Yoshihiro Kubozono *Editor*

Physics and Chemistry of Carbon-Based Materials

Basics and Applications

Physics and Chemistry of Carbon-Based Materials

Yoshihiro Kubozono
Editor

Physics and Chemistry of Carbon-Based Materials

Basics and Applications

Editor
Yoshihiro Kubozono
Research Institute for Interdisciplinary
Science
Okayama University
Okayama, Japan

ISBN 978-981-13-3416-0 ISBN 978-981-13-3417-7 (eBook)
https://doi.org/10.1007/978-981-13-3417-7

Library of Congress Control Number: 2019930441

© Springer Nature Singapore Pte Ltd. 2019
This work is subject to copyright. All rights are reserved by the Publisher, whether the whole or part of the material is concerned, specifically the rights of translation, reprinting, reuse of illustrations, recitation, broadcasting, reproduction on microfilms or in any other physical way, and transmission or information storage and retrieval, electronic adaptation, computer software, or by similar or dissimilar methodology now known or hereafter developed.
The use of general descriptive names, registered names, trademarks, service marks, etc. in this publication does not imply, even in the absence of a specific statement, that such names are exempt from the relevant protective laws and regulations and therefore free for general use.
The publisher, the authors and the editors are safe to assume that the advice and information in this book are believed to be true and accurate at the date of publication. Neither the publisher nor the authors or the editors give a warranty, express or implied, with respect to the material contained herein or for any errors or omissions that may have been made. The publisher remains neutral with regard to jurisdictional claims in published maps and institutional affiliations.

This Springer imprint is published by the registered company Springer Nature Singapore Pte Ltd.
The registered company address is: 152 Beach Road, #21-01/04 Gateway East, Singapore 189721, Singapore

Preface

Carbon being one of the most fundamental elements in nature, carbon-based materials have attracted a great deal of attention during the past century. All organisms on Earth consist of carbon-based structures, and many materials important to human society are based on carbon. Carbon is the Group 14 element that has four valence electrons and forms different types of chemical bonds (covalent bonds) using several hybridizations (sp, sp^2, and sp^3). Chemists are quite familiar with this flexibility, as it allows the formation of a wide variety of very interesting materials. The chemistry of electrically conductive carbon is currently one of the most important research areas in science. Many researchers and engineers are working on the design and synthesis of new carbon-based materials that will play important roles in human society as electronic polymers, plastics, medicines, and fuel, with the range of potential applications constantly increasing.

However, physicists have not been as familiar with carbon and carbon-based materials as chemists. The research targets of solid-state physics emphasized solids other than carbon until late in the twentieth century, when epochal discoveries drastically changed the trend of solid-state physics. The discovery of superconductivity in metal-intercalated graphite and fullerene attracted the interest of many physicists, who established a research community. Interestingly, superconductivity was also discovered in carbides. Subsequently, the discovery of carbon nanotubes expanded the scope of research, not only in solid-state physics but also extending into mesoscopic physics. A decisive push toward the next step was the discovery of exciting physics in graphene, the name given to one layer of the stack of planar layers of carbon atoms that form graphite. The discovery that electrons governed by relativistic quantum physics play an important role in graphene's properties drew the attention of a large number of physicists at the beginning of the twenty-first century. Currently, this intensified scrutiny is expanding to topological materials. Thus, without exaggeration, carbon occupies a central position in solid-state physics and mesoscopic physics.

Carbon's importance currently extends beyond abstract science into the technology of electronics. Organic materials tested successfully for usability in transistor applications include polycyclic hydrocarbons like pentacene, fullerene, carbon

nanotubes, diamond, and graphene, and this has stimulated the development of all-carbon transistors that may someday support most of society's electronics. The desire to replace the traditional inorganic materials in electronics with new carbon-based substitutes has gradually diffused to the communities of chemists, physicists, and applied physicists, although it cannot be said that the trend has become dominant in mainstream electronic engineering. Currently, the likeliest future for carbon-based electronics may be their complementary use in electronics together with conventional inorganic materials, i.e., maximizing the advantages of each, such as ease of design, printable fabrication, flexibility, wearability, and wide applicability. The similar future is considered for the use of carbon-based materials in solar cells.

This book includes both the fundamental science and many applications of carbon-based materials. The fundamental theory relevant to these materials, their synthesis and characterization, their physical properties (physics), and their applications are fully described, which will contribute to the advancement of not only basic science in this research field but also of the technology based on these materials. The book's targets are researchers and engineers in the field and graduate students who specialize in physics, chemistry, and materials science. Thus, this book addresses the physics and chemistry of the most interesting materials in the twenty-first century.

Okayama, Japan Yoshihiro Kubozono
August 2018

Contents

1 Graphite and Intercalated Compound Superconductors: Atomic and Electronic Structures 1
Ritsuko Eguchi and Fumihiko Matsui

2 Physics of Graphene: Basic to FET Application 29
Hidenori Goto

3 Physics of Heavily Doped Diamond: Electronic States and Superconductivity 65
Takanori Wakita, Kensei Terashima, and Takayoshi Yokoya

4 Physics of Carbon Nanotubes and New Type of Carbon Network Materials: Electronic and Magnetic Properties 97
Susumu Okada and Mina Maruyama

5 Electronic and Geometric Structures of Cluster Encapsulated Fullerenes 121
Takafumi Miyazaki and Shojun Hino

6 Superconductivity of Carbides 149
Kaya Kobayashi, Kazumasa Horigane, Rie Horie, and Jun Akimitsu

7 Organic Chemistry of π-Conjugated Polycyclic Aromatic Hydrocarbons: Acenes and Phenacenes 211
Hideki Okamoto

8 Transistor Application and Intercalation Chemistry of π-Conjugated Hydrocarbon Molecules 229
Yoshihiro Kubozono, Shino Hamao, Takahiro Mikami, Yuma Shimo, Yasuhiko Hayashi, and Hideki Okamoto

9 Nanostructure Control of Crystalline Organic Thin Films by Solution Processes 253
Hiroko Yamada

10 Solar Cell Applications of π-Conjugated Molecules 293
Kouki Akaike and Kaname Kanai

Chapter 1
Graphite and Intercalated Compound Superconductors: Atomic and Electronic Structures

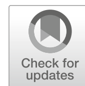

Ritsuko Eguchi and Fumihiko Matsui

Abstract Graphite is a carbon allotrope with a unique anisotropy. The in-plane bonds of carbon have a strong covalent bonding characteristic, while out-of-plane bonding of carbon is due to the weak van der Waals interaction. Graphite can be easily exfoliated, i.e., a sheet of graphite called graphene can be easily separated. By intercalating metallic atoms, the property of graphite can be drastically altered. For example, CaC_6 is known as a graphite intercalation compound (GIC) superconductor having transition temperature of 11.5 K at ambient pressure. In the first half of this chapter, the brief history of GIC discovery as a superconducting material is outlined, and then the current understanding of GIC superconducting mechanism is described. In the second half of this chapter, the experimental verification of the atomic and electronic structures of the pristine graphite and GIC using photoelectron spectroscopy and diffraction is introduced. Finally, this chapter is summarized and expanded into future prospects.

Keywords Graphite · Intercalation · Photoelectron spectroscopy · Photoelectron diffraction

1.1 Introduction

Graphite is a carbon allotrope with a unique anisotropy. The in-plane bonds of carbon have a strong covalent bonding characteristic, namely, σ bonds due to sp^2 hybridization. A layer of honeycomb network structure is formed by sharing three

R. Eguchi (✉)
Okayama University, Okayama, Japan
e-mail: eguchi-r@okayama-u.ac.jp

F. Matsui
Institute for Molecular Science, Okazaki, Japan

Nara Institute of Science and Technology, Ikoma, Japan
e-mail: matui@ims.ac.jp

© Springer Nature Singapore Pte Ltd. 2019

Y. Kubozono (ed.), *Physics and Chemistry of Carbon-Based Materials*,
https://doi.org/10.1007/978-981-13-3417-7_1

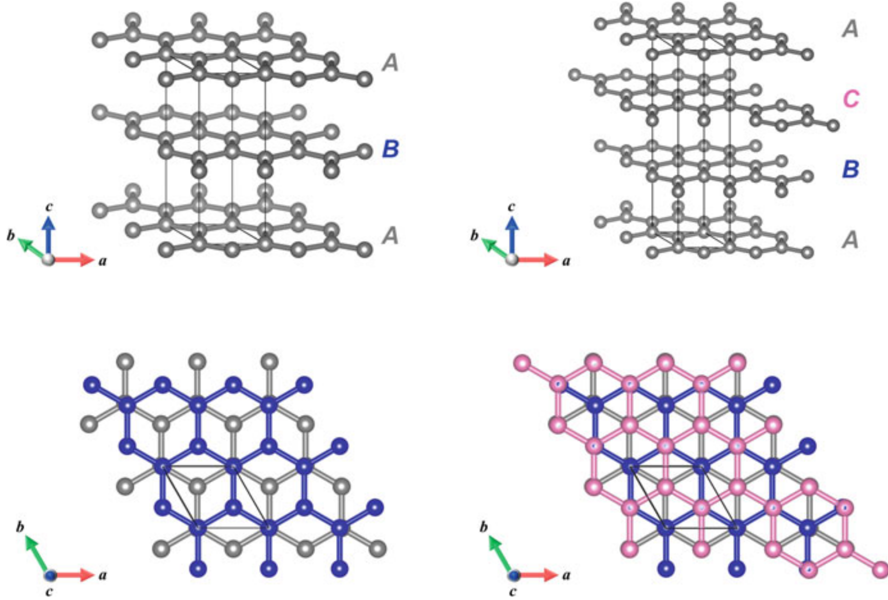

Fig. 1.1 Crystal structures of graphite stacked in *ABABAB* (left column) and *ABCABC* (right column) sequences. Hexagonal cell is shown in both crystal structures

sp^2 electrons of three adjacent carbons. The in-plane CC bond length is 1.421 Å. Moreover, the out-of-plane bonding of carbon is the result of the weak van der Waals interaction caused by delocalized π orbitals. The interplanar spacing of the carbon layer is about 3.35 Å. Graphite can be easily exfoliated, i.e., a sheet of graphite called graphene can be easily separated. The physical properties of graphene are explained in detail in Chap. 2. The carbon layer in graphite is stacked in two different forms, which are *AB* sequence (*ABABAB* ...) and *ABC* sequence (*ABCABC* ...), as shown in Fig. 1.1. The former is called α-graphite having a hexagonal structure, and the latter is called β-graphite having a rhombohedral structure. The hexagonal α-graphite is more stable than the rhombohedral β-graphite. In the case of α-graphite, there are tri-coordinated and penta-coordinated carbon atoms; however, in the case of β-graphite, only the tetra-coordinated carbon exists. A β-graphite can be converted to diamond without repositioning its bonds. The physical properties of diamond are described in detail in Chap. 3.

Graphite intercalation compounds (GIC) are old and new superconducting materials. Currently, the maximum transition temperature (T_c) value of a GIC superconductor (CaC_6) at ambient pressure is 11.5 K [1, 2]. Members of the GIC superconducting family have not changed for many years, except the T_c of BaC_6, which was confirmed as 65 mK in 2015 [3]. Recently, a new series of bimetal-intercalated graphite superconductor, $Ca_xK_{1-x}C_y$, was successfully synthesized [4]. When K and Ca atoms are intercalated, graphite flakes turn into golden superconducting compounds (Fig. 1.2). This chapter focuses on the superconductivity

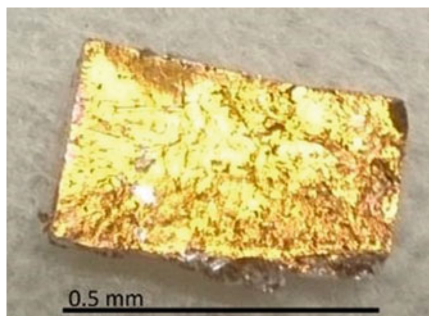

Fig. 1.2 Photograph of Ca- and K-intercalated graphite flake sample

of the GICs. In the first half of this chapter, the brief history of GIC discovery as a superconducting material is outlined, and then the current understanding of the GIC superconducting mechanism is described. In the second half of this chapter, the experimental verification of the atomic and electronic structures of the pristine graphite and GIC using photoelectron spectroscopy and diffraction is introduced. Finally, this chapter is summarized and expanded into future prospects.

1.2 Graphite Intercalation Compounds (GICs)

Over the years, GICs have attracted a considerable amount of attention from chemists and physicists due to their exciting electronic properties. In GICs, atoms and molecules are inserted into the space between the honeycomb carbon layers as intercalants. Intercalation provides a variation of many physical properties in graphite. Intercalated metals and molecules exist as intercalants of electron donor or acceptor type. This means that intercalation with different chemical species and concentrations may change the free carrier concentration in a graphite. As a result, GIC exhibits various electronic, thermal, and magnetic characteristics.

The synthesis of the first GIC, graphite sulfate, was reported by Schaffaütl in 1841 [5]. The systematic study of GICs began in the early 1930s, and "stage" was determined using X-ray diffraction techniques. Subsequently, its physical properties were systematically studied in the early 1940s. Since the discovery of GICs, comprehensive reviews of GICs have been reported: by Rüdorff in 1959 [6], Ebert in 1976 [7], H. Selig and L. B. Eber in 1980 [8], Ebert and Scanlon in 1980 [9], and Forsman et al. in 1983 [10]. A representative review of GICs was reported by M.S. Dresselhaus and G. Dresselhaus in 2002 [11]. GICs have been used as an anode material in batteries represented by the lithium-ion battery. Furthermore, superconductivity was observed in metal-intercalated graphite. In this chapter, based on the literature reported so far, we focused on the superconductivity of metal-intercalated graphite and its physical and chemical properties.

GICs possess a characteristic structure, in which atoms and molecules are inserted in the space between carbon layers. Another way of looking at the structure is to focus on the fact that one or several consecutive carbon layers are present

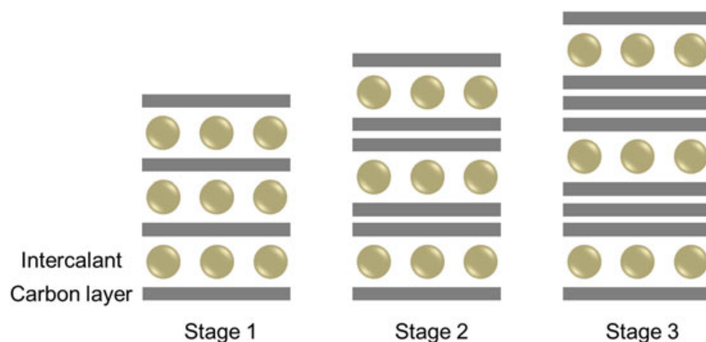

Fig. 1.3 Schematic represent of the different stages in GICs

between the intercalated atom layers. Depending on the number of consecutive carbon layers located in between the intercalated atom layers, the structural name of a GIC is defined. For example, the first stage (or stage 1) for one carbon layer, the second stage (or stage 2) for two carbon layers, and the third stage (or stage 3) for three carbon layers, and so on. Figure 1.3 shows a schematic diagram of the different stages in GICs.

As mentioned above, intercalated metals and molecules act as electron donor- or acceptor-type intercalants. Intercalants of the electron donor type are alkali and alkaline earth metals and rare earth metals (such as Li, Na, K, Cs, Ca, Sr, Ba, Sm, Eu, Yb, and Tm). Intercalants of the electron acceptor type are halogens, acids, and metal halides (such as Br_2, ICl, IBr, $AlCl_3$, $FeCl_3$, $CuCl_2$, $SbCl_5$, $MoCl_5$, AsF_5, SbF_5, HNO_3, H_2SO_4, H_3PO_4, and HF) [11]. In addition to these representative binary and ternary (binary-element-intercalated) GICs, more complex materials are also reported. For a donor intercalant, liquid ammonia is used as a solvent for the intercalation of metals, such as Li, Na, K, Rb, Cs, Co, Sr, and Ba, to form a stoichiometric compound $C_{12}M(NH_3)_2$ (M = metals).

Various synthetic methods have been developed for the preparation of GICs, such as two-zone vapor transport technique (Fig. 1.4a), liquid intercalation method, and electrochemical method. To prepare a target material, various parameters, such as temperature, vapor pressure, gas, and reaction time, must be accurately controlled in each method. For metal-intercalated graphite exhibiting superconductivity, pioneers used vapor transport technique for synthesizing GICs. However, intercalation of alkaline earth metals into graphite has proven to be much more difficult than that of any alkali metals. For CaC_6, vapor Ca reacts only on the surface region of graphite, and intercalation into graphite crystals is insufficient. This reduces the quality of the sample and does not show a sharp drop in magnetization at T_c and diamagnetic saturation. To overcome this problem, a new reaction method for graphite and metals has been developed. This reaction is carried out between pyrolytic graphite platelets and molten lithium-calcium alloy at about 350 °C, under pure argon atmosphere (Fig. 1.4b) [1]. The reaction time can be between few days to 10 days. Despite

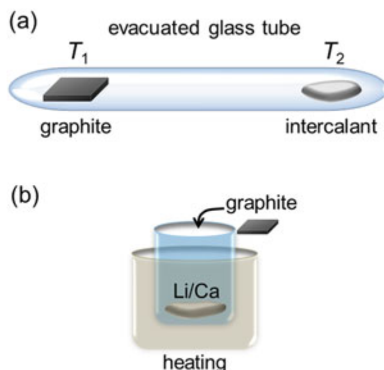

Fig. 1.4 (**a**) Two-zone vapor transport technique and (**b**) reaction technique using metal alloy

the lower Ca concentration compared to the Li content, Li is not present in the final reaction product, and Ca is homogeneously intercalated in the bulk graphite. The quality of the sample was improved using this method, showing a sharp drop in magnetization and a crystal structure of CaC_6. Using this method with Ca/K/Li alloy, the synthesis of ternary GIC, $Ca_xK_{1-x}C_y$, became possible.

1.3 Superconductivity in GICs

In 1965, superconductivity of $T_c = 0.14$ K was observed in KC_8, the interlayer K-intercalated graphite [12, 13], which is a stage 1 compound. This was the first observation of superconductivity in GICs. Note that, no superconductivity was observed in KC_{24} (stage 2), KC_{36} (stage 3), and KC_{48} (stage 4), suggesting that the alternating arrangement of metal and graphene layers (stage 1 structure) is important for superconductivity to occur in GICs. The K-intercalated graphite was prepared by heating highly purified K metal with highly oriented pyrolytic graphite (HOPG) in an evacuated tube. It was possible to obtain a gold compound as KC_8. The magnetic susceptibility of KC_8 under a magnetic field H//*c* exhibited type I characteristic, while that under H⊥*c* exhibited type II characteristic [13], where *c* represents the perpendicular direction with respect to the carbon plane, as shown in Fig. 1.1. A KC_8 compound produced with stoichiometric amounts of the elements ($T_c = 0.39$ K) showed a higher anisotropy in the H_{c2} values, 25 Oe for a magnetic field H⊥*c* and 250 Oe for H//*c* [12]. A large variation in H_{c2} (H_c), as a function of magnetic field directions, was observed as a result of the anisotropy of mean free path, reflecting the two-dimensional (2D) crystal structure. Thus, the mean free path and the electrical conductivity in the carbon plane are much higher than those along the *c* axis. This anisotropy behavior was observed in other metal-intercalated graphite superconductors, such as CaC_6, YbC_6, and SrC_6, which is described later.

Subsequently, the Rb- and Cs-intercalated graphite, RbC_8 and CsC_8, were also discovered using an annealing synthesis method in the same manner as KC_8;

however, these GICs exhibited quite low T_c (less than 1 K) [12, 14, 15] like KC_8 [12, 13]. Furthermore, the high-pressure syntheses were successfully achieved in other metal intercalations, which increased the T_c up to 1.9 K at 33 kbar (=0.33 GPa) for LiC_2 [16], 5 K for NaC_2 [17], and 1.5–5.5 K for KC_3, KC_4, and KC_6 [17, 18]. These results imply that there are metastable phases, such as MC_2 or MC_3, that are different from MC_8 (M: metal atom).

Moreover, ternary GICs, such as $KHgC_8$ (1.9 K) [19], $RbHgC_8$ (1.44 K) [19], $KTl_{1.5}C_4$ (2.7 K) [20], and $CsBi_{0.55}C_4$ (4.05 K) [21], were also synthesized. In these GICs, not only an electron transfer from intercalants to graphite but also a change in spacing between the graphite layers may affect superconductivity significantly. The spacing between graphite layers strongly depends on the T_c, which is described later. Thus, superconductivity of GICs was a significant research subject up to the late 1980s–early 1990s. However, in 1991, the discovery of metal-intercalated C_{60} fullerene compounds with higher T_c (=18 K) [22] drastically changed this situation and research on fullerene intercalated compounds attracted attention of many researchers.

In 2005, the discovery of superconductivity in CaC_6 ($T_c = 11.5$ K [1]) and YbC_6 ($T_c = 6.5$ K [2]) made a major breakthrough in the GIC research. CaC_6 provided the highest T_c (=11.5 K) among the GICs discovered so far. The T_c further increased under high pressure ($T_c = 15.1$ K at 7.5 GPa) [23]. The increase in T_c originated from a pressure-induced phonon softening related to an in-plane Ca phonon mode. Unfortunately, above 8 GPa, T_c suddenly decreased to 5 K, suggesting the occurrence of phase transition (probably a structural phase transition). After the discovery of superconductivity in CaC_6 and YbC_6, the other alkaline earth metal (or alkaline earth plus alkali metal)-intercalated graphite, SrC_6 ($T_c = 1.65$ K) [24] and $Li_3Ca_2C_6$ ($T_c = 11.15$ K) [25], were also reported. Recently, a new GIC superconductor, BaC_6 ($T_c = 0.065$ K), was discovered [3], and the binary-element-intercalated graphite compounds, $Ca_xK_{1-x}C_y$ ($T_c \leq 11.5$ K), were synthesized [4]. Thus, the family of superconducting GICs has been well established; however, the no superconductors with T_c greater than 11.5 K have been reported yet.

The characteristic behaviors and parameters of GIC superconductors are exhibited in various experiments. The magnetization as a function of magnetic field, $M(H)$, of CaC_6 indicated clear critical points, H_{c1} and H_{c2}, which means that CaC_6 is a type II superconductor. H_{c2} was about 2500 Oe at 2 K with the magnetic field oriented along the c axis ($H_{c2}(\parallel c)$), while that measured with the magnetic field in the ab plane was about 7000 Oe ($H_{c2}(\perp c)$) [1]. Such anisotropy of the critical field was observed in YbC_6 and SrC_6, where $H_{c2}(\perp c)/H_{c2}(\parallel c)$ (the anisotropy parameter) is approximately 2 [2, 24]. This anisotropy depends on the ratio of the electron masses along the two directions, $\parallel$c and $\perp$c, which was followed by the Ginzburg-Landau theory. The value of the anisotropy parameter (2) was smaller than that for a pure graphite (7). This difference indicates that the band structure and Fermi surface are more three-dimensional (3D) in GIC superconductors as compared to those in pure graphite [2].

The crystal structure of KC_8 and RbC_8 shows the AαAβAγAδA stacking along the c axis, which corresponds to the face-centered orthorhombic structure (space

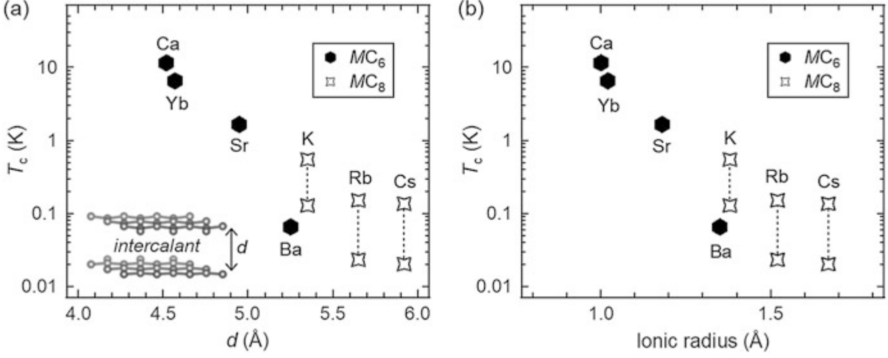

Fig. 1.5 Plots of T_c as a function of (**a**) d and (**b**) ionic radius in MC_6 (M: Ca [1, 2], Yb [2], Sr [24], and Ba [3]) and MC_8 (M: K [12, 13], Rb [12, 15], and Cs [12])

group: *Fddd)*. Here, "A" refers to the honeycomb carbon layer, and "α," "β," "γ," and "δ" refer to the metal layers (or different location) [14]. Moreover, the crystal structure of CaC_6 refers to the AαAβAγA stacking (rhombohedral structure, space group; $R\overline{3}$m) [1]. The structures of YbC_6 [2], SrC_6 [26], and BaC_6 [3] correspond to the AαAβA stacking (hexagonal structure, space group: $P6_3/mmc$). The spacing, d, between the carbon layers increases depending on the size of intercalant atoms; the value of d is 4.52 Å for CaC_6 [1], 4.57 Å for YbC_6 [2], 4.95 Å for SrC_6 [24], 5.25 Å for BaC_6 [3], and 5.35 Å for KC_8 [11]. The value of T_c of GIC superconductors strongly depends on the value of d, indicating that the smaller d realizes GIC superconductors with higher T_c. Moreover, CaC_6 has the smallest value of d as compared to the other GICs, BaC_6 [3] and MC_8 (M: K, Rb, and Cs) [12–15], which have values of T_c less than 1 K; exceptionally T_c for YbC_6 is higher than 1 K [2]. The summary of T_c as a function of d is shown in Fig. 1.5a.

The highest T_c (=15.1 K) of Ca was realized at 7.5 GPa due to the further shrinkage of d [3, 24]. This is probably because the electron-phonon coupling sensitively changes against both in-plane intercalant and out-of-plane C phonon modes, resulting in the change of T_c [24], i.e., the small size of an intercalant decreases the d to produce high-T_c GIC. This relationship between T_c and ionic radius of the intercalants is also shown in Fig. 1.5b. The ionic radii are referred to M^{2+} ions for MC_6 and M^{1+} ions for MC_8. The application of pressure to GIC can decrease the d value directly to realize a high-T_c GIC. As mentioned previously, the highest T_c of CaC_6 was achieved under the pressure of 7.5 GPa [23]. The T_c values varied with dT_c/dP ~0.50 K GPa^{-1} in the pressure range of 0–1.2 GPa [27]. The KC_8 and SrC_6 compounds showed T_c of 1.7 K at 1.5 GPa [28] and 2 K at 1 GPa [24], respectively. The T_c value of SrC_6 increased with dT_c/dP ~0.35 K GPa^{-1} [24]. In YbC_6, T_c also increased with the applying pressure and reached the value of 7.1 K at 1.8 GPa with dT_c/dP ~0.37 K GPa^{-1} [27]. Thus, all GIC superconductors showed pressure dependence similar to that of CaC_6.

New superconducting $Ca_xK_{1-x}C_y$ compounds were successfully synthesized in 2016 [4]. These compounds were synthesized by immersing HOPG or Kish graphite in melted Li/K/Ca alloy (Fig. 1.4b). The T_c value of $Ca_xK_{1-x}C_y$ continuously increased with the increasing x, indicating the binary-element intercalation of Ca and K in graphite. Interestingly, the structure of $Ca_xK_{1-x}C_y$ ($0 \leq x \leq 0.6$) is the same as that of KC_8, i.e., face-centered orthorhombic structure (space group: *Fddd*). Therefore, $Ca_xK_{1-x}C_y$ was represented as "$Ca_xK_{1-x}C_8$" [4]. The d value of $Ca_xK_{1-x}C_8$ ($0 \leq x < 1$) was independent of x, which is nearly equal to one fourth of the lattice constant c (21.4 Å); $d = 5.35$ Å, which is enlarged as compared to that of CaC_6 (4.50 Å). The x independence of d ($x < 1$) suggested that the structure of $Ca_xK_{1-x}C_8$ was dominated by the K atom because of the larger ionic radius of K^+ (1.38 Å) than that of Ca^{2+} (1.00 Å).

The pressure dependence of resistance in $Ca_xK_{1-x}C_8$ ($x = 0.6$) was measured in a pressure range from 2.0 to 43 GPa [4]. A T_c value of 10.5 K was observed at 2.0 GPa. With more pressure, T_c increased and reached a maximum T_c value of 11.6 K at 3.3 GPa and then rapidly decreased to 4 K at 15 GPa. Thereafter, T_c slowly decreased, and no superconducting transition down to 1.9 K was observed at 43 GPa. This behavior is qualitatively similar to that observed for CaC_6. The successful synthesis of superconducting binary-element-intercalated graphite may open a path for finding new graphite superconductors through a combination of various metals. Furthermore, details of the electronic and atomic structures for $Ca_xK_{1-x}C_y$ were elucidated by the photoelectron holography (PEH) technique, as discussed in Sect. 1.5 later. The 3D atomic arrangement around the intercalant atom was visualized, which provides a deeper understanding of the mechanism of superconductivity.

1.4 Superconducting Mechanism of GIC Superconductors

The physical properties of CaC_6 have been extensively studied to elucidate the superconducting mechanism because the highest T_c value of GICs was reported in CaC_6 under ambient and high pressure. The intercalants of alkali and alkaline earth metals provide electrons to the graphene layers in GICs, resulting in partially filled graphene π bands. In addition, the interlayer band, which is delocalized over the interstitial space of carbon layers, forms the free-electron-like Fermi surface. This interlayer band is hybridized with the π^* bands. This aspect is different from that of the simple electron doping of the π^* bands. The results of soft X-ray photoelectron spectroscopy suggested that not only the C 2p states but also the Ca 3d-derived states are located at the Fermi level [29]. The theoretical study suggested that the presence of the interlayer band was essential for stabilizing the superconductivity in GICs [30]. The interlayer band originated from the s band of the intercalant Ca. Thus, the interlayer band plays an important role for the superconductivity of GICs. The electron-phonon coupling, λ, due to the out-of-plane C phonon and in-plane Ca phonon was large enough to explain the relatively high T_c of GICs [31]. To experimentally elucidate the contribution of the Ca phonon to superconductivity,

the Ca isotope effect coefficient was reported in 2007 [32]. Based on the BCS theory [33], the isotopic effect shows that T_c depends on the mass of the nuclei, because a change in mass affects the lattice vibrations, which play an important role in the formation of the electron pairing in superconducting states. This means that it can indicate the phonon modes that are directly involved in the mechanism of superconductivity. The temperature-dependent magnetic susceptibility of CaC_6 synthesized using ^{40}Ca and ^{44}Ca clearly showed the shift in T_c, where a lower T_c was observed in ^{44}Ca intercalated graphite as compared to that of ^{40}Ca intercalated graphite. This result indicates that superconductivity is dominated by coupling of the electrons by the Ca phonon modes.

The superconducting mechanism of GICs is deeply debated based on the experimental and theoretical studies on superconducting CaC_6. The result of the in-plane magnetic penetration depth suggested isotropic *s*-wave pairing, and the value of $2\Delta(0)/k_B T_c$ (=3.6 ± 0.2) indicated a weakly coupled superconductor [34], where $2\Delta(0)$ and k_B are the superconducting gap and Boltzmann constant, respectively. Note that the BCS theory predicted the universal value of $2\Delta(0)/k_B T_c$, that is, 3.528. The specific heat measurements showed the anomaly characteristics of superconducting transition just at T_c, which indicates bulk superconductivity [35]. The temperature and magnetic dependence of electronic-specific heat provided a fully gapped superconducting parameter, namely, an isotropic *s*-wave BCS gap. The λ value of 0.70 ± 0.04 suggested that the high T_c of CaC_6 was explained by the intermediate coupling of the BCS scenario [35]. Scanning tunneling spectroscopy (STS) provided a clear superconducting gap in the quasiparticle density of states. An isotropic gap of $\Delta(0)$ was evaluated to be 1.6 ± 0.2 meV by fitting with the gap function of a conventional BCS theory, and $2\Delta(0)/k_B T_c = 3.66$ was slightly higher than the value expected in the weak coupling limit [36]. Furthermore, the presence of gap anisotropy was discussed, based on theoretical [37] and experimental [38] studies.

1.5 Atomic Structure of Graphite and GIC

1.5.1 Principle of Photoelectron Diffraction and New Holography Algorithm

To elucidate the mechanism of superconductivity, it is essential to directly visualize the 3D atomic arrangement around the intercalant atom. There are various types of approaches to atomic level structural analysis, such as X-ray diffraction, scanning transmission electron microscopy, and scanning probe microscopy. In this section, the PEH technique is described. When an atom is excited with X-ray, a photoelectron is emitted. Photoelectrons from localized core levels are excellent element-specific probes for atomic structure analysis. Due to the shallow probing depth of photoelectrons, PEH is a powerful method to study the local surface

and subsurface atomic structures in 3D. Information on the photoelectron-emitting atoms and the atomic arrangement around them is recorded as a photoelectron hologram in the photoelectron intensity angular distribution (PIAD). Forward focusing peaks (FFPs) at local interatomic directions [39–41] and diffraction rings around them appearing in the photoelectron hologram show the 3D atomic positions of the surrounding atoms with respect to the photoelectron-emitting atoms. A conventional reconstruction algorithm for PEH was based on the Fourier transform of the photoelectron hologram. However, the reconstructed image was greatly distorted by the effect of FFP without phase information. Recently, the scattering-pattern-extraction algorithm with maximum entropy method (SPEA-MEM), which is a new holographic algorithm for atomic arrangement reconstruction, was developed [42]. 3D images of atomic arrangements around the photoelectron-emitting atoms can be obtained directly from element-specific photoelectron holograms.

The photoelectron wave function in the case of a simple s-wave with kinetic energy E_{k} is expressed as an outgoing wave: $\Psi_0 = \exp(ikr)/r$. Wave number $k = \sqrt{2m_{\mathrm{e}}E_{\mathrm{k}}}/\hbar$ is the length of the wave vector $\mathbf{k}$. r is the distance from the excited atom. m_{e} is the mass of the electron. The photoelectron wave function Ψ_0 emitted from the atom is partially scattered by the surrounding N atoms, resulting in a scattered wave $\Psi^{\mathrm{s}} = \sum_{i=1}^{N} \psi_i^{\mathrm{s}}$. Consequently, interference occurs between the direct and scattered waves. We observe it as PIAD $I(\theta, \phi) = |\Psi_0 + \Psi^{\mathrm{s}}|^2$.

Strictly speaking, the kinetic energy of the photoelectron $E_{\mathrm{k}}^{\mathrm{cryst}}$ should be defined from the inner potential of the crystal, E_0. The difference between $E_{\mathrm{k}}^{\mathrm{cryst}}$ and E_{k} is $V_0 = E_0 + W$. The work function of the surface is represented by W. For graphite, V_0 is 17.17 eV. This value is obtained from the measurement value of the k_{z} band dispersion of the valence band, which is described later [43].

For example, a photoelectron scattering process with a 13-atom graphene cluster is simulated. Figure 1.6a shows the real part of the photoelectron wave function. The amplitude was rescaled by multiplying the distance r from the excited atom indicated by the central white circle. The kinetic energy of photoelectrons E_{k} was 500 eV. Figure 1.6b shows the variation in photoelectron intensity in real space $\chi(\mathbf{r}) = \left(I - {\Psi_0}^2\right)/{\Psi_0}^2$. The intensity of the photoelectron "tail" is formed at the position of the scatterer atom just like that in a comet. A photoelectron hologram $\chi(\theta, \phi)$ is an angular distribution measured by a detector located far from the sample. This photoelectron intensity tail is detected as FFP. Furthermore, if the phase difference between ψ_i^{s} and Ψ_0 is $2\pi n$ (n: integer number), the two waves constructively interfere and form diffraction rings around the FFP. Figure 1.6c shows the relationship between the atomic arrangement in real space and the hemispherical photoelectron hologram. The intensity of photoelectrons increases in the direction in which the diffraction rings overlap.

The measured C1s PIADs from graphite are shown in Fig. 1.7 [44]. A 2 mm diameter graphite single crystal was cleaved in air and mounted on a sample holder. The normal direction of the surface was aligned along the photon incident axis. The kinetic energies were (a) 500 eV and (b) 800 eV. Note that the diffraction ring arcs

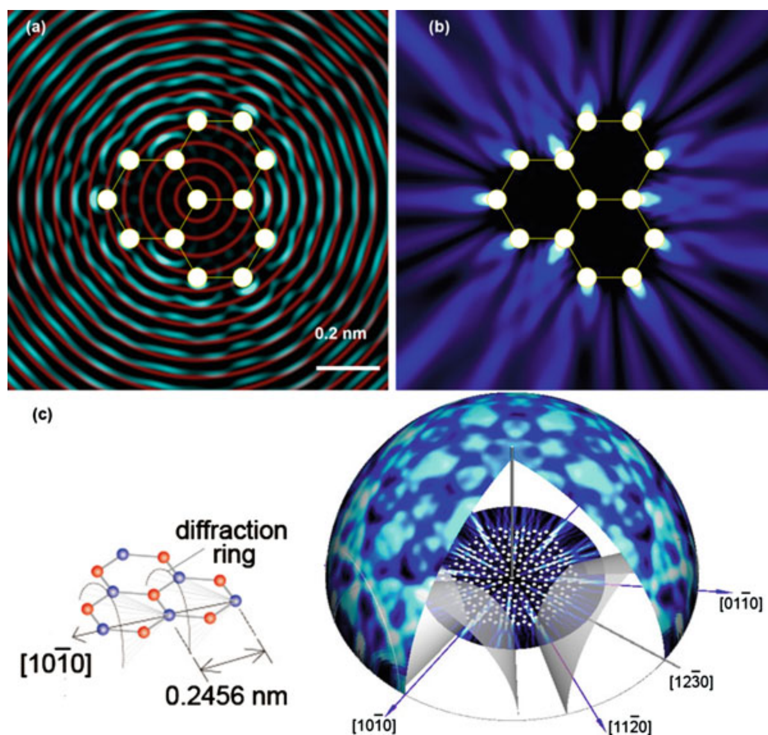

Fig. 1.6 (**a**) Real part of the photoelectron wave function from the central carbon atom in a C_{13} cluster, (**b**) photoelectron intensity in the real space $\chi(\mathbf{r})$, and (**c**) simulated photoelectron hologram $\chi(\theta, \phi)$ from a C_{253} graphene cluster

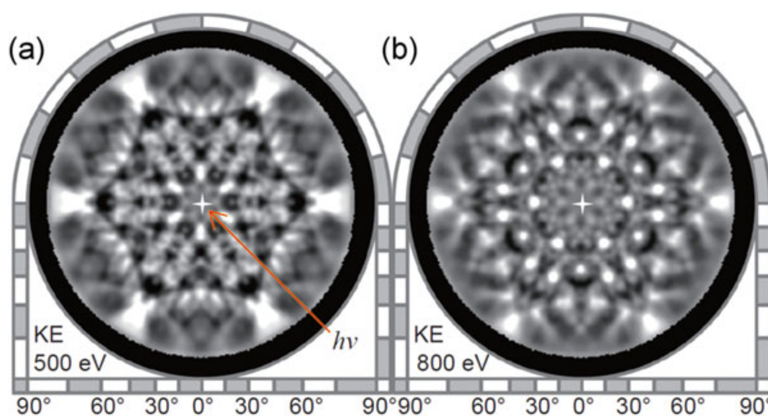

Fig. 1.7 C1s photoelectron holograms from graphite. Kinetic energy was (**a**) 500 eV and (**b**) 800 eV [44]. (Copyright 2012 The Physical Society of Japan)

of the two PIADs have different radii corresponding to the different wave numbers of the photoelectrons.

The PEH reconstruction algorithm, SPEA-MEM, uses a fitting-based approach of diffraction rings and FFP with simulated data under maximum entropy method scheme [42]. In this case, the fitting of diffraction intensity oscillations as a function of the polar angle from the scatterer atom direction of the various CC atomic distances was applied to the entire set of the measurement data. As shown in Fig. 1.8, the real space images of several graphite layers above the photoelectron-emitting atom as well as the layers containing emitting atom were clearly reproduced [44]. The in-plane lattice vector and interlayer spacing of graphite were determined with an accuracy of 1% (Fig. 1.8a) and 3% (Fig. 1.8d), respectively. The atomic structure of graphite is shown in Fig. 1.9a. There are four types of atomic sites in the unit cell; thus, atomic images seen from each atomic site are superimposed. Note that some of the reconstructed spots are stronger. For the emitting atom layer image shown in Fig. 1.8a, the second nearest atomic image from the center emitting atom position appears brighter than the first nearest atomic image. This is because the atomic images from the two different sites overlap at the same position, as shown in Fig. 1.9b. Contrarily, for the atomic image of the upper layer shown in Fig. 1.8b, the first nearest atomic image appears more intense. The schematic diagram of Fig. 1.9c–i illustrates how different stacking structures result in modulation of reconstructed atomic image intensity. As shown in Fig. 1.9c–e, there are various types of graphene stacking structures. The "*B*" layer can be stacked on an "*A*" layer with a translational shift equal to the CC bond length in the CC bond direction shown in Fig. 1.9d, or the "*B*" layer can be stacked with a translational shift in the opposite direction, as shown in Fig. 1.9e. The stacked structure can be determined from the modulation of the atomic image contrast, as shown in Fig. 1.4f–i. For the layers stacked in the *AA* and *AB* sequences, the bright spots form triangular (Fig. 1.9f) and hexagonal (Fig. 1.9i) lattices, respectively.

The contrast modulation of the graphene lattice in one layer above (Fig. 1.8b) strongly indicates that the two adjacent layers are stacked in the *AB* sequence. In contrast, the contrast modulation of the graphene lattice in two layers above (Fig. 1.8c) indicates that the graphene layer is stacked in the same way as the emitting atom layer. Therefore, the reconstructed 3D atomic image shows that this graphite crystal has an *ABAB* (Bernal) stacking structure. Further, contrast modulation can be used to determine the in-plane and stacking structure of few-layered graphene [45] and GICs [46].

1.5.2 Atomic Arrangement Imaging of GIC Cleaved Surface

This PEH method was applied for the structural analysis of (Ca,K)C_8, superconductor ($T_c = 9.9$ K). The photoelectron spectra of the cleaved surface of (Ca, K)C_8 showed only the C 1*s* and K 2*p* peaks. The Ca 2*p* peak intensity was less than a few hundredths of the intensity of the K 2*p* peak. The observation of the K dominant

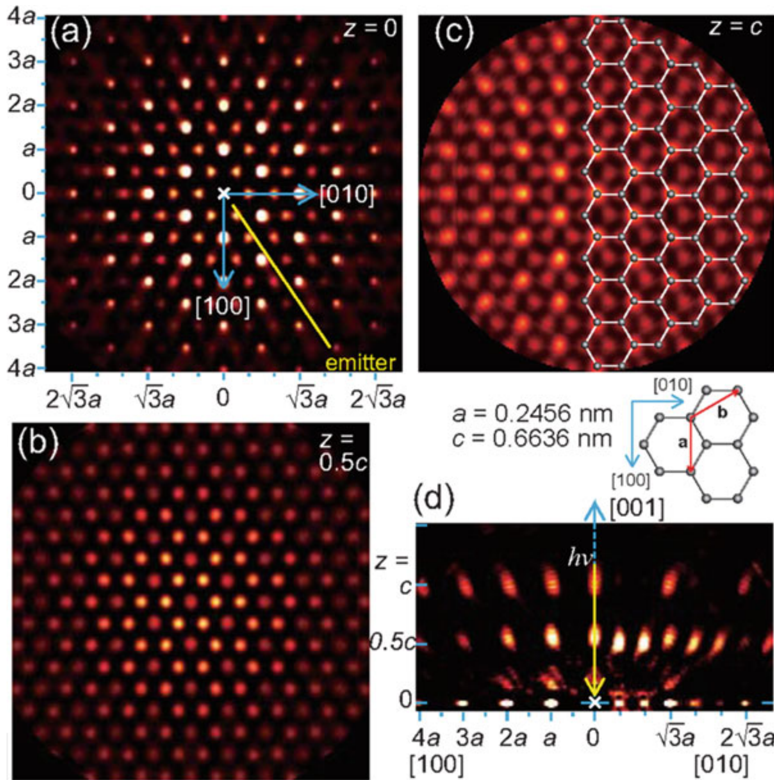

Fig. 1.8 Reconstructed atomic arrangement image of graphite from C1*s* PD patterns [44]. The (**a**) graphite layer including the emitter atom, and the (**b**) first and (**c**) second layers above the emitter atom are shown. (**d**) Vertical cross sections of the real space images for the *xz* (left) and *yz* (right) planes. (Copyright 2012 The Physical Society of Japan)

structure on the cleaved surface means that the Ca atoms are dispersed in bulk and are likely to form high-T_c domains. Figure 1.10a, b shows the full hemisphere C 1*s* and K 2*p* photoelectron holograms with a kinetic energy of 600 eV [46]. The incident direction of the soft X-ray was aligned along the surface normal. From these holograms, the atomic image from the cleavage surface was directly reconstructed. Graphene atomic images were collected on the in-plane cross sections of layers 3.3 Å and 5.7 Å above the photoelectron-emitting C atoms, and the stacking structures were determined as *AB* and *AA* type, respectively. An intercalant metal atomic layer was observed between two *AA*-stacked graphenes, as shown in Fig. 1.10c, d. A K atomic image showing 2 × 2 periodicity, occupying each second central position of the C hexagonal prism, was reconstructed.

These results revealed that a preferential cleavage takes place in the K atom insertion layer without the Ca atoms. This is likely to be the most fragile part of the crystal samples. It is important to note that the cleavage planes do not necessarily represent the average bulk structure. The surface and bulk structures and

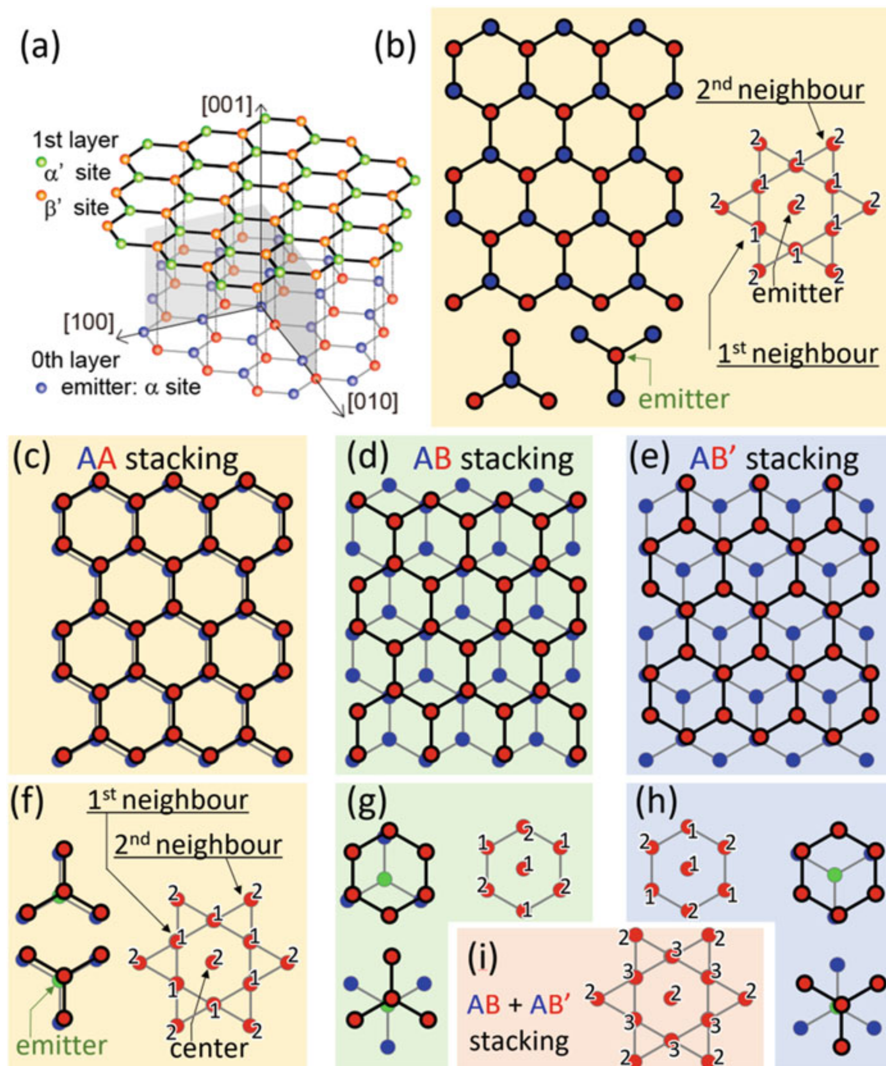

Fig. 1.9 (**a**) Graphite crystal model. Atomic configuration models of (**b**) emitter atom layer, (**c**) *AA*, (**d**) *AB*, and (**e**) *AB*' bilayer stacking structures. Graphene clusters can be stacked on top of the *A* graphene layer in three different ways. (**f–i**) The schematic structure model in each stacking geometry and the expected signal intensity ratio at the center; the first- and second-neighboring atoms in the reconstructed real space images

composition may be substantially different, especially in layered systems. Special precautions must be taken when using sensitive methods, such as ultraviolet angle-resolved photoelectron spectroscopy (ARPES) or scanning probe microscopy.

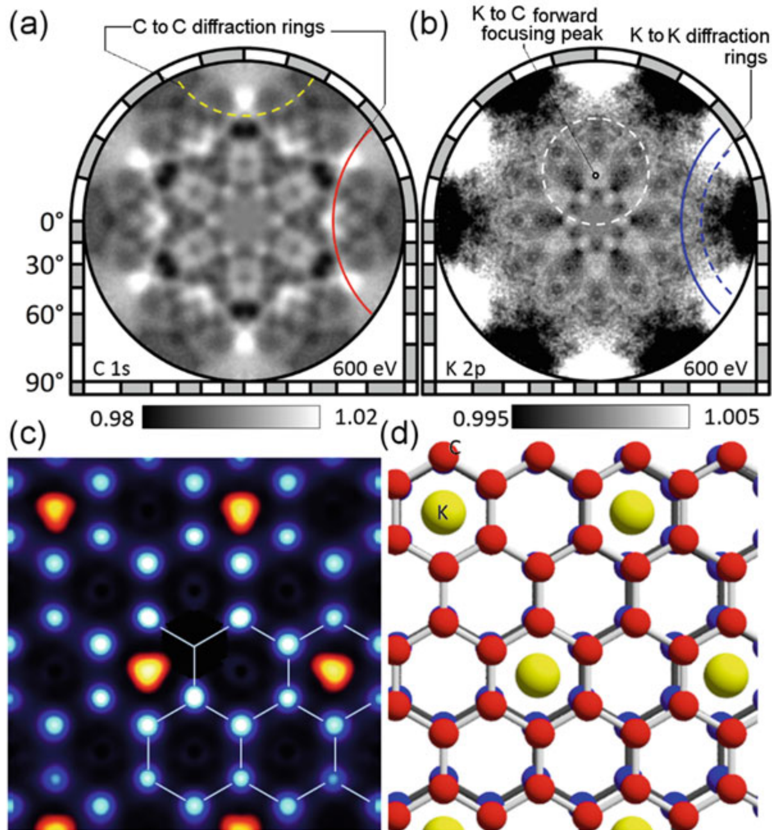

Fig. 1.10 **(a)** C 1 s and **(b)** K 2p photoelectron intensity angular distributions (holograms) from (Ca,K)C_y. **(c)** Atomic arrangement image of C (blue) and K (orange) layers. **(d)** Structure model of the cleaved surface region of (Ca,K)C_y [46]. (Copyright 2016 The Author(s))

Surface phonons are often softened by bulk truncation, structural modification, and interaction with adsorbates. Recently, superconductivity of In [47] and Pb monoatomic layers [48] and FeSe ultrathin films [49] has been discovered and attracted substantial fundamental interest. As mentioned above, PEH is one of the most effective methods to study the surface and subsurface atomic structures in 3D. This method of directly visualizing the atomic arrangement by element selective PEH is expected to be a powerful tool for developing new superconducting materials.

1.6 Electronic Structure of Graphite and GIC

1.6.1 Transition Matrix Elements and Photoelectron Structure Factors

The electronic and chemical properties of a material are mainly determined by the movement of electrons near the Fermi level. The valence electron interaction and photoelectron interference are projected as PIAD patterns in momentum space. The valence band and core level photoelectron energy distribution curves reflect the density of states and compositions, respectively. Based on the principle of energy and momentum conservation in photoelectron emission process, photoelectron spectra resolved in all emission directions provide rich information on the atomic and electronic structures.

The ARPES of a valence band is a powerful technique to study such electrons. 2D Fermi surface mapping reveals the driving force of the electronic structure phase transition, such as charge density wave and superconductivity. Under higher kinetic energy conditions, the Brillouin zone appears within a small solid angle, where the transition matrix elements are approximately constant. 3D Fermi surfaces can be mapped using high angle-resolved electron spectrometer [50]. It is noteworthy that photoelectron spectroscopy using high photon energy probes the intrinsic bulk electronic states because of the long inelastic mean free path of the high kinetic energy electrons [51–53]. However, we encounter diffraction effects under higher kinetic energy conditions. In this chapter, the measurement of band dispersion by ARPES will be described. Furthermore, the photoelectron intensity variation among different Brillouin zones is discussed in detail.

Interlayer interactions induce the well-known degeneracy of the π band to two bands, a lower binding energy band π_{L} and a higher binding energy band π_{H}. In the photoelectron spectrum, the π_{L} and π_{H} bands appear alternately for each Brillouin zone along the $\mathbf{k}_{\mathrm{z}}$ direction. Consequently, oscillation of the binding energy as a function of the photon energy was observed at the bottom of the π band dispersion. This is explained by considering the constitutive and deconstructive interference of the p_{z} orbitals in the unit cell called the *photoelectron structure factor*. An analytical formula of the photoelectronic structure factor of graphite is shown.

We start with the transition matrix, M, between the initial and final states under the dipole approximation scheme. PIAD $I(\theta, \phi)$ is proportional to the square of M.

$$I\,(\theta, \phi) \propto D\,(E_{\mathrm{B}}, \mathbf{q})\,|\mathrm{M}|^2 \delta_{E_{\mathrm{f}}, h\nu + E_{\mathrm{i}}} \delta_{\boldsymbol{k}, \boldsymbol{q}+\boldsymbol{G}}$$

$$\mathrm{M} = \langle \mathrm{f} | \boldsymbol{e} \cdot \boldsymbol{r} | \mathrm{i} \rangle$$

$D(E_{\mathrm{B}}, \mathbf{q})$ is the density of states in the Brillouin zone at binding energy E_{B} and at $\mathbf{q}$. The two delta functions ensure the law of energy and momentum conservation. Therefore, the relations $E_{\mathrm{f}} = h\nu + E_{\mathrm{i}}$ and $\boldsymbol{G} = \boldsymbol{k} - \boldsymbol{q} = \alpha \boldsymbol{a}^* + \beta \boldsymbol{b}^* + \gamma \boldsymbol{c}^*$ (α, β, γ :integer

numbers) hold for the primary photoelectron excitation process. The dipole operator $\boldsymbol{e} \cdot \boldsymbol{r}$ is expressed using spherical harmonics.

$$\boldsymbol{e} \cdot \boldsymbol{r} = \sum_{\sigma=-1}^{1} \sqrt{\frac{4\pi}{3}} e_\sigma Y_{1\sigma} (\theta, \phi)$$

For $\sigma = 1$ helicity, $e_1 = 1$, $e_0 = 0$, and $e_{-1} = 0$. For x-polarization, $e_{\pm 1} = \mp 1/\sqrt{2}$ and $e_0 = 0$.

The initial state $|\mathrm{i}\rangle$ with the wave vector $\mathbf{q}$ and energy E_i is written by a Bloch state in tight-binding approximation as

$$|\mathrm{i}\rangle = \frac{1}{\sqrt{N}} \sum_j \sum_{n\nu} e^{i\boldsymbol{q}\cdot\boldsymbol{R}'} u_{n\nu} (\boldsymbol{q}) \varphi_{n\nu} \left(\boldsymbol{r} - \boldsymbol{R}'\right),$$

$$\boldsymbol{R}' \equiv R_j + \tau_n,$$

where N is the total number of atoms and $\boldsymbol{R}'$ is the position vector of the nth atom at τ_n in the jth unit cell at R_j. $\varphi_{n\nu}(\boldsymbol{r})$ is the νth orbital of the nth atom, which is the product of a radial function $R_{nl}(r)$ and a spherical harmonics $Y_{lm}(\theta, \phi)$. $u_{n\nu}(\boldsymbol{q})$ is its LCAO coefficient. The final state $|\mathrm{f}\rangle$ with the wave vector $\mathbf{k}$ and energy E_f is also a Bloch state in bulk and is written as

$$|\mathrm{f}\rangle = 4\pi \sum_{l'm'} i^{l'} e^{-i\delta_{l'}} Y^*_{l'm'} (\theta_k, \phi_k) Y_{l'm'} (\theta, \phi) R_{E_\mathrm{f},l'}(r).$$

Using the above equations for the initial and final states, a formula for the matrix elements is derived. $\mathbf{G} = \mathbf{k} - \mathbf{q}$ is a reciprocal vector.

$$\begin{aligned} \mathrm{M} &= \tfrac{1}{\sqrt{N}} \sum_j \sum_{n\nu} e^{-i(\boldsymbol{k}-\boldsymbol{q})\cdot R'} u_{n\nu} (\boldsymbol{q}) A_{n\nu} \\ &= \sum_{n\nu} \exp(-i\boldsymbol{G} \cdot \tau_n) u_{n\nu} (\boldsymbol{q}) A_{n\nu} \end{aligned}$$

where the “angular distribution from atomic orbital ADAO” $A_{n\nu}$ is defined as follows [54]:

$$A_{n\nu} \equiv \langle \mathrm{f}(\boldsymbol{r}) | \boldsymbol{e} \cdot \boldsymbol{r} | \varphi(\boldsymbol{r}) \rangle = \sum_{l'=1\pm 1} R_{l'} \sum_{m'} e_\sigma Y_{l'm'} (\theta_k, \phi_k) c^1 \left(l', m', l, m\right)$$

$$\sigma = m' - m$$

$R_{l'}$ is the radial part of the transition matrix element and is a constant complex number depending on l, l', and photon energy. The Gaunt coefficient $c^1(l', m', l, m)$ is nonzero only when $\sigma = \pm 1$ or 0.

If the initial state consists of only one type of atomic orbital, the ADAO term can be separated out of the absolute value as

$$|\mathrm{M}|^2 = \left|\sum_n \exp\left(-i\boldsymbol{G}\cdot\tau_n\right) u_n\left(\boldsymbol{q}\right)\right|^2 |A\left(\theta,\phi\right)|^2 = |F\left(\boldsymbol{k}\right)|^2 |A\left(\theta,\phi\right)|^2.$$

where “photoemission structure factor PSF” $F(\boldsymbol{k})$ [55] is introduced as

$$F\left(\boldsymbol{k}\right) = \sum_n \exp\left(-i\boldsymbol{G}\cdot\tau_n\right) u_n\left(\boldsymbol{q}\right).$$

The term $|F|^2$ is the intensity distribution in the reciprocal **k** space independent of the kinetic energy of photoelectrons or the angle of incidence of photons. This factor is derived from the interference of photoelectron waves from different groups of atoms in the unit cell and is similar to the structural factor of X-ray or electron diffraction that replaces the scattering factors by the coefficient of each atomic orbit in the LCAO wave function [56]. The PIAD from the valence band can be understood as the product of the band dispersion, PSF, and ADAO in simple cases. In the following description, it is shown how these terms work on the actual systems using single-crystal graphite data.

There are four carbon atoms in the unit cell of a graphite. The intralayer bond of carbon has strong covalent properties, i.e., σ bonds with sp^2 hybridization. The layer of the honeycomb network structure is formed by sharing three sp^2 electrons of three adjacent carbon atoms. Moreover, the interlayer bond of carbon is caused by the weak van der Waals interactions produced by delocalized π orbitals. As shown in Figs. 1.1 and 1.11a, there are three- and five-coordinated carbon atoms in the Bernal stacked structure.

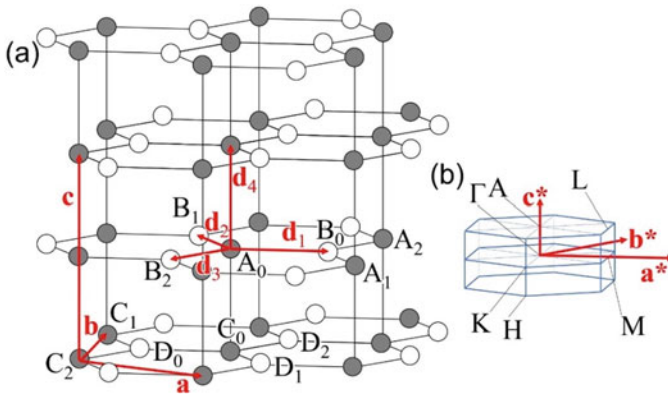

Fig. 1.11 (**a**) Graphite atomic structure and (**b**) Brillouin zone

The four C $2p_z$ orbitals p_A, p_B, p_C, and p_D, in the unit cell form the π band dispersions. The wave function of the π band $\varphi(\mathbf{q}, \mathbf{r})$ is as follows:

$$\begin{aligned}\varphi(\mathbf{q},\mathbf{r}) &= \frac{1}{\sqrt{N}}\sum_n e^{i\mathbf{q}\cdot\mathbf{r}_{A_n}}u_A p_A + e^{i\mathbf{q}\cdot\mathbf{r}_{B_n}}u_B p_B + e^{i\mathbf{q}\cdot\mathbf{r}_{C_n}}u_C p_C + e^{i\mathbf{q}\cdot\mathbf{r}_{D_n}}u_D p_D \\ &= \frac{1}{\sqrt{N}}\sum_n e^{iq\cdot R_n}\left[e^{i\mathbf{q}\cdot\mathbf{d}_4/2}\left(u_A p_A + e^{i\mathbf{q}\cdot\mathbf{d}_1}u_B p_B\right)\right. \\ &\qquad \left. + e^{-i\mathbf{q}\cdot\mathbf{d}_4/2}\left(u_C p_C + e^{-i\mathbf{q}\cdot\mathbf{d}_1}u_D p_D\right)\right]\end{aligned}$$

$\mathbf{d}_1$, $\mathbf{d}_2$, $\mathbf{d}_3$, and $\mathbf{d}_4$ are the position vectors of the neighboring C atoms. The in-plane and interlayer phase factors are introduced as follows:

$$g(\mathbf{q}) = e^{i\mathbf{q}\cdot\mathbf{d}_1} + e^{i\mathbf{q}\cdot\mathbf{d}_2} + e^{i\mathbf{q}\cdot\mathbf{d}_3}$$

$$h(\mathbf{q}) = e^{i\mathbf{q}\cdot\mathbf{d}_4} + e^{-i\mathbf{q}\cdot\mathbf{d}_4} = 2\cos\mathbf{q}\cdot\mathbf{d}_4$$

The matrix elements $H_{ij} = \langle p_i | H | p_j \rangle$ are classified as follows: Coulomb integrals, $H_{ii} = \varepsilon_p$, and resonance integrals between two p orbitals, $H_{AB} = H_{CD} = -V_{pp\pi}$ and $H_{AC} = V_{pp\sigma}$. The secular equation is

$$\begin{pmatrix} \varepsilon_p - E & V_{pp\pi}g & V_{pp\sigma}h & 0 \\ V_{pp\pi}g^* & \varepsilon_p - E & 0 & 0 \\ V_{pp\sigma}h & 0 & \varepsilon_p - E & V_{pp\pi}g^* \\ 0 & 0 & V_{pp\pi}g & \varepsilon_p - E \end{pmatrix}\begin{pmatrix} u_A \\ u_B \\ u_C \\ u_D \end{pmatrix} = 0$$

which leads to

$$E_{\pi_L} = \varepsilon_p - \frac{1}{2}\sqrt{\left(2V_{pp\pi}|g|\right)^2 + \left(V_{pp\sigma}|h|\right)^2} - \frac{V_{pp\sigma}|h|}{2}$$

$$E_{\pi_H} = \varepsilon_p - \frac{1}{2}\sqrt{\left(2V_{pp\pi}|g|\right)^2 + \left(V_{pp\sigma}|h|\right)^2} + \frac{V_{pp\sigma}|h|}{2}$$

$$E_{\pi_L^*} = \varepsilon_p + \frac{1}{2}\sqrt{\left(2V_{pp\pi}|g|\right)^2 + \left(V_{pp\sigma}|h|\right)^2} - \frac{V_{pp\sigma}|h|}{2}$$

and

$$E_{\pi_H^*} = \varepsilon_p + \frac{1}{2}\sqrt{\left(2V_{pp\pi}|g|\right)^2 + \left(V_{pp\sigma}|h|\right)^2} + \frac{V_{pp\sigma}|h|}{2}.$$

Note that $\varepsilon_p \mp \sqrt{\left(2V_{pp\pi}|g|\right)^2 + \left(V_{pp\sigma}|h|\right)^2}/2$ corresponds to the binding energy of the π (−) and π^* (+) band dispersions, for graphene. The third term $\mp V_{pp\sigma}|h|/2$ represents the further degeneration of the π (−) and π^* (+) bands. The LCAO

coefficients for the π bands (π_H and π_L) are as follows. $u_A = \pm u_C \propto \varepsilon_p - E$, $u_B \propto V_{pp\pi} g^*$, and $u_D \propto \pm V_{pp\pi} g$. $u_A{}^2 + u_B{}^2 + u_C{}^2 + u_D{}^2 = 1$. The following equation is for the PSF of the π band. The plus and minus signs correspond to the H and L bands, respectively.

$$F = e^{-i\mathbf{G}\cdot\mathbf{d}_4/2}\left(u_A + e^{-i\mathbf{q}\cdot\mathbf{d}_1} u_B\right) \pm e^{i\mathbf{G}\cdot\mathbf{d}_4/2}\left(u_C + e^{i\mathbf{q}\cdot\mathbf{d}_1} u_D\right)$$

Finally, the PSF formula for graphite Brillouin zone is obtained [43]. Note that $\mathbf{G}\cdot\mathbf{d}_1 = 2\pi(2\alpha+\beta)/3$ and $\mathbf{G}\cdot\mathbf{d}_4 = \pi\gamma$. For the even Brillouin zone along the $\boldsymbol{k}_z$ direction (γ=2n)

$$\left|F_{\pi_L}\right|^2 = \frac{2}{\left(\varepsilon_p - E_{\pi_L}\right)^2 + V_{pp\pi}{}^2 gg^*}\left[V_{pp\pi}\sum_{x=1}^{3}\sin\left(\mathbf{G}\cdot\mathbf{d}_1 + \mathbf{q}\cdot\mathbf{d}_x\right)\right]^2$$

$$\left|F_{\pi_H}\right|^2 = \frac{2}{\left(\varepsilon_p - E_{\pi_H}\right)^2 + V_{pp\pi}{}^2 gg^*}\left[\varepsilon_p - E_{\pi_H} - V_{pp\pi}\sum_{x=1}^{3}\cos\left(\mathbf{G}\cdot\mathbf{d}_1 + \mathbf{q}\cdot\mathbf{d}_x\right)\right]^2.$$

For the odd Brillouin zone along the $\boldsymbol{k}_z$ direction (γ=2n + 1):

$$\left|F_{\pi_L}\right|^2 = \frac{2}{\left(\varepsilon_p - E_{\pi_L}\right)^2 + V_{pp\pi}{}^2 gg^*}\left[\varepsilon_p - E_{\pi_L} - V_{pp\pi}\sum_{x=1}^{3}\cos\left(\mathbf{G}\cdot\mathbf{d}_1 + \mathbf{q}\cdot\mathbf{d}_x\right)\right]^2,$$

$$\left|F_{\pi_H}\right|^2 = \frac{2}{\left(\varepsilon_p - E_{\pi_H}\right)^2 + V_{pp\pi}{}^2 gg^*}\left[V_{pp\pi}\sum_{x=1}^{3}\sin\left(\mathbf{G}\cdot\mathbf{d}_1 + \mathbf{q}\cdot\mathbf{d}_x\right)\right]^2.$$

Figure 1.12a, b shows the structure factor for the π_H and π_L bands, respectively. The C 2p_z atomic orbitals at Γ for the π_H and π_L bands are depicted together as Fig. 1.12c, d, respectively. Note that the p_z orbitals in the π_L band (bonding) are aligned to be in antiphase, and the p_z orbitals in the π_H band (anti-bonding) are aligned to have the same phase. The alignment of these π_L and π_H bands produces destructive and constructive interference, respectively, in the first Brillouin zone and vice versa in the second Brillouin zone.

The cross sections of the valence band dispersion of graphite close to the plane of symmetry of HAH and LAL are shown in Fig. 1.13. The photon energy was set and maintained at 80 eV. The analyzer was set and maintained at 60° off from the incident light. The acceptance angle mode of the analyzer was ±30° perpendicular to the plane containing the incident light, its electric vector, and the direction to the center of the analyzer entrance slit. The valence band consists of one π band and three σ bands. A schematic 3D band dispersion is shown in Fig. 1.13b. The red, yellow, green, and blue bands correspond to π, σ_3, σ_2, and σ_1 (or 2s) band, respectively. The π band from the Fermi level to the binding energy of 8 eV consists

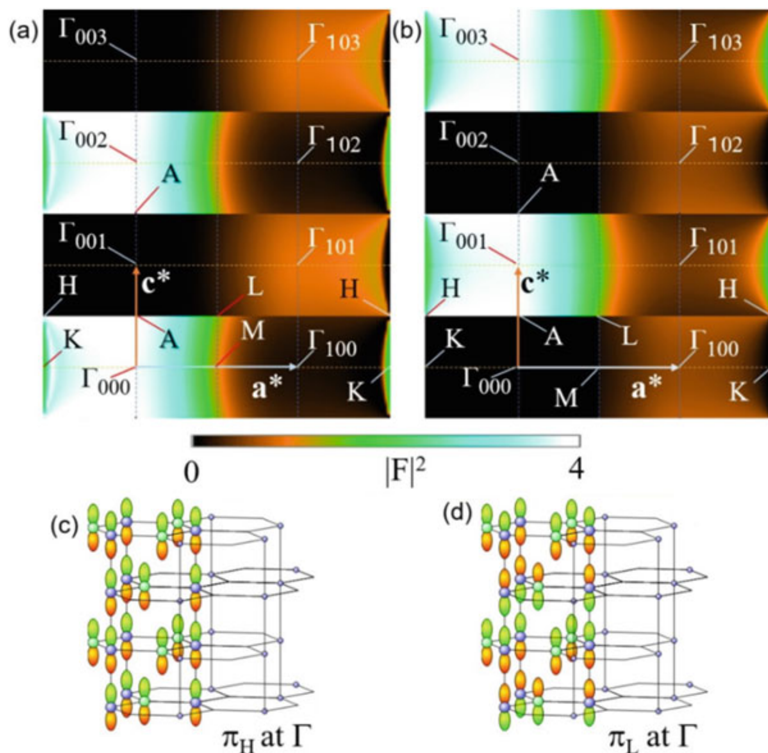

Fig. 1.12 Square of structure factors (PSF), $|F|^2$, for (**a**) π_H band and (**b**) π_L band. The color scale indicates the PSF intensity with white and black corresponding to 1 and 0, respectively. C $2p_z$ atomic orbitals at Γ for (**c**) π_H and (**d**) π_L bands [43]. (Reprinted with permission from [43]. Copyright 2018 American Physical Society)

of a C $2p_z$ orbital. Two σ bands from about 5–12 eV are made from the C $2p_x$ and $2p_y$ orbitals. The σ_1 band of 12–20 eV is mainly from the C 2*s* orbitals.

The left and center columns of Fig. 1.14 are the PIADs of graphite obtained using He II (40.8 eV) and linearly polarized synchrotron radiation, respectively. In the latter case, the photon energy was adjusted to 45.2 eV to suppress the influence of Umklapp scattering. The brightness is proportional to the photoelectron intensity. The graphite has honeycomb carbon sheets, whose electronic structure exhibits sixfold symmetry. The hexagon in Fig. 1.14 represents the first Brillouin zone of graphite. As shown in Fig. 1.14i, the center of the hexagon is the Γ/A point, the vertex is the K/H point, and the midpoint of one side is the M/L point.

The photoelectrons at the Fermi level shown in Fig. 1.14a, e are from the vicinity of the H points, where the π bands degenerate. In the case of non-polarized light excitation, all six points are bright; however, only four points are observed in the case of linearly polarized light excitation. This is due to the characteristic of p_z ADAO, as shown in Fig. 1.14l.

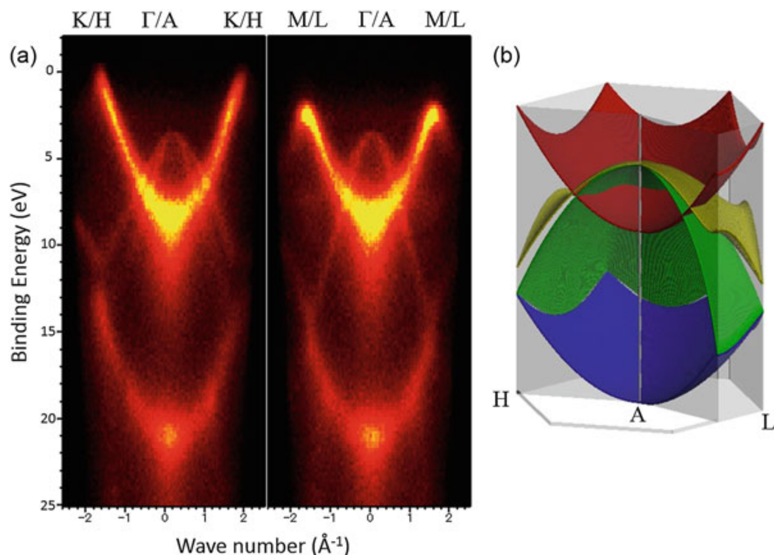

Fig. 1.13 (**a**) Valence band dispersion of graphite along the KΓMK/HALH symmetry plane. The photon energy was 80 eV. (**b**) 3D band diagram of graphite at the HALH plane

As the binding energy increases to 2.0 eV, the π band is dispersed to the M/L points. Although six M points appear to be bright, the outside region of the M point of the second Brillouin region remains dark. This is explained by the PSF of the π band shown in Fig. 1.14i. The photoelectron intensity along the KM/HL line outside the first Brillouin region is calculated as zero, which is consistent with the experimental observations. This intensity inequality between the first and second Brillouin zones means that this π band is a "same-phase (bonding) band."

A σ band appears at the Γ/A point with the binding energy of 4.0 eV. The π band appearing as a ring-shaped feature is dispersed to the Γ/A point, and the σ band is dispersed toward the M/L points. As shown in Fig. 1.14h, for linearly polarized light, note that the σ band intensity is observed only at the four M/L points. This indicates that the σ band is composed of the p_x and p_y atomic orbitals.

The overall characteristics of the intensity distribution are determined by the ADAO, A_ν, and modified by the PSF. The PIAD measurements, along with the combination of a display-type analyzer and linearly polarized light, allow the analysis of atomic orbitals and bonding characters. From A_ν, it is possible to determine the atomic orbital that forms the bands, and the bonding nature can be determined from the PSF. In other words, phase relations between the atomic orbitals in the unit cell can be deduced [43, 55, 56, 57].

The valence band dispersion of the graphite π band along the $\mathbf{k}_z$ axis was measured using the photon energy of 60–230 eV. The oscillation in binding energy was observed for π band dispersion during photon energy scanning. The binding

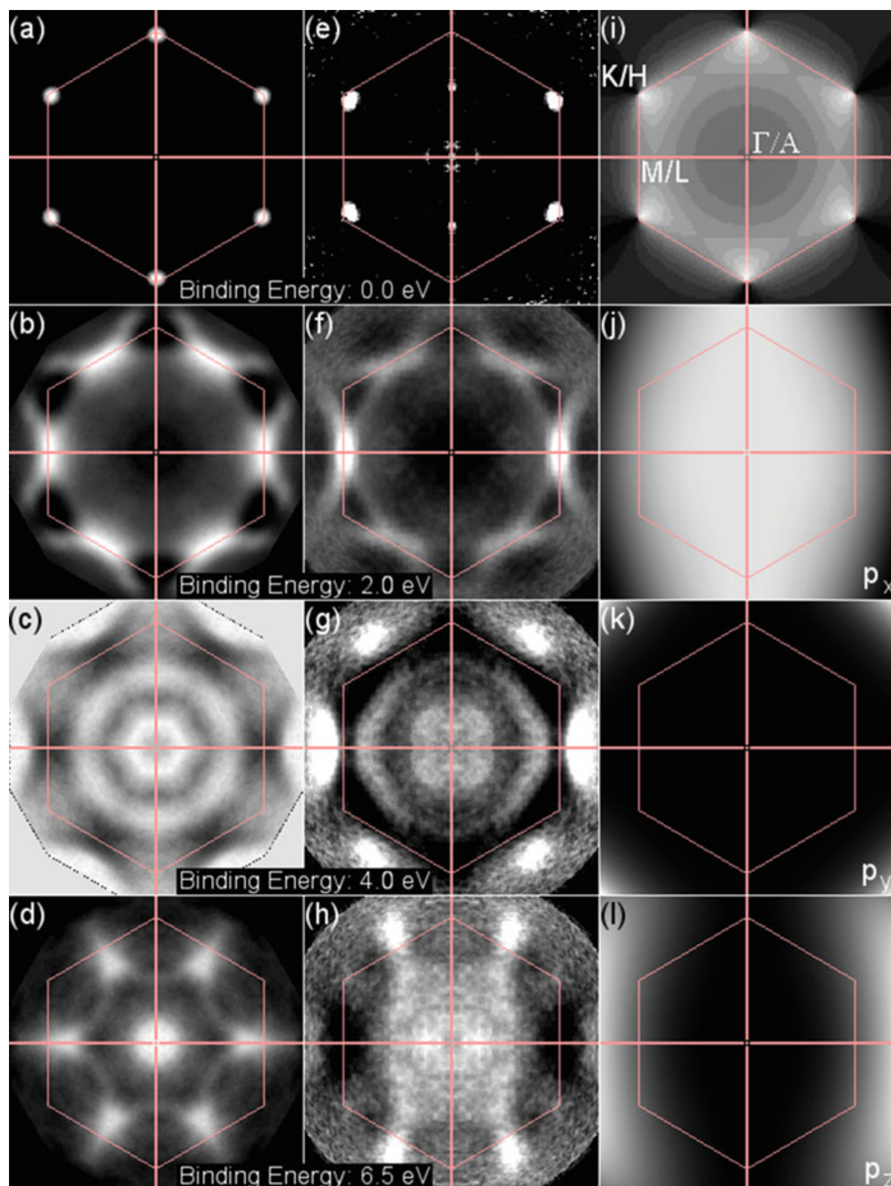

Fig. 1.14 (**a**–**d**) PIADs of graphite excited by the He II (40.8 eV) radiation. The hexagon represents the Brillouin zone. (**e**–**h**) PIADs excited by the linearly polarized synchrotron radiation (45.2 eV). The electric vector is along the horizontal direction. (**i**) Structure factor of the graphite π band. ADAO from (**j**) p_x, (**k**) p_y, and (**l**) p_z atomic orbitals calculated for the photoelectron kinetic energy of 36 eV

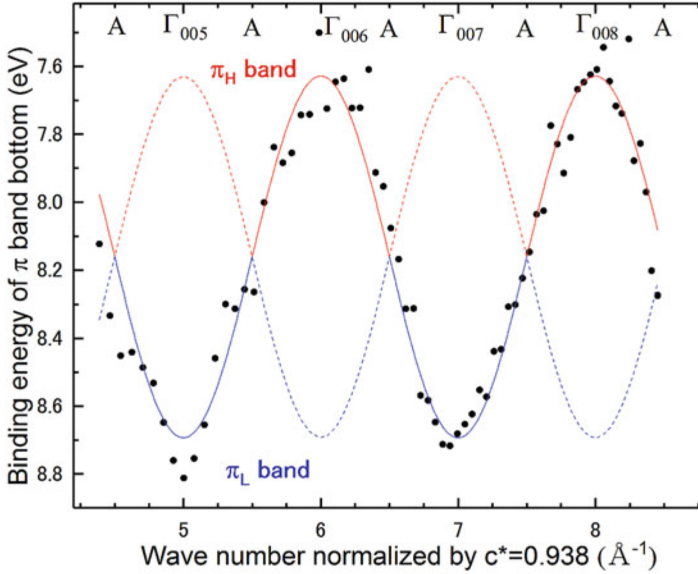

Fig. 1.15 Graphite band dispersion measured at Γ/A as a function of the photon energy. Binding energy at the bottom of the π band dispersion plotted as a function of wave number [43] (Reprinted with permission from [43]. Copyright 2018 American Physical Society)

energy at the bottom of the π band, as a function of photon energy, is plotted in Fig. 1.15. The horizontal axis is the wave number normalized by the reciprocal lattice c^*. The integer positions correspond to the Γ points. Considering the inner potential as a fitting parameter, the kinetic energy of each data point was converted into wave number so that the minimum and maximum values appear at Γ point.

At odd number points, the binding energy at the bottom of the π band is low. At even number points, the binding energy is high. The former corresponds to the π_L band. The latter corresponds to the π_H band. This oscillation is well explained by the PSF effect in the $\mathbf{k}_z$ direction, as shown in Fig. 1.12a, b. The π_L band is formed by the p_z orbitals that are in antiphase with each other forming deconstructive interference at $k_\mathrm{z} = 2nc^*$ Γ points. The π_H band is formed by the p_z orbitals aligned in the same phase forming constructive interference at $k_\mathrm{z} = 2nc^*$ Γ points. Thus, the PSF effect leads to complete disappearance of one π band and a 4 π band dispersion.

Fitting was done by finding the position of Γ points using a simple sine curve. From this fitting, the resonance integral between the interlayer p_z orbitals, $V_{pp\sigma}$ was derived as 0.5 eV. Furthermore, the inner potential of the graphite from the vacuum level was determined to be 17.17 eV. This value roughly corresponds to the midpoint between the bottom of π and σ bands at the Γ point.

1.6.2 Valence Band Dispersion of GIC

The details of the electronic structures of CaC_6 were clarified by the ARPES experiment. ARPES is powerful technique to experimentally determine the band dispersion of the valence band and Fermi surfaces. Details of ARPES are given in Sect. 1.6.1. The ARPES study of CaC_6 was reported in 2009 [58]. Its results suggested that the graphene sheet plays an important role in GIC superconductivity and no interlayer bands are observed. The electron-phonon coupling on the Fermi surface, derived from the π^* band, was strong and anisotropic. Moreover, Sugawara et al. reported that a small electron pocket derived from the π^* band appears near the Fermi level at the K point [59]. The triangular Fermi surface at the K point was formed in the π^* band, and almost no opening of the superconducting gap was observed. This result was explained by the simple rigid band shift by electron doping. In addition, they pointed out that an extra structure at the Γ point was observed. Neither a simple rigid band shift nor the π^* band, folding due to the superstructure of the Ca intercalant, explained this observation [59]. It was suggested that the free-electron-like spherical Fermi surface observed at point Γ is due to the interlayer coupling of CaC_6. The superconducting gap was estimated to be between 1.8 ± 0.2–2.0 ± 0.2 meV at different momentum points around the Γ point, and $2\Delta(0)/k_B T_c$ was determined to be 4.1 ± 0.5 [59], indicating an intermediate or strong coupling regime. Two superconducting gaps of $\Delta E_{\pi^*} = 0.5 \pm 0.1$ meV and $\Delta E_{IL} = 0.4 \pm 0.1$ meV are present in both π^* and the intermediate layer [60]; thus, it was suggested recently that both bands are involved in superconductivity. Therefore, although the electronic structure is still being studied, the ARPES research at high energy resolution can provide the electronic structure of the GIC superconductor to clarify the origin of superconductivity.

1.7 Future Perspectives of GIC Superconductor

The most critical problem in the research of GIC superconductors is that the materials exhibiting T_c higher than 11.5 K found for CaC_6 [1, 2] have never been synthesized in the past decade. Figure 1.16 shows the evolution of transition temperatures T_c in GIC superconductors [61]. The trial for designing new GIC with higher T_c through intercalation of single element has always failed. As described in Sect. 1.3, the binary-element-intercalated graphite (the ternary GICs) compounds were successfully synthesized in the late 1980s, and new GICs have been discovered in recent years, e.g., $Ca_xK_{1-x}C_y$ ($x = 0.33$–0.7). Their structure and pressure dependence of superconductivity were fully investigated [4], and this study expanded the viewpoint of the GIC research to design new GIC compounds. Although T_c did not exceed 15.1 K for CaC_6 at 7.5 GPa, the intercalation of binary or ternary elements may be effective to enhance the GIC superconductors.

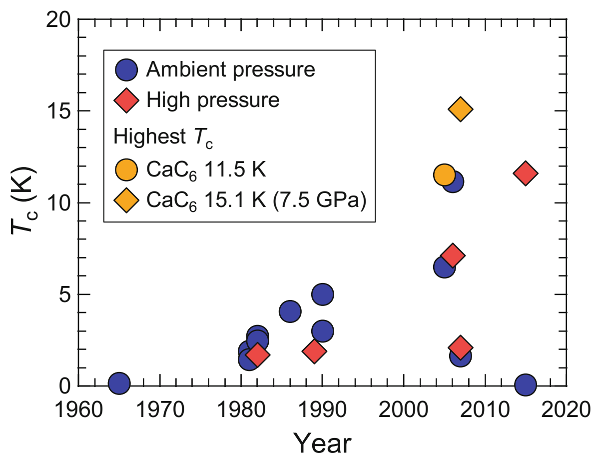

Fig. 1.16 Evolution of transition temperatures (T_c) in GIC superconductors

The strategy for realizing a higher T_c than 11.5 K at ambient pressure (or 15.1 K at high pressure) is still unclear. However, the recent discovery of superconductivity in graphene may become a key for realizing higher T_c in GICs. Moreover, the surface region of GIC may have different superconducting phases from those of bulk crystals. If the superconducting phase in the confined region can be selectively detected, this region may be utilized for electronic devices. The techniques of scanning tunneling spectroscopy (STS), conduction atomic force microscopy (AFM), and magnetic force microscopy (MFM) may be available for detecting superconducting phase in the surface region. As described in Sect. 1.5, the PEH of $Ca_{0.6}K_{0.4}C_8$ was successfully measured to clarify its surface structure [46]. The PEH method is effective to clarify the surface structure of the GIC superconductors, implying that the superconducting phase structure in the surface region can be determined as well. The microprobe and holography techniques may enable the detection and utilization of high-T_c superconducting phase appeared only in the confined region different from bulk superconductivity. Part of Sects. 1.3, 1.4, and 1.6.2 refers to [61] (Copyright 2016 IOP publishing).

References

1. N. Emery, C. Hérold, M. d'Astuto, V. Garcia, C. Bellin, J.F. Marêché, P. Lagrange, G. Loupias, Phys. Rev. Lett. **95**, 087003 (2005)
2. T.E. Weller, M. Ellerby, S.S. Saxena, R.P. Smith, N.T. Skipper, Nat. Phys. **1**, 39–41 (2005)
3. S. Heguri, N. Kawade, T. Fujisawa, A. Yamaguchi, A. Sumiyama, K. Tanigaki, M. Kobayashi, Phys. Rev. Lett. **114**, 247201 (2015)
4. H.T.L. Nguyen, S. Nishiyama, M. Izumi, L. Zheng, X. Miao, Y. Sakai, H. Goto, N. Hirano, Y. Oishi, T. Kagayama, K. Shimizu, Y. Kubozono, Carbon **100**, 641–646 (2016)
5. P. Schaffaütl, J. Prakt. Chem. **21**, 155 (1841)
6. W. Rüdorff, Adv. Inorg. Chem. Radiochem. **1**, 223 (1959)

7. L.B. Ebert, Annu. Rev. Mater. Sci. **6**, 181–211 (1976)
8. H. Selig, L.B. Ebert, Adv. Inorg. Chem. Radiochem **23**, 281–327 (1980)
9. L.B. Ebert, J.C. Scanlon, Ind. Eng. Chem. Prod. Res. Dev. **19**, 103 (1980)
10. W.C. Forsman, T. Dziemianowicz, K. Leong, D. Carl, Synth. Met. **5**, 77–100 (1983)
11. M.S. Dresselhaus, G. Dresselhaus, Adv. Phys. **51**, 1–186 (2002)
12. N.B. Hannay, T.H. Geballe, B.T. Matthias, K. Andres, P. Schmidt, D. MacNair, Phys. Rev. Lett. **14**, 225–226 (1965)
13. Y. Koike, H. Suematsu, K. Higuchi, S. Tanuma, Solid State Commun. **27**, 623–627 (1978)
14. A. Hérold, D. Billaud, D. Guérard, P. Lagrange, M.E. Makrini, Physica B **105**, 253–260 (1981)
15. M. Kobayashi, T. Enoki, H. Inokuchi, M. Sano, A. Sumiyama, Y. Oda, H. Nagano, Synth. Metals **12**, 341–346 (1985)
16. I.T. Belash, A.D. Bronnikov, O.V. Zharikov, A.V. Pal'nichenko, Solid State Commun. **69**, 921–923 (1989)
17. I.T. Belash, A.D. Bronnikov, O.V. Zharikov, A.V. Pal'nichenko, Synth. Met. **36**, 283–302 (1990)
18. V.V. Avdeev, O.V. Zharikov, V.A. Nalimova, A.V. Pal'nichenko, K.N. Semenenko, Pis'ma Zh. Eksp. Teor. Fiz. **43**, 376–378 (1986)
19. L.A. Pendrys, R. Wachnik, F.L. Vogel, P. Lagrange, G. Furdin, M.E. Makrini, A. Hérold, Solid State Commun. **38**, 677–681 (1981)
20. R.A. Wachnik, L.A. Pendrys, F.L. Vogel, P. Lagrange, Solid State Commun. **43**, 5–8 (1982)
21. P. Lagrange, A. Bendriss-Rerhrhaya, J.F. Mareche, E. McRae, Synth. Met. **12**, 201–206 (1985)
22. A.F. Hebard, M.J. Rosseinsky, R.C. Haddon, D.W. Murphy, S.H. Glarum, T.T.M. Palstra, A.P. Ramirez, A.R. Kortan, Nature **350**, 600–601 (1991)
23. A. Gauzzi, S. Takashima, N. Takeshita, C. Terakura, H. Takagi, N. Emery, C. Hérold, P. Lagrange, G. Loupias, Phys. Rev. Lett. **98**, 067002 (2007)
24. J.S. Kim, L. Boeri, J.R. O'Brien, F.S. Razavi, R.K. Kremer, Phys. Rev. Lett. **99**, 027001 (2007)
25. N. Emery, C. Hérold, J.F. Marêché, C. Bellouard, G. Loupias, P. Lagrange, J. Solid State Chem. **179**, 1289–1292 (2006)
26. D. Guerard, M. Chaabouni, P. Lagrange, M.E. Makrini, A. Hérold, Carbon **18**, 257–264 (1980)
27. R.P. Smith, A. Kusmartseva, Y.T.C. Ko, S.S. Saxena, A. Akrap, L. Forró, M. Laad, T.E. Weller, M. Ellerby, N.T. Skipper, Phys. Rev. B **74**, 024505 (2006)
28. L.E. DeLong, V. Yeh, V. Tondiglia, P.C. Eklund, S.E. Lambert, M.B. Maple, Phys. Rev. B **26**, 6315–6318 (1982)
29. H. Okazaki, R. Yoshida, K. Iwai, K. Noami, T. Muro, T. Nakamura, T. Wakita, Y. Muraoka, M. Hirai, F. Tomioka, Y. Takano, A. Takenaka, M. Toyoda, T. Oguchi, T. Yokoya, Phys. Rev. B **80**, 035420 (2009)
30. G. Csányi, P.B. Littlewood, A.H. Nevidomskyy, C.J. Pickard, B.D. Simons, Nat. Phys. **1**, 42–45 (2005)
31. M. Calandra, F. Mauri, Phys. Rev. Lett. **95**, 237002 (2005)
32. D.G. Hinks, D. Rosenmann, H. Claus, M.S. Bailey, J.D. Jorgensen, Phys. Rev. B **75**, 014509 (2007)
33. J. Bardeen, L. Cooper, J.R. Schrieffer, Phys. Rev. **108**, 1175 (1957)
34. G. Lamura, M. Aurino, G. Cifariello, E.D. Gennaro, A. Andreone, N. Emery, C. Hérold, J.F. Marêché, P. Lagrange, Phys. Rev. Lett. **96**, 107008 (2006)
35. J.S. Kim, R.K. Kremer, L. Boeri, F.S. Razavi, Phys. Rev. Lett. **96**, 217002 (2006)
36. N. Bergeal, V. Dubost, Y. Noat, W. Sacks, D. Roditchev, N. Emery, C. Hérold, J.-F. Marêché, P. Lagrange, G. Loupias, Phys. Rev. Lett. **97**, 077003 (2006)
37. A. Sanna, G. Profeta, A. Floris, A. Marini, E.K.U. Gross, S. Massidda, Phys. Rev. B **75**, 020511(R) (2007)
38. R.S. Gonnelli, D. Daghero, D. Delaude, M. Tortello, G.A. Ummarino, V.A. Stepanov, J.S. Kim, R.K. Kremer, A. Sanna, G. Profeta, S. Massidda, Phys. Rev. Lett. **100**, 207004 (2008)
39. R.J. Baird, C.S. Fadley, L.F. Wagner, Phys. Rev. B **15**, 666 (1977)
40. S. Takahashi, S. Kono, H. Sakurai, T. Sagawa, J. Phys. Soc. Jpn. **51**, 3296 (1982)
41. W.F. Egelhoff Jr., Phys. Rev. B **30**, 1052 (1984)

42. T. Matsushita, F. Matsui, J. Electron Spectrosc. Relat. Phenom. **195**, 365–374 (2014)
43. F. Matsui, H. Nishikawa, H. Daimon, M. Muntwiler, M. Takizawa, H. Namba, T. Greber, Phys. Rev. B **97**, 045430 (2018)
44. F. Matsui, T. Matsushita, H. Daimon, J. Phys. Soc. Jpn. **81**, 114604 (2012)
45. F. Matsui, R. Ishii, H. Matsuda, M. Morita, S. Kitagawa, T. Matsushita, S. Koh, H. Daimon, Jpn. J. Appl. Phys. **52**, 110110 (2013)
46. F. Matsui, R. Eguchi, S. Nishiyama, M. Izumi, E. Uesugi, H. Goto, T. Matsushita, K. Sugita, H. Daimon, Y. Hamamoto, I. Hamada, Y. Morikawa, Y. Kubozono, Sci. Rep. **6**, 36258 (2016)
47. T. Uchihashi, P. Mishra, M. Aono, T. Nakamura, Phys. Rev. Lett. **107**, 207001 (2011)
48. T. Zhang, P. Cheng, W.-J. Li, Y.-J. Sun, G. Wang, X.-G. Zhu, K. He, L. Wang, X. Ma, X. Chen, Y. Wang, Y. Liu, H.-Q. Lin, J.-F. Jie, Q.-K. Xue, Nat. Phys. **6**, 104–108 (2010)
49. J.-F. Ge, Z.-L. Lie, C. Liu, C.-L. Gao, D. Qian, Q.-K. Xue, Y. Liu, J.-F. Jia, Nat. Mater. **14**, 285–289 (2015)
50. M. Yano, A. Sekiyama, H. Fujiwara, T. Saita, S. Imada, T. Muro, Y. Onuki, S. Suga, Phys. Rev. Lett. **98**, 036405 (2007)
51. A. Sekiyama, T. Iwasaki, K. Matsuda, Y. Saitoh, Y. Onuki, S. Suga, Nature **403**, 396 (2000)
52. K. Horiba, M. Taguchi, A. Chainani, Y. Takata, E. Ikenaga, D. Miwa, Y. Nishino, K. Tamasaku, M. Awaji, A. Takeuchi, M. Yabashi, H. Namatame, M. Taniguchi, H. Kumigashira, M. Oshima, M. Lippmaa, M. Kawasaki, H. Koinuma, K. Kobayashi, T. Ishikawa, S. Shin, Phys. Rev. Lett. **93**, 236401 (2004)
53. Y. Takata, K. Tamawaku, T. Tokushima, D. Miwa, S. Shin, T. Ishikawa, M. Yabashi, K. Kobayashi, J.J. Kim, T. Yao, T. Yamamoto, Appl. Phys. Lett. **84**, 4310 (2004)
54. S.M. Golberg, C.S. Fadley, S. Kono, J. Electron Spectrosc. Relat. Phnom. **21**, 285 (1981)
55. H. Daimon, S. Imada, H. Nishimoto, S. Suga, J. Electron Spectrosc. Relat. Phenom. **76**, 487 (1995)
56. H. Nishimoto, T. Nakatani, T. Matsushita, S. Imada, H. Daimon, S. Suga, J. Phys. Condens. Matter **8**, 2715 (1996)
57. F. Matsui, Y. Hori, H. Miyata, N. Suganuma, H. Daimon, H. Totsuka, K. Ogawa, T. Furukubo, H. Namba, Appl. Phys. Lett. **81**, 2556 (2002)
58. T. Valla, J. Camacho, Z.-H. Pan, A.V. Fedorov, A.C. Walters, C.A. Howard, M. Ellerby, Phys. Rev. Lett. **102**, 107007 (2009)
59. K. Sugawara, T. Sato, T. Takahashi, Nat. Phys. **5**, 40–43 (2009)
60. S.-L. Yang, J.A. Sobota, C.A. Howard, C.J. Pickard, M. Hashimoto, D.H. Lu, S.-K. Mo, P.S. Kirchmann, Z.-X. Shen, Nat. Commun. **5**, 3493 (2014)
61. Y. Kubozono, R. Eguchi, H. Goto, S. Hamao, T. Kambe, T. Terao, S. Nishiyama, L. Zheng, X. Miao, H. Okamoto, J. Phys. Condens. Matter **28**, 334001 (2016)

Chapter 2
Physics of Graphene: Basic to FET Application

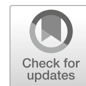

Hidenori Goto

Abstract Graphene is a single layer of carbon atoms that are arranged in a two-dimensional honeycomb network. Since the successful isolation of graphene in 2004, its peculiar nature has been extensively studied. The linear dispersion relation, which is described by the massless Dirac equation, induces striking phenomena explained by relativistic quantum physics. In addition, the carrier mobility of graphene considerably exceeds that of silicon, which makes graphene a promising material for future electronics. This chapter aims at introducing the basic properties of graphene concisely to a broad readership. After summarizing the development of the study on graphene briefly, we provide the theoretical description of the electronic properties and experimental procedures to study graphene field-effect transistor (FET). Finally, two methods for carrier doping in graphene are discussed based on our recent study.

Keywords Graphene · Two-dimensional material · Field-effect transistor · Mesoscopic physics · Carrier doping

2.1 Introduction

2.1.1 History of Study on Graphene and 2D Electron System

The electronic structure of graphene has been theoretically studied since the 1940s [1–3]. The peculiar electronic properties, such as linear dispersion relation and anomalous magnetic response, which are discussed in Sect. 2.2, were already predicted at that time. The two-dimensional (2D) structure had been believed to be unstable against long-range fluctuation [4]; thus, it was surprising that the graphene

H. Goto (✉)
Research Institute for Interdisciplinary Science, Okayama University, Okayama, Japan
e-mail: p57f8bcq@cc.okayama-u.ac.jp

© Springer Nature Singapore Pte Ltd. 2019

Y. Kubozono (ed.), *Physics and Chemistry of Carbon-Based Materials*,
https://doi.org/10.1007/978-981-13-3417-7_2

was firstly isolated from graphite using a simple technique with an adhesive tape [5–7], and its intriguing properties were found successively [8, 9].

Prior to the discovery of graphene, a variety of 2D electron systems had been studied. For example, the transport property of disordered 2D systems was understood by the interference of wave functions or weak Anderson localization [10, 11]. The notion about phase coherence in wave function initiated mesoscopic physics [12]. Moreover, clean 2D systems had been studied in Si inversion layer or GaAs/AlGaAs heterojunction, in which electrons are confined in a potential valley at the interface. The magnetotransport in these systems enabled us to explore the novel macroscopic quantum phenomena, integer and fractional quantum Hall effects [13–15]. Besides, a dilute 2D system that forms a solid lattice called Wigner crystal has also been studied using electrons floated on the surface of liquid helium [16].

Graphene is classified into various clean 2D systems. The differences from the previous systems are as follows. (1) Graphene is a monoatomic layer, which can be isolated from other materials. Thus, it is possible to study the intrinsic properties of graphene by suspending it in vacuum or by putting it in between inert materials. (2) The kinetic energy of carrier in graphene is proportional to its momentum, which is contrasting to the common knowledge in classical and quantum physics, where the kinetic energy is quadratic in the momentum. This means that the carrier in graphene obeys the massless Dirac equation or Weyl equation rather than the Schrödinger equation. Consequently, graphene provides a unique opportunity to study relativistic quantum physics within the framework of condensed matter physics. In addition, the peculiar band structure suppresses back scattering of carriers to enhance their mobility. Further, future electronic devices utilizing high mobility are expected, although some problems, such as the opening of the band gap, must be solved. Even after over 10 years from the discovery [5–7], this inexhaustible study has revealed the peculiar properties and application possibilities of graphene.

Graphene exhibits too many interesting phenomena to cover all the topics completely in this chapter. To have a better understanding for various properties of graphene and related materials, textbooks and review papers [17–23] are provided at the end of the chapter. Standard textbooks about quantum mechanics [24, 25], solid-state physics [26, 27], and semiconductor physics [28, 29] are also listed as references to underlying fundamental physics.

2.1.2 Extension of Study on Graphene and Future Perspectives

The findings of graphene have stimulated the interest in other materials. First, the method of isolating graphene, which is called micromechanical cleavage technique, has been applied to other 2D layered materials (2DMs) in which layers are stacked with the weak van der Waals force [30, 31]. These materials include black phosphorus (BP), as shown in Fig. 2.1b [32, 33]; hexagonal boron nitride (h-BN),

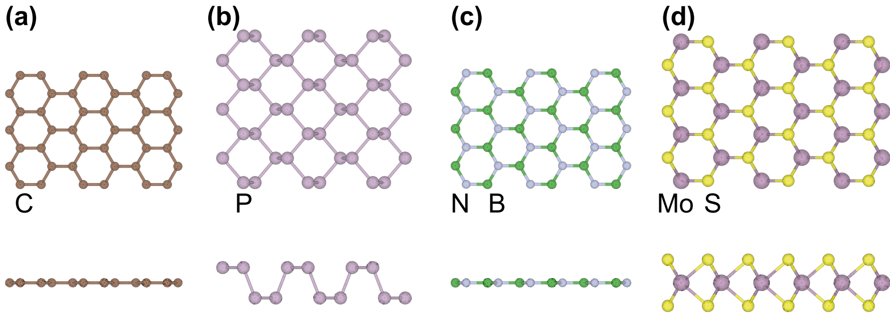

Fig. 2.1 Schematic top and side views of various 2D materials. (**a**) Graphene, (**b**) black phosphorus, (**c**) hexagonal boron nitride, and (**d**) molybdenum disulfide

as shown in Fig. 2.1c; and transition metal dichalcogenides (TMDs) such as MoS_2, as shown in Fig. 2.1d [34, 35]. These materials have similar crystal structure to graphene (Fig. 2.1a); however, they show distinct transport properties. Graphene is a zero-gap semiconductor, BP is a semiconductor, h-BN is an insulator, and TMDs are metals or semiconductors depending on materials and crystal structures. The combination of metallic, semiconducting, and insulating 2DMs with van der Waals force may realize innovative 2D devices which are flexible, transparent, and light in weight [36].

Further, monoelemental layered materials other than graphene have attracted much attention in recent years. In addition to phosphorene from BP [32, 33], silicene from Si [37], germanene from Ge [38], and so on [39, 40] were predicted, and some of them have been realized experimentally. These novel 2DMs have buckled honeycomb structure similar to graphene, and they are expected to have the following merits over graphene. These materials have an intrinsic band gap, which is superior to graphene for application to semiconducting and optical devices. In addition, strong spin-orbit interaction in these materials may induce novel phenomena, such as quantum spin Hall effect [41, 42], which is not observed in graphene. Furthermore, the valley degree of freedom in the band structure can be utilized to valleytronics [43–45]. The stability in the atmospheric condition is a key issue for the practical application of these materials.

Furthermore, a theoretical study on graphene has introduced the Dirac or Weyl equation and topological notion to solid-state physics [41, 42, 46]. In particular, the concept of topological insulator (TI) was proposed based on the graphene structure [42], which opened new research discipline. The TI has a band gap in bulk; however, no-gap state at the surface [47–49]. The surface state has a linear dispersion in which momentum and spin has correlation similar to those in graphene, i.e., the direction of the real spin is locked by that of the momentum in TI. The study of topological quantum materials, such as Weyl semimetal and Dirac semimetal [50], has also been initiated. These semimetals are regarded as an extension of graphene to the 3D space, i.e., a carrier is described by an analogue of 3D Weyl equation.

2.2 Theoretical Aspects

In this section, the crystal and electronic structures of graphene are described in accordance with references [51, 52]. The characteristic transport phenomena induced by the linear dispersion relation are also explained.

2.2.1 Crystal Structure

The atomic number of carbon is 6, which means that a carbon atom has six electrons in the atomic orbitals ($1s^2$, $2s^2$, and $2p^2$), among which two electrons of $1s^2$ are bound in the inner shell and other four ($2s^2$ and $2p^2$) are valence electrons. One of the $2s$ electrons is excited so that ($2s$, $2p_{\mathrm{x}}$, $2p_{\mathrm{y}}$, and $2p_{\mathrm{z}}$) orbitals can be hybridized. In graphene, three orbitals of $2s$, $2p_{\mathrm{x}}$, and $2p_{\mathrm{y}}$ are hybridized to sp^2 orbitals. These three sp^2 orbitals lie in an identical x-y plane and extend to 120° in angle to each other. The sp^2 orbitals form strong σ bonds, which lead to a planer honeycomb network. The residual $2p_{\mathrm{z}}$ electron, called π electron, forms the weak π bond. The π electron not only leads to weak van der Waals interaction between the graphene layers but also works as a carrier of electric conduction.

Figure 2.2a shows the honeycomb network of graphene. The unit cell indicated by a diamond shape includes two atoms, A (white circle) and B (gray circle). The honeycomb network itself is not the Bravais lattice because the arrangement of atoms is different when viewed from A or B atom. However, each atom forms a hexagonal lattice; thus, they are called A or B sublattice. The primitive vectors are indicated by $\boldsymbol{a}_1$ and $\boldsymbol{a}_2$, although the other ways to select them are allowed. Lattice length a is 2.46 Å, and the distance of the nearest neighbor atoms is $a/\sqrt{3} = 1.42$ Å.

Figure 2.2b shows the reciprocal lattice structure and its unit vectors, $\boldsymbol{b}_1$ and $\boldsymbol{b}_2$. These vectors satisfy the relation of $\boldsymbol{a}_i \cdot \boldsymbol{b}_j = 2\pi\ \delta_{i,j}$, where $\delta_{i,j}$ is Kronecker's delta, i.e., $\delta_{i,j} = 1$ when $i = j$ and 0 in other cases. The first Brillouin zone is obtained by the Wigner-Seitz method [26], and it takes the shape of a regular hexagon. The points with high symmetry, Γ, K, K′, and M points are indicated in the first Brillouin zone. The other vertices of the hexagon are equivalent to K or K′ point because those can be transferred to K or K′ point by the translation of $\boldsymbol{b}_1$ and/or $\boldsymbol{b}_2$. Since two $2p_{\mathrm{z}}$ electrons are provided by A and B atoms in the unit cell, the first Brillouin zone is perfectly filled with the electrons, i.e., the Fermi level is situated at the zone boundary [26].

Finally, the evolution of the crystal structure from graphene to graphite is discussed. A bilayer graphene consists of two graphene layers, where two layers are shifted from each other by $+\boldsymbol{\delta}_i$ or $-\boldsymbol{\delta}_i$ indicated in Fig. 2.2a. The A sublattice in the top layer is right above the B sublattice in the bottom layer or vice versa; thus, this structure is called AB stacking. The trilayer graphene is obtained by putting one more layer on bilayer. There are two arrangements for the topmost layer, called ABA or ABC stacking. In ABA stacking, the top layer is arranged in the same position as

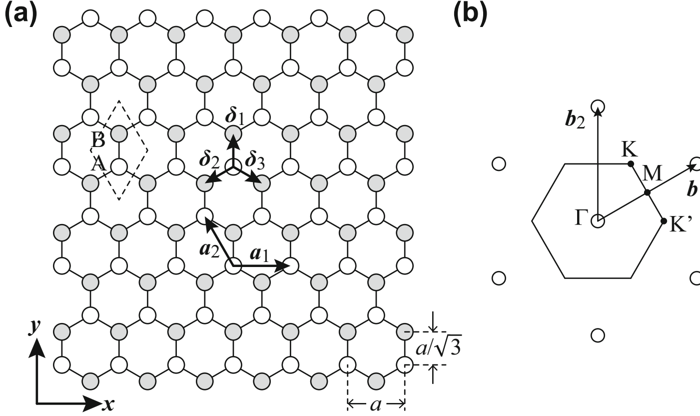

Fig. 2.2 Crystal lattice and reciprocal lattice of graphene. (**a**) Crystal structure of graphene. The white and gray circles construct A and B sublattices, respectively. $\boldsymbol{a}_1$ and $\boldsymbol{a}_2$ indicate primitive lattice vectors whose length is a. $\boldsymbol{\delta}_i$ ($i = 1$–3) indicate vectors from an A atom to B atoms of the nearest neighbor. Choosing x and y axes as in the figure, $\boldsymbol{a}_1 = a(1, 0)$, $\boldsymbol{a}_2 = a\left(-\frac{1}{2}, \frac{\sqrt{3}}{2}\right)$, $\boldsymbol{\delta}_1 = \frac{a}{\sqrt{3}}(0, 1)$, $\boldsymbol{\delta}_2 = \frac{a}{\sqrt{3}}\left(-\frac{\sqrt{3}}{2}, -\frac{1}{2}\right)$, and $\boldsymbol{\delta}_3 = \frac{a}{\sqrt{3}}\left(\frac{\sqrt{3}}{2}, -\frac{1}{2}\right)$. The dashed diamond shows a unit cell, whose area is $S = \frac{\sqrt{3}}{2}a^2$. The horizontal and vertical edges are called zigzag and armchair edges for their shapes, respectively. (**b**) The reciprocal lattice of graphene is shown by white circles. $\boldsymbol{b}_1$ and $\boldsymbol{b}_2$ indicate the primitive reciprocal lattice vectors. The regular hexagon is the first Brillouin zone in which the points with high symmetry, Γ, K, K′, and M are indicated, where $\boldsymbol{b}_1 = \frac{4\pi}{\sqrt{3}a}\left(\frac{\sqrt{3}}{2}, \frac{1}{2}\right)$, $\boldsymbol{b}_2 = \frac{4\pi}{\sqrt{3}a}(0, 1)$, $\Gamma = (0, 0)$, $\mathrm{K} = \frac{4\pi}{3a}\left(\frac{1}{2}, \frac{\sqrt{3}}{2}\right)$, and $\mathrm{K}' = \frac{4\pi}{3a}(1, 0)$, and $\mathrm{M} = \frac{2\pi}{\sqrt{3}a}\left(\frac{\sqrt{3}}{2}, \frac{1}{2}\right)$

the bottom layer. In ABC stacking, the shift of the top layer from the middle layer is the same as the shift of the middle layer from the bottom layer. The band structure of graphene layers depends on layer number and stacking manner significantly [53]. The distance between layers in graphite is $c = 3.34$ Å.

2.2.2 Band Structure

We consider the electronic properties of π electron with a tight-binding model [26]. We set the coordinates of A and B atoms in the jth unit cell to $\boldsymbol{R}_{\mathrm{A},j}$ and $\boldsymbol{R}_{\mathrm{B},j}$, and the atomic orbital functions around these atoms to $\varphi_\mathrm{A}(\boldsymbol{r} - \boldsymbol{R}_{\mathrm{A},j})$ and $\varphi_\mathrm{B}(\boldsymbol{r} - \boldsymbol{R}_{\mathrm{B},j})$. In the tight-binding approximation, the wave functions of A and B sublattices are constructed of the atomic orbital functions as follows:

$$\Phi_\mathrm{A}(\boldsymbol{r}) = \frac{1}{\sqrt{N}}\sum_{j=1}^{N} e^{i\boldsymbol{k}\cdot\boldsymbol{R}_{\mathrm{A},j}}\varphi_\mathrm{A}\left(\boldsymbol{r} - \boldsymbol{R}_{\mathrm{A},j}\right), \quad \Phi_\mathrm{B}(\boldsymbol{r}) = \frac{1}{\sqrt{N}}\sum_{j=1}^{N} e^{i\boldsymbol{k}\cdot\boldsymbol{R}_{\mathrm{B},j}}\varphi_\mathrm{B}\left(\boldsymbol{r} - \boldsymbol{R}_{\mathrm{B},j}\right), \tag{2.1}$$

where N is the number of unit cells. $\Phi_A(\boldsymbol{r})$ and $\Phi_B(\boldsymbol{r})$ are wave functions in periodical potential; thus, these functions must satisfy the Bloch's theorem. This was proved by replacing $\boldsymbol{r}$ with $\boldsymbol{r}+\boldsymbol{T}$, where $\boldsymbol{T}$ is a translational vector in the crystal lattice.

$$\Phi_A(\boldsymbol{r}+\boldsymbol{T}) = \frac{1}{\sqrt{N}}\sum_{j=1}^{N} e^{i\boldsymbol{k}\cdot\boldsymbol{R}_{A,j}}\varphi_A\left(\boldsymbol{r}+\boldsymbol{T}-\boldsymbol{R}_{A,j}\right) = \frac{1}{\sqrt{N}}\sum_{j=1}^{N} e^{i\boldsymbol{k}\cdot\left(\boldsymbol{R}'_{A,j}+\boldsymbol{T}\right)}\varphi_A\left(\boldsymbol{r}-\boldsymbol{R}'_{A,j}\right)$$
$$= e^{i\boldsymbol{k}\cdot\boldsymbol{T}}\frac{1}{\sqrt{N}}\sum_{j=1}^{N} e^{i\boldsymbol{k}\cdot\boldsymbol{R}'_{A,j}}\varphi_A\left(\boldsymbol{r}-\boldsymbol{R}'_{A,j}\right) = e^{i\boldsymbol{k}\cdot\boldsymbol{T}}\Phi_A(\boldsymbol{r}) \quad ,$$

where $\boldsymbol{R}'_{A,j} = \boldsymbol{R}_{A,j} - \boldsymbol{T}$ is also the coordinate of A atom; thus, the last equation holds. The wave function $\Psi(\boldsymbol{r})$ of the system is expressed by linear combination of the Bloch functions $\Phi_A(\boldsymbol{r})$ and $\Phi_B(\boldsymbol{r})$:

$$\Psi(\boldsymbol{r}) = c_A\Phi_A(\boldsymbol{r}) + c_B\Phi_B(\boldsymbol{r}), \tag{2.2}$$

where c_A and c_B are the complex coefficients. Equations (2.1) and (2.2) are inserted into the Schrödinger equation, $H\Psi(\mathbf{r}) = E\Psi(\mathbf{r})$. Further, the equation is multiplied by $\varphi_A{}^*(\boldsymbol{r} - \boldsymbol{R}_{A,i})$ or $\varphi_B{}^*(\boldsymbol{r} - \boldsymbol{R}_{B,i})$ from the left side and integrated over $\boldsymbol{r}$. We consider the hopping and overlap integrals only between the nearest neighbor atoms as follows:

$$\begin{aligned}
&\int \varphi_A^*\left(\boldsymbol{r}-\boldsymbol{R}_{A,i}\right)\varphi_A\left(\boldsymbol{r}-\boldsymbol{R}_{A,j}\right)\, d\boldsymbol{r} = \delta_{i,j} \quad ,\\
&\int \varphi_B^*\left(\boldsymbol{r}-\boldsymbol{R}_{B,i}\right)\varphi_B\left(\boldsymbol{r}-\boldsymbol{R}_{B,j}\right)\, d\boldsymbol{r} = \delta_{i,j} \quad ,\\
&\int \varphi_A^*\left(\boldsymbol{r}-\boldsymbol{R}_{A,i}\right)\varphi_B\left(\boldsymbol{r}-\boldsymbol{R}_{B,j}\right)\, d\boldsymbol{r} = s_0\delta_{\boldsymbol{R}_{A,i},\boldsymbol{R}_{B,j}-\boldsymbol{\delta}_l}\ (l=1,2,3) \quad ,\\
&\int \varphi_A^*\left(\boldsymbol{r}-\boldsymbol{R}_{A,i}\right)H\varphi_A\left(\boldsymbol{r}-\boldsymbol{R}_{A,j}\right)\, d\boldsymbol{r} = \alpha\delta_{i,j} \quad ,\\
&\int \varphi_B^*\left(\boldsymbol{r}-\boldsymbol{R}_{B,i}\right)H\varphi_B\left(\boldsymbol{r}-\boldsymbol{R}_{B,j}\right)\, d\boldsymbol{r} = \alpha\delta_{i,j} \quad ,\\
&\int \varphi_A^*\left(\boldsymbol{r}-\boldsymbol{R}_{A,i}\right)H\varphi_B\left(\boldsymbol{r}-\boldsymbol{R}_{B,j}\right)\, d\boldsymbol{r} = -\gamma_0\delta_{\boldsymbol{R}_{A,i},\boldsymbol{R}_{B,j}-\boldsymbol{\delta}_l}\ (l=1,2,3) \quad ,
\end{aligned}$$

where $\delta_{\boldsymbol{R}_{A,i},\boldsymbol{R}_{B,j}-\boldsymbol{\delta}_l}\ (l = 1, 2, 3)$ selects the nearest neighbor atoms, as shown in Fig. 2.2a. The hopping integral is $-\gamma_0 = -2.8\sim -3.16$ eV [20], and the overlap integral s_0 is assumed to 0 for simplicity. Besides, the energy of the $2p_z$ orbital α is set to 0. Within this approximation, we obtain two equations:

$$-\gamma_0 f(\boldsymbol{k})\, c_B = Ec_A \quad ,$$

$$-\gamma_0 f^*(\boldsymbol{k})\, c_A = Ec_B \quad ,$$

which are unified in a matrix form

$$-\gamma_0\begin{pmatrix} 0 & f(\boldsymbol{k}) \\ f^*(\boldsymbol{k}) & 0 \end{pmatrix}\begin{pmatrix} c_A \\ c_B \end{pmatrix} = E\begin{pmatrix} c_A \\ c_B \end{pmatrix}, \tag{2.3}$$

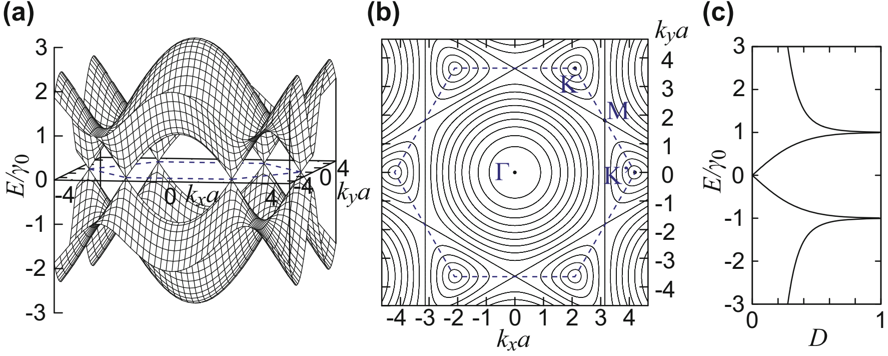

Fig. 2.3 Dispersion relation of graphene based on tight-binding model. (**a**) Band structure of graphene drawn in a periodic zone scheme. (**b**) The contour plot of energy dispersion. The contour lines are drawn against $|E/\gamma_0|$ from 0 to 3 with an increment of 0.2. The lines are convergent to K and K′ points at $E/\gamma_0 = 0$ and Γ point at $|E/\gamma_0| = 3$. The dashed hexagon indicates the first Brillouin zone. (**c**) Density of states per unit cell

where

$$f(\boldsymbol{k}) = \sum_{j=1}^{3} e^{i\boldsymbol{k}\cdot\boldsymbol{\delta}_j} = \exp\left(\frac{ik_y a}{\sqrt{3}}\right) + 2\exp\left(-\frac{ik_y a}{2\sqrt{3}}\right)\cos\left(\frac{k_x a}{2}\right) \tag{2.4}$$

is introduced for the off-diagonal elements. By solving the secular equation,

$$\begin{vmatrix} E & \gamma_0 f(k) \\ \gamma_0 f^*(k) & E \end{vmatrix} = 0,$$

we obtain eigenvalues

$$E_\pm = \pm\gamma_0 |f(\boldsymbol{k})| \tag{2.5}$$

for eigenvectors $\frac{1}{\sqrt{2}}\begin{pmatrix} 1 \\ \mp f^*/|f| \end{pmatrix}$. E_+ and E_- correspond to the energy of conduction and valence bands, respectively. The dispersion relation, $E_\pm = \pm\gamma_0|f(\boldsymbol{k})|$, is shown in Fig. 2.3a, where

$$|f(\boldsymbol{k})| = \sqrt{1 + 4\cos\left(\frac{k_x a}{2}\right)\cos\left(\frac{\sqrt{3}k_y a}{2}\right) + 4\cos^2\left(\frac{k_x a}{2}\right)}\ .$$

The contour plot of the energy dispersion is shown in Fig. 2.3b. One can see that $E/\gamma_0 = 0$ at K and K′ points where the Fermi energy is situated. These independent two points are together called a valley according to semiconducting materials. The contour lines at $|E/\gamma_0| = 1$ are straight lines and form a regular hexagon. The vertices of the hexagon are M point which is a saddle point. The maximum or minimum value, $|E/\gamma_0| = 3$, is taken at Γ point. The density of states $D(E)$ is proportional to the increment of the area enclosed by the contour line from E to $E + dE$. Thus,

$$D(E) \propto \oint \frac{\sqrt{{dk_x}^2 + {dk_y}^2}}{\left|\mathrm{grad}_k E\right|} = \int \frac{dk_x}{\left|\partial E/\partial k_y\right|} \ ,$$

where $D(E)$ is analytically expressed by the first elliptic integral [20] and shown in Fig. 2.3c. Note that $D(E) = 0$ at $E = 0$ and is divergent at $|E/\gamma_0| = 1$.

2.2.3 *Electronic Property*

2.2.3.1 Linear Dispersion Relation

Further, the band structure around the K and K′ points is discussed. The off-diagonal element $f(\boldsymbol{k})$ and $f^*(\boldsymbol{k})$ in Eq. (2.3) is 0 at these points. For example, at K′ point of $\boldsymbol{K}' = 4\pi/3a(1, 0)$

$$f\left(\boldsymbol{K}'\right) = \sum_{j=1}^{3} e^{i\boldsymbol{K}'\cdot\boldsymbol{\delta}_j} = \exp(0i) + \exp\left(-2\pi i/3\right) + \exp\left(2\pi i/3\right) = 1 + \omega^2 + \omega = 0,$$

where $\omega = (-1 + i\sqrt{3})/2$ is the cubic root of 1. The intralayer coupling between A and B atoms vanishes at K and K′ point; thus, the energy of each sublattice is degenerated at $E = 0$. This is the reason why the gap is not opened in graphene. In the vicinity of K′ point, we expand $f(\boldsymbol{K}' + \boldsymbol{k})$ for small $\boldsymbol{k}$.

$$\begin{aligned} f\left(\boldsymbol{K}' + \boldsymbol{k}\right) &= f\left(\boldsymbol{K}'\right) + \boldsymbol{k}\cdot\left(\mathrm{div}_{\boldsymbol{k}} f\left(\boldsymbol{k}\right)|_{\boldsymbol{k}=\boldsymbol{K}'}\right) = \boldsymbol{k}\cdot\left(\sum_{j=1}^{3} i\boldsymbol{\delta}_j e^{i\boldsymbol{K}'\cdot\boldsymbol{\delta}_j}\right) \\ &= i\boldsymbol{k}\cdot\left(\boldsymbol{\delta}_1 + \boldsymbol{\delta}_2\omega^2 + \boldsymbol{\delta}_3\omega\right) = i\boldsymbol{k}\cdot\left\{\tfrac{1}{2}\left(2\boldsymbol{\delta}_1 - \boldsymbol{\delta}_2 - \boldsymbol{\delta}_3\right) + \tfrac{\sqrt{3}i}{2}\left(\boldsymbol{\delta}_3 - \boldsymbol{\delta}_2\right)\right\} \\ &= i\boldsymbol{k}\cdot\left(\tfrac{\sqrt{3}a}{2}\boldsymbol{e}_y + \tfrac{\sqrt{3}a}{2} i\boldsymbol{e}_x\right) = \tfrac{\sqrt{3}a}{2}\left(-k_x + ik_y\right), \end{aligned}$$

where two vectors $(1/2)\,(2\boldsymbol{\delta}_1 - \boldsymbol{\delta}_2 - \boldsymbol{\delta}_3)$ and $(\sqrt{3}/2)\,(\boldsymbol{\delta}_2 - \boldsymbol{\delta}_3)$ have the same length $\sqrt{3}a/2$ and are normal to each other. Thus, the matrix in Eq. (2.3) is written as

$$H = \gamma \begin{pmatrix} 0 & k_x - ik_y \\ k_x + ik_y & 0 \end{pmatrix} = \gamma\,|k| \begin{pmatrix} 0 & e^{-i\theta} \\ e^{i\theta} & 0 \end{pmatrix} \ , \tag{2.6}$$

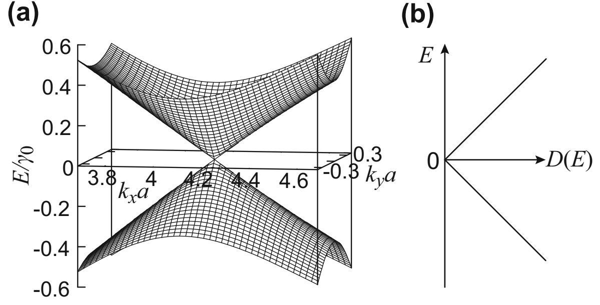

Fig. 2.4 Enlarged energy band around the Dirac point. (**a**) Linear dispersion relation around K′ point and (**b**) density of states around $E = 0$

where $\gamma = \frac{\sqrt{3}}{2}\gamma_0 a$ and $\boldsymbol{k} = (k_x, k_y) = |k|(\cos\theta, \sin\theta)$. By solving the secular equation, we obtain eigenvalues

$$E_{\pm} = \pm\gamma\ |\boldsymbol{k}| \equiv \pm\hbar v_{\mathrm{F}}\ |\boldsymbol{k}| \tag{2.7}$$

for eigenvectors $\frac{1}{\sqrt{2}}\begin{pmatrix} 1 \\ \pm\, e^{i\theta} \end{pmatrix}$. The band structure is shown in Fig. 2.4a. Conical valence and conduction bands are contacted to each other at their apexes called the Dirac point. In Eq. (2.7), the Fermi velocity is introduced by $v_{\mathrm{F}} = \gamma/\hbar \sim 10^6$ m/s. The linear dispersion relation expressed by Eq. (2.7) is the same for photon, $E = c|\boldsymbol{p}|$ by regarding light velocity c as v_{F} and momentum $\boldsymbol{p}$ as $\hbar\boldsymbol{k}$. The expression for photon is given from Einstein's relation, $E = \hbar\omega$; de Broglie's relation, $\boldsymbol{p} = \hbar\boldsymbol{k}$; and light velocity, $c = \omega/|\boldsymbol{k}|$, where ω is the angular frequency and $\boldsymbol{k}$ is the wave number vector of photon. The energy of the relativistic particles is obtained by $E = \sqrt{c^2\boldsymbol{p}^2 + m^2c^4}$. This is reduced to the quadratic dispersion, $E = mc^2 + p^2/2m$, when $m \neq 0$ and $p/m << c$, while the linear dispersion, $E = c|\boldsymbol{p}|$, when $m = 0$. For this reason, the carrier in graphene is sometimes called massless Dirac fermion. However, it should be noted that the carrier in graphene actually moves as if it has a mass of $m^* = \hbar k/v_{\mathrm{F}}$ based on semiclassical approximation [54]. Nevertheless, the massless character at the Dirac point is a distinguished property of graphene.

Concerning the linear dispersion relation, we notice that both group velocity $v_{\mathrm{g}} = dE/dk$ and phase velocity $v_{\mathrm{p}} = E/k$ are equal to v_{F} for $E > 0$. In quantum mechanics, v_{g} indicates the velocity of a wave packet, which corresponds to the classical motion of a particle, while v_{p} shows the velocity of each wave constructing the wave packet. In general, v_{g} is not equal to v_{p} due to the nonlinear dispersion relation, which spreads the width of wave packet after a certain amount of time has elapsed. For the carrier in graphene, such broadening of the wave packet does not occur because of no dispersion.

The Fermi surface is circular at low energy; thus, the carrier density at energy $E = \pm\gamma|k|$ is

$$n = \frac{4 \times \pi k^2}{(2\pi)^2} = \frac{k^2}{\pi} = \frac{E^2}{\pi\gamma^2}\ ,$$

where the factor 4 comes from the degeneracy due to spin and valley. By differentiating n with E, one can obtain the density of states $D(E)$ per unit area

$$D(E) = \frac{dn}{dE} = \frac{2|E|}{\pi\gamma^2} \quad . \tag{2.8}$$

Figure 2.4b shows the E dependence of $D(E)$. $D(E) = 0$ at $E = 0$ and increases in proportion to $|E|$. Note that the linear band dispersion and linear density of states are in contrast to those in conventional 2D systems. In a conventional system, the dispersion relation takes a quadratic form, $E = \hbar^2k^2/2m^*$, and the density of states $D(E) = gm^*/2\pi\hbar^2$ is constant, where m^* is the effective mass in the band and g is the degeneracy of spin and valley.

The discussion around K′ point also holds around K point. For $\boldsymbol{K} = 4\pi/3a(-1, 0)$, we obtain $f(\boldsymbol{K}+\boldsymbol{k}) = \frac{\sqrt{3}a}{2}\left(k_x + ik_y\right)$. This also gives the same band dispersion and density of states as K′ point.

2.2.3.2 Absence of Back Scattering

To discuss the motion of carriers at the vicinities of K and K′ points, effective mass or $\boldsymbol{k}\cdot\boldsymbol{p}$ approximation is applied to the tight-binding model [55]. Then, Hamiltonian is given by replacing a wave vector $\boldsymbol{k}$ in Eq. (2.6) with an operator $\widehat{\boldsymbol{k}} \equiv \nabla/i$ [55]. The equation at the vicinity of K′ is given by $H\Psi(\boldsymbol{r}) = E\Psi(\boldsymbol{r})$, where

$$H = \gamma\begin{pmatrix} 0 & \widehat{k}_x - i\widehat{k}_y \\ \widehat{k}_x + i\widehat{k}_y & 0 \end{pmatrix} = \gamma\left[\widehat{k}_x\begin{pmatrix} 0 & 1 \\ 1 & 0 \end{pmatrix} + \widehat{k}_y\begin{pmatrix} 0 & -i \\ i & 0 \end{pmatrix}\right] = \gamma\left(\widehat{k}_x\sigma_x + \widehat{k}_y\sigma_y\right) = \gamma\widehat{\boldsymbol{k}}\cdot\boldsymbol{\sigma}, \tag{2.9}$$

$$\Psi(\boldsymbol{r}) = \begin{pmatrix} F_{\mathrm{A}}(\boldsymbol{r}) \\ F_{\mathrm{B}}(\boldsymbol{r}) \end{pmatrix} = \begin{pmatrix} F_{\mathrm{A}} \\ F_{\mathrm{B}} \end{pmatrix} e^{i\boldsymbol{k}\cdot\boldsymbol{r}} \quad .$$

$F_{\mathrm{A}}(\boldsymbol{r})$ and $F_{\mathrm{B}}(\boldsymbol{r})$ are the envelope functions of Bloch function with wave vector K′ for A and B sublattices, respectively, and note that the definition of wave function is different from Eq. (2.2) on tight-binding model. Here, $\sigma_x = \begin{pmatrix} 0 & 1 \\ 1 & 0 \end{pmatrix}$, $\sigma_y = \begin{pmatrix} 0 & -i \\ i & 0 \end{pmatrix}$, and $\sigma_z = \begin{pmatrix} 1 & 0 \\ 0 & -1 \end{pmatrix}$ are Pauli matrices, which are related to the amplitudes of $F_{\mathrm{A}}(\boldsymbol{r})$ and $F_{\mathrm{B}}(\boldsymbol{r})$. Thus, σ is called pseudospin and not related to real electron spin. Solving the effective mass equation, we obtain eigenvalues $E = \pm\gamma|\boldsymbol{k}|$ for eigenfunctions, $\Psi_{\pm}(r) = F_{\pm}(\theta)\, e^{i\boldsymbol{k}\cdot\boldsymbol{r}}$, $F_{\pm}(\theta) = \frac{1}{\sqrt{2}}\begin{pmatrix} 1 \\ \pm e^{i\theta} \end{pmatrix}$.

The equation in the eigenstates, $\gamma\widehat{\boldsymbol{k}}\cdot\boldsymbol{\sigma}\Psi_{\pm} = \pm\gamma\,|\boldsymbol{k}|\,\Psi_{\pm}$, is transformed into $\left(\widehat{\boldsymbol{k}}\cdot\boldsymbol{\sigma}/|\boldsymbol{k}|\right)\ \Psi_{\pm} = \pm\Psi_{\pm}$. The operator on the left hand side, $\widehat{\boldsymbol{k}}\cdot\boldsymbol{\sigma}/|\boldsymbol{k}|$, shows the

component of pseudospin projected to the wave vector, which is called the chirality. The eigenstates of energy are also those of chirality. The fact that the eigenvalue of the chirality is ± 1 means that $\boldsymbol{\sigma}$ is parallel or antiparallel to $\boldsymbol{k}$ for positive or negative E, respectively. This is also confirmed by calculating the expectation values of the pseudo spins: $\langle \sigma_x \rangle = \langle \Psi_\pm | \sigma_x | \Psi_\pm \rangle = \pm \cos\theta$, $\langle \sigma_y \rangle = \pm \sin\theta$, and $\langle \sigma_z \rangle = 0$ for $\Psi_\pm(r) = \frac{1}{\sqrt{2}} \begin{pmatrix} 1 \\ \pm e^{i\theta} \end{pmatrix} e^{i\boldsymbol{k}\cdot\boldsymbol{r}}$.

The correlation between the directions of the wave vector and pseudospin leads to an intriguing scattering phenomenon. Consider that the carrier with $E > 0$ is scattered from wave vector $\boldsymbol{k}$ to $\boldsymbol{k}'$ where the angle between $\boldsymbol{k}$ and $\boldsymbol{k}'$ is θ. Assuming that the scattering potential does not affect the pseudospin, the scattering probability is

$$p(\theta) \propto \left| \langle \boldsymbol{k}' | V | \boldsymbol{k} \rangle \langle F(\theta) | F(0) \rangle \right|^2 \propto |\langle F(\theta) | F(0) \rangle|^2 = \left| \frac{1}{2} \left(1, e^{-i\theta}\right) \begin{pmatrix} 1 \\ e^{i0} \end{pmatrix} \right|^2 = \cos^2 \frac{\theta}{2},$$

where $e^{i\boldsymbol{k}\cdot\boldsymbol{r}}$ is expressed by $|\boldsymbol{k}\rangle$.The result shows that $p(\theta)$ is maximum at $\theta = 0$ and minimum at $\theta = \pi$. In particular, $p(\pi) = 0$ means the absence of back scattering [55]. Although the scattering to the direction of $\theta \neq \pi$ is possible, it can be observed that the multiple scattering to backward direction is also suppressed by the interference of time-reversed paths. For example, we consider the third-order scattering process from $\boldsymbol{k}$ to $-\boldsymbol{k}$. The scattering amplitude contains summation of terms $\langle -\boldsymbol{k}|V|\boldsymbol{k}''\rangle\langle \boldsymbol{k}''|V|\boldsymbol{k}'\rangle\langle \boldsymbol{k}'|V|\boldsymbol{k}\rangle\langle F(\pi)|F(\theta'')\rangle\langle F(\theta'')|F(\theta')\rangle\langle F(\theta')|F(0)\rangle$ for wave vector $\boldsymbol{k}'$ and $\boldsymbol{k}''$, where the energy denominator is abbreviated for simplicity. Consider the contribution of two time-reversed trajectories indicated in Fig. 2.5 to the summation. $\langle \boldsymbol{k}''|V|\boldsymbol{k}'\rangle = \langle -\boldsymbol{k}'|V|-\boldsymbol{k}''\rangle$ when V has time reversal symmetry [24]; thus, the orbital parts, $\langle -\boldsymbol{k}|V|\boldsymbol{k_2}\rangle\langle \boldsymbol{k_2}|V|\boldsymbol{k_1}\rangle\langle \boldsymbol{k_1}|V|\boldsymbol{k}\rangle$ and $\langle -\boldsymbol{k}|V|-\boldsymbol{k_1}\rangle\langle -\boldsymbol{k_1}|V|-\boldsymbol{k_2}\rangle\langle -\boldsymbol{k_2}|V|\boldsymbol{k}\rangle$, are identical. Moreover, the pseudospin parts $\langle F(\pi)|F(\theta_2)\rangle\langle F(\theta_2)|F(\theta_1)\rangle\langle F(\theta_1)|F(0)\rangle = e^{-i\frac{\pi}{2}} \cos\frac{\pi-\theta_2}{2} \cos\frac{\theta_2-\theta_1}{2} \cos\frac{\theta_1}{2}$ and $\langle F(-\pi)|F(\theta_1-\pi)\rangle\langle F(\theta_1-\pi)|F(\theta_2-\pi)\rangle\langle F(\theta_2-\pi)|F(0)\rangle = e^{i\frac{\pi}{2}} \cos\frac{\pi-\theta_2}{2} \cos\frac{\theta_2-\theta_1}{2} \cos\frac{\theta_1}{2}$ have the same absolute value with different sign. Consequently, two trajectories interfere so that they are cancelled. This result is also

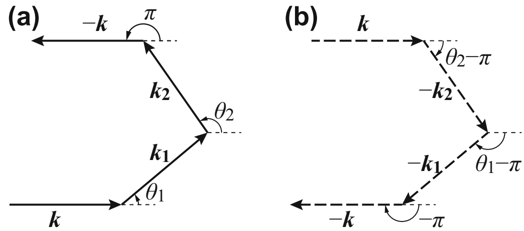

Fig. 2.5 Trajectories of an electron which scatters to back direction. (**a**) Solid path and (**b**) dashed path indicate two time-reversed trajectories. The scattering amplitude of the two trajectories is cancelled

explained by Berry's phase. When an electron makes a round trip in the K′ valley, the pseudospin is also rotated by 2π. Note that wave function gains the Berry's phase of π when the pseudospin is rotated by 2π. The path indicated with a solid line gains the phase of $\pi/2$, while the path with a dashed line gains the phase of $-\pi/2$. Thus, two wave functions have different phase of π, and the interference works to be cancelled. In this way, back scattering is significantly suppressed in graphene. The interference is broken by phase decoherence due to electron-electron, electron-phonon, or spin-flip scattering. Further, the intervalley scattering breaks the interference, although it needs a significant change in the wave vector and can occur only for short-ranged scattering due to defects or edges.

Some readers may notice that the phenomenon is similar to weak anti-localization in disordered 2D systems [56]. In the absence of spin-orbit interaction, the time-reversed paths from $\boldsymbol{k}$ to $-\boldsymbol{k}$ interferes so that the interference is intensified and wave functions are localized [10, 11]. The spin-orbit scattering develops the phase of spin components in the two paths oppositely, and consequently, the two paths interfere to be cancelled. Thus, the coupling of spin and orbit takes an important role for the interference, and its effect is most prominent in graphene. Note again that pseudospin in graphene is not real spin but results from the crystal structure with two sublattices.

Physics discussed at K′ point holds at other valleys with little modification. At the K point of $4\pi/3a(-1, 0)$, the above discussion holds by replacing k_x with $-k_x$. When an electron with $E > 0$ goes around K′ or K point in the clockwise direction, $\boldsymbol{\sigma}$ rotates clockwise about K′ point, while counterclockwise about K point.

2.2.3.3 Magnetic Field Effect

The electronic property of 2D materials is significantly affected by the perpendicular magnetic field, $\boldsymbol{B}$. Lorentz force due to the magnetic field causes circular motion of charged carriers, and the orbital energy is quantized to Landau levels. The effect of magnetic field on the orbital motion is included by replacing $\widehat{\boldsymbol{k}}$ in the Hamiltonian with $\widehat{\boldsymbol{k}}' = \widehat{\boldsymbol{k}} + e\boldsymbol{A}/\hbar$, where $\boldsymbol{A}$ is the vector potential defined as $\boldsymbol{B} = \mathrm{rot}\,\boldsymbol{A}$. Neglecting the Zeeman energy, the Hamiltonian in a conventional 2D system is

$$H = \frac{\hbar^2 \widehat{k}'^2}{2m} = \hbar\omega_c\left(a^+ a + \frac{1}{2}\right) .$$

The creation and annihilation operators are introduced by $a^+ = \frac{l}{\sqrt{2}}\left(\widehat{k}'_x + i\widehat{k}'_y\right)$ and $a = \frac{l}{\sqrt{2}}\left(\widehat{k}'_x - i\widehat{k}'_y\right)$, respectively, where $\omega_c \equiv \frac{eB}{m}$ is the cyclotron frequency and $l \equiv \left(\frac{\hbar}{eB}\right)^{1/2}$ is the magnetic length. These operators satisfy the following relation: $[a, a^+] = 1$, $a\,|n\rangle = \sqrt{n}\,|n-1\rangle$, $a^+\,|n\rangle = \sqrt{n+1}\,|n+1\rangle$, and $a^+ a|n\rangle = n|n\rangle$. Thus, the energy levels are split to Landau levels $|n\rangle$ with eigen energies $E_n = (n + 1/2)\,\hbar\omega_c$ $(n = 0,\ 1,\ 2,\ \ldots)$.

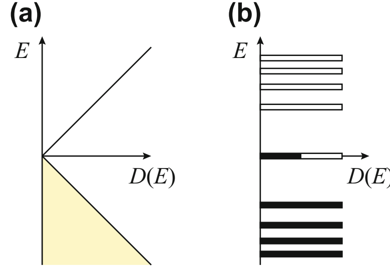

Fig. 2.6 Density of states in graphene. (**a**) Density of states $D(E)$ is a linear function of energy E when no magnetic field is applied. The shaded states are occupied by electrons. (**b**) The Landau levels under a large perpendicular magnetic field. The states at $E < 0$ and half of the states at $E = 0$ are occupied

In contrast, the Hamiltonian for graphene around K′ point is

$$H = \gamma \begin{pmatrix} 0 & \widehat{k_x'} - i\widehat{k_y'} \\ \widehat{k_x'} + i\widehat{k_y'} & 0 \end{pmatrix} = \frac{\sqrt{2}\gamma}{l} \begin{pmatrix} 0 & a \\ a^+ & 0 \end{pmatrix} .$$

The eigen energies are given by $E_n = \pm\frac{\gamma}{l}\sqrt{2n}$ against eigenstates $\begin{pmatrix} 0 \\ |0\rangle \end{pmatrix}$ for $n = 0$ and $\begin{pmatrix} \pm|n-1\rangle \\ |n\rangle \end{pmatrix}$ for $n = 1, 2, \ldots$. The zero energy state in graphene is in contrast to that in the conventional 2D system, where the minimum energy is not zero but a finite value, $E_0 = 1/2\ \hbar\omega_c$. This is because an electron acquires Berry's phase of π when it makes a circler motion around the K or K′ point. The electronic property under magnetic field has been one of the most important research fields in graphene [8, 9, 57–59].

As shown in Fig. 2.6, there is no density of states at $E = 0$ under no magnetic field, while Landau levels for $n = 0$ appear at $E = 0$ under the magnetic field. As a result, the orbital energy of the electrons increases by applying a magnetic field. The increase of free energy F with B means the negative magnetization $\left(M \equiv -\frac{\partial F}{\partial B} < 0\right)$ or diamagnetism. This is the reason why the large diamagnetism is observed in graphene and graphite [2].

2.3 Experimental Aspects

In this section, an experimental procedure is described in the context of fabrication and measurement of graphene FET. The operation of graphene FET and *p*-*n* junction is compared with those of conventional inorganic semiconductors, according to which the characteristic transport property of graphene is emphasized. In addition, the advantages and disadvantages of graphene for application are summarized.

2.3.1 Fabrication of Graphene FET

2.3.1.1 Preparation of Graphene

So far, many methods have been developed to prepare graphene. These are classified into two categories: top-down and bottom-up methods. A typical example of the top-down method is mechanical exfoliation of graphite using an adhesive tape [5]. This method can produce high-quality graphene, although the size of flakes becomes much smaller than that of the initial graphite. Other examples of the top-down method are thermal expansion of graphite intercalated compounds [60] and the reduction of oxidized graphite [61]. A common difficulty for the top-down methods is that the size and thickness of graphene layer cannot be controlled. To solve this problem, the bottom-up methods such as chemical vapor deposition (CVD) are developed [62]. A precise control of deposition condition, such as the kinds of used gasses, substrates, and growth temperature, has improved the quality of graphene. The thermal decomposition of SiC substrate also produces large area of graphene with controlled layer number [63]. In the following sections, sample fabrication using exfoliated graphene is described based on our study.

2.3.1.2 Identification of Graphene

The mechanical cleavage method can produce graphene under dry condition. After repeating the exfoliation of graphite several times, the adhesive face of the tape with thin graphite layers is put down on a SiO_2/Si substrate. Rubbing the back of the tape allows some graphene flakes to be transferred on the substrate. This method enables us to find many graphene flakes with different layer number, N. The electronic property of graphene layers significantly depends on N; thus, it must be distinguished definitely. For this purpose, the various methods have been used such as optical microscopy, Raman spectroscopy, and atomic force microscopy (AFM). Figure 2.7 shows how we determine N with these three methods [64].

First, N is easily distinguished by the contrast of the optical microscope image when the thickness of SiO_2 on the Si substrate is optimized [65]. Figure 2.7a shows an optical micrograph of graphene flakes prepared on the SiO_2 layer of 300 nm. It is observed that the color becomes deep with increasing the layer number. When the color image is split to R/G/B channels, the contrast of few-layer graphene is most prominent in G channel. The intensity in G channel is digitized and quantified by using an image analyzing software such as imageJ [66] to determine N.

Second, Raman spectroscopy, which is a versatile tool to investigate the electronic structure of graphitic materials, is applicable to identification of N [67, 68]. Graphene has prominent two peaks at around 1590 and 2700 cm^{-1}, which are called G and 2D peaks, respectively. As shown in Fig. 2.7b, the ratio of intensity of these peaks $I(G)/I(2D)$ and the shape of 2D peak significantly depend on N [69]. Raman D peak is observed at around 1350 cm^{-1} when defects are present, which is useful

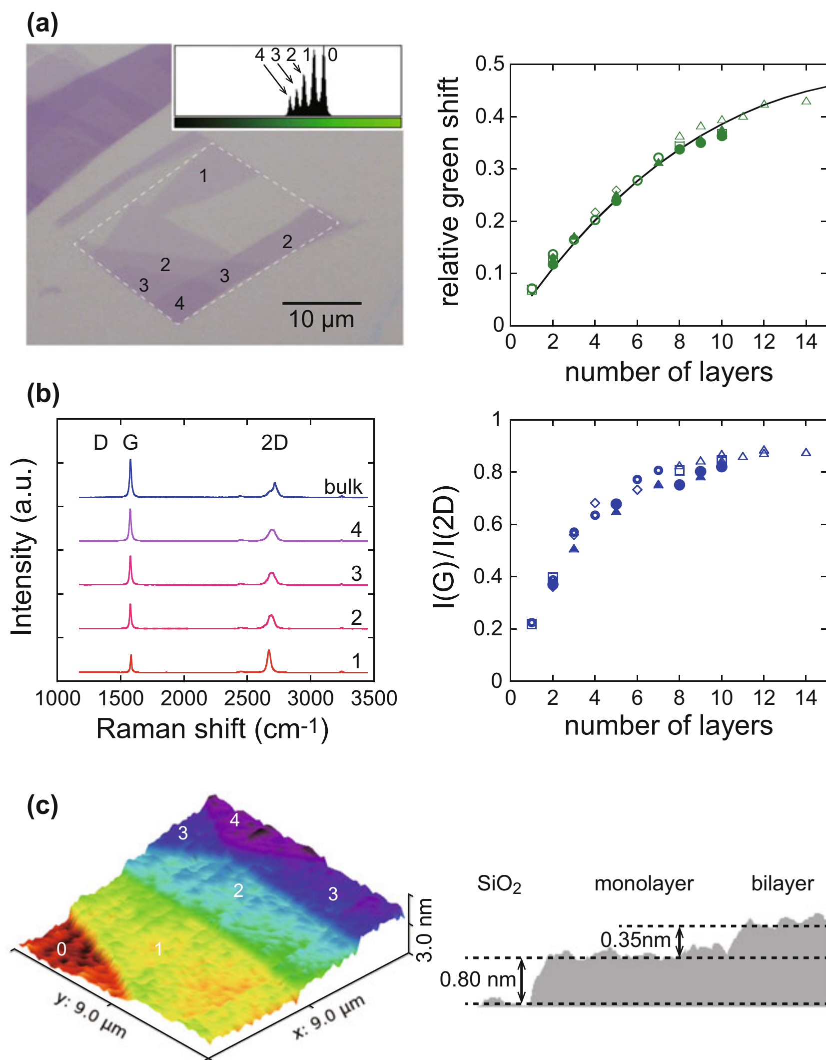

Fig. 2.7 Three methods to distinguish layer number of graphene flakes. (**a**) Left: microscope image of graphene flakes. Inset: histogram of green intensities in the microscope image enclosed with dashed lines. The number, 0–4, indicates the layer number of graphene, which gives the peak of the histogram. Right: layer number dependence of relative green shift (RGS). RGS is defined by $(G_s - G_f)/G_s$, where G_f and G_s are the green intensities of FLG and the substrate, respectively. (**b**) Left: Raman spectra of the N-layer graphene ($N = 1$–4) and bulk graphite. The spectra are normalized to give the same 2D peak intensity. Right: layer number dependence of ratio of G and 2D peak intensities. (**c**) Left: atomic force microscope image. Right: height steps across the surfaces of SiO_2, mono-, and bilayer graphene. Some of the figures were used in the supplementary information of [64] (Copyright 2013 The Author(s))

to verify the quality of graphene. In addition, Raman spectroscopy is effective to distinguish the ABA and ABC stacking manner of few-layer graphene [70] and geometries of armchair and zigzag edges [71].

Finally, AFM can measure the height of the graphene layer from the substrate directly. As shown in Fig. 2.7c, the distance between monolayer and bilayer graphene was measured to be 0.35 nm, which agrees well with the literature value, 0.334 nm. The distance between the SiO_2 surface and monolayer graphene was 0.80 nm, which is reasonable considering the additional van der Waals distance between the two materials [9]. AFM is also applicable to investigate the flatness of graphene layer [72, 73].

2.3.1.3 Preparation of Devices

After finding out the suitable graphene flakes, we attach electrodes to them. The exfoliated flakes are at most 10 μm in size; thus, microfabrication techniques, such as photolithography or electron-beam lithography (EBL), are required to design the electrodes. Graphene has the chemical stability for organic solvent and heating process, which makes microfabrication of graphene easy. The flakes on substrates are coated with polymer resists, which change the solubility after an exposure of UV light or electron beam. The resolution of the photolithography is in principle limited by the wavelength of the light, however, to several μms because of imperfect contact between a photomask and a substrate. EBL is superior to the photolithography for the high resolution and the accurate alignment. The flexible design of electrodes is also advantage of EBL for the purpose of laboratory research. Figure 2.8 shows typical procedure to make a graphene Hall bar with EBL.

2.3.2 Characteristics of Graphene FET

2.3.2.1 Output and Transfer Characteristics

First, we introduce the characteristics of typical inorganic FET in metal-oxide-semiconductor (MOS) structure to compare them with graphene FET. Figure 2.9a shows a schematic of inorganic MOS-FET, which is made of *p*-type semiconductor exhibiting an enhanced *n*-channel operation. The device has three electrodes: drain, source, and gate electrodes labeled with D, S, and G. D and S are highly *n* doped, thus, noted with n_+. The drain voltage V_d is applied to D, while S is grounded, i.e., source voltage V_s is 0. Drain current I_d flowing between D and S is controlled by V_d and gate voltage V_g. At $V_g = 0$, $I_d = 0$ because of the n_+-p-n_+ structure. By applying positive V_g, the conduction band bends downward at the interface. Consequently, electrons accumulate at the interface called inversion layer (refer Fig. 2.9b), and I_d starts to flow because of the n_+-n-n_+ structure. A set of I_d-V_d curves for several V_g values is called output characteristics (Fig. 2.9c). I_d increases in proportion to

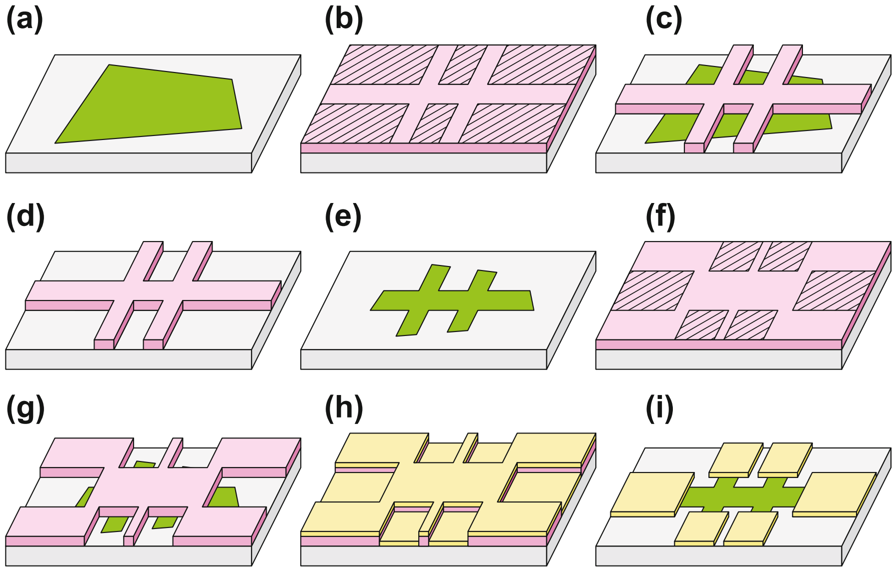

Fig. 2.8 Preparation procedure of graphene device with Hall bar structure. (**a**) Transfer of graphene flakes on SiO_2/Si substrate. (**b**) Resist coating and prebake. Hatched regions are exposed by electron beam. (**c**) Development after exposure of electron beam. (**d**) Oxygen plasma etching. The residual resist works as an etching mask. (**e**) Removal of the resist. (**f**) Resist coating and prebake. Hatched regions are exposed by electron beam. (**g**) Development after exposure to electron beam. (**h**) Vacuum deposition of metal for electrodes. (**i**) Lift-off. The disused metal is removed

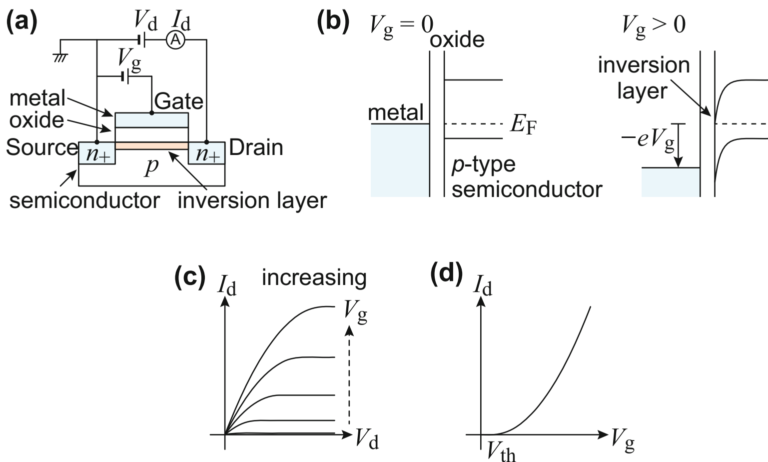

Fig. 2.9 Structure and characteristics of MOS-FET. (**a**) Schematic structure and terminal configuration. (**b**) Energy band diagrams at $V_g = 0$ and $V_g > 0$. (**c**) Output characteristic based on the simple model. (**d**) Transfer characteristic in the saturation region

V_d at small V_d satisfying $V_d << V_g - V_{th}$ (linear region), and it saturates with large V_d for $V_d >> V_g - V_{th}$ (saturation region). Moreover, $I_d - V_g$ curve is called transport characteristics (Fig. 2.9d). With the increasing V_g, I_d starts to increase at the threshold voltage V_{th}. From the transport curve, we can evaluate the mobility of the device, which is an important parameter characterizing the FET operation. The mobility is defined by $\mu \equiv v/E$, where v is the drift velocity of carriers and E is an applied electric field. Depending on the magnitude of V_d, mobility is obtained by the following formulae [28]:

$$I_d = \frac{W\mu}{L} C_o \left(V_g - V_{th}\right) V_d \text{ in the linear region,} \tag{2.10}$$

$$I_d = \frac{W\mu}{2L} C_o \left(V_g - V_{th}\right)^2 \text{ in the saturation region,} \tag{2.11}$$

where L and W are channel length and width, respectively, and C_o is the capacitance of gate insulator per unit area. For a detailed deduction of these equations and physical meaning of the both regions, see Ref. [28].

Compared with inorganic MOS-FETs, graphene FET shows very different characteristics because of the linear energy dispersion with no energy gap. Figure 2.10a shows the structure of typical four-terminal graphene FET which is often used for research purpose. The current I flows between the electrodes at both ends (noted by I_+ and I_-) and the potential difference V between two electrodes placed inside (noted by V_+ and V_-) is measured. The V-I curves measured at various V_g show a linear Ohmic relation, as in Fig. 2.10c. The sheet conductance σ is evaluated

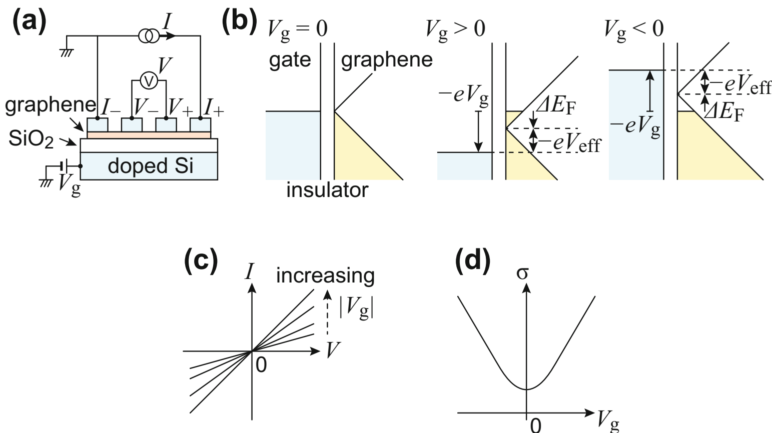

Fig. 2.10 Structure and characteristics of graphene FET. (**a**) Schematic structure and terminal configuration of the four-terminal graphene FET. (**b**) Band diagrams of a gate electrode and graphene. The Fermi level of graphene is controlled by V_g. (**c**) Output and (**d**) transfer characteristics

by $\sigma = \frac{L}{W}\frac{dI}{dV}$, where L is the distance between the voltage electrodes and W the width of graphene channel. In this chapter, σ always means the sheet conductance with a unit of S ($=\Omega^{-1}$) and is hereafter simply termed conductivity. Typical σ-V_g curve is illustrated in Fig. 2.10d. As described in Sect. 2.2.2, the Fermi energy E_F of non-doped graphene is situated at the Dirac point. Thus, the conductivity σ takes minimum at around $V_g = 0$. When positive V_g is applied, electrons are accumulated in graphene, and the conductivity increases (refer Fig. 2.10b). Moreover, application of negative V_g accumulates holes, also increasing the conductivity. In this way, graphene FET shows ambipolar behavior, which operates by both *n*- and *p*-type carriers. The carrier density induced by gate voltage is given by $n = C_o V_g/e = \alpha V_g$, where $C_o = \varepsilon_0\varepsilon/d$ is geometrical capacitance determined by relative permittivity ε and thickness d of the gate insulator. $\varepsilon_0 = 8.854 \times 10^{-14}$ F cm^{-1} is permittivity of vacuum, and positive/negative n means the electron/hole density, respectively. $C_o = 11.5$ nFcm^{-2} and $\alpha = 7.18 \times 10^{10}$/cm^2 V for 300 nm-thick SiO_2 with $\varepsilon = 3.9$. Corresponding to Eq. (2.10) for MOS-FET in the linear region, the conductivity is expressed by

$$\sigma = |n|e\mu = C_o\,|V_g - V_n|\,\mu \ . \tag{2.12}$$

$V_n \sim 0$ is the charge neutrality point, meaning that σ takes the minimum value at $V_g = V_n$. This equation is oversimplified because the conductance at V_n and the energy dependence of scattering are neglected. For comprehensive discussion of σ-V_g curve, see Ref. [54, 73, 74]. Furthermore, V_g in Eq. (2.12) should be replaced by V_{eff} indicated in Fig. 2.10b; the potential difference between the gate electrode and graphene decreases from V_g to V_{eff}, after the shift of Fermi energy due to the carrier accumulation. This correction can be neglected when C_o is very small as in the case of 300 nm-thick SiO_2. However, the effect becomes important for large C_o, which will be discussed in Sect. 2.4.1.

From Eq. (2.12), the mobility is given by

$$\mu = \frac{1}{C_o}\left|\frac{d\sigma}{dV_g}\right|. \tag{2.13}$$

The hole mobility μ_h and electron mobility μ_e are obtained in the regimes at $V_g < V_n$ and $V_g > V_n$, respectively. For the graphene FET prepared on SiO_2/Si substrate, σ often increases linearly with respect to $|V_g|$, as shown in Fig. 2.10d, indicating that μ is independent of V_g. Similarly, μ of MOS-FET is also considered to have a constant value. However, there is an important difference between the two FETs. Based on the Drude model [26], the mobility is given by

$$\mu = \frac{e\tau}{m^*} \ . \tag{2.14}$$

For MOS-FET, constant scattering time, τ, and effective mass, m^*, give constant mobility. In contrast,

$$\mu = \frac{e\tau v_F}{\hbar k_F} = \frac{e\tau v_F}{\hbar\sqrt{\pi n}} = \frac{e\tau v_F}{\hbar\sqrt{\pi\alpha\left|V_g\right|}}$$

holds for the graphene FET. Thus, constant mobility means that τ depends on $|V_g|^{1/2}$. Such scattering is known to be long-ranged Coulomb scattering by charged impurities [54, 74, 75]. For graphene devices on the SiO_2/Si substrates, this is one of the most important scattering factors limiting the mobility.

2.3.2.2 Graphene *p-n* Junction

The transport property through the graphene *p-n* junction is very different from that in a conventional *p-n* junction made of inorganic semiconductors. This is also because of the linear dispersion in graphene and interpreted by the tunneling phenomena in relativistic quantum physics.

It is well known that the *p-n* junction formed by inorganic semiconductors is used for rectification of electric current. Figure 2.11 shows the band diagram of the *p-n* junction and a principle of the rectification. The alignment of the Fermi energy between the *p*- and *n*-type semiconductors forms built-in potential ΔE (>0) at the interface. When a positive voltage is applied to the *p* side, the current increases abruptly with a decrease in ΔE. In contrast, when a negative voltage is applied to the *p* side, ΔE increases to suppress the current. This explains the rectifying *IV* characteristics of the *p-n* diode.

In contrast, the graphene *p-n* junctions do not exhibit this rectifying property. Figure 2.12a shows a band diagram and Fermi circle of the graphene *p-n* junction. The potential energy indicated by the dashed line is higher in the *p* region than that

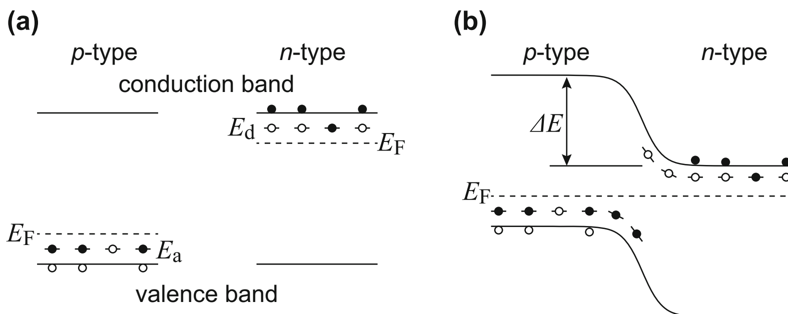

Fig. 2.11 *p-n* junction of conventional semiconductors. (**a**) Band diagrams of *p*- and *n*-type semiconductors. E_a and E_d indicate the acceptor and donor levels, respectively. (**b**) Band diagram of a *p-n* junction. As a result of the alignment of E_F, the potential step ΔE is built at the interface

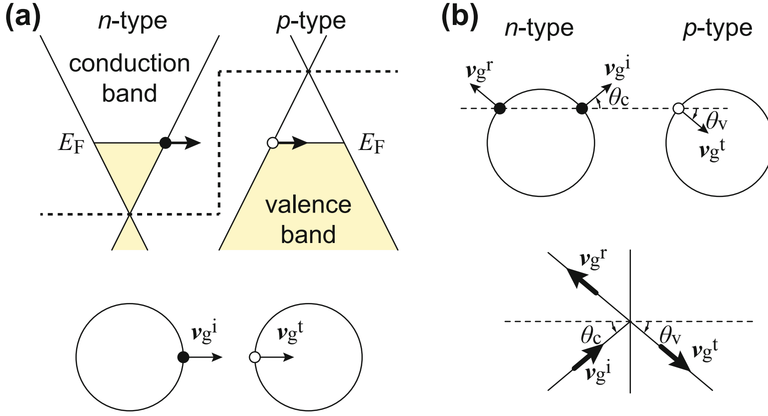

Fig. 2.12 *p-n* junction of graphene FET. (**a**) Band diagrams and Fermi circles of *n*- and *p*-doped graphene. An electron of the black circle with group velocity $\boldsymbol{v}_g{}^i$ is incident normal to the interface. It is transmitted as a hole of the white circle with group velocity $\boldsymbol{v}_g{}^t$. (**b**) Fermi circles of graphene *p-n* junction in which an obliquely incident electron is transmitted or reflected. The arrows $\boldsymbol{v}_g{}^i$, $\boldsymbol{v}_g{}^t$, and $\boldsymbol{v}_g{}^r$ indicate group velocity of incident, transmitted, and reflected electron waves, respectively

in the *n* region, which is realized by applying different gate voltages locally. When an electron was injected from *n* to *p*-doped graphene, the electron does not reflect but can transmit through the interface with a probability of 1. This is because the electron in the *n* region is transformed to the hole in the *p* region with the same group velocity, $\boldsymbol{v}_g{}^i = \boldsymbol{v}_g{}^t$. For the graphene *n-p-n* junction, an electron in one *n* region can be transmitted to the other *n* region through the *p* region. This perfect tunneling through a potential barrier is called Klein tunneling, which is suggested in relativistic quantum dynamics. This phenomenon is in contrast to the conventional quantum physics, where an electron can tunnel the potential barrier with certain probability. In this way, graphene offers a unique opportunity to study relativistic quantum phenomena [76, 77].

Further, let us look at the junction from a top side. As described, a normally injected electron from the *n* side is transmitted to the *p* side without reflection. Figure 2.12b shows the Fermi circle of *n*- and *p*-doped graphene and shows how an obliquely injected electron is transmitted and reflected. The momentum parallel to the interface, which is indicated by the dashed line, is preserved. Thus, an injected electron with group velocity $\boldsymbol{v}_g{}^i$ is reflected with $\boldsymbol{v}_g{}^r$ in the *n* region or transmitted to $\boldsymbol{v}_g{}^t$ in the *p* region. The transmission probability is $T = \cos^2\theta_c / \cos^2(\theta_c/2 + \theta_v/2)$ [78]. When the magnitude of a wave vector in the *n*- and *p*-doped graphene is equal, $\theta_c = -\theta_v$ and $T = \cos^2\theta_c$. As shown in the lower panel in Fig. 2.12b, an electron wave packet is refracted as if it is transmitted to a material with the negative refractive index [78, 79]. This type of peculiar refraction is a popular topic in optics with metamaterials [80] and may be studied using an electron wave in graphene.

2.3.3 Advantages and Disadvantages of Graphene for Device Application

2.3.3.1 Advantages of Graphene

Graphene has a lot of advantages in device application. They are classified according to specific properties of graphene.

A1: (linear energy dispersion) high carrier mobility, long coherence length, and long spin relaxation length
A2: (strong sp^2 bonding) chemically inert and stable, flexible and robust, and high heat conductivity
A3: (atomically thin layer) transparent, lightweight, large specific surface area, and less short-channel effect
A4: (carbon-based material) low cost and easy fabrication of devices
A5: (no energy gap) good contact with metal electrodes

In particular, high mobility is one of the most prominent properties of graphene. The larger μ means the better performance of FET; high mobility enables rapid operation, low power dissipation, and high sensitivity. Compared with $\mu = 1450$ cm^2/Vs for Si at 300 K [28], the typical μ value reaches 10,000 for graphene on SiO_2/Si substrates. The mobility is expressed by $\mu = e\tau/m^*$ (Eq. (2.14)). In graphene, τ is significantly enhanced because of the absence of back scattering. τ is also enhanced in high-quality graphene without impurities or lattice defects. In addition, m^* ($\sim\hbar k/v_F$) is extremely small around the Dirac point, which also increases μ. The mobility of graphene is still limited by the scattering because of the charge impurities on SiO_2/Si. The mobility can be improved furthermore by suspending graphene in vacuum [81–83] or by putting graphene on chemically inert and atomically flat h-BN [73, 84]. Actually, μ of 0.2–1 $\times$ 10^6 cm^2/Vs was achieved for suspended graphene at low temperature [81, 83].

Large μ offers unique opportunity to study some new physical phenomena. First, an increase in τ enhances the mean free path (or elastic scattering length) l ($\equiv v_F\tau$) over 1 μm [81]. When the sample size L is much larger than l, transport is diffusive. In the graphene, the opposite condition ($L < l$) can be prepared, which realizes the ballistic transport with no scattering in the system. Second, a large μ also increases the coherence length and spin relaxation length. These characteristic lengths express how long the coherence of phase or spin is preserved. Such long characteristic lengths are useful to study mesoscopic physics and spintronics [85, 86].

Strong sp^2 bonding [87] between the carbon atoms is important in mechanical applications, such as microelectromechanical systems (MEMS) [88]. It is also known that thermal conductivity is extremely enhanced in monolayer graphene due to the 2D character [89].

Graphene is an extremely thin material; thus, the transparent property [90] is suitable for electrodes in solar cell [91]. The large specific surface area is applicable to supercapacitors. Furthermore, atomically thin graphene may not suffer from

short-channel effect [28], which causes inevitable problems when miniaturizing FET devices.

Because of no energy gap, Schottky barrier [28] is not formed at the interface between graphene and metal electrodes, which establishes their good electrical contact. This made graphene good candidate for research targets. An example is the superconducting proximity effect [92, 93], which is not observed if there is large contact resistance between graphene and superconducting electrodes.

2.3.3.2 Disadvantages of Graphene

A major problem for an application is that graphene has no energy gap. Finite current can flow even at the Dirac point, and perfect OFF state is not realized (see Fig. 2.10d). Thus, the on/off ratio of the graphene FET, which is defined by the ratio of the maximum and minimum current, is relatively low. In addition, the output characteristic is linear and not saturated as shown in Fig. 2.10c, which decreases the cutoff frequency for the radiofrequency application [94]. Consequently, it may be difficult to prepare practical logic devices and high-speed devices from graphene [94]. Thus, TMDs and other 2DMs with a band gap have attracted much attention recently. Some methods are proposed to open the band gap by breaking the symmetry of graphene layers as follows:

1. Monolayer graphene with the breaking of AB sublattice symmetry [43]
2. Bilayer graphene under a perpendicular electric field [95, 96]
3. ABC-stacked trilayer graphene under a perpendicular electric field [97, 98]
4. Graphene nanoribbons [99, 100]
5. Graphene derivatives such as graphane [101]

The size of a band gap is variable by the magnitude of electric field for (2) and (3) and by the width of graphene nanoribbon for (4). One problem is that the mobility may be decreased with opening the band gap. To reconcile high mobility and large band gap is a challenge for the future.

2.4 Application of Graphene FET: Carrier Accumulation in Graphene

In the final section, an application example of graphene FET is given based on our recent study [64, 102–104]. We attempt carrier doping in graphene with two methods by evaluating the carrier density quantitatively. As a result, the problem that prevents the effective carrier accumulation is clarified.

The electronic structure of graphene has two singularities. One is the topological singularity at $E = 0$ (K/K′ point or the Dirac point). This singularity leads to Berry's phase which affects the motion of carriers as described at Sect. 2.2.3. The other is

van Hove singularity at $E = \pm\gamma_0 \sim \pm3.0$ eV (M point). The electron correlation is enhanced at this energy because the density of states diverges as in Fig. 2.3c. In addition, the Fermi surface is a regular hexagon with high symmetry at M point (refer Fig. 2.3b), which can give rise to various ordered phenomena, such as superconductivity, ferromagnetism, and spin/charge density waves [105–108]. For superconductivity, occurrence of chiral d-wave superconductivity [108] is predicted besides conventional s-wave superconductivity.

However, such an exotic state has not been realized due to the experimental difficulty of achieving the high energy state. As shown in Fig. 2.3b, the carrier density required to reach the van Hove singularity is 1/4 carriers per carbon atom, i.e., 9.5×10^{14} cm^{-2}. So far, two methods have been often used to control the number of carriers. One utilizes an electric field effect in the FET structure (gating method) as shown in Fig. 2.10b. The other uses electron transfer between the dopants and target materials (doping method). In general, these two methods are assumed to work equivalently for carrier accumulation. Both methods have been used to control the carrier density and electric conductance in semiconductors [28]. Furthermore, each method has been successfully utilized to induce superconductivity in materials, such as $SrTiO_3$ [109, 110] and TMDs [111, 112], by enhancing the carrier density. In this section, we explore the possibility of high-density carrier accumulation in graphene using these two methods.

2.4.1 *Electric Field Effect on Few-Layer Graphene with Ionic Liquid Gate*

First, carrier accumulation with the gating method is discussed. The carrier density n induced by V_g is expressed as $n = C_g V_g/e$, where $C_g = \varepsilon_0\varepsilon/d$ is the geometrical capacitance, which was denoted with C_o in Sect. 2.3. As described in Sect. 2.3.1, SiO_2 with ε of 3.9 and d of 300 nm is often used for the gate electric for graphene FETs, which leads to $C_g = 11.5$ nF cm^{-2}. The maximum gate voltage applicable to 300 nm-thick SiO_2 is at most $V_g \sim 100$ V, which can induce carrier density of $n = C_g V_g/e \sim 7.2 \times 10^{12}$ cm^{-2}. Therefore, to accumulate higher density of carriers in graphene with the gating method, it is necessary to use a gate dielectric with much larger capacitance. C_g can be enhanced by increasing ε or by decreasing d. To use high-κ (high dielectric constant) materials such as $Pb(Zr_{0.47}Ti_{0.53})O_3$ (PZT, $\varepsilon > 1000$), $SrTiO_3$ (STO, $\varepsilon = 140$), Ta_2O_5 ($\varepsilon = 25$) [28], etc. is one approach to increase C_g. The other approach, a reduction of d, is achieved by using an electric double layer (EDL) for a gate dielectric [113]. When applying gate voltage to a target material via an electrolyte such as an ionic liquid, the EDL is formed at the interface between the material and the electrolyte, which works as a very thin gate dielectric. Although the applicable gate voltage is limited to several volts to avoid chemical reaction, the achievable carrier density is nevertheless expected to be 10^1–10^2 times larger than that with

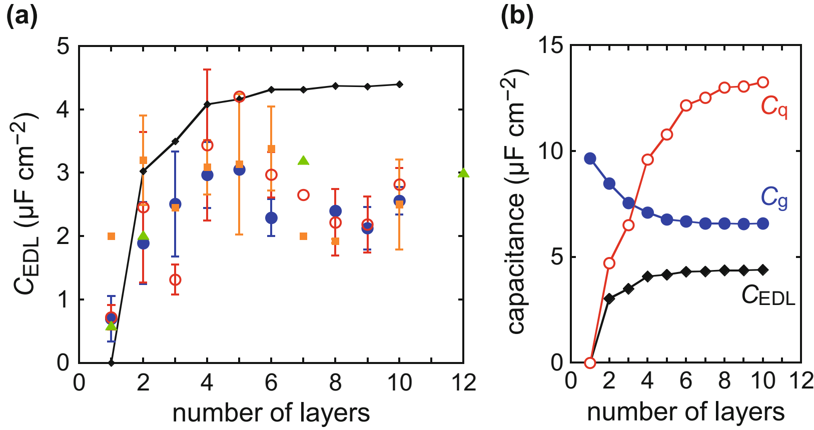

Fig. 2.13 Layer number dependence of capacitance at EDL. (**a**) Experimental capacitances evaluated with three methods. The blue solid circles and red open circles indicate the C_{EDL} values measured in hole-carrier and electron-carrier regimes, respectively, using two-terminal devices. The green triangles indicate the C_{EDL} values evaluated from Hall coefficients. The orange squares indicate the C_{EDL} values directly measured with AC. The black solid line shows calculated C_{EDL}. (**b**) Calculated capacitances as a function of N. Geometrical capacitance C_g, quantum capacitance C_q, and EDL capacitance C_{EDL} are indicated by blue, red, and black lines, respectively. Reproduced from our previous report [64] (Copyright 2013 The Author(s))

conventional gate insulator. For example, C_g of EDL formed between an ionic liquid, [1-butyl-3-methylimidazolium][hexafluorophosphate] (bmim[PF_6]), and an Au electrode is 9.7 μF cm^{-2} [114], which is 10^3 times larger than C_g of 300 nm-thick SiO_2. When applying $V_g = 2$ V using bmim[PF_6], carriers of $C_g V_g / e = 1.2 \times 10^{14}$ cm^{-2} can be accumulated in the Au electrode. Among a variety of ionic liquids, there is an ionic liquid that has extremely large C_g [115]. Furthermore, applicable V_g can be raised at low temperature [116]. Thus, the electric field effect using ionic liquid gate may enable us to reach the van Hove singularity in graphene.

According to our previous study [64], we discuss the capacitance C_{EDL} between the ionic liquid, bmim[PF_6], and few layers of graphene to explore the possibility of novel physical property in highly doped graphene. Figure 2.13a shows C_{EDL} values as a function of layer number, N, which is experimentally evaluated with three methods. As shown in Fig. 2.13a, measured C_{EDL} is much smaller than $C_g = 9.7$ μF cm^{-2} obtained for the Au electrodes. C_{EDL} is minimum for monolayer graphene. With an increase in N, C_{EDL} increases and takes the maximum value of 3 μF cm^{-2} at $N \sim 4$. With a further increase in N, C_{EDL} slightly decreases to saturate. Even at maximum C_{EDL}, the carrier concentration is estimated to be 4×10^{13} cm^{-2} for $V_g = 2$ V.

The reason why C_{EDL} for monolayer graphene is so small is explained by the concept of quantum capacitance [117–119], as mentioned in Sect. 2.3.2. As shown in Fig. 2.10b, when the positive gate voltage V_g is applied to the ionic liquid, the

Fermi energy changes by ΔE_F ($\Delta E_F < 0$) so that the actual voltage difference V_{eff} between the ionic liquid and graphene becomes smaller than V_g. Thus, the applied voltage is divided into two components: $-eV_g = \Delta E_F - eV_{\mathrm{eff}}$ or

$$V_g = \frac{-\Delta E_F}{e} + V_{\mathrm{eff}} \equiv \frac{Q}{C_q} + \frac{Q}{C_g} \equiv \frac{Q}{C_{\mathrm{EDL}}} \quad , \tag{2.15}$$

where V_{eff} is the effective voltage difference between the ionic liquid and graphene, which accumulates charges $\pm Q$ according to $Q = C_g V_{\mathrm{eff}}$. We consider that the deficient voltage due to $-\Delta E_F/e$ is applied to an imaginary capacitor, whose capacitance is $C_q \equiv \frac{eQ}{-\Delta E_F} = \frac{e^2 D(E)}{2}$, called quantum capacitance. As a result, the total capacitance $C_{\mathrm{EDL}} \equiv Q/V_g$ is expressed by a series connection of two capacitors, $C_{\mathrm{EDL}} = \left(C_q^{-1} + C_g^{-1}\right)^{-1}$. For graphene, C_q is extremely small because of the small $D(E)$ around the Dirac point. When the conventional SiO_2 gate dielectric is used, the C_g is still smaller than C_q of graphene, and the effect of C_q does not appear. However, for the ionic liquid gate, C_g of EDL can exceed C_q, which leads to $C_{\mathrm{EDL}} \sim C_q << C_g$. Thus, the ionic liquid-gated graphene is a unique system where the effect of C_q becomes prominent because of large C_g and small C_q.

The expressions for C_g and C_q of monolayer graphene can also be deduced from the electrostatic energy condensed between the ionic liquid and graphene. As shown in Fig. 2.14a, application of gate voltage changes total energy U_{EDL} which consists of two kinds of contributions; one is electric field energy U_g condensed between the ionic liquid and graphene, and the other is the band filling energy U_q to accumulate electron to change the Fermi energy. U_g and U_q are expressed by the following equations (refer Fig. 2.14a) and related to the capacitances C_g and C_q, respectively:

$$U_g = \frac{1}{2}\int \boldsymbol{E}\cdot\boldsymbol{D}d\boldsymbol{r} = \frac{1}{2}\varepsilon_{\mathrm{IL}}\varepsilon_0 \boldsymbol{E}^2 d \equiv \frac{Q^2}{2C_g} \quad , \tag{2.16}$$

$$U_q = \int_0^{E_F} E D(E) dE \equiv \frac{Q^2}{2C_q} \quad , \tag{2.17}$$

where $\boldsymbol{E}$ and $\boldsymbol{D}$ ($=\varepsilon\varepsilon_0\boldsymbol{E}$) in Eq. (2.16) indicate the electric field and electric displacement, respectively, while E in Eq. (2.17) indicates the energy of an electron measured from the Dirac point. From Eqs. (2.16) and (2.17), one obtain familiar expressions $C_g = \varepsilon_0\varepsilon/d$ and $C_q = e^2D(E)/2$. Furthermore, the equation of total energy $U_{\mathrm{EDL}} = U_g + U_q$ agrees with the energy of the series capacitors, $1/C_{\mathrm{EDL}} = 1/C_g + 1/C_q$. Note that the expression of C_q is different from the conventional quantum capacitance for 2D materials, $C_q = e^2D(E)$ [117]. This is because $D(E)$ for graphene is a linear function of E, while it is constant for conventional 2D electron systems. Even in the graphene, if the capacitance is estimated from AC impedance, which is measured with small AC voltage superimposed by the DC voltage, $C_q = e^2D(E)$ should be used by neglecting E dependence of $D(E)$.

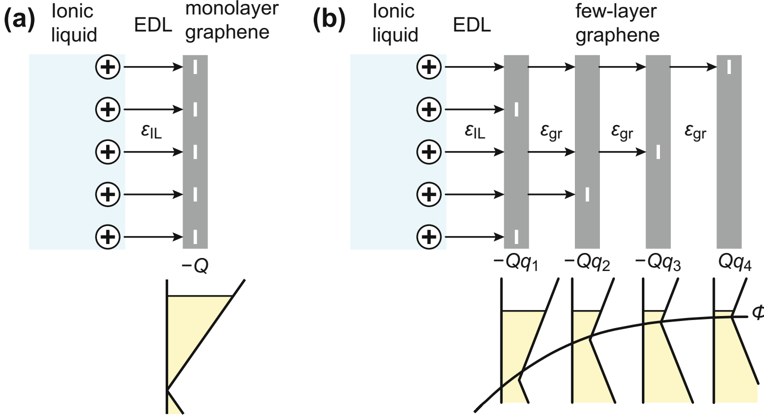

Fig. 2.14 Electrostatic energy in EDL capacitor between an ionic liquid and (**a**) monolayer graphene/(**b**) few-layer graphene. Total energy consists of the electric field energy U_g and band filling energy U_q, which are illustrated at upper and lower panels, respectively. U_g and U_q are related to the geometrical and quantum capacitances, respectively

The above discussion about the monolayer graphene can be developed for N-layer graphene (refer Fig. 2.14b). The positive and negative charges, $\pm Q$ ($Q > 0$), are placed on each side of EDL; $+Q$ is at the side of an ionic liquid, while $-Qq_1, \ldots, -Qq_N$ are distributed in 1, …, Nth layers of FLG. The ordinals are given from the interface. U_g and U_q are written by referring to Fig. 2.14b and extending Eqs. (2.16) and (2.17)

$$U_g = \frac{Q^2}{2C_{IL}} + \frac{Q^2}{2C_{gr}} \sum_{i=1}^{N-1} \left(1 - \sum_{j=1}^{i} q_j \right)^2 \equiv \frac{Q^2}{2C_g} \quad , \tag{2.18}$$

$$U_q = \frac{1}{N} \sum_{i=1}^{N} \int_0^{E_{Fi}} E D_N(E) dE \equiv \frac{Q^2}{2C_q} \quad , \tag{2.19}$$

where U_g is sum of the field energy in the EDL and ith and $i+1$th layer of graphene ($i = 1$ to $N-1$). C_{IL} and C_{gr} are the geometrical capacitances in EDL and adjacent graphene layers, respectively. $D_N(E)$ is the density of states for N-layer graphene, and $D_N(E)/N$ is that per one layer. E_{Fi} is the Fermi energy of ith layer. Assuming the constant $D_N(E) = D_N(0)$ for simplicity, Eq. (2.19) is reduced to

$$U_q = \frac{D_N(0)}{2N} \sum_{i=1}^{N} {E_{Fi}}^2 = \frac{Q^2 N}{2e^2 D_N(0)} \sum_{i=1}^{N} {q_i}^2 \equiv \frac{Q^2}{2C_q}. \tag{2.20}$$

U_g is minimum when $q_1 = 1$ and $q_2 = \ldots = q_N = 0$, while U_q is minimum when $q_1 = \ldots = q_N = 1/N$. The actual distribution of q_i is determined by minimizing the total energy $U_{EDL} = U_g + U_q$ under the restriction of $\sum_{i=1}^{N} q_i = 1$. This can be solved using the method of Lagrange multipliers. Once q_is are determined, C_g and C_q are obtained from Eqs. (2.18) and (2.20). Calculated capacitances C_g, C_q, and C_{EDL} are shown in Fig. 2.13b as a function of layer number N. With increasing N, C_q increases, while C_g decreases. C_{EDL} is determined by smaller capacitance of C_g and C_q; thus, C_{EDL} increases to saturate with an increase in N. The calculated C_{EDL} is also indicated in Fig. 2.12a, which shows a good agreement with the experimental data.

Physical meaning of layer number dependence of three capacitances is explained as follows. C_q is proportional to $D_N(E)$ which increases with N. However, note that the electric field is screened by three to four layers and cannot penetrate into the thicker layer than the screening length. Thus, C_q increases with N and $D_N(E)$, but saturates in thicker graphene layers. Moreover, decrease in C_g is due to the penetration of electric field into the interior layer of FLG. This corresponds to the expansion of d of the EDL capacitor, and the advantage of thin EDL is spoiled. With the increasing N, C_g also saturates because of the screening of the electric field. The magnitude relation of C_q and C_g is inversed at $N = 4$; thus, C_{EDL} of thicker FLG is determined by C_g, which is significantly smaller than C_g for $N = 1$.

Finally, we investigate the condition of an ionic liquid to reach the van Hove singularity of the monolayer graphene. From Eq. (2.15), the required gate voltage is

$$V_g = \frac{\gamma_0}{e} + \frac{ne}{C_g} \quad . \tag{2.21}$$

Inserting $\gamma_0/e = 3$ V and $n = 9.5 \times 10^{14}$ cm^{-2} into Eq. (2.21), we obtain $V_g = 3 + 160/C_g$, where the units of V_g and C_g are V and μF cm^{-2}, respectively. For example, if we can apply V_g of 5 V to an ionic liquid with C_g of 80 μF cm^{-2}, Fermi energy can shift to the van Hove singularity.

2.4.2 *Doping Effect on Monolayer Graphene with Electron Transfer Molecules*

Further, we discuss carrier doping by utilizing electron transfer between graphene and adsorbed molecules. Combining graphene with organic molecules can offer rich physics through carrier accumulation or energy-band modification. First, a high density of carriers may be accumulated in graphene densely covered with molecules. If a carrier of 9.5×10^{14} cm^{-2} (0.25/carbon atom) is accumulated, the Fermi energy E_F reaches the van Hove singularity, leading to various ordered states [105–108]. Further, if the molecule is exactly deposited to cause a difference in the potential

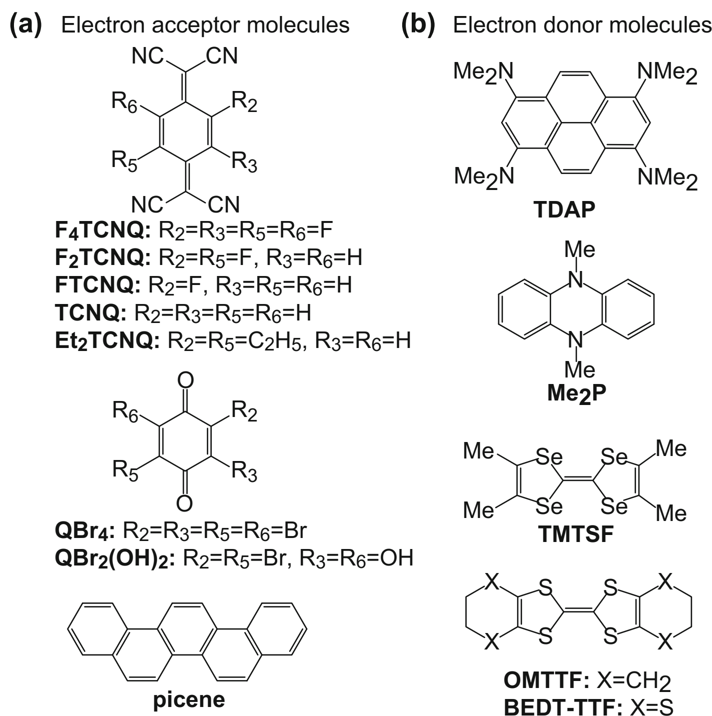

Fig. 2.15 Molecular structures used in this study. (**a**) Electron acceptor molecules and (**b**) electron donor molecules. TDAP is added to the molecules used in our previous report [103]

energy between two sublattices of graphene, a novel graphene with an energy gap would be produced. Although the effects of the adsorbed molecules and atoms on the electronic properties of graphene have been extensively studied [120–124], there has been no quantitative study on what property of molecules influences electron transfer between molecules and graphene. In this section, we investigate the carrier accumulation in graphene by depositing diverse electron acceptor/donor molecules on graphene. Details of this study are reported in Ref. [103].

Figure 2.15 shows the eight electron acceptor molecules and five donor molecules used in this study; one donor molecule, 1,3,6,8-tetrakis(dimethylamino) pyrene (TDAP), was added since our previous report [103]. The molecules were thermally deposited on graphene under a vacuum of 10^{-4} Pa, and the gate voltage dependence of conductivity $\sigma(V_g)$ was measured in situ. The V_g for which $\sigma(V_g)$ provides the minimum value is called a "charge neutrality point" (V_n). The carrier density induced for graphene, $N_{carrier}$, was evaluated from a variation of the V_n value when the molecules are adsorbed on graphene. The shift of V_n was investigated by increasing the molecular thickness, i.e., against the number density $N_{molecule}$ of the adsorbed molecule. The $N_{carrier}$ value increased linearly with $N_{molecule}$, but it started to saturate at a very low molecular coverage corresponding to approximately 0.1

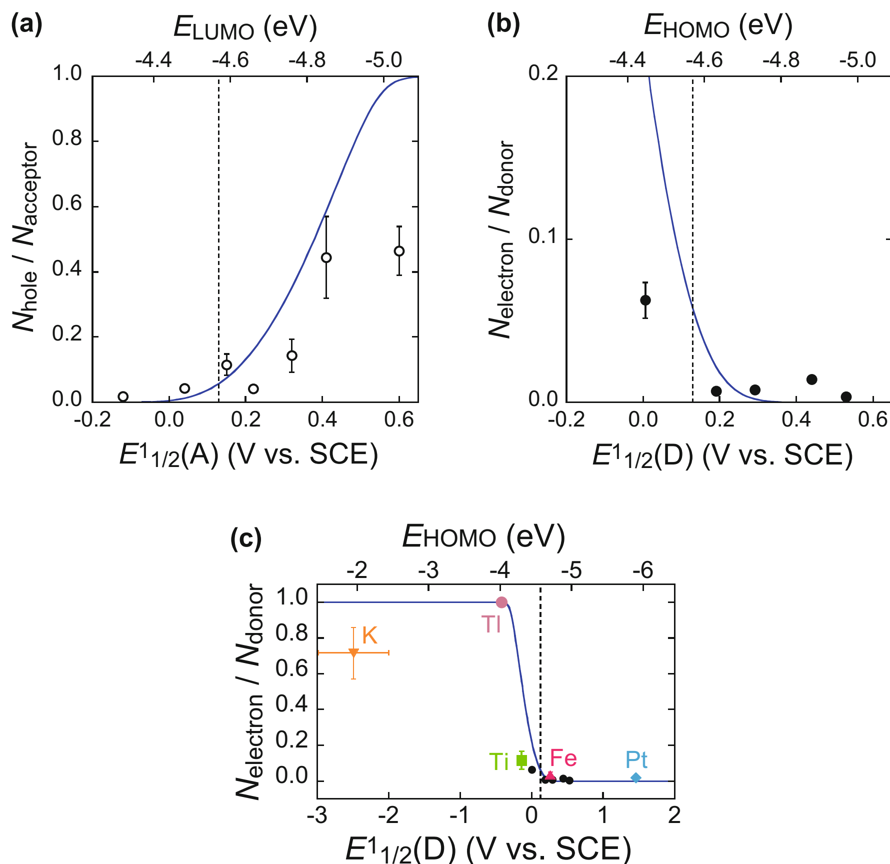

Fig. 2.16 Doping efficiency of various molecules. (**a**) Doping efficiency of electron acceptor molecules as a function of redox potential or LUMO level. (**b**) Doping efficiency of electron donor molecules as a function of redox potential or HOMO level. The dashed lines indicate Fermi energy of non-doped graphene. The blue lines indicate calculated results. (**c**) Comparison of our data with doping efficiency of adsorbed atoms reported by other groups [122–124] (Reproduced from our previous report [103] by permission of John Wiley & Sons Ltd)

monolayers. The carrier doping efficiency, $N_{\mathrm{carrier}} / N_{\mathrm{molecule}}$, was determined at the linear region of $N_{\mathrm{molecule}} \sim 10^{13}$ cm^{-2} (refer Fig. 2.1d of Ref. [103]). Hereafter, the above doping efficiency is denoted as $N_{\mathrm{hole}}/N_{\mathrm{acceptor}}$ or $N_{\mathrm{electron}}/N_{\mathrm{donor}}$ for electron acceptor/donor molecules. Figure 2.16a, b shows plots of $N_{\mathrm{hole}}/N_{\mathrm{acceptor}}$ and $N_{\mathrm{electron}}/N_{\mathrm{donor}}$ as functions of the redox potential $E^1{}_{1/2}$(A) and $E^1{}_{1/2}$(D) of the molecules, respectively [103]. $E^1{}_{1/2}$(A) and $E^1{}_{1/2}$(D) are directly related to the LUMO and HOMO levels (E_{LUMO} and E_{HOMO}), respectively [125], which are also indicated in Fig. 2.16. The dashed vertical lines shown in the graphs correspond to the Fermi energy of graphene, $E_F{}^0$ ($= -4.57$ eV [126]). These graphs show the intuitive consequence in which electron transfer enhances at $E_{\mathrm{LUMO}} < E_F{}^0$

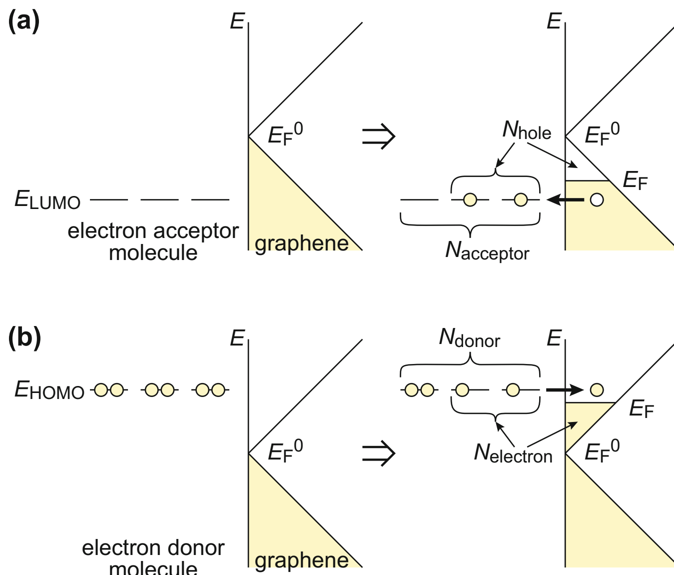

Fig. 2.17 Electron transfer process between molecules and graphene. Energy diagrams of molecules and graphene are shown before and after electron transfer. (**a**) Electron transfer from graphene to acceptor molecules. (**b**) Electron transfer from donor molecules to graphene

or $E_{HOMO} > E_F{}^0$. As shown in Fig. 2.16, it is notable that a new data point (at $E^1{}_{1/2}(D) = 0.006$ V [127]) from TDAP added to this report clearly shows the rise of $N_{electron}/N_{donor}$ when $E_{HOMO} \geq E_F{}^0$. However, a weak dependence of the doping efficiency on the redox potential cannot simply be explained by considering only the energy difference ($E_{LUMO} < E_F{}^0$ or $E_{HOMO} > E_F{}^0$) described above.

Figure 2.17a, b shows the energy diagram of graphene and the electron acceptor molecules. The occupancy of the LUMO level is given by the modified Fermi distribution function:

$$\frac{N_{hole}}{N_{acceptor}} = \left[1 + \frac{1}{2}\exp\left(\frac{E_{LUMO} - E_F}{k_B T}\right)\right]^{-1}, \tag{2.22}$$

where the degeneracy factor, 1/2, comes from the spin degeneracy of the LUMO level. k_B and T are the Boltzmann factor and temperature, respectively. After the electrons are transferred to the molecules, the E_F of graphene decreases so that $N_{hole} = \int_{E_F - E_F^0}^{0} D(E)dE$ holds. Note that graphene has a small density of states, $D(E)$, which is expressed as $D(E) = 2|E|/\pi\gamma^2$ (Eq. 2.8) because of the linear energy band of graphene. The relationship between N_{hole} and $N_{acceptor}$ is expressed as

$$\frac{N_{\text{hole}}}{N_{\text{acceptor}}} = \left[1 + \frac{1}{2}\exp\left(\frac{-E^1_{1/2}\,(\text{A}) + 0.13 + \gamma\sqrt{\pi N_{\text{hole}}}}{k_{\text{B}}T}\right)\right]^{-1}. \quad (2.23)$$

The details of derivations of the Eq. (2.23) are included in the supporting information of Ref. [103].

N_{hole} was numerically calculated as a function of N_{acceptor} by using Eq. (2.23), and the doping efficiency at $N_{\text{acceptor}} = 1 \times 10^{13}$ cm^{-2} is shown as a function of $E^1{}_{1/2}$(A) in Fig. 2.16a with a blue curve (theoretical curve). The theoretical curve follows the experimental plots (Fig. 2.16a). This model also explains why N_{carrier} saturates at a very low N_{molecule}. As the approach of E_{F} to E_{LUMO} suppresses electron transfer, the maximum hole number is evaluated from the equation $N^{\text{max}}_{\text{hole}} = \int^{0}_{E_{\text{LUMO}}-E^0_{\text{F}}} D(E)dE$. $N^{\text{max}}_{\text{hole}}$ was estimated to be at most 1.6×10^{13} cm^{-2} even when using the strongest electron acceptor, F_4TCNQ. This value is consistent with the $N^{\text{max}}_{\text{hole}}$ value of 1×10^{13} cm^{-2} obtained previously for F_4TCNQ-deposited graphene [121].

The model was simultaneously applied to electron donor molecules, and an equation similar to Eq. (2.23) was derived as

$$\frac{N_{\text{electron}}}{N_{\text{donor}}} = \left[1 + \frac{1}{2}\exp\left(\frac{E^1_{1/2}\,(\text{D}) - 0.13 + \gamma\sqrt{\pi N_{\text{electron}}}}{k_{\text{B}}T}\right)\right]^{-1}. \quad (2.24)$$

The theoretical curve of $N_{\text{electron}}/N_{\text{donor}}$ against $E^1{}_{1/2}$(D) showed an agreement with the experimental data, as shown in Fig. 2.16b. In addition to our data, the doping efficiencies of metal atoms K [122], Ti, Fe, Pt [123], and Tl [124], which were reported previously, were plotted as a function of $E^1{}_{1/2}$(D) evaluated from their work functions [128] (Fig. 2.16c). All reported data points fall onto the theoretical curve, indicating the validity of our model. Thus, we clarified that the electron transfer was determined by the energy difference between E_{F} and LUMO/HOMO levels. Thus, the doping efficiency could definitely be scaled by the redox potential without considering any other parameters such as molecular size and symmetry. Furthermore, the important conclusion derived from this study is that the maximum carrier concentration that can be experimentally accumulated is limited by the small $D(E)$ of graphene. Finally, we give the condition of electron transfer molecules to reach the van Hove singularity. From the above discussion, the electron acceptor molecule with $E_{\text{LUMO}} \leq E_{\text{F}}{}^0 - \gamma_0 \sim -7.6$ eV or electron donor molecule with $E_{\text{HOMO}} \geq E_{\text{F}}{}^0 + \gamma_0 \sim -1.6$ eV is required, although to achieve this condition may be difficult.

To summarize, it is difficult to produce highly carrier-doped graphene because of the small $D(E)$ of graphene. For E_{F} of graphene to reach a van Hove singularity (M-point), combining both the gating method and doping method may be effective because the conditions imposed on an ionic liquid and an electron transfer molecule are alleviated. Other perspective is to decrease the energy of the van Hove singularity. For example, the energy is lowered by uniform expansion of graphene, which facilitates carrier doping by molecular adsorption or the electric field.

Acknowledgments The author acknowledges his research collaborators, Prof. A. Kanda and Prof. Y. Ootuka from Tsukuba University, Prof. K. Tsukagoshi from NIMS, Prof. A. Fujiwara from Kwansei Gakuin University, and Prof. Y. Kubozono, Dr. E. Uesugi, Mr. H. Akiyoshi, Mr. T. Uchiyama, and Mr. A. Takai from Okayama University. The author is grateful to Prof. N. Ikeda and Prof. M. Mifune from Okayama University for the measurements of atomic force microscopy and Raman microspectroscopy. The author is also grateful to Prof. G. Saito and Dr. Y. Yoshida from Meijo University for providing a variety of electron transfer molecules.

References

1. P.R. Wallace, Phys. Rev. **71**, 622 (1947)
2. J.W. McClure, Phys. Rev. **104**, 666 (1956)
3. J.C. Slonczewski, P.R. Weiss, Phys. Rev. **109**, 272 (1958)
4. N.D. Mermin, Phys. Rev. **176**, 250 (1968)
5. K.S. Novoselov et al., Science **306**, 666 (2004)
6. A.K. Geim, Rev. Mod. Phys. **83**, 851 (2011)
7. K.S. Novoselov, Rev. Mod. Phys. **83**, 837 (2011)
8. K.S. Novoselov et al., Nature **438**, 197 (2005)
9. Y. Zhang, Y.-W. Tan, H.L. Stormer, P. Kim, Nature **438**, 201 (2005)
10. P.W. Anderson, Phys. Rev. **109**, 1492 (1958)
11. E. Abrahams, P.W. Anderson, D.C. Licciardello, T.V. Ramakrishnan, Phys. Rev. Lett. **42**, 673 (1979)
12. Y. Imry, *Introduction to Mesoscopic Physics*, 2nd edn. (Oxford University Press, Oxford, 2008)
13. T. Ando, A.B. Fowler, F. Stern, Rev. Mod. Phys. **54**, 437 (1982)
14. K.V. Klitzing, G. Dorda, M. Pepper, Phys. Rev. Lett. **45**, 494 (1980)
15. D.C. Tsui, H.L. Stormer, A.C. Gossard, Phys. Rev. Lett. **48**, 1559 (1982)
16. Y. Monarkha, K. Kono, *Two-Dimensional Coulomb Liquids and Solids* (Springer, Berlin, 2004)
17. A.K. Geim, K.S. Novoselov, Nat. Mater. **6**, 183 (2007)
18. A.K. Geim, Science **324**, 1530 (2009)
19. K.S. Novoselov et al., Nature **490**, 192 (2012)
20. A.H. Castro Neto, F. Guinea, N.M.R. Peres, K.S. Novoselov, A.K. Geim, Rev. Mod. Phys. **81**, 109 (2009)
21. S.D. Sarma, S. Adam, E.H. Hwang, E. Rossi, Rev. Mod. Phys. **83**, 407 (2011)
22. H. Aoki, M. S. Dresselhaus (eds.), *Physics of Graphene* (Springer, Cham, 2014)
23. A.C. Ferrari et al., Nanoscale **7**, 4598 (2015)
24. J.J. Sakurai, *Modern Quantum Mechanics* (Addison Wesley, Boston, 1993)
25. J.J. Sakurai, *Advanced Quantum Mechanics* (Addison Wesley, Boston, 1967)
26. C. Kittel, *Introduction to Solid State Physics*, 8th edn. (Wiley, New York, 2004)
27. N.W. Ashcroft, N.D. Mermin, *Solid State Physics* (Holt, Rinehart and Winston, New York, 1976)
28. S.M. Sze, *Semiconductor Devices*, 3rd edn. (Wiley, New York, 2012)
29. J.H. Davies, *The Physics of Low-dimensional Semiconductors* (Cambridge University Press, Cambridge, 1997)
30. K.S. Novoselov et al., Proc. Natl. Acad. Sci. U. S. A. **102**, 10451 (2005)
31. A.K. Geim, I.V. Grigorieva, Nature **499**, 419 (2013)
32. L. Li et al., Nat. Nanotechnol. **9**, 372 (2014)
33. H. Liu et al., ACS Nano **8**, 4033 (2014)
34. B. Radisavljevic, A. Radenovic, J. Brivio, V. Giacometti, A. Kis, Nat. Nanotechnol. **6**, 147 (2011)

35. K.F. Mak, C. Lee, J. Hone, J. Shan, T.F. Heinz, Phys. Rev. Lett. **105**, 136805 (2010)
36. K. Kang et al., Nature **550**, 229 (2017)
37. L. Tao et al., Nat. Nanotechnol. **10**, 227 (2015)
38. M.E. Davila, G.L. Lay, Sci. Rep. **6**, 20714 (2016)
39. Y. Xu et al., Phys. Rev. Lett. **111**, 136804 (2013)
40. S. Zhang, Z. Yan, Y. Li, Z. Chen, H. Zeng, Angew. Chem. Int. Ed. **54**, 3112 (2015)
41. C.L. Kane, E.J. Mele, Phys. Rev. Lett. **95**, 226801 (2005)
42. C.L. Kane, E.J. Mele, Phys. Rev. Lett. **95**, 146802 (2005)
43. R.V. Gorbachev et al., Science **346**, 448 (2014)
44. M. Sui et al., Nat. Phys. **11**, 1027 (2015)
45. Y. Shimazaki et al., Nat. Phys. **11**, 1032 (2015)
46. F.D.M. Haldane, Phys. Rev. Lett. **61**, 2015 (1988)
47. M.Z. Hasan, C.L. Kane, Rev. Mod. Phys. **82**, 3045 (2010)
48. X.-L. Qi, S.-C. Zhang, Rev. Mod. Phys. **83**, 1057 (2011)
49. Y. Ando, J. Phys. Soc. Jpn. **82**, 102001 (2013)
50. A.A. Burkov, Nat. Mater. **15**, 1145 (2016)
51. T. Ando, J. Phys. Soc. Jpn. **74**, 777 (2005)
52. E. McCann, cond-mat:arXiv 1205.4849
53. M. Koshino, Phys. Rev. B **81**, 125304 (2010)
54. S. Adam, E.H. Hwang, V.M. Galitski, S.D. Sarma, Proc. Natl. Acad. Sci. U. S. A. **104**, 18392 (2007)
55. T. Ando, T. Nakanishi, R. Saito, J. Phys. Soc. Jpn. **67**, 2857 (1998)
56. S. Kobayashi, Surf. Sci. Rep. **16**, 1 (1992)
57. K.S. Novoselov et al., Science **315**, 1379 (2007)
58. K.I. Bolotin, F. Ghahari, M.D. Shulman, H.L. Stormer, P. Kim, Nature **462**, 196 (2009)
59. C.R. Dean et al., Nat. Phys. **7**, 693 (2011)
60. X. Li, X. Wang, L. Zhang, S. Lee, H. Dai, Science **319**, 1229 (2008)
61. C.K. Chua, M. Pumera, Chem. Soc. Rev. **43**, 291 (2014)
62. K.S. Kim et al., Nature **457**, 706 (2009)
63. K.V. Emtsev et al., Nat. Mater. **8**, 203 (2009)
64. E. Uesugi, H. Goto, R. Eguchi, A. Fujiwara, Y. Kubozono, Sci. Rep. **3**, 01595 (2013). https://doi.org/10.1038/srep01595
65. P. Blake et al., Appl. Phys. Lett. **91**, 063124 (2007)
66. C.A. Schneider, W.S. Rasband, K.W. Eliceiri, Nat. Methods **9**, 671 (2012)
67. L.M. Malard, M.A. Pimenta, G. Dresselhaus, M.S. Dresselhaus, Phys. Rep. **473**, 51 (2009)
68. A.C. Ferrari et al., Phys. Rev. Lett. **97**, 187401 (2006)
69. D. Graf et al., Nano Lett. **7**, 238 (2007)
70. C.H. Lui et al., Nano Lett. **11**, 164 (2011)
71. B. Krauss et al., Nano Lett. **10**, 4544 (2010)
72. C.H. Lui, L. Liu, K.F. Mak, G.W. Flynn, T.F. Heinz, Nature **462**, 339 (2009)
73. C.R. Dean et al., Nat. Nanotechnol. **5**, 722 (2010)
74. T. Ando, J. Phys. Soc. Jpn. **75**, 074716 (2006)
75. K. Nomura, A.H. MacDonald, Phys. Rev. Lett. **96**, 256602 (2006)
76. M.I. Katsnelson, K.S. Novoselov, A.K. Geim, Nat. Phys. **2**, 620 (2006)
77. A.F. Young, P. Kim, Nat. Phys. **5**, 222 (2009)
78. V.V. Cheianov, V. Fal'ko, B.L. Altshuler, Science **315**, 1252 (2007)
79. G.-H. Lee, G.-H. Park, H.-J. Lee, Nat. Phys. **11**, 925 (2015)
80. D. Schurig et al., Science **314**, 977 (2006)
81. K.I. Bolotin et al., Solid State Commun. **146**, 351 (2008)
82. X. Du, I. Skachko, A. Barker, E.Y. Andrei, Nat. Nanotechnol. **3**, 491 (2008)
83. E.V. Castro et al., Phys. Rev. Lett. **105**, 266601 (2010)
84. L. Wang et al., Science **342**, 614 (2013)
85. N. Tombros, C. Jozsa, M. Popinciuc, H.T. Jonkman, B.J. van Wees, Nature **448**, 571 (2007)
86. W. Han, R.K. Kawakami, M. Gmitra, J. Fabian, Nat. Nanotechnol. **9**, 794 (2014)

87. C. Lee, X. Wei, J.W. Kysar, J. Hone, Science **321**, 385 (2008)
88. S.M. Kim et al., Appl. Phys. Lett. **99**, 023103 (2011)
89. S. Ghosh et al., Nat. Mater. **9**, 555 (2010)
90. R.R. Nair et al., Science **320**, 1308 (2008)
91. Y. Wang, S.W. Tong, X.F. Xu, B. Özyilmaz, K.P. Loh, Adv. Mater. **23**, 1514 (2011)
92. H.B. Heersche, P. Jarillo-Herrero, J.B. Oostinga, L.M.K. Vandersypen, A.F. Morpurgo, Nature **446**, 56 (2007)
93. C.W.J. Beenakker, Rev. Mod. Phys. **80**, 1337 (2008)
94. F. Schwierz, Nat. Nanotechnol. **5**, 487 (2010)
95. J.B. Oostinga, H.B. Heersche, X. Liu, A.F. Morpurgo, L.M.K. Vandersypen, Nature Mater. **7**, 151 (2008)
96. Y. Zhang et al., Nature **459**, 820 (2009)
97. C.H. Lui, Z. Li, K.F. Mak, E. Cappelluti, T.F. Heinz, Nat. Phys. **7**, 944 (2011)
98. W. Bao et al., Nat. Phys. **7**, 948 (2011)
99. M.Y. Han, B. Özyilmaz, Y. Zhang, P. Kim, Phys. Rev. Lett. **98**, 206805 (2007)
100. G.Z. Magda et al., Nature **514**, 608 (2014)
101. D.C. Elias et al., Science **323**, 610 (2009)
102. H. Goto, E. Uesugi, R. Eguchi, Y. Kubozono, Nano Lett. **13**, 5153 (2013)
103. H. Akiyoshi et al., Adv. Electron. Mater. **1**, 1500073 (2015)
104. T. Uchiyama et al., Sci. Rep. **7**, 11322 (2017)
105. J.L. McChesney et al., Phys. Rev. Lett. **104**, 136803 (2010)
106. D. Makogon, R. van Gelderen, R. Roldan, C. Morais Smith, Phys. Rev. B **84**, 125404 (2011)
107. G. Li et al., Nature Phys. **6**, 109 (2010)
108. R. Nandkishore, L.S. Levitov, A.V. Chubukov, Nat. Phys. **8**, 158 (2012)
109. K. Ueno et al., Nat. Mater. **7**, 855 (2008)
110. J.F. Schooley et al., Phys. Rev. Lett. **14**, 305 (1965)
111. J.T. Ye et al., Science **338**, 1193 (2012)
112. G.V.S. Rao, M.W. Shafer, S. Kawarazaki, A.M. Toxen, J. Solid State Chem. **9**, 323 (1974)
113. K. Ueno et al., J. Phys. Soc. Jpn. **83**, 032001 (2014)
114. Y. Kaji et al., Org. Electron. **12**, 2076 (2011)
115. S. Ono, K. Miwa, S. Seki, J. Takeya, Appl. Phys. Lett. **94**, 063301 (2009)
116. H. Yuan et al., Adv. Funct. Mater. **19**, 1046 (2009)
117. S. Luryi, App. Phys. Lett. **52**, 501 (1988)
118. A. Das et al., Nat. Nanotechnol. **3**, 210 (2008)
119. J. Ye et al., P. Natl. Acad. Sci. U. S. A. **108**, 13002 (2011)
120. J. Park et al., Adv. Mater. **24**, 407 (2012)
121. C. Coletti et al., Phys. Rev. B **81**, 235401 (2010)
122. J.-H. Chen et al., Nat. Phys. **4**, 377 (2008)
123. K. Pi et al., Phys. Rev. B **80**, 075406 (2009)
124. C. Straßer et al., Nano Lett. **15**, 2825 (2015)
125. H. Meng et al., Chem. Mater. **15**, 1778 (2003)
126. Y.-J. Yu et al., Nano Lett. **9**, 3430 (2009)
127. G. Saito, S. Hirate, K. Nishimura, H. Yamochi, J. Mater. Chem. **11**, 723 (2001)
128. H.B. Michaelson, J. Appl. Phys. **48**, 4729 (1977)

Chapter 3
Physics of Heavily Doped Diamond: Electronic States and Superconductivity

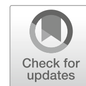

Takanori Wakita, Kensei Terashima, and Takayoshi Yokoya

Abstract Diamond is a popular material, not only as a gem but also for basic and applied research owing to its extraordinary properties. The discovery of superconductivity in heavily doped diamond has increased its importance. Although the highest superconducting critical temperature (T_c) is 10 K, it is regarded as a superconductor with a potentially high T_c, owing to the strong covalent bonding between carbon atoms and the light atomic mass of carbon. In this chapter, after reviewing the fundamentals of the electronic states of pristine and doped diamond, we describe the electronic states, together with the vibrational properties, of boron-doped superconductive diamond, which have been revealed by photoemission spectroscopy and other experimental techniques.

Keywords Heavily doped diamond · Electronic states · Superconductivity · Photoemission spectroscopy · Impurity band

3.1 Introduction

Diamond is one of the most popular gem materials. Diamond is also known as a technologically important material [1], owing to its extraordinary properties such as its high hardness, high thermal conductance at room temperature, very small thermal expansion, high breakdown voltage, and so on. The hardness and high thermal conductivity warrant its use in, for example, glass cutters and heat sinks, respectively. For the synthesis of electrical and optical devices, doped semiconducting diamond made with a chemical vapor deposition (CVD) technique has been utilized [2], mainly because of the capability of controlling the dopant

T. Wakita (✉) · K. Terashima · T. Yokoya
Research Institute for Interdisciplinary Science, Okayama University, Tsushima-naka, Okayama, Japan
e-mail: wakita@cc.okayama-u.ac.jp; k-terashima@cc.okayama-u.ac.jp; yokoya@cc.okayama-u.ac.jp

© Springer Nature Singapore Pte Ltd. 2019

Y. Kubozono (ed.), *Physics and Chemistry of Carbon-Based Materials*,
https://doi.org/10.1007/978-981-13-3417-7_3

concentration. Recently, the nitrogen-vacancy center in diamond has been paid attention to as a qubit in quantum computers [3].

In terms of the electronic structure, diamond is classified as an insulator with a 5.50 eV bandgap at room temperature [4]. Although impurity-doped diamond has been studied for several decades, it was not until the twenty-first century that heavily boron-doped diamond was found to be a superconductor [6]. According to the BCS theory of a superconductivity, in the superconducting phase, electrons form Cooper pairs, and they are condensed into a coherent state that can be described with one wave function. The superconducting critical temperature (T_c) is expressed by

$$k_B T_c = 1.13\hbar\omega_D \exp\left(-\frac{1}{N(E_F)\cdot V}\right), \tag{3.1}$$

where k_B is the Boltzmann constant, $\hbar$ is the Dirac constant, ω_D is the Debey frequency, $N(E_F)$ is the density of states at the Fermi energy (E_F), and V is the interaction potential. This formula shows that the higher ω_D is beneficial to an increase in T_c. Therefore, diamond is a promising material for high-temperature superconductivity, owing to its high ω_D originating from the strong covalent bonding between carbon atoms and the lighter atomic mass of carbon.

Understanding of the superconductivity in diamond is not straightforward, as it emerges in the vicinity of the semiconductor-to-metal transition, where the mechanism of the superconductivity depends on the electronic states that are indeed realized. Hence, experimental and theoretical investigations of the electronic states are crucial. On the experimental side, photoemission spectroscopy (PES) offers the advantage of directly observing the electronic states of a material over a wide energy range, from the valence band to the core levels, including the superconducting gap as well as yielding momentum information of the valence band. In addition, the results can be compared with the theoretical models in an intuitive manner. PES has, therefore, played a crucial role in the study of the electronic and chemical states of heavily boron-doped diamond, as described in Sect. 3.3.

In this chapter, we describe the electronic states of pristine and doped diamond as well as of heavily boron-doped superconducting diamond. For the experimental data of boron-doped diamond superconductor, we mainly focus on PES results. Some results from related studies using other methods are also presented. This chapter is organized as follows. In Sect. 3.2, we explain the basic knowledge of the electronic states of pristine (insulating) and doped (semiconducting) diamond. We describe the doping dependence of the electronic states in detail in the latter part of this section, expecting that it will contribute to future investigations by young researchers. Readers familiar with the subjects in this part can skip it. In Sect. 3.3, we describe the physical properties and electronic states of superconductive diamond. Finally, in Sect. 3.4, we present a summary and give future prospects of the study of superconducting diamond.

3.2 Electronic States of Diamond

3.2.1 Crystal Structure and Basic Electronic States

3.2.1.1 Crystal Structure

Selected physical properties of diamond are listed in Table 3.1, with those of silicon and germanium for comparison. Diamond is one of the allotropes of carbon, others of which include graphite, graphene, fullerene, and carbon nanotubes. Figure 3.1a shows the conventional unit cell of diamond, which belongs to the O_h^7-$Fd3m$ space group, with a lattice parameter of 3.57 Å at 300 K. The unit cell contains two crystallographically inequivalent carbon atoms, namely, sites $C1$ and $C2$, which are identical in their chemical states. A carbon (C) atom has six electrons, with the electronic configuration of $1s^2 2s^2 2p^2$. The bonds between C atoms in diamond are formed with the four sp^3 hybrid orbitals (φ_{111}, $\varphi_{1\bar{1}\bar{1}}$, $\varphi_{\bar{1}1\bar{1}}$, and $\varphi_{\bar{1}\bar{1}1}$), consisting of a linear combination of four states, $2s$ (φ_{2s}), $2p_x$ (φ_{2p_x}), $2p_y$ (φ_{2p_y}), and $2p_z$ (φ_{2p_z}), in the $1s^2 2s 2p^3$ configuration,

$$\begin{aligned}
\varphi_{111} &= 1/2(\varphi_{2s} + \varphi_{2p_x} + \varphi_{2p_y} + \varphi_{2p_z}) \\
\varphi_{1\bar{1}\bar{1}} &= 1/2(\varphi_{2s} + \varphi_{2p_x} - \varphi_{2p_y} - \varphi_{2p_z}) \\
\varphi_{\bar{1}1\bar{1}} &= 1/2(\varphi_{2s} - \varphi_{2p_x} + \varphi_{2p_y} - \varphi_{2p_z}) \\
\varphi_{\bar{1}\bar{1}1} &= 1/2(\varphi_{2s} - \varphi_{2p_x} - \varphi_{2p_y} + \varphi_{2p_z})
\end{aligned} \tag{3.2}$$

Although the $1s^2 2s 2p^3$ configuration has a higher energy by 4 eV than $1s^2 2s^2 2p^2$ [7], the covalent bond formation between the neighboring sp^3 orbitals reduces the total energy of the system sufficiently to stabilize a tetrahedral local

Table 3.1 Basic physical parameters of pristine diamond, silicon, and germanium at 300 K [1, 7, 10, 12]

Physical property	Diamond	Silicon	Germanium
Space group of crystal structure	$O_h^7(Fd3m)$	$O_h^7(Fd3m)$	$O_h^7(Fd3m)$
Lattice constant (Å)	3.57	5.43	5.65
Bandgap (eV)	5.48	1.12	0.66
Electron mobility (cm^2/Vs)	2000	1450	3900
Hole mobility (cm^2/Vs)	1600	505	1800
Breakdown electric field (MV/cm)	5.6	0.3	0.1
Saturation electron velocity ($\times 10^7$cm/s)	2.7	1.0	0.6
Thermal conductivity (W/cmK)	20.9	1.48	0.6
Debye temperature (K)	1860	645	374
Dielectric constant	5.7	11.9	16.2

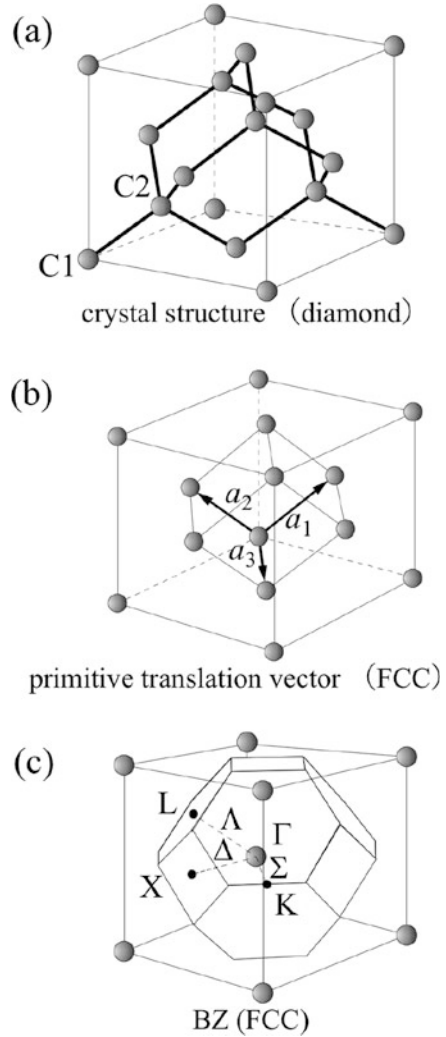

Fig. 3.1 (**a**) Crystal structure, (**b**) primitive translation vector, and (**c**) Brillouin zone(BZ) of diamond [10]

structure. A diamond crystal, then, consists of a three-dimensional (3D) network of the tetrahedral connections of C atoms with $Fd3m$ symmetry (so-called *diamond structure*), instead of the two-dimensional hexagonal atomic network in graphite formed with the sp^2 hybrid orbital. The 3D network of the bonding and antibonding states of the covalent bonds constitutes the valence and conduction bands, respectively (Fig. 3.2 [11]). The distance between the C atoms in a diamond crystal is 1.544 Å, which is 66 % of the Si–Si distance in a Si crystal. The close distance between the C atoms corresponds to a wide energy gap between the bonding and antibonding states, giving rise to the large bandgap between the valence and conduction bands, and the strong covalent bonding between C atoms makes diamond the hardest material.

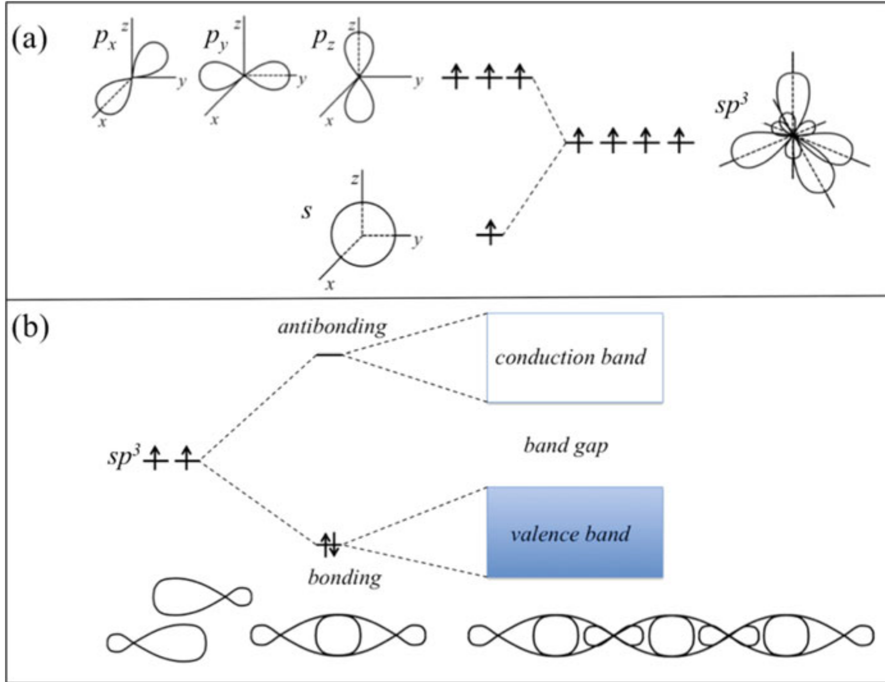

Fig. 3.2 Upper: Boundary surface diagrams for s and p atomic orbitals and that for the sp^3 hybrid orbital. Lower: Conceptional picture of electron energy level: one electron energy levels for hybrid orbitals, bonding and antibonding electron levels for interacting atoms, and formation of bands for a large number of interacting atoms [11]

3.2.1.2 Electronic Band Structure

The diamond structure can be regarded as a pair of intersecting FCC lattices, which are displaced from each other along the [111] axis by 1/4th of the body diagonal length of the unit cell. The diamond lattice has the same primitive unit vector as the FCC lattice and, therefore, also the same reciprocal lattice and Brillouin zone (BZ) (see Fig. 3.1). The upper panel of Fig. 3.3 shows the calculated band dispersion of diamond along the high symmetry lines of the BZ derived by a first principles calculation using the WIEN2k package [17], which shows good overall agreement with literature [15].

The whole valence bands have both the energy maximum and the bottom at the Γ point in the BZ with the calculated bandwidth of ~21.5 eV. Along the ΓX and ΓL lines, we see three bands. The higher binding energy (E_B) band, which is downward convex (E_B = 14–21.5 eV), has a strong s orbital character. The flat band around 13 eV has both the s and p orbital characters. The other two bands, which are upward convex and show larger dispersion, (E_B = 0–15 eV) have a strong p orbital character. The orbital characters of each band can be seen from the total

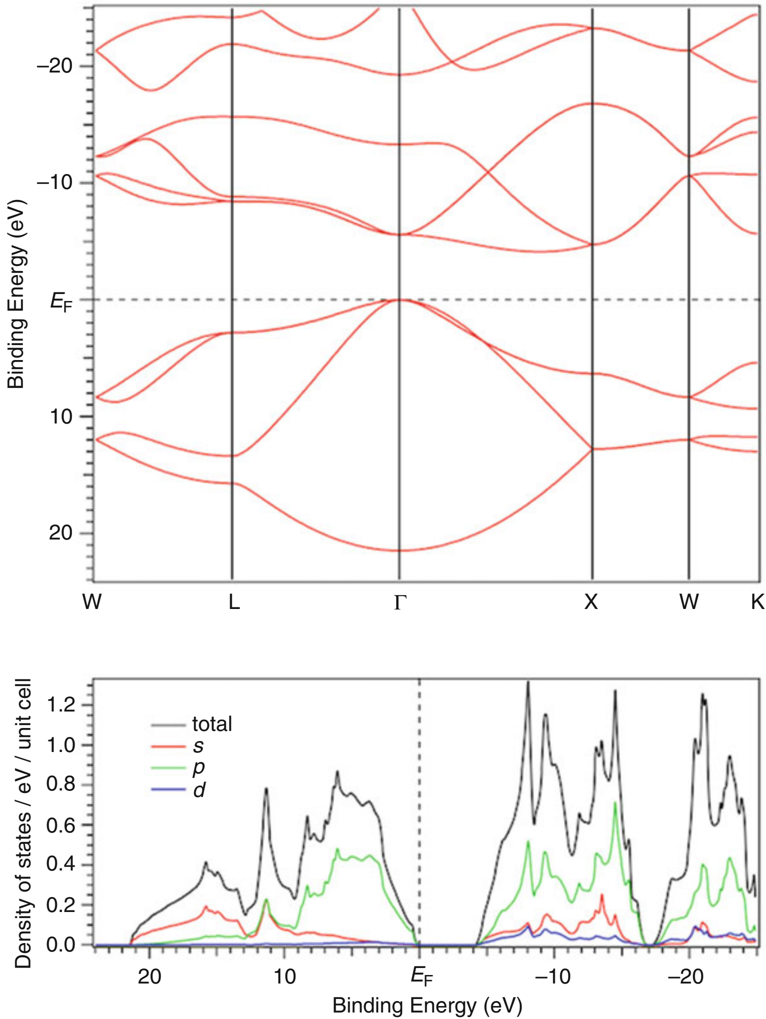

Fig. 3.3 Upper: Band structure of diamond obtained by first principles calculation using the WIEN2k package [17], where input parameters are set as follows: lattice parameter $a = 3.567$ Å, $RK_{\max} = 7$, and k-point = 1000. The Perdew-Burke-Ernzerhof [16] form of the generalized gradient approximation was used as the exchange-correlation functional. Lower: Total and partial density of states of diamond

and partial density of states in the lower panel of Fig. 3.3. The top band is doubly degenerate, and, actually, it splits into two bands along the *LW* and *WK* lines. Hence, the total number of bands is four. These four bands with spin-up and -down states originate from eight electron states of two C atoms in the unit cell (each atom has four valence electron states). The diamond structure does not have an inversion symmetry at the center of the bond between the two nearest-neighbor

C atoms. This gives rise to a splitting (6–13 meV[5]) of the p bands at Γ near E_F owing to spin-orbit coupling (the band calculation in Fig. 3.3 does not include this effect). The conduction band has a local minimum along the ΓX line. Thus, the bandgap is indirect with a width of 5.50 eV [4] (Fig. 3.3 shows a smaller value of the bandgap than the experimentally obtained one, since the calculated bandgap generally depends on the form of exchange-correlation functional).

3.2.2 Semiconducting Behavior and Energy Diagram

3.2.2.1 Natural Diamond

In the early studies of natural diamonds using infrared and ultraviolet absorption spectroscopy, it was found that there are two types of natural diamonds: one has nitrogen (N) impurities and the other does not [1]. These are called type I and II diamonds, respectively (Table 3.2). Most natural diamonds tend to incorporate N atoms, where the N impurities appear to be distributed into small aggregates, and these are called type Ia diamond. The diamonds synthesized by high-pressure and high-temperature methods usually contain N atoms as well, but these N atoms are in isolated substitutional lattice sites. This type of diamond is very rare in nature and is classified as type Ib diamond. Type II diamond, which hardly has any N impurities, is also very rare in nature. It was found that one specimen of type II diamond shows an exceptional behavior of appreciable electrical conductivity, and such diamonds are called type IIb diamond to distinguish them from the insulating type II diamonds, which are called type IIa diamond [1]. Type IIb diamond is extremely rare in nature.

3.2.2.2 Impurity Doping to Diamond

After the discovery of type IIb diamond, it was found that it is a p-type semiconductor including boron (B) atoms as impurities [1]. This finding has opened a path to

Table 3.2 Classification of natural diamond [1]

Type	Features
Ia	N atoms are included. Most natural diamonds tend to incorporate N atoms, where the N impurities appear to be distributed into small aggregates.
Ib	N atoms are included. The N atoms are on isolated substitutional lattice sites. This type of diamond is very rare in nature. The diamond synthesized by high-pressure and high-temperature methods usually contains N atoms in this form.
IIa	N atoms are hardly included. This type of diamond is very rare in nature.
IIb	N atoms are hardly included, but B atoms are incorporated. As a result of B doping, the system shows a semiconducting behavior. This type of diamond is extremely rare in nature.

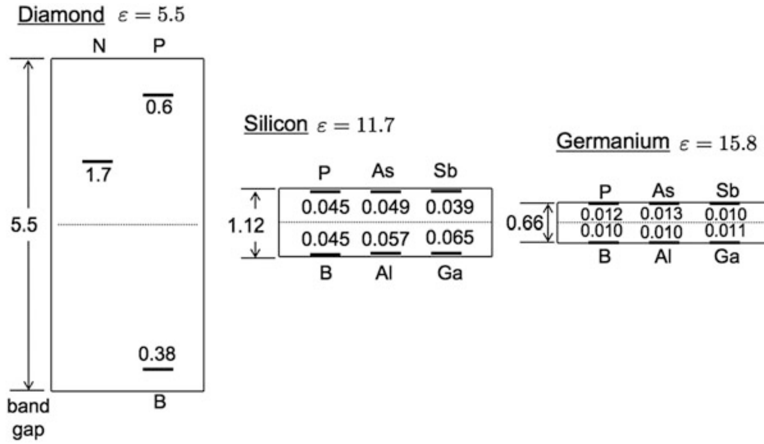

Fig. 3.4 Impurity levels of doped atoms in diamond, silicon and germanium. The values (in eV) are measured from top of the valence band for accepters and from the bottom of the conduction band for donors [7]

electrical applications of diamond, although it has been a long process to establish the synthesis method of diamond with a controlled impurity concentration [14]. After much effort, diamond is currently used as a semiconductor by doping with appropriate atoms, similar to other semiconductors, such as Si. As for electron- or n-type doping, one might think that doping with N atoms would be appropriate, because N atoms have one extra valence electron as compared to C atoms. As found for type Ib diamond, however, N-doped diamond remains insulating because the ionization energy of the donor level is too deep (1.7 eV) [1] and the thermal excitation of electrons into the conduction band at room temperature is nearly zero. Instead, phosphorous is known as a promising dopant owing to the formation of a relatively shallow donor level with the ionization energy of 0.6 eV [19]. Regarding hole-doping, as found for type IIb diamond, B atoms form an accepter level with the ionization energy of 0.37 eV, owing to a deficiency of one valence electron as compared to C atoms [1]. The impurity levels of dopants in diamond are summarized in Fig. 3.4.

3.2.2.3 Bohr's Hydrogen Atom Model

The concentration of B atoms in type IIb diamond was estimated to be $\sim 5 \times 10^{16}\,\text{cm}^{-3}$ [1], and that of P atoms in reference [19] was estimated to be approximately $10^{18}\,\text{cm}^{-3}$. Dividing the impurity concentrations by the atomic density of diamond $1.76 \times 10^{23}\,\text{cm}^{-3}$ shows that the doping level of the former is 0.000028% and that of the latter is 0.00057%, indicating that both are in the *lightly* doped regime for diamond (we will later see the impurity concentration dependence of the physical properties of diamond, including the *heavily* doped regime). The magnitude of the

ionization energy of a shallow impurity level in such a lightly doped semiconductor is approximately expressed using Bohr's hydrogen atom model [7–10, 12],

$$E_{\mathrm{imp}} = \frac{e^4 m_e}{2(4\pi\epsilon\epsilon_0\hbar)^2} \simeq \left(\frac{13.6}{\epsilon^2}\frac{m_e}{m_0}\right)\ \mathrm{eV}, \tag{3.3}$$

where e is the magnitude of an electron charge, ϵ is the static relative dielectric constant of the material, m_0 is the electron rest mass, and m_e is the effective mass of an electron in the periodic potential of the crystal. In comparison with the expression for the magnitude of the ionization energy of atomic hydrogen $e^4 m_0/2(4\pi\epsilon_0\hbar)^2$ ($\simeq$13.6 eV), e^2 and the electron mass are replaced by e^2/ϵ and m_e, respectively. The Bohr radius of the impurity state (the effective Bohr radius, a_{B}^*) is expressed in the same way,

$$a_{\mathrm{B}}^* = 4\pi\epsilon\epsilon_0 \frac{\hbar^2}{m_e e^2} \simeq \left(\frac{0.53\,\epsilon}{m_e/m_0}\right)\ \text{Å}. \tag{3.4}$$

Taking a simple average of the longitudinal and the transverse effective masses (m_l and m_t) in diamond as m_e for electrons ($m_l = 1.56m_0$, $m_t = 0.28m_0$ [18], and the average is $0.92m_0$) with $\epsilon = 5.7$ [1], we then obtain $E_{\mathrm{imp}} \simeq 0.39$ eV and $a_{\mathrm{B}}^* \simeq 3.3$ Å. For holes, we obtain $E_{\mathrm{imp}} \simeq 0.20$ eV and $a_{\mathrm{B}}^* \simeq 6.4$ Å, if we take a simple average of the light-hole and heavy-hole effective masses (m_{lh} and m_{hh}) in diamond as m_e ($m_{lh} = 0.26m_0$, $m_{hh} = 0.57m_0$ [18], and the average $\simeq 0.47\,m_0$). The discrepancies between the above experimental values and the calculated values will be improved by taking into account the effect of the short-range part of the impurity potential and the precise electronic structure of the band edges [8].

3.2.2.4 Comparison with Si in Hydrogen Atom Model

For the impurity levels in lightly doped Si, we can calculate E_{imp} and a_{B}^* in the same manner with the effective electron masses of Si ($m_l = 0.97m_0$, $m_t = 0.19m_0$, $m_{lh} = 0.16m_0$, and $m_{hh} = 0.52m_0$ [7]) and $\epsilon = 11.7$, leading to $E_{\mathrm{imp}} \simeq 0.058$ eV and $a_{\mathrm{B}}^* \simeq 10.7$ Å for electrons and $E_{\mathrm{imp}} \simeq 0.034$ eV and $a_{\mathrm{B}}^* \simeq 18.2$ Å for holes. It is clear that the values of E_{imp} for diamond are larger by approximately one order of magnitude than those for Si. The experimental values of E_{imp} for the shallow impurity levels in Si show the same trend with the calculated ones as seen in Fig. 3.4 [7], which also shows the values of Ge for comparison. This trend is mainly because of the relatively large difference in the static relative dielectric constant ϵ, as E_{imp} is proportional to the square of $1/\epsilon$ but to the first power of m_e, and the latter shows a relatively small difference between diamond and silicon.

The magnitude of ϵ in a semiconductor is related to the size of the bandgap [9]. If a bandgap vanishes, the material becomes a metal, meaning that ϵ becomes infinite, owing to the property of metals whereby electrons in them move arbitrarily far from

their original positions within a crystal under the influence of an external electric field. In a material with a narrow bandgap, the spatial distribution of electrons is still easily deformed by an external electric field, resulting in a large value of ϵ. Conversely, a wider bandgap can lead to a smaller value of ϵ. In fact, ϵ of diamond (a wide bandgap material) is small, almost half the value of that of Si. The small ϵ value results not only in a large value of E_{imp}, as seen above, but also in a small value of a_{B}^{*}, which is proportional to ϵ. Actually, the values of a_{B}^{*} in diamond obtained above are approximately 1/3 of those in Si for both electrons and holes. These features concerning ϵ are also important in the nonmetal-to-metal (NM-M) transition under increase of the carrier concentration, as will be seen later.

3.2.2.5 Hydrogen Crystal Model of the NM-M Transition in a Doped Semiconductor

When the dopant concentration (n) in a semiconductor increases, a nonmetal-to-metal (NM-M) transition occurs around a certain critical concentration (n_c). The simplest explanation for this transition is to consider it as the result of an increase in the overlapping of the ground state wave functions of electrons on neighboring impurity atoms. By considering the NM-M transition in a virtual hydrogen crystal, the n_c can be roughly estimated [7]. If we imagine a virtual crystal of hydrogen atoms with a simple cubic lattice and a variable lattice constant a, then the crystal in an insulating phase with large values of a would show a transition into a metallic phase when a becomes smaller than a certain critical value a_{c}. The values of a_{c} and n_{c} can be calculated from the metallic side by considering a critical condition for the lattice constant in the formation of an electron bound state due to a screened Coulomb potential produced by a hydrogen nucleus (proton). The Coulomb potential energy in a metallic phase acting on an electron is screened by other electrons. This screened Coulomb potential energy is expressed by using the Thomas–Fermi approximation as follows [7],

$$U(r) = -\frac{e^2}{4\pi\epsilon\epsilon_0 r}\exp(-k_s r). \tag{3.5}$$

Here we assume ϵ=1 for the hydrogen crystal and then k_s=$(4(3/\pi)^{1/3}n_0^{1/3}/a_{\mathrm{B}})^{1/2}$ where n_0 is the electron concentration. $1/k_s$ is called Thomas-Fermi screening length.

The numerical calculation in reference [21] shows that this potential has a bound state when $1/k_s$ is larger than $0.83991a_{\mathrm{B}}$, demonstrating that the system in this model can be an insulator under such a condition. Using the relation $n_0 = 1/a^3$ for a simple cubic lattice, we obtain the relations $a_{\mathrm{c}} = 4(3/\pi)^{1/3}(0.83991)^2 a_{\mathrm{B}} \simeq 2.78a_{\mathrm{B}}$ and $n_{\mathrm{c}} = 1/a_{\mathrm{c}}^3 \simeq 0.047/a_{\mathrm{B}}^3$. These relations are usually expressed as $n_{\mathrm{c}}^{1/3}a_{\mathrm{B}} \simeq (0.047)^{1/3} \simeq 0.36$. For various semiconductors, it has been reported that the experimentally obtained criterion $n_{\mathrm{c}}^{1/3}a_{\mathrm{B}}^{*} \simeq 0.26 \pm 0.05$ has almost universal

applicability [30]. It should be emphasized here that a smaller value of a_{B}^{*} will lead to a larger value of n_{c}, and one of the examples of such a case is diamond as seen below.

3.2.2.6 Other Models for NM-M Transition: Mott–Hubbard Model and Anderson Localization

The above hydrogen crystal model for the NM-M transition is based on the criterion for the bound state due to the screened Coulomb potential. The NM-M transition in a system with one electron per unit cell such as the hydrogen crystal is also predicted by a tight binding model with an electron–electron Coulomb interaction U on the same lattice site, known as the Mott–Hubbard model [31]. If U is larger than the bandwidth W, this model leads to a band splitting into two bands, the lower and the upper Hubbard bands separated by U (Fig. 3.5 [32]). Each electron is accommodated in the lower Hubbard band and localized at each atomic site, and thus the system is insulating. When U is comparable to W ($U \approx W$), the splitting of the Hubbard bands disappears, and the NM-M transition occurs in a continuous manner as a function of U (Mott–Hubbard transition) [32].

Another scenario for the NM-M transition proposed for a doped semiconductor is one in which the transition is triggered by disorder [33, 34], which is known as the Anderson transition. When a quantum mechanical system is sufficiently disordered by impurity incorporation, the diffusion of electrons can be completely suppressed owing to coherent backscattering off random impurities, resulting in the localization of electrons (Anderson localization). In the simplest model for this

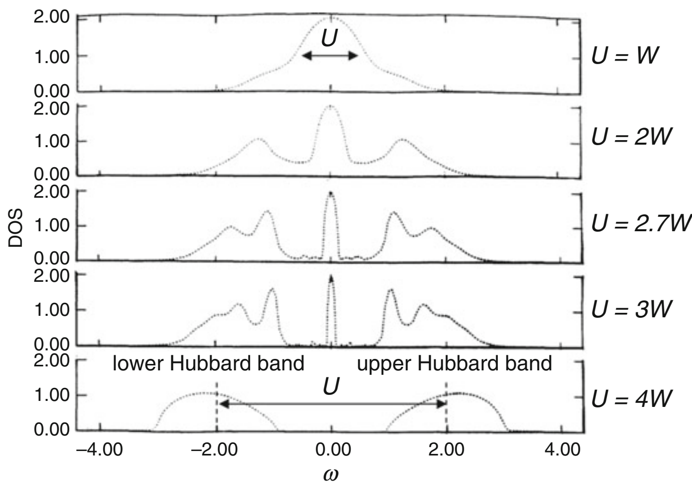

Fig. 3.5 Density of states at zero temperature as a function of U, where $W = 1$. (Reprint with permission from [32] Copyright 1993 by American Physical Society)

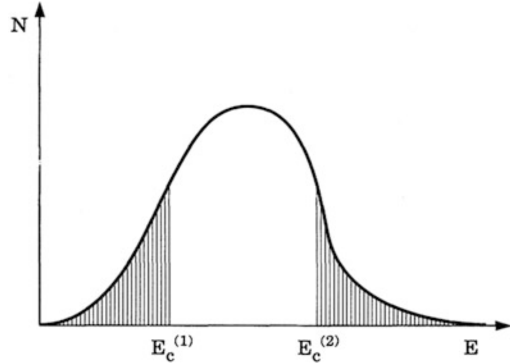

Fig. 3.6 Schematic picture of the DOS N against the energy E in the Anderson model when the energy distribution of the random site energies is not so wide as to localize the whole band. $E_c^{(1.2)}$ are the mobility edges, and the states in the shaded regions are localized. (Reprint with permission from [35] Copyright 1994 by American Physical Society)

localization, randomly distributed site energies are assumed; in other words, only the diagonal matrix elements of the Hamiltonian are considered to be disordered (so-called diagonal disorder). If the energy distribution of the random site energies is not so wide as to localize the whole band, only the electrons with energies near the band edge would be localized, because the smaller energy differences between the states near the band edge and the impurity states will lead to stronger scattering than the larger differences between the states in the band center and the impurity states will do. Then, the NM-M transition can occur when, as the impurity concentration increases, the chemical potential of charge carriers crosses a certain energy E_c, which separates the localized states in the band tail from the extended states in the band center (Fig. 3.6). E_c is called the mobility edge.

Both of these two models ushered in a new quantum mechanical view of NM-M transitions. It is, however, concluded that neither the Mott–Hubbard model nor the Anderson localization picture alone is sufficient to explain the experimental observations for NM-M transitions in doped semiconductors [35]. A pure Mott–Hubbard transition picture could be inadequate because of the existence of high disorder in most materials that display a NM-M transition. Owing to ubiquity of Coulomb interactions among electrons in materials, a pure Anderson localization picture is also too simple. Hence, it is important to consider a NM-M transition in a doped semiconductor in terms of both the disorder and the interactions among electrons [35].

3.2.2.7 Impurity Concentration Dependence of Electronic State

To see how the electronic state in a doped semiconductor depends on the impurity concentration, it will be instructive to start by looking at the temperature dependence of the electric conductivity $\sigma(T)$ in a doped semiconductor, which is generally expressed by the following equation,

$$\sigma(T) = \sigma_0 \exp(-E_a/k_B T), \tag{3.6}$$

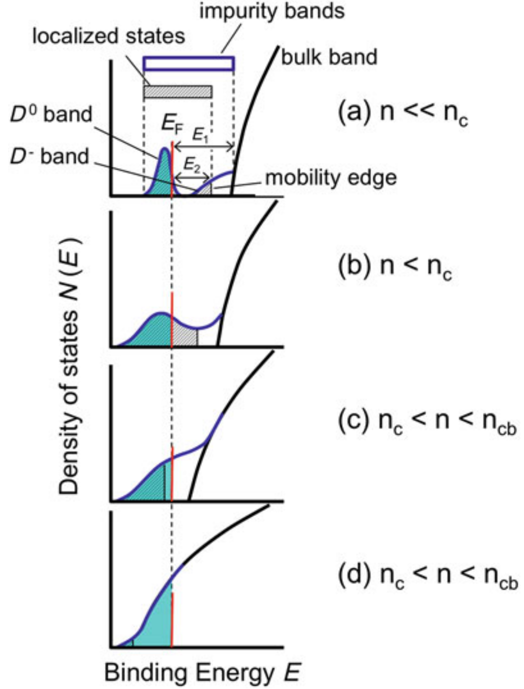

Fig. 3.7 Hypothetical schematic picture of the change in the electronic states due to impurity doping in semiconductor. $D^0 + D^-$ bands are the impurity states and the shaded regions are localized states. (Reprint with permission from [20] Copyright 1978 by Scottish Universities Summer Schools in Physics)

where E_a is the activation energy. $\sigma(T)$ will be zero at $T = 0$. When the impurity concentration increases and exceeds the critical concentration n_c, $\sigma(T)$ becomes finite at $T = 0$, and the system becomes metallic. Figure 3.7 shows a hypothetical sketch of the change in the density of states depending on the impurity concentration in a doped semiconductor [20], which is depicted mainly based on the temperature dependence of the electric conductivity and the Hall coefficient of Ga-doped Ge. The density of states (DOS) of the bulk band is assumed to be proportional to $\sqrt{E}$. The vertical axis is increased such that the height of the impurity level seems to be constant, even if the height of the impurity level increases according to an increase in the impurity concentration.

In the following description of the impurity concentration dependence of $\sigma(T)$ and the electronic state of the system, we will use the terms applicable to electrons for convenience, and it is always possible to rephrase them with the terms proper for holes. When the impurity concentration is low ($n \ll n_c$), the electron conduction is caused by the excitation of electrons from the localized neutral impurity (D^0) level to the conduction band with an activation energy E_1. When the impurity concentration increases but is still in the range of $n \ll n_c$, a D^0 band is formed owing to the increase in the interaction between the D^0 levels. At the same time, conduction with an activation energy E_2 is clearly observed in the low temperature range, where $E_2 < E_1$. To illustrate this conduction, the D^- band model was proposed [22]. Owing to the decrease in the average distance between impurities

following the increase in n, doubly occupied D^- sites are formed by the excitation of electrons from the D^0 site to another neighboring D^0 site. The wave function of the D^- site is approximately 3–4 times larger than that of the D^0 site and forms a wider band than the D^0 band (Fig. 3.7a). However, in the D^- band consisting of randomly existing D^- sites, the electrons are considered to be localized at the carrier concentration below the mobility edge. In the D^- band model, therefore, the conduction with E_2 is explained to be due to the transition from the localized states to the mobility edge within the D^- band. As the concentration further increases, the D^0 and D^- bands (so-called impurity bands) begin to merge owing to disorder and a stronger overlap of the wave functions (Fig. 3.7b). At $n = n_c$, E_F exceeds the mobility edge, leading to $E_2 = 0$, and a transition to a metallic state occurs (Fig. 3.7c). At this concentration, E_F is presumed to remain below the bottom of the conduction band. When the concentration exceeds n_{cb}, the impurity bands and the conduction band completely merge. For $n \geq n_{cb}$, E_F enters the conduction band, and a truly metallic conduction is observed, similar to that of an impure metal (Fig. 3.7d).

In the impurity concentration range of $n_c < n < n_{cb}$, the screening by free carriers increases as n increases, leading to a rapid increase in the static relative dielectric constant. As a result, the bottom of the conduction band shifts downward, as depicted in Fig. 3.7. There is, then, a plausible argument that this shift is large enough that the impurity and conduction bands already overlap with each other at n_c. Such an argument as to whether E_F is actually below the bottom of the conduction band at n_c will be discussed later.

3.2.2.8 Effect of Compensation

A so-called *compensated* semiconductor contains a small amount of the other type of dopant, which ionizes a fraction of the major dopants through electron transfer from donors (D^0) to acceptors (A^0). As a result, a compensated system has both ionized donors (D^+) and acceptors (A^-). This ionization reduces the carrier concentration and provides unoccupied impurity states at D^+ (for electrons) and A^- (for holes) sites. In such a system, conduction with an activation energy E_3 is observed in the range from low to high impurity concentration at low temperature, where E_3 is smaller than E_2 ($E_3 < E_2 < E_1$). This conduction occurs by phonon-assisted hopping from neutral (D^0) to ionized (unoccupied) impurity sites (D^+) (this description is for electrons). In the D^0-D^+ band formed following the increase in n, Anderson localization occurs owing to fluctuation in the energy level (diagonal disorder) due to the random electrostatic field of the ionized impurities, until E_F exceeds the mobility edge. In strongly compensated systems, the conduction with E_2 does not appear. This is probably because the energy difference between E_F and the mobility edge in the D^- band increases due to large diagonal disorder in strongly compensated systems, and E_2 becomes larger than E_1. Eventually, only the conductions with E_1 and E_3 are observed in strongly compensated systems [20].

3.2.2.9 Identification of the Nature of the NM-M Transition

Regarding the conduction with the activation energy E_2 observed in uncompensated systems, an interpretation other than the D^- band model has been also proposed. This interpretation presumes that the conduction occurs by the electron excitation to the upper Hubbard band, produced as a result of the relatively large Coulomb repulsion energy at the D^- site with the relatively small width of the D^0 band in the low-concentration region. In this case, the transition to the metallic state is caused by a disappearance of the splitting of the Hubbard bands resulting from the increase in the bandwidth accompanying the increase in n (Mott–Hubbard transition).

However, the scaling analysis of the doping dependence of the electrical conductivity at low temperature for uncompensated Ga-doped Ge shows that, in the range of $\pm 1\%$ of n_c, the critical exponent μ is approximately equal to 1 ($\mu \approx 1$) [24], which is consistent with that predicted for the Anderson transition [25]. In strongly compensated samples, the critical exponent $\mu \approx 1$ indicating Anderson transition is obtained over a wider concentration range near n_c, meaning that the Anderson localization and, therefore, the impurity band play a main role in the NM-M transition in the strongly compensated system.

For uncompensated samples, it is considered that an unintended and unavoidable small amount of compensation is responsible for the critical exponent $\mu \approx 1$ observed in the very narrow concentration region near n_c [24]. In the very close vicinity of n_c in an uncompensated sample with an unintended small compensation, the Anderson localization effect may be enhanced by the decrease in the effect of Coulomb repulsion due to the increase in the D^0 bandwidth and the number of carriers and by the divergence of the localization length on the nonmetal side (by the divergence of the correlation length due to the relatively small number of carriers on the metal side).

Outside of the $\mu \approx 1$ region of n for uncompensated samples, $\mu \approx 0.5$ is observed [24]. There seems to be no widely accepted theoretical interpretation for this observation at present, although there are many theoretical proposals that attribute this anomalous critical exponent, for example, to strong intervalley scattering for n-type semiconductors [13] and to strong electron correlation [24].

3.2.2.10 Role of the Impurity Band

The conclusion that E_F is in an impurity band below the conduction band at the NM-M transition was led from several experimental results such as, for example, far-infrared reflection [26], Raman scattering [27], and tunneling spectroscopy [23]. From the measurement of the Hall coefficient, it was also concluded that the hump structure in the temperature dependence of the Hall coefficient, observed in the impurity concentration range of $n_c < n < n_{cb}$, indicates the existence of

two bands: an impurity band and a conduction band with two kinds of electron mobilities [20].

In contrast, de Haas–Shubnikov oscillations for n-type Ge with a high impurity concentration agree with those expected from the conduction band mass parameters in pure Ge including the anisotropy, although the hump in the temperature dependence of the Hall coefficient was still observed. Furthermore, it was shown that the hump structure of the Hall coefficient can be explained if one assumes that (i) E_F lies in the conduction band and (ii) the Coulomb scattering deviates distinctly from the usual scattering when the wavelength of the electron is greater than the average value of the distance between impurities [28]. This shows that the available evidence for the NM-M transition in an impurity band below the conduction band may not be unshakeable [20].

At concentrations clearly exceeding n_{cb}, the DOS observed by far-infrared reflection spectroscopy was reproduced well by the Drude model [26]. This means that the DOS at such a high impurity concentration is essentially proportional to $\sqrt{E}$, except for the tail states, which are modulated by the potential fluctuations due to the random distribution of impurities [20, 23].

3.2.2.11 Boron-Doped Diamond

For a homoepitaxial film of B-doped diamond, the n_c of 4.5×10^{20} cm^{-3} (0.25%) has been reported [29]. In diamond, because the static relative dielectric constant is small, the effective Bohr radius is also small, as mentioned above. Consequently, the absolute value of n_c is larger than for other conventional semiconductors as seen in Fig. 3.8. This feature may lead to an increase in unintended compensation and disorder near the critical concentration, which will affect the values of n_c and n_{cb}. Hence, inevitable questions regarding the NM-M transition in a B-doped diamond are:

1. How strongly are the impurity and host bands merged with each other at the NM-M transition?
2. How strongly does the disorder affect the NM-M transition?

In this context, one of the important findings for a B-doped diamond is that the DOS at E_F remains large down to the NM-M transition when n approaches n_c from the metallic side, which has been concluded from the superconducting properties of the B-doped diamond [29]. Interestingly, the superconducting transition occurs in the vicinity of the NM-M transition in the heavily B-doped diamond, pointing to the close relationship between the two physical processes.

In the next section, we will describe the experimental and the theoretical findings on the physical properties and the electronic states of superconductive diamonds which have been revealed until present. One will find that these findings also shed light on the above issues related with the NM-M transition.

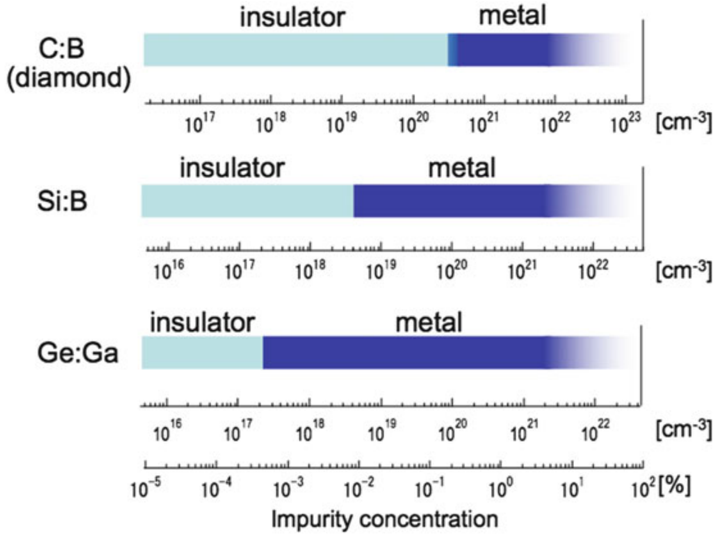

Fig. 3.8 Phase diagrams as a function of impurity concentration for B-doped diamond (C:B), B-doped silicon (Si:B) and Ga-doped germanium (Ge:Ga), respectively

3.3 Superconductivity in Heavily Doped Diamond

3.3.1 Superconducting Properties

The first report on the superconductivity of diamond was made by a Russian group for heavily B-doped bulk samples synthesized with a high-temperature and high-pressure technique [6] (Fig. 3.9). The reproducibility was soon confirmed by a study using heavily B-doped films made with a microwave plasma-assisted chemical vapor deposition (MPCVD) process [36]. MPCVD offers the advantage of synthesizing homoepitaxial diamond films with the capability of controlling the B concentration. As the B concentration is increased, the magnitude of the resistivity decreases. The temperature-dependent resistivity shows metallic behavior around room temperature but shows a slight increase at low temperature, which was attributed to the inhomogeneity probably arising from a nonuniform distribution of B [37].

The superconductivity of B-doped diamond was found to occur just after the NM-M transition, and T_c increases as the B concentration is increased [38]. The lattice parameters of bulk samples increase as a function of the B concentration and exhibit a maximum lattice constant of 3.578 Å for a sample with a B concentration of 4%. (The lattice constant of an undoped sample at 300 K: $a = 3.567$ Å). The increasing trend in a with respect to the B concentration is linear for lower B concentrations but shows a deviation for higher B concentrations. This deviation was attributed to the incorporation of B atoms at interstitial sites and possible B aggregates, such

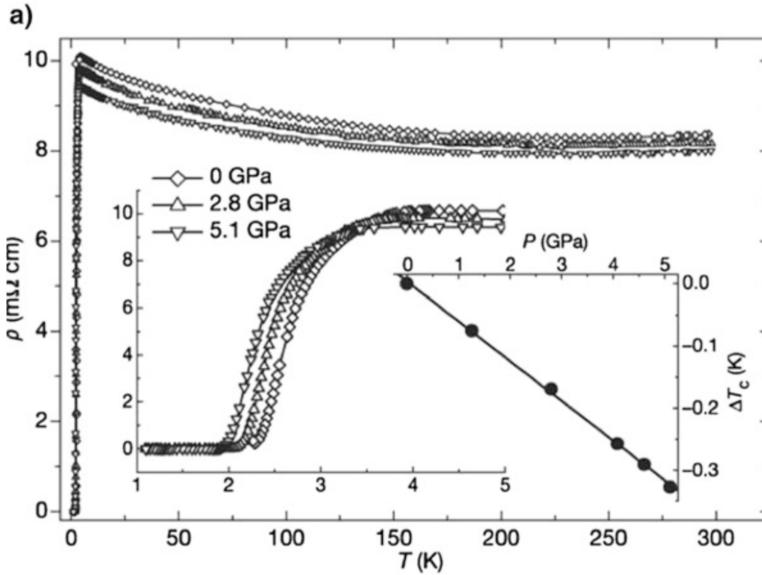

Fig. 3.9 Temperature-dependent electrical resistivity of B-doped diamond synthesized with a high-temperature and high-pressure technique. Zero resistivity around 2 K is clearly observed. (Reprint with permission from [6] Copyright 2004 by Springer Nature)

as interacting substitutional B pairs and multiboron complexes with vacancies or interstitials [39]. For studies using films, it was found that the dependences of T_c on B concentration, or carrier concentration, show different behaviors for (001) and (111) films [40] (Fig. 3.10). Whereas the B concentration n_B *vs* T_c curves of (001) films saturate around 4 K, those of a (111) film increase continuously until 8 K. The difference in n_B with respect to T_c was found to be correlated with the presence or absence of the anisotropic lattice expansion of the crystal structure. The highest T_c of 10 K determined from the resistivity at zero temperature was realized for (111) oriented films [55].

The upper critical field at $T = 0$ was estimated from its temperature dependence, and the value depends on the reports: 9.0–14 T (bulk sample with the hole concentration $n_H \sim 1.8 \times 10^{21}$ cm^{-3} [37]) and 1.4 T ((001) film with $n_B = 1.9 \times 10^{21}$ cm^{-3} [38]). Correspondingly, the Ginzburg–Landau coherence length $\xi_{GL} = [\phi_0/2\pi H_{c2}(0)]^{1/2}$ was 48–60 Å [37] and 150 Å [38]. The specific heat measurements [38] showed anomalies at T_c, indicating the bulk nature of the superconductivity. The analyses gave a specific heat coefficient A of 0.113 mJ/(mol·K^2) and sample-averaged Debye temperature Θ_D of 144 K, which is approximately 23% smaller than the Debye temperature of undoped diamond, indicative of lattice softening due to B doping. $\Delta C/\gamma T_c = 0.5$ is smaller than the value of 1.43 expected for weak-coupling superconductivity.

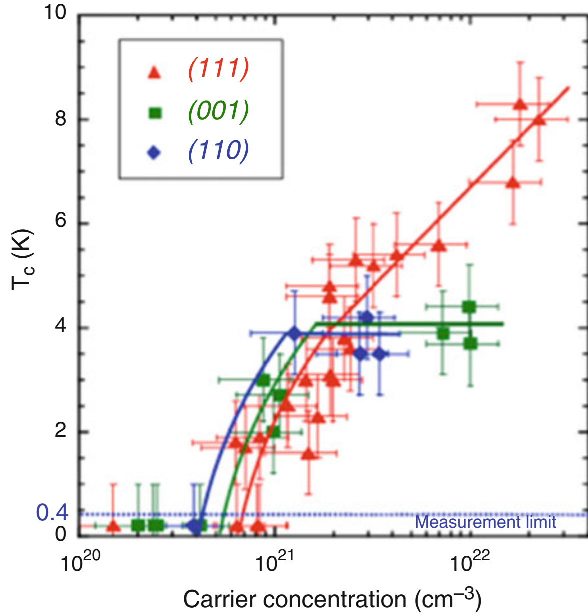

Fig. 3.10 T_c as a function of carrier concentration for boron-doped MPCVD diamond films with different orientations. (Reprint with permission from [40] Copyright 2010 by American Physical Society)

3.3.2 *Theoretical Studies on Electronic Structure and Models for Superconductivity*

As described above, lightly B-doped diamond is a *p*-type semiconductor. For the heavily B-doped diamond, there are two types of descriptions for the metallic electronic states in the extreme cases. One is that the metallic states emerge from the impurity band, which are grown from the impurity level. Because the bandwidth of these states are narrow, electron correlation can play an important role. The other is that the metallic states can be described by a degenerate semiconductor, where the wave function of the doped B hybridizes with that of C atoms and forms a hybridized band, which has been predicted from band structure calculations.

Band structure calculations with different approaches have been used to study the metallic band structure and mechanism of the superconductivity of doped diamond. One approach uses a virtual crystal approximation (VCA), in which the crystal is made of virtual atoms with nuclear charge Z of $(1 - x)Z_C + xZ_B$ [41, 42]. These calculations provided a picture that the holes at the top of the zone-centered degenerate bonding valence band couple strongly to the optical bond-stretching phonon modes, which is the likely mechanism of the superconductivity. The other uses a large supercell (SC) with one B atom in substitution [43, 44]. Hence, B atoms in a SC model are treated explicitly, but it is placed periodically, the latter of which leads to the artifact of zone folding. Although the study using the SC model provided a consistent picture for phonon-mediated superconductivity, the important role of B vibration for the electron–phonon coupling was also pointed out. Coherent potential

approximation (CPA) [45], which is another approach to the treatment of randomly positioned dopant atoms, showed similar valence band dispersions to those of VCA, which were smeared due to a lifetime effect. As for n-type diamond, a higher value of T_c was predicted from VCA owing to the higher DOS of the conduction band [46], but superconductivity has not yet been experimentally observed for n-type diamond.

There are several reports describing the metallic and superconducting states that emerge in the impurity band, from the motivation of the larger activation energy of the impurity state and superconductivity occurring in the vicinity of the semiconductor–metal transition. Baskaran discussed the superconductivity occurring in the narrow impurity band with electron–electron correlation [47]. Shirakawa et al. have studied the effect of B disorder on the superconducting properties using CPA [48]. On the basis of the disordered attractive Hubbard model in three dimensions, it was discussed that the superconductivity in the boron-doped diamond is close to or in the crossover regime from the superconductivity in the degenerate valence band to the one in the impurity band [49]. The metallization of clustering B atoms was also discussed [50].

3.3.3 Experimental Studies of Heavily Boron-Doped Diamond

In this section, we will see the spectroscopic experimental results for heavily boron-doped diamond.

3.3.3.1 Electronic Structure with the Wider Energy Scale

Figure 3.11 shows the photoemission spectrum of heavily B-doped diamond measured with a 1200 eV photon and with the wider energy range. The sharp peak around 280 eV is the C 1s core level signal. The broad hump around 320 eV is the plasmon satellite [51], which corresponds to the excitation of the group of valence electrons by a photoelectron. The energy difference with respect to the main C 1s line is ~35 eV. No oxygen signal around 530 eV guarantees the cleanliness of the surface. A 50-times intensity-enlarged spectrum near E_F shows a peak near E_F and around 185 eV, which are the valence band and the B 1s core level signals, respectively. The detailed information of the B 1s core levels will be discussed in Sect. 3.4.

3.3.3.2 Valence Band Density of States

When the valence band electrons with different momenta in the initial states in the first BZ are excited by higher photon energy, the excited photoelectrons are emitted in smaller solid angles. Hence, the DOS of the valence band is obtained

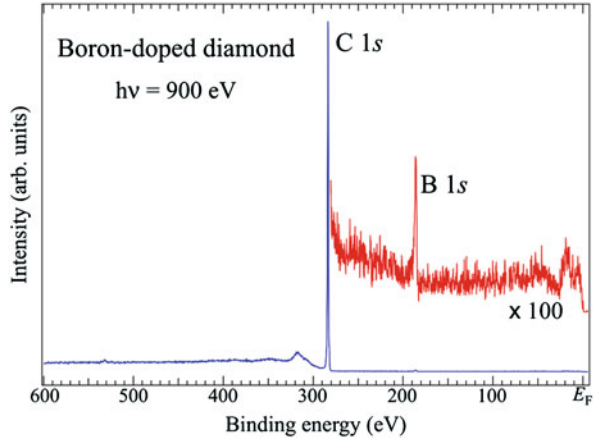

Fig. 3.11 PES spectra of B-doped superconductive diamond measure with wide energy range

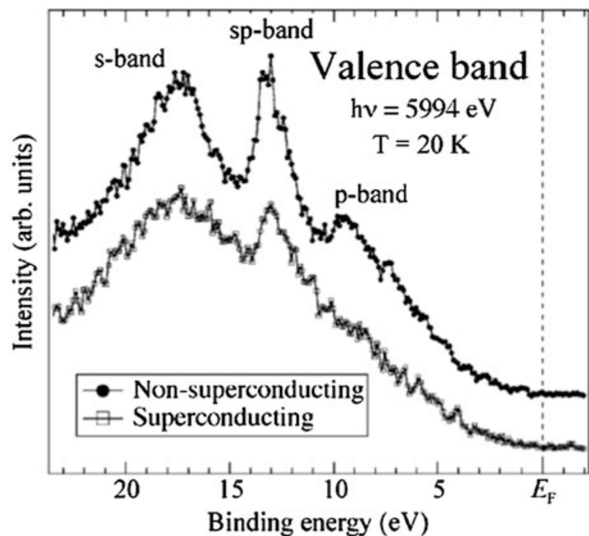

Fig. 3.12 Valence band PES spectra of lightly B-doped nonsuperconductive and highly B-doped superconductive diamond. (Reprint with permission from [52] Copyright 2007 by MYU TOKYO)

approximately from angle-integrated photoemission spectra measured with high photon energy, where each orbital component is multiplied by the photoemission excitation probability. The valence band spectra of lightly doped nonsuperconducting and heavily doped superconducting diamond measured at 20 K and using photon energy of 5994 eV are shown in Fig. 3.12 [52]. The lightly B-doped diamond has three structures at 9.5, 13, and 17.5 eV. According to band calculations (Fig. 3.3), these structures can be ascribed to the C 2*p*, 2*sp*, and 2*s* dominant states, respectively. The valence band spectrum of the heavily B-doped diamond has also three structures, but they are found to be broader than those of the lightly B-doped diamond.

3.3.3.3 Valence Band Dispersions

Band dispersions of the valence bands are visualized by angle-resolved photoemission spectra (ARPES) with relatively low photon energy. The lower photon energy guarantees a higher momentum resolution. Figure 3.13 shows ARPES intensity maps of the valence band measured with photon energy of 825 eV for MPCVD homoepitaxially grown (111)-oriented diamond films with different B concentrations (BDD1 and BDD2 in Table 3.3). [52]. The gray parts correspond to band dispersions. The measured momentum region is illustrated in the inset. There is a convex-downward band at higher binding energies and convex-upward bands at lower binding energies, which have the energy bottom and top, respectively, at the Γ point. The total number of bands, as is evident from ΓL direction, is four, originating from the eight electrons from two atoms in the conventional unit cell. Note that the

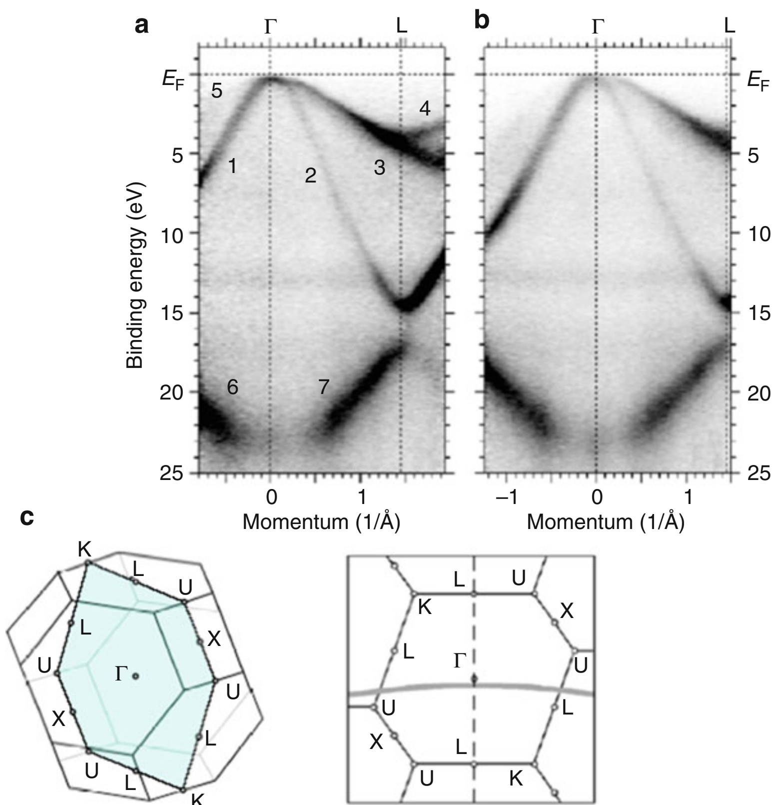

Fig. 3.13 Valence band dispersions of lightly B-doped nonsuperconductive (top left) and mediumly B-doped superconductive (top right) diamond measured with ARPES, together with measured momentum locations in BZ. (Reprint with permission from [53] Copyright 2006 by Elsevier Science Ltd.)

Table 3.3 Boron concentration of samples used for ARPES and physical constants deduced from the ARPES [53]

Samples	BDD1	BDD2	BDD3
$n_{\mathrm{B,SIMS}}$ (cm^{-3})	2.89×10^{20}	1.18×10^{21}	8.37×10^{21}
E_{F} (eV) wrt. VBM	0.0	0.2 ± 0.1	0.4 ± 0.2
n_{ARPES} (cm^{-3})	–	5.5×10^{20}	1.9×10^{21}
τ (fs)	–	5.1	2.8

dispersion nearest to E_{F} consists of two bands. The valence band dispersions were found to be very similar to what the band calculations predict, but the experimental bandwidth (23.5 ± 0.5 eV) is wider than that of the calculations (21.5 eV). The shape of the band does not change significantly in the superconductive sample. These results indicate that the overall electronic structure is retained under B doping. In the sample with the highest B concentration, any dispersionless features near E_{F}, which is the signature of the existence of the impurity band, have not been clearly observed.

Figure 3.14 shows the B concentration dependence of ARPES intensity maps near E_{F} [53], showing systematic change in the electronic structure, which is intimately related to the conducting property of the film. In the lowest-doped film, the top of the valence band is clearly seen as a bright upward convex feature at Γ. This indicates that the chemical potential of this sample is located slightly above the top of the valence band. The intensity of the top of the band decreases in the medium-doped sample. In the heaviest-doped film, the top region of the band is truncated. Further confirmation of band crossing E_{F} has been obtained by other X-ray ARPES studies [54], where the higher signal-to-noise ratio of the data demonstrates the band crossing with separated structures in the momentum distribution curves.

A line profile curve of the ARPES intensity map along the momentum axis at a particular binding energy is called the momentum distribution curve (MDC). The peak positions in the MDC at E_{F} correspond to Fermi momentum k_{F}. From estimated k_{F}, we deduced the energy shifts of the band with respect to the lowest B-doped film. The obtained values of the shifts were then converted to the effective carrier concentrations of the samples, which are listed in Table 3.3. The values are smaller than those of the B concentrations, whereas they are consistent with that estimated from Hall measurements. These results indicate the low effectiveness of carrier doping, which will be discussed later.

The lifetime (τ) of the carrier can be estimated from the peak width (Δk) in the MDC at E_{F} by using the Heisenberg's uncertainty relation between time and energy: $\tau = \hbar/(v_{\mathrm{F}}\Delta k)$, where v_{F} is the Fermi velocity. The estimated τ were 2.8 and 5.1 fs for the medium- and heaviest-doped samples, respectively, although this gives the lowest limit of the lifetime as the observed MDC width includes the contribution of the three-dimensionality of the electronic structure. Interestingly, the lifetime was found to be correlated with T_{c} [55].

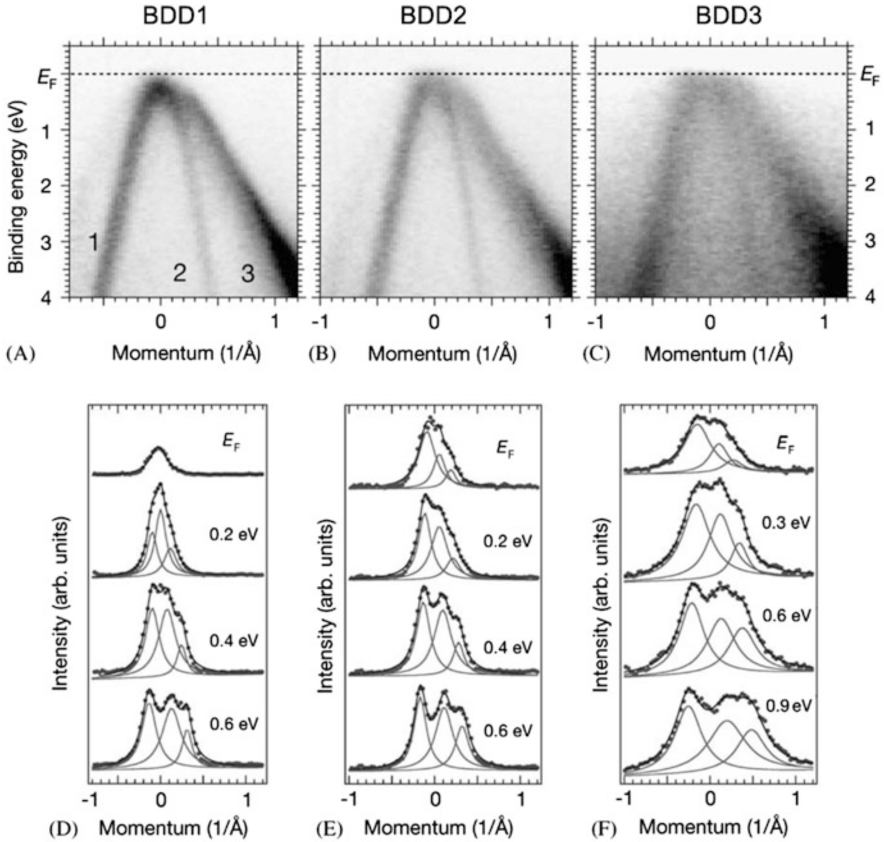

Fig. 3.14 Valence band dispersions near E_F of lightly B-doped nonsuperconductive (top left), mediumly B-doped superconductive (top middle), and heavily B-doped superconductive (top right) diamond measured with ARPES. The bottom figures are momentum distribution curves (dots), together with results of curve fittings. (Reprint with permission from [53] Copyright 2006 by Elsevier Science Ltd.)

3.3.3.4 Fermi Surface

The Fermi surface (FS) is a constant-energy surface at E_F in the BZ, which is intimately related to the physical properties of solids. Heavily B-doped diamond is expected to have three Fermi surfaces centered at the Γ point in the BZ (Fig. 3.15). In Fig. 3.16, the ARPES intensities at E_F are plotted as functions of $k_\perp$ and $k_\parallel$, where the higher intensity parts correspond to the FS cross sections [55]. The observed FS cross sections show good agreement with the calculated ones superimposed on the figure. Because the total volume surrounded by the FSs corresponds to the carrier concentration, we can estimate the carrier concentration from the total volume of the calculated FSs. The obtained carrier concentration is 3.1×10^{21} cm^{-3}. The carrier

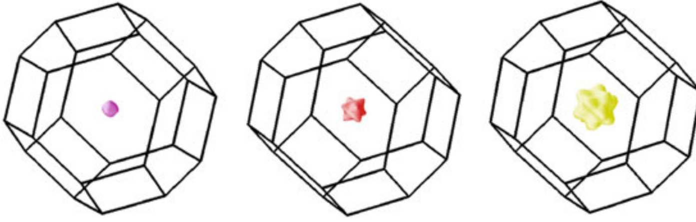

Fig. 3.15 Calculated energy contours of diamond at $E_B = 0.4\,\text{eV}$ below E_F, which correspond to Fermi surfaces of hole-doped diamond in the case of rigid shift. Three Fermi surfaces are expected to exist

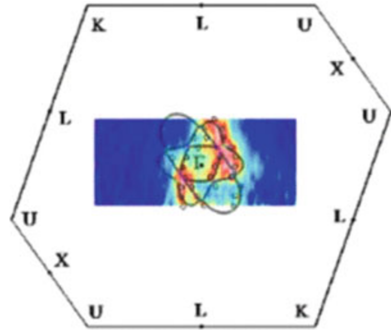

Fig. 3.16 Fermi surface mapping of heavily B-doped superconductive diamond, as compared with calculated Fermi surface cross sections. (Reprint with permission from [55] Copyright 2015 by AIP Publishing)

concentrations in B-doped diamond derived from the ARPES data were also found to be correlated with T_c as with the lifetimes mentioned above [55].

3.3.3.5 Impurity State

The evolution of electronic states near or within the bandgap as a function of B concentration were studied by X-ray emission spectroscopy (XES) and X-ray absorption spectroscopy (XAS) [57–59]. XAS utilizes the excitation of a core electron of a particular element to an unoccupied state and XES the relaxation followed by the core electron excitation. Both processes are governed by a selection rule of photon-mediated transition of electrons. Consequently, they can provide the element-specific and orbital-selective partial DOS of the valence band (XES) and of unoccupied states (XAS), respectively. From the combined study of XES and XAS [59], it was suggested that the impurity state exists near the top of the valence band in nonsuperconducting B-doped diamond, which may be localized. In contrast, the impurity state of superconducting B-doped diamond seems to be merged with the valence band, meaning that holes in the merged state play an important role in the occurrence of superconductivity of B-doped diamond. For a B-doped diamond film with carrier concentration under the n_c (carrier concentration measured by Hall measurements $n_{\text{Hall}} = 1.3 \times 10^{20}\,\text{cm}^{-3}$), the formation of an impurity band close

to the top of the valence band has been also reported from optical reflectivity measurement [56]. Besides such an impurity band, XAS revealed that new states appear in the bandgap under a heavy B doping. As the origin of the new states, the formation of B–B and B–H species has been proposed from the angle-dependent intensity variation in the XAS spectra [60].

3.3.3.6 Phonon Dispersion and Electron Phonon–Coupling

Phonon dispersion of type I and type II diamond was reported in 1960, which was measured with inelastic neutron scattering (INS) [61]. It showed the optical and acoustic phonon modes along several high symmetry lines. INS measurements for superconductive films show strong softening of optical–phonon modes near the BZ center, which supports theoretical models suggesting a phonon-mediated paring mechanism via coupling of optical modes to FSs around the zone center. In contrast, no coupling was observed for the acoustic modes [62]. An electron–phonon coupling parameter is estimated experimentally to be approximately $\lambda = 0.33$ [63]. Very strong coupling between electrons and a phonon mode at $1330\,\mathrm{cm}^{-1}$ (164.9 meV) was revealed from the dip structure in the reflectance and optical conductivity spectra for a lightly doped sample ($n_{\mathrm{Hall}} = 1.3 \times 10^{20}\,\mathrm{cm}^{-3}$) [56]. The strong coupling of doped carrier to the high-energy optical phonons ($\sim$150 meV $= \sim$1210 cm^{-1}) was also demonstrated by multiphonon side bands of the Fermi edge in the PES spectrum in the superconducting sample (B concentration determined by secondary ion mass spectroscopy $n_{\mathrm{B,SIMS}} = 8.4 \times 10^{21}\,\mathrm{cm}^{-3}$) [64].

3.3.3.7 Superconducting Gap

The superconducting phase is characterized by the formation of Cooper pairs, which give rise to an energy gap stabilizing the superconducting state. The DOS(ω) of a superconductor near E_{F} as a function of energy (ω) is expressed by the BCS function

$$\mathrm{DOS}(\omega, \Delta) = N(0)\frac{|\omega|}{\sqrt{\omega^2 - |\Delta|^2}}. \tag{3.7}$$

Owing to the opening of the superconducting gap, this function has divergences adjacent to the superconducting gap (Fig. 3.17), which is sometimes called the condensation peak. The value of the superconducting gap is a measure of how the Cooper pair is bonded. The BCS theory predicts the reduced gap value as follows:

$$\frac{2\Delta}{k_{\mathrm{B}}T_{\mathrm{c}}} \simeq 3.5. \tag{3.8}$$

When this value is higher (equal or lower) than 3.5, the superconductor is classified as a strong-coupling (weak-coupling) superconductor. The phenomenological BCS function (Dynes function) is also used frequently:

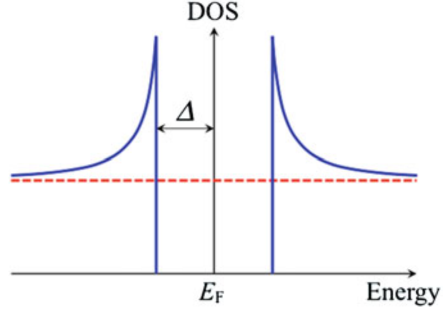

Fig. 3.17 Schematic drawing of superconducting DOS (lines) and normal state DOS (broken lines) near E_F

$$\mathrm{DOS}(\omega, \Delta, \Gamma) = \mathrm{Re}\left[\frac{(\omega - i\Gamma)}{\sqrt{(\omega - i\Gamma)^2 - |\Delta|^2}}\right], \tag{3.9}$$

where Γ is the broadening parameter, which is practically used as a fitting parameter in the analysis of the gap shapes obtained experimentally. Whereas Γ was originally introduced to express the recombination time of the Cooper pair, it can also express the distribution of the gap size originating from the sample homogeneity and/or the symmetry of the superconducting state.

The superconducting gap of heavily doped diamond has been studied by several spectroscopic techniques. High-resolution photoemission studies of (111) film shows the reduction in intensity near E_F across T_c, which is indicative of the opening of the superconducting gap (Fig. 3.18) [65]. The spectral shape was found rather broad and does not show a clear condensation peak. The fitting analysis using the broadened BCS function and assuming a BCS-like temperature dependence of $\Delta(T)$ gave the magnitude of the superconducting gap at 0 K (Δ(0 K)) of 1.01 meV. This gives the reduced gap value $2\Delta/k_B T_c = 3.56$, classifying the superconductivity of diamond as a weakly coupled BCS superconductor. The value of Γ is comparable to Δ, which is related to the broader spectral shape.

Scanning tunneling microscopy/spectroscopy (STM/STS) experiments on (111)-oriented epitaxial films of heavily B-doped diamond grown by MPCVD were reported. These showed a broader superconducting spectral shape giving Δ = 0.83–0.87 meV and Γ $\sim$ 0.38 meV at 0.47 K, leading to reduced gap values of 3.57–3.7. The tunneling conductance spectra measured at 0.47 K do not show strong spatial dependence. However, STS studies of high-quality single-crystalline (100) B-doped diamond below 100 mK showed a clear superconducting gap with sharp condensation peaks in the tunneling DOS, yielding $2\Delta/k_B T_c \sim 3.48$ [66].

The optical spectroscopy of heavily B-doped diamond revealed changes in the reflectively across T_c, which can be explained by the BCS function in the dirty limit [67]. The reduced gap value was estimated to be $\sim$3, smaller than that of the mean-field BCS value. The reason for this was explained in terms of the anisotropic superconducting gap.

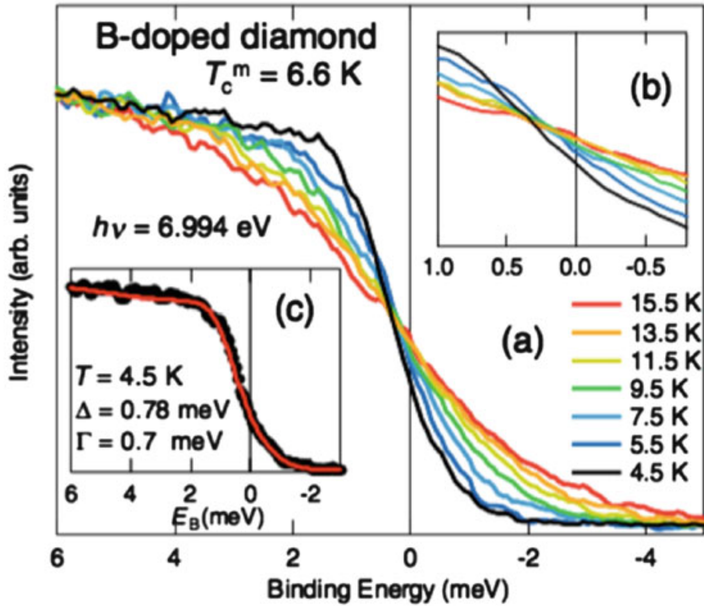

Fig. 3.18 Temperature-dependent high-resolution PES spectra of heavily B-doped superconductive diamond. Reduction in the intensity at E_F below T_c indicates opening of superconducting gap. (Reprint with permission from [65] Copyright 2007 by American Physical Society)

3.3.4 Lower Efficiency of Carrier Doping (Chemical Sites)

As discussed above, the carrier concentration of the heavily B-doped diamond is much smaller than that of the B concentration. This means that some of the doped B atoms are inactive or even compensate the introduced carriers, suggesting the existence of some of the B atoms incorporated into sites other than substitutional sites in the diamond lattice. How the doped B atoms could be incorporated into the crystal is an important issue, because such knowledge will yield insights into how to increase the effective carrier concentration and possibly to increase T_c.

Experimentally, multiple chemical sites were reported from NMR studies [68]. The NMR spectra consist of a sharp peak and a broad structure. The intensity of the sharp peak has a good correspondence to the superconductivity, which was ascribed to be a substitutionally introduced B atom. For the broad feature, it was conjectured that the structure is originated from the neutral B–H complex. Photoemission measurements for the B 1*s* core levels also show several chemical sites (Fig. 3.19) [69]. The photon energy dependence and B concentration dependence have shown the existence of several bulk chemical sites. Within the observed three bulk site components, the intensity of that with the lowest binding energy was found to be correlated to T_c (Fig. 3.20). This indicates that one of the bulk chemical sites is responsible for yielding carriers and thus the metallic and superconducting states.

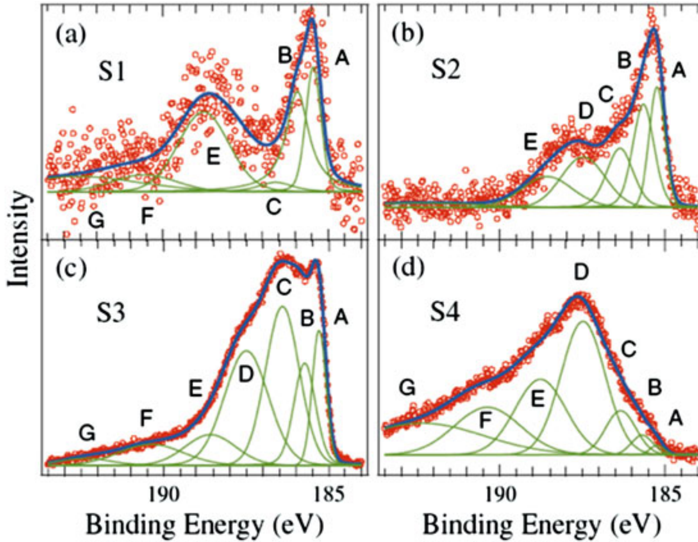

Fig. 3.19 B 1*s* core level spectra (circles) of four samples with different B concentration and synthesis conditions, together with fitting results (curves). (Reprint with permission from [69] Copyright 2009 by The Physical Society of Japan)

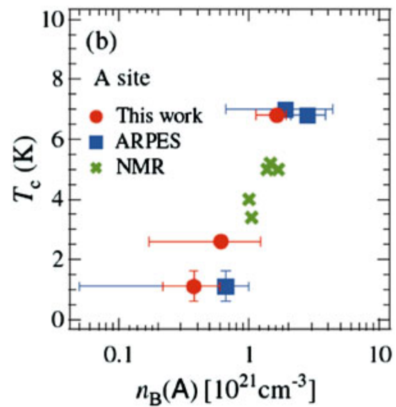

Fig. 3.20 Relation between T_c and relative area of one chemical component of the B 1*s* core level spectrum, compared with other studies. (Reprint with permission from [69] Copyright 2009 by The Physical Society of Japan)

Photoelectron holography, which can observe three-dimensional local structure around an impurity atom, can be used to determine the local structure around a doped B atom [70]. The photoelectron holography study revealed that the doped B atoms have a tendency to incorporate into one of the two C sites in the diamond structure, where the B atoms form three covalent bonds with C atoms underneath them instead of one bond at the other site during the film growth process in the (111) plane. However, the energy resolution of the study could not resolve the difference in the local structures around the B atoms in different chemical sites. High-resolution

photoelectron holography studies could determine the local structure of a B atom that plays a crucial role for carrier introduction and will be performed in the near future.

3.4 Summary and Future Prospects

In this chapter, we described the electronic structure of pristine (insulating), lightly doped (semiconducting), and heavily B-doped (metallic and superconducting) diamond. The exceptional properties of diamond can be explained in terms of the electronic states, which stem from the bonding of the C atoms and the crystal structure. The superconductivity of diamond is interesting, as it occurs in a material with such exceptional properties and in the carrier concentration region where the NM-M transition takes place, with importance of disorder. Because the electronic states are the key to understand the physical properties, reliable and precise measurements can deepen our knowledge of the physical properties. In this regard, it may be worth noting the advancement of the experimental method: many of the experimental studies described in the latter part of this chapter are indebted to third-generation synchrotron radiation facilities with high photon density. The advancements of both experimental and theoretical techniques, including supercomputers, will give further insight into many-body interactions of electrons in diamond.

Acknowledgements This research was partially supported by the Grant-in-Aid for Scientific Research from the Japan Society for the Promotion of Science (17H05220).

References

1. J.E. Field (ed.), *The Properties of Diamond* (Academic Press, London, 1979)
2. L.S. Pan, D.R. Kania (ed.), *Diamond: Electronic Properties and Applications* (Springer Science+Business Media, New York, 1995)
3. T.D. Ladd et al., Nature **464**, 45 (2010)
4. O. Madelung, *Semiconductors: Data Handbook*, 3rd edn. (Springer, Berlin/Heidelberg/New York, 2004)
5. J. Serrano, M. Cardona, T. Ruf, Solid State Commun. **113**, 411 (2000)
6. E.A. Ekimov et al., Nature **428**, 542 (2004)
7. C. Kittel, *Introduction to Solid State Physics*, 8th edn. (Wiley, New York, 2005)
8. G. Grosso, G.P. Parravicini, *Solid State Physics* (Academic, Orland, 2000)
9. N.W. Ashcroft, N.D. Mermin, *Solid State Physics* (Holt, Rinehart and Winston, New York, 1976)
10. P.Y. Yu, M. Cardona, *Fundamentals of Semiconductors: Physics and Materials Properties* 3rd edn. (Springer, Berlin/Heidelberg/New York, 2005)
11. W.A. Harrison, *Electronic Structure and the Properties of Solids: The Physics of the Chemical Bond* (Dover, New York, 1989)
12. S.M. Sze, *Semiconductor Devices, Physics and Technology*, 2nd edn. (Wiley, New York, 2002)
13. N.F. Mott, *Metal-Insulator Transitions*, 2nd edn. (Taylor & Francis, London/New York, 1990)

14. C.E. Nebel, J. Ristein (ed.), *Thin-film diamond II* (Elsevier Academic Press, Amsterdam, 2004)
15. M. Rohlfing, P. Krüger, J. Pollmann, Phys. Rev. B **48**, 17791 (1993)
16. J.P. Perdew, K. Burke, M. Ernzerhof, Phys. Rev. Lett. **77**, 3865 (1996)
17. P. Blaha, K. Schwarz, G.K.H. Madsen, D. Kvasnicka, J. Luitz, *Wien2k: An Augmented Plane Wave + Local Orbitals Program for Calculating Crystal Properties* (Vienna University of Technology, Wien, 2001)
18. N. Naka, K. Fukai, Y. Handa, I. Akimoto, Phys. Rev. B **88**, 035205 (2013)
19. S. Koizumi, T. Teraji, H. Kanda, Diam. Relat. Mater. **9**, 935 (2000)
20. H. Fritzsche, The metal-nonmetal transition in doped semiconductors, in *The Metal Non-Metal Transition in Disordered Systems* ed. by L.R.F. Friedman, D.P. Tunstall. Proceedings of the nineteenth Scottish Universities Summer School in Physics, St. Andrews, Edinburgh (1978)
21. F.J. Rogers, H.C. Graboske Jr., D.J. Harwood, Phys. Rev. A **1**, 1577 (1970)
22. H. Fritzsche, J. Phys. Chem. Solids **6**, 69 (1958)
23. P.P. Altermatt, A. Schenk, G. Heiser, J. Appl. Phys. **100**, 113714 (2006)
24. K.M. Itoh, M. Watanabe, Y. Ootuka, E.E. Haller, T. Ohtsuki, J. Phys. Soc. Jpn. **73**, 173 (2004)
25. E. Abrahams, P.W. Anderson, D.C. Licciardello, T.V. Ramakrishnan, Phys. Rev. Lett. **42**, 673 (1979)
26. A. Gaymann, H.P. Geserich, H. v. Löhneysen, Phys. Rev. Lett. **71**, 3681 (1993)
27. J. Doehler, Phys. Rev. B **12**, 2917 (1975)
28. T. Kurosawa, M. Matsui, W. Sasaki, J. Phys. Soc. Jpn. **42**, 1622 (1977)
29. T. Klein, P. Achatz, J. Kacmarcik, C. Marcenat, F. Gustafsson, J. Marcus, E. Bustarret, J. Pernot, F. Omnes, Bo E. Sernelius, C. Persson, A Ferreira Da Silva, C. Cytemann, Phys. Rev. B **75**, 165313 (2007)
30. P. P. Edwards and M. J. Sienko, Phys. Rev. B **17**, 2575 (1978)
31. J. Hubbard, Proc. R. Soc. London, Sec. A **276**, 23 (1963)
32. X.Y. Zhang, M.J. Rozenberg, G. Kotliar, Phys. Rev. Lett. **70**, 1666 (1993)
33. P.W. Anderson, Phys. Rev. **109**, 1492 (1985)
34. A. Lagendijk, B. van Tiggelen, D.S. Wiersma, Phys. Today **62**, 24 (2009)
35. D. Belitz, T.R. Kirkpatrick, Rev. Mod. Phys. **66**, 261 (1994)
36. Y. Takano et al., Appl. Phys. Lett. **85**, 2851–2853 (2004)
37. V.A. Sidorov et al., Phys. Rev. B **71**, 060502(R) (2005)
38. E. Bustarret et al., Phys. Rev. Lett. **93**, 237005 (2004)
39. V.V. Brazhkin et al., Phys. Rev. B **74**, 140502(R) (2006)
40. A. Kawano et al., Phys. Rev. B **82**, 085318 (2010)
41. L. Boeri, J. Kortus, O.K Andersen, Phys. Rev. Lett. **93**, 237002 (2004)
42. K.-W. Lee, W.E. Pickett, Phys. Rev. Lett. **93**, 237003 (2004)
43. X. Blasé, Ch. Adessi, D. Connetable, Phys. Rev. Lett. **93**, 237004 (2004)
44. H.J. Xiang, Z. li, J. Yamg, J.G. Hou, Q. Zhu, Phys. Rev. B **70**, 212504 (2004)
45. K.-W. Lee, W.E. Pickett, Phys. Rev. B **73**, 075105 (2006)
46. Y. Ma et al., Phys. Rev. B **72**, 014306 (2005)
47. G. Baskaran, J. Supercond. Nov. Magn. **21**, 45–49 (2008)
48. T. Shirakawa et al., J. Phys. Soc. Jpn. **76**, 014711 (2007)
49. Y. Yanase, N. Yorozu, J. Phys. Soc. Jpn. **78**, 034715 (2009)
50. Y.G. Pogorelov et al., Phys. Rev. B **72**, 075213 (2005)
51. K. Yamamoto, H. Yoshida, Diamond Relat. Mater. **13**, 736 (2004)
52. T. Yokoye et al., New Diamond Front. Carbon Technol. **17**, 11 (2007)
53. T. Yokoya et al., Sci. Technol. Adv. Mater. **7**, S12, (2006)
54. H. Okazaki et al., J. Phys. Chem. Solid **69**, 2978–2981 (2008)
55. H. Okazaki et al., Appl. Phys. Lett. **106**, 052601 (2015)
56. D. Wu et al., Phys. Rev. B **73**, 012501 (2006)
57. J. Nakamura et al., Phys. Rev. B **70**, 245111 (2004)
58. J. Iihara et al., Jap. J. Appl. Phys. **44**, 6612–6617 (2005)
59. J. Nakamura et al., J. Phys. Soc. Jpn. **77**, 054711 (2008)
60. J. Nakamura et al., Physica C **470**, 5671–5672 (2010)

61. J.L. Warren et al., Phys. Rev. **158**, 805 (1967)
62. M. Hoesch et al., Sci. Technol. Adv. Mater. **7**, S31 (2006)
63. M.Hoesch et al., Phys. Rev. B **75**, 140508 (2007)
64. K. Ishizaka et al., Phys. Rev. Lett. **100**, 166402 (2008)
65. K. Ishizaka et al., Phys. Rev. Lett. **98**, 047003 (2007)
66. B. Sacepe, Phys. Rev. Lett. **96**, 097006 (2006)
67. M. Ortolani et al., Phys. Rev. Lett. **97**, 097002 (2006)
68. H. Mukuda et al., Phys. Rev. B **75**, 033301 (2007)
69. H. Okazaki et al., J, Phys. Soc. Jpn. **78**, 034703 (2009)
70. Y. Kato et al., Appl. Phys. Lett. **91**, 251914 (2007)

Chapter 4
Physics of Carbon Nanotubes and New Type of Carbon Network Materials: Electronic and Magnetic Properties

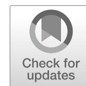

Susumu Okada and Mina Maruyama

Abstract In this chapter, using the density functional theory with the appropriate approximations for the exchange-correlation potential of interacting electrons, we explain the electronic structure of carbon nanotubes under the external electric field and the magnetic properties of two-dimensional (2D) sp^2 C networks with topological defects. The capacitances of the CNTs with ellipsoidal and squashed cross sections implemented in the conducting channel in the field-effect transistor are different from that of the pristine CNT owing to the distribution of accumulated carriers depending on the CNT deformation and arrangements with respect to the electric field direction. The 2D networks induce the spin polarization and long-range magnetic spin ordering depending on their network topology, boundary condition, and topological defect implanted in the networks.

Keywords CNT-FET · Electric field · Electronic structures · Topological defects · Magnetic properties

4.1 Introduction

Ever since the discovery of fullerene and carbon nanotubes, low-dimensional materials consisting of carbon atoms with threefold coordination have occupied a premier position in the nanoscale sciences [1]. These materials are obtained by imposing boundary conditions on graphene with an appropriate shape and size. These conditions result in a variety of carbon allotropes with one or zero dimensions. For instance, carbon nanotubes are a one-dimensional allotrope of carbon that can be considered as a rolled-up sheet of graphene with appropriate connecting conditions between the two edges [2–4]. As another example, fullerene has a hollow-cage structure with zero dimensions, where the cage structure consists

S. Okada (✉) · M. Maruyama
Graduate School of Pure and Applied Sciences, University of Tsukuba, Tennodai, Tsukuba, Japan
e-mail: sokada@comas.frsc.tsukuba.ac.jp; mmaruyama@comas.frsc.tsukuba.ac.jp

© Springer Nature Singapore Pte Ltd. 2019

Y. Kubozono (ed.), *Physics and Chemistry of Carbon-Based Materials*,
https://doi.org/10.1007/978-981-13-3417-7_4

of 12 pentagons and a number of hexagons [5–7]. It is known that differences in the boundary conditions imposed on nanoscale graphene sheets produce a rich variety of electronic properties in these low-dimensional carbon allotropes. For example, seamless cylindrical structures result in either metallic or semiconducting electronic structures, depending on the helical angles in the hexagonal networks on the cylinders [3, 4]. In addition, the occupied electronic states of fullerenes were pointed out to correspond to the spherical harmonic states (Y_{lm}) in ordinary atoms, due to the spherical structure [8].

According to the characteristic electronic properties of these low-dimensional carbon allotropes, they have also attracted much attention in the field of nanoscale engineering; they can be used as constituent units in both nanoscale electronic devices and nanoscale functional materials. Carbon nanotubes in particular are regarded as key emerging materials for next-generation nanometer-scale electronic devices, because of their characteristic electronic and geometric structures. Indeed, it has been demonstrated that individual semiconductor carbon nanotubes can function as field-effect transistors (FETs), by forming hybrid structures with insulating substrates and metal electrodes [9–12], and a mat of carbon nanotubes was shown to function as a flexible integrated circuit [13]. In the FET structures, CNTs intrinsically possess defects and structural deformations that seriously modulate the electronic structure of CNTs as stated above. For CNTs with atomic and topological defects in FET structures, the carrier accumulation strongly depends on the mutual orientation of the defects with respect to the applied external electric field by the electron polarization around the defects [14, 15]. In addition to the defects, structural deformations are also induced by forming hybrid structures with foreign materials, such as other CNTs, insulating substrates, and metal electrodes [16–20]. In such situations, CNTs possess ellipsoidal and squashed cross sections due to the substantial interaction with foreign materials. Although several researches have investigated the electronic properties of CNTs under an external electric field [21–26], the fundamental properties of carrier accumulation into CNTs with FET structures by an electric field are not fully understood. In particular, it is still unclear how the structural deformations of CNTs affect the electronic properties and charge accumulation under an electric field, which is an important issue for the application of CNTs in semiconducting electronic devices.

Polymerization and oligomerization of hydrocarbon molecules can provide structurally well-defined π electron networks with various dimensionalities. These low-dimensional or porous graphene networks have attracted much attention because of their high surface areas and electronic structure modulation, which are promising for application in energy and electronic devices in the near future [27–30]. The electronic structures of such polymers and oligomers strongly depend on the combination of hydrocarbon molecules and polymer chains, which allows us to tailor their physical and chemical properties by fabrication under optimum external conditions [31–34]. This indicates that porous magnetic carbon nanomaterials may be synthesized by polymerizing hydrocarbon molecules with radical spins. Phenalenyl is one possible candidate as a constituent unit of such magnetic materials [35–39]. Dimerization of triphenylphenalenyl and cyclodehydrogenated phenalenyl leads to complexes containing two phenalenyls possessing singlet and

triplet spin coupling as their stable states [40–43]. Despite intensive experimental and theoretical work on two phenalenyls connected via a covalent π network, the possible electronic structures of 2D networks consisting of phenalenyl molecules have not yet been investigated in detail. The threefold symmetry of the phenalenyl network causes honeycomb networks of radical spins or nonbonding state to be distributed on phenalenyls with appropriate interconnect units, leading to interesting electron systems that are characterized by competition between slow massless electrons and radical spin at E_F.

For the electronic structure calculations, we use the density functional theory [44, 45] with local density approximation [46, 47] for CNT-FET and generalized gradient approximation [48] for the magnetic C nanostructures. A Vanderbilt ultrasoft pseudopotential was used to describe the electron-ion interaction [49].

4.2 Electrostatic Properties of Carbon Nanotubes Under an Electric Field

In this section, we demonstrate the fundamental electronic properties of zigzag (20,0)CNTs with ellipsoidal and squashed cross sections in CNT-FET structure under an electric field based on first-principles total-energy calculations using density functional theory [50]. To simulate the CNT-FET device structure, we consider the structural model shown in Fig. 4.1, in which the CNT is located below the planar gate electrode simulated by an effective screening medium with the infinite permittivity to mimic an ideal metal electrode. The center of the deformed CNTs is located at 15.88 Å below the electrode. In addition, we consider the other CNT arrangements in which the deformed CNTs possess the same spacing between the electrode and the CNT wall of 3.18 and 6.28 Å. An electric field is applied between the electrode and the CNT up to the gate voltage, which injected 0.5 carriers into CNTs per unit cell. The CNTs with squashed and ellipsoidal shapes were obtained by performing the structural optimization on (20,0) CNTs under zero field with a structural constraint that the topmost and the bottommost dimer rows are fixed. The lattice parameter along the tube axis is fixed at 4.26 Å corresponding to the single periodicity of zigzag CNTs. To investigate the electronic properties of an

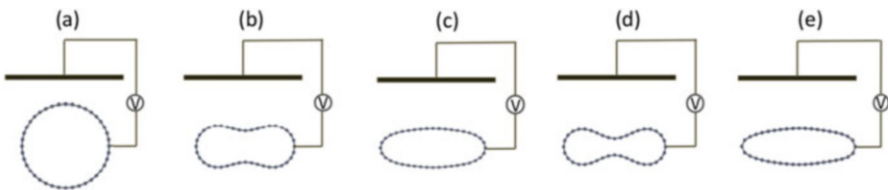

Fig. 4.1 Structural models of deformed CNT under an electric field. The (20,0) CNTs with (**a**) circular, (**b**) moderately squashed (MS), (**c**) moderately ellipsoidal (ME), (**d**) tightly squashed (TS), and (**e**) tightly ellipsoidal (TE) cross sections are arranged below the planar electrode denoted by black thick lines

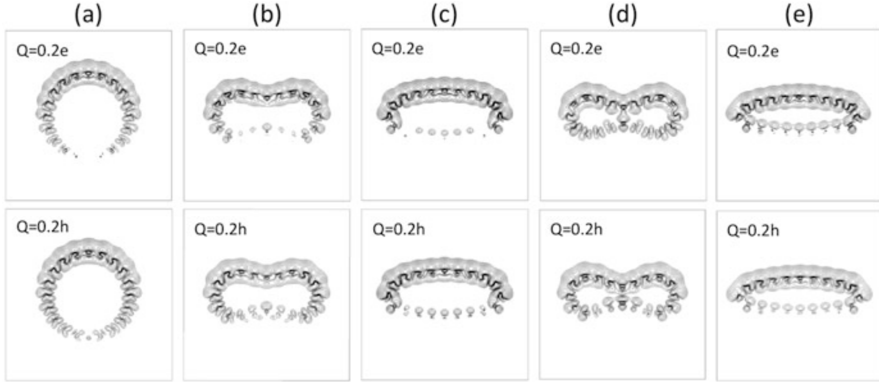

Fig. 4.2 Contour plots of accumulated carriers by the electric field of (20,0) CNT with (**a**) circular, (**b**) moderately squashed (MS), (**c**) moderately ellipsoidal (ME), (**d**) tightly squashed (TS), and (**e**) tightly ellipsoidal (TE) cross sections. In each panel, 0.2e and 0.2h denote 0.2 electrons and 0.2 holes per unit cell, respectively

isolated CNT, each CNT is separated by an 8 Å interwall spacing from its periodic images. During the calculations under the conditions with a finite electric field, the atomic geometries were kept the same as those with a zero electric field.

Figure 4.2 shows the distributions of accumulated electrons (0.2e/cell) and holes (0.2h/cell) in CNTs with circular, squashed, and ellipsoidal cross sections by the external electric field. In this case, the center of the CNT is located at 15.88 Å below the electrode. For all CNTs, the accumulated carriers are primarily distributed on the outer part of the CNT wall at the electrode side for both electron and hole accumulations. In addition to the main distribution, the holes and electrons are also slightly induced on the inner wall of the CNTs at the electrode side under positive and negative bias voltages, respectively. Furthermore, for the case of CNTs with squashed and ellipsoidal shapes, electrons and holes are induced in the inner and outer walls, respectively, at the opposite side to the electrode. In accordance with the carrier distribution induced by the electric field, the hybrid system consisting of the deformed CNT and electrode can be regarded as two capacitors connected in series. In contrast to the CNTs with structural deformations, charge redistribution in the pristine CNT induced by the electric field exhibits different natures: the accumulated/depleted carriers oscillate along their circumference.

Figure 4.3 shows the contour plots of electrostatic potential and the vector plots of corresponding electric field under the electron (0.2e/cell) and hole (0.2h/cell) accumulations. The potential gradient or the electric field is primary concentrated at the electrode side of the CNTs, while the electric field is absent around the opposite side of the CNTs, because of the concentration of the accumulated carriers at the electrode side of the CNTs. On the other hand, the detailed electrostatic potential and electric field strongly depend on the shape of CNTs: for the pristine and squashed CNTs, the field concentration occurs around the part of the CNT wall with a large curvature as in the case of the conducting materials with a protruding portion

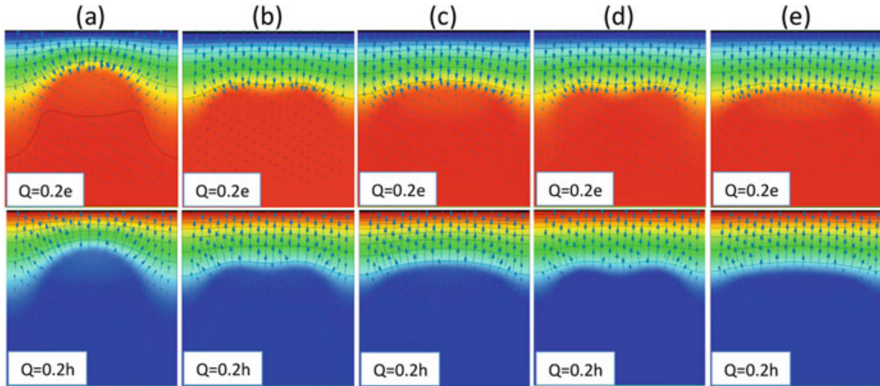

Fig. 4.3 (Color online) Contour and vector plots of electrostatic potential and electric field, respectively, of (20,0)CNT with (**a**) circular, (**b**) moderately squashed (MS), (**c**) moderately ellipsoidal (ME), (**d**) tightly squashed (TS), and (**e**) tightly ellipsoidal (TE) cross sections. In each panel, 0.2e and 0.2h denote 0.2 electrons and 0.2 holes per unit cell, respectively

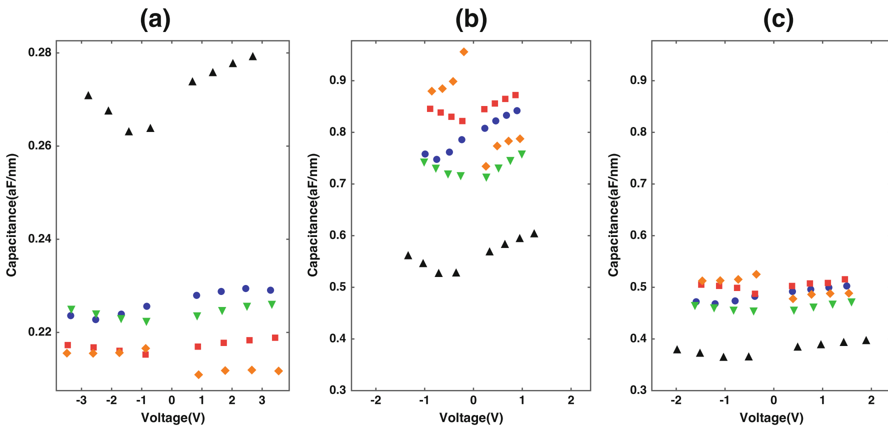

Fig. 4.4 (**a**) Capacitances of pristine and deformed (20,0)CNTs situated below the electrode by the spacing of 15.88 Å between the center of CNTs and the electrode. Capacitance of pristine and deformed (20,0)CNTs arranged with the spacing between the electrode and the CNT walls of (**b**) 3.18 and (**c**) 5.29 Å. Triangles, circles, inverse triangles, squares, and rhombuses denote capacitances of CNTs with circular, moderately squashed (MS), moderately ellipsoidal (ME), tightly squashed (TS), and tightly ellipsoidal (TE) cross sections, respectively

in the classical electrodynamics. In contrast, for the CNTs with the ellipsoidal cross section, the almost constant field emerges around the outer wall of the CNTs, since the CNTs possess a flat region with respect to the electrode.

Figure 4.4 shows the calculated total capacitance of CNTs,

$$C = \frac{dQ}{d\mu} = \frac{C_0 D}{C_0 + D}$$

where C_0 and D denote the geometrical capacitance and density of states of CNT, respectively [26], as a function of the gate voltage. The capacitance strongly depends on both the gate voltage and CNT cross sections. The pristine CNT possesses the largest capacitance among the five CNTs studied here. The largest capacitance of the pristine CNT is ascribed to the structural model studied here, that is, the center of the CNT is located at 15.88 Å below the electrode. Thus, the spacing between the electrode and the wall of the pristine CNT is smaller than that of the other deformed CNTs, leading to the largest geometrical (classical) capacitance C_0. Indeed, the capacitance decreases with increasing structural deformation of CNTs causing the increase in the spacing between the CNT and the electrode. For instance, the moderately ellipsoidal and squashed CNTs possess a smaller capacitance than that with the tightly deformed cross sections. In addition to the spacing between the electrode and the CNT wall, the cross section of CNTs also affects the capacitance. For the deformed CNT with the same length in its minor axis, the capacitance of the squashed CNT is larger than that of the ellipsoidal CNT. In the case of the CNT with the squashed cross section, the two convex regions of the wall cause a larger capacitance than that of the CNT with an ellipsoidal cross section.

It is worth investigating how the distribution of accumulated carriers and electric field depend on the relative arrangement of the deformed CNT to the electric field. Figure 4.5 shows the contour and vector plots of the accumulated carrier and electric field, respectively, of the deformed CNTs tilted to the electric field under 0.2e/cell and 0.2h/cell injections. For all CNTs with the parallel arrangement to the electric field ($\theta = 90$ deg.), accumulated electrons are mainly concentrated at the top of the CNT facing to the electrode. Furthermore, accumulated/depleted carriers oscillate along the circumference as in the case of the CNT with the circular cross section. Owing to the large curvature of the CNTs with squashed and ellipsoidal cross sections with respect to the electrode, the electric field highly concentrates around the protruding region. With decreasing the CNT orientation to the field, the charge oscillation and field concentration decrease.

To check the effect of the structural deformation on the capacitances, we calculate the capacitance of pristine and deformed CNTs possessing the same spacing between the electrode and the CNT wall of 3.18 and 6.28 Å. Figure 4.4b, c show the capacitances under the spacing of 3.18 and 6.28 Å, respectively. The capacitance of all CNTs is larger under the spacing of 3.18 Å than under the spacing of 6.28 Å. In addition to the spacing, the capacitance increases with increasing deformation, which causes the increases in the lateral area of the deformed CNT with respect to the gate electrode. Indeed, under the fixed CNT-electrode spacing, the CNT with a tightly squashed shape possesses the largest capacitance. Thus, the results indicate that the deformation of the CNT sensitively affects its capacitance in the FET structure.

Since the rotation of the CNT modulates the distribution of accumulated/depleted carriers by the electric field, the capacitances of the CNTs with squashed and ellipsoidal cross sections may depend on the relative arrangement to the electric field. Figure 4.6 shows the calculated capacitances of the deformed CNTs with the rotational angles of 30°, 60°, and 90° with respect to the electric field under

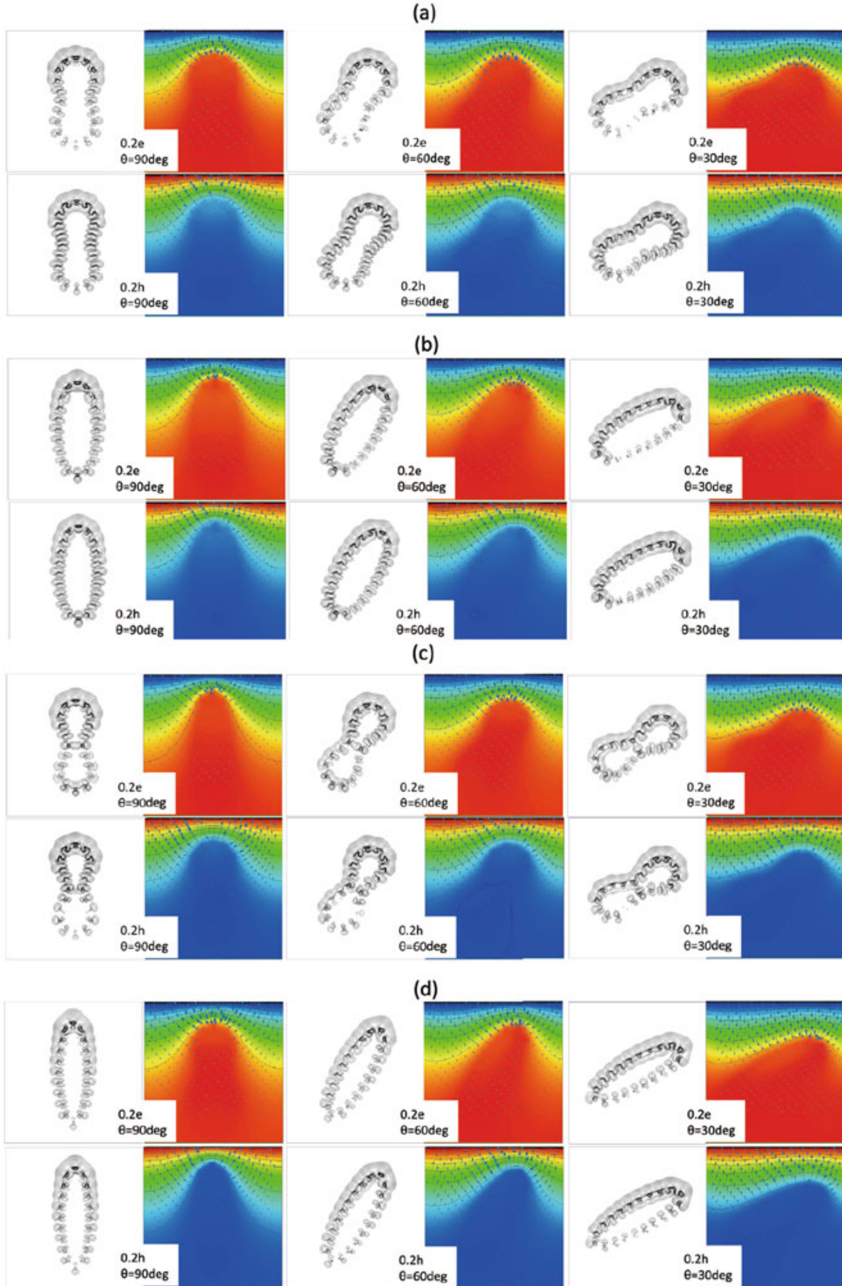

Fig. 4.5 (Color online) Contour and vector plots of accumulated carriers and electric field, respectively, of (20,0)CNT with (**a**) moderately squashed (MS), (**b**) moderately ellipsoidal (ME), (**c**) tightly squashed (TS), and (**d**) tightly ellipsoidal (TE) cross sections under the rotational angles of $\theta = 30°$, $60°$, and $90°$ with respect to the electric field under the carrier injection of 0.2 electrons and 0.2 holes per unit cell

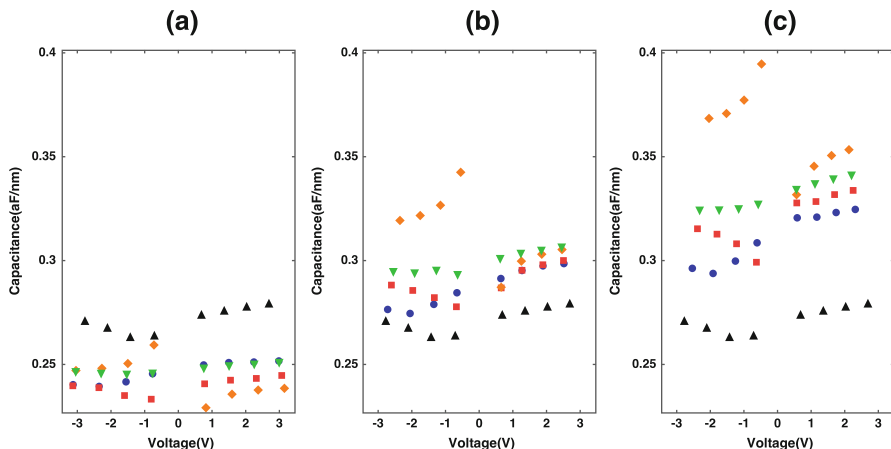

Fig. 4.6 Capacitances of pristine and deformed (20,0)CNTs with the rotational angles of (**a**) 30°, (**b**) 60°, and (**c**) 90°. Triangles, circles, inverse triangles, squares, and rhombuses denote capacitances of CNTs with circular, moderately squashed (MS), moderately ellipsoidal (ME), tightly squashed (TS), and tightly ellipsoidal (TE) cross sections, respectively

the fix distance of 15.88 Å between the electrode and the center of the CNTs. The capacitance strongly depends on their mutual arrangement to the electric field. By increasing the rotational angle, the capacitances of the deformed CNTs monotonically increase. The capacitance is determined by the competition between the decrease in the vacuum spacing and the increase in the area of the CNT with respect to the electrode. Therefore, the CNT orientation with respect to the electric field also affects the carrier accumulation of the CNT with structural deformations in FET structures.

4.3 Magnetism of the 2D Carbon Materials with Topological Defects

In this section, we focus on 2D covalent networks consisting of fused pentagon trimers (acepentalene structure) of which three edges are shared by its three adjacent trimers [51]. Although acepentalene molecule is a bowl-shape molecule (Fig. 4.7a), we assume the molecule possesses flat conformation. We consider two representative networks: A network can be regarded as the honeycomb network of fused acepentalenes of which consists edges are shared by its three adjacent units leading to network consisting of pentagonal rings and large dodecagonal pores (fused pentagon network) (Fig. 4.7b). In addition, we also consider the networks structure of fused pentagon trimers each of which are connected to its three adjacent molecules directly (Fig. 4.7b) and via four-member ring (acepentalene

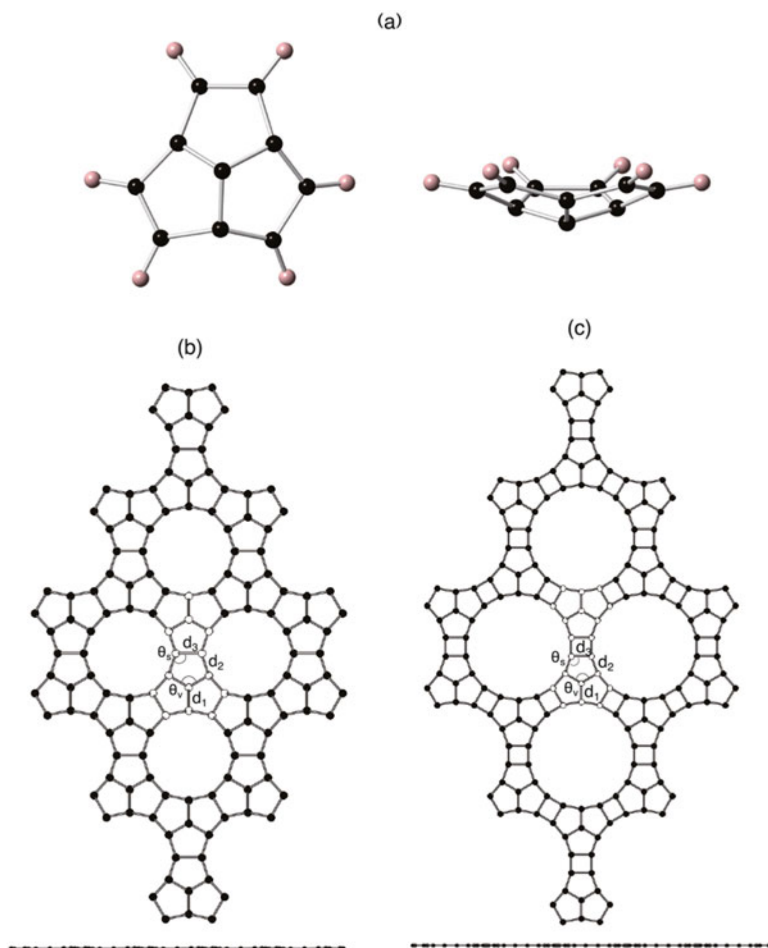

Fig. 4.7 Top and side views for optimized geometries of (**a**) an isolated acepentalene molecule, (**b**) the fused pentagon network, and (**c**) the acepentalene polymer

polymer) (Fig. 4.7c). With this choice of initial geometry, the resulting material has a honeycomb lattice containing 14 C atoms per unit cell for fused pentagon network and 20 C atoms per unit cell for acepentalene polymer network.

Figure 4.8 shows the total energies per atom as a function of lattice parameter a of the fused pentagon network and the acepentalene polymer. We found that the optimum lattice constant is 9.5 and 7.1 Å for the acepentalene polymer and the 2D fused pentagonal network, respectively. The larger lattice parameter of the polymeric acepentalene is ascribed to the four-member ring situated between two acepentalene structures. The calculated total energy of the acepentalene polymer is 0.90 eV/atom with respect to the energy of graphene. The polymeric acepentalene is less stable by 0.29 eV/atom than the fused pentagon network. Therefore, the

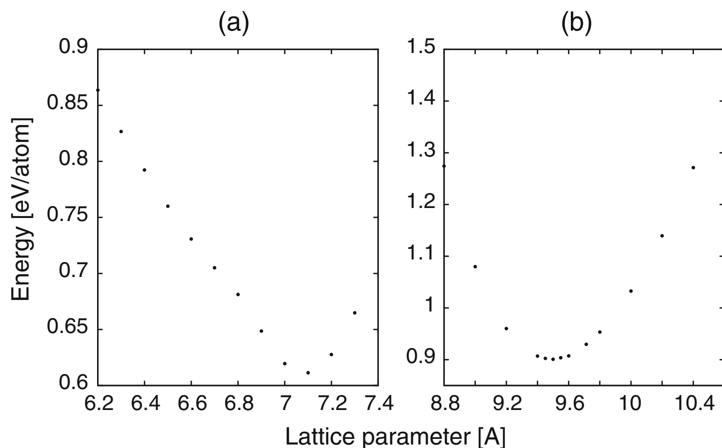

Fig. 4.8 Total energies per atom of (**a**) the acepentalene polymer and (**b**) the fused pentagonal network as a function of the hexagonal lattice parameter a. The energies are measured with respect to the energy of an isolated graphene

polymeric acepentalene is energetically unfavorable solid carbon among many possible conformations [52–54]. It has been demonstrated that the four-member ring in polymeric fullerene usually decreases the total energy of the system with increase of the covalent bond with its adjacent fullerenes. In sharp contrast, in the case of the polymeric acepentalene, planar structure of the acepentalene structure causes substantial energy cost for formation of four-member rings within the pentagonal networks. Since polycyclic hydrocarbon molecules occasionally contain four-member ring in their stable structure, the polymeric acepentalene sheet is expected to exist under ambient condition.

The kinetic stability of the polymerized acepentalene network is worth investigating. We investigated the geometric structure of the 2D covalent networks at temperatures of 1000 and 2000 K by performing ab initio molecular dynamics simulations for a few picosecond simulation times. The simulations showed that the both sheets retain its 2D planar covalent network structure at temperatures up to 2000 K. Therefore, once the sheets are synthesized by an appropriate experimental method, it is expected to retain its characteristic structure under ambient conditions, although the networks show a higher total energy than other carbon allotropes.

Figure 4.9 shows the electronic structure of the fused pentagon network with an equilibrium lattice constant. We found that the acepentalene polymer is a metal in which three branches cross the Fermi level, leading to a finite density of state at the Fermi level (Fig. 4.9a). As shown in Fig. 4.9c, an isolated acepentalene molecule has an energy gap of 1 eV between the highest occupied state and the lowest unoccupied state. The metallic nature of the sheet constructed from the acepentalene units indicates that the interunit covalent bonds extend the distribution of three electrons throughout the sheet. In the case of the fused pentagonal network, the sheet is also a metal. However, in contrast to the acepentalene polymer, the fused pentagon

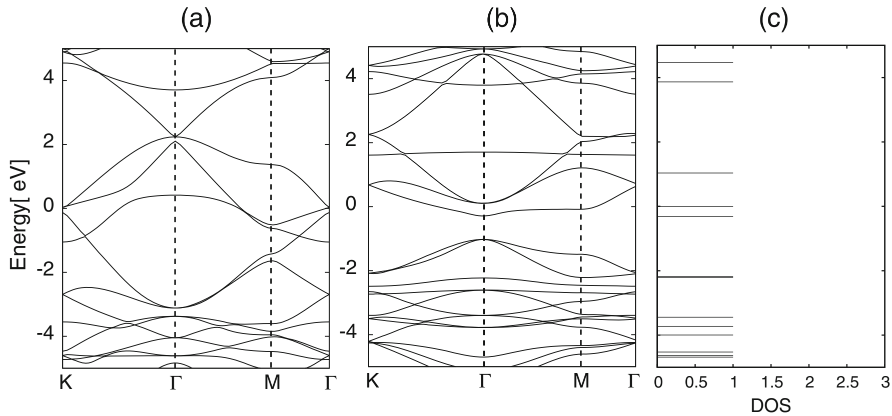

Fig. 4.9 Electronic energy bands near the Fermi level of (**a**) the acepentalene polymer and (**b**) the fused pentagonal network. The energies are measured with respect to the Fermi level. (**c**) Electronic structure of an isolated acepentalene molecule near the Fermi level. The energy is measured from that of the highest occupied state

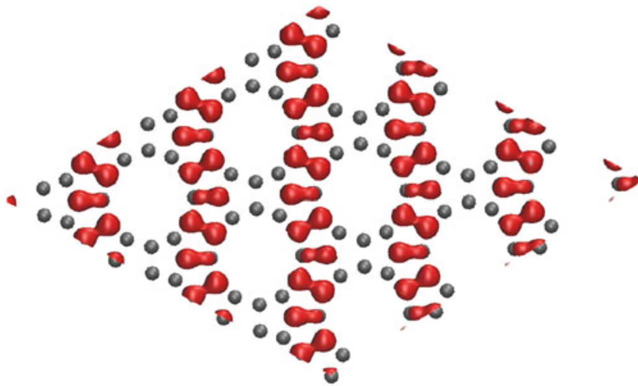

Fig. 4.10 Isosurfaces of the spin density of the fused pentagon sheet. The isosurfaces correspond to 0.001 e/a.u. Gray spheres indicate the atomic positions of the fused pentagon network

network has a flat dispersion band that crosses the Fermi level (Fig. 4.9c). The flat dispersion band has a dispersion of about 0.1 eV around the Γ point. Thus, it is expected that the flat-band state induces spin polarization on the sheet according to the Fermi level instability associated with the flat dispersion band. The flat dispersion band splits into lower and upper branches for the majority and minority spin states, respectively, indicating that the sheet exhibits magnetic ordering. The calculated exchange splitting between the branches of the flat dispersion band is about 0.10 eV, and the induced magnetic moment is 0.62 μ_B/nm^2.

Figure 4.10 shows the isosurfaces of the polarized electron spins of the fused pentagon network. We found that the polarized electron spins are ferromagnetically

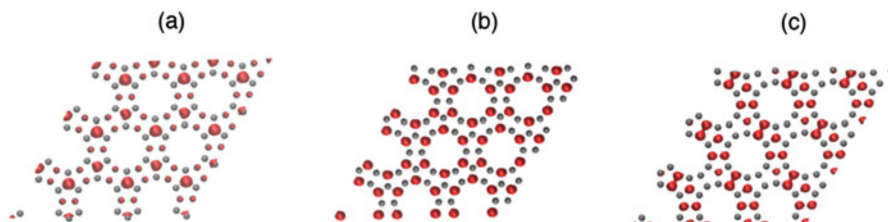

Fig. 4.11 Isosurfaces of the squared wave function of (**a**) the flat dispersion band at the Γ point in Fig. 4.9b, (**b**) the dispersive band just above the Fermi level at the K point in Fig. 4.9, and (**c**) the other dispersive band with higher energy indicated at K point. The isosurfaces correspond to 0.8 e/a.u. Gray spheres indicate the atomic position of the fused pentagon network

aligned and extend throughout the sheet. Therefore, the fused pentagon network is a 2D ferromagnet consisting of only sp^2 carbon atoms whose covalent bonds are fully saturated. Furthermore, the extended nature of the spin distribution indicates that the flat dispersion band is not induced by the localized state at certain atomic sites but is induced by extended π electron states throughout the sheet. The wave function associated with the flat-band state at the Γ point exhibits the extended π electron nature (Fig. 4.11a), indicating that the delicate balance among the extended π state of C atoms induces the flat dispersion band of the sheet. Furthermore, it should be noted that the spin distribution is similar to the wave function distribution of the electronic state-labelled δ at K point (Fig. 4.11c). Similar flat dispersion bands have also been observed in hexagonal network materials with zigzag edges or interfaces [55–58]. Therefore, the fused pentagon network extends the research field associated with C allotropes with the flat dispersion band.

Since the polarized spin has striped distribution along the zigzag direction of the honeycomb network of fused pentagons, the antiparallel spin distribution is expected to occur on this system. To corroborate the issues, we calculate the electronic structure of the sheet with double periodicity normal to the spin strips, which contains two strips of spin density in its unit cell. Under this extended unit cell, we compare the total energy of ferromagnetic state with that of the antiparallel spin strip state. Our calculation shows that the antiparallel spin configuration between adjacent strips emerges as a metastable state in addition to the ferromagnetic state. Calculated total energy of the antiparallel sate is higher than that of the ferromagnetic state by 2.6 meV/atom. Therefore, the ferromagnetic spin state is the ground state of the honeycomb network of the fused pentagons.

The fused pentagon network also exhibits another interesting feature in the electronic energy band near the Fermi level, in addition to the flat dispersion band. Three states are bunching up together with a small gap of about 0.1 eV at the K point just above the flat dispersion band. Two of the three states possess almost linear dispersion with respect to the wave number, similar to the π and π^* states of graphene and graphite. Therefore, the massive Dirac electrons are expected to be located on the fused pentagon network which does not contain any graphene-like hexagonal covalent network structure. The wave function of these states exhibits

nonbonding nature as in the case of the π state of the graphene and graphite at the Dirac point. The lowest branch of the state is distributed on the atoms adjacent to the vertex of three pentagons. The upper branch is distributed on the atoms at the vertex of three pentagons and the atoms shared by the two acepentalene structures. This suggests that a graphene-like electronic structure is expected to occur in the honeycomb network material with internal atomic structures.

Since the planar materials usually form a stacking structure similar to the case of graphite and transition metal chalcogenides. Furthermore, because of the bowl shape of the isolated acepentalene molecule, the fused pentagon network sheet is expected to form covalent bonds with adjacent sheets, leading to the three-dimensional network structure. Therefore, we investigated the relative stability and geometric structures of the fused pentagon sp^2 C sheets having stacking structures. By changing the interlayer spacing, we found that the layered system comprising the fused pentagon sheets has an energy minimum at the interlayer spacing of 3.2 Å. The calculated energy gain that arises from the interlayer interaction is 20 meV/atom. At the equilibrium interlayer spacing, each fused pentagon sheet retains its planar structure and does not form covalent bonds with adjacent layers.

4.4 Magnetism of 2D Network of Polymeric Hydrocarbons

In this section, we aim to theoretically investigate the possible structures of 2D porous hydrocarbon networks of sp^2 C obtained by assembling phenalenyl molecules in a hexagonal manner with phenyl interconnects and their electronic and magnetic properties using density functional theory [59, 60]. Figure 4.12 shows the optimized structures of 2D porous hydrocarbon networks consisting of phenalenyl connected via phenyl with various arrangements under the hexagonal cell parameter of 19.4 Å. For all phenyl arrangements, the phenalenyl units retained a planar structure as their stable conformation. As illustrated in Fig. 4.12a, two phenalenyl units per unit cell form a hexagonal lattice in which phenyl units connect adjacent phenalenyl units through covalent bonds like those of graphene. Simultaneously, three phenyl units form a Kagome lattice in which phenalenyl acts as an interunit bond. Because of the planar conformations of both phenyl and phenalenyl, the porous hydrocarbon sheet possesses a 2D π electron system. Rotation of phenyl modulates the π electron system: by rotating one of the three phenyl units, the π electrons form a 1D network in which the alternating phenalenyl and phenyl units form zigzag chains (1D structure in Fig. 4.12b). By rotating two phenyl units, π electrons are segmented into a phenalenyl dimer containing a phenyl unit (dimer structure in Fig. 4.12c). Finally, π electrons are localized on each phenalenyl and phenyl in the monomer structure depicted in Fig. 4.12d.

The total energies of the porous hydrocarbon sheets with various phenyl conformations are listed in Table 4.1. Among the four structures, the planar structure is the least stable with a total energy higher by 0.8 eV per cell than that of the ground state conformation. The total energy monotonically decreases by increasing the

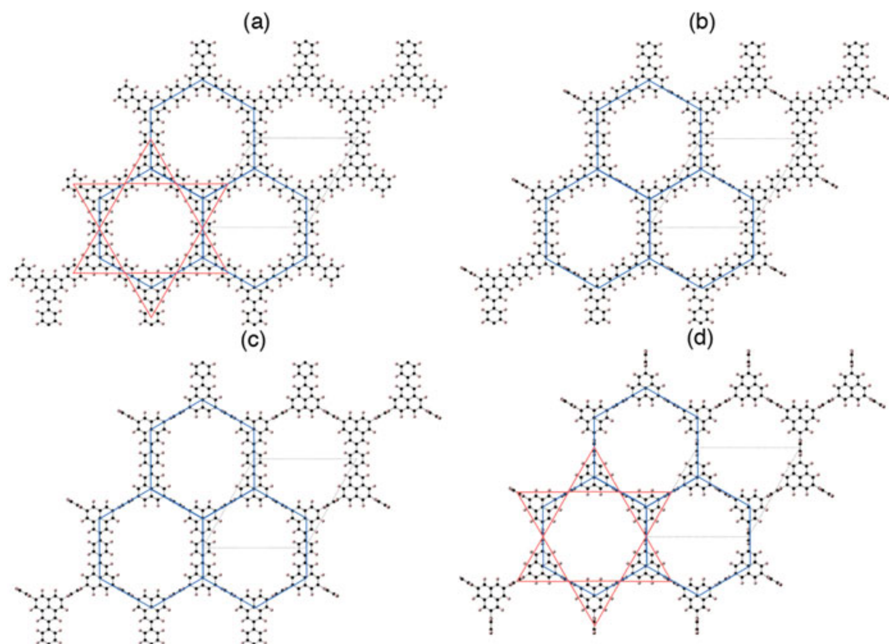

Fig. 4.12 Optimized structures of porous hydrocarbon sheets consisting of phenalenyl and phenyl groups with (**a**) planar, (**b**) 1D, (**c**) dimer, and (**d**) monomer conformation. Black and pink balls denote carbon and hydrogen atoms, respectively. Black dotted lines show the unit cell of each network. Blue hexagons and red triangles show hexagonal and Kagome networks of phenalenyl and phenyl units, respectively

Table 4.1 Relative total energies of porous hydrocarbon sheets consisting of phenalenyl and phenyl groups with antiferromagnetic (AF), ferromagnetic (F), and nonmagnetic (NM) states. The energies are measured from that with the planar conformation without spin polarization

Structures	AF state [meV]	F state [meV]	NM [meV]
2D	803	817	1116
Chain	301	310	612
Dimer	159	163	471
Monomer	0	0	313

number of rotated phenyl units, although the π conjugation decreases. The decrease of the total energy with respect to the rotation of phenyl units is caused by the steric hindrance between hydrogen atoms attached to the phenyl and phenalenyl. Since the hydrogen atoms attached to the phenyl and phenalenyl are positively charged, the hydrogen atoms tend to separate each other to reduce the Coulomb's repulsive interaction. The dynamical stability of the porous hydrocarbon sheets was investigated by ab initio molecular dynamics simulations conducted at a constant temperature up to 3000 K for simulation times of 1 ps. Under all temperatures, all structures retained their initial network topologies. On the other hand, at the

elevated temperatures, the phenyl units are tilted by angles of 20°–40° from the planar arrangement owing to the steric hindrance between hydrogen atoms attached to the phenalenyl and phenyl. The sheet hardly retains the planar conformation under the finite temperature.Thus, we confirm that the 2D networks of phenalenyl and phenyl proposed here are both statically and dynamically stable and are expected to be stable under ambient conditions once they are synthesized experimentally.

Figure 4.13 presents the electronic structures of 2D porous hydrocarbon sheets consisting of phenalenyl and phenyl. The planar structure possesses a characteristic feature around E_F (Fig. 4.13a). The porous hydrocarbon sheet is a zero-gap semiconductor with a pair of linear dispersion bands at E_F. In addition to the

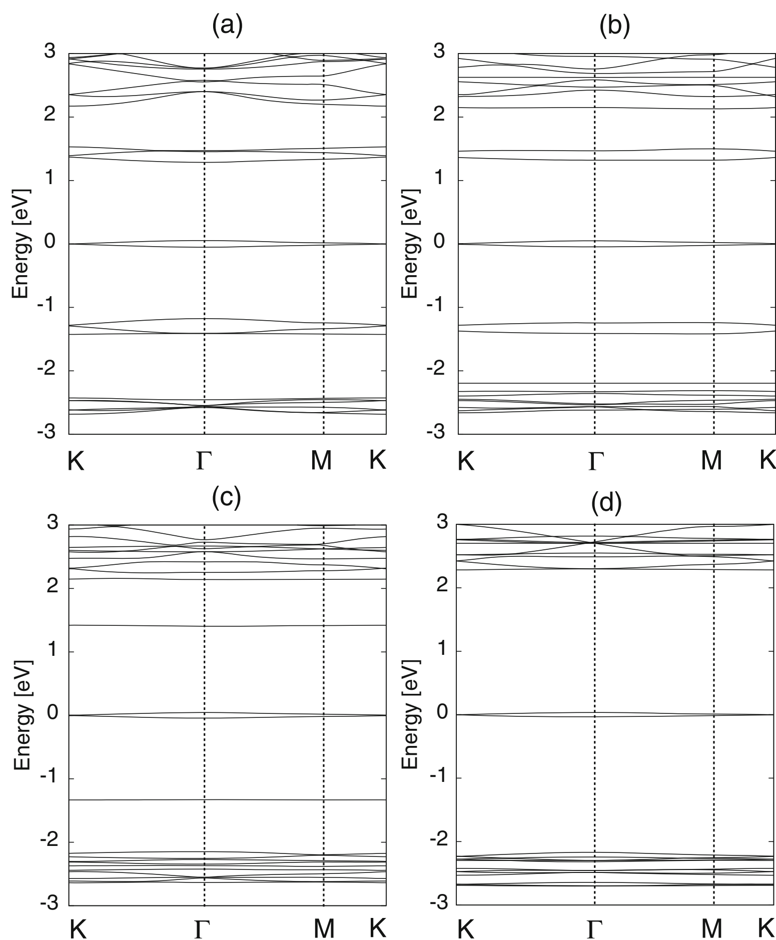

Fig. 4.13 Electronic structures of porous hydrocarbon sheets consisting of phenalenyl and phenyl groups with (**a**) planar, (**b**) 1D, (**c**) dimer, and (**d**) monomer conformation. Energies are measured from that of E_F

linear dispersion bands, we find three bunched states just above and below the linear dispersion bands. One of the three branches exhibits perfect flat-band nature, while the remaining two have finite band dispersion, consistent with their Kagome band structure [61, 62]. These observations indicate that Dirac cone and Kagome flat bands coexist in the porous hydrocarbon sheet of phenalenyl and phenyl with flat conformation. The Dirac cone is robust, while the Kagome bands are fragile against the rotation of phenyl: a Dirac cone is observed for all porous hydrocarbon sheets, regardless of the phenyl conformation. In contrast, the Kagome flat bands are absent for the sheets with 1D and dimer structures, because the electron system of the phenyl unit does not retain the symmetry of the Kagome lattice.

We evaluated the tight-binding parameters of the Dirac cone and Kagome band in the different sheet conformations from their bandwidth. The calculated transfer integrals of the Dirac cone t_D are 17, 16, 14, and 10 meV for the planar, 1D, dimer, and monomer conformations, respectively. Because of the narrow bandwidth, the Fermi velocities of the Dirac cone are 1.2×10^4, 1.4×10^4, 0.5×10^4, 1.6×10^4 m/s for the planar, 1D, dimer, and monomer conformations, respectively. Therefore, the porous hydrocarbon sheets are possible fields for strongly correlated electron systems that induce peculiar physical phenomena.A low Fermi velocity may cause large Fermi level instability even though the sheets possess zero density of states at E_F. For the Kagome bands, we also evaluated the transfer integral t_K. The calculated t_K are 27 and 21 meV for the planar and monomer conformations, respectively.

To clarify the physical origin of the Dirac cone in the planar system, we investigated the squared wave functions of the states at the K point (Fig. 4.14a). The wave functions are localized on phenalenyl units even though this porous hydrocarbon sheet possesses a 2D planar π electron network. By focusing on the wave function distribution within each phenalenyl, the state exhibits nonbonding nature in each phenalenyl unit. This indicates that the electron states associated with the Dirac cone can be ascribed to the singly occupied states of isolated phenalenyl monomers. In addition to the nonbonding nature within each phenalenyl unit, the wave function also exhibits nonbonding nature between adjacent phenalenyl units. Thus, the pair of linear dispersion bands at E_F is ascribed to the hexagonally arranged singly occupied state or radical spin state of phenalenyl units. Similar nonbonding nature within and between phenalenyl units was also found for the porous hydrocarbon sheets with 1D, dimer, and monomer conformations (Fig. 4.14b–d).

Next, we examined the wave function associated with the Kagome band. Figure 4.15 shows the isosurfaces of the squared wave functions of Kagome bands just below E_F at the Γ point. For the planar conformation, the wave functions are mainly distributed on the phenyl unit with the character of the HO states of phenyl molecules and are extended throughout the networks. Therefore, the flat dispersion band is ascribed to the delicate balance of the electron transfer among the HO state of the three phenyl units of the Kagome network, as in the case of the usual Kagome flat band state. In contrast, for the 1D and dimer conformations that lack the Kagome flat band, the states below E_F exhibit anisotropic nature, because of the orthogonality between the π states of the planar network and rotated phenyl

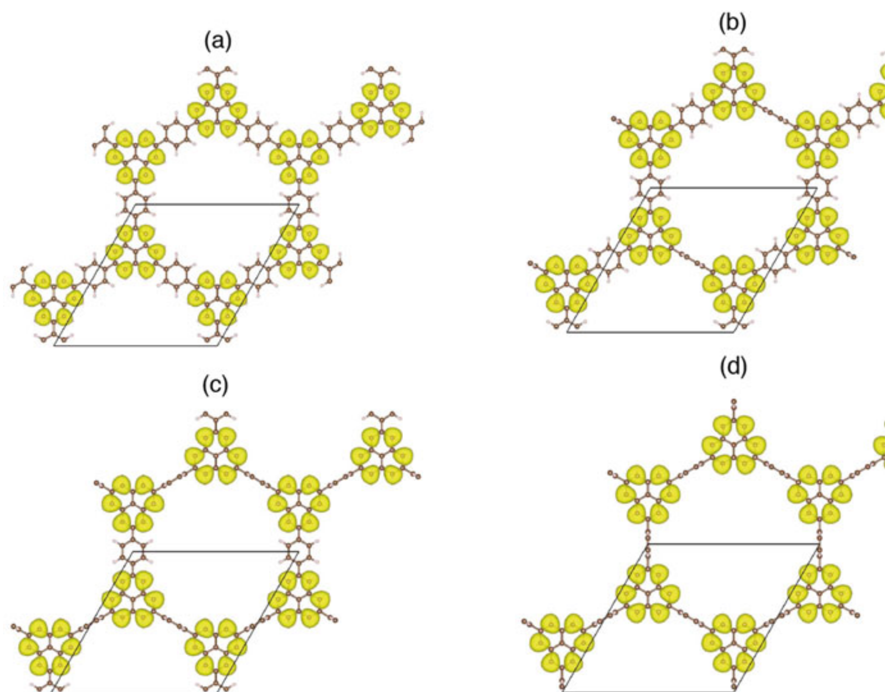

Fig. 4.14 Isosurfaces of the wave function of the Dirac cone of porous hydrocarbon sheets consisting of phenalenyl and phenyl groups with (**a**) planar, (**b**) 1D, (**c**) dimer, and (**d**) monomer conformation at the K point

units (Fig. 4.15b, c). For the monomer conformation, which possesses a Kagome flat band, the wave functions are more localized at the phenyl unit with the HO state nature and weakly extended throughout the network (Fig. 4.15d). This weak extended nature leads to the smaller t_K of the monomer conformation than that of the planar conformation.

The narrow band width of the Dirac cone of the porous hydrocarbon sheets results in a large density of states near E_F, which induces the Fermi level instability, causing magnetic ordering on the sheet, even though the sheets possess zero density of states at E_F because of the pair of linear dispersion bands at the K point. Figure 4.16 illustrates the spin density of the porous hydrocarbon sheets $\rho_s(\mathbf{r})$ evaluated by the equation

$$\rho_s(\mathbf{r}) = \rho_\alpha(\mathbf{r}) - \rho_\beta(\mathbf{r})$$

where $\rho_\alpha(\mathbf{r})$ and $\rho_\beta(\mathbf{r})$ are the charge densities of α and β spin components, respectively. We found that all the porous hydrocarbon sheets show spin polarization. Polarized electrons are localized on the phenalenyl units; the α and β spins are distributed on one of two sublattices of the phenalenyl units, as in the case of the

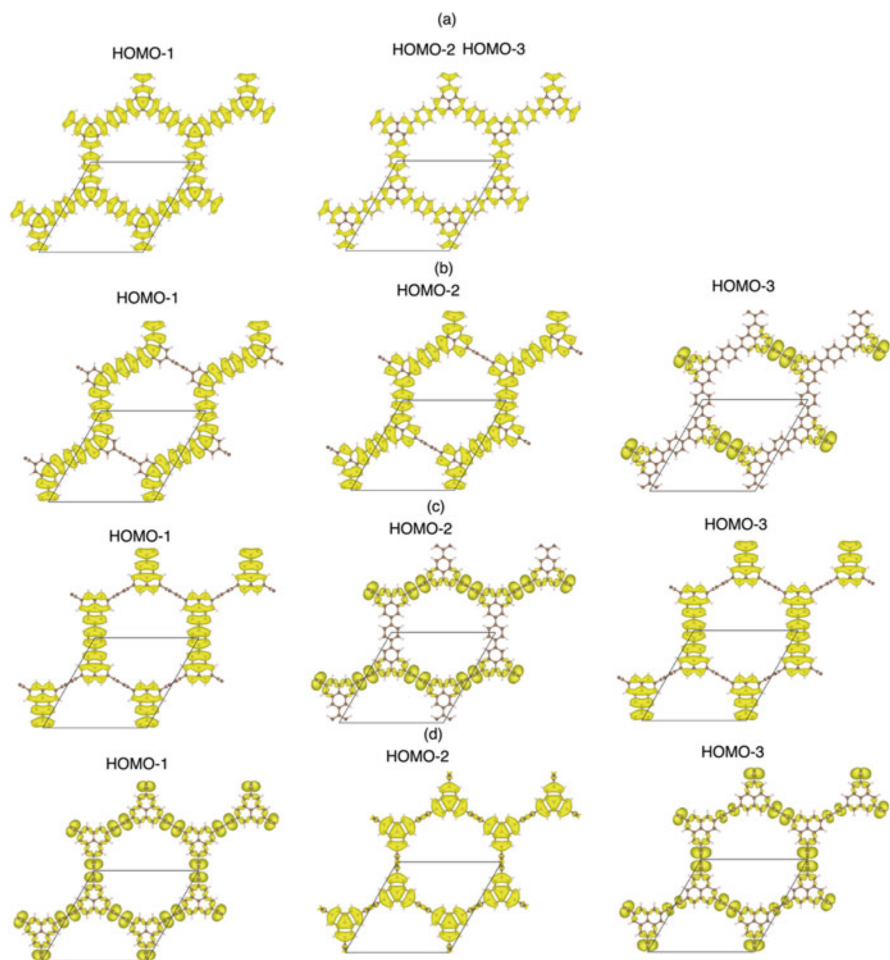

Fig. 4.15 Isosurfaces of the wave function of the Kagome flat dispersion band of porous hydrocarbon sheets consisting of phenalenyl and phenyl groups with (**a**) planar, (**b**) 1D, (**c**) dimer, and (**d**) monomer conformation at the Γ point

spin density of an isolated phenalenyl. Because of the spin density of the phenalenyl unit, each phenalenyl unit possesses $S = 1/2$ radical spin corresponding to the difference between the numbers of two sublattices. Furthermore, the $S = 1/2$ spin of the phenalenyl unit exhibits AF and F spin ordering throughout the sheets.

The total energies of the porous hydrocarbon sheets with AF and F states are listed in Table 4.1. The total energy of each sheet with spin polarization is about 300 meV lower than that of the corresponding sheet with nonmagnetic states for all phenyl conformations. Furthermore, the total energy of the AF state is lower than that of the F state by 14, 9, and 4 meV for the planar, 1D, and dimer conformations, respectively. These values indicate that the $S = 1/2$ spin on the phenalenyl

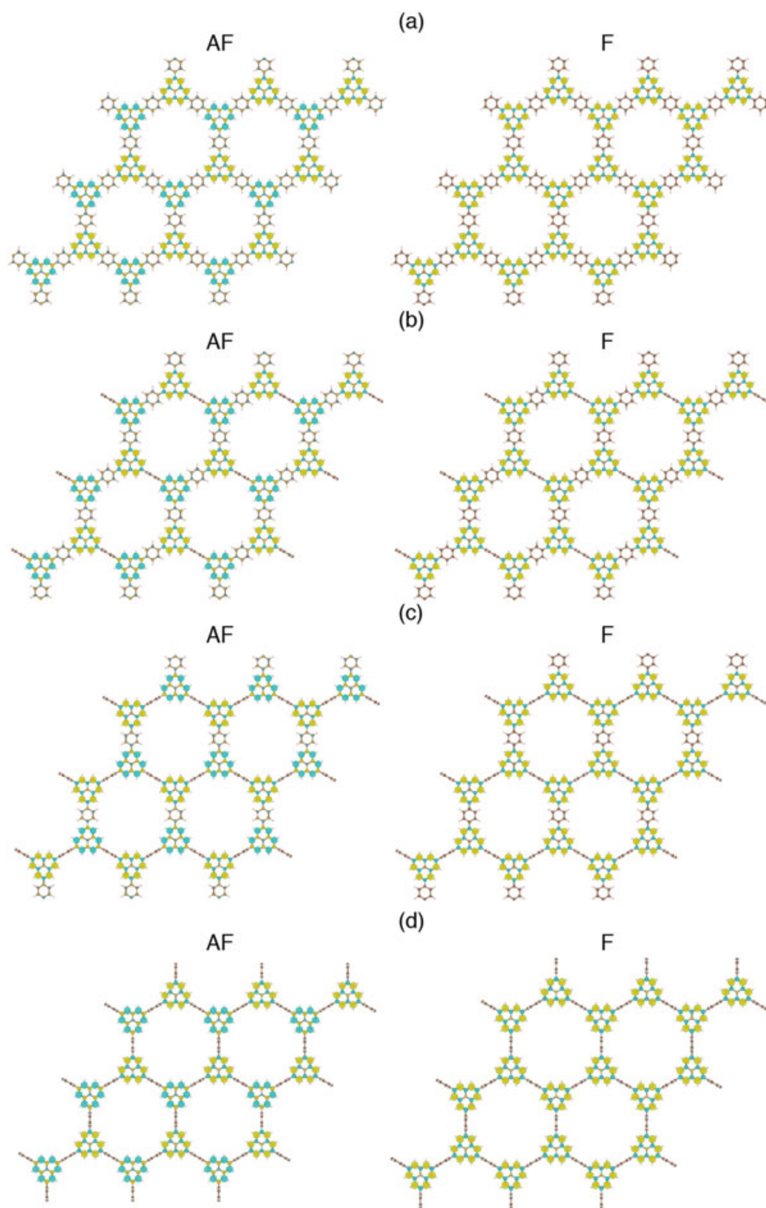

Fig. 4.16 Spin densities of porous hydrocarbon sheets consisting of phenalenyl and phenyl groups with (**a**) planar, (**b**) 1D, (**c**) dimer, and (**d**) monomer conformation with antiferromagnetic and ferromagnetic states. Colors indicate the sign of the polarized electron spin

unit interacts with its neighboring sites with weak singlet spin interaction J. The calculated spin interaction J per phenalenyl pair is about 10 meV. Note that the AF and F states are degenerate for the sheet with monomer conformation, because the total energies of these states are the same within numerical error. Thus, this sheet does not exhibit long-range magnetic ordering. In addition, the rotation of the phenyl unit may turn off the spin interaction between adjacent phenalenyl units because of the monotonic decrease of the energy difference between the AF and F states. Therefore, the magnetic states of the porous hydrocarbon sheets can be tuned by controlling the orientation of phenyl units with respect to the phenalenyl units: the planar, 1D, and dimer conformations are a $S = 1/2$ AF sheet, magnetically independent array of $S = 1/2$ AF chains, and magnetically isolated singlet spin dimer network, respectively.

Figure 4.17 shows the electronic energy bands of the AF and F states of the porous hydrocarbon sheets with various phenyl conformations. In all cases, the spin polarization modulates the pair of linear dispersion bands at E_F. For the AF state, flat dispersion bands emerge above and below E_F instead of a Dirac cone because of the antiparallel coupling between two $S = 1/2$ radical spins of phenalenyl units. The energy gap between the upper and lower branches of the states associated with

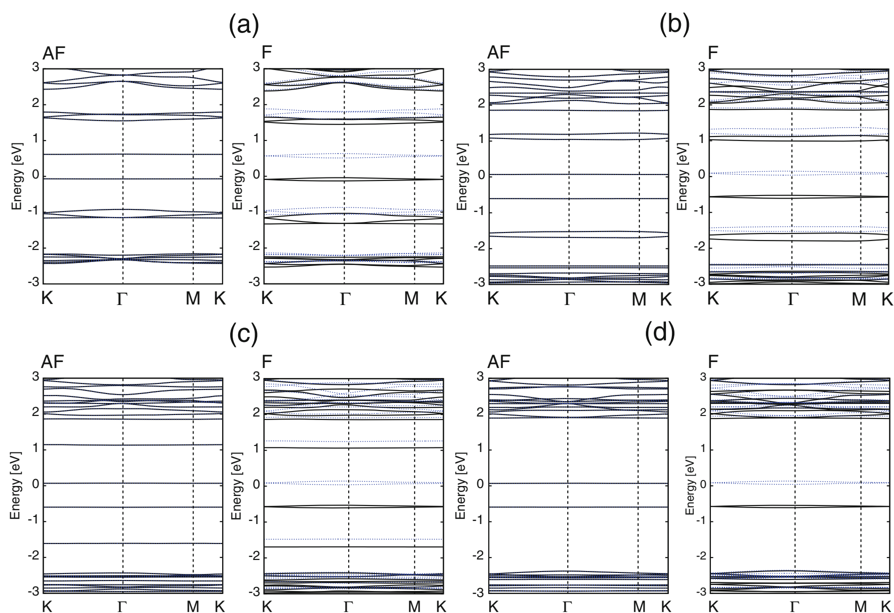

Fig. 4.17 Electronic structures of porous hydrocarbon sheets consisting of phenalenyl and phenyl groups with (**a**) planar, (**b**) 1D, (**c**) dimer, and (**d**) monomer conformation with antiferromagnetic and ferromagnetic states. E_F is located at zero. Black lines and blue dotted lines denote majority and minority spin bands, respectively

Table 4.2 Dependence of the number of polarized electron spins ($\Delta\rho$) on hole concentration

Number of hole doping	1	2	3	4	5	6	7
$\Delta\rho$	1	0	1	2	3	2	1

the spin polarization is 0.69–0.67 eV. For the F state, the Dirac cone is split into α and β spin states with a spin exchange energy of 0.65 eV, almost retaining its characteristic shape. In addition to the Dirac cone, electronic states near E_F are also modulated by the spin polarization. For instance, the Kagome band is split into α and β spin states with an energy difference of 0.16 eV.

The unusual electron systems near E_F of the porous hydrocarbon sheets may exhibit further interesting physical properties upon hole injection into the Dirac cone and Kagome band. Because of the localized and extended natures of the electronic states associated with the Dirac cone and Kagome band, respectively, hole injection changes spin polarization in the porous hydrocarbon sheet. By injecting holes into the porous hydrocarbon sheet with flat conformation by a counter planar electrode, we find that the number of polarized electron spins strongly depends on the number of holes injected (Table 4.2). The spin density in the porous hydrocarbon sheet also strongly depends on the hole concentration (Fig. 4.18). For a low-hole concentration corresponding to hole injection into the Dirac cone, the polarized electron spin exhibits qualitatively the same distribution as that of the undoped system. For a high-hole concentration at which E_F crosses the Kagome band, the spin density exhibits different characteristics to that of the undoped case: the polarized electron spin is distributed on not only the phenalenyl but also the phenyl units, reflecting the extended nature of the wave functions associated with the Kagome band. Furthermore, in contrast to the non-doped network, the porous hydrocarbon sheet with a high-hole concentration exhibits F spin ordering in its ground state. It should be noted that the carrier density to induce the magnetism associated with the Kagome flat band is about 0.8×10^{14} cm^{-2}. Thus, the magnetic state of the porous hydrocarbon sheet is tunable using ionic gating by the formation of electrical double layers (EDLs) which can inject carrier density up to 8×10^{14} cm^{-2}.

Since the phenyl prefers the tilted/rotated conformation in their ground state owing to the steric hindrance between hydrogen atoms attached to phenalenyl and phenyl, we further investigate the detailed energetics and spin interaction of a constituent unit of the porous hydrocarbon network. Here, we consider a phenalenyl dimer connected via phenyl as for the structural model of the porous hydrocarbon network (Fig. 4.19a). Figure 4.19b shows the total energy of the model molecule as a function of the rotational angle of phenyl with respect to the phenalenyl moieties. By rotating the phenyl, the total energy of the molecule monotonically decreases and possesses a minimum at the angle of about 35°. The total energy of the molecule with the rotation angle of 35° is lower by about 120 meV than that of the flat arrangement. Then, by further increasing the angle, the total energy monotonically increases. Therefore, the phenyl connecting the phenalenyl units of the freestanding porous hydrocarbon sheet may be rotated by about 35° under the ambient condition

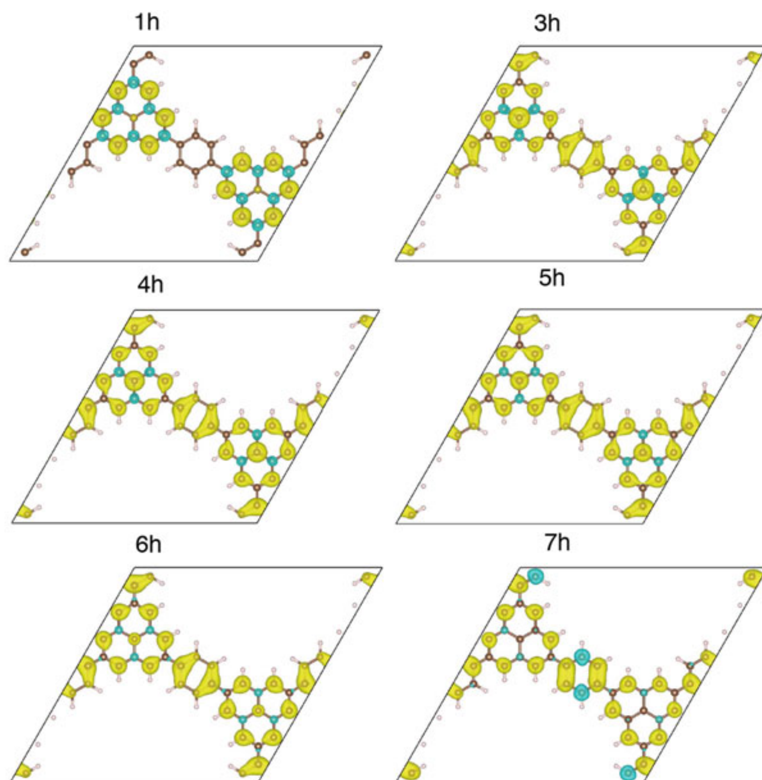

Fig. 4.18 Spin densities of a porous hydrocarbon sheet consisting of phenalenyl and phenyl groups with planar conformation and hole concentrations of 1*h* to 7*h*

as their ground state conformation. On the other hand, the porous hydrocarbon sheet may retain its flat conformation by adsorbing on appropriate substrates, such as graphene and h-BN, since the energy gain upon the interaction between the sheet and substrates compensates the energy loss upon the rotation of phenyl.

In addition to the energetics, it is worth to investigate how the spin interaction depends on the mutual rotational angle of the phenyl, because the spin interaction is terminated by the phenyl with the angle of 90°. Figure 4.19c shows the antiferromagnetic spin exchange energy J of the localized electron spin on phenalenyl moiety as a function of the rotational angle. The antiferromagnetic spin exchange interaction is the largest at the planar conformation and monotonically decrease with increasing the rotational angle of phenyl. The spin exchange interaction at the stable angle of 35° is approximately half of that of the flat conformation, indicating that the spin interaction among the phenalenyl still extends throughout the sheet under the conformation with tilted phenyl. Thus, the sheet still exhibits the antiferromagnetic ordering under the ground state conformation.

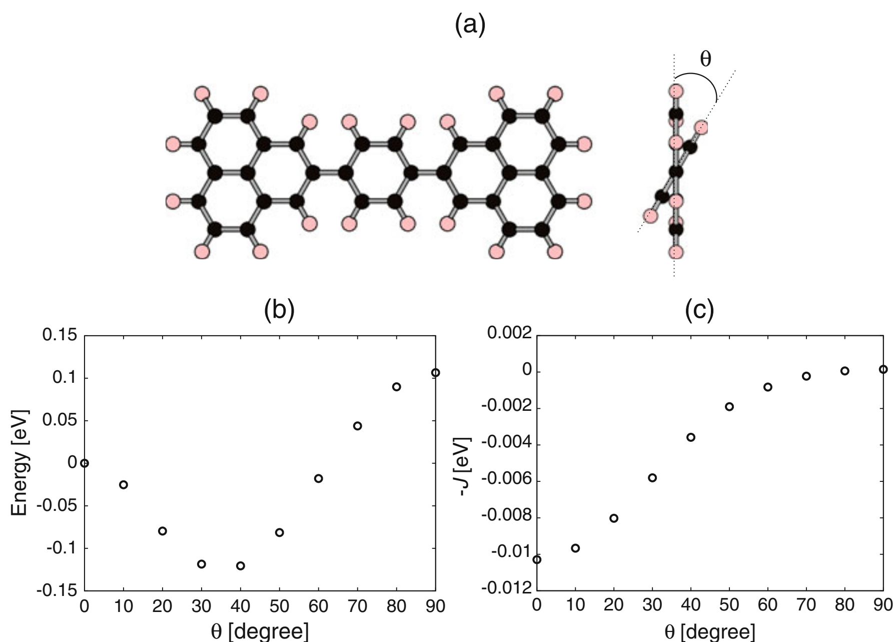

Fig. 4.19 (**a**) A geometric structure of a phenalenyl dimer connected via phenyl (phenalenyl-phenyl-phenaleny). Black and pink circles denote carbon and hydrogen atoms, respectively. (**b**) Calculated total energy of phenalenyl-phenyl-phenaleny as a function of the rotational angle of phenyl unit. Energy is measured from that under the flat conformation. (**c**) Spin exchange energy of phenalenyl-phenyl-phenaleny as a function of the rotational angle of phenyl unit

References

1. M.S. Dresselhaus, G. Dresselhaus, P.C. Eklund, *Science of Fullerenes and Carbon Nanotubes* (Academic, San Diego, 1996)
2. S. Iijima, Nature (London) **354**, 56 (1991)
3. N. Hamada, S. Sawada, A. Oshiyama, Phys. Rev. Lett. **68**, 1579 (1992)
4. R. Saito, M. Fujita, M.S. Dresselhaus, G. Dresselhaus, Appl. Phys. Lett. **60**, 2204 (1992)
5. H.W. Kroto, J.R. Heath, S.C. O'Brien, R.F. Curl, R.E. Smalley, Nature (London) **318**, 162 (1985)
6. W. Krätschmer, K. Fostiropoulous, D.R. Hoffman, Nature (London) **347**, 354 (1990)
7. P.W. Fowler, D.E. Manolopoulos, *An Atlas of Fullerenes* (Oxford University Press, Oxford, 1995)
8. S. Saito, A. Oshiyama, Phys. Rev. Lett. **66**, 2637 (1991)
9. S.J. Tans, A.R.M. Verschueren, C. Dekker, Nature **393**, 49 (1998)
10. R. Martel, T. Schmidt, H.R. Shea, T. Hartel, Ph. Avouris, Appl. Phys. Lett. **73**, 2447 (1998)
11. Y. Nosho, Y. Ohno, S. Kishimoto, T. Mizutani, Appl. Phys. Lett. **86**, 073105 (2005)
12. Y. Nosho, Y. Ohno, S. Kishimoto, T. Mizutani, Nanotechnology **17**, 3412 (2006)
13. D.-M. Sun, M.Y. Timmermans, Y. Tian, A.G. Nasibulin, E.I. Kauppinen, S. Kishimoto, T. Mizutani, Y. Ohno, Nat. Nanotechnol. **6**, 156 (2011)
14. U. Ishiyama, N.-T. Cuong, S. Okada, Jpn. J. Appl. Phys. **53**, 115102 (2014)
15. U. Ishiyama, N.-T. Cuong, S. Okada, Jpn. J. Appl. Phys. **54**, 065101 (2015)

16. M.S.C. Mazzoni, H. Chacham, Appl. Phys. Lett. **76**, 1561 (2000)
17. N.G. Chopra, L.X. Benedict, V.H. Crespi, M.L. Cohen, S.G. Louie, A. Zettel, Nature **377**, 135 (1995)
18. H. Mehrez, A. Svizhenko, M.P. Anantram, M. Elstner, T. Frauenheim, Phys. Rev. B **71**, 155421 (2005)
19. J.-Q. Lu, J. Wu, W. Duan, F. Liu, B.-F. Zhu, B.-L. Gu, Phys. Rev. Lett. **90**, 156601 (2003)
20. C. Gómez-Navarro, J.J. Sáenz, J. Gómez-Herrero, Phys. Rev. Lett. **96**, 076803 (2006)
21. K. Tada, K. Watanabe, Jpn. J. Appl. Phys. **39**, 268 (2000)
22. C. Kim, B. Kim, Phys. Rev. B **65**, 165418 (2002)
23. H. Zhang, Y. Miyamoto, Appl. Phys. Lett. **95**, 053109 (2009)
24. A. Yamanaka, S. Okada, Appl. Phys. Express **5**, 095101 (2012)
25. A. Yamanaka, S. Okada, Appl. Phys. Express **6**, 045101 (2013)
26. K. Uchida, S. Okada, Phys. Rev. B **76**, 155436 (2007)
27. J. Wu, W. Pisula, K. Müllen, Chem. Rev. **107**, 718 (2007)
28. K. Müllen, J.P. Rabe, Acc. Chem. Res. **41**, 511 (2008)
29. M. Fujihara, Y. Miyata, R. Kitaura, Y. Nishimura, C. Camacho, S. Irle, et al., J. Phys. Chem. C **116**, 15141 (2012)
30. H.E. Lim, Y. Miyata, M. Fujihara, S. Okada, Z. Liu, Arifin, et al., ACS Nano **9**, 5034 (2015)
31. A.I. Cooper, Adv. Mater. **21**, 1291 (2009)
32. J. Gao, D. Jiang, Chem. Commun. **52**, 1498 (2016)
33. X. Liu, J. Tan, A. Wang, X. Zhang, M. Zhao, Phys. Chem. Chem. Phys. **16**, 23286 (2014)
34. C. Sánchez-Sánchez, S. Brüller, H. Sachdev, K. Müllen, M. Krieg, H.F. Bettinger, et al., ACS Nano **5**, 9228 (2015)
35. Y. Morita, S. Suzuki, K. Sato, T. Takui, Nat. Chem. **3**, 197 (2011)
36. V. Boekelheide, C.E. Larrabee, J. Am. Chem. Soc. **72**, 1245 (1950)
37. D.H. Reid, Tetrahedron **3**, 339 (1958)
38. K. Nakasuji, M. Yamaguchi, I. Murata, K. Yamaguchi, T. Fueno, H. Ohya-Nishiguchi, et al., J. Am. Chem. Soc. **111**, 9265 (1989)
39. Z. Sun, J. Wu, J. Mater. Chem. **22**, 4151 (2012)
40. T. Kubo, Chem. Rec. **15**, 218 (2015)
41. T. Kubo, A. Shimizu, M. Uruichi, K. Yakushi, M. Nakano, D. Shiomi, et al., Org. Lett. **9**, 81 (2007)
42. Z. Mou, K. Uchida, T. Kubo, M. Kertesz, J. Am. Chem. Soc. **136**, 18009 (2014)
43. Z.-H. Cui, A. Gupta, H. Lischka, M. Kertesz, Phys. Chem. Chem. Phys. **17**, 23963 (2015)
44. P. Hohenberg, W. Kohn, Phys. Rev. **136**, B864 (1964)
45. W. Kohn, L.J. Sham, Phys. Rev. **140**, A1133 (1965)
46. J.P. Perdew, A. Zunger, Phys. Rev. B **23**, 5048 (1981)
47. D.M. Ceperley, B.J. Alder, Phys. Rev. Lett. **45**, 566 (1980)
48. J.P. Perdew, K. Burke, M. Ernzerhof, Phys. Rev. Lett. **77**, 3865 (1996)
49. D. Vanderbilt, Phys. Rev. B **41**, 7892 (1990)
50. A. Hasegawa, S. Okada, Jpn. J. Appl. Phys. **55**, 045101 (2016)
51. M. Maruyama, S. Okada, Appl. Phys. Express **6**, 095101 (2013)
52. C. Su, H. Jiang, J. Feng, Phys. Rev. B **87**, 075453 (2013)
53. H. Kollmar, V. Staemmler, J. Am. Chem. Soc. **99**, 3583 (1977)
54. Y. Liu, G. Wang, Q.-S. Huang, L.-W. Guo, X. Chen, Phys. Rev. Lett. **108**, 225505 (2012)
55. M. Fujita, K. Wakabayashi, K. Nakada, K. Kusakabe, J. Phys. Soc. Jpn. **65**, 1920 (1996)
56. M. Fujita, K. Nakada, G. Dresselhaus, M. Dresselhaus, Phys. Rev. B **54**, 17954 (1996)
57. S. Okada, A. Oshiyama, Phys. Rev. Lett. **87**, 146803 (2001)
58. S. Okada, M. Igami, K. Nakada, A. Oshiyama, Phys. Rev. B **62**, 9896 (2000)
59. M. Maruyama, N.T. Cuong, S. Okada, Carbon **109**, 755 (2016)
60. M. Maruyama, S. Okada, Carbon. https://doi.org/10.1016/j.carbon.2017.08.040
61. K. Shiraishi, H. Tamura, H. Takayanagi, Appl. Phys. Lett. **78**, 3702 (2001)
62. H. Ishiia, T. Nakayama, J. Inoue, Surf. Sci. **514**, 206 (2002)

Chapter 5
Electronic and Geometric Structures of Cluster Encapsulated Fullerenes

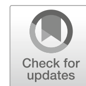

Takafumi Miyazaki and Shojun Hino

Abstract Fullerene cages often encapsulate mono-metal atom, multiple-metal atoms, metal–carbide clusters, metal nitrides, and so on. The entrapped metal atoms donate electrons to the fullerene cages which induces the change of their electronic structure. It has been known so far that the amounts of transferred electrons depend on the number of entrapped atoms and the entrapped species. Ultraviolet photoelectron spectroscopy is a powerful technique to determine the electronic structure and has been used to reveal the electronic structure of fullerenes as well as their cage structure with an aid of theoretical calculation. The electronic structure of endohedral fullerenes revealed by photoelectron spectroscopy is described in this chapter. Geometrical structure of endohedral fullerenes deduced by theoretical calculation is also presented.

Keywords Endohedral fullerene · Photoelectron spectroscopy · DFT calculation · Electronic structure · Geometrical structure

5.1 Introduction

Thirty years already passed since the discovery of C_{60} [1]. Provoked by the superconductivity of alkali metal-dosed C_{60} [2], investigation of fullerene physics and chemistry has made a great progress. The discovery and separation of higher fullerenes such as C_{70}, C_{82}, C_{84}, and so on, and that some of them encapsulated atoms (endohedral fullerenes), are remarkable results brought by the investigation. Until now, there have been a lot of attempts to synthesize and isolate endohedral

T. Miyazaki (✉)
Research Laboratory for Surface Science, Okayama University, Okayama, Japan
e-mail: tmiyazaki@okayama-u.ac.jp

S. Hino
Graduate School of Science and Engineering, Ehime University, Matsuyama, Japan
e-mail: hino@gakushikai.jp

© Springer Nature Singapore Pte Ltd. 2019

Y. Kubozono (ed.), *Physics and Chemistry of Carbon-Based Materials*,
https://doi.org/10.1007/978-981-13-3417-7_5

fullerenes containing mono- or di-metal atom [3–8], metal nitrides [9–12], and metal–carbon clusters [13–15].

5.2 Synthesis and Isolation of Endohedral Fullerenes

Soot containing mono-metal, di-metal, and metal–carbide endohedral fullerene were produced by direct-current arc heating of a M_2O_3 (M = Er, Lu, Tm, Ce, La)/graphite composite rod in a He atmosphere. $Er@C_{82}$ (I) [16], $Er_2@C_{82}$ (I) and $Er_2@C_{82}$ (III) [17], $Lu@C_{82}$ (I) [18], $Ce_2@C_{80}$ [19], $La_2@C_{80}$ [20], $Lu_2@C_{82}$ (II) [21], $Lu_2C_2@C_{82}$ (III) [22], $Tm_2@C_{82}$ (III) [5, 23], $Tm_2C_2@C_{82}$ (III) [24], and $Sc_3C_2@C_{80}$ [25] were extracted using *o*-xylene from the soot and isolated using multiple-stage high-performance liquid chromatography with toluene as an eluent. Soot containing $Sc_3N@C_{68}$ [26] and $Sc_3N@C_{78}$ [27] were produced by direct-current arc heating of a Sc_2O_3/graphite composite rod in a mixed He/N_2 atmosphere. They were extracted using o-xylene from the soot and isolated using multiple-stage high-performance liquid chromatography with toluene as an eluent.

5.3 The UPS and XPS Measurement of Specimens

Photoelectron spectroscopy is a useful technique to investigate the electronic structure of materials. Ultraviolet photoelectron spectroscopy (UPS) is a powerful tool to determine the upper valence band structure of materials. Cleanness of the surface of the specimen is the key factor in the measurement of UPS. Since endohedral fullerenes are obtained as powder, thieir sublimation is desirable to obtain films of clean surface. As the sublimation temperature of endohedral fullerenes is as high as around 830 K or up and they are vulnerable to high temperature, the abundance of the specimen and delicate temperature control of the sublimation crucible are essential.

5.4 Density Functional Theory (DFT) Calculation of Endohedral Fullerenes

Molecular orbitals of endohedral fullerenes were calculated by the density functional theory (DFT) with a Gaussian 03 and 09 program module. There is no theoretical reasoning that Kohn–Sham orbital energies obtained from DFT calculation are compatible with Koopmans' theorem, but Janak's theorem [28] is an analogue to Koopmans' theorem in DFT calculation, and that Kohn–Sham orbital energies correspond the highest occupied and the lowest unoccupied molecular orbitals energy levels. Further, it has been found that simulated spectra generated

from Kohn–Sham orbital energies reproduce the UPS very well and the comparison was helpful to estimate the cage geometry.

The geometry of $La_2@C_{80}$ and $Ce_2@C_{80}$ was optimized at the Hartree–Fock level using the CEP-31G basis set. The DFT calculation was performed on the optimized structures of $Ce_2@C_{80}$ and $La_2@C_{80}$ using the B3LYP hybrid functional to obtain the Kohn–Sham orbital energies with basis sets Sapporo-DZP and/or uB3LYP/6–31 + G-(d) for C atoms and TK/NOSeC-V-TZP function for Ce and La atoms [29, 30]. The simulated spectra were generated by broadening the calculated Kohn–Sham orbital energies with Gaussian functions of 0.2 eV full width at half maximum.

According to the NMR analysis of $Sc_3N@C_{68}$ and crystallographic analysis of the $Sc_3N@C_{68}$ adduct [26], geometry of $Sc_3N@C_{68}$ seems to be isomer 6140 [31], and this was adopted as the initial geometry for geometry optimization at the B3LYP level using 6–311 g basis sets. A Sc_3N cluster was placed to maintain the D_3 symmetry. Kohn–Sham orbital energies were obtained on the geometry optimized $Sc_3N@C_{68}$ structure using 6–31G-(d) for C atoms and a TK/NOSeC-V-TZP function [29, 30] for Sc atoms. Simulated spectrum was generated by broadening the calculated Kohn–Sham orbital energies with Gaussian functions of 0.15 eV full width at half maximum. Hartree–Fock level calculation was also performed and simulated spectrum was obtained. The DFT origin simulated spectrum reproduced the UPS far better than the one obtained from the Hartree–Fock calculation.

The geometry of $Sc_3N@C_{78}$ was optimized at the Hartree–Fock level using the 6–31G basis set. Simulated spectrum generated by broadening the calculated eigenvalues at the Hartree–Fock level with Gaussian functions of 0.2 eV full width at half maximum differed significantly from the observed UPS. The DFT calculation was also performed on the optimized $Sc_3N@C_{78}$ structure using the B3LYP hybrid functional to obtain the Kohn–Sham orbital energies with basis sets of 6–31G-(d) for C atoms and the TK/NOSeC-V-TZP function [32] for Sc atoms. Simulated spectrum obtained by the same procedure described above using Kohn–Sham orbital energies reproduced the UPS far better than those obtained from the Hartree–Fock calculation. Mulliken charges and natural population analysis (NPA) charge of $Sc_3N@C_{78}$ were calculated on the Hartree–Fock level optimized structure using B3LYP and Lanl2dz functions.

5.5 Electronic Structure of Mono-metal Atom Entrapped Fullerenes

Review article on the ultraviolet photoelectron spectra of mono-metal endohedral fullerenes $La@C_{82}$, $Sc@C_{82}$, $Gd@C_{82}$, $Tb@C_{82}$, $Tm@C_{82}$, and $Pr@C_{82}$ was given by S. Hino [33]. In this report another mono-metal atom entrapped fullerenes after the publication of the handbook will be presented.

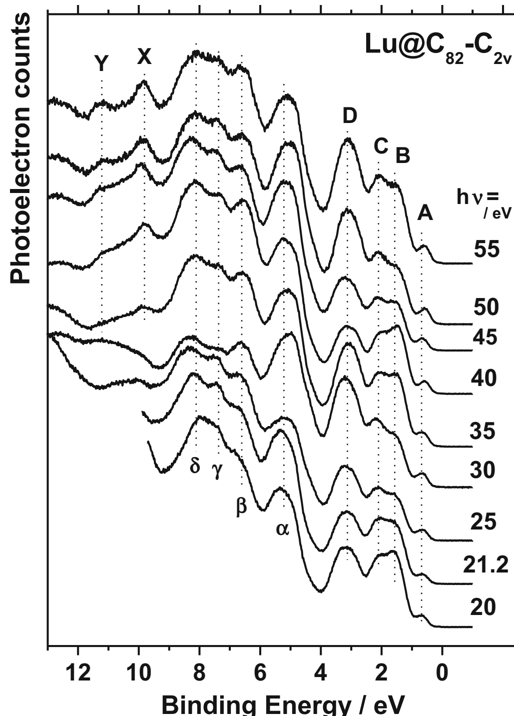

Fig. 5.1 The incident photon energy-dependent UPS of Lu@C_{82}-C_{2v} at $h\nu = 20 \sim 55$ eV. (Reproduced with permission from [34]. Copyright (2013) Elsevier)

[Lu@C_{82}-C_{2v}]

Lutetium atom entrapped fullerenes have been isolated [18], and the cage symmetry of Lu@C_{82} (I) has been determined to be $C_{2\mathrm{v}}$ (82:9) by the NMR analysis. The valence band UPS of Lu@C_{82}-C_{2v} obtained with $h\nu$ = 20–55 eV incident photon energy is shown in Fig. 5.1 [35]. The onset energy (E_{onset}) of Lu@C_{82}-C_{2v} is 0.25 eV, which are much smaller than that of empty C_{82} (1.2 eV), which means encapsulation of metal atom inside the cage contributes to narrow the band gap of fullerene but Lu@C_{82} is still semiconductive. There are 11 structures labeled A–E and α–ζ in the UPS of Lu@C_{82}-C_{2v}, which can be divided into two parts. These structures that appeared in the deeper than 5 eV region are mainly due to σ-electrons that constitute the C_{82} skeletal C–C bonds and those between 0 and 5 eV are due to π-electrons. The UPS of Lu@C_{82}-C_{2v} is analogous to those of Tb@C_{82}-C_{2v} and La@C_{82}-C_{2v}, which indicates that entrapped species do not seriously affect the electronic structure of the cage. However, there are two structures (X and Y) in the 9–11 eV region, which are not observed in the UPS of other endohedral fullerenes.

They are not observed when the incident photon energy is less than 35 eV, but they become distinct and their intensity becomes stronger in accordance with the increase of the incident photon energy. This behavior is quite different from that of other endohedral fullerenes and seems to be the characteristic ones to the entrapped Lu atom. The ionization potentials of Lu $4f_{7/2}$ and $4f_{5/2}$ are 7.5 eV and 8.9 eV,

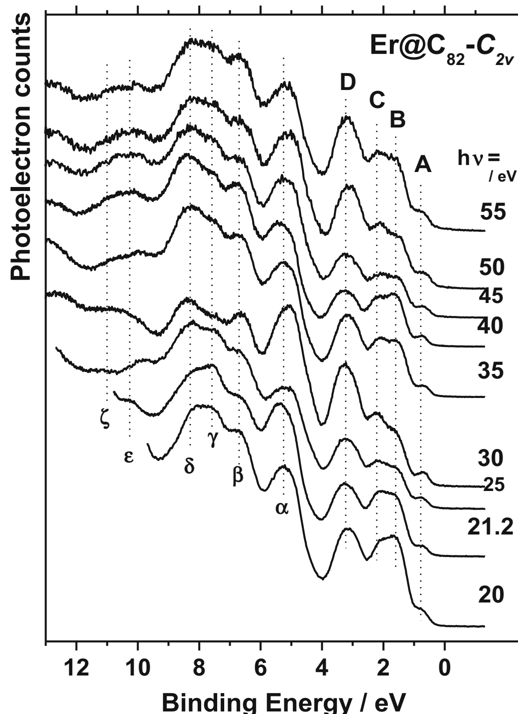

Fig. 5.2 The incident photon energy-dependent UPS of Er@C_{82}-C_{2v} at $h\nu = 20 \sim 55$ eV. (Reproduced with permission from [37]. Copyright (2010) Elsevier)

respectively [36]. The electronic configuration of Lu atom is [Xe] $(4f)^{14}$ $(5d)^{1}$ $(6\,s)^{2}$. Structures of X and Y appear between 9.3–9.8 eV and 10.8–11.2 eV, respectively, which are higher than those of Lu metal atoms by 2.0–2.5 eV. As entrapped Lu atom donates electrons to the cage (presumably the oxidation state entrapped of Lu atom is +3), Lu atom is electron wanting state. Hence the ionization potential of entrapped Lu 4f levels moves to a deeper level. Possibly structures X and Y are due to Lu4$f_{7/2}$ and Lu4$f_{5/2}$.

[Er@C_{82}-C_{2v}]

Erbium atom entrapped fullerenes have been isolated, and the cage symmetry of the main isomer Er@C_{82} (I) was determined to be C_{2v} (82:9) by NMR structural analysis [16, 17]. The upper valence band UPS of Er@C_{82}-C_{2v} obtained with $h\nu = 20$–55 eV incident photons is shown in Fig. 5.2 [37]. Ten structures labeled A − D and α–ζ were clearly observed. All spectra were normalized by the peak height of the structure α. The intensity of these structures changed, when the incident photon energy was tuned, which is a typical behavior of fullerenes. The spectral onset energy (E_{onset}) of Er@C_{82} (I) is 0.38 eV below the Fermi level, and this is much smaller than that of empty C_{82} (1.2 eV).

Structures α–ζ that appeared in the deeper binding energy region (E_b > 5 eV) of the UPS of Er@C_{82}-C_{2v} are due to σ-electrons that constitute the C_{82} skeletal

C–C bonds. Structures labeled A–D that appeared in the upper binding energy region (E_b < 5 eV) of the UPS are derived from π-electrons. The E_{onset} of Er@C_{82}-C_{2v} is slightly larger than those of La@C_{82} (0.25 eV) and Tb@C_{82} (0.24 eV). Nuclear charges of the entrapped atoms might influence the onset energy.

These deeper binding energy region (E_b > 5 eV) UPS resemble each other. Entrapped atoms seem to hardly affect the electronic structure of fullerene skeleton. Upper valence band (E_b < 5 eV) spectral shape of Er@C_{82}-C_{2v}, Tb@C_{82}-C_{2v}, and La@C_{82}-C_{2v} was substantially identical, which means that Er@C_{82}-C_{2v}, Tb@C_{82}-C_{2v}, and La@C_{82}-C_{2v} have analogous electronic structure. The UPS of Er@C_{82}-C_{2v} in the upper valence region is considerably different from those of Tm@C_{82}-C_{2v}. Thus, there was a large difference in the electronic structures of Er@C_{82}-C_{2v} and Tm@C_{82}-C_{2v}. So another reason has been also required to understand their spectral difference. The oxidation state might be the reason. The oxidation state of La in La@C_{82} and Tb in Tb@C_{82} was +3, while that of Tm in Tm@C_{82} was +2. That is, the fullerene cage accepted different amounts of the electrons from the entrapped atom. Accordingly, the electronic structure fullerene itself was modified differently with the accepted amounts of electrons. The upper valence band UPS of Er@C_{82}-C_{2v} was well reproduced by the simulated spectrum assuming a C_{82}^{3-}-C_{2v}, confirming the cage structure deduced from NMR analysis.

5.6 Electronic Structure of Di-metal Atoms Entrapped Fullerenes

When the fullerene cage entraps in plural atoms, its electronic structure seems to be more complicated than that of mono-metal atom entrapped fullerene. Not only the interaction between the entrapped atoms and the cage but also that between the entrapped atom themselves must be considered. DFT calculation is helpful to interpret the UPS. In the following section, the UPS of di-metal atoms encapsulated fullerenes Ce_2@C_{80}, La_2@C_{80}, Er_2@C_{82}, Lu_2@C_{82}, and Tm_2@C_{82} are presented, and also the results of the DFT calculation are presented.

[Ce_2@C_{80}-D_{3d}]

Cerium atom entrapped fullerenes have been isolated [19, 38]. Figure 5.3 shows the UPS of Ce_2@C_{80} obtained with the incident photon energy of 20–55 eV [40]. The spectral onset of Ce_2@C_{80} was 0.89 eV below the Fermi level. The UPS of Ce_2@C_{80} differs from those of C_{80} [41] particularly in the upper value region. However, its lower UPS resemble those of M_2@C_{80}: might be a structure appeared at about 5.5 eV which is a typical structure in the UPS of fullerenes and a broad band between 6.0 and 9.5 eV which is due to σ-electrons constituting fullerene backbone. All spectra were normalized by the peak height of the structure α. The intensity of these structures changed, when the incident photon energy was tuned, as is observed in the UPS of fullerenes.

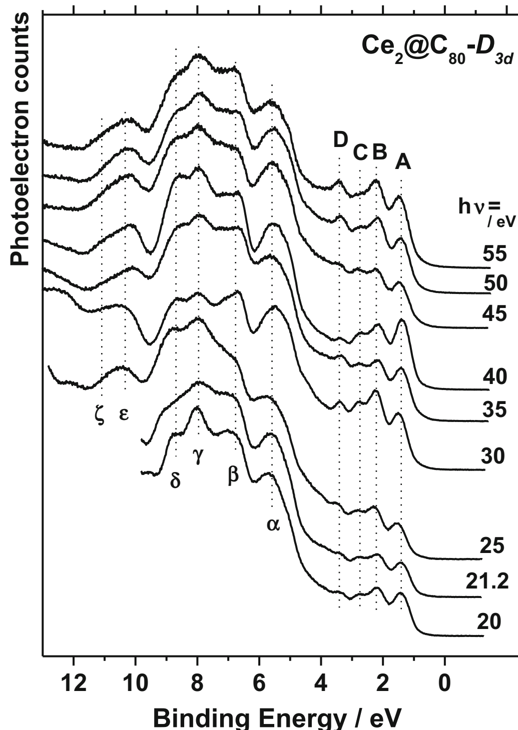

Fig. 5.3 The incident photon energy-dependent UPS of $Ce_2@C_{80}$-D_{3d} at $h\nu = 20 \sim 55$ eV. (Reproduced with permission from [39]. Copyright (2015) Elsevier)

Geometry optimization of $Ce_2@C_{80}$ gave three stable structures having symmetry of D_{5d}, D_{2h}, and D_{3d}. Since the formation energy of $Ce_2@C_{80}$-D_{5d} is much higher than that of other two, actual $Ce_2@C_{80}$ might not take this geometry. The formation energies of the other two are very close so that the geometry of $Ce_2@C_{80}$ can't be decided by the comparison of the formation energy. Kohn–Sham orbital energies are calculated using Sapporo-DZP for C atoms and TK/NOSeC-V-TZP basis sets for La and Ce atoms [29, 30]. Figure 5.4 shows Kohn–Sham orbital energies (bars) and simulated spectra generated by broadening the Kohn–Sham orbital energies with Gaussian functions [40]. As the UPS is referenced to the Fermi level and Kohn–Sham orbital energies are referenced to vacuum level, simulated spectra are shifted by 4.4 eV so that the UPS and simulated spectra can be easily compared. As the simulated spectrum obtained from D_{3d} geometry reproduces the UPS very well, $Ce_2@C_{80}$ might have D_{3d} symmetry. Figure 5.5 shows calculated energy diagrams of $Ce_2@C_{80}$-D_{3d}, C_{80}-D_{3d}, and the entrapped Ce atoms [40]. Wave functions of some frontier orbitals of $Ce_2@C_{80}$ and C_{80} are also depicted in the figures. The HOMO-3 and HOMO-2 wave functions of $Ce_2@C_{80}$ are almost identical with the LUMO and LUMO+1 of C_{80}, and similar resemblance is observed in the HOMO-4 of $Ce_2@C_{80}$ and the LUMO+2 of C_{80}. That is, the upper three levels of $Ce_2@C_{80}$ are derived from the unoccupied molecular orbitals of C_{80}, and six electrons of the entrapped Ce atoms are transferred to HOMO-2,

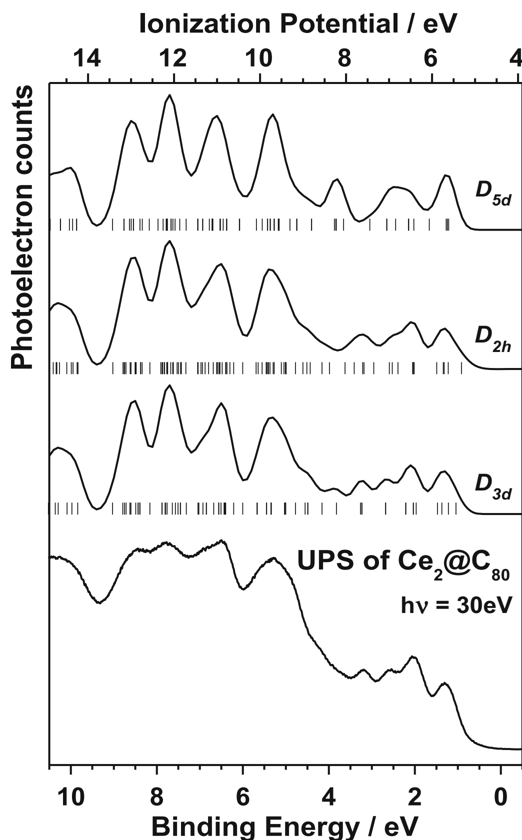

Fig. 5.4 The UPS of $La_2@C_{80}$ obtained with 30 eV excitation photon and the simulated spectrum obtained by broadening of the Kohn–Sham orbital energies. Bars under each simulation spectrum indicate the energy of calculated ionization potentials. (Reproduced with permission from [39]. Copyright (2015) Elsevier)

HOMO-3, and HOMO-4 orbitals. Thus, the formal oxidation state of $Ce_2@C_{80}$ can be described as $Ce_2^{6+}@C_{80}^{6-}$.

[$La_2@C_{80}$-D_{3d}]

Figures 5.6 shows the UPS of $La_2@C_{80}$ obtained with the incident photon energy of 20–60 eV [40]. The spectral onset of $La_2@C_{80}$ was 0.77 below the Fermi level. There are ten structures labeled A-D and α–ζ in the UPS. The UPS of $La_2@C_{80}$ and $Ce_2@C_{80}$ is almost identical and hard to distinguish one another. As was done in $Ce_2@C_{80}$, geometry optimization has been performed, and three optimized geometries having D_{5d}, D_{2h}, and D_{3d} symmetry were obtained. Figure 5.7 shows a calculated Kohn–sham orbital energies and simulated spectrum of each geometry [40]. Simulated spectrum derived from $Ce_2@C_{80}$-D_{3d} geometry reproduces the UPS very well. That means that the structures of $Ce_2@C_{80}$ and $La_2@C_{80}$ are the same and have D_{3d} symmetry. There is an argument on the structures of these two endohedral fullerenes, early stage X-ray diffraction analysis combined with maximum entropy method (MEM) [42] suggested $La_2@C_{80}$-I_h cage, and theoretical calculations [34, 43–46] insisted that metal atom entrapped C_{80}-I_h did not retain

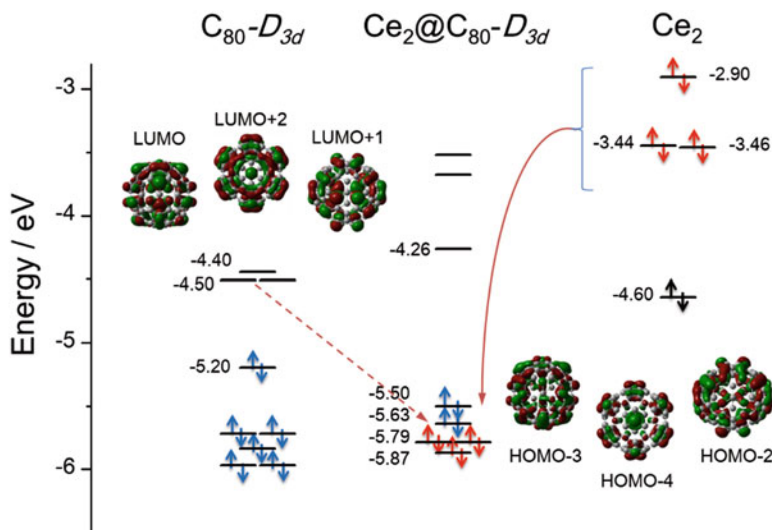

Fig. 5.5 Energy diagrams of empty C_{80}, $Ce_2@C_{80}$, Ce atoms obtained by DFT calculation. The Kohn–Sham orbital energies of frontier orbitals are inserted, and the wave function distributions of frontier orbitals are also shown. The electron configuration of $Ce_2@C_{80}$ could be $(Ce_2)^{6+}@C_{80}{}^{6-}$. (Reproduced with permission from [39]. Copyright (2015) Elsevier)

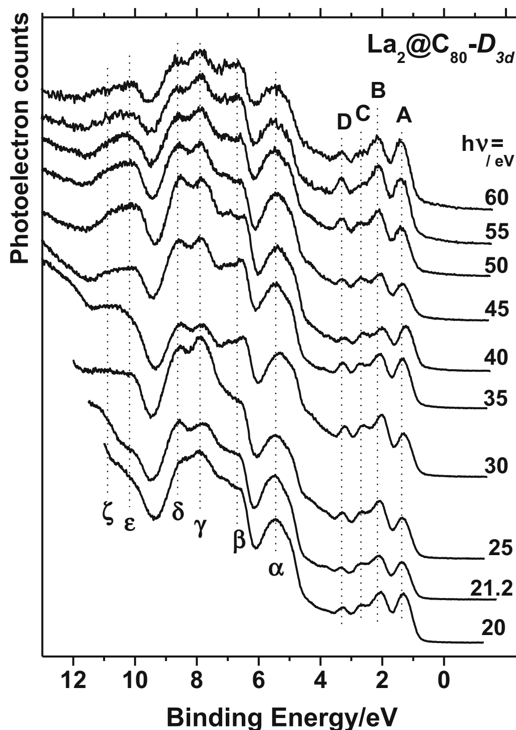

Fig. 5.6 The incident photon energy-dependent UPS of $La_2@C_{80}$-D_{3d} at $h\nu = 20 \sim 55$ eV. (Reproduced with permission from [39]. Copyright (2015) Elsevier)

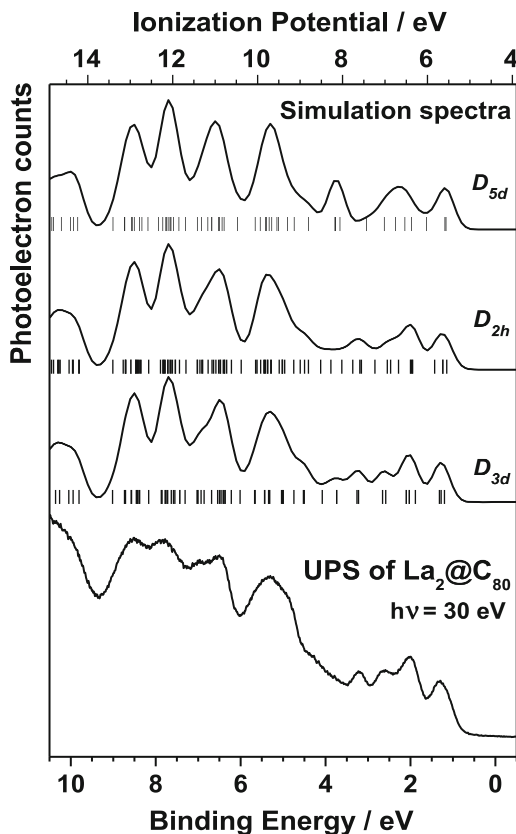

Fig. 5.7 The UPS of $La_2@C_{80}$ obtained with 30 eV excitation photon and the simulated spectrum obtained by broadening of the Kohn–Sham orbital energies. Bars under each simulation spectrum indicate the energy of calculated ionization potentials. (Reproduced with permission from [39]. Copyright (2015) Elsevier)

the original symmetry and encapsulation of metal atoms induced the degradation of symmetry. Crystallographic structure of a $La_2@C_{80}$ adduct also supported this conclusion that the encapsulation of metal atoms is favorable for the stability of the fullerene cage [39].

Early theoretical calculation on $La_2@C_{80}$ suggested that entrapped two La atoms rotated in the C_{80}-D_{2h} cage [43]. X-ray crystallographic analysis of its adduct, $La_2@C_{80}$ $(CH_2)(C_6H_5)_3N$, revealed that the rotation was frozen [47]. On the other hand, vibrational mode analysis using DFT calculation of $La_2@C_{80}$ suggested D_{3d} symmetry that is the global minimum in total energy [45]. This proposal was questioned by recent DFT calculations [34, 46] that supported D_{2h} geometry; using relativistic basis sets could be a crucial factor to support D_{2h}. Present finding might settle the argument on the geometry of C_{80}-I_h endohedral fullerenes.

Figure 5.8 shows calculated energy diagrams of $La_2@C_{80}$, C_{80} of the same cage symmetry and the entrapped La atoms [40]. Wave functions of some frontier orbitals of $La_2@C_{80}$ and C_{80} are also depicted in the figure. The upper three levels of $La_2@C_{80}$ are derived from the unoccupied molecular orbitals of C_{80}, and electrons

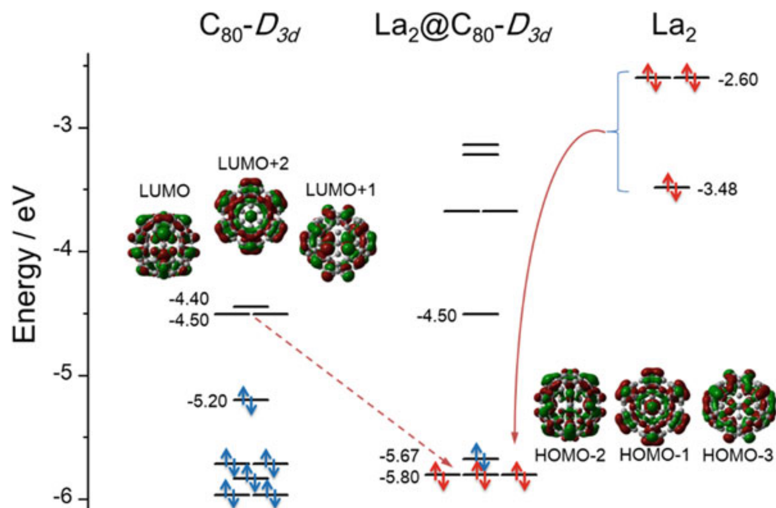

Fig. 5.8 Energy diagrams of empty C_{80}, $La_2@C_{80}$ obtained by DFT calculation. The Kohn–Sham orbital energies of frontier orbitals are inserted, and the wave function distributions of frontier orbitals are also shown. The electron configuration of $La_2@C_{80}$ could be $(La_2)^{6+}@C_{80}{}^{6-}$. (Reproduced with permission from [39]. Copyright (2015) Elsevier)

of the entrapped La atoms are transferred to these levels. Comparison of the UPS with theoretically generated simulation spectra indicates that the most plausible structure of $La_2@C_{80}$ has D_{3d} symmetry. The formal oxidation state of $La_2@C_{80}$ is $La^{6+}@C_{80}{}^{6-}$ as is in the case of $Ce_2@C_{80}$.

[$Er_2@C_{82}$-C_s and $Er_2@C_{82}$-C_{3v}]

Erbium atom encapsulated C_{82} fullerenes, $Er_2@C_{82}$ (I) and $Er_2@C_{82}$ (III), have been isolated [17], and their cage symmetry (structure) the Fowler's nomenclature [31] has been determined by the NMR measurements; according to the cage structure of the $Er_2@C_{82}$ (I) is C_s (82: 6) and that of the $Er_2@C_{82}$ (III) is C_{3v} (82: 8). The UPS of $Er_2@C_{82}$-C_s and $Er_2@C_{82}$-C_{3v} obtained with $h\nu = 20 \sim 55$ eV incident photon energy is shown in Figs. 5.9 and 5.10, respectively [48]. The E_{onset} of $Er_2@C_{82}$-C_s and $Er_2@C_{82}$-C_{3v} are 0.84 and 0.81 eV, respectively. The XPS $Er4d_{5/2}$ level of $Er_2@C_{82}$ is very close to that of Er_2O_3 (Er^{3+}). Thus, the oxidation state of Er in $Er_2@C_{82}$ might be +3. It should be noted that the UPS of these endohedral fullerenes differs from each other particularly in the upper band region.

Cage symmetry itself seems to determine the upper orbital energy levels of the multiple-atom entrapped fullerenes as was described in the mono-metal atom entrapped fullerenes.

[$Lu_2@C_{82}$-C_{2v}]

Two-lutetium atoms encapsulated C_{82} fullerenes, $Lu_2@C_{82}$ (II), have been isolated [21, 35], and their NMR study revealed C_{2v} (82:9) cage symmetry. The valence

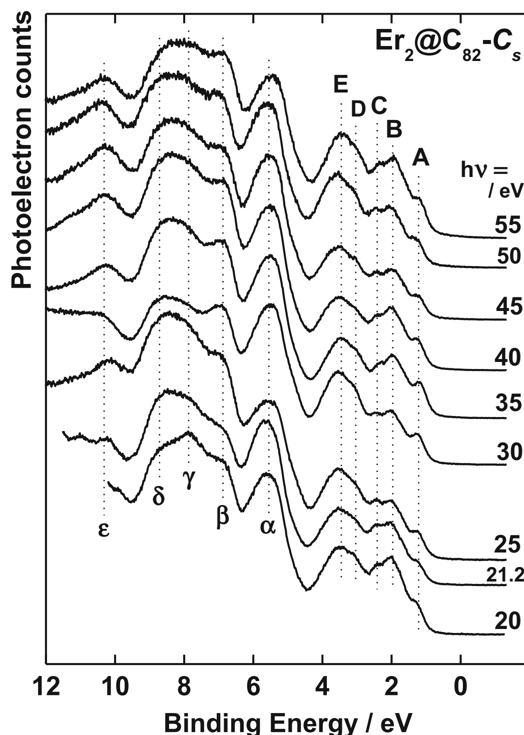

Fig. 5.9 The incident photon energy-dependent UPS of $Er_2@C_{82}$-C_s at hν = 20 ∼ 55 eV. (Reproduced with permission from [48]. Copyright (2012) Elsevier)

band UPS of $Lu_2@C_{82}$-C_{2v} obtained with $h\nu = 20$–55 eV incident photon energy is shown in Fig. 5.11. There is a clear gap between the spectral onset (0.64 eV) and the Fermi level which means this endohedral fullerene is semiconductive as the other metal atom encapsulated endohedral metallofullerenes. Two structures X and Y are observed in the UPS obtained with 45 eV or higher incident photon energy. These are due to $Lu4f_{7/2}$ and $Lu4f_{5/2}$ levels as was described in the section of $Lu@C_{82}$-C_{2v}.

[$Tm_2@C_{82}$-C_{3v}]

Two-thulium atoms encapsulated C_{82} fullerene, $Tm_2@C_{82}$ (III), has been isolated, and their NMR analysis indicated C_{3v} (82:8) cage symmetry [5, 23, 24]. The UPS of $Tm_2@C_{82}$-C_{3v} obtained with $h\nu = 20 \sim 60$ eV incident photon energy is shown in Fig. 5.12 [49]. Ten structures labeled A−D and α–ζ were clearly observed. All spectra were normalized by the peak height of the structure α. The intensity of these structures changed, when the incident photon energy was tuned, which is a typical behavior of fullerenes. The spectral onset energy (E_{onset}) of $Tm_2@C_{82}$-C_{3v} is 0.90 eV below the Fermi level, and this is slightly smaller than that of empty C_{82} (1.2 eV). Structures α–ζ that appeared in the deeper binding energy region ($E_b > 5$ eV) of the UPS of $Er@C_{82}$-C_{2v} are due to σ-electrons that constitute the C_{82} skeletal C–C bonds. Structures labeled A–D that appeared in the upper binding energy region ($E_b < 5$ eV) of the UPS are derived from π-electrons.

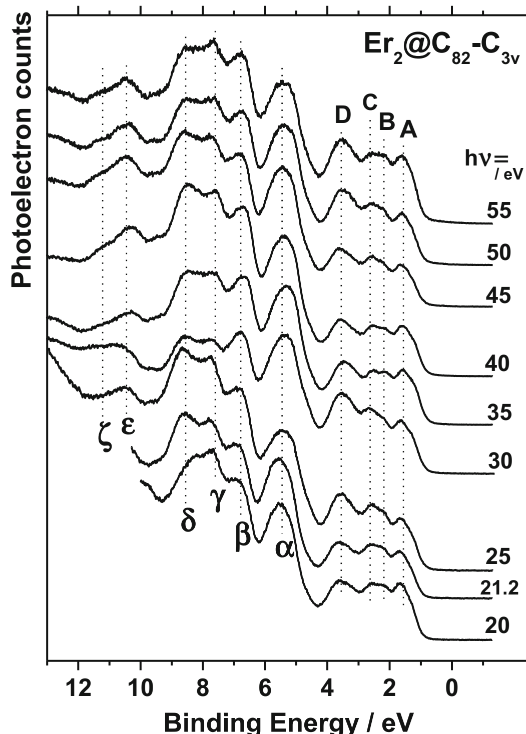

Fig. 5.10 The incident photon energy-dependent UPS of $Er_2@C_{82}$-C_{3v} at $h\nu = 20 \sim 55$ eV. (Reproduced with permission from [48]. Copyright (2012) Elsevier)

Spectral shape of $Er_2@C_{82}$-C_{3v}, $Lu_2@C_{82}$-C_{3v}, and $Tm_2@C_{82}$-C_{3v} was virtually identical, which means that $Er_2@C_{82}$-C_{3v}, $Lu_2@C_{82}$-C_{3v}, and $Tm_2@C_{82}$-C_{3v} have analogous electronic structures. The upper valence band UPS of $Tm_2@C_{82}$-C_{3v} is considerably different from those of $Er_2@C_{82}$-C_s and $Lu_2@C_{82}$-C_{2v}. Thus, there was a large difference in the electronic structures of $Tm_2@C_{82}$-C_{3v}, $Er_2@C_{82}$-C_s, and $Lu_2@C_{82}$-C_{2v}.

X-ray photoelectron spectrum of $Tm_2@C_{82}$-C_{3v} reveals that the $Tm4d_{5/2}$ levels of $Tm_2@C_{82}$ are very close to those of Tm_2O_3 (Tm^{3+}), which indicates that the oxidation state of entrapped Tm atoms is +3. This finding is rather surprising. The electronic structure of $Tm@C_{82}$ is $Tm^{2+}@C_{82}{}^{2-}$. The oxidation state is thought to be held when the number of entrapped atoms increased. The oxidation state of Er in $Er@C_{82}$ or $Er_2@C_{82}$ is the same +3, and this applied to other metal atom(s) entrapped fullerenes such as $Y@C_{82}$ and $Y_2@C_{82}$ $Lu@C_{82}$ and $Lu_2@C_{82}$. $Tm^{2+}@C_{82}{}^{2-}$ electronic configuration suggests that C_{82} cage does not have enough capacity to deprive three electrons of Tm atom. However, XPS^{3+} result of $Tm_2@C_{82}$ indicates Tm atoms lose each three electrons, and possibly plus three electrons are accommodated in the C_{82} cage. It should be noted that the amounts of electron transfer from the entrapped metal atom(s) to the cage aren't always governed by metal atom species.

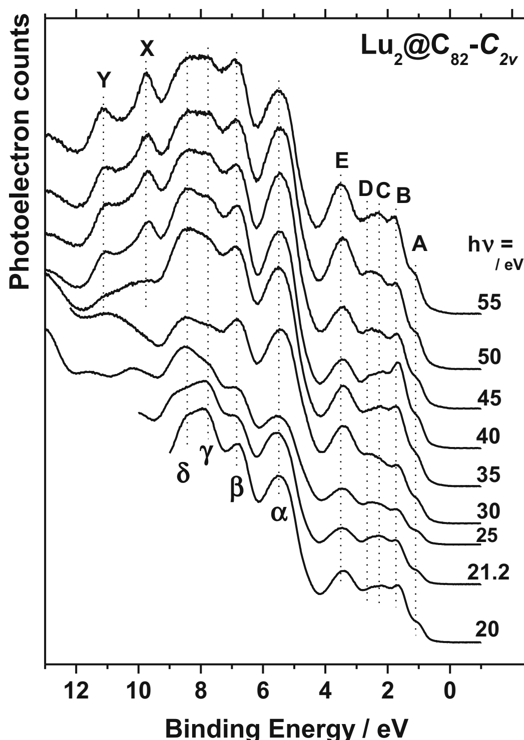

Fig. 5.11 The incident photon energy-dependent UPS of $Lu_2@C_{82}$-C_{2v} at $h\nu = 20 \sim 55$ eV. (Reproduced with permission from [34]. Copyright (2013) Elsevier)

5.7 Electronic Structure of Metal–Carbide Entrapped Fullerenes

Metal carbide consisting of more than four atoms can be entrapped inside the fullerene cage. Since the inner space of the cage is so limited, the interaction among the entrapped atoms might be large, and their structural configuration is of interest. UPS alone is not efficient to elucidate the structure of entrapped atoms, but comparison of the UPS and DFT calculated simulation spectra gives a clue to determine the structure of entrapped carbide. Since the amounts of carbide entrapped endohedral fullerene is so limited to obtain reliable X-ray crystallographic data, the comparison described above might be one of the most potent method to elucidate the structure of entrapped carbide.

[$Er_2C_2@C_{82}$-C_s and $Er_2C_2@C_{82}$-C_{3v}]

Erbium–carbide encapsulated C_{82} fullerenes, $Er_2C_2@C_{82}$ (I) and $Er_2C_2@C_{82}$ (III), have been isolated, and their NMR study revealed their cage symmetry, C_s (82:6) for $Er_2C_2@C_{82}$ (I) and C_{3v} (82:8) for $Er_2C_2@_{82}$ (III) [17]. The UPS of $Er_2C_2@C_{82}$-C_s and $Er_2C_2@C_{82}$-C_{3v} obtained with $h\nu = 20 \sim 55$ eV incident photon energy are shown in Figs. 5.13 and 5.14, respectively. The spectral onset energies of

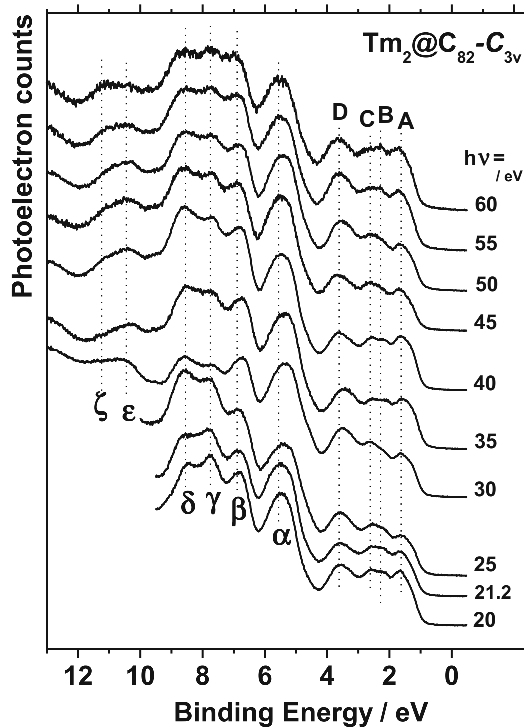

Fig. 5.12 The incident photon energy-dependent UPS of $Tm_2@C_{82}$-C_{3v} at $h\nu = 20 \sim 55$ eV. (Reproduced with permission from [49]. Copyright (2014) Elsevier)

$Er_2C_2@C_{82}$-C_{3v} and $Er_2C_2@C_{82}$-C_s are 0.81 and 0.94 eV, respectively [48]. In the UPS of $Er_2C_2@C_{82}$-C_s, there are five structures labeled A–E derived from π-electrons and the six structures labeled α–ζ derived from σ-electrons. In the UPS of $Er_2C_2@C_{82}$-C_{3v}, there are four structures labeled A–D derived from π-electrons and the six structures labeled α–ζ due to σ-electrons. Structures α–ζ in both spectra resemble each other, which means the electronic structures of both C_{82}-C_s and C_{82}-C_{3v} skeletal cage don't differ so much. On the other hand, there is an explicit difference in structures A–D (E). Upper valence band UPS of the different cage structure (symmetry) with the same carbon number fullerene differ from each other, which means this region can be used to distinguish fullerenes from one another.

[$Lu_2C_2@C_{82}$-C_{2v}]

Lutetium–carbide encapsulated C_{82} fullerenes $Lu_2C_2@C_{82}$ (II) have been isolated, and their NMR study revealed their cage symmetry to be C_{2v} (82:9) [40]. The valence band UPS of $Lu_2C_2@C_{82}$-C_{2v} obtained with $h\nu = 20 \sim 55$ eV incident photon energy is shown in Fig. 5.15 [35]. Eleven structures labeled A−E, α–δ, and X and Y were clearly observed. All spectra were normalized by the peak height of structure α. The intensity of these structures changed, when the incident photon energy was tuned, which is a typical behavior of fullerenes. Their onset energy (E_{onset}) of $Lu_2C_2@C_{82}$-C_{2v} is 0.64 eV. Again this endohedral fullerene is

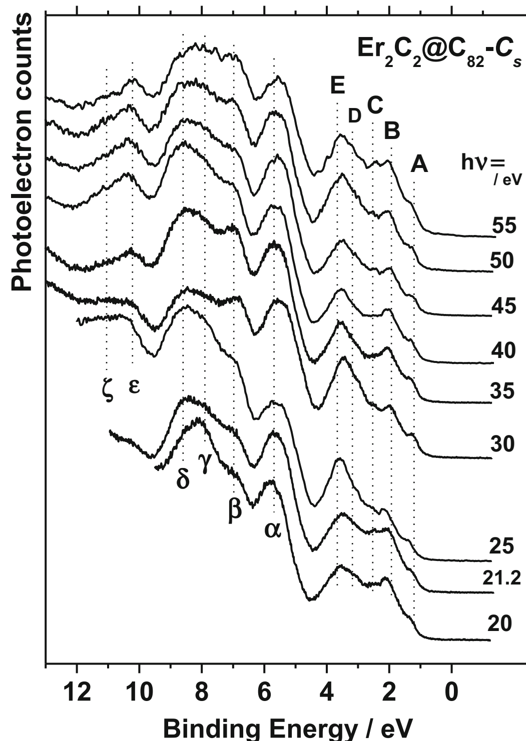

Fig. 5.13 The incident photon energy-dependent UPS of $Er_2C_2@C_{82}$-C_s at $h\nu = 20 \sim 55$ eV. (Reproduced with permission from [48]. Copyright (2012) Elsevier)

semiconductive. Structures α–δ that appeared in the deeper binding energy region ($E_b > 5$ eV) of the UPS of $Lu_2C_2@C_{82}$-C_{2v} are due to σ-electrons that constitute the C_{82} skeletal C–C bonds. Structures labeled A–E that appeared in the upper binding energy region ($E_b < 5$ eV) of the UPS are derived from π-electrons. The UPS of $Lu_2C_2@C_{82}$-C_{2v} is quite different from those of $Lu@C_{82}$-C_{2v}, which can be interpreted in terms of the amounts of transferred electrons from the entrapped atom(s) to the cage: the C_{82} cage that entrapped two Lu atoms accepts more electrons than that of one Lu atom in it. Spectral resemblance is found in the UPS of $Lu_2C_2@C_{82}$-C_{2v} and $Y_2C_2@C_{82}$-C_{2v} except for structures X and Y. This difference is plausible since structures X and Y are Lu4f level origin.

The UPS of $Lu_2@C_{82}$-C_{2v} [40] also resembles those of $Lu_2C_2@C_{82}$, but there are two major differences. One is the relative intensity of structure E of $Lu_2C_2@C_{82}$-C_{2v} which is much higher than its counterpart of $Lu_2@C_{82}$-C_{2v}. DFT calculation suggests an existence of an orbital attributed to entrapped C–C atoms at the energy region of structure E. That is, the enhancement of structure E of $Lu_2C_2@C_{82}$ is due to the superposition of the electronic level of C–C atoms. Another difference is the energy positions of structures X and Y. Their positions of $Lu_2C_2@C_{82}$-C_{2v} are shallower than those of $Lu@C_{82}$-C_{2v} or $Lu_2@C_{82}$-C_{2v} by 0.5 eV. This difference suggests that electrons on Lu atoms of $Lu_2C_2@C_{82}$-C_{2v} are more

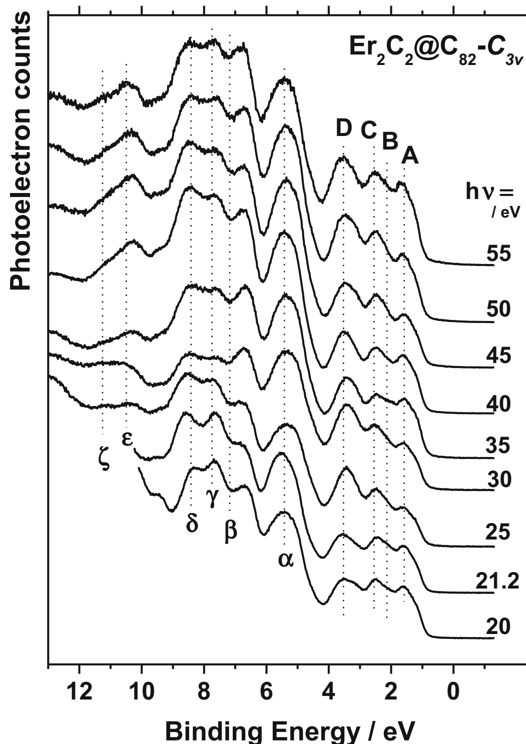

Fig. 5.14 The incident photon energy-dependent UPS of $Er_2C_2@C_{82}$-C_{3v} at $h\nu = 20 \sim 55$ eV. (Reproduced with permission from [48]. Copyright (2012) Elsevier)

abundant than those of Lu@C_{82}-C_{2v} or Lu_2@C_{82}-C_{2v}. Possible reason of this energy level difference might be electron back donation or hybridization among the orbitals of entrapped Lu and carbon atoms in $Lu_2C_2@C_{82}$-C_{2v}. In the case of $Lu_2C_2@C_{82}$-C_{2v}, there is additional interaction between entrapped Lu atoms on the top of that in Lu@C_{82}-C_{2v}. Since entrapped Lu atoms in Lu_2@C_{82}-C_{2v} are ions because of electron donation to the cage, these two ions have repulsive interaction. In the case of $Lu_2C_2@C_{82}$, the situation becomes much more complicated, since four atoms are confined in a very tight area. Lu atoms donate electrons to the cage and possibly to entrapped C_2 atoms, attractive interaction between entrapped C_2 and Lu atoms might be induced. Their atomic orbitals might overlap and induce orbital hybridization, which brings back donating of once C_2 atom accepted electron. That is, electron population of Lu atoms in $Lu_2C_2@C_{82}$-C_{2v} might be $Lu^{+3-\delta}$.

[$Tm_2C_2@C_{82}$-C_{3v}]

Thulium–carbide encapsulated C_{82} fullerenes, $Tm_2C_2@C_{82}$ (III), have been isolated, and their NMR analysis supported C_{3v} (82:8) cage symmetry [5, 23, 24]. The UPS of $Tm_2C_2@C_{82}$-C_{3v} obtained with $h\nu = 20 \sim 60$ eV incident photon energy is shown in Fig. 5.16 [48]. Structures labeled A–D that appeared between 0 and 5.5 eV energy region are principally due to π-electrons, and structures labeled A–D and α–ζ that appeared in the deeper energy region than 5.5 eV are mainly due to σ-electrons that constitute the C_{82} skeletal C–C bonds. The UPS of $Y_2C_2@C_{82}$-

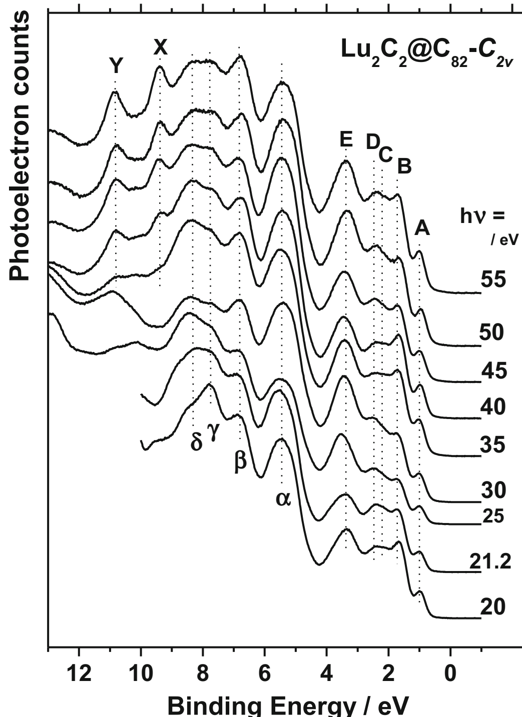

Fig. 5.15 The incident photon energy-dependent UPS of $Lu_2C_2@C_{82}$-C_{2v} at $h\nu = 20 \sim 55$ eV. (Reproduced with permission from [34]. Copyright (2013) Elsevier)

C_{3v}, $Er_2C_2@C_{82}$-C_{3v}, and $Tm_2C_2@C_{82}$-C_{3v} are also identical, which suggests their analogous electronic structure. Molecular orbitals of $Y_2C_2@C_{82}$-C_{3v} have been calculated, and an inspection of the orbitals reveals that the molecular orbitals due to encapsulated C_2 unit lie at the energy region of 3.5 eV which is responsible to form structure D. From the analogy to the discussion in previous section, the oxidation state of Tm in $Tm_2C_2@C_{82}$-C_{3v} is (or Tm+3-δ) and entrapped C_2 atoms accept electrons. Possible electronic configuration might be $(Tm_2C_2)^{4+}@C_{82}{}^{4-}$.

[$Sc_3C_2@C_{80}$]

Figure 5.17 shows the UPS of $Sc_3C_2@C_{80}$ measured at various incident photon energies [50]. The spectra exhibit seven peaks denoted as A–C and α–ζ in the figure. The onset energy of the UPS (Eonset), which is the energy separation between the Fermi level and the valence band maximum, is 0.2 eV for $Sc_3C_2@C_{80}$. This value is much smaller than the Eonset of $La_2@C_{80}$ (0.77 eV) [40] and $Sc_3N@C_{80}$ (1.1 eV) [11]. The Fermi level of the n-type semiconducting fullerene thin film usually does not situate at the mid gap but closer to the conduction band minimum [51], so the band gap of $Sc_3C_2@C_{80}$, $La_2@C_{80}$, and $Sc_3N@C_{80}$ is probably between the E_{onset} and twice of the E_{onset}. The small onset energy of $Sc_3C_2@C_{80}$ is qualitatively consistent with the previous DFT calculation by Sato et al. [52] in which the band gap of $Sc_3C_2@C_{80}$, $La_2@C_{80}$, and $Sc_3N@C_{80}$ is estimated to be 0.07, 0.41, and 1.23 eV, respectively.

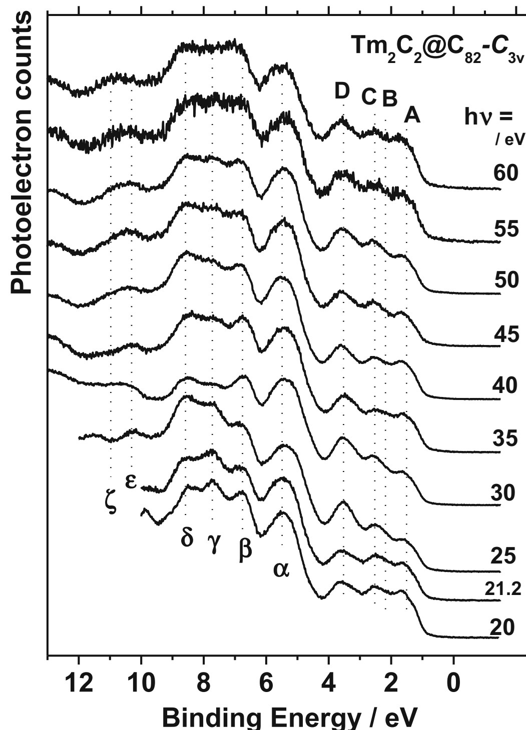

Fig. 5.16 The incident photon energy-dependent UPS of $Tm_2C_2@C_{82}$-C_{3v} at $h\nu = 20 \sim 60$ eV. (Reproduced with permission from [49]. Copyright (2014) Elsevier)

Geometry optimization of $Sc_3C_2@C_{80}$ yields two energy stable structures (iomers 1 and 2). The simulated spectra for both structures do not reproduce the UPS well, but a spectrum obtained by adding the simulated spectra of isomer 1 and 2 reproduces the UPS very well. These findings indicate that the coexistence of these two structures should be adopted to consider the electronic structure of $Sc_3C_2@C_{80}$. Finally, comparison of the calculated wave functions of $Sc_3C_2@C_{80}$ and empty C_{80} (I_h symmetry) revealed that the oxidation state of both isomers was $(Sc_3C_2)^{6+}@C_{80}{}^{6-}$. That is, entrapped cluster donates six electrons to the C_{80} cage. $Sc_3C_2@C_{80}$ thin film is not a semimetal as predicted by the previous band calculation, but a semiconductor with a small band gap (more than 0.2 eV). Considering the coexistence of two different structures of $Sc_3C_2@C_{80}$ reduces the discrepancy between the measured UPS and the theoretical spectra calculated on a single molecule. It seems important for the band calculation of $Sc_3C_2@C_{80}$ to consider two stable structures. $Sc_3C_2@C_{80}$ is one of the well-studied endohedral fullerenes. Recent band calculation suggests the possibility of its semimetallic behavior due to the small band gap (0.07 eV). We measured the ultraviolet photoelectron spectra (UPS) of $Sc_3C_2@C_{80}$ and estimated the lower limit of the band gap to be 0.2 eV. A simulated spectrum obtained by averaging the results of DFT calculations on two stable Sc_3C_2 geometries reproduces the UPS well. In conclusion, $Sc_3C_2@C_{80}$ thin film is not a semimetal but a semiconductor.

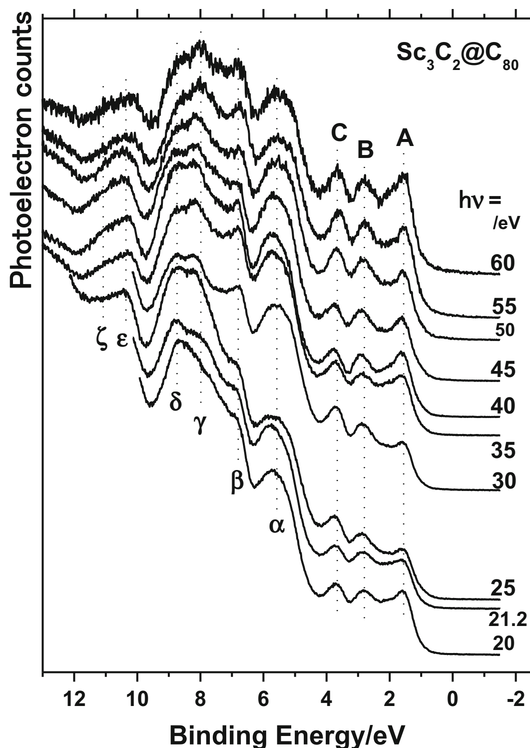

Fig. 5.17 The incident photon energy-dependent UPS of $Sc_3C_2@C_{80}$ at $h\nu = 20 \sim 60$ eV. (Reproduced with permission from [50]. Copyright (2015) Elsevier)

The discrepancy between the experimental and previously calculated results might be attributed to the coexistence of two Sc_3C_2 geometries.

5.8 Electronic Structure of Metal Nitride Entrapped Fullerenes

Interaction between entrapped metal atoms and C_2 atoms in the carbide entrapped endohedral fullerenes seems to be rather small because hardly any bonding is formed between the metal atoms and C_2 atoms. On the other hand, situation of nitride entrapped fullerenes might be quite different since bonding formation between entrapped nitrogen and metal atoms is highly expected. Entrapped nitride may take either pyramidal shape with a nitrogen atom at the top or triangle shape with a nitrogen atom at the center of triangle. Fullerene inner space is so limited. C_{68} and C_{78} cages are going to be considered. Inner space of C_{68} is much narrower than that of C_{78}. The shape of metal nitride in these fullerene cages is a great concern. The UPS of nitride encapsulated fullerenes $Sc_3N@C_{78}$ and $Sc_3N@C_{68}$ are going to be given, and the structure of entrapped Sc_3N is considered with an aid of DFT calculation.

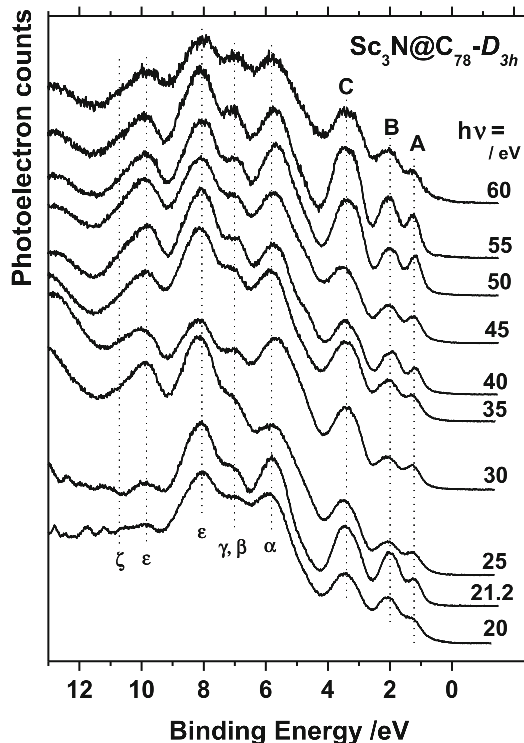

Fig. 5.18 The incident photon energy-dependent UPS of $Sc_3N@C_{78}$ at $h\nu = 20 \sim 60$ eV. Reprinted with permission from [51]. Copyright (2013) American Chemical Society

[$Sc_3N@C_{78}$-D_{3h}]

Isolation of endohedral fullerene, $Sc_3N@C_{78}$-D_{3h}, has been reported [27], and its cage symmetry was determined to be D_3 from the NMR analysis. Figure 5.18 shows the valence band UPS of $Sc_3N@C_{78}$ obtained with $h\nu = 20$–60 eV photon energy [53]. The spectral onset was 0.75 eV below the Fermi level. There are eight explicit structures labeled A–C and α–ζ in the UPS of $Sc_3N@C_{78}$. Approximate peak positions of the structures are indicated with dotted lines.

The intensity of the structures appearing in the UPS of $Sc_3N@C_{78}$ oscillates in accordance with the incident photon energy change, which means that this molecule has analogous photoelectric behavior to other fullerenes. The UPS of $La_2@C_{78}$ and $Ti_2C_2@C_{78}$ have been reported [54]. These endohedral fullerenes have the same D_{3d} symmetry. That is, $Sc_3N@C_{78}$, $La_2@C_{78}$, and $Ti_2C_2@C_{78}$ have the same cage structure. When fullerene cage entraps a metal atom, their electronic structure depends only on the cage symmetry as long as the amount of the transferred electrons to the cage is the same. Present result suggests that the amounts of transferred electrons in these endohedral fullerenes differ from each other. Transferred electrons are calculated to be 3.8 ($Sc_3N@C_{78}$), 4.6 ($La_2@C_{78}$), and 2.6 ($Ti_2C_2@C_{78}$) by DFT population analysis. Rearrangement of molecular orbital of the fullerene cage upon encapsulation of cluster could be also the reason of their spectral difference. The UPS is well reproduced by a simulated spectrum obtained

from geometry optimized structure in which entrapped Sc_3N takes triangle shape with N atom at the center. XPS of $Sc_3N@C_{78}$ was measured, and chemical shifts of Sc3d, and N1 s peaks suggest Sc^+ and N^- or N^{2-} state. Since N^{2-} state is less plausible, the electronic configuration of $Sc_3N@C_{78}$ might be $(Sc^+)_3N^-@C_{78}{}^{2-}$.

[$Sc_3N@C_{68}$]

Isolated fullerenes tend to obey an empirical rule so-called isolated pentagon rule (IPR) in which pentagon rings try to be separated from each other to lower the total energy of the fullerene cage. C_{60} and other isolated higher fullerenes satisfy this rule.

However, $Sc_2@C_{66}$ [56] and $Sc_3N@C_{68}$ [26] were found and isolated, and they do not obey the IPR so that they are called non-IPR fullerenes. The non-IPR structure of $Sc_2@C_{66}$ was confirmed by X-ray diffraction analysis conducted by the Rietveld/maximum entropy method and NMR spectroscopy. The NMR analysis of $Sc_3N@C_{68}$ indicated that it has either D_3 or S_6 symmetry. Their formation energy calculation of the candidate $Sc_3N@C_{68}$ isomers suggested that D_3 isomer (No. 6140 after the nomenclature by Fowler and Manolopoulos) was the most plausible candidate for $Sc_3N@C_{68}$. This estimation was later supported by X-ray crystal structure analysis of the $Sc_3N@C_{68}$ [Ni(OEP)]-$2C_6H_6$ adduct [57]. However, the structure of the endohedral fullerene obtained from the fullerene adduct complex does not always reflect the structure of endohedral fullerene itself [58], since the structure or the position of the entrapped species often changes upon adduct formation. Hence, actual structural determination is an important issue with regard to endohedral fullerenes. Moreover, why non-IPR fullerenes can be produced is a more important issue, because this answer could provide a clue on the fullerene formation mechanism. Stability of the fullerene cage might depend on the cage formation energy and the electronic structure of the cage represented by the energy of the highest occupied molecular orbital (HOMO) and the gap between HOMO and the lowest unoccupied molecular orbital (LUMO). Figure 5.19 shows the valence band UPS of $Sc_3N@C_{68}$ obtained with $h\nu = 20$–60 eV photon energy [55].

The spectral onset is 1.1 eV below the Fermi level, which is the largest value among endohedral fullerenes [53, 54, 59–62] and is comparable to that of the higher fullerenes [63, 64]. There are 7 structures labeled A to G due to π-electrons and 6 structures labeled α–δ due to σ-electrons in this figure. Geometry optimization of $Sc_3N@C_{68}$ has been performed by a DFT method, and it yields one structure as shown in Fig. 5.20, which resembles the one deduced from X-ray crystallographic structure analysis of $Sc_3N@C_{68}$ adduct [57]. A simulated spectrum generated from this geometry reproduces the UPS very well particularly in the upper valence band region as is shown in Fig. 5.20 [55]. That is, it is highly probable that actual $Sc_3N@C_{68}$ takes the geometry shown in Fig. 5.21 [55]. Sc_3N cluster takes triangle form as that in $Sc_3N@C_{78}$.

This inner space of $Sc_3N@C_{68}$ is much smaller than that of $Sc_3N@C_{78}$. To accommodate Sc_3N cluster inside cage, C_{68} is compressed in the perpendicular direction of the Sc_3N triangle and is elongated in the direction of the triangle plane when compared with empty C_{68} (no. 6140).

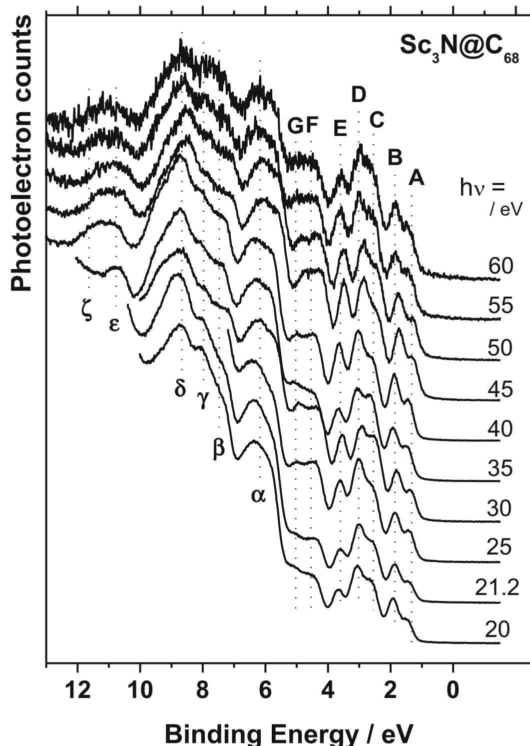

Fig. 5.19 The incident photon energy-dependent UPS of non-IPR $Sc_3N@C_{68}$ at $h\nu = 20 \sim 60$ eV. (Reproduced with permission from [55]. Copyright (2013) Elsevier)

XPS of $Sc_3N@C_{68}$ was measured, and chemical shift of Sc2p suggests either Sc^{2+} or Sc^{3+} state. XPS of $Sc_3N@C_{68}$ [53] and $Sc_3N@C_{80}$ [11] were also measured. Their peak positions of Sc3d and N1s shift according to the cage size. The smaller the cage size, the shallower Sc3d and N1 s binding energy. This fact can be interpreted in terms of the degree of the interaction between Sc and N atoms. Their interaction must be large in the smaller cage because of shorter Sc-N distance. Once transferred electrons from Sc atoms to N atom are more back donated in the smaller cage. Thus, both Sc and N atoms became electron rich in the smaller cage.

5.9 Prospect of Endohedral Fullerenes

Fullerenes have attracted a lot of attentions from researchers ranging from physicists, chemists to product seeking engineers. Spherical geometry of fullerenes themselves is interesting, and their aromatic nature draws attentions of researchers. Discovery of super conduction of alkali metal-dosed C_{60} was a striking astonishment, and there was a prospect of finding of another fullerene based super conductors. Unfortunately, it seems that C_{60} is only candidate to yield superconductors.

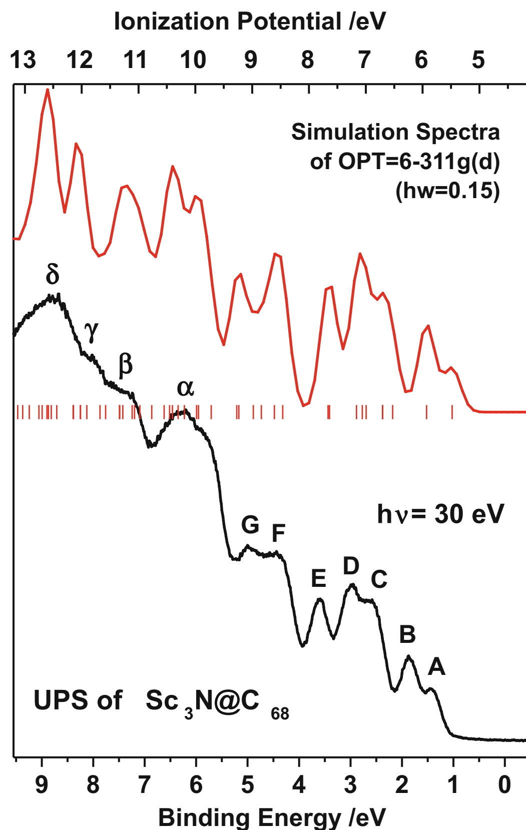

Fig. 5.20 The UPS of non-IPR $Sc_3N@C_{68}$ at $h\nu = 30$ eV and the simulated spectrum. (Reproduced with permission from [55]. Copyright (2013) Elsevier)

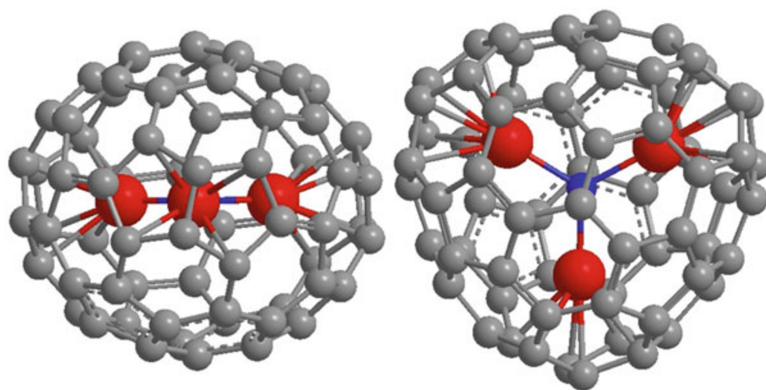

Fig. 5.21 Optimized geometry of non-IPR $Sc_3N@C_{68}$ obtained from the initial geometry. (Reproduced with permission from [55]. Copyright (2013) Elsevier)

Thus, the research on fullerenes is now gradually declining. The reason is rather simple. C_{60} and C_{70} can be produced with enough quantity, but other fullerenes such as higher fullerenes or endohedral fullerenes cannot be easily synthesized, and their isolation is a hard work. Application of fullerenes is rather limited, and the cost of their synthesis does not meet the application demands. If useful application is discovered and cheaper synthesis method is found, the investigation on fullerene science will be developed. Fullerenes are still exotic material, and we could extract interesting knowledge from them. Particularly endohedral metallofullerenes are of interest, since their electronic structure can be easily modified by changing encapsulated atoms. We hope lots of researchers pay attention to fullerenes.

References

1. H.W. Kroto, J.R. Heath, S.C. O'brien, R.F. Curl, R.E. Smalley, Nature **318**, 162 (1985)
2. A.F. Hebard, M.J. Rosseinsky, R.C. Haddon, D.W. Murphy, S.H. Glarum, T.T.M. Palstra, A.P. Ramirez, A.R. Kortan, Nature **350**, 600 (1991)
3. Y. Chai, T. Guo, C. Jin, R.E. Haufler, L.P.F. Chibante, J. Fure, L. Wang, J.M. Alford, R.E. Smalley, J. Phys. Chem. **95**, 7564 (1991)
4. H. Shinohara, H. Sato, M. Ohkohchi, Y. Ando, T. Kodama, T. Shida, T. Kato, Y. Saito, Nature **357**, 52 (1992)
5. Z. Xu, T. Nakane, H. Shinohara, J. Am. Chem. Soc. **118**, 11309 (1996)
6. R.D. Johnson, M.S. de Vries, J. Salem, D.S. Bethune, C.S. Yannoni, Nature **355**, 239 (1992)
7. L. Soderbolm, P. Wurz, K.R. Lykke, D.H. Parker, F.W. Lytle, J. Phys. Chem. **96**, 7153 (1992)
8. R. Beyers, C.-H. Kiang, R.D. Johnson, J.R. Salem, M.S. Devries, C.S. Yannoni, D.S. Bethune, H.C. Dorn, P. Burbank, K. Harich, S. Stevenson, Nature **370**, 196 (1994)
9. S. Stevenson, G. Rice, T. Glass, K. Harich, F. Cromer, M.R. Jordan, J. Craft, E. Hadju, R. Bible, M.M. Olmstead, K. Maitra, A.J. Fisher, A.L. Balch, H.C. Dorn, Nature **401**, 55 (1999)
10. H. Shiozawa, H. Rauf, T. Pichler, D. Grimm, X. Liu, M. Knupfer, M. Kalbac, S. Yang, L. Dunsch, B. Buchner, D. Batchelor, Phys. Rev. B **72**, 195409 (2005)
11. L. Alvarez, T. Pichler, P. Georgi, T. Schwieger, H. Peisert, L. Dunsch, Z. Hu, M. Knupfer, J. Fink, P. Bressler, M. Mast, M.S. Golden, Phys. Rev. B **66**, 035107 (2002)
12. S. Yang, L. Dunsch, J. Phys. Chem. B **109**, 12320 (2005)
13. T. Inoue, T. Tomiyama, T. Sugai, T. Okazaki, T. Suematsu, N. Fujii, H. Utsumi, K. Nojima, H. Shinohara, J. Phys. Chem. B **108**, 7573 (2004)
14. B. Cao, M. Hasegawa, K. Okada, T. Tomiyama, T. Okazaki, K. Suenaga, H. Shinohara, J. Am. Chem. Soc. **123**, 9679 (2001)
15. C.-R. Wang, T. Kai, T. Tomiyama, T. Yoshida, Y. Kobayashi, E. Nishibori, M. Takata, M. Sakata, H. Shinohara, Angew. Chem. Int. Ed. **40**, 397 (2001)
16. N. Tagmatarchis, E. Aslanis, H. Shinohara, K. Prassides, J. Phys. Chem. B **104**, 11010 (2000)
17. Y. Ito, T. Okazaki, S. Okubo, M. Akachi, Y. Ohno, T. Mizutani, T. Nakamura, R. Kitaura, T. Sugai, H. Shinohara, ACS Nano **1**, 456 (2007)
18. A. Miyamoto, H. Okimoto, H. Shinohara, Y. Shibamoto, Eur. Radiol. **16**, 1050 (2006)
19. J. Ding, S. Yang, Angew. Chem. Int. Ed. **35**, 2234 (1996)
20. M.M. Alvarez, E.G. Gillan, K. Holczer, R.B. Kaner, K.S. Min, R.L. Whetton, J. Phys. Chem. **95**, 1056 (1991)
21. H. Umemoto, K. Ohashi, T. Inoue, N. Fukui, T. Sugai, H. Shinohara, Chem. Commun. **46**, 5653 (2010)
22. H. Shinohara, Rep. Prog. Phys. **63**, 843 (2000). and references therein
23. U. Kirbach, L. Dunsch, Angew. Chem. Int. Ed. **35**, 2380 (1996)

24. T. Kodama, N. Ozawa, Y. Miyake, K. Sakaguchi, H. Nishikawa, I. Ikemoto, K. Kikuchi, Y. Achiba, J. Am. Chem. Soc. **124**, 1452 (2002)
25. H. Shinohara, M. Inakuma, N. Hayashi, H. Sato, Y. Saito, T. Kato, S. Bandow, J. Phys. Chem. **98**, 8597 (1994)
26. S. Stevenson, P.W. Fowler, T. Heine, J.C. Duchamp, G. Rice, T. Glass, K. Harich, E. Hajdu, R. Bible, H.C. Dorn, Nature **408**, 428 (2000)
27. M.M. Olmstead, A.D. Bettencourt-Dias, J.C. Duchamp, S. Stevenson, D. Marciu, H.C. Dorn, A.L. Balch, Angew. Chem. Int. Ed. **40**, 23 (2001)
28. J.F. Janak, Phys. Rev. B **18**, 7165 (1978)
29. T. Koga, S. Yamamoto, T. Shimazaki, H. Tatewaki, Theor. Chem. Accounts **108**, 41 (2002)
30. Y. Osanai, M. Sekiya, T. Noro, T. Koga, Mol. Phys. **101**, 65 (2003)
31. P.W. Fowler, D.E. Manolopoulos, *An Atlas of Fullerenes* (Oxford Press, Oxford, 1995)
32. A.A. Popov, L. Dunsch, J. Am. Chem. Soc. **129**, 11835 (2007)
33. K.D. Sattler (ed.), *Handbook of Nanophysics*(CRC, 2004)
34. K. Muthukumar, J.A. Larsson, J. Mater. Chem. **18**, 3347 (2008)
35. T. Miyazaki, R. Sumii, H. Umemoto, H. Okimoto, T. Sugai, H. Shinohara, S. Hino, Chem. Phys. Lett. **555**, 222 (2013)
36. M. Cardona, L. Ley, *Photoemission in Solids I* (General Principles Springer-Verlag, Berlin, 1978)
37. T. Miyazaki, R. Sumii, H. Umemoto, H. Okimoto, Y. Ito, T. Sugai, H. Shinohara, S. Hino, Chem. Phys. **378**, 11 (2010)
38. L. Dunsch, S. Yang, Small **3**, 1298 (2007)
39. M. Yamada, T. Wakahara, T. Nakahodo, T. Tsuchiya, Y. Maeda, T. Akasaka, K. Yoza, E. Horn, N. Mizorogi, S. Nagase, J. Am. Chem. Soc. **128**, 1402 (2006)
40. T. Miyazaki, S. Okita, T. Ohta, H. Yagi, R. Sumii, H. Okimoto, Y. Ito, H. Shinohara, S. Hino, Chem. Phys. **447**, 71 (2015)
41. T.R. Cummins, M. Burk, M. Schmidt, J.F. Armbruster, D. Fuchs, P. Adelmann, S. Schupper, R.H. Michel, M.M. Kapps, Chem. Phys. Lett. **261**, 228 (1996)
42. E. Nishibori, M. Takata, M. Sakata, A. Taninaka, H. Shinohara, Angew. Chem. Int. Ed. **40**, 2998 (2001)
43. K. Kobayashi, S. Nagase, T. Akasaka, Chem. Phys. Lett. **245**, 230 (1995)
44. K. Kobayashi, S. Nagase, T. Akasaka, Chem. Phys. Lett. **261**, 502 (1996)
45. H. Shimotani, T. Ito, Y. Iwasa, A. Aninaka, H. Shinohara, E. Nishibori, M. Takata, M. Sakata, J. Am. Chem. Soc. **126**, 364 (2004)
46. J. Zhang, C. Hao, S. Li, W. Mi, P. Jin, J. Phys. Chem. C **111**, 7862 (2007)
47. T. Akasaka, S. Nagase, K. Kobayashi, M. Walchi, K. Yamamoto, H. Funasaku, M. Kato, T. Hoshino, T. Erata, Angew. Chem. Int. Ed. **36**, 1643 (1997)
48. T. Miyazaki, R. Sumii, H. Umemoto, H. Okimoto, Y. Ito, T. Sugai, H. Shinohara, T. Zaima, H. Yagi, S. Hino, Chem. Phys. **397**, 87 (2012)
49. T. Miyazaki, Y. Tokumoto, R. Sumii, H. Yagi, N. Izumi, H. Shinohara, S. Hino, Chem. Phys. **47**, 431–432 (2014)
50. H. Yagi, T. Miyazaki, S. Okita, T. Zaima, H. Okimoto, N. Izumi, Y. Nakanishi, H. Shinohara, S. Hino, Chem. Phys. Lett. **634**, 98 (2015)
51. M. Shiraishi, K. Shibata, R. Maruyama, M. Ata, Phys. Rev. B **68**, 235414–2351-5 (2003)
52. S. Sato, S. Seki, G. Luo, M. Suzuki, J. Lu, S. Nagase, T. Akasaka, J. Am. Chem. Soc. **134**, 11681 (2012)
53. S. Hino, M. Zenki, T. Zaima, Y. Aoki, S. Okita, T. Ohta, H. Yagi, T. Miyazaki, R. Sumii, H. Okimoto, Y. Ito, H. Shinohara, J. Phys. Chem. C **116**, 165 (2012)
54. S. Hino, M. Kato, D. Yoshimura, H. Moribe, H. Umemoto, Y. Ito, T. Sugai, H. Shinohara, M. Otani, Y. Yoshimoto, S. Okada, Phys. Rev. B **75**, 125418 (2007)
55. S. Hino, N. Ogasawara, T. Ohta, H. Yagi, T. Miyazaki, T. Nishi, H. Shinohara, Chem. Phys. **421**, 39 (2013)
56. C.-R. Wang, T. Kai, T. Tomiyama, T. Yoshida, Y. Kobayashi, E. Nishibori, M. Takata, M. Sakata, H. Shinohara, Nature **408**, 426 (2000)

57. M. Yamada, T. Wakahara, T. Nakahodo, T. Tsuchiya, Y. Maeda, J. Am. Chem. Soc. **128**, 1402 (2006)
58. M.M. Omstead, H.M. Lee, J.C. Duchamp, S. Stevenson, D. Marciu, H.C. Dorn, A.L. Balch, Angew. Chem. Int. Ed. **42**, 900 (2003)
59. S. Hino, H. Takahashi, K. Iwasaki, M. Matsumoto, T. Miyazaki, S. Hasegawa, K. Kikuchi, Y. Achiba, Phys. Rev. Lett. **71**, 4261 (1993)
60. S. Hino, N. Wanita, K. Iwasaki, D. Yoshimura, N. Ozawa, T. Kodama, K. Sakaguchi, H. Nishikawa, I. Ikemoto, K. Kikuchi, Chem. Phys. Lett. **402**, 217 (2005)
61. S. Hino, N. Wanita, K. Iwasaki, D. Yoshimura, T. Akachi, T. Inoue, Y. Ito, T. Sugai, H. Shinohara, Phys. Rev. B **72**, 195424 (2005)
62. S. Hino, T. Miyazaki, Y. Aoki, N. Wanita, M. Kato, R. Sumii, T. Akachi, T. Inoue, Y. Ito, T. Sugai, H. Shinohara, Bull. Chem. Soc. Jpn. **82**, 963 (2009)
63. S. Hino, H. Takahashi, K. Iwasaki, T. Miyazaki, K. Kikuchi, Chem. Phys. Lett. **230**, 165 (1994)
64. S. Hino, K. Umishita, K. Iwasaki, T. Miyazaki, K. Kikuchi, Phys. Rev. B **53**, 7496 (1996)

Chapter 6
Superconductivity of Carbides

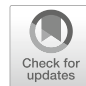

Kaya Kobayashi, Kazumasa Horigane, Rie Horie, and Jun Akimitsu

Abstract Carbon-based superconductors can be roughly categorized into two groups. The first includes relatively new superconductors, such as boron-doped diamond, graphite-intercalated compounds (GIC), carbon nanotube (CNT) superconductors and fullerene superconductors.

Here, we review relatively "old materials," which are materials that can be described within the "BCS (Bardeen-Cooper-Schrieffer) frame." The contents of this chapter are as follows:

1. MX-type compounds (B1-type superconductors and SiC)
2. MC_2 compounds (YC_2 and LaC_2)
3. Ln_2C_3 (La_2C_3 and Y_2C_3)
4. Boron carbide (RNi_2B_2C and YB_2C_2)

We introduce the present experimental and theoretical understanding of carbon-based superconductors.

Keywords Superconductivity · Intermetallic compound

6.1 MX-Type Compounds

6.1.1 B1-Type Superconductors

After the discovery of superconductivity in Hg by H. Kamerlingh Onnes [1], a number of superconductors among metal elements (Pb, Nb, etc.), metal-nonmetal compounds and intermetallic compounds have been discovered. In the early history of new superconductors, B1(NaCl)-type compounds were discovered as the first superconductors with a transition temperature (T_c) above 10 K. In this section, we

K. Kobayashi · K. Horigane · R. Horie · J. Akimitsu (✉)
Research Institute for Interdisciplinary Science, Okayama University, Okayama, Japan
e-mail: akimitsu@okayama-u.ac.jp

© Springer Nature Singapore Pte Ltd. 2019

Y. Kubozono (ed.), *Physics and Chemistry of Carbon-Based Materials*,
https://doi.org/10.1007/978-981-13-3417-7_6

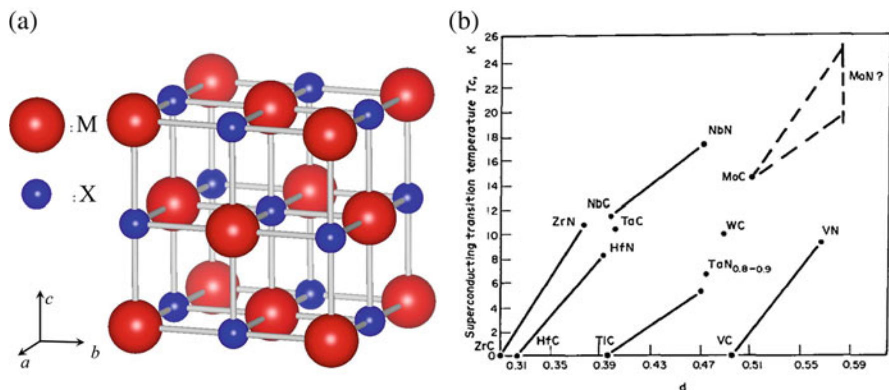

Fig. 6.1 (**a**) B1(NaCl)-type structure of MX (M = Nb, Mo, Ta, W, etc. and X = N or C). (**b**) T_c in B1-type MX as a function of valence electron density d ($=n/a_0^3$), where n is the number of valence electrons per cell [2]

introduce transition-metal carbide and nitride superconductors alongside their T_c data. We first introduce the overall information regarding B1-type superconductors and subsequently discuss the density of states (DOS) at the Fermi energy and phonon softening, which are important for fully understanding T_c.

6.1.1.1 B1-Type Structures and Their T_c's

Before discussing individual materials, we present a general view of B1-type superconductors. Figure 6.1a shows the crystal structure of MX, where M is a transition metal (M = Nb, Ta, W, Mo, etc.) belonging to a group from IIIa to VIa and X is C or N. Its space group is $O^5{}_h$-Fm3m. The characteristic feature of the bonding state of these compounds is that charge transfer occurs from the metal element to the nonmetal element and covalent and ionic bonds coexist alongside metallic bonds. These characteristics make these materials superior in terms of their superconductivity, high heat resistance, and high hardness [3]. Transition metal nitrides (MN) have higher T_c values than transition metal carbides (MC) in all MX compounds.

Figure 6.1b shows a plot of T_c vs valence electron density d (valence electrons per cell) in B1-type MX compounds [2]. It is noted that the T_c in MN is always higher than that of MC, as shown in Fig. 6.1b. This can be ascribed to the higher valence electron density in MN than in MC. This feature is also explained by higher density of states (DOS) at the Fermi level in nitride than in carbide because the atomic number of N atoms is larger than that of C atoms, as will be discussed later. The characteristic of MX is that defects exist at both M and X sites. These defects increase the resistance of the normal metal phase and suppress T_c. Even in 1:1 stoichiometric compounds, there are several defects in TiC or NbN and a 25% atomic concentration of defects in VC.

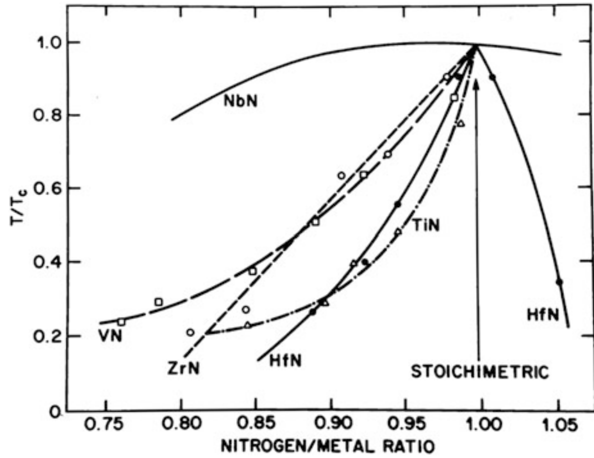

Fig. 6.2 Effect of deviations from stoichiometry on T_c for various nitrides [4]

We emphasize here that maintaining stoichiometry is the primary factor for maximizing T_c. When the stoichiometry improves, the attractive phonon interaction between electrons (electron-phonon interaction) will increase. Figure 6.2 shows how deviations from ideal stoichiometry affect T_c for various nitrides [4]. NbN has the highest T_c value (17.3 K) [5], which was the first MX superconductor discovered in 1941. T_c decreased when vacancies or anti-site defects increased. From Fig. 6.2, they found that the ideal 1:1 stoichiometry is important for obtaining a higher T_c value. Due to lattice instabilities in these B-1 type compounds (MN and MC), they are easy to decompose with anion vacancies, which reduces T_c and can be explained with Matthias's rule.

Substitution at anion sites has been studied, and $NbN_{0.7}C_{0.3}$ has the highest T_c value (17.8 K) among alloys between carbides and nitrides [6, 7], where the anion site defects are considered to disappear. The details of other alloys are summarized in Ref. [8].

Table 6.1 lists the T_c values in B1-type superconductors MX (X: C or N). Maintaining the fcc sub-lattice structure in B1-type superconductors is important for obtaining a compound with a higher T_c value. For example, rapid quenching from the melt is crucially important [12] for maintaining the B1-type structure.

WC normally has a hexagonal structure (B_h) and is not superconducting down to 0.3 K. However, Willens and Buehler succeeded in obtaining a B1 phase WC by using the rapid-quenching technique, which exhibited superconductivity with $T_c = 10.0$ K [12]. The hexagonal structure of MoC has $T_c = 9.3$ K, but Willens and Buehler also succeeded in obtaining B1 phase MoC by rapid-quenching technique, which showed a higher T_c value of 14.3 K [12]. By rapid quenching from the melt, solid solutions with NaCl-type structure can be obtained for binaries among NbC, TaC, WC, and MoC. The T_c values in these binaries show that the density of states at the Fermi level is important and that stoichiometry is again the main factor for achieving a maximum T_c value.

Table 6.1 T_c of B1(NaCl)-type carbides (MC) and B1(NaCl)-type nitrides (MN)

Carbides	T_c [K]	Nitrides	T_c [K]
NbC	11.6	NbN	17.3[5, 9]
TaC	11.4[10]	MoN	13.0–14.8[11]
MoC	14.3[12, 13]	TaN	14.0[9]
WC	10.0[10, 12, 13]	ZrN	10.7[9]
TiC	3.4	VN	9.25[10]
RuC	2.0[14, 15]	TiN	5.5
HfC	0.25	HfN	8.8
ZrC	0.25	ThN	3.2
VC	<0.05	UN	5.6
ScC	<1.38	ScN	<1.38
YC	<1.38	YN	<1.40
Hex-MoC	9.3	RuN	∼12
		$NbC_{0.3}N_{0.7}$	17.8[6, 7]
		NbN-NbC	18.0[16]
		$(NbN)_{0.8}(TiC)_{0.2}$	18
		Hex-MoN	16.4

6.1.1.2 Density of States in MC and MN

As described above, the T_c values in transition-metal nitrides are higher than those of carbides in general. NbN has the highest T_c value among B1-type superconductors. These T_c values have been discussed in terms of the DOS at E_F. Here, we show some examples of the DOS in nitrides and carbides. The electronic band structures of NbC and NbN using full-potential linearized augmented plane wave method (FP-LAPW)are shown in Fig. 6.3 [17].

The DOS of the valence and conduction bands are characterized by two regions separated by a gap; the lower region is s character of the nonmetal atoms (C, N), with a very small contribution of the Nb-d component. In the second region, exactly in the first peak, we can see that the nonmetal-p density of states dominates on the two compounds, but the mixture of the $d(t_{2g})$ and $d(e_g)$ manifolds in this range of energy is considerably higher in NbC than in NbN. In the range between 0.85 Ry and E_F, the niobium d-component of the DOS dominates, and it can be seen that in this energy range, the t_{2g} manifold exceeds all other components. This t_{2g} charge can form dd_σ bonds between neighboring niobium atoms because the nonmetal p contributions to the DOS are small, so not the pd_π but the dd_σ bonds are most important.

From Fig. 6.3, they estimated the values of the DOS at Fermi energy. DOS of NbC is 9.8527 states/Ry unit cell, and this value is in good agreement with the experimental values reported by Toth [8] from electronic specific heat measurement (9.79 states/Ry unit cell). Furthermore, this value is much better than that obtained by Schwarz [18] using the APW method (8.5 states/Ry unit cell). In the case of NbN, the value is 11.025 states/Ry unit cell, which is close to the experimental

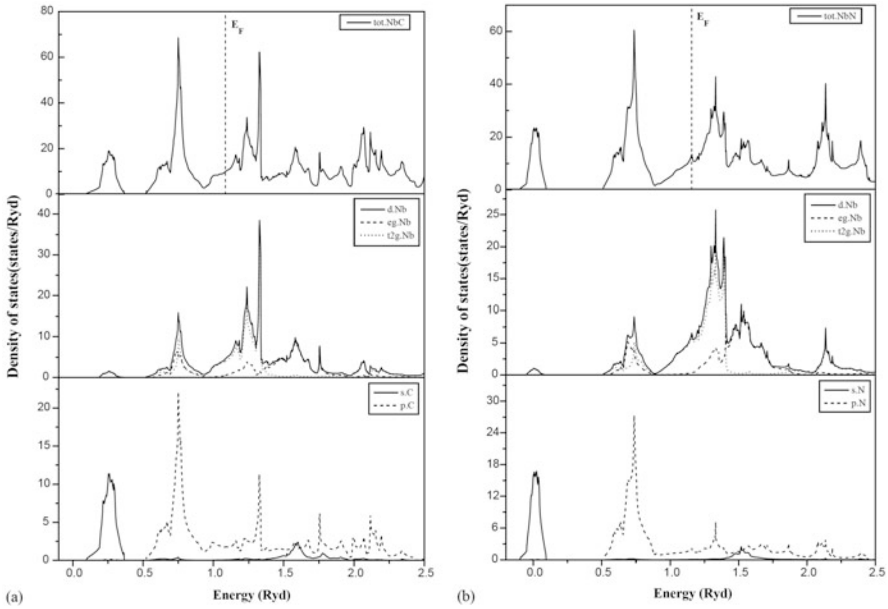

Fig. 6.3 The density of states (DOS) obtained by the LDA calculation of (**a**) NbC and (**b**) NbN (in states per Ry unit cell) [17]

value (11.4288 states/Ry unit cell) [8]. From these values, the DOS at Fermi energy for NbN is larger than that for NbC, which causes a higher DOS and a higher T_c value.

Figure 6.4 shows the DOS in (a) MoC, (b) $MoC_{0.75}N_{0.25}$, and (c) MoN [19]. The DOS in MoC consists of three primary regions: I, a region of carbon s states with a small degree of hybridized d states from molybdenum; II, a region of hybridized carbon p states and molybdenum d states; and III, predominately molybdenum d states with a small degree of hybridized p states from carbon. Region II can be considered as the bonding part of the Mo-d nonmetal-p hybridization couples, while region III is the corresponding antibonding part with d-d direct bonds existing between neighboring Mo atoms.

As seen in the case of MoC and MoN, the DOS at E_F is purer d in MoN than in MoC. Hence, the DOS in nitride at E_F is also higher than that of carbide in Mo compounds, which is the reason why the T_c value in nitride is higher than that of carbide. Based on BCS theory, a material with higher DOS at E_F has a higher T_c value, but MoC and MoN are exceptions. Pickett et al. [20] and Ihara et al. [21] expected T_c to be about 29 K for MoN, but a lower T_c was observed experimentally for this B1 structure in MoN films; the superconducting transition temperature was found to be only around 3 K [22]. However, the character of nitrides is sensitive to the composition ratio and preparation method.

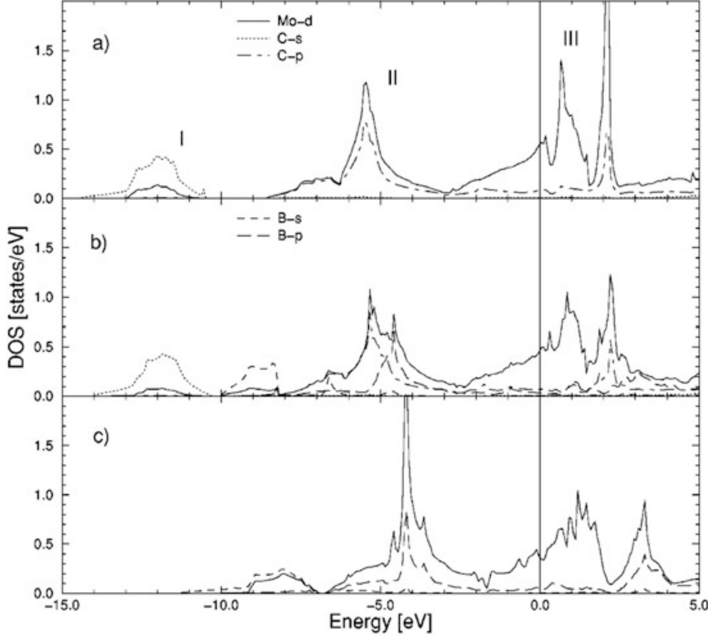

Fig. 6.4 Density of states in MoC substituted with nitrogen: (**a**) MoC, (**b**) $MoC_{0.75}N_{0.25}$, and (**c**) MoN [19]

6.1.1.3 Phonon Softening on MC and MN

Figure 6.5a shows the transverse acoustic (TA) phonon dispersion of ZrC ($T_c < 1$ K), $NbC_{0.98}$ ($T_c = 11$ K), $Nb(N_{0.5}C_{0.5})_{0.95}$, and $Nb(N_{0.8}C_{0.2})_{0.93}$ ($T_c = 17.5$ K) along the {111} direction of the zone boundary at the L point. As the proportion of N increases, the phonon energy decreases near the L point, and phonon softening is larger for a higher T_c value. According to BCS theory, T_c can be calculated using Eq. (6.1):

$$T_c = 1.14\ \Theta_D \exp\left[-\left(\lambda - \mu\right)^{-1}\right], \tag{6.1}$$

where Θ_D is the Debye temperature, μ is the average Coulomb repulsion energy, $\lambda = N(E_F)\overline{V}$ is the electron-phonon interaction parameter, $N(E_F)$ is the density of states at the Fermi energy, and $\overline{V}$ is the average electron-phonon interaction. The Debye temperature $\theta_D = \hbar\omega_D/k_B$, where $\hbar\omega_D$ is an average phonon energy. To estimate T_c from Eq. (6.1), variations in θ_D, $N(E_F)$, and λ as a function of the ratio of C to N are shown in Fig. (6.5b). $N(E_F)$ hardly changes if the ratio of C to N is changed. T_c has a maximum when the proportion of N is 70% ($NbN_{0.7}C_{0.3}$), but θ_D has a minimum value at this ratio, as shown in Fig. (6.5b). It seems to be incompatible with the formula (6.1). However, phonon softening in $NbN_{0.7}C_{0.3}$ is maximized, and the electron-phonon interaction $\overline{V}$ is maximized at this ratio. This $\overline{V}$ value maximizes λ, as shown in Fig. (6.5b).

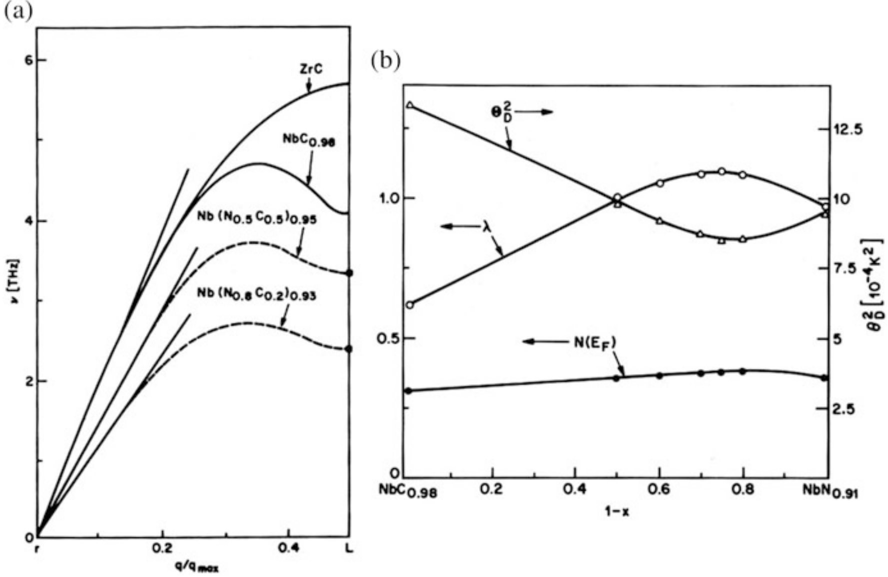

Fig. 6.5 (**a**) Dispersion of TA phonons along the {111} direction for alloys of $NbC_{0.98}$ with $NbN_{0.91}$. (**b**) Variations of θ_D, microscopic electronic parameters λ, $N(E_F)$ with nitrogen concentration [23]

In Eq. (6.1), $\overline{V}$ is on the shoulder of the exponent. Hence, its contribution is much larger than that of θ_D.

As described above, T_c varies depending on whether the composition of the superconductor is MC or MN, and it depends on the stoichiometric ratio, DOS, and electron-phonon interaction. Although the study of B1-type superconductors has a long history, their practical application has been delayed because these materials are difficult to process. However, recent advances in thin-film fabrication processes have accelerated applications in superconducting wires [24] and Josephson devices [25–28].

6.1.2 SiC

6.1.2.1 Introduction

The possibility of superconductivity in a wide-gap semiconductor has been theoretically suggested by Gurevich et al. [29] and Cohen [30]. In 2004, Ekimov et al. discovered superconductivity in boron-doped diamond [31], and, subsequently, an enhanced T_c value in the film as high as 11 K has renewed interest in low-carrier-density superconductivity in doped semiconductors [32]. High T_c was suggested in boron-doped diamond, where б-bonds transform into bands by carrier doping to a semiconductor [33]. Stimulated by this discovery, Z. A. Ren et al. discovered

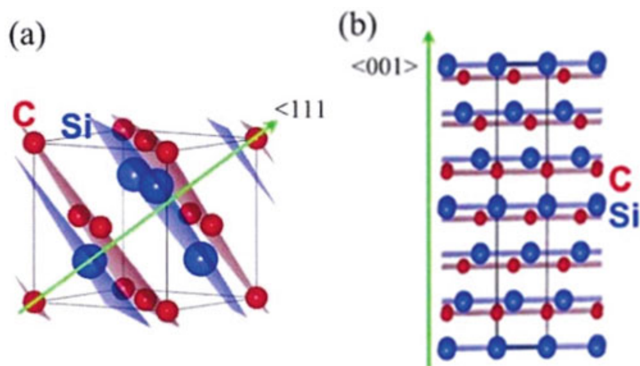

Fig. 6.6 Unit cell of (**a**) cubic 3C-SiC and (**b**) hexagonal 6H-SiC [36]

superconductivity in boron-doped SiC with a critical transition temperature T_c~1.4 K [34]. Undoped SiC is a wide-gap semiconductor with a band gap of 2~3 eV, which makes it ideal for uses in power devices [35]. SiC basically consists of tetrahedrally bonded silicon and carbon atoms. However, SiC has many stable prototypes, including cubic zinc-blende, and hexagonal and rhombohedral polytypes.

6.1.2.2 Crystal Structure and Its Physical Properties

Figure 6.6 shows the cubic zinc-blende structure labeled 3C-SiC or β-SiC, in which Si and C occupy ordered sites in a diamond framework and hexagonal (nH-SiC) and rhombohedral polytypes (nR-SiC), consisting of C and Si layers stacked in a primitive unit cell. Lightly doped SiC has been studied for nitrogen (N), phosphorus (P), boron (B), and aluminum (Al) used as donors or acceptors. Recently, a metallic transition was observed in n-type nitrogen-doped 4H-SiC with carrier concentration above 10^{19} cm^{-3} but without a report of superconductivity [37]. Z. A. Ren et al. reported superconductivity from resistivity and magnetization measurements in p-type boron-doped SiC with a carrier concentration 1~2 × 10^{21} cm^{-3} and a critical transition temperature T_c~1.4 K [34].

Figure 6.7 shows the magnetic susceptibility of B-doped 3C-SiC and 6H-SiC under a magnetic field of 1 Oe (zero-field cooling process), suggesting the occurrence of superconductivity with T_c~1.5 K (3C-SiC:B) and T_c~1.4 K (6H-SiC:B) with a superconducting volume fraction almost 100% due to the shielding effect [36].

From typical powder X-ray diffraction (PXRD) patterns, the main phases in each sample were indexed as cubic zinc-blende 3C-SiC and hexagonal 6H-SiC phases, as shown in Fig. 6.8. In addition, we found some unreacted Si, but no boron peaks were detected [38]. The refined lattice parameters of the 3C-SiC and 6H-SiC phases

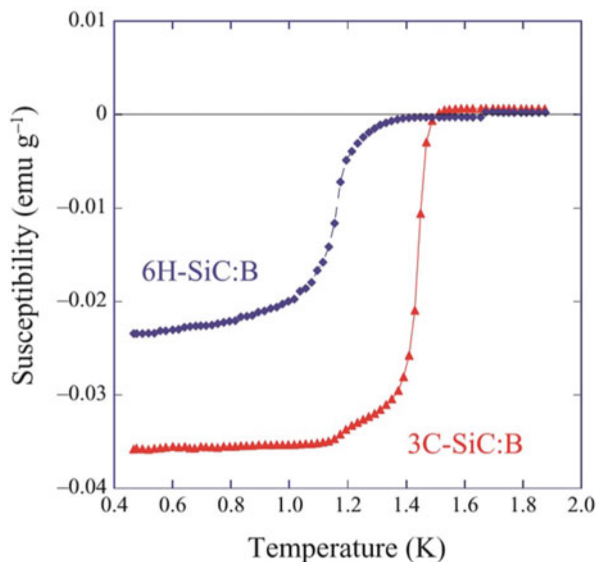

Fig. 6.7 Temperature dependence of susceptibility in B-doped 3C-SiC (3C-SiC:B) and B-doped 6H-SiC (6H-SiC:B) [36]

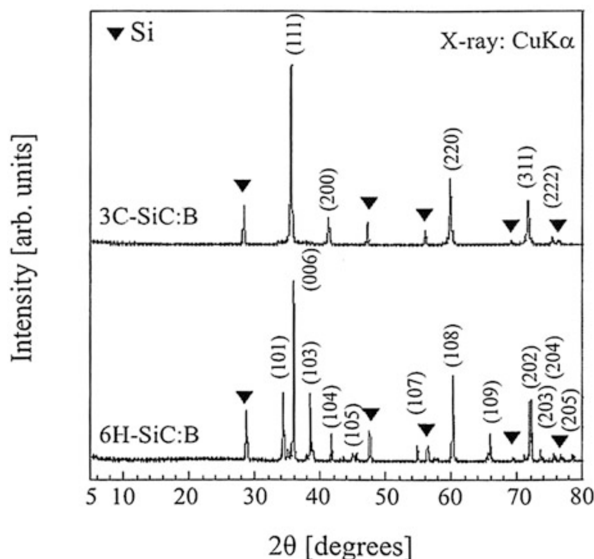

Fig. 6.8 Powder X-ray diffraction patterns in B-doped 3C-SiC (3C-SiC:B) and B-doped 6H-SiC (6H-SiC:B)

show minor changes between 0.1% and ~0.2%. Those small changes in the lattice parameters suggest that boron substitutes at carbon sites in these samples.

Figure 6.9 shows the electrical resistivities of 3C-SiC:B and 6H-SiC:B [36]. The inset magnifies the region near T_c. Both samples exhibit metallic conductivity, reflecting the high carrier doping level. B-doped 3C-SiC exhibits a much smaller resistivity that is almost linear with temperature. However, B-doped 6H-SiC shows a broad feature near 150 K, suggesting the weak localization of carriers. The inset

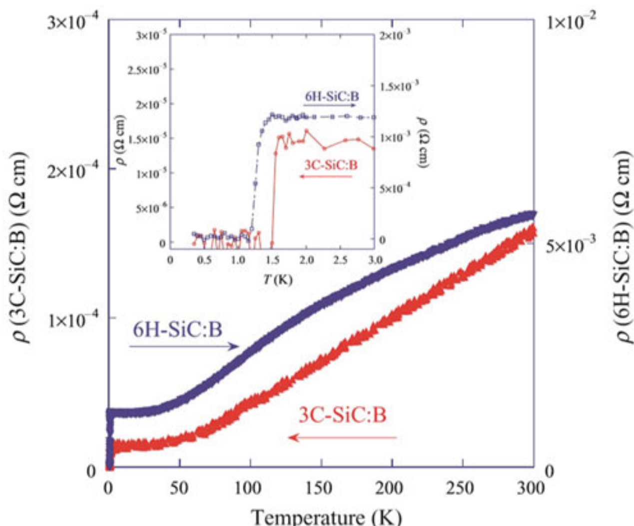

Fig. 6.9 Temperature dependence of resistivity in B-doped 3C-SiC (3C-SiC:B) and B-doped 6H-SiC (6H-SiC:B). The inset magnifies the region near T_c [36]

in Fig. 6.9 shows an expanded view at low temperature. Different T_c values can be seen in 6H-SiC and 3C-SiC, which agrees well with the data obtained from the susceptibility measurements. After the experimental discovery of superconductivity in SiC, J Noffsinger et al. [39] investigated the origin of superconductivity in boron-doped SiC using a first-principles approach by considering a large set of structural models. They found that superconductivity arises from conventional phonon-mediated paring. From their calculation, the transition temperature (T_c) ranges from 1.1 K for a B concentration of 3.7% to 6.3 K for 12.5%. In a SiC superconductor, acoustic phonons and Fermi surface nesting play an important role, in contrast to the related B-doped Si and diamond system.

6.1.2.3 Phase Diagram of SiC:B

To determine the phase diagram in the magnetic field-temperature (H-T) plane for both samples, the resistivities were measured while changing the temperature for fixed magnetic field strengths (T-scan) and by changing the magnetic field strength at fixed temperatures (H-scan). During the T-scan, only one transition was observed at zero applied magnetic field, while a large supercooling effect was observed in both samples at finite field strengths. Hysteresis was also observed during the H-scan under 130 Oe in B-doped 3C-SiC and 100 Oe in B-doped 6H-SiC. The (i) in-field hysteresis, (ii) absence of hysteresis at zero applied field, and (iii) very small value of the critical field provide strong evidence for type-I superconductivity both in SiC polytypes.

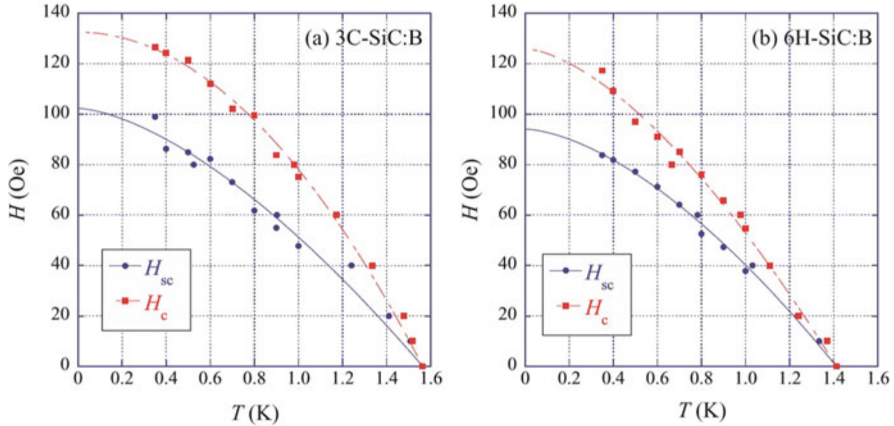

Fig. 6.10 *H-T* phase diagram for (**a**) B-doped 3C-SiC(3C-SiC:B) and (**b**) B-doped 6H-SiC (6H-SiC:B), determined from the onset of superconductivity during a *T*-scan and *H*-scan of resistivity [36]

The *H-T* phase diagram determined from the resistivity data (*T*-scan and *H*-scan) is shown in Fig. 6.10. Applying the conventional formula $H_c(T) = H_c(0)[1-(T/T_c(0))^{\alpha}]$, the thermodynamic critical field $H_c(0)$ is estimated to be 132 ± 3 Oe with α ~2.0 for B-doped 3C-SiC and 125 ± 5 Oe with α~ 1.6 for B-doped 6H-SiC during the warming process. The same procedure applied to the cooling process yields α~ 1.6 in both SiC polytypes. This transition is identified as the upper limit of the intrinsic supercooling limit. The corresponding transition fields are denoted H_{sc} (the subscript "sc" stands for supercooling) with an estimated $H_{sc}(0) = 102 \pm 6$ Oe for B-doped 3C-SiC and 94 ± 3 Oe for B-doped 6H-SiC.

Applying the Ginzburg-Landau (GL) theory of type-I superconductivity to these data, one can estimate an upper limit of the GL parameter κ from the difference of the critical fields obtained from a field-cooling run and a subsequent warming run [40, 41], where $\kappa(0) \leq H_{sc}(0)/\left(1.695 \times \sqrt{2}H_c(0)\right)$. This formula yields κ~ 0.32 for B-doped 3C-SiC and 0.31 for B-doped 6H-SiC, in agreement with the analysis of the Hall effect and specific heat data [38, 42]. This supports the type-I nature of superconductivity in B-doped SiC. Note that the value of κ is less than 0.41, which is required in a model based on supercooling instead of superheating [41, 43, 44].

6.1.2.4 Physical Properties of SiC:Aℓ

After the discovery of superconductivity in boron-doped SiC, Muranaka et al. successfully observed superconductivity in Al-doped SiC [36]. From a typical PXRD pattern (not shown in this article), three phases were identified, including 3C-SiC, unreacted Si, and unreacted Al. The main phase in the 3C-SiC:Al sample is indexed as cubic zinc-blende 3C-SiC. For the main phase in 3C-SiC, the refined

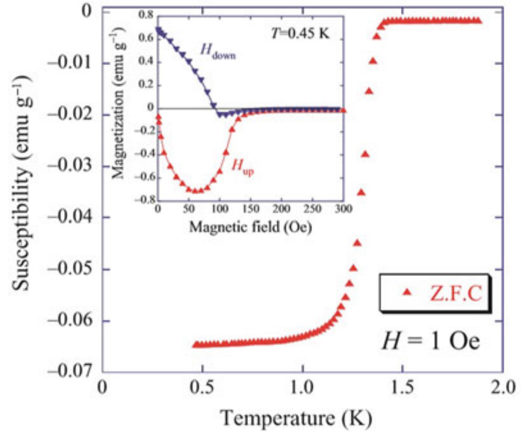

Fig. 6.11 Temperature dependence of DC magnetic susceptibility in SiC:Al. The inset shows the magnetization versus magnetic field at $T = 0.45$ K [36]

lattice parameter a increased after sintering by ~0.1% from 4.338 to 4.342. Minute changes in the lattice parameters suggest that Al substitutes Si sites in 3C-SiC. We expect that the presence of liquid Si facilitates Al diffusion due to much faster mass transport compared to solid sintering, thus enhancing the Al substitution efficiency.

EPMA analysis with area scans (within $50 \times 50\ \mu m^2$) at various positions only detected Si, C, and Al. From Hall measurements at room temperature, the effective hole concentration was found to be $n \sim (3.86\text{–}7.06) \times 10^{20}\ cm^{-3}$.

As shown in Fig. 6.11, the magnetic susceptibility of SiC:Al in a magnetic field of 1 Oe (zero-field cooling process) significantly decreases at 1.4 K, suggesting the occurrence of superconductivity. The estimated superconducting volume fraction at 0.45 K is almost 100% due to the shielding effect. The inset of Fig. 6.11 shows a magnetization vs magnetic field (M-H) curve, which shows typical type-II superconducting behavior. These M-H curves and the value of T_c exclude the possibility that superconductivity is caused by an impurity, such as Al ($T_c = 1.175$ K). From the M-H curves, we estimate the lower critical field Hc_1 is 53 Oe.

In Fig. 6.12, the resistivity of 3C-SiC:Al shows metallic behavior at room temperature, reflecting the high level of carrier doping. There is a sharp drop in resistivity at 1.5 K and zero resistivity below 1.35 K (inset in Fig. 6.12).

The phase diagram in the magnetic field-temperature (H-T) plane was deduced from resistivity measurements (figure not shown). Neither hysteresis nor supercooling behavior was observed in a T-scan or H-scan, which is consistent with the transition to superconductivity under an applied magnetic field being of second order. Thus, type-II superconductivity occurs in 3C-SiC:Al, in contrast with type-I superconductivity in 3C-SiS:B.

Figure 6.13 shows the T_c value and upper critical field H_{c2} determined from the onset of resistivity, as well as the irreversibility field Hirr determined from zero resistivity. Applying the conventional formula $H_{c2}(T) = H_{c2}(0)\cdot[1\text{-}(T/T_c)^2]$,

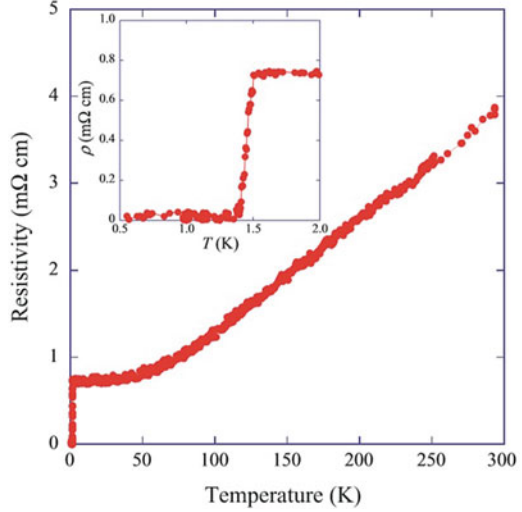

Fig. 6.12 Temperature dependence of resistivity in 3C-SiC:Al. The inset shows a magnified region near T_c [36]

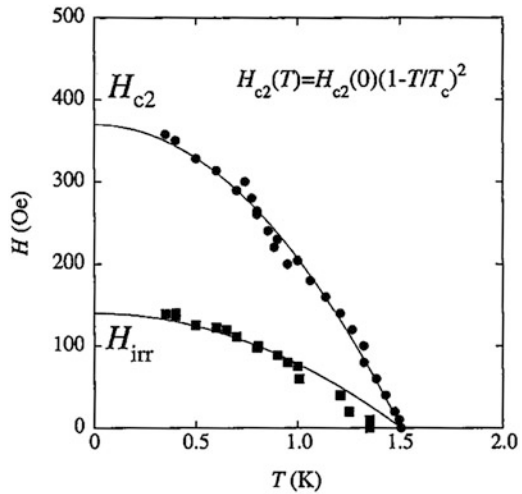

Fig. 6.13 Temperature dependence of the upper critical field H_{c2} and the irreversibility field H_{irr} in 3C-SiC:Al [36]

we plot the T-dependence of $H_2(T)$ with $H_{c2}(0) = 370 \pm 3$ Oe and H_{irr}(T) with $H_{irr}(0) = 140 \pm$ Oe.

Table 6.2 lists the specific heat coefficients γ_n [42], basic normal-state parameters, Fermi wave number k_F, effective mass m^*, Fermi velocity υ_F, mean free path ℓ, the superconducting state parameter, penetration depth λ, coherence length ξ, and the Ginzburg-Landau parameter κ_{GL}. These parameters were estimated following the process described in [38]. The parameters in 3C-SiC:B, C(Diamond):B, and Si:B are included for comparison. A value of $\kappa_{GL}{\sim}1.8$ provides evidence for type-II superconductivity. Our results also imply that 3C-SiC:Al is a dirty-limit superconductor because ξ (0) $\gg$ l, similar to SiC:B.

Table 6.2 Parameters of the studied SiC:Al, SiC:B, C(Diamond):B, and Si:B samples [36] and original references therein

	SiC:Al	SiC:B	C:B	Si:B
n (cm^{-3})	7.06×10^{20}	1.91×10^{21}	1.80×10^{21}	2.80×10^{21}
γ_n (mJ molK^{-2})	0.35	0.294	0.113	–
ρ_0 (mΩ cm)	0.746	0.06	2.5	0.13
RRR	5.3	10.0	0.9	1.2
T_c (onset) (K)	1.5	1.45	4.50	0.35
$H_c(0)$ (Oe)	–	115	–	–
$H_{sc}(0)$ (Oe)	–	80	–	–
$H_{c2}(0)$ (Oe)	370	–	4.2×10^4	4000
k_F (nm^{-1})	2.8	3.8	3.8	–
m^* (m_{e1})	2.0	1.2	1.7	–
υ_F(m s^{-1})	1.6×10^5	3.8×10^5	–	–
l (nm)	2.2	14	0.34	–
$\xi(0)$ (nm)	148	360	80(9)	(20)
$\lambda(0)$ (nm)	281	130	160	–
κ_{GL}	1.8	0.35	2(18)	–

6.1.2.5 Summary

The report reviews boron-doped SiC (3C- and 6H-SiC polytypes) and Al-doped 3C-SiC synthesized by a substitutional sintering method and characterization of bulk superconductivity in those materials. Both 3C-SiC:B and 6H-SiC:B reveal type-I superconductivity at $T_c = 1.5$ K. However, Al-doped 3C-SiC (3C-SiC:Al) reveals type-II superconductivity at $T_c = 1.4$ K. From the results, superconductivity in carrier-doped semiconductors can be interpreted in terms of the depth of acceptor levels in p-type semiconductors. One can only speculate on the physical reasons behind this difference. One possibility could be a much different Fermi velocity υ_F in the case of SiC:B due to a different shape of the Fermi surface. Further experimental and theoretical work is required to resolve this question.

6.2 MC_2 Compounds

6.2.1 Introduction

The crystal structures of dicarbides MC_2 are primarily categorized into the well-known tetragonal CaC_2-type structure (*I4/mmm*, Fig. 6.14a), cubic high-temperature modified CaC_2 structure (*Fm-3 m*, Fig. 6.14b), low-temperature modified CaC_2 (*C2/c*, Fig. 6.14c) crystallized in a ThC_2-type structure, and metastable modified structure CaC_2(*C2/m*) [45, 46]. Superconductivity in MC_2 such as YC_2 ($T_c = 3.88$ ~4.02 K) [47, 48] has tetragonal CaC_2-type structure that can be considered as a

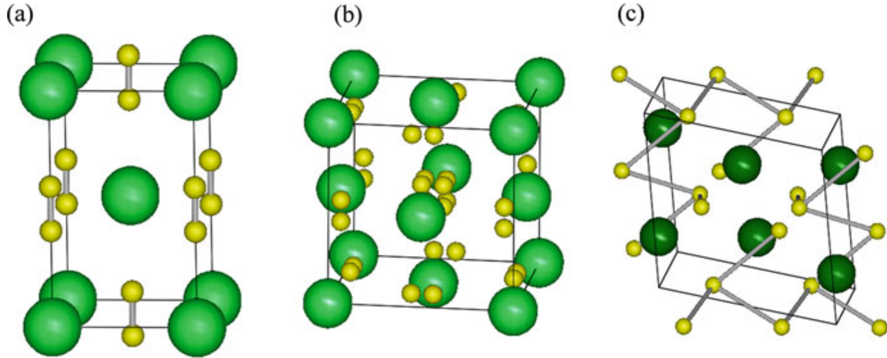

Fig. 6.14 Crystal structure of (**a**) CaC_2-type (tetragonal, *I4/mmm*), (**b**) KCN-type (cubic, *Fm-3 m*), and (**c**) ThC_2-type (monoclinic, *C2/c*) MC_2 superconductors. Yellow spheres correspond to C atoms

tetragonally distorted NaCl-type arrangement in which lanthanide atoms occupy Na sites with characteristic C_2 dimers on the Cl sites. As the cation varies from La to Lu in MC_2, the lattice constant decreases with increasing atomic number. The unit cell volume decreases, which is consistent with the lanthanide contraction. Up to now, superconductivity in dicarbides has been found in YC_2, LaC_2 ($T_c = 1.61{\sim}1.8$ K) [49–51], and LuC_2 ($T_c = 3.33$ K) [49].

In this review, we introduce experimental and theoretical results regarding the physical properties of MC_2 and superconductivity in MC_2, which can be explained within the BCS framework.

6.2.2 *Physical Properties of YC_2*

Giorgi et al. reported that YC_2 (tetragonal CaC_2 type) was found to be superconducting at 3.88 K [47]. However, Gulden et al. characterized a superconducting state of YC_2 and found that YC_2 is a superconductor with $T_c = 4.02$ K [48], which is slightly higher than the previous reported experimental value of 3.88 K. This is due to local carbon defects induced by heating conditions. Rapid cooling leads to a reduction of T_c from 4.02 K to 2.85 K, and the c-axis decreases from 6.1786 Å to 6.1151 Å. This c-axis reduction, being strongly coupled to T_c, comes from local carbon defects, suggesting that C_2 dimers may play a key role in MC_2 superconductivity. Moreover, Gulden et al. examined the substitution effect in YC_2. Figure 6.15a shows how T_c varies with C defects and Y site substitution in YC_2. It was found that partial substitution with Ca and Th reduces T_c. This substitution effect is in contrast to the case of Th-doped Y_2C_3, where Th substitution leads to a significant increase in T_c [52]. Substitution of magnetic rare-earth atoms like Gd induces a dramatic decrease in T_c.

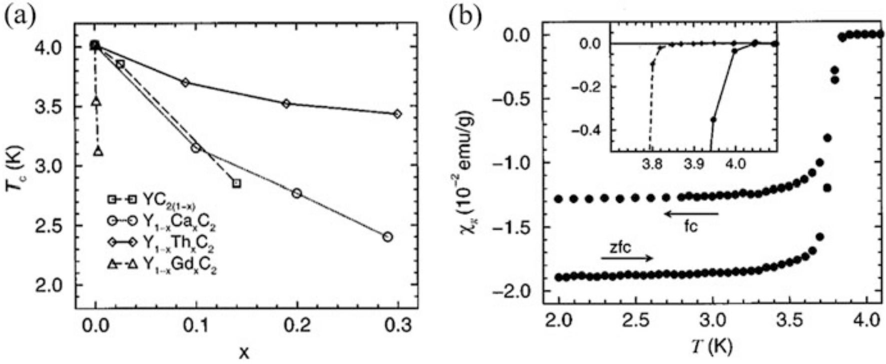

Fig. 6.15 (**a**) T_c variation with C defects and Gd, Th, or Ca substitution of the cation Y. (**b**) Magnetic susceptibility of $YC_{1.95}$. The inset shows the onset of magnetic susceptibility of YC_2 (solid line) and $Y^{13}C_2$ (dotted line) on an enlarged scale [48]

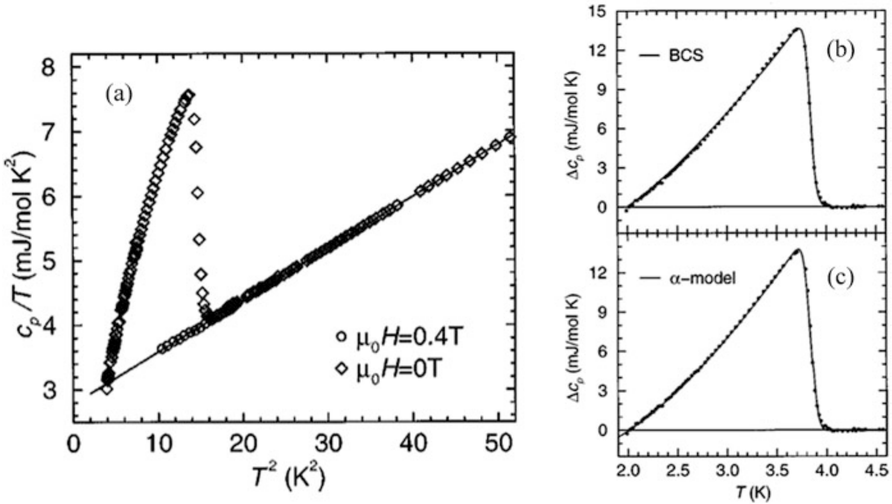

Fig. 6.16 (**a**) Specific heat capacity C_p/T vs T^2 of YC_2. (**b**), (**c**) Difference ΔC_p of specific heats in YC_2 in the superconducting and the normal states. Fits of the BCS model and the α-model are given by the full lines [48]

In order to understand the mechanism governing superconductivity, Gulden et al. examined the isotope effect of superconductivity in YC_2. The $^{12}C/^{13}C$ isotope effect on T_c in YC_2 amounts to $\Delta T_c = -0.17$ K (inset in Fig. 6.15b). This corresponds to an isotope exponent of $\alpha = 0.51$, which agrees well with the prediction of weak coupling from BCS theory.

Specific heat measurements in YC_2 can also be explained by weak coupling from BCS theory. Figure 6.16a shows the specific heat in YC_2. The specific heat of YC_2 can be well described by the following formula:

$$C = C_{el} + C_{ph} = \gamma T + \beta T^3 \tag{6.2}$$

where γ is the electronic heat capacity coefficient and β is the lattice heat capacity coefficient. γ and the Debye temperature Θ_D (estimated from $\beta = N(12/5)\pi^4 R\Theta_D{}^{-3}$) of YC_2 were 2.782(5) mJ/molK^2 and 418(1) K, respectively. Figure 6.16b shows a fit of ΔC_p data to the BCS model.

Although the BCS model can capture the features of ΔC_p, the model predicts low values in the range from 3.6 K to 3.8 K and high values below $T = 3.6$ K. A model for the thermodynamic properties of a superconductor with BCS-like Cooper pairing and variable electron-phonon coupling strength was suggested by Padamsee et al. [53]. In this model, the only adjustable parameter is the value of the ratio $\alpha = \Delta(0)/k_B T_c$ (α-model). Figure 6.16c shows a fit of ΔC_p data to the α-model. This model can describe the heat capacity results more precisely, and the value of α was 1.82(1), which is very close to the BCS weak-coupling limit of $\alpha_{BCS} = 1.764$.

6.2.3 Physical Properties of LaC_2

Babizhetskyy et al. investigated the physical properties of LaC_2 by powder X-ray and neutron diffraction, magnetic susceptibility, and heat capacity measurements [51]. Neutron powder diffraction patterns were refined from the tetragonal CaC_2 type structure and did not show any broadening or splitting of reflections at 4 K, indicating that a structural transition from tetragonal CaC_2 type to monoclinic ThC_2 type can be excluded.

Figure 6.17 shows AC magnetic susceptibility measurements in two samples, one prepared with excess carbon (starting composition $La_{0.28}C_{0.72}$, sample No. 109) and the other sample with starting composition $La_{0.35}C_{0.65}$ (C poor, sample No. 112). Whereas sample No. 109 shows superconductivity at 1.695 K, T_c of sample No. 112 is higher (1.80 K) than that of sample No. 109. Interestingly, both onset transition

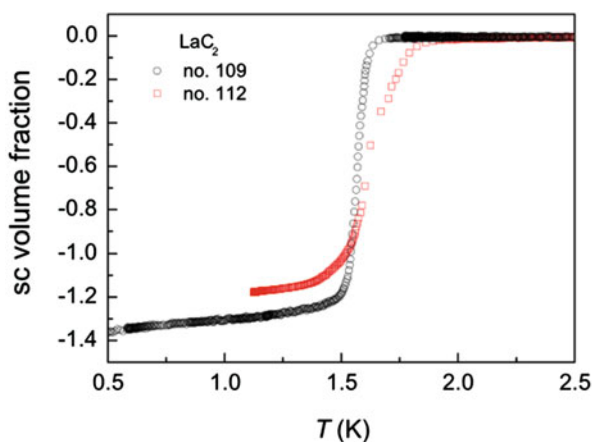

Fig. 6.17 AC magnetic susceptibility of LaC_2 (samples No. 109 and 112) [51]

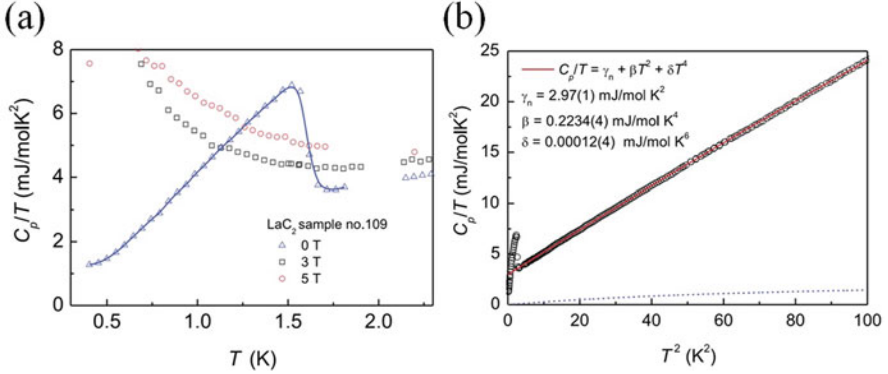

Fig. 6.18 (**a**) Heat capacity in LaC_2 (sample No. 109) measured without and with an applied magnetic field. The solid line shows a fit of the data to the α-model. (**b**) C_p/T vs T^2 in LaC_2. The red solid line represents a fit of the heat capacity data in the normal state ($T > 3$ K) to a polynomial in T^2 [51]

Table 6.3 Comparison of T_c, the Sommerfeld term in the superconducting and normal states, γ_{sc}, γ_n, and the Debye temperature in YC_2 and LaC_2 [51]

Sample	T_c [K]	γ_n(mJ mol^{-1} K^{-2})	γ_{sc}(mJ mol^{-1} K^{-2})	$\Theta_D(0)$ (K)	λ
YC_2	3.83(1)	2.78	2.79	418	0.55
LaC_2(no.109)	1.61(2)	2.97(1)	2.41(5)	296(2)	0.49(1)

temperatures are higher than the values in a previous report ($T_c = 1.61$ K) [49, 50]. From a structural perspective, the C-C distance in sample No. 109 is noticeably shorter than that of sample No. 112. This result suggests that superconductivity in the MC_2 system is coupled to the C-C distance.

Figure 6.18a shows the heat capacity in LaC_2 (sample No. 109) measured without and with applying a magnetic field. The solid line in Fig. 6.18a shows a fit of the data to the α-model. The estimated value of $2\Delta(0)/k_B T_c = 3.64$ agrees well with the value expected from weak coupling in BCS theory. Above T_c, the specific heat of LaC_2 can be well described by Eq. (6.1) (Fig. 6.18b), and the values of γ and Θ_D in LaC_2 were calculated to be 2.97(1) mJ/molK^2 and 296(2) K, respectively. Based on the above parameters, Babizhetskyy et al. discussed the T_c values of LaC_2 and YC_2 within the framework of McMillan theory [54]. McMillan's equation for T_c is

$$T_c = \frac{\Theta_D}{1.45} \exp\left(-\frac{1.04\,(1+\lambda)}{\lambda - \mu^*\,(1+0.62\lambda)}\right) \tag{6.3}$$

where μ^* is the effective Coulomb repulsion. All parameters obtained from this equation are summarized in Table 6.3. The values of Θ_D and λ in LaC_2 are smaller than those in YC_2. These smaller Θ_D and λ values probably affect the suppression of T_c in LaC_2.

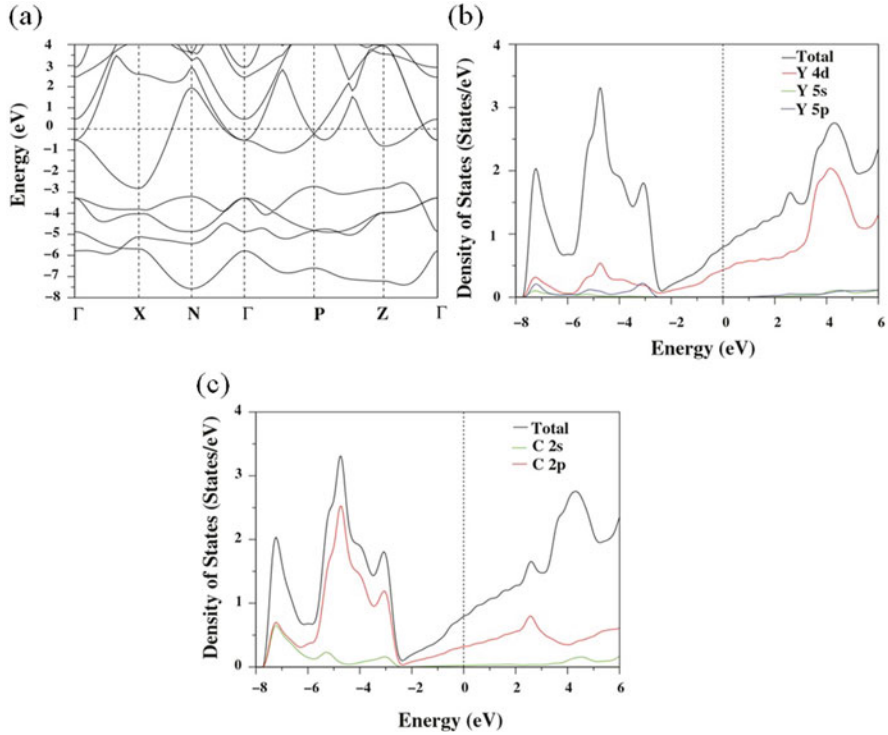

Fig. 6.19 (**a**) The electronic band structure for YC_2 along selected symmetry lines in the body-centered tetragonal Brillouin zone. Zero energy corresponds to the Fermi level. (**b**), (**c**) Total and partial eDOS curves [55]

6.2.4 Theoretical Calculation of Band Structure and Phonon Dispersion in YC_2 and LaC_2

From the experimental results of both materials, phonons probably play the role of superconductivity in this MC_2 system. In this section, we introduce a theoretical study of the electronic band structure and phonon dispersion in YC_2 and LaC_2 using the plane-wave pseudopotential method and density functional theory [55].

Figures 6.19 and 6.20 show the electronic band structures and eDOS in YC_2 and LaC_2, respectively. In both materials, the Fermi level is crossed by at least one electronic band, resulting in metallic behavior. In the case of YC_2, the band close to the Fermi level arises from Y 4*d* and C 2*p* states. Thus, hybridization between Y 4*d* and C 2*p* states occurs at energies ranging from −2 eV to the Fermi level. Contributions from $N(E_F)$ from the Y 4*d* and C 2*p* states are approximately 55% and 42%, respectively. This result indicates that the chemical and physical properties of YC_2 are dominated by the Y 4*d* and C 2*p* states. In the case of LaC_2, La 5*d* and C

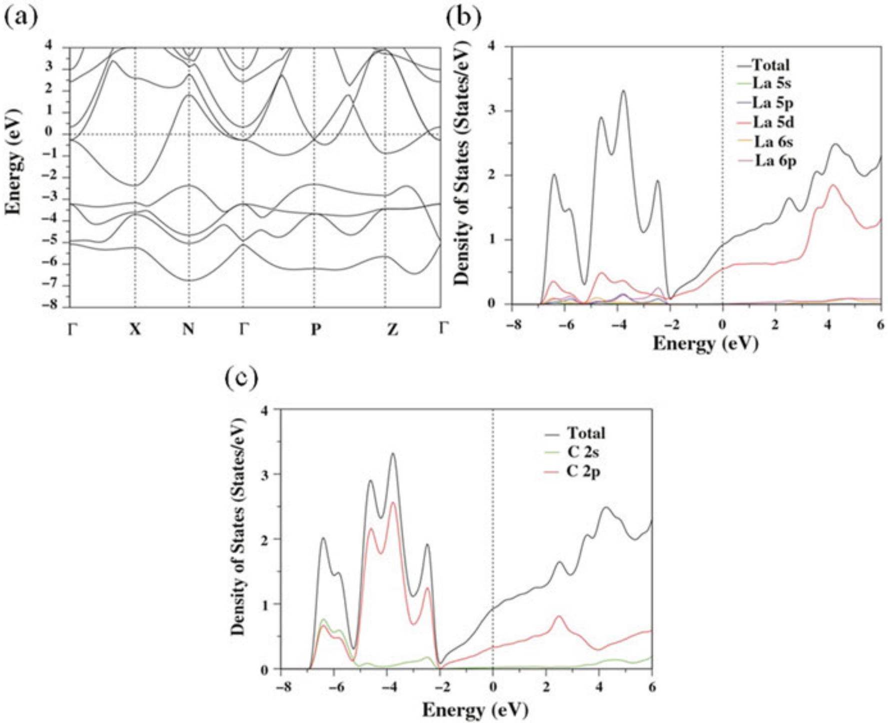

Fig. 6.20 (**a**) The electronic band structure for LaC_2 along selected symmetry lines in the body-centered tetragonal Brillouin zone. Zero energy corresponds to the Fermi level. (**b**), (**c**) Total and partial eDOS curves [55]

2*p* states also affect the DOS at the Fermi level, and contributions of $N(E_F)$ from the La 5*d* and C 2*p* states are approximately 61% and 38%, respectively.

Figure 6.21 shows the phonon dispersion along some symmetry directions in YC_2 and LaC_2. In the case of YC_2, the Y-related acoustic phonon branches can be seen in the low-frequency region (LFR) from 0 to 5.2 THz. C atoms also contribute to this region. Thus, Y-C hybridization can be seen. In the intermediate-frequency region (IFR) between 9.3 and 13.7 THz, vibration of C atoms is the primary contributor to phonon dispersion. The high-frequency region (HFR) from 46.4 to 48.9 is dominated by vibration of C atoms due to the C-C bond stretching. The phonon dispersion of YC_2 is very similar to that of LaC_2.

In order to analyze the strength of electron-phonon coupling in both materials, the electron-phonon coupling parameter λ was calculated from the Eliashberg spectral function ($\alpha^2 F(\omega)$). λ in YC_2 and LaC_2 was calculated to be 0.55 and 0.54, respectively. λ in YC_2 and LaC_2 is much lower than the value in strong electron-phonon coupling materials such as MgB_2 ($\lambda = 0.7 \sim 0.9$) [56, 57]. TüTüncü et al. further analyzed the contribution of LFR, IFR, and HFR phonons to the electron-phonon coupling parameter λ. They found that the largest contribution to

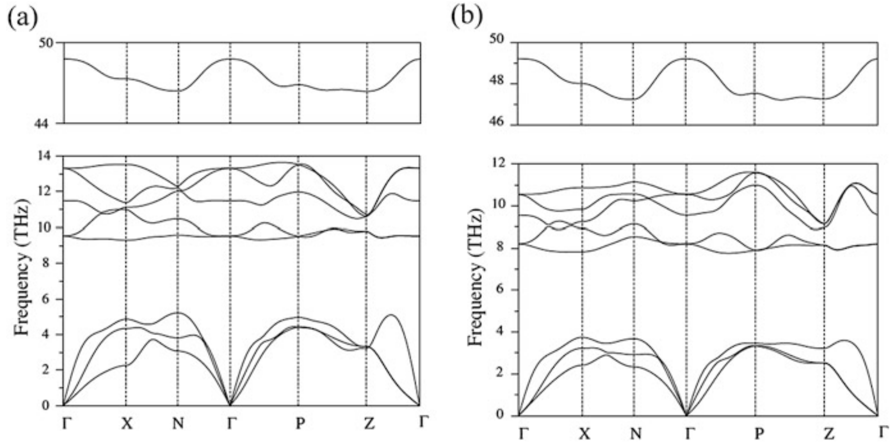

Fig. 6.21 The phonon dispersion relation for (**a**) YC_2 and (**b**) LaC_2 along some symmetry directions in the body-centered tetragonal Brillouin zone [55]

λ comes from Y (La) atoms from strong coupling between *d*-electrons and acoustic vibrations (in the LFR range). The intermediate frequency phonon modes also contribute considerably to λ. This result suggests that vibration of C atoms plays an important role in superconductivity.

6.2.5 Relationship Between the Superconducting Transition Temperature T_c and C-C Distance

The crystal structure of dicarbides MC_2 has a C_2 unit as a common structural feature, and several researchers point out the importance of the C-C distance [48, 58]. Figure 6.22a shows a schematic MO diagram of the $(C_2)^{2-}$ ion. In the case of insulating CaC_2, the structure contains $C \equiv C$ triple bonds (~1.20 Å). The antibonding π* states that lie near the Fermi level are empty in this case. On the other hand, LaC_2 has a longer C-C distance (1.303 Å), and the structure can be described as $M^{3+}(C_2)^{2-}(e^-)$. Conduction electrons occupy the antibonding π* states, resulting in metallic behavior in LaC_2. This idea suggests the possibility of tuning T_c by changing the C-C distance because the C-C distance is strongly coupled to the filling of antibonding π* states.

Based on the above discussion, Babizhetskyy et al. summarized the relationship between the C-C distance and T_c [51]. Figure 6.22b shows how the superconducting transition temperature T_c depends on the C-C distance in several carbide materials. Clearly, T_c is maximized when the C-C distance is close to ~1.30 Å. This result indicates a clear relationship between the C-C distance and superconductivity.

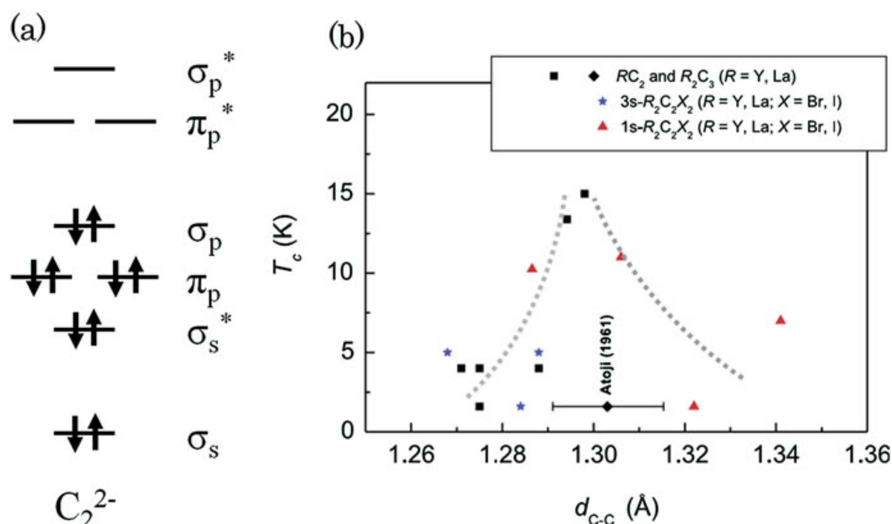

Fig. 6.22 (**a**) Schematic MO diagram of $(C_2)^{2-}$ ions [9]. (**b**) Superconducting transition temperature T_c as a function of the C-C distance in several carbide materials. The dotted lines guide the eye [51]

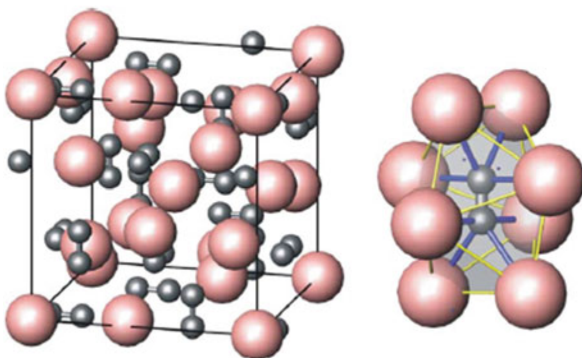

Fig. 6.23 Pu_2C_3-type cubic crystal structure of La_2C_3. Dicarbide anions occupy voids in bisphenoids in the metal substrate. Note: in contrast to the standard crystallographic setting, the origin of the indicated unit cell is shifted into a La position. (Left) Carbon dumbbell located in a La cage of eight atoms [59]

6.3 Ln_2C_3

6.3.1 *Rare-Earth Sesquicarbide Superconductors*

The majority of rare-earth sesquicarbides (La to Ho, except Pm) crystallize in a body-centered cubic D_{5c} (Pu_2C_3 type) structure [*I-43d*, space group 220, $Z = 8$ formula units in the cubic cell], as shown in Fig. 6.23. The structure is non-centrosymmetric. Due to the structure, exotic superconductivity is expected to

occur in this class of materials. A couple of rare-earth compounds and an actinide compound are known to exhibit superconductivity (La, Y, and Th_2C_3). Details are discussed in separate subsections.

Lanthanum sesquicarbide was found to be superconducting at 12 K in 1969 [60], with little study performed on the material due to the difficulties in handling the material. Isostructural doped-Y_2C_3 also shows superconductivity with T_c ranging from 6 to 12 K [61], which is expected to be closely related to the superconductivity in La_2C_3. The resemblance, however, has not been discussed due to the lack of basic information regarding superconductivity in both materials. In addition to superconductivity, rare-earth sesquicarbide shows insulating behaviors with several magnetic phases [62]. The sesquicarbides are synthesized using arc melting. Krupka et al. suggested that Y_2C_3 and other compounds can be prepared using high pressure and high temperature, yielding an isostructural form [61]. Sesquicarbides with Ln = Er, Tm, Yb, and Lu have metastable structure that form only under high pressure [63]. Ho_2C_3 was observed to be dimorphic. Subsequent investigation revealed this holds true for Ln = Er to Lu [64], and none of them are superconducting. Thus, superconductivity only appears in Ln = La and Y and Ac = Th and their substituted compounds. The T_c values are relatively high and are comparable to A15 compounds, bringing the material family to be a popular field to study. Moreover, the exotic superconducting mechanism is discussed along with the non-centrosymmetric crystal structure. Detailed experiments on various physical properties were carried out to clarify the mechanism. Some examples are discussed below.

In the Pu_2C_3 structure, C_2 dumbbells are located inside the rare-earth metal atomic cage (Fig. 6.24). Since the C-C bond is quite short, the phonon frequency for the C-C stretching phonon modes is expected to be very high. Thus, a relatively high T_c value in Y_2C_3 and La_2C_3 is ascribed to electron-phonon coupling between high-frequency phonons and C-C antibonding states at the Fermi level.

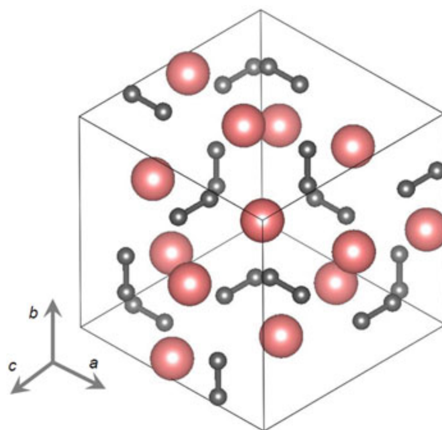

Fig. 6.24 Crystal structure of La_2C_3 projected along **[111]**

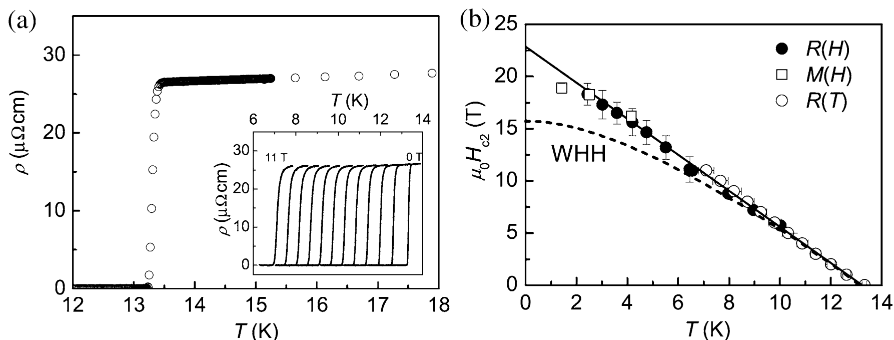

Fig. 6.25 (**a**) Low-temperature electrical resistivity of La_2C_3, showing the superconducting transition at 13.4 K. The inset demonstrates a decreased superconducting transition in the magnetic fields. (**b**) Upper critical field of La_2C_3 determined from magnetoresistance (R(H) and R(T)) and magnetization M(H) measurements (Figs. 6.8 and 6.9 from [62])

6.3.2 La_2C_3

La_2C_3 crystallizes with cubic Pu_2C_3 structure containing C-C dumbbells in a distorted dodecahedral coordination ("bisphenoid") formed by eight La atoms (Fig. 6.23). The cage surrounding La is thought to carry the main phonon mode and influences superconductivity through electron-phonon coupling.

In contrast to Y_2C_3, which requires high-pressure synthesis methods, samples of La_2C_3 are readily accessible by arc melting of the constituents. In early works, La_2C_3 is reported to have a T_c value of 11 K [60]. Detailed studies revealed that those early prepared samples contained homogeneous carbon content ranging from 45.2% to 60.2% [65, 66]. Investigations of a series of $La_2C_{3-\delta}$ samples with 0.3 $\geq \delta \geq$ 0 indicate a separation into two superconducting phases with rather sharp T_c values of ~6 K and 13.3–13.4 K (Fig. 6.25). The high T_c values are attributed to stoichiometric La_2C_3, i.e., negligible C deficiency, which was confirmed individually in the samples from neutron powder diffraction patterns [62]. Due to the important role of C deficiency in the system and a strong dependence of the superconducting transition temperature on the lattice parameter, one would expect strong pressure to affect the superconducting properties. The lattice parameters can be controlled through deficiency of carbon sites, as was observed in other carbides. This was also studied in terms of the annealing process. This is also discussed from the aspect of sample quality in the study, which we describe in the Y_2C_3 section. This was studied up to 30 GPa and focused on two points: how pressure affects the structural degrees of freedom in the Pu_2C_3-type phase and the stability of the phase in the context of pressure synthesis of rare-earth carbides. The results suggest that the system shows little dependence on the external pressure [59].

Magnetic susceptibility measurements indicate that La_2C_3 is a type-II superconductor. The upper critical field H_{c2} is reported to follow the Werthamer-Helfand-

Hohenberg (WHH) equation in early work [67]. However, systematic studies combined with neutron scattering measurements revealed that the upper critical field is clearly enhanced and exceeds WHH yet is still below the Pauli limit [68]. This indicates that La_2C_3 does not hold an exotic pairing mechanism, even with the non-centrosymmetric crystal structure and spin-orbit coupling.

H_{c2} studies in La_2C_3 found $\lambda_{ph} \sim 0.8$, suggesting moderate electron-phonon coupling [67]. However, such a moderate electron-phonon coupling appears to be too small to generate a relatively high T_c value in sesquicarbide superconductors. One of the difficulties in prior studies on rare-earth sesquicarbides is that the electronic properties and structural parameters can drastically vary depending on synthesis due to C deficiency. This is confirmed from detailed neutron scattering experiments along with electronic structure calculations [68]. They also performed specific heat measurements to obtain information on λ_{ph}. For electron-phonon coupling in superconductors, Carbotte proposed that the characteristic thermodynamic quantities follow empirical formulas that can be described in terms of one adjustable parameter ω_{ln}/T_c, where ω_{ln} is the logarithmic averaged phonon frequency [69]. All samples Kim et al. measured show that the thermodynamic properties were scaled by these parameters, and the results give the averaged logarithmic phonon frequency as 110 ± 27 K. This ω_{ln} value is only 30% of the Debye temperature ($\omega_D \approx 350$ K). Such a reduced ω_{ln} value compared to ω_D indicates the importance of the low-energy phonon modes in superconductivity. Following the discussion regarding Y_2C_3 [70], the phonon mode in La-C can be converted to $\sim$140 cm^{-1}, which is still too high for the observed $\omega_{ln} \approx 76 \pm 15$ cm^{-1}. Other relevant phonon modes for superconductivity in La_2C_3 could occur due to tilting vibration of the C-C dimer. In AC_2 (A = Ca, Sr, and Ba), dimers lose their connections with the surrounding cage at low temperature, and the rare-earth carbon halides show lower phonon modes in Raman scattering studies [71]. Compared to the octahedral metal atom cages, the size of a bisphenoid La cage is larger; thus the binding of the C-C dimer to the La cage could be even weaker. Consequently, the tilting modes of the C-C dimer in La_2C_3 are expected to have lower frequencies, which can provide a sizable contribution to electron-phonon coupling. Using the modified McMillan formula, Kim et al. could explain the relatively high T_c value within the strong electron-phonon coupling scheme [68].

The non-centrosymmetric structure of La_2C_3 could serve as a candidate for multiband superconductivity or a mixture of s- and p-wave superconductivity. This could be tested in high-resolution photoemission studies. Results from high-resolution experiment showed a clear quasiparticle peak just below the Fermi energy, which is indicative of a superconducting gap opening. The quasiparticle peak is broad and rounded compared to that of conventional superconductors. Numerical fittings revealed that the spectrum is hardly reproduced with a single *s*- or *p*-wave gap but is satisfactorily explained by two gaps with the gap values of 0.5 and 1.7 meV. All these experiments suggested two-gap superconductivity in La_2C_3 [72]. Detailed specific heat measurement also suggested s-wave superconductivity in La_2C_3. However, it was reported as a single gap [68].

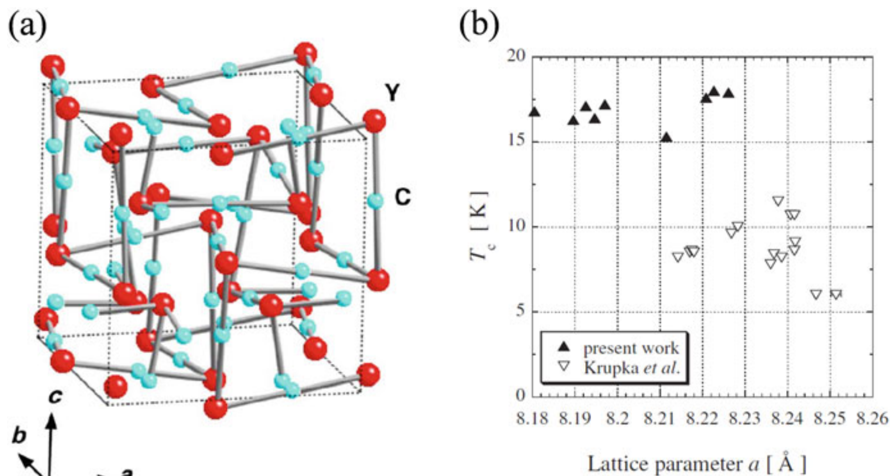

Fig. 6.26 (**a**) Crystal structure of Y_2C_3 in the high T_c phase obtained from neutron diffraction results [75]. (**b**) T_c as a function of lattice constant [74]

Recently, sesquicarbide superconductors were revisited due to their non-centrosymmetric structure. In addition to the expectation of exotic superconductivity, the anomalous behavior in the superconducting state was observed in a nuclear magnetic resonance (NMR) experiment [73]. The enhanced $(T_1T)^{-1}$ signal well below T_c indicates that either triplet coupling of pairing in the superconducting condensate or anomalous vortex motion yields the signal enhancement.

6.3.3 Y_2C_3

Old reports show T_c variations of 6–11.5 K [61] in Y_2C_3 samples synthesized at ultrahigh pressures of 1.5–2.5 GPa and at high temperatures of 1200–1500 °C. Those reports have larger lattice constants compared to high T_c compounds synthesized at high pressure [74] (see Fig. 6.26). As was discussed in the dicarbide LnC_2 section, the bonding length of C-C plays the major role in superconductivity of the sesquicarbide material family as indicated by band calculations [70]. Superconductivity in Y_2C_3 strongly depends on the synthesis conditions. In addition to C deficiency, superconductivity also has a dependence on substitution of Y, which will be discussed in detail later. The substitution of actinide Th enhanced T_c up to 17 K [61]. Subsequently, synthesis at higher pressures of 3.5–4.5 GPa resulted in a higher T_c value of 18 K [74, 76].

X-ray diffraction results show that the Y_2C_3 compound has a body-centered cubic Pu_2C_3-type structure and that the lattice parameters varied in the 8.181–8.251 Å range [61, 74]. The difficulty lays in the large difference of elements in this binary system; ^{6}C atoms are far lighter than ^{39}Y atoms. Thus, neutron scattering

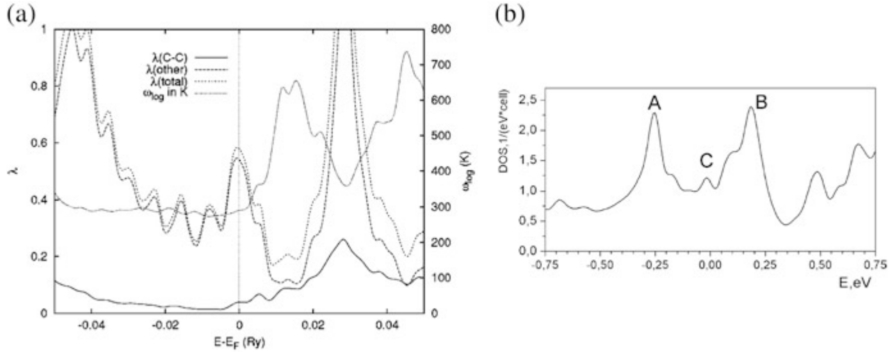

Fig. 6.27 (**a**) Electron-phonon coupling λ and average phonon frequency as a function of energy. The heavy dashed (heavy solid) line denotes the full symmetry Y (C) derived mode as a function of energy, normalized as if these modes are representative. The light dashed line shows the total λ with this assumption. The light dotted line is a logarithmic average of these two frequencies with λ, which would enter the prefactor of the McMillan equation [70]. (**b**) Total density of states in Y_2C_3 near the Fermi energy ($E_F = 0$) [77]

Table 6.4 Selected interatomic distances and lattice constant *a* (both in nm) [75]

	High-T_c	Low-T_c
Y–C^{i}	0.2510(1)	0.2507(1)
Y–C	0.2641(2)	0.2647(2)
Y–C^{ii}	0.2810(1)	0.2806(1)
Y–Y^{iii}	0.3391(2)	0.3395(1)
Y–Y^{iv}	0.35668(1)	0.35669(1)
C–C^{v}	0.1298(4)	0.1290(4)
a	0.82372(3)	0.82374(3)

experiment was performed on high T_c and low T_c samples to investigate the precise crystal structure [75]. The obtained crystal structure is presented in Fig. 6.27, and the distance between atoms are presented in Table 6.4. The occupancy results calculated for both high and low T_c samples show little difference. In addition, the atomic displacement is negligibly small for both Y and C. The displacement parameters for Y, B_Y and for C, B_C were calculated from Rietveld refinement analysis. The high T_c samples have B_Y values of 0.0007 nm^2, and the low T_c samples have B_Y values of 0.0008 nm^2, while B_C varies from 0.069 nm^2 for high T_c samples to 0.0059 nm^2 for low T_c samples. By comparison, it is clear that Y atoms are extremely rigid compared to C atoms. While the lattice parameter does not differ from high to low T_c samples, the C-C distance show clear difference, confirming the importance of C-C bonding in superconductivity [75].

One ab initio calculation showed that the C-C stretching phonon frequency in Y_2C_3 is 1442 cm^{-1} for an almost pure C-C bond, while a Y-dominant mode shows frequency as low as 175 cm^{-1}. Electronic structure calculations for Y_2C_3 demonstrated that the high-frequency C-C bond stretching phonon modes contribute less than 10% of the total electron-phonon coupling, and rather low-frequency Y(-C)

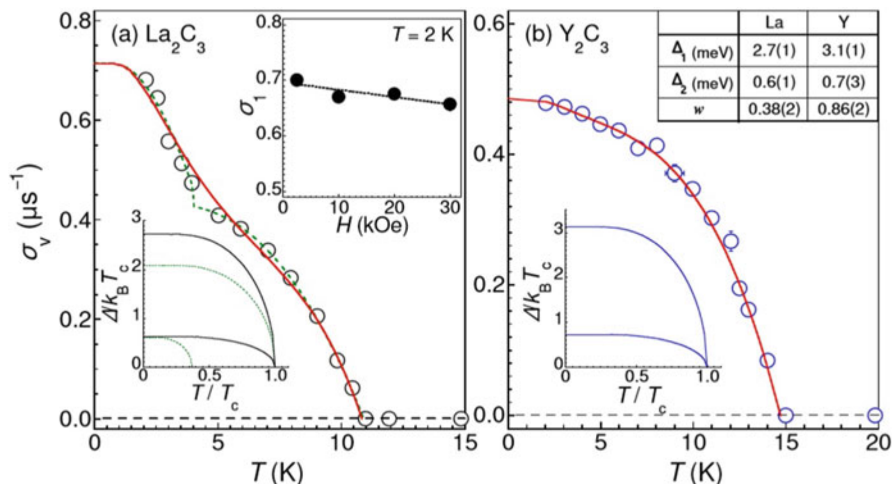

Fig. 6.28 Temperature dependence of the muon spin relaxation rate for (**a**) La_2C_3 at 2.5 kOe and (**b**) Y_2C_3 at 5.0 kOe. Error bars (not shown) are smaller than the symbol size. Solid and dashed curves indicate the result of the fitting analysis using the double gap model described in the text. Insets show the relaxation rate in the superconducting state (σ_1) as a function of the magnetic field for La_2C_3 and the order parameters [$\Delta(T)/k_B T_c$] for the respective cases [78]

phonons must be considered to be the relevant modes for superconductivity. The calculation shows an electron-phonon coupling peak in the vicinity of the Fermi energy at stoichiometric band filling and low contribution from C-C bonding [70]. This peak feature in the vicinity of Fermi energy is also presented in comparison to YC_2, suggesting this is the origin of the dependence on synthesis condition and annealing [77]. The features of λ and DOS are presented in Fig. 6.28. The peak in the DOS is also observed as a function of lattice constant [79]. A recent study investigating the stability and mechanical properties in a Y-C binary system with first principles calculation showed that Y_2C_3 with the discussed crystal structure [75] has the largest bulk modulus, shear modulus, Young's modulus, and hardness among all Y-C binary compounds. The Debye temperature calculated in the study was 550.5 K, which agrees well with other studies [80].

An early report on the high T_c phase of Y_2C_3 also pointed out the importance of an enhanced $H_{c2}(0)$ value and its contribution to superconductivity [76]. They estimate $H_{c2}(0)$ to be 43.5 T and 18.3 T for different samples at 18 K and 11 K, respectively. The enhanced $H_{c2}(0)$ value is close to the Pauli paramagnetic limit. Such a large enhancement may indicate the contribution from spin-triplet superconductivity. This idea was tested under extremely high magnetic fields [81]. They performed tunnel-diode resonant circuit measurements in pulsed magnetic fields. The obtained $H_{c2}(0)$ values varied between 25 and 30 T for a sample at 15.5 K. The orbital limit and Pauli paramagnetic limit for the sample in question were found to be 24.5 T and 28.8 T, respectively. The obtained value of $H_{c2}(0) \sim 30$ T is larger than both limits, and an $H_{c2}(T)$ curve shows an upturn at low temperature.

Table 6.5 Superconducting parameters of Y_2C_3 samples with various T_c values [67]

T_c(K)	11.6	13.9	15.2
γ(mJ Mol^{-1} K^{-2})	4.7	6	6.3
$\Theta_D(0)$ (K)	540	530	530
$\mu_0 H_{c2}$(T)	22.7	24.7	26.8
$2\Delta/k_B T_c$	3.6	3.9	4.1
ξ(Å)	38	36	35

This kind of behavior is typical in non-centrosymmetric superconductors with large antisymmetric spin-orbital coupling. However, strong electron-phonon coupling may induce larger critical fields.

Superconducting parameters are obtained via specific heat measurements [82, 83]. Measurements from multiple samples with different T_c values show variation in $H_{c2}(0)$ and the electron specific heat coefficient γ. The obtained parameters are shown in Table 6.5. All samples show relatively high Debye temperatures of $\Theta_D \sim 530$ K, which are comparable to that of YNi_2B_2C. This is indirect evidence that the phonon mode comes from light elements because YNi_2B_2C superconductivity comes from Ni-B layers. The results also show a clear dependence of T_c on γ. The value of γ depends on the DOS in the vicinity of the Fermi energy, thus the aforementioned phonon mode enhancement might play an important role in determining T_c. Clear evidence we can derive from the specific data relates to whether or not superconductivity in these systems is fully gapped. The results from Akutagawa et al. clearly show that Y_2C_3 is a fully gapped *s*-wave superconductor. Similar behavior was observed in tunneling break-junction measurements [84]. ^{13}C NMR measurements were performed on a sample with $T_c = 15.7$ K [85]. They observed a reduced Knight shift below T_c, indicating spin-singlet superconductivity. A nuclear spin-lattice relaxation study revealed that Y_2C_3 in the superconducting state is a multigap superconductor that exhibits a large gap of $2\Delta/k_B T_c = 5$ at the main band and a small gap $2\Delta/k_B T_c = 2$ at others. This kind of multigap behavior was also observed in μSR spectroscopy [78]. Figure 6.28 shows a comparison between La_2C_3 and Y_2C_3. The results obtained from both compounds were analyzed using the phenomenological two-gap model and agreed well with the model. The quasiparticle observed in the magnetoresistance also agrees with the model [78]. Subsequently, detailed penetration depth measurements were carried out using a tunneling diode resonant circuit [86], and detailed $H_{c2}(T)$ results were obtained at low temperatures. The sharp enhancement measured in previous studies is shown in Fig. 6.29. The H_{c2} curve is well described by a two-gap model in the vicinity of T_c, but the clear enhancement below 2 K strongly suggests that asymmetric spin-orbit coupling splits the electronic bands, thus mixing the spin-singlet and spin-triplet pairing states and leading to the existence of line nodes [86]. To analyze this possibility, Chen et al. calculated the temperature dependence of the nuclear magnetic relaxation rate $(T_1T)^{-1}$ in the Dresselhaus-type non-centrosymmetric superconductor Y_2C_3 employing the $(s+f)$-wave parity-mixing model, where the *d*-vector is chosen to be parallel to the Dresselhaus spin-orbit coupling vector. They found that the $(s + f)$-wave model can explain the experimental results

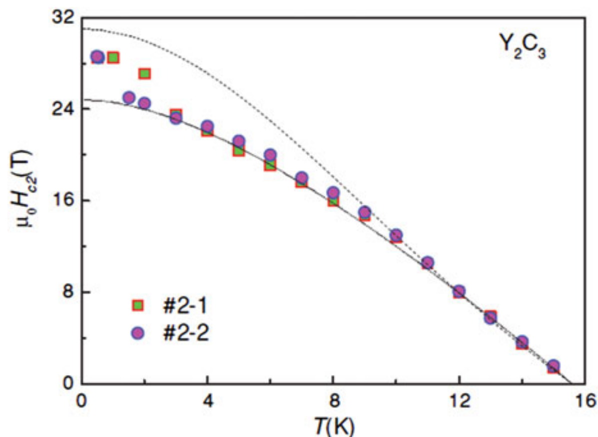

Fig. 6.29 The upper critical field versus temperature for two Y_2C_3 samples. The dotted and the dashed lines are fits to the weak-coupling WHH method and GL theory, respectively [86]

fairly well over a wide range of temperatures for a ratio of s- and f-wave parity superconductivity gaps $\kappa = \Delta_s/\Delta_f = 0.5$ [87]. The current data is insufficient to explain the low-temperature behavior.

6.3.4 Y_2C_3-Th_2C_3 and Substitution Effect

Following the first report of synthesizing Y_2C_3 in a body-centered-cubic Pu_2C_3-type structure, Th-substituted samples were synthesized with the goal of achieving superconductivity [52]. The phase diagram shows the wide range of crystallographic stability in the Pu_2C_3 structure. In general, the superconducting transition is fairly broad, occurring over a span of 0.3–2 K. Thorium doping can modulate T_c and enhances it up to 17 K in $(Y_{0.7}Th_{0.3})_2C_{3.1}$ [52]. T_c has a peak in the lattice constant dependence, as shown in Fig. 6.30. The non-monotonic curve shows that the maximum T_c value at 8.35 Å is larger than in Y_2C_3 samples. This agrees with the calculated electronic structure studied from first principles [88]. The C-C bond length of the substituted sample is discussed as being dependent on the Y/Th metal and C/Mt. carbon-total metal atomic ratios [52]. Elements other than Th incorporated in Y_2C_3 resulted in enhanced T_c compared to pure Y_2C_3. Au, Ge, Nb, Ti, Ca, Ru, Sn, and Bi produce a similar effect on T_c, while Zr, Mo, W, V, and Cr enhance T_c within a small doping range (see Table 6.6). The upper critical field of $(Y, Th)_2C_3$ follows the WHH equation [67] and is estimated to reach 28.0 ± 0.24 T [90], which keeps similar values as Y_2C_3. A similar enhancement of T_c is also observed in Th-doped La_2C_3 [91].

This substitution eventually led to synthesis of new actinide carbide Th_2C_3 at 2.0–3.5 GPa [92]. Rare-earth elements are also introduced to nonsuperconducting

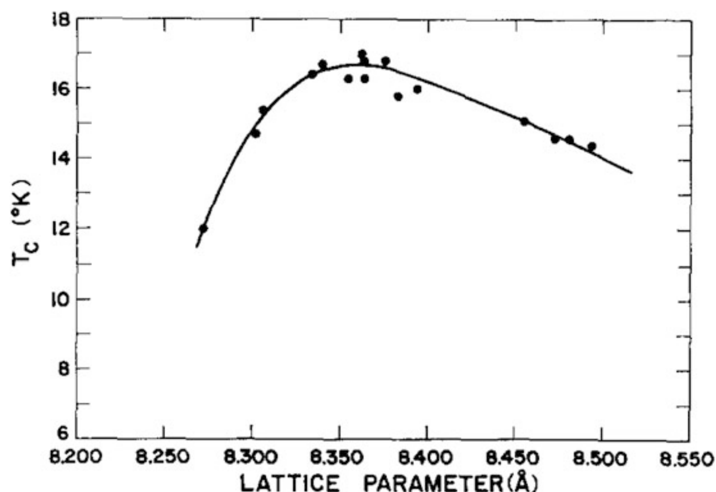

Fig. 6.30 T_c as a function of lattice parameters in $(Y, Th)_2C_3$ [52]

Th_2C_3 with body-centered-cubic Pu_2C_3 crystal structure, yielding samples with various T_c values ranging from 4.1 to 11.7 K [64]. Both Th-doped Y_2C_3 and Th_2C_3 were synthesized at high pressure (3.0 GPa or more), and the lattice parameter can vary depending on the synthesis conditions [89].

Rare-earth sesquicarbide superconductors doped with Th, such as $(Y_{1\text{-}x}Th_x)_2C_3$ and $(La_{1\text{-}x}Th_x)_2C_3$), would have non-centrosymmetric crystal structure due to the resemblance between Th^{3+} and U/Pu. In addition to the crystal structure, the presence of Th can function equivalent to 4f electrons in a heavy-fermion superconductor [93]. Thus, the material family is an interesting group for studying spin-orbit interaction, non-centrosymmetric crystal structure, and superconductivity. Despite the high expectation, these materials are yet to be studied.

6.4 Boron Carbide

6.4.1 Rare-Earth Quaternary Boron Carbides

Superconductivity in quaternary borocarbides was discovered in 1993. The first report is in YNi_4B with $T_c = 15$ K, and superconductivity is in negligibly small order (volume fraction of superconductivity is $\sim 2\%$) [94]. The materials were studied from the perspective of an anomalous lattice volume via valence fluctuations in rare-earth elements. Intensive studies revealed that carbon is necessary to induce superconductivity. Thus, $YNi_4BC_{0.2}$ [95] and $LnNi_2B_2C$ [96] were synthesized and exhibited largely improved signals with zero resistance, i.e., bulk superconductivity. The crystal structure was then found [97] to have body-centered tetragonal $ThCr_2Si_2$

Table 6.6 Superconducting transition temperature and lattice parameters in $(Th,R)_2C_3$ [89]

System composition			
R.E. element	Nominal Th/R.E. atomic ratio	Superconducting transition temperature (°K)	Lattice parameter a_0 (Å) (b.c.c. sesquicarbide phase)
Ce	9/1	< 4	8.5445 ± 4
Pr	9/1	< 4	8.5563 ± 4
	8/2	< 4	8.5602 ± 5
Nd	9/1	< 4	8.5555 ± 4
Gd	9/1	Magnetic	8.5439 ± 4
Tb	9/1	Magnetic	8.5415 ± 4
Dy	9/1	Magnetic	8.5482 ± 7
	8/2	Magnetic	8.5296 ± 7
Ho	9/1	5.4	8.5448 ± 5
	8/2	5.5	8.526 ± 1
	7/3	5.2	8.499 ± 2
	6/4	Magnetic	8.471 ± 2
Er	9.5/0.5	6.8	8.5434 ± 4
	9/1	8.2	8.5400 ± 8
	8/2	8.2	8.523 ± 2
	7/3	8.1	8.486 ± 2
	6/4	7.0	8.455 ± 2
	5/5	4.6	8.412 ± 3
	4/6	Magnetic	8.361 ± 2
	3/7	Magnetic	8.297 ± 2
	2/8	Magnetic	8.237 ± 4
	1/9	Magnetic	8.194 ± 3
Lu	9/1	10.3	8.5278 ± 7
	8/2	10.9	8.495 ± 1
	7/3	11.7	8.461 ± 1
	6/4	11.6	8.426 ± 1
Sc	9/1	6.7	8.5362 ± 9
	8/2	6.8	8.531 ± 1
	7/3	7.2	8.5297 ± 3
	6/4	7.1	8.529 ± 1
	5/5	6.5	8.543 ± 2
	4/6	6.0	8.550 ± 5
	3/7	5.4	Not determined

structure (space group I4/*mmm*). The crystal structure of YNi_2B_2C is shown in Fig. 6.31a. There are several different compounds related to those superconductors, denoted RM_2B_2C, where R is a rare-earth element and M is a transition metal (M = Ni, Pd, Pt, Ru, etc.). The interplay of structural, electronic, and magnetic properties are discussed below.

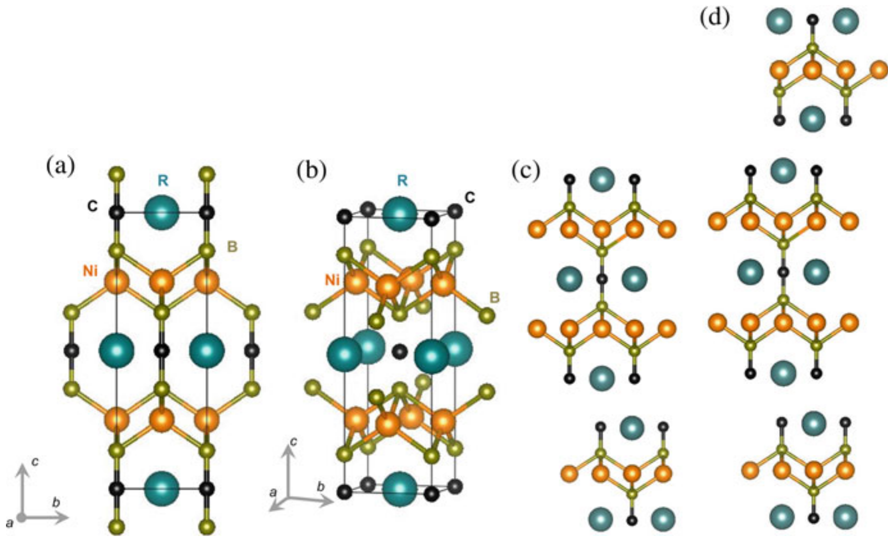

Fig. 6.31 (**a**) Unit cell of the tetragonal structure (I4/*mmm*) in RNi_2B_2C materials. The structure is a filled-in version of the $ThCrSi_2$ structure, with C atoms occupying a special position (1/2, 1/2, 0) in the unit cell. The structure was first reported in [97]. Crystal structures of (**b**) *RM*BC, (**c**) RM_2B_2C, (**d**) $R_3M_4B_4C_3$ showing stacking within **[001]** (small dark spheres, *M*; small light spheres, B; large light spheres, *R*; larger dark spheres, C)

The layered structure of borocarbides is reminiscent of high T_c cuprates, where superconductivity is supposed to be induced by doping CuO_2-planes separated by rare-earth metal oxide (buffer) layers. Superconductivity appears in CuO_2-planes. In contrast to the 2D cuprate electronic structure, borocarbides are essentially three-dimensional (3D) superconductors. In addition, strong phonon softening observed in a number of superconducting borocarbides, such as YNi_2B_2C and $LaNi_2B_2C$ [98], indicates these materials are s-wave superconductors. A strongly anisotropic energy gap was observed in several measurements, which is unusual in conventional s-wave superconductors. This suggests the superconductivity of the materials possess a complex pairing mechanism.

6.4.1.1 Superconductivity of RNi_2B_2C and General Features of the Material Family

Since the discovery of the RNi_2B_2C series [95, 96], research on these materials has flourished. There were three physical reasons for this interest. First, the members of this series are magnetic superconductors for the most of latter half rare-earth elements. The elements rarely appear in superconductors except in buffer layers of cuprates. Second, many of them show antiferromagnetic (AFM) order transitions at a temperature (T_N) that is comparable to T_c; thus the salient energy

scales for AFM order and superconductivity can be varied over a wide range and examined in two very different limits ($T_c > T_N$ and $T_N > T_c$). Third, high-quality samples can be readily produced in single crystal form using Ni_2B flux [99]; thus numerous experiments for determining the superconductivity properties were easily performed.

The highest T_c values occur in $R Ni_2B_2C$, which could be used to form a series of $(RC)_m(NiB)_n$ with layered structures (Fig. 6.31b–d). The homologous structure consists of a planar *R*C layer separated by a couple of $(NiB)_2$ layers. In an *R*C plane, the carbon C sits in the center of rare-earth *R* square. The structure of *R*NiBC ($n = 2$) and RNi_2B_2C ($n = 1$) occurs in ...(B-Ni_2-B)-*R*C-*R*C... and ...(B-Ni_2-B)-*R*C... stacking sequences, respectively. The variation of compounds is nitride and is represented as $(RC)_m(NiN)_n$. Two nitrides are known to be superconducting, i.e., LaNiBN and $La_3Ni_2B_2N_3$ [100]. The latter is the only one known for the $m = 3$, $n = 1$ type of this series and is superconducting with $T_c \sim 12$ K.

The stacking structure of Lu_2NiBC_2 with monoclinic unit cell ($n = 4$) was obtained from high-resolution electron microscopy imaging [101]. For the $R = \mathrm{Y}$ compound, Y_2NiBC_2 was found to form a primitive tetragonal unit cell based on X-ray powder diffraction but with a different stacking sequence of (B-Ni_2-B)-YC-YC-YC-YC-... (i.e., a larger rock-salt-like slab of YC) fitting better within the row of compounds. Stacking variants with larger numbers of Ni_2B_2 layers than *R*C slabs lead to $Y_3Ni_4B_4C_3$ ($n = 3/2$, I4/*mmm*) with sequence ...(B-Ni_2-B)-YC-YC-(B-Ni_2-B)-YC..., $Y_5Ni_8B_8C_5$ ($n = 5/2$, I4/*mmm*) with sequence ...(B-Ni_2-B)-YC-(B-Ni_2-B)-YC-(B-Ni_2-B)-YC-(B-Ni_2-B)-YC-YC..., and $Y_5Ni_6B_6C_5$ ($n = 5/3$, I4/*mmm*) with sequence (B-Ni_2-B)-YC-YC-(B-Ni_2-B)-YC-YC-... The crystal structure of $Y_3Ni_4B_4C_3$ was determined via single-crystal X-ray diffraction analysis and was found to correspond to the T^* phase of cuprates with alternating *R*NiBC blocks and RNi_2B_2C structures. This kind of intergrowth structure allows some material engineering to explore the material family. There are several crystal structures in this material family that are fascinating in themselves yet are beyond our interest in this book (e.g., see [102]).

Below, we describe materials with body-centered-tetragonal $ThCr_2Si_2$ structure and exceptionally high stability. Take an example in YNi_2B_2C in Fig. 6.31a. The structure consists of square Ni_2B_2 and *R*C sheets alternately stacked along the *c* axis. C atoms occupy the center of the square (special position, unoccupied in the $ThCr_2Si_2$ structure) formed by four *R* atoms. The in-plane lattice parameter *a* and interlayer spacing *c* change as the ionic radii of rare-earth elements increases. When rare-earth elements are present in the compounds, the lattice parameter is expected to play an important role in determining the valence and electronic structure of the material. The dependence in the Ni series is discussed in the following section. In addition to those lattice parameters, the position of boron z(B) is discussed to determine various distances, such that within the linear complex $[BCB]^{4-}$ ion and to a somewhat smaller extent the *M*-B distance. The value of z(B) is the relative distance between B and the RC plane (e.g., see Fig. 6.31a, where z(B) is measured from the top RC plane and is normalized by the lattice parameter c). Within the *M*-B layer, the angle between B-*M*-B can vary due to slight distortions, as shown in Fig. 6.32.

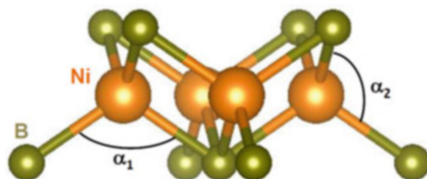

Fig. 6.32 NiB_2 layer with edge-sharing tetrahedral structure in borocarbides RNi_2B_2C. The definitions of angles α_1 and α_2 are described in the main text

Table 6.7 T_c and T_N in superconducting-magnetic RNi$_2$B$_2$C (R = Dy, Ho, Er, and Tm)

Material	T_c [K]	T_N[K}
$DyNi_2B_2C$[a]	6	11
$HoNi_2B_2C$[b]	8, 5	8.5, 6.3[b], 5
$ErNi_2B_2C$[c,e]	11	6.8, 2.3
$TmNi_2B_2C$[d,e]	10.6	1.5

Data taken from [103]

[a]Superconductivity occurs in an antiferromagnetic lattice and is strongly sensitive to nonmagnetic impurities

[b]Superconductivity nearly disappears at $T_{c2} = 6$ K and returns quickly at $T_{c3} = 5$ K

[c]Below 2.3 K, weak ferromagnetism coexists with superconductivity, even as T approaches 0

[d]Distinct magnetic ordering, quadrupole ordering, and its influence on magnetism [104]

[e]Several new phenomena are discussed along with Fermi liquid behavior in magnetic superconductors (not in this book)

In addition to the structural variation, the compounds allow R and M to correspond to multiple elements. The family also hosts numerous exotic magnetic behaviors, where a number of compounds show T_c values that are comparable to T_N [101, 102]. Some superconducting compounds are listed in Table 6.7 with T_c and T_N values.

Considering that rare-earth nickel compounds have the potential for hydrogen absorption and hydrogen is known to influence T_c, we note that YNi_2B_2C takes hydrogen to an extent of 0.25 atomic fraction and neither affects the structure nor the T_c value to any significant extent [105].

6.4.1.2 Variation of Compounds and Superconductivity in RM_2B_2C

Quaternary borocarbides allow several transition metals (M) to form $(MB)_2$ layers. While the Ni series has the highest T_c values and accommodate good single crystal growth, there are several other transition metal compounds that show superconductivity and/or long-range magnetic order. T_c shows a non-monotonic dependence on the ionic radius of R (Fig. 6.33a). Below are some of the examples of superconducting compounds.

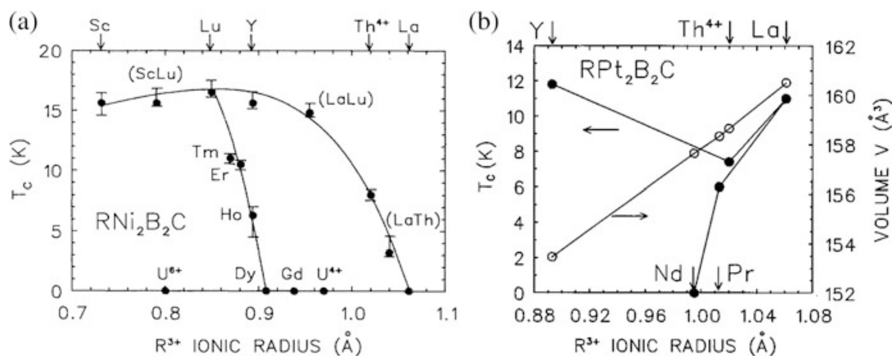

Fig. 6.33 (**a**) Variation of T_c with ionic radius of R^{3+} ions in a RNi$_2$B$_2$C system (R = Sc, Y, La, Gd, Dy, Ho, Er, Tm, Lu). The Th^{4+} ionic radius is used for R = Th. Both U^{4+} and U^{6+} are used for UNi$_2$B$_2$C. The solid lines guide the eyes [106]. (**b**) Variation of T_c and tetragonal unit cell volume V with R^{3+} ionic radius in RPt$_2$B$_2$C (R = Y, La, Pr, Nd). The Th^{4+} ionic radius is used for R = Th [107]

Table 6.8 T_c of R-Pd-B-C superconductors

Material	T_c [K]	References
$YPd_5B_3C_{0.3}$	22.6	[100]
$Y_{1.25}Pd_{4.5}B_{4.25}C_x$	23	[100]
$YPd_{2-x}Rh_xB_2C$ (x = 0–0.25)	12–22	[109]
YPd_4BC_x	~10, ~22	[110]
YPd_2B_2C	~23	[111]
$ThPd_4BC$ (multiphase)	14, 20	[112]
$ThPd_2B_2C$ (multiphase)	12, 17	[112]
$LuPd_4BC_{0.2}$	9	[110]
$LaPd_2B_2C$	1.8	[113]

One of the early variations is Pd with relatively high T_c ~ 23 K in YPd_5B_3C [108]. The downside is the stability of the material; it loses the superconductivity when annealed above 900 °C. Following the discovery, several compounds showing superconductivity were synthesized and are listed in Table 6.8. Subsequently, pseudoternary phase diagrams were obtained via a survey over a wide range of Y-Pd-B-C contents through X-ray diffraction and magnetic susceptibility measurements [111]. Quenched samples showed superconductivity for various elemental ratios. The strongest signal is observed in the compound with similar ratio to that of Y-Ni-B-C, i.e., YPd_2B_2C. They showed that superconductivity is metastable and only exists in rapidly quenched samples. This simple fcc-cubic structure diminishes when annealed above 750 °C along with the superconductivity, confirming that the crystal structure is related to superconductivity. Another group reported that the phase holds as a tetragonal I4/*mmm* structure, reminiscent of the Ni series. The primary electronic states at the Fermi level come from Pd in the system, as determined from Pd L_3-edge X-ray absorption near-edge spectra [109]. This is also supported by the energy-dispersive X-ray analysis [114]. Despite all the

intensive work, superconductivity in a single-phase Y-Pd-B-C specimen was not reported. With substitution of Ni by Pd, examination of $Y(Ni_yPd_{1-y})_2B_2C$ revealed that the substituted compound is formed by a peritectic reaction. This substitution shows the region where the superconducting signal appears and where the fcc-phase and tetragonal structure coexist, providing evidence that the tetragonal structure does not directly correspond to superconductivity and adding an extra puzzle to superconductivity in the material [115]. Transition metal Pd and rare-earth Y can be substituted by other rare-earth elements ranging from La to Yb up to 10% [116]. The introduction of rare earth as impurities modulates changes in T_c, where ΔT_c follows de Gennes scaling. Off-stoichiometric $DyPd_5B_3C_{0.35}$ also shows superconductivity, where both T_c and T_N are lower than 1.7 K. The results obtained from these Pd compounds suggest strong magnetic pair breaking and rather weak Ruderman-Kittel-Kasuya-Yosida (RKKY) interaction among rare-earth ions [116]. The results contrast the results obtained from the Ni series. In addition to rare-earth elements R, $ThPd_2B_2C$ shows superconductivity at $T_c = 14.5$ K [117]. They also reported an undetermined phase showing $T_c = 21$ K, which has not yet been confirmed to the best of our knowledge.

Regarding Pt, materials with R = Y, La, Ce, Pr, Nd, and Dy are known to be isostructural with the ability to accommodate nonstoichiometry [118]. It was reported that signals resembling superconductivity were observed at 10 K for R = La and Y and 6 K for Pr. The lattice parameters may be modulated via the nonstoichiometry of either B or C. This deficiency plays an important role in determining T_c values in these systems [118]. Subsequently, Cava et al. studied the Pt series of superconducting crystals in detail (La, Y and Pr) and showed Au and Pt should be doped together or nonstoichiometrically to obtain high-quality samples [119]. Other compounds with R = Ce and Nd were reported to show no superconductivity. The former is discussed as a candidate heavy-fermion system based on the temperature dependence of the resistivity, specific heat, and magnetic susceptibility [110]. Subsequently, high-quality single crystals with R = Ce were synthesized, and detailed magnetic and thermodynamic measurements showed that $CePt_2B_2C$ is similar to those of Ce-based Kondo lattices or heavy-fermion compounds like $YbNi_2B_2C$. The resistivity has a weak temperature dependence down to 60 K, below which it decreases rapidly. Resistivity follows a strictly linear temperature dependence below 10 K, which is similar to that observed in heavy-fermion $YbRh_2Si_2$ with non-Fermi-liquid behavior. The specific heat of $CePt_2B_2C$ also shows a temperature dependence similar to that of $YbRh_2Si_2$, which is expected to arise from its proximity to a quantum phase fluctuation. Those behaviors support the idea that $CePt_2B_2C$ is a heavy-fermion system with properties similar to that of non-Fermi liquid $YbRh_2Si_2$. It is expected that $CePt_2B_2C$ shows superconductivity in the vicinity of 8 K from the two superconducting neighboring rare-earth compounds $LaPt_2B_2C$ and $PrPt_2B_2C$. On the contrary, $CePt_2B_2C$ does not show any superconducting behavior, which is perceived as indirect supporting evidence of the Kondo effect and heavy-fermion behavior present in the system. The magnetic susceptibility of $CePt_2B_2C$ follows the Curie-Weiss law in the 100–300 K temperature range with $\mu_{eff} = 2.5\mu_B$, as expected for trivalent Ce ions. This

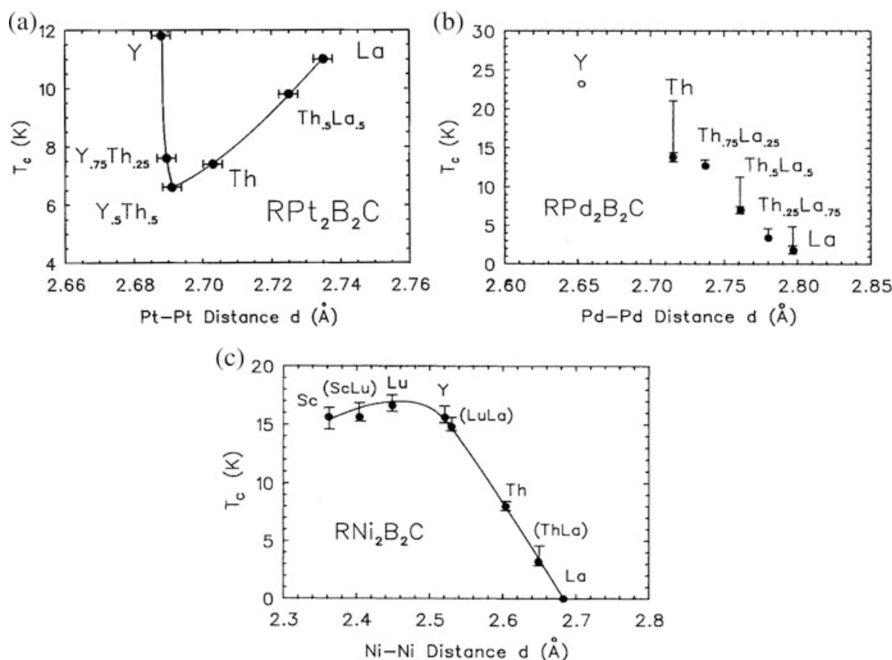

Fig. 6.34 (**a**) Variation of T_c with the Pt-Pt in-plane distance for nonmagnetic RPt_2B_2C [107]. (**b**) Variation of T_c with the nearest-neighbor Pd-Pd in-plane distance for quaternary and pseudoternary components in the RPd_2B_2C system. The open circle indicates the YPd_2B_2C superconductor prepared with nonstoichiometric composition [113]. (**c**) Variation of T_c with the nearest-neighbor Ni-Ni in-plane distance in nonmagnetic RNi_2B_2C [106] (all *M*-*M* distances are derived from the lattice constant *a*, as described in the main text)

is in contrast to the valence fluctuation behavior exhibited in nonsuperconducting $CeNi_2B_2C$. This suggests that hybridization of rare-earth elements and the structural parameters would modulate the magnetic properties along with superconductivity. The latter $R =$ Nd compound is reported to show a magnetic transition at 9.5 K [120] and superconductivity at 3 K [121]. Thus, superconductivity in $R =$ Nd is expected to coexist with magnetic order below T_c. Rare-earth and actinide compounds in the Pt series were synthesized, and some showed superconductivity. $ThPt_2B_2C$, which is isostructural to $LuNi_2B_2C$, shows superconductivity at 6.5 K, while a uranium compound shows no superconductivity [117]. Contrary to the smoothly decreasing T_c value with the increasing ionic radii for nonmagnetic RNi_2B_2C ($R =$ Y, Th, and La) compounds [106], nonmagnetic RPt_2B_2C ($R =$ Y, Th, and La) compounds show an anomalous variation in T_c versus ionic radius with a local minimum at 7 K in $ThPt_2B_2C$ (Fig. 6.33b). Since the insertion of different *R* ions can influence the in-plane and *c*-axis Pt-Pt interatomic distances, the electronic structure and the Pt(5*d*)-dominated conduction bandwidth are expected to change as a result. Figure 6.34 shows changes in T_c with strong dependence on the nearest-neighbor in-plane Pt-Pt distance (d(Pt-Pt) $= a/\sqrt{2}$, where *a* is the tetragonal in-plane lattice parameter)

for various amounts of Th. The smooth variation of the Pt-Pt distance and T_c during (Th, R) substitution ruled out the possibility of sample inhomogeneity.

The Pt-Pt bond lengths of 2.688–2.735 Å are smaller than the fcc Pt value of 2.77 Å, suggesting the presence of metal-metal bonding in this phase. Such an anomalous T_c-d(Pt-Pt) relationship, along with other physical properties, suggests the importance of the Pt(5d)-dominated conduction band [107]. On the contrary, the smooth variation of the Ni(3d) and Pd(4d) bands in isostructural RT_2B_2C systems (T = Ni, Pd) are reflected through a smoothly decreasing T_c value with T-T in-plane distance $d(T\text{-}T)$, where no superconductivity was observed down to 0.3 K in $LaNi_2B_2C$ with the longest d(Ni-Ni) value; a lower T_c value of 2 K was observed for $LaPd_2B_2C$ with the longest d(Pd-Pd) value [113].

In the series with M = Ru, only R = Y is reported to be superconducting at T_c = 9.7 K for YRu_2B_2C, which is isostructural to $LuNi_2B_2C$ [122]. There was no following report of superconductivity in related materials. The only reported Ru compound YRu_2B_2C has a similar lattice parameter a as YRh_2B_2C and YPd_2B_2C but a significantly smaller c parameter [122].

6.4.1.3 Rare-Earth Dependence of Borocarbides RNi$_2$B$_2$C

Large variations of rare-earth metals in RNi_2B_2C (isostructural to $LuNi_2B_2C$) were reported [123]. Various materials were studied from the perspective of structure and superconductivity along with long-range magnetic order. For R = Dy, Ho, Er, and Tm, the system was studied for the interplay between superconductivity (T_c = 6.5, 8.5, 10.5, and 10.8 K, respectively) and magnetic order (T_N = 10.5, 6.0, 5.9, and 1.5 K, respectively). Upon cooling the compounds with Ho, Er, and Tm, magnetic order emerged in the presence of superconductivity, while the Dy compound becomes superconducting in the magnetically ordered state. There are several interesting rare-earth-dependent behaviors that coexist in these compounds. One is that the compounds with the rare-earth metal ions which do not carry a localized magnetic moment (Y, Lu) are type-II superconductors [99, 105, 124, 125] and display the highest T_c values in the series (16 and 15.5 K, respectively). For all Ni compounds, only those compounds with smaller rare-earth metals show superconductivity. The rare-earth element changes the lattice parameters, as shown in Fig. 6.35.

6.4.1.4 Structural Changes with R Modulation in Ni Series

Crystallographic values determining the crystal structure of the tetragonal $LuNi_2B_2C$-type structures are a, c, and z(B), the latter being the only variable position parameter where a boron atom sits above the R-C plane. There is generally a small deviation in the YM_2B_2C data from the expected dependencies on the ionic radii, given that $r(Y^{3+})$ is comparable to $r(Ho^{3+})$ (see Fig. 6.36). For the metastable

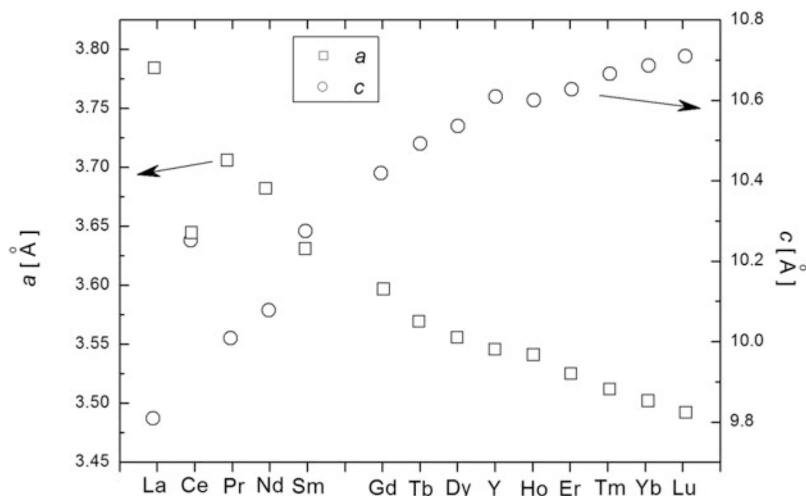

Fig. 6.35 Lattice parameters *a* and *c* in tetragonal RNi_2B_2C. Data points are taken from the literature

compound $ScNi_2B_2C$, one set of unit cell parameters was omitted from the list as the *c* unit cell parameters were apparently too small.

X-ray and neutron diffraction studies on Ni compounds indicate all crystallographic sites to be essentially fully occupied with significant site mixing, although neutron and positron annihilation experiments suggest possible carbon vacancies despite the uncertainty regarding whether the structure allows nonstoichiometry [126, 127]. Variation of the unit cell parameters in YNi_2B_2C at equilibrium with different phases and a clear temperature dependence of T_c on the unit cell volumes from about 10 (small volume) to 15 K (large volume) indicate a considerable homogeneity range in YNi_2B_2C [128]. The system is also studied for boron content in the range of $1 \leq x < 2$ in YNi_2B_xC to clarify the phase equilibria and obtain the correlation between T_c onset and boron deficiency [129]. Local disorder of B and C was also discussed to be responsible for locally higher T_c values, leading to diamagnetic contributions slightly above the bulk superconducting transition temperature [130]. There are reports that show a clear dependence on the physical properties, i.e., T_c, T_N, electrical resistivity, and magnetic order in $HoNi_2B_2C$ [131] and $ScNi_2B_2C$ [132], as well as on the annealing history of the samples. The annealing history was traced back to the formation of vacancies and to some disorder of C and B up to a considerable level of 8.6%, based on neutron powder diffraction measurements from $YNi_2{}^{10}B_2C$ [133]. We should note here that ^{11}B and C are nearly indistinguishable both in X-ray and neutron diffraction measurements and that ^{10}B with a clearly different diffraction length in neutron scattering is a highly absorbing element. High-resolution electron microscopy indicated significant concentrations of stacking faults that modify the local composition, which is a common feature in homologous compounds. The same trend will hold true

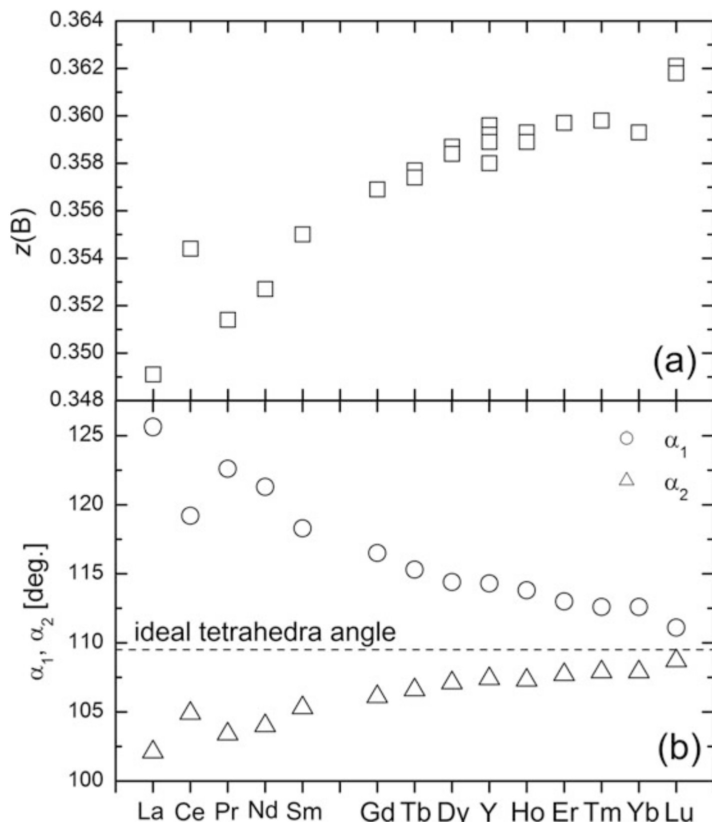

Fig. 6.36 (**a**) Site parameters z(B). (**b**) Angles of Ni-B, α_1, and α_2 in $R\mathrm{Ni_2B_2C}$ borocarbides for various R. The description of α_1 and α_2 is shown in Fig. 6.32

for all discussed borocarbides, based on the observed dependencies of physical properties on thermal history of the samples [131, 134, 135]. The example is $HoNi_2B_2C$, where the unit cell parameter depends on B and C contents. This agrees well with the aforementioned vacancies in B/C sites and mixing of B/C. Further investigation demonstrated at least a small homogeneity range within these two constituents hosts superconductivity. Small deviations from ideal composition trigger the disappearance of superconductivity. Excess boron position in $HoNi_2B_{2.1}C$ is studied and revealed that they are apparently introduced at interstitial positions between HoC and Ni_2B_2 layers and strongly modulates the superconductivity [131]. Amorphous YNi_2B_2C powders did not show any superconductivity, although superconductivity appears upon annealing with a significantly lower T_c value than other well-crystallized samples. The T_c value in such samples can be accelerated with prolonged annealing or with higher annealing temperatures due to increasing recrystallization, which also provides some insight on superconductivity.

Figure 6.35 shows the unit cell parameters *a* and *c* as a function of incorporated rare-earth metal atoms. The unit cell parameters *a* and *c* show contrasting trends when the rare-earth *R* atom is changed in RNi_2B_2C. This kind of systematic change dependent on $r(R^{3+})$ is expected for a given transition metal. Because *c* increases and *a* decreases as $r(R^{3+})$ decreases, the overall volume contraction as *R* changes from La to Lu is only about 11% (including the Sc material, about 15%). As the only deviation from the monotonic dependences, Ce compounds exhibit a smaller volume and *a*, but they exhibit larger *c* and *c*/*a* ratio, indicating a mixed or intermediate valence state of approximately $Ce^{3.75+}$, as extrapolated from volume measurements [97, 112, 136, 137]. Physical properties are in accordance with an intermediate valence state of Ce. Ce apparently stays in the intermediate state, even in diluted systems, e.g., when substituted for Y in $Y_{1-x}Ce_xNi_2B_2C$ [138]. This contradicts the results from Pt compounds, where Ce is in a monovalence state.

Changing *R* from Lu to La in Ni compounds decreases *z*(B) in a linear manner concomitant to the decreasing *c* unit cell parameter, resulting in almost independent interatomic distances within the $[B_2C]^{4-}$ ion, which might be expected from the rigid nature of this entity (see Fig. 6.36). These distances are expectedly shorter than those in the B-C framework compounds. There is some small deviation in $YbNi_2B_2C$ and $CeNi_2B_2C$, both of which hold for valence fluctuations and are discussed below.

The coordination of Ni, which modifies the electronic state of the compounds, is nearly tetrahedral as B forms layers of edge-sharing tetrahedral $[NiB_{4/4}]$ (see Fig. 6.32). There are two characteristic B-*M*-B angles to be considered, which are denoted α_1 and α_2 according to Fig. 6.32 and are shown in Fig. 6.37. Both angles are connected by a simple mathematical relation due to the symmetry of *M*. Given the nearly constant distance *d*(B-Ni), the angle α_1 is mainly coupled to the Ni-Ni distance, *d*(Ni-Ni). α_2 also changes with *d*(Ni-Ni) to a smaller extent and gives a measure of the "thickness" of the Ni triple layer sandwiched by B. α_1 in all studied compounds is larger than the ideal tetrahedral angle, while α_2 is smaller. Within the Ni series, the strongest distortion from an ideal tetrahedron is found for the largest rare-earth metal La, and distortion decreases with smaller ionic radii approaching Lu. In compounds with larger rare-earth ions, the tetrahedra become increasingly compressed along the **[001]** direction, concomitant to the increasing *d*(Ni-Ni) distance and only slightly increasing *d*(Ni-B) distance. Exceptions are again observed for the Ce compound with a smaller deviation from the ideal tetrahedral angle than would be expected given the ionic radius of Ce^{3+}. The Yb compound is also an exception and has a slightly larger distortion than expected from Yb^{3+}. The superconducting members with R = Y, Dy, Ho, Er, Tm, and Lu exhibit tetrahedral B_4Ni with $\alpha_1 < 114.5°$ and $\alpha_2 > 107°$, which represent the closest values to the ideal tetrahedral angle of 109.7° within the Ni series. This behavior is somewhat similar to the behavior observed in iron pnictide superconductors. The only exception is the Yb compound with no superconducting transition, but the angles are close to the values in $TmNi_2B_2C$. X-ray absorption spectroscopy at the B-*K* edge revealed significant changes with increasing rare-earth metal size along R = Lu, Tm, Er, Y, Ho, Tb, and Sm, which were interpreted as reflecting increased

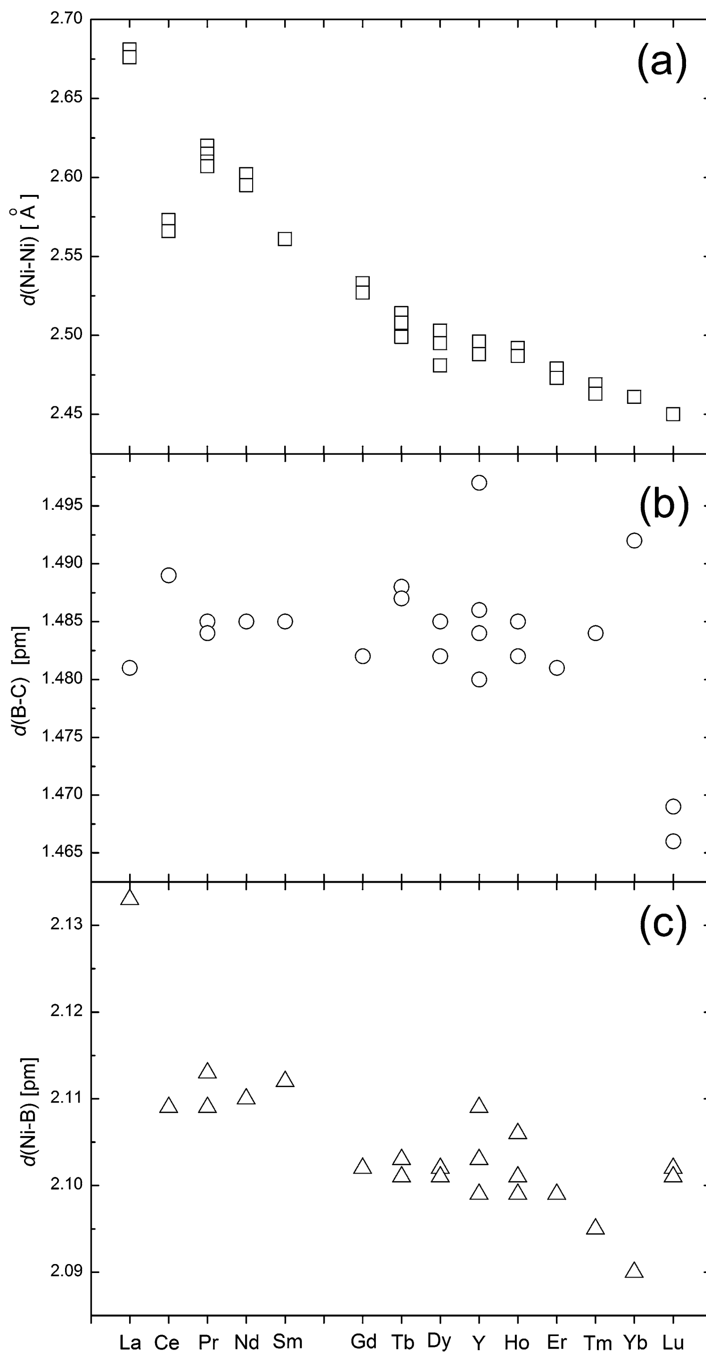

Fig. 6.37 (**a**) The Ni-Ni bond length, (**b**) the B-C bond length, and (**c**) the Ni-B bond length of RNi2B2C are shown for various R. The latter two bond lengths show no R dependence, emphasizing the rigidity of these bonds, in contrast to Ni-Ni bond

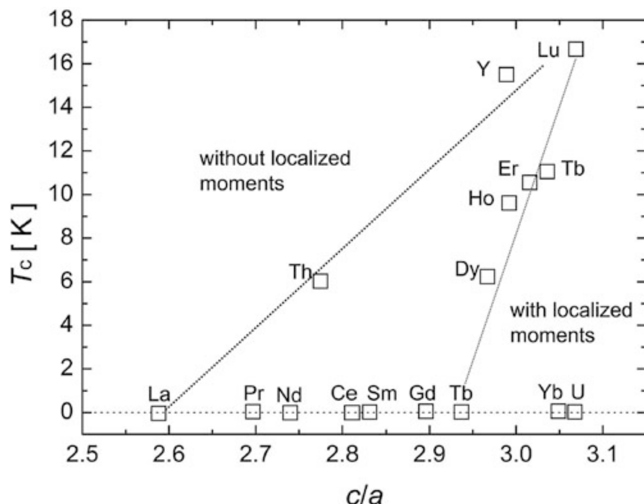

Fig. 6.38 Variation of T_c in $R\mathrm{Ni_2B_2C}$ and its dependence in the *c*/*a* ratio as a measure of the distortion in $\mathrm{NiB_4}$ tetrahedra. Straight lines individually connect the superconductor containing rare-earth metals with and without localized magnetic moments

Table 6.9 T_c and lattice parameters of $R\mathrm{Ni_2B_2C}$ nonmagnetic superconductor and nonsuperconducting $\mathrm{LaNi_2B_2C}$

Material	T_c [K]	*a* [nm]	*c* [nm]
$\mathrm{LuNi_2B_2C}$	16.5	0.3472	1.0658
$\mathrm{YNi_2B_2C}$	15.5	0.3533	1.0566
$\mathrm{ScNi_2B_2C}$	15	0.335	1.068
$\mathrm{ThNi_2B_2C}$	8	~0.370	~1.019
$\mathrm{LaNi_2B_2C}$	No superconductivity	0.38	0.986

deformation of the $\mathrm{B_4Ni}$ tetrahedra along this row [139]. These angles within the $\mathrm{NiB_4}$ tetrahedra being close to the ideal tetrahedral angle were frequently discussed as a relevant prerequisite for superconductivity in borocarbides. For example, in the substitution series $\mathrm{Lu_{1\text{-}x}R_xNi_2B_2C}$ (R = Y, La) with small $x \leq 0.1$, T_c linearly decreases for a given *c*/*a* ratio [140, 141].

Figure 6.38 shows the T_c values in $R\mathrm{Ni_2B_2C}$ compounds as a function of the *c*/*a* ratio using data from the literature. Superconductors containing rare-earth metals with and without localized magnetic moments are individually connected by straight lines. Similar T_c dependencies can be obtained upon plotting against other structural parameters like *d*(Ni-Ni) or internal structural distances between atomic planes, which all somehow depend on the size of R [142]. In the unsubstituted borocarbides of trivalent rare-earth elements, T_c correlates with the ionic radii of R but only in the Pauling system. As was previously discussed, the lattice parameter modulates the majority of the electronic properties of materials in the series, and superconducting properties are strongly tuned by including the appropriate rare-earth element. This is illustrated in Table 6.9 for nonmagnetic $R\mathrm{Ni_2B_2C}$ superconductors.

6.4.1.5 Substitution of *R* in *R*Ni_2B_2C

The majority of RNi_2B_2C materials form an $LuNi_2B_2C$-type structure; thus it is relatively easy to prepare and investigate the pseudoquaternary compounds $(R_{1-x}R'_x)Ni_2B_2C$. It should be noted, however, that for large differences in the ionic radii R^{3+} and R'^{3+}, such as (Lu, La) and (Y, La), there are large miscibility gaps for x around 0.5 [143]. Therefore, data on physical properties, such as T_c, measured for x-values within the gap have only limited significance because the corresponding samples have two phases [106]. In such systems, the superconducting properties are affected by internal stress (connected to strain, sometimes called chemical pressure), as was observed in $(Y_{1-x}La_x)Ni_2B_2C$ [144] and in the mixed magnetic system $(R, R') = (Y, R_{mag})$ or (Lu, R_{mag}) [145]. The complete effect of chemical pressure has not been thoroughly analyzed, yet the R variation results in T_c modulation (see Fig. 6.34). Substitution at either metal site typically reduces T_c due to increasing disorder, as was shown in a number of examples. For example, substitution of $Y_{0.9}R_{0.1}Ni_2B_2C$ decreases T_c by 6 K for $R = Ce$, 5 K for Gd, 1.4 K for Dy, 0.8 K for Ho, 0.4 K for Er, 13 K for Yb, and completely disappears for $R = U$ [138, 141, 146–149]. In some of the metastable phases, such as $ScNi_2B_2C$, the substitution of rare-earth elements stabilizes the structure and is expected to be relevant to $LuNi_2B_2C$-type superconductivity. The superconducting phase is stabilized by approximately tuning the R-site radius, namely, by substituting Y^{3+} (0.90 Å) at the Sc^{3+} (0.73 Å) site, thereby increasing the average R-site radius in the system [150].

Several research groups have investigated compounds with both elements R and R' being nonmagnetic, in particular $(R, R') = (Y, Lu)$ [151–153]. The primary problem relates to how the properties of such mixed systems deviate from those of their two parent systems and from a fictional "gray" system with an "average" or effective R ion in an average lattice. In addition to the lattice parameters, Zarestky et al. found an additional optical phonon mode in mixed $(Lu, Y)Ni_2B_2C$ crystals, which is not present in the parent compound [153].

In the effective "gray" system, the value of T_c is expected to sit on the line connecting the two parental compounds. However, in a real pseudoquaternary system like $Y_xLu_{1-x}Ni_2B_2C$, T_c is considerably lower than the expected line. A non-monotonic dependence on x was observed with a minimum at $x = 0.5$ [141, 151]. This behavior has been attributed to disorder induced by local lattice distortions due to different ionic radii of Y and Lu. Quantitative analysis shows that the sensitivity to site disorder is most pronounced for $H_{c2}(0)$, which will be discussed later, with somewhat weaker sensitivity for T_c. Therefore, the parameter $H_{c2}(0)$ can be considered to be the most sensitive measure of perfection of a clean-limit multiband superconductor.

Systematic doping of rare-earth elements at a Y site was performed in $Y_{1-x}R_xNi_2B_2C$ (R = Er, Ho, Dy, Gd, $0 \leq x \leq 1.0$) compounds [148]. The presence of magnetic ions destroys superconductivity. In general, the suppression of T_c strongly depends on the de Gennes factor $(g_J-1)^2J(J + 1)$, where g_J- is the Lande g factor and J is the total angular momentum of the R^{3+} ion estimated from Hund's

rule for the ground state and the magnetic moments. For a magnetic moment with small de Gennes factor, superconductivity only slightly changes with incorporation of a large number of magnetic ions. The result implies a small but non-negligible exchange coupling between conduction electrons and the localized 4*f* moments. Coupling between conduction electrons and the magnetic moments not only affects superconductivity but also the formation of magnetic ordering. The variation of T_c and T_N with magnetic ion concentration (dT_c/dx and dT_N/dx) can basically be scaled by the de Gennes factor. The small Curie-Weiss temperature also suggests that coupling between R^{3+} moments is not too strong. From this, exchange coupling between R^{3+} moments is attributed to an indirect RKKY-type interaction. The exchange parameter between a conduction electron and a magnetic moment is about 13 meV in this class of quaternary superconductors, which is weak when compared to intermetallic superconductors.

6.4.2 Coexistence with Magnetic Order Reentrant Superconductivity

One of the main features of quaternary borocarbides is, as was described in Sect. 4.1, coexisting magnetic order in a temperature range comparable with superconductivity. The magnetic order temperatures in other previously known magnetic superconductors are relatively low. RRh_4B_4 (R = Pr, Nd, Sm, Tm) exhibits magnetic order below 2 K, such as $PrRh_4B_4$ which has T_c of ~4.6 K and T_N of ~1.8 K [154]. In the case of a few high T_c cuprates ($T_c > 77$ K), magnetic order does occur well below T_c, for example, $GdBa_2Cu_3O_{7-\delta}$ has T_c of ~90 K and T_N of ~2 K [155]. Furthermore, T_N remains the same in $GdBa_2Cu_3O_6$, which is an insulator, showing that conduction electrons play no role in the magnetic transition in this system. In both cases above, magnetic order in the rare-earth plane is somewhat decoupled from the superconducting electrons, which are effectively confined to Cu-O planes in cuprates. Contrary to those materials, quaternary borocarbides have high T_N values, which implies that the magnetic interaction is not due to a direct dipole interaction but is mediated through conduction electrons through the well-known RKKY-type exchange interactions. This raises the question whether conduction electrons also carry magnetism. The question is relevant in the analogy to cuprates due to the $3d^9$ configuration of Ni in the quaternary borocarbides. Furthermore, a band structure calculation shows that the major contribution in the vicinity of the Fermi energy comes from the Ni-derived 3*d* states [156]; however, high-resolution neutron scattering measurements detected no magnetism at Ni sites [136] but rather found magnetic order in *R* ions. Ni atoms with nearly $3d^9$ configuration in RNi_2B_2C do not have a stable moment, which has to do with hybridization.

NMR and muon spin resonance (μSR) studies in nonmagnetic YNi_2B_2C (or $LuNi_2B_2C$) suggest the presence of dynamic fluctuations associated with Ni moments, though no time-averaged finite static Ni moment was detected.

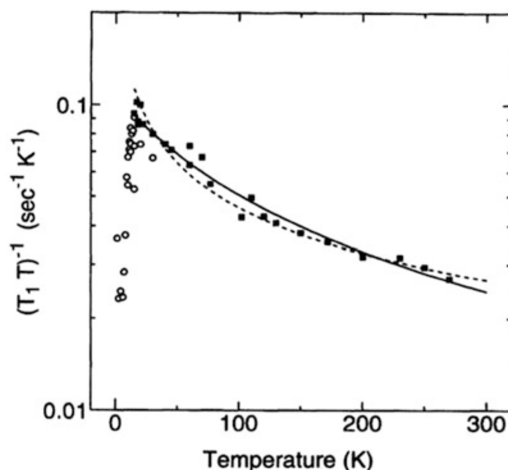

Fig. 6.39 Analysis of the temperature dependence of $(T_1T)^{-1}$ for ^{11}B. Solid squares and open circles are the measured values of relaxation in the normal and superconducting states, respectively [157]

Figure 6.39 shows $(T_1T)^{-1}$ of ^{11}B ($I = 3/2$) nuclei in YNi_2B_2C as a function of temperature deep into the superconducting phase. It is clear that with decreasing temperature, $(T_1T)^{-1}$ is strongly enhanced in the 20–270 K temperature range compared to that given by the Korringa law, which is generally observed in a Fermi liquid. Nearly Curie-Weiss-like behavior of $(T_1T)^{-1}$ arising primarily from the antiferromagnetic spin fluctuation is explained by invoking Moriya's self-consistent renormalization theory [157]. Similar behavior is observed for ^{11}B in $LuNi_2B_2C$ [158], ^{13}C in YNi_2B_2C [159], and ^{61}Ni in $LuNi_2B_2C$ [160]. A hyperfine coupling constant derived from a ^{61}Ni Knight shift is about an order of magnitude smaller than the contributions arising from 3*d* core polarization in transition metals, suggesting moment that is too weak to be detected or no moment at all. These results showing magnetic moments arising from rare-earth elements along with results obtained from neutron scattering measurements are described below.

6.4.2.1 Long-Range Magnetic Order

Magnetic orders in RNi_2B_2C compounds for magnetic R = Dy, Tm, Er, and Ho have been studied, thanks to the comparable energy scale of superconductivity and magnetic order since the discovery of the magnetic superconductivity [96]. Systematic surveys were carried out on compounds that show superconductivity and magnetic order simultaneously [161]. The relatively higher T_N values compared to predecessors suggest magnetic energies are dominated by exchange rather than dipolar (electromagnetic) interactions, while comparable superconducting condensation energies ensure that the interplay between superconductivity and magnetism should be much stronger than was concluding in earlier reports on a comparable energetic footing.

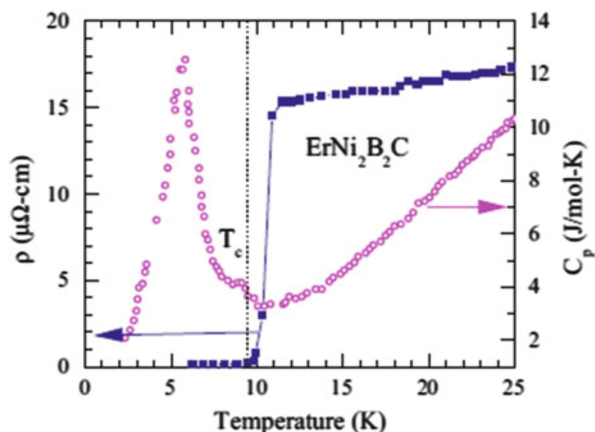

Fig. 6.40 *T*-dependence of resistivity (right axis) and heat capacity (left axis) in $ErNi_2B_2C$. The dashed vertical line indicates T_c. The jump in heat capacity around 6 K indicates magnetic ordering [162] (data taken from [105])

Early studies reported magnetism and magnetic transitions from magnetic susceptibility measurements (e.g., see [161]). The bulk magnetic transition is confirmed by specific heat measurements in various magnetic compounds. Figure 6.40 shows one example, $ErNi_2B_2C$, where T_c is higher than T_N. The large jump in specific heat indicates a magnetic transition below the superconducting transition temperature. Detailed magnetic structure studies were not accessible until high-quality polycrystalline samples or single crystals were available.

The electronic structure calculation in $LuNi_2B_2C$ shows a 3D nature, despite its layered structure [156]. Interest flows toward anisotropy in the magnetic structure of the material. A systematic study on various RNi_2B_2C including nonsuperconducting compounds [136] showed the magnetic structure has variations that depend on *R* (Fig. 6.41).

6.4.2.2 $HoNi_2B_2C$

$HoNi_2B_2C$ is a case where $T_c \sim T_N$ (8 K) [161] that attracts the most interest.

As shown in Fig. 6.42, resistivity versus temperature curves measured at zero magnetic field show a sharp transition into the superconducting state at $T_c \sim 8$ K. Even below T_c, the resistivity shows an anomalous behavior that is called reentrant behavior. Near-reentrant superconductivity is observed for relatively small fields (e.g., 0.13 T for a polycrystalline sample). Considering the T_c and T_N values for $R =$ Er and Tm compounds (see Table 6.7), the behavior does not depend on the value of H in the vicinity of T_N where the reentrant behavior is observed. Therefore, T_N is considered to be some intrinsic temperature indicating a magnetic phase transition.

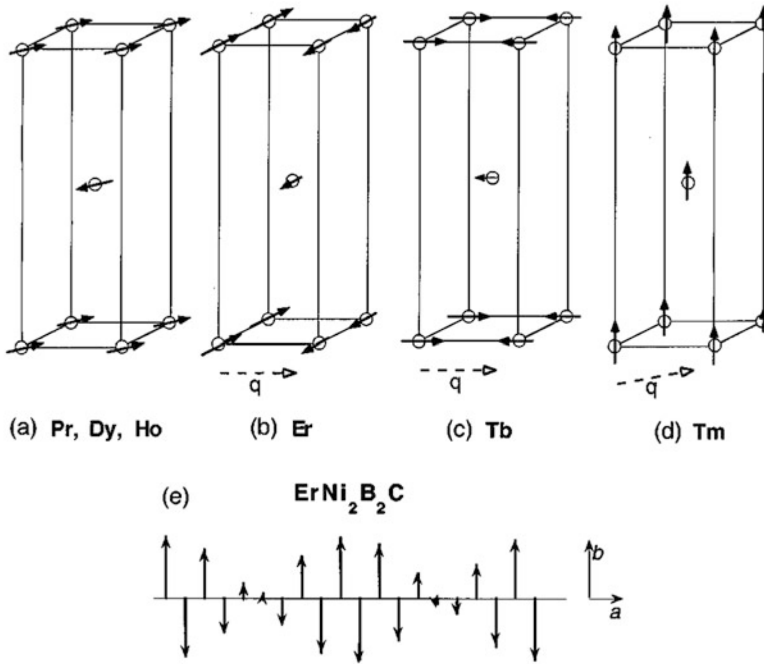

Fig. 6.41 Magnetic structures observed for (**a**) Pr, Dy, and Ho at low *T*, which consists of ferromagnetic sheets of spins in the a-b plane that are coupled antiferromagnetically along the c axis. The wave vector describing the structure is **[001]**. (**b**) Er, which is a transversely polarized spin-density wave with wave vector parallel to **[001]**. (**c**) Tb, which is longitudinally polarized spin-density wave with wave vector along **[100]**. (**d**) Tm, which is a transversely polarized spin-density wave with wave vector along **[110]**. (**e**) Transverse spin-density wave for a-axis modulation in $ErNi_2B_2C$, shown over several unit cells [136]

When investigating $HoNi_2B_2C$, one has to be aware that the magnetic and superconducting properties between T_N and T_c are quite sensitive to the preparation procedure and to small deviations from ideal stoichiometry [131]. The stoichiometric $HoNi_2B_2C$ shows successive magnetic transitions at low temperatures [136]. The behavior is also detected in specific heat measurements. The change corresponds to transitions from commensurate to incommensurate antiferromagnetic order. This behavior was thoroughly studied with neutron scattering measurements. Spiral modulation along the *c*-axis is detected in the intermediate temperature region between two different magnetic transition temperatures. This kind of structure is obtained due to crystalline electric fields and the RKKY interaction, thus supporting the picture of ferromagnetic sheets. Furthermore, an *a*-axis modulated incommensurate magnetization structure is observed in a small temperature range above T_N. This behavior is described in Fig. 6.43.

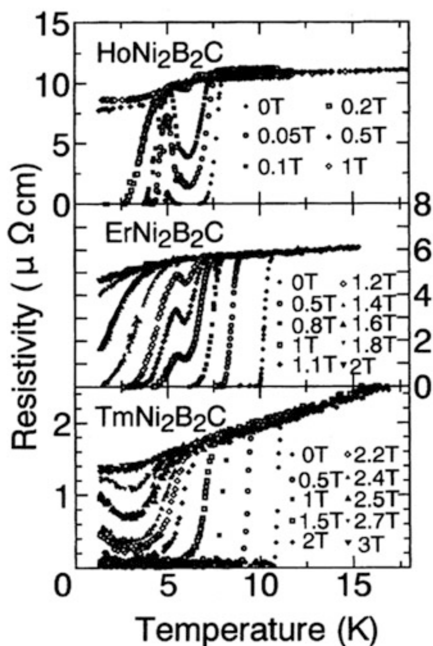

Fig. 6.42 T-dependent resistivities under various magnetic fields in $HoNi_2B_2C$, $ErNi_2B_2C$, and $TmNi_2B_2C$. Characteristic structures due to the magnetic modulations are observed below T_c [161]

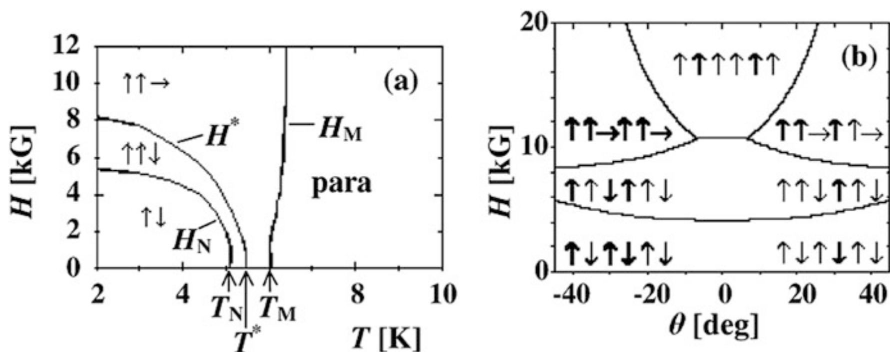

Fig. 6.43 Magnetic phase diagrams of $HoNi_2B_2C$. (**a**) Field applied along the tetragonal a-axis. Arrows indicate the magnetic structure. (**b**) Phase diagram at T = 2 K, where the vertical axis is the magnetic field and the horizontal is the angle of the field with the respect to the nearest magnetically easy [115] direction [143]

6.4.2.3 $ErNi_2B_2C$

$ErNi_2B_2C$ has lower T_N than T_c. The magnetic transition occurs at 6.8 K in a transversely polarized spin-density wave with modulation vector (0.55, 0, 0) parallel to the a-axis and the Er magnetic moments parallel to b (or vice versa) [163]. Coexistence of magnetism and superconductivity was first found in $ErNi_2B_2C$ crystals via small-angle neutron scattering measurements [164].

In addition to antiferromagnetic order coexisting with superconductivity, there are indications of weak ferromagnetism at lower temperatures [165]. This is discussed in relation with phonon behavior, but the overall behavior induced by the ferromagnetic order arose in the presence of magnetic fields. This behavior is entangled with the magnetophonon dispersion that compensates the suppressed phonon behavior along with the suppression of superconductivity.

6.4.3 Band Structure

Since the discovery of superconductivity coexisting with long-range magnetic orders, there is interest focused on the coupling of Cooper pairs and the exotic superconducting mechanism. Early electronic structure calculations suggested a simple BCS electron-phonon coupling can explain the superconductivity [156]. They showed that the DOS at the Fermi energy is mostly contributed from Ni (Fig. 6.44). This agrees well with the Mössbauer measurement showing that conduction occurs in Ni-B layers in Fe-doped $ReNi_2B_2C$ [166]. Despite the layered structure and its similarity to cuprate superconductors, the electronic state is reported to be 3D. This isotropic behavior is observed on $R\mathrm{Ni}_2\mathrm{B}_2\mathrm{C}$ (R = Y, Ho, Er, Lu) single crystals from electric resistivity measurements in their normal state [167]. They also reported small deviation from isotropic behavior above 150 K in R = Er and Ho compounds, suggesting crystal-electric field interaction effects. In magnetic compounds with R = Er and Ho, the in-plane resistivity shows the same temperature dependence as the nonmagnetic compounds, with an extra temperature-independent term. This is expected to be a perturbation that originates from magnetic buffer layers. Three-dimensionality is also presented in the compressibility of electronic states under pressure [168].

In addition to coexisting magnetic order and superconductivity, quaternary borocarbide superconductors are discussed as candidates for exotic superconducting pairing. Originally, this material was discussed as a simple phonon-mediated *s*-wave superconductor [169, 170]. Subsequent thermodynamic measurements show deviation from the single band BCS mechanism and have led to different suggestions. These include *s*- or *d*-wave [171] or $s + g$-wave pairing obtained from the anisotropic gap structure detected in point-contact measurements [172]. Led by rather elaborate Fermi surfaces with open and closed sheets [156, 173–175], multiband behavior was suggested [176–181]. This anisotropic superconducting gap structure was studied over a wide range of materials at various temperatures. YNi_2B_2C was studied via point-contact spectroscopy, and the material exhibits a fully gapped structure along the *c* direction and sharp minima in the basal plane, consistent with the $s + g$ symmetry [172]. Measurements of de Haas-van Alphen oscillations in $LuNi_2B_2C$ single crystals revealed that the multiband contributions are present in the detected signals [182]. They also performed angular-dependent measurements using the cyclotron mass (m_{exp}) obtained from the signal well above the critical field in the normal state using the Lifshitz-Kosevich (LK)

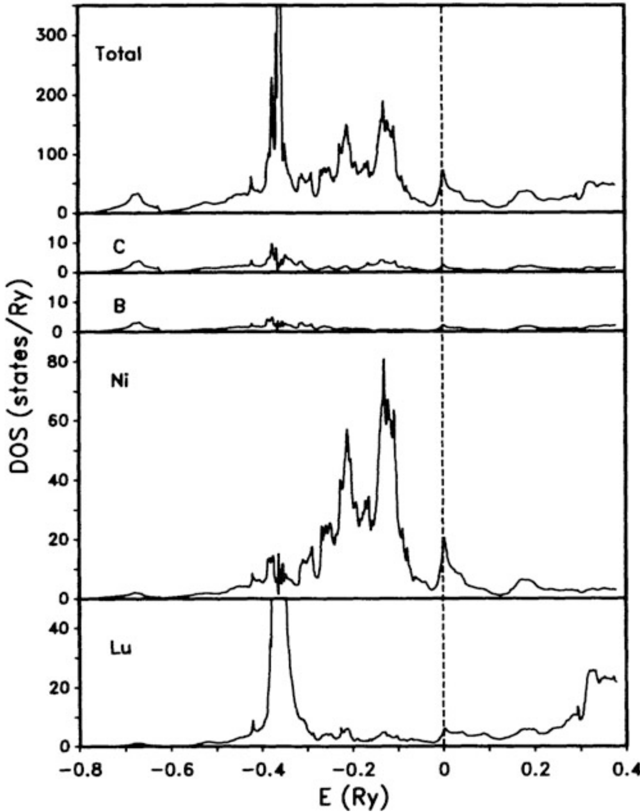

Fig. 6.44 Total- and site-projected DOS in $LuNi_2B_2C$. The prominent peak at the Fermi energy (zero energy) has Lu, B, and C character complementing the strong Ni *d* character. The peak at approximately −0.35 Ry is from the Lu $5f$ bands [156]

formula. They could derive the anisotropy of the bands by comparing the obtained data and calculated data estimated from the model proposed by theorists (Fulde-Ferrell-Larkin-Ovchinnikov) (m_{FFLO}). The band-resolved angular dependence of the anisotropic deviation in mass ($\lambda = m_{exp}/m_{FFLO}$-1) was obtained and is expected to be directly related to the Cooper-pairing coupling parameter. For all three bands that contribute to the physical properties, different bands revealed different coupling strengths, although there may be some unsolved anisotropy due to the use of quasi-classical LK analysis [182].

6.4.4 Phonon Scattering

Inelastic neutron scattering experiments in single-crystal $YNi_2{}^{11}B_2C$ (to avoid the absorption of neutrons by ^{10}B) revealed not only a gradual phonon softening

observed in elastic neutron scattering diffraction but also enhanced sharp phonon peaks below T_c in the transverse acoustic branch [183]. The intensity of the observed peaks strongly depends on the magnetic field and vanishes at H_{c2}, which is perceived as clear evidence of a phonon mode related to electron-phonon coupling, superconductivity. Moreover, the energy of the peak ($\approx$ 4.0 meV) is close to the superconducting gap as estimated from BCS theory. We should note that the temperature dependence of the peak position is found to be weaker than what one would expect from BCS theory.

Strong electron-phonon coupling suggests BCS-like *s*-wave superconductivity in these materials. The aforementioned strongly anisotropic superconductivity gap, which is unusual for conventional s-wave superconductors, indicates a complex pairing mechanism that involves both antiferromagnetic and electron-phonon interactions. To investigate the idea, Yanson et al. performed point-contact spectroscopy in $R\mathrm{Ni_2B_2C}$ with R = La, Y, and Ho for nonsuperconducting, nonmagnetic superconducting, and magnetic superconducting compounds. They obtained spectra showing strong electron-phonon interaction in the compounds, but the coupling followed the order La < Y < Ho. Thus, they could derive the importance of electron-phonon interaction. They also reported the interaction is enhanced in the magnetic fields [98].

6.4.5 *YB_2C_2*

6.4.5.1 Introduction

Extensive studies of crystal structure and physical properties in rare-earth diborocarbide compounds RB_2C_2 were reported by Sakai et al. and Bauer et al. in the 1980s [184–186]. They proposed the crystal structure in RB_2C_2 has *P-42c* symmetry, which consists of R and BC layers as shown in Fig. 6.45a. As for the magnetic properties, an antiferromagnetic transition was observed in RB_2C_2 (R = Ce, Nd,

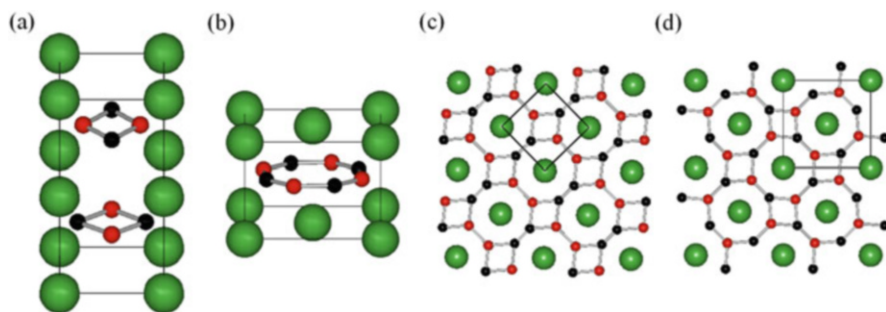

Fig. 6.45 Crystal structure of RB_2C_2 with (**a**), (**c**) *P-42c* and (**b**), (**d**) *P4/mbm* symmetry. Red and black atoms correspond to B and C atoms, respectively

Sm, Gd, Tb, Er, and Tm) compounds, and superconductivity was found in YB_2C_2 (T_c = 3.6 K) and LuB_2C_2 (T_c = 2.4 K). However, neutron powder diffraction studies suggested that RB_2C_2 crystallizes in the same LaB_2C_2-type crystal structure with *P4/mbm* symmetry, as shown in Fig. 6.45b [187, 188]. The crystal structure difference between *P-42c* and *P4/mbm* symmetry is due to the arrangement of B and C atoms in the network. Theoretical calculations also supported the result that the structure with *P4/mbm* symmetry is much more stable than the originally claimed *P-42c* symmetry [189]. Moreover, Michor et al. reinvestigated the superconducting properties of YB_2C_2 and discovered a superconducting transition at 1.0 K [190].

In this review, we focus on recent experimental and theoretical results regarding the physical properties of YB_2C_2 and the superconductivity of YB_2C_2, which can be explained within the weak-coupling BCS framework.

6.4.5.2 Physical Properties of YB_2C_2

Sakai et al. reported that YB_2C_2 (tetragonal CaC_2 type) was found to be superconducting at 3.6 K [184]. However, the T_c value in YC_2 varies from 4.02 K to 2.85 K due to the local carbon defects, and this T_c value is very close to T_c in YB_2C_2 [48]. Recently, Michor et al. fabricated clean single-phase YB_2C_2 samples and reinvestigated the superconducting properties of this material [190].

Figure 6.46a shows the specific heat of YB_2C_2. A sharp bulk superconducting transition can be seen at 1.0 K. The specific heat anomaly at T_c $\Delta C_p/T \sim$ 4.5 mJ/molK^2 and the normal-state specific heat with linear-T electronic Sommerfeld coefficient $\gamma = 3.15(5)$ mJ/molK^2 yield the thermodynamic ratio $\Delta Cp/(\gamma_n T_c)$

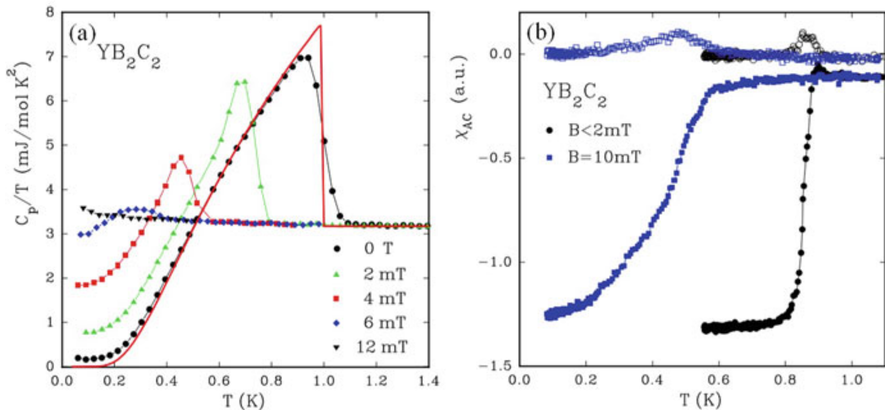

Fig. 6.46 (**a**) C_p vs T in YB_2C_2. The solid red line shows a fit to the BCS model. (**b**) Temperature-dependent real part χ' (full symbols) and imaginary part χ'' (open symbols) of the AC susceptibility in YB_2C_2 measured at an AC field amplitude of about 1 mT and superimposed DC fields as labeled [190]

~1.43. In fact, the zero-field specific heat result can be explained using the weak-coupling BCS theory. Figure 6.44b shows AC susceptibility measurements in YB_2C_2. The slightly lower value of $T_c = 0.85$ K measured in a zero field is attributed to a small remanent field (1~2 mT).

In order to estimate the electron-phonon coupling constant λ, they discussed the value of λ using the McMillan theory. Taking the experimental value of $T_c = 1.0$ K and $\Theta_D = 680$ K (estimated from heat capacity measurements) and assuming a typical value $\mu^* = 0.13$, the McMillan formula yields $\lambda = 0.4$. This value is not strong compared to other strong electron-phonon coupling materials like MgB_2 ($\lambda = 0.7 \sim 0.9$).

6.4.5.3 Theoretical Calculations of Structural Stability and Band Structure in YB_2C_2

Khmelevsky et al. calculated the structural stability and electronic structure of superconducting YB_2C_2 using the full-potential LAPW method within the framework of ab initio density functional theory [189]. From the calculated total energy for both *P-42c* and *P4/mbm* structures, it was found that the structure with *P4/mbm* symmetry is much more stable than the originally claimed *P-42c* symmetry. The total energy difference between both materials is 1.35 eV/fu. They also optimized the structural parameters and found that the displacements from the claimed experimental values [184] were 0.007 nm for the optimized *P-42c* geometry, while optimizing the parameters for the *P4/mbm* structure leads to nearly perfect agreement with the initially estimated values [187] (differences <0.001 nm). Thus, they concluded that the LaB_2C_2-type crystal structure with *P4/mbm* symmetry is the plausible model to describe YB_2C_2.

Figure 6.47 shows the calculated total and atom-resolved DOS in YB_2C_2. In the case of MgB_2, the partial occupancy of boron in the p_{xy} band leads to a high density

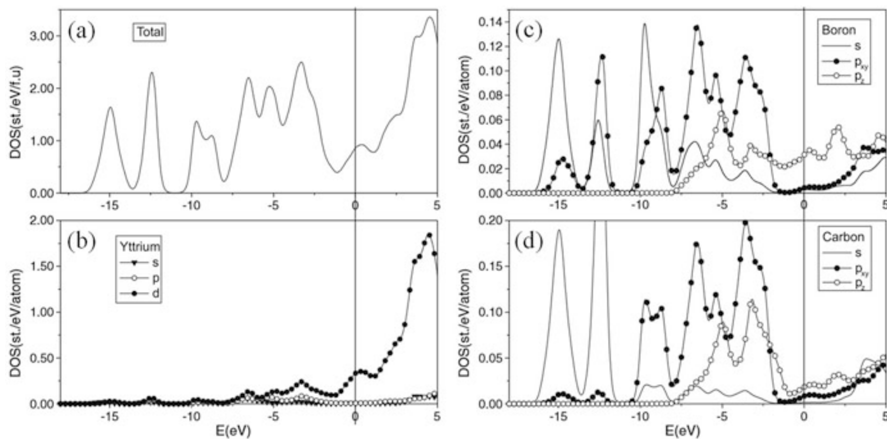

Fig. 6.47 (**a**) Total density states in YB_2C_2 with *P4/mbm* geometry. (**b–d**) Atomic- and orbital-resolved densities of states [189]

of states at the Fermi level [56]. On the other hand, the p_{xy} states of B and C in YB_2C_2 are nearly absent at the Fermi level (Fig. 6.47c,d). The main contribution to $N(E_F)$ comes from Y d-bands, which are weakly hybridized with p_z-states from the B_2C_2 planes (Fig. 6.47b). This result suggests that superconductivity in YB_2C_2 primarily originates from Y d-bands.

6.5 Conclusion

We have reviewed superconductivity in carbide compounds, whose T_cs are unfortunately limited in the 10 K to 20 K range. During the development of these superconductors, we focused on high-frequency phonons induced by the incorporation of a light element. The maximum T_c value in sesquicarbides and wide band-gap semiconductors are currently 18 K and 11 K, respectively. Thus, other routes must be sought for the development of new high-T_c superconductors. Recently, much attention has focused on the new superconductor H_3S ($T_c \backsimeq 200$ K) at ultrahigh pressure ($200 \backsimeq$GPa), which can be described by the BCS theory. This probably shows that light element superconductors provide one of the most promising paths to a room-temperature superconductor by taking account of the relationship between electronic states and bonding states.

References

1. H.K. Onnes, Akad. van Wetenschappen **14**, 113 (1911)
2. Y.-X. Zhao, S. He, Solid State Commun. **45**, 281 (1983)
3. L.E. Toth, *Transition Metal Carbides and Nitrides* (Academic Press, New York, 1971)
4. J.K. Hulm, R.D. Blaugher, AIP Conf. Proc. **4**, 1 (1972)
5. K.S. Keskar, T. Yamashita, Y. Onodera, Jpn. J. Appl. Phys. **10**, 370 (1971)
6. B.T. Matthias, Phys. Rev. **92**, 874 (1953)
7. M.W. Williams, K.M. Ralls, M.R. Pickus, J. Phys. Chem. Solids **28**, 333 (1966)
8. L.E. Toth, *Transition Metal Carbides and Nitrides* (Elsevier, Saint Louis, 2014)
9. Zhao You-Xiang, He Shou-an, in *High Pressure in Science and Technology*, **22**, North Holland, 51 (1983)
10. B.W. Roberts, J. Phys. Chem. Ref. Data **5**, 581–821 (1976)
11. J.M. Vandenberg, B.T. Matthias, Mat. Res. Bull. **9**, 1085 (1974)
12. R.H. Williens, E. Buehler, Appl. Phys. Lett. **7**, 25 (1965)
13. R.H. Williams, E. Buehler, B.T. Matthias, Phys. Rev. **159**, 327 (1967)
14. E.M. Savitskii, V.V. Baron, Y.V. Efimov, M.I. Bychkova, L.F. Myzenkova, *Superconducting Materials*, vol 107 (Plenum Press, New York, 1981)
15. P. Villars, L.D. Calvert, *Pearson's Handbook of Crystallographic Data for Intermetallic Phases*, vol 1–3 (ASM, Cleveland, 1985)
16. N. Pessall, J.K. Hulm, M.S. Walker, Westinghouse Research Laboratories, Final Rep. AF **33**(615), 2729 (1967)
17. T. Amriou, B. Bouhafs, H. Amourag, B. Khelifa, S. Bresson, C. Mathieu, Physica B **325**, 46 (2003)
18. K. Schwarz, J. Phys. C Solid State Phys. **8**, 809 (1975)

19. H.W. Hugosson, L. Nordström, U. Jansson, B. Johansson, O. Eriksson, Phys. Rev. B **60**, 15123 (1999)
20. W.E. Pickett, B.M. Klein, D.A. Papaconstantopoulos, Physica B **107**, 667 (1981)
21. H. Ihara, K. Senzaki, Y. Kimura, M. Hirabayashi, N. Terada, Advance. Cryo. Engin. **32**, 603–616 (1986)
22. G. Linker, R. Smithey, O. Meyer, J. Phys. F **14**, L115 (1984)
23. P. Roedhammer, E. Gmelin, W. Weber, J.P. Remeika, Phys. Rev. B **15**, 711 (1977)
24. D. Dew-Hughes, R. Jones, Appl. Phys. Lett. **36**, 856 (1980)
25. J.R. Gavaler, A.T. Santhanam, A.I. Braginski, M.A. Janacko, IEEE Trans. Magn. **MAG 17**, 573 (1981)
26. J.R. Gavaler, M.A. Janacko, A. Patterson, C.K. Jones, J. Appl. Phys. **42**, 54 (1971)
27. K.E. Gray, R.T. Kampwirth, D.W. Capone, R. Vaglio, Physica B+C **135**, 164 (1985)
28. F. Shinoki, A. Shoji, S. Kosaka, S. Takada, H. Hayakawa, Appl. Phys. Lett. **38**, 285 (1981)
29. V.L. Gurevich, A.I. Larkin, Y.A. Firsov, Sov. Phys. Solid State **4**, 185 (1962)
30. M.L. Cohen, Rev. Mod. Phys. **36**, 240 (1964)
31. E.A. Ekimov, V.A. Sidorov, E.D. Bauer, N.N. Mel'nik, N.J. Curro, J.D. Thompson, S.M. Stishov, Nature **428**, 542 (2004)
32. Y. Takano, T. Takenouchi, S. Ishii, S. Ueda, T. Okutsu, I. Sakaguchi, H. Umezawa, H. Kawarada, M. Tachiki, Diam. Relat. Mater. **16**, 911 (2007)
33. H. Fukuyama, J. Supercond. Nov. Magn. **19**, 201 (2006)
34. Z.A. Ren, J. Kato, T. Muranaka, J. Akimitsu, M. Kriener, Y. Maeno, J. Phys. Soc. Jpn. **76**, 103710 (2007)
35. N.G. Wright, A.B. Horsfall, K. Vassilevski, Mater. Today **11**, 16 (2008)
36. T. Muranaka, Y. Kikuchi, T. Yoshizawa, N. Shirakawa, J. Akimitsu, Sci. Technol. Adv. Mater. **9**, 044204 (2008)
37. A.F. Da Silva, J. Pernot, S. Contreras, B.E. Sernelius, C. Persson, J. Camassel, Phys. Rev. B **74**, 245201 (2006)
38. M. Kriener, Y. Maeno, T. Oguchi, Z.-A. Ren, J. Kato, T. Muranaka, J. Akimitsu, Phys. Rev. B **78**, 024571 (2008)
39. J. Noffsinger, F. Steven, S.G. Lovie, M.L. Cohen, Phys. Rev. B **79**, 104511 (2009)
40. H. J. Fink, D. S. Mclachlan, B. Rothberg-Bibby*, Progress in Low Temperature Physics,* ed. By D. F. Brewer (North-Holland, Amsterdam, Vols. VIIB, Chap. 6) (1978).
41. S. Yonezawa, Y. Maeno, Phys. Rev. B **72**(180), 504 (2005)
42. M. Kriener, T. Muranaka, Z.-A. Ren, J. Kato, J. Akimitsu, Y. Maeno, J. Phys.: Conf. Ser. **150**, 052130 (2009)
43. J. Feder, Solid State Comm. **5**, 299 (1967)
44. V.I. Marchenko, E.R. Podolyak, Sov. Phys. JETP **97**, 154 (2003)
45. M. Atoji, J. Chem. Phys. **35**, 1950 (1961)
46. M. Knapp, U. Ruschewitz, Chemistry **7**, 874 (2001)
47. A.L. Giorgi, E.G. Szklarz, M.C. Krupka, T.C. Wallace, N.H. Krikorian, J. Less-Common Met. **14**, 247 (1968)
48. T. Gulden, R.W. Henn, O. Jepsen, R.K. Kremer, W. Schnelle, A. Simon, C. Felser, Phys. Rev. B **56**, 9021 (1997)
49. R.W. Green, E.O. Thorland, J. Croat, S. Legvold, J. Appl. Phys. **40**, 3161 (1969)
50. T. Sakai, G. Adachi, T. Yoshida, J. Shiokawa, J. Less-Common Met. **81**, 91 (1981)
51. V. Babizhetskyy, O. Jepsen, R.K. Kremer, A. Simon, B. Ouladdiaf, A. Stolovits, J. Phys.: Condens. Matter **26**, 025701 (2014)
52. M.C. Krupka, A.L. Giorgi, N.H. Krikorian, E.G. Sklarz, J. Less-Common Met. **19**, 113 (1969)
53. H. Padamsee, J.E. Neighbor, C.A. Shiffman, J. Low Temp. Phys. **12**, 387 (1973)
54. W.L. McMillan, Phys. Rev. **167**, 331 (1968)
55. H.M. Tütüncü, G.P. Srivastava, Journal of Applied Physics **117**(153), 902 (2015)
56. J. Kortus, I.I. Mazin, K.D. Belashchenko, V.P. Antropov, L.L. Boyer, Phys. Rev. Lett. **86**, 4656 (2001)

57. R. Osborn, E.A. Goremychkin, A.I. Kolesnikov, D.G. Hinks, Phys. Rev. Lett. **87**, 017005 (2001)
58. A. Simon, Angew. Chem. Int. Edn Engl. **36**, 1788 (1997)
59. X. Wang, I. Loa, K. Syassen, R.K. Kremer, A. Simon, M. Hanfland, K. Ahn, Phys. Rev. B **72**, 064520 (2005)
60. A.L. Giorgi, E.G. Szklarz, M.C. Krupka, N.H. Krikorian, J. Less-Common Met. **17**, 121 (1969)
61. M.C. Krupka, A.L. Giorgi, N.H. Krikorian, E.G. Szklarz, J. Less-Common Met. **17**, 91 (1969)
62. R. K. Kremmer, J. S. Kim et al., in *High Tc Superconductors and Related Transition Metal Oxides*, ed. By A. Bussmann-Holder, H Keller (Springer, Berlin/Heidelberg, 2007) pp 213–226.
63. K.A. Gschneidner Jr., F.W. Calderwood, Bull. All. Phase Diag. **7**, 421 (1986)
64. V.I. Novokshnov, J. Inorg. Chem. **25**, 375 (1980)
65. F.H. Spedding, K. Gschneidener Jr., A.H. Daane, J. Am. Chem. Soc. **80**, 4499 (1958)
66. A. Simon, T. Gulden, Z. Anorg. Allg. Chem. **630**, **2191** (2004)
67. T.L. Francavilla, F.L. Carter, Phys. Rev. B **14**, 128 (1976)
68. J.S. Kim, W. Xie, R.K. Kremer, V. Babinzhetskyy, O. Jepsen, A. Simon, K.S. Ahn, B. Raquet, H. Rakoto, J.-M. Broto, B. Ouladdiaf, Phys. Rev. B **76**, 014516 (2007)
69. J.P. Carbotte, Rev. Mod. Phys. **62**, 1027 (1990)
70. D.J. Singh, I.I. Mazin, Phys. Rev. B **70**, 052504 (2004)
71. R.W. Henn, T. Strach, R.K. Kremer, A. Simon, Phys. Rev. B **58**, 14364 (1998)
72. K. Sugawara, T. Sato, S. Souma, T. Takahashi, A. Ochiai, Phys. Rev. B **76**, 132512 (2007)
73. A. Potočnik, P. Jeglič, K. Kobayashi, K. Kawashima, S. Kuchida, J. Akimitsu, D. Arčon, Phys. Rev. B **90**, 104507 (2014)
74. G. Amano, S. Akutagawa, T. Muranaka, Y. Zenitani, J. Akimitsu, J. Phys. Soc. Jpn. **73**, 530 (2004)
75. T. Mochiku, T. Nakane, H. Kito, H. Takeya, S. Harjo, T. Ishigaki, T. Kamiyama, T. Wada, K. Hirata, Physica C **426–431**, 421 (2005)
76. T. Nakane, T. Mochiku, Appl. Phys. Lett. **84**, 2859 (2004)
77. I.R. Shein, A.L. Ivanovskii, Solid State Commun. **131**, 223 (2004)
78. S. Kuroiwa, Y. Sauma, J. Akimitsu, M. Hiraishi, M. Miyazaki, K.H. Satoh, S. Takeshita, R. Kadono, Phys. Rev. Lett. **100**, 097002 (2008)
79. Y. Nishiyama, T. Shishidou, T. Oguchi, J. Phys. Soc. Jpn. **76**, 064714 (2007)
80. X.-P. Gao, Y.-H. Jiang, R. Zhou, J. Feng, J. Alloy. Comp. **587**, 819 (2014)
81. H.Q. Yuan, J. Chen, J. Singleton, S. Akutagawa, J. Akimitsu, J. Phys. Chem. Solids **72**, 577 (2011)
82. B. Cort, G.R. Stewart, A.L. Giorgi, J. Low Temp. Phys. **54**, 149 (1984)
83. S. Akutagawa, J. Akimitsu, J. Phys. Soc. Jpn. **76**, 024713 (2007)
84. T. Ekino, A. Sugimoto, A.M. Gabovich, H. Kinoshita, J. Akimitsu, Physica C **484**, 52 (2013)
85. A. Harada, S. Akutagawa, Y. Miyamichi, H. Mukuda, Y. Kitaoka, J. Akimitsu, J. Phys. Soc. Jpn. **76**, 023704 (2007)
86. J. Chen, M.B. Salamon, S. Akutagawa, J. Akimitsu, J. Singleton, J.L. Zhang, L. Jiao, H.Q. Yuan, Phys. Rev. B **83**(144), 529 (2011)
87. C. Chen and B. Jin, ArXiv:1608.01190v1 (2016).
88. Y. Nishikayama, T. Shishido, T. Oguchi, J. Phys. Soc. Jpn. **76**, 064714 (2007)
89. M.C. Krupka, A.L. Giorgi, E.G. Szklarz, J. Less-Common Met. **30**, 217 (1973)
90. T.L. Francavilla, F.L. Carter, A.W. Webb, Phys. Lett. A **59**, 388 (1976)
91. A.L. Giorgi, E.G. Szklarz, N.H. Krikorian, M.C. Krupka, J. Less-Common Met. **22**, 131 (1970)
92. M.C. Krupka, J. Less-Common Met. **20**, 135 (1970)
93. I.A. Sergienko, Physica B **581**, **359**–**361** (2004)
94. C. Mazumdar et al., Solid State Commun. **87**, 413 (1993)
95. R. Nagarajan et al., Phys. Rev. Lett. **72**, 274 (1994)

96. R.J. Cava, H. Takagi, B. Batlogg, H.W. Zandbergen, J.J. Krajewski, W.F. Peck Jr., R.B.v. Dover, R.J. Felder, T. Siegrist, K. Mizuhashi, J.O. Lee, H. Eisaki, S.A. Carter, S. Uchida, Nature **367**, 146 (1994)
97. T. Siegrist, H.W. Zandbergen, R.J. Cava, J.J. Krajewski, W.F. Peck Jr., Nature **367**, 254 (1994)
98. I.K. Yanson, V.V. Fisun, A.G.M. Jansen, P. Wyder, P.C. Canfield, B.K. Cho, C.V. Tomy, D.M.K. Paul, Phys. Rev. Lett. **78**, 935 (1997)
99. M. Xu, P.C. Canfield, J.E. Ostenson, D.K. Finnemore, B.K. Cho, Z.R. Wang, D.C. Johnston, Physica C **227**, 321 (1994)
100. R.J. Cava, H.W. Zandbergen, B. Batlogg, H. Eisaki, H. Takagi, J.J. Krajewski, W.F. Peck Jr., E.M. Gyorgy, S. Uchida, Nature **372**, 245 (1994)
101. P.C. Canfield, P.L. Gammel, D.J. Bishop, Phys. Today **10**, 40 (1998)
102. R. Niewa, L. Shlyk, B. Blaschkowski, Z. Kristallogr. **226**, 352 (2011)
103. L.C. Gupta, Adv. Phys. **55**, 691 (2006)
104. N.H. Andersen, J. Jensen, T.B.S. Jensen, M.v. Zimmermann, R. Pinholt, A.B. Abrahamsen, K.N. Toft, P. Hedegård, P.C. Canfield, Phys. Rev. B **73**, 02504 (2006)
105. C. Godart, L.C. Gupta, R. Nagarajan, S.K. Dhar, H. Noel, M. Potel, C. Mazumdar, Z. Hossain, C. Levy-Clement, G. Schiffmacher, B.D. Padalia, R. Vijayaraghavan, Phys. Rev. B **51**, 489 (1995)
106. C.C. Lai, M.S. Lin, Y.B. You, H.C. Ku, Phys. Rev. B **51**, 420 (1995)
107. F.S. Jeng, Y.B. You, H.C. Ku, Phys. Rev. B **53**, 3492 (1996)
108. R.J. Cava, H. Takagi, B. Batlogg, H.W. Zandbergen, J.J. Krajewski, W.F. Peck Jr., R.B. van Dover, R.J. Felder, T. Siegrist, K. Mizuhashi, J.O. Lee, H. Eisaki, S.A. Carter, S. Uchida, Nature **367**, 146 (1994)
109. L.-S. Hsu, Y.K. Wang, G.Y. Guo, Y.-J. Huang, M.-D. Lan, Mat. Res. Soc. Symp. Proc. **731**, W8.13 (2002)
110. Z. Hossain, C. Geiber, L.C. Gupta, R. Nagarajan, C. Godart, J. Phys. Condens. Matter **14**, 7045 (2002)
111. V. Ström, K.S. Kim, A.M. Grishin, K.V. Rao, J. Mater. Res. **11**, 572 (1995)
112. L.C. Gupta, R. Nagarajan, Z. Hossain, C. Mazumdar, S.K. Dhar, C. Godart, C. Levy-Clement, B.D. Padalia, R. Vijayaraghavan, J. Mag. Mag. Mat. **140–141**, 2053 (1995)
113. P.J. Jiang, M.S. Lin, J.H. Shieh, Y.B. You, H.C. Ku, J.C. Ho, Phys. Rev. B **51**, 16436 (1995)
114. L.M. Dezaneti, Y.Y. Xue, Y.Y. Sun, K. Ross, C.W. Chu, Physica C **334**, 123 (2000)
115. H. Bitterlich, W. Löser, G. Behr, Matt. Lett. **57**, 59 (2002)
116. G. Ghosh, A.D. Chinchure, R. Nagarajan, C. Godart, L.C. Gupta, Phys. Rev. B **63**, 212505 (2001)
117. J.L. Sarrao, M.C. de Andrade, J. Herrmann, S.H. Han, Z. Fisk, M.B. Maple, R.J. Cava, Physica C **229**, 65 (1994)
118. R.J. Cava, B. Batlogg, T. Sigrist, J.J. Krajewski, W.F. Peck Jr., S. carter, R.J. Felder, H. Takagi, R.B. van Dover, Phys. Rev. B **49**, 12384 (1994)
119. R.J. Cava et al., Physica C **226**, 170 (1994)
120. M. Buchgeister, G. Fuchs, J. Klosowski, U. Wiesner, J. Zawadzki, Physics C **255**, 19 (1995)
121. P.L. Paulose, S.K. Dhar, A.D. Chinchure, E. Alleno, C. Godart, L.C. Gupta, R. Nagarajan, Physica C **399**, 165 (2003)
122. Y.Y. Hsu, H.C. Chiang, H.C. Ku, J. Appl. Phys. **83**, 6789 (1998)
123. R.J. Cava, H. Takagi, H.W. Zandbergen, J.J. Krajewski, W.F. Peck Jr., T. Siegrist, B. Batlogg, R.B. van Dover, R.J. Felder, K. Mizuhashi, J.O. Lee, H. Eisaki, S. Uchida, Nature **367**, **252** (1994)
124. S.B. Roy, Z. Hossain, A.K. Pradhan, C. Mazumdar, P. Chaddah, R. Nagarajan, C. Godart, L.C. Gupta, Physica C **228**, 319 (1994)
125. J.S. Kim, W.W. Kim, G.R. Stewart, Phys. Rev. B **50**, 3485 (1994)
126. B.C. Chakoumakos, M. Paranthaman, Physica C **227**, 143 (1994)
127. C.S. Sundar, A. Bharanthi, Y. Hariharan, T.S. Radhakrishanan, Z. Hossain, R. Nagarajan, L.C. Gupta, R. Vijayaraghavan, Phys. Rev. B **53**, R2971 (1996)

128. A. Belger, U. Jaenicke-Rössler, D. Lipp, B. Wehner, P. Paufler, G. Behr, Physica C **306**, 277 (1998)
129. H. Szillat, H. Kuhn, T. Schuster, P. Majewski, M. Seeger, F. Aldinger, H. Kronmüller, Physica C **280**, 43 (1997)
130. A. Lascialfari, T. Mishonov, A. Rigamonti, I. Zucca, G. Behr, W. Loser, S.L. Drechsler, Eur. Phys. J. B **35**, 325 (2003)
131. A. Dertinger, R.E. Dinnebier, A. Kreyssig, P.W. Stephens, S. Pagola, M. Loewenhaupt, S. Van Smaalen, H.F. Braun, Phys. Rev. B **63**(184), 518 (2001)
132. Z.M. Tomilo, P.V. Molchan, A.S. Shestak, V.M. Finskaya, N.A. Prytkova, S.N. Ustinovich, Physica C **361**, 95 (2001)
133. A.D. Hillier, R.I. Smith, R. Cywinski, Appl. Phys. A **74**, S823 (2002)
134. C.-G. Oertel, L. Ledig, J. Eckert, W. Skrotzki, Crystal. Res. Technol. **35**, 427 (2000)
135. S.L. Bud'ko, P.C. Canfield, Phys. Rev. B **71**, 024409 (2005)
136. J.W. Lynn, S. Skanthakumar, Q. Huang, S.K. Sinha, Z. Hossain, L.C. Gupta, R. Nagarajan, C. Godart, Phys. Rev. B **55**, 6584 (1997)
137. T. Siegrist, R.J. Cava, J.J. Krajewski, W.F. Peck Jr., J. Alloys. Compd. **216**, 135 (1994)
138. E. Alleno, Z. Hossain, C. Godart, R. Nagarajan, L.C. Gupta, Phys. Rev. B **52**, 7428 (1995)
139. E. Pellegrin, C.T. Chen, G. Meigs, R.J. Cava, J.J. Krajewski, W.F. Peck Jr., Phys. Rev. B **51**, 16,159 (1995)
140. D.R. Sánchez, S.L. Bud'ko, E.M. Baggio-Saitovitch, J. Phys.: Condens. Matter **12**, 9941 (2000)
141. J. Freudenberger, S.-L. Drechsler, G. Fuchs, A. Kreyssig, K. Nenkov, S.V. Shulga, K.-H. Müller, L. Schultz, Physica C **306**, 1 (1998)
142. L.M. Volkova, A. Polyshchuk, A. Magarill, F.E. Herbeck, J. Supercond. **15**, 663 (2002)
143. K. –H. Muller et al., in *Handbook of the Physics and Chemistry of the Rare Earths*, **38** (2008)
144. D.R. Sanchez, S.L. Bud'ko, E.M. Saitovitch, J. Phys: Condens. Matter. **12**, 9941–9948 (2000)
145. H. Michor, M. El-Hagary, L. Naber, E. Bauer, G. Hilscher, Phys. Rev. B **61**, R6487 (2000)
146. T. Takabatake, Y. Maeda, T. Konishi, H. Fujii, J. Phys. Soc. Jpn. **63**, 2853 (1994)
147. H. Michor, W. Perthold, T. Holubar, N.M. Hong, G. Hilscher, Physica C **235–240**, 2553 (1994)
148. M.D. Lan, T.J. Chang, C.S. Liaw, J. Phys. Chem. Solids **59**, 1285 (1998)
149. K. Eversmann, A. Handstein, G. Fuchs, L. Cao, K.-H. Müller, Physica C **266**, 27 (1996)
150. G.V.M. Kiruthika, G. Behr, R. Kulkarni, S.K. Dhar, L.C. Gupta, Physica C **405**, 245 (2004)
151. G. Fuchs, K.–.H. Muller, J. Freudenberger, K. Nenkov, S.–.L. Drechsler, S.V. Shulga, D. Lipp, A. Gladun, T. Cichorek, P. Gegenwart, Prama J. Phys. **58**, 791 (2002)
152. K.D.D. Rathnayaka, D.G. Naugle, B.K. Cho, P.C. Canfield, Phys. Rev. B **53**, 5688 (1996)
153. J.L. Zarestky, C. Stassis, A.I. Goldman, P.C. Canfield, G. Shirane, S.M. Shapiro, J. Phys. Chem. Solids **63**, 811 (2002)
154. K. Kumagai, T. Ooyama, H. Nakajima, M. Shimotomai, Physica B+C **148**, 133 (1987)
155. B.D. Dunlap, M. Slaski, Z. Sungaila, D.G. Hinks, K. Zhang, C. Segre, S.K. Malik, E.E. Alp, Phys. Rev. B **37**, R592 (1988)
156. W.E. Pickett, D.J. Singh, Phys. Rev. Lett. **72**, 3702 (1994)
157. T. Kohara, T. Oda, K. Ueda, Y. Yamada, A. Mahajan, K. Elankumaran, Z. Hossian, L.C. Gupta, R. Nagarajan, R. Vijayaraghavan, C. Mazumdar, Phys. Rev. B **51**, R3985 (1995)
158. K. Ikushima, J. Kikuchi, H. Yasuoka, R.J. Cava, H. Takagi, J.J. Krajewski, W.W. Peck Jr., J. Phys. Soc. Jpn. **63**, 2878 (1994)
159. Y. Iwamoto, K. Ueda, T. Kohara, Solid State Communications **113**, 615 (2000)
160. K. Ikushima, H. Yasuoka, A. Ohno, H. Takagi, R.J. Cava, J.J. Krajewski, W.F. Peck Jr., J. Phys. Soc. Jpn. **66**, 1130 (1997)
161. H. Eisaki, H. Takagi, R.J. Cava, B. Batlogg, J.J. Krajewski, W.F. Peck Jr., K. Mizuhashi, J.O. Lee, S. Uchida, Phys. Rev. B **50**, R647 (1994)
162. C. Mazumdar, R. Nagarajan, Physica C **514**, 173 (2015)
163. J. Zarestky, C. Stassis, A.I. Goldman, P.C. Canfield, P. Dervenagas, B.K. Cho, D.C. Johnston, Phys. Rev. B **51**, R678 (1995)

164. U. Yaron, P.L. Gammel, A.P. Ramirez, D.A. Huse, D.J. Bishop, A.I. Goldman, C. Stassis, P.C. Canfield, K. Mortensen, M.R. Eskildsen, Nature **382**, 236 (1996)
165. M. El Massalami, R.E. Rapp, F.A.B. Chaves, H. Takeya, C.M. Chaves, Phys. Rev. B **67**, 224407 (2003)
166. D.R. Sánchez, H. Micklitz, M.B. Fontes, S.L. Bud'ko, E. Baggio-Saitovitch, Phys. Rev. Lett. **76**, 507 (1996)
167. I.R. Fisher, J.R. Cooper, P.C. Canfield, Phys. Rev. B **56**(10), 820 (1997)
168. O.M. Cappannini, C.O. Rodriguez, N.E. Christensen, Physica C **306**, 101 (1998)
169. T. Ekino, H. Fujii, M. Kosugi, Y. Zenitani, J. Akimitsu, Physica C **235–240**, 2529 (1994)
170. R. Movshovich, M.F. Hundley, J.D. Thompson, P.C. Canfield, B.K. Cho, A.V. Chubukov, Physica C **227**, **381** (1994)
171. P. Martínez-Samper, H. Suderow, S. Vieira, J.P. Brison, N. Luchier, P. Lejay, P.C. Canfield, Phys. Rev. B **67**, 014526 (2003)
172. P. Raychaudhuri, D. Jaiswal-Nagar, G. Sheet, S. Ramakrishnan, H. Takeya, Phys. Rev. Lett. **93**(156), 802 (2004)
173. L.F. Mattheiss, Phys. Rev. B **49**(13), 279 (1994)
174. H. Kim, C.-D. Hwang, J. Ihm, Phys. Rev. B **52**, 4592 (1995)
175. S.B. Dugdale, M.A. Alam, I. Wilkinson, R.J. Hughes, I.R. Fisher, P.C. Canfield, T. Jarlborg, G. Santi, Phys. Rev. Lett. **83**, 4824 (1995)
176. S.V. Shulga, S.-L. Drechsler, G. Fuchs, K.-H. Müller, K. Winzer, M. Heinecke, K. Krug, Phys. Rev. Lett. **80**, 1730 (1998)
177. N.L. Bobrov, S.I. Beloborod'ko, L.V. Tyutrina, I.K. Yanson, D.G. Naugle, K.D.D. Rathnayaka, Phys. Rev. B **71**, 014512 (2005)
178. Y.G. Naidyuk, O.E. Kvitnitskaya, I.K. Yanson, G. Fuchs, K. Nenkov, A. Wälte, G. Behr, D. Souptel, S.-L. Drechsler, Physica C **460–462**, 105 (2007)
179. S. Mukhopadhyay, G. Sheet, P. Raychaudhuri, H. Takeya, Phys. Rev. B **72**, 014545 (2005)
180. S. Manalo, H. Michor, M. El-Hagary, G. Hilscher, E. Schachinger, Phys. Rev. B **63**, 104508 (2001)
181. K.-H. Müller, G. Fuchs, S.-L. Drechsler, I. Opahle, L. Helmut Eschrig, Schultz, Günter Behra, W. Löser, D. Souptel, A. Wälte, K. Nenkov, Y. Naidyuk, H. Rosner. Physica C **99**, **460–462** (2007)
182. B. Bergk, V. Petzold, H. Rosner, S.–.L. Drechsler, M. Bartkowiak, O. Ignatchik, A.D. Bianchi, I. Sheikin, P.C. Canfield, J. Wosnitza, Phys. Rev. Lett. **100**, 257004 (2008)
183. H. Kawano, H. Yoshizawa, H. Takeya, K. Kadowaki, Phys. Rev. Lett. **77**, 4628 (1996)
184. T. Sakai, G. Adachi, J. Shiokawa, J. Less-Common Met. **84**, 107 (1982)
185. T. Sakai, G. Adachi, J. Shiokawa, Solid State Communications **40**, 445 (1981)
186. J. Bauer, O. Bars, Acta Crystallogr. B **36**, 1540 (1980)
187. T. Onimaru, H. Onodera, K. Ohoyama, H. Yamauchi, Y. Yamaguchi, J. Phys. Soc. Jpn. **68**, 2287 (1999)
188. K. Ohoyama, K. Kaneko, K. Indoh, H. Yamauchi, A. Tobo, H. Onodera, Y. Yamaguchi, J. Phys. Soc. Jpn. **70**, 3291 (2001)
189. S. Khmelevskyi, P. Mohn, J. Redinger, H. Michor, Supercond. Sci. Technol. **18**, 422 (2005)
190. H. Michor, E.W. Scheidt, S. Manalo, M. Müller, E. Bauer, G. Hilscher, J. Phys.: Conf. Ser. **150**, 052160 (2009)
191. S. Akutagawa, T. Ohashi, H. Kitano, A. Maeda, J. Goryo, H. Matsukawa, J. Akimitsu, J. Phys. Soc. Jpn. **77**, 064701 (2008)

Chapter 7
Organic Chemistry of π-Conjugated Polycyclic Aromatic Hydrocarbons: Acenes and Phenacenes

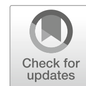

Hideki Okamoto

Abstract Polycyclic aromatic hydrocarbons (PAHs) are of great importance from the aspect of fundamental sciences as well as materials science, especially in organic electronics. In this chapter, the electronic features, synthesis strategies, and representative reactions of two series of π-conjugated PAHs, acenes and phenacenes, are described. In the last two decades, pentacene has been widely investigated as an organic electronic material, e.g., as the active layer of organic field-effect transistors (OFETs). Picene, which is an isomer of pentacene with a phenacene structure, was also found to serve as an active layer in high-performance OFETs. While pentacene is unstable under exposure to light and oxygen, picene is quite stable under such conditions. The electronic and chemical features of acene and phenacene are thus compared to understand the differences in the nature of the two structural categories of PAHs.

Keywords Polycyclic aromatic hydrocarbons · Acene · Phenacene

7.1 Introduction

Polycyclic aromatic hydrocarbons (PAHs) are of much interest because of their unique electronic structures, molecular structures, and potential application to organic functional materials. In the past two decades, PAHs have attracted much attention in organic electronics, especially, as organic semiconductors applicable to organic field-effect transistors (OFETs) [1–4], organic photovoltaics (OPVs) [5–7], and organic light-emitting diodes (OLEDs) [8, 9]. The discovery of high-performance p-channel OFET devices using pentacene as the active layer [10] led to an explosive growth of electronic devices using PAHs as well as the development of novel organic electronic materials. As for high-performance OFET

H. Okamoto (✉)
Division of Earth, Life, and Molecular Sciences, Graduate School of Natural Science and Technology, Okayama University, Okayama, Japan
e-mail: hokamoto@okayama-u.ac.jp

© Springer Nature Singapore Pte Ltd. 2019

Y. Kubozono (ed.), *Physics and Chemistry of Carbon-Based Materials*,
https://doi.org/10.1007/978-981-13-3417-7_7

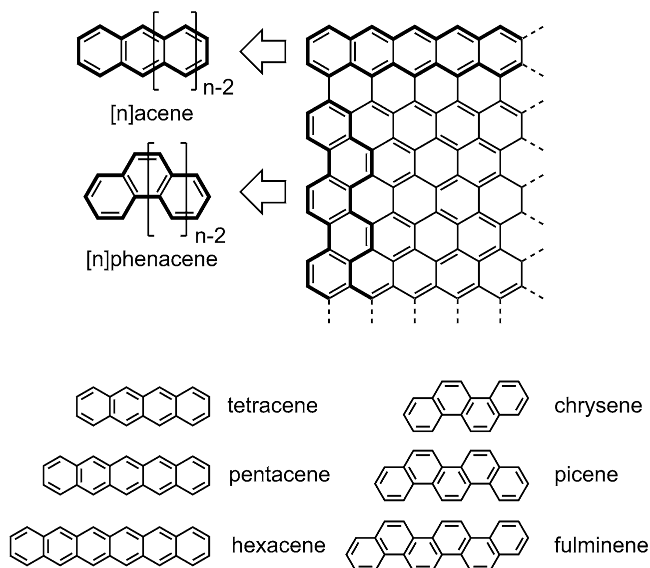

Fig. 7.1 General structures of acene and phenacene

devices, apart from PAHs which consist of only carbon and hydrogen atoms, those containing chalcogen atoms such as sulfur and selenium have also been successfully applied [11]. It is worth noting that some PAHs produced superconductors upon doping with alkali or alkali-earth metals; thus, potassium-doped picene exhibited superconductivity at superconducting transition temperatures $T\mathrm{c} = 7$ and 18 K [12–15].

Nowadays, PAHs are of great significance in material sciences. The purpose of this chapter is to provide an overview of the electronic features, synthetic methods, and representative reactions of PAHs. To this end, two kinds of PAH series, i.e., acenes and phenacenes, are chosen to highlight the appreciable differences between their natures. Figure 7.1 shows the general chemical structures of the two series of PAHs. Acenes ([n]acenes) have benzene rings fused in a linear array (n denotes the number of benzene rings incorporated in the structure). The acene structure is considered to be a graphene ribbon with a zigzag edge. In contrast, phenacenes are considered to be armchair-edge graphene ribbons. Lower analogs of acene and phenacene with four to six benzene rings are illustrated in Fig. 7.1. Phenacenes of $n \geq 7$ are called as [n]phenacenes because they have no trivial names. The differences in the chemical structures induce drastic variations in the physical and chemical properties between acenes and phenacenes. In the following sections, the contrasting physical and chemical features of these two series of PAHs will be reviewed.

7.2 Electronic Features of Acenes and Phenacenes

7.2.1 *Stability of Polycyclic Aromatic Compounds*

The aromatic stability of monocyclic aromatic compounds is defined by Hückel's $4n + 2$ rule [16–18]. In order to understand the aromaticity of PAH systems, Clar's π sextet rule was formulated and successfully adapted to qualitatively discuss the aromatic character of benzenoid species [19, 20]. In the conventional Kekulé structure of benzene, three double bonds are alternately placed in the hexagonal framework as shown in Scheme 7.1a. Clar's sextet illustrates the Kekulé benzene ring with a hexagon including a circle, indicating that the ring is in a stable 6π resonance state. Thus, the PAHs with a larger number of Clar sextet rings are considered to be more stabilized by the resonance. Anthracene is drawn as a

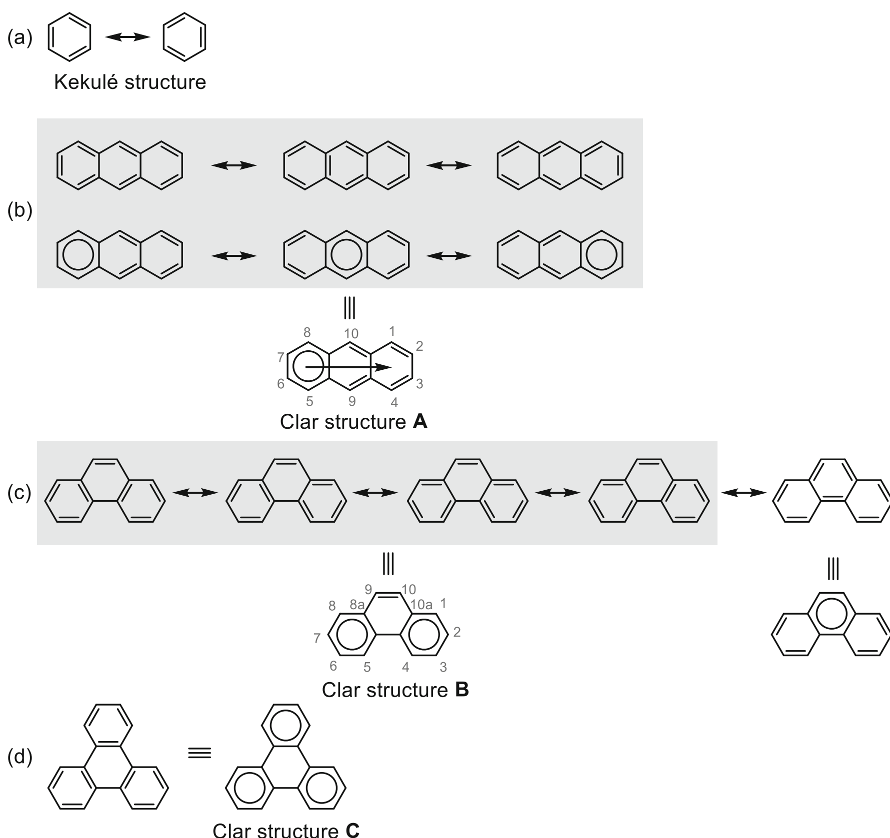

Scheme 7.1 Kekulé and Clar structures of typical PAHs: benzene (**a**), anthracene (**b**), phenanthrene (**c**), and triphenylene (**d**)

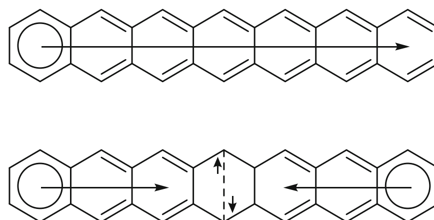

Fig. 7.2 Singlet closed-shell (upper) and open-shell (lower) Clar structures of heptacene. (Reprinted from [20] Copyright 2013 M. Solà, licensed under CC BY 3.0)

resonance hybrid of Kekulé structures (Scheme 7.1b, upper). By using Clar's π sextet concept, the Kekulé structure of anthracene can be formulated as shown in Scheme 7.1b (lower). One can draw only one Clar's sextet for each Kekulé resonance structure of anthracene. The three Clar sextet resonance structures may be merged into one representation as Clar structure **A**. The arrow illustrates that the Clar's sextet resonance part can be drawn in one of the three rings connected by the arrow. In the case of phenanthrene, one can draw two sextet resonance rings within the molecule as shown in Clar structure **B** (Scheme 7.1c). Triphenylene (Scheme 7.1d) can be expressed as Clar structure **C** with no double bonds. Triphenylene contains three Clar sextets and an empty central ring with no double bonds. Such a structure is called as a fully benzenoid hydrocarbon and is known to be stable [20].

In many cases, the Clar structures reflect the experimental characteristics of PAHs. A typical case can be seen for the structure of phenanthrene. There are double ($C_9 = C_{10}$) and single (C_{8a}-C_9, C_1-C_{10a}) bonds in the Clar structure **B**. The experimentally determined mean values of the bond lengths are 1.350 Å for the $C_9 = C_{10}$ bond and 1.452 Å for the C_{8a}-C_9 and C_1-C_{10a} bonds; these values are consistent with those expected for structure **B** [21]. Chemically, the $C_9 = C_{10}$ bond often behaves like a C=C double bond. The stabilities of acenes and phenacenes are very different from each other. It has been recognized that large acenes are unstable even under ambient light and air, while phenacenes are quite stable. Theoretical calculations suggest that, for large acenes, an open-shell singlet biradical character is predominant in the ground state [22]. Solà provided a schematic explanation that two Clar aromatic sextets are possible in open-shell heptacene (Fig. 7.2, lower), while only one Clar aromatic sextet is involved in the closed-shell structure (Fig. 7.2, upper) [20].

It has been noted that there is a relationship between the aromatic natures and absorption behavior of PAHs [23, 24]. In Fig. 7.3, the structures of heptacene and its isomers are illustrated and their absorption maximum wavelengths (λ_{max}) are listed. It can be seen that λ_{max} tends to undergo a blue shift upon increasing the number of Clar sextet resonance structures. These facts suggest that the optical band gap increased with an increase in the stability of PAH isomers.

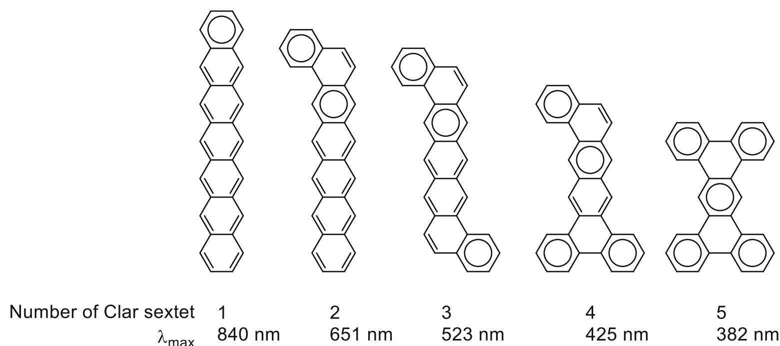

Fig. 7.3 Correlation between the number of Clar sextets and absorption maximum wavelengths (λ_{max}) observed in $C_{30}H_{18}$ PAH compounds. The absorption wavelengths are sourced from ref. 23

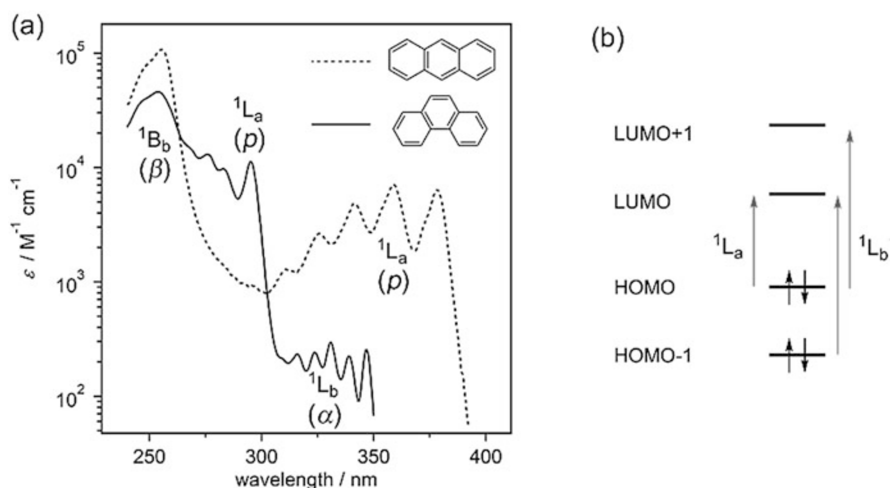

Fig. 7.4 (**a**) Electronic absorption spectra of anthracene and phenanthrene in chloroform. (**b**) Orbital diagrams of the ^1L_a and ^1L_b bands. The ^1L_a and ^1L_b bands are, respectively, described as *p* band *α* bands according to Clar's definition

7.2.2 Electronic Spectra of Acene and Phenacene

The electronic absorption spectra of anthracene and phenanthrene are displayed in Fig. 7.4 as representatives of acene and phenacene, respectively. The spectra show a clear contrast between the absorption behavior of acene and phenacene [25]. The first absorption band of anthracene (^1L_a band) corresponds to a transition from HOMO (highest occupied molecular orbital) to LUMO (lowest unoccupied molecular orbital) (Fig. 7.4b, left arrow). The molecular absorption coefficient (ε) of the band is close to 1×10^4 M^{-1} cm^{-1}. In the case of phenanthrene, the first absorption band is much lower in intensity and is assigned to the ^1L_b

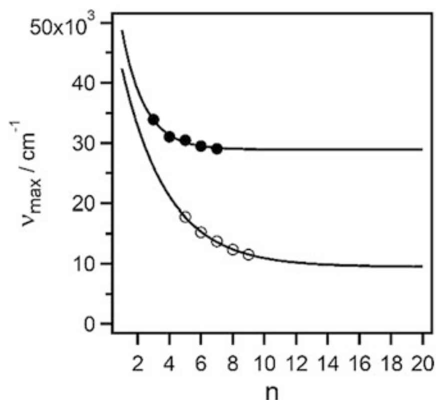

Fig. 7.5 Dependence of the absorption maximum wavenumber (ν_{max}) of the *p* band on the number of benzene rings (*n*): ν_{max} for acenes (○) in a solid argon matrix and phenacenes (•) in a $CHCl_3$ solution. Curve fitting with the function $\nu_{max} = y_0 + a\mathrm{e}^{-bn}$ yields $y_0 = 9490\ \mathrm{cm}^{-1}$ for acenes and $y_0 = 28{,}900\ \mathrm{cm}^{-1}$ for phenacenes. The data points for acenes are sourced from ref. 26, while those for phenacenes are from ref. 27 and the references therein

band, which consists of a mixed electronic transition of (HOMO – 1)–LUMO and HOMO–(LUMO +1) (Fig. 7.4b, right arrows). For phenanthrene, the absorption band corresponding to the HOMO-LUMO transition (^1L_b, *p* band) appears at around 300 nm.

In the acene series, the absorption band in the longer wavelength region undergoes a remarkable red shift as the number of benzene rings increases. In contrast, the band corresponding to the phenacene series undergoes only a slight red shift. Figure 7.5 compares the dependence of the absorption wavelengths of the *p* band (HOMO-LUMO transition) of acene and phenacene on the number of benzene rings, n. The dependence for acene series is represented as $\nu_{max} = y_0 + a\mathrm{e}^{-bn}$ (cm^{-1}), where *a* and *b* are fitting constants and n is number of benzene rings in acene [26]. From this exponential fit, the optical gap for the *p* band of polyacene is deduced to be constant at 1054 nm (1.18 eV). Thus, the effective conjugation length is expected to be $n = 24$–25 [26]. A similar treatment for the phenacene series suggests that the optical band gap for larger phenacnes is expected to be 346 nm (3.56 eV), which is much larger than that of the acene series and reflects their chemical stability.

7.3 Synthesis of Acenes and Phenacenes

7.3.1 Synthesis of Acenes by Elimination Reactions

It is well recognized that large acenes are unstable under ambient conditions, such as exposure to light and oxygen, and are hardly soluble in common solvents. Thus,

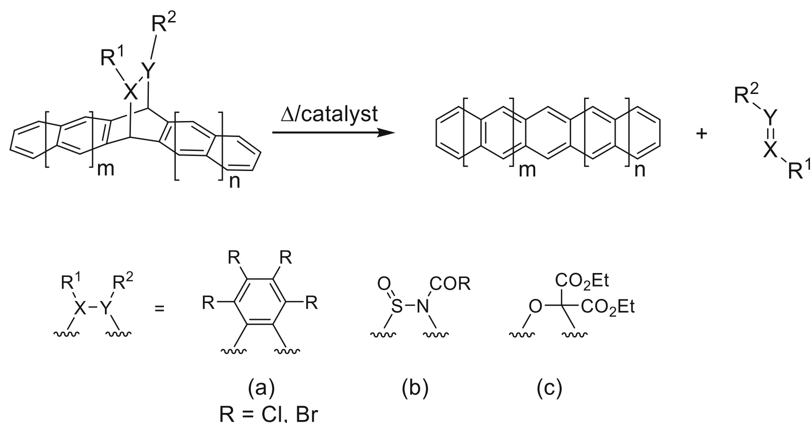

Scheme 7.2 Synthesis of acenes by elimination reactions

large acenes were synthesized via precursors in which the acene π conjugation is interrupted by a R^1-X-Y-R^2 bridge (Scheme 7.2). The protecting bridges are designed to be cleanly removed through cheletropic reactions by heat, catalysis, or light and to enhance the solubility of the precursors. Some of the representative protecting bridges are depicted in Scheme 7.2. The synthetic strategies and the applications to solution-processed OFET device fabrication were recently reviewed [28]. During the pentacene synthesis by using the precursors ($m = n = 1$), the protecting bridges, shown in Scheme 7.2, were removed by heating generally at 100–200 °C.

Acene frameworks were also constructed by the elimination of monocarbonyl precursors in which the acene π system was interrupted with a C=O bridge (Scheme 7.3). The decarbonylation reaction proceeds by heating or photoirradiation. Pentacene has been prepared by decarbonylation reaction of two kinds of precursors, i.e., precursors with symmetric ($m = n = 1$) and antisymmetric ($m = 2$, $n = 0$) structures [28, 29]. It is noteworthy that hexacene was produced by the thermal decarbonylation of a monocarbonyl precursor ($m = 2$, $n = 1$) [30]. The hexacene thus prepared was used as an active layer of a high-performance OFET device to achieve a very high charge mobility (4.3 $cm^2 V^{-1} s^{-1}$). On the basis of theoretical calculations, it has been predicted that the activation barrier for thermal decarbonylation increases as the fused benzene-ring number increases [31]. Thermal decarbonylation of the symmetrical precursor ($m = n = 1$) is predicted to take place at 400 K [31]. Experimentally, the precursor produced pentacene by the thermolysis at 150 °C (423 K) [29]. In the case of hexacene synthesis with the monocarbonyl precursor ($m = 2$, $n = 1$), the decarbonylation reaction proceeded at higher temperature (180 °C, 453 K) [30].

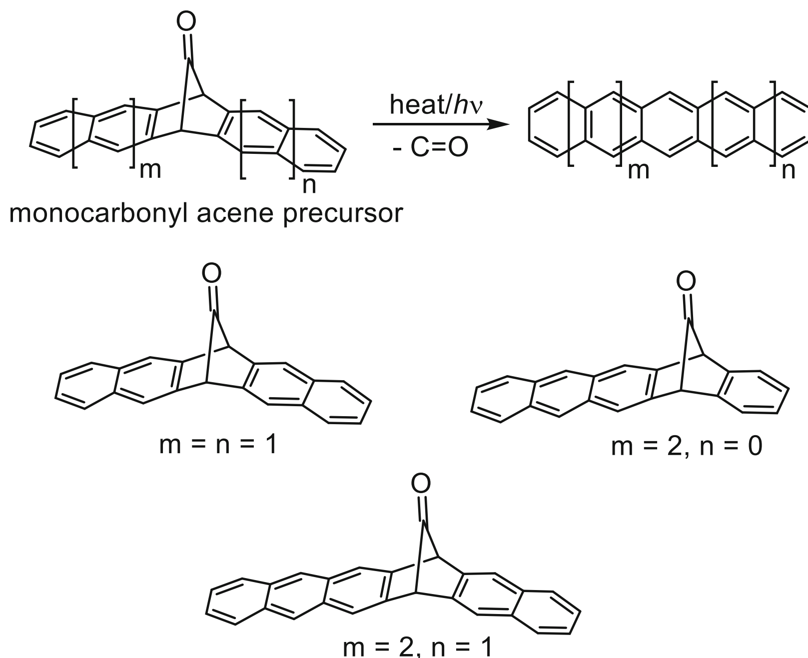

Scheme 7.3 Synthesis of acenes by the thermal decarbonylation of monocarbonyl precursors

7.3.2 Preparation of Higher Acenes by Bisdecarbonylation Reaction of Diketone Precursors (Strating-Zwanenburg Reaction)

Annelated bicyclo[2.2.2]octa-5,7-diene-2,3-dione (diketone precursors) have been recognized as versatile precursors to acenes as they can undergo clean extrusion of CO molecules upon photoirradiation. This reaction was first observed for the photolysis of the precursor of $m = n = 0$ (Scheme 7.4) [32]. The diketone precursor was found to be thermally unreactive, but it efficiently converted to anthracene with the evolution of CO molecules. This strategy has been widely used for the synthesis of extremely large acenes up to heptacene [33]. Precursors possessing two diketone moieties, such as the bis(diketone) precursors, were used for the photochemical formation of octacene and nonacene under matrix-isolation conditions [26]. The formed octacene and nonacene were characterized by their electronic absorption spectra showing λ_{max} at 806 and 865 nm, respectively.

The largest acene that could be experimentally characterized thus far is decacene [34]. A tetra-epoxide precursor was deoxygenated on an Au(111) surface under scanning tunneling microscopy (STM) conditions using the so-called on-surface chemistry strategy (Scheme 7.5). The HOMO-LUMO energy gap was determined to be 1.17 eV on an Au(111) surface.

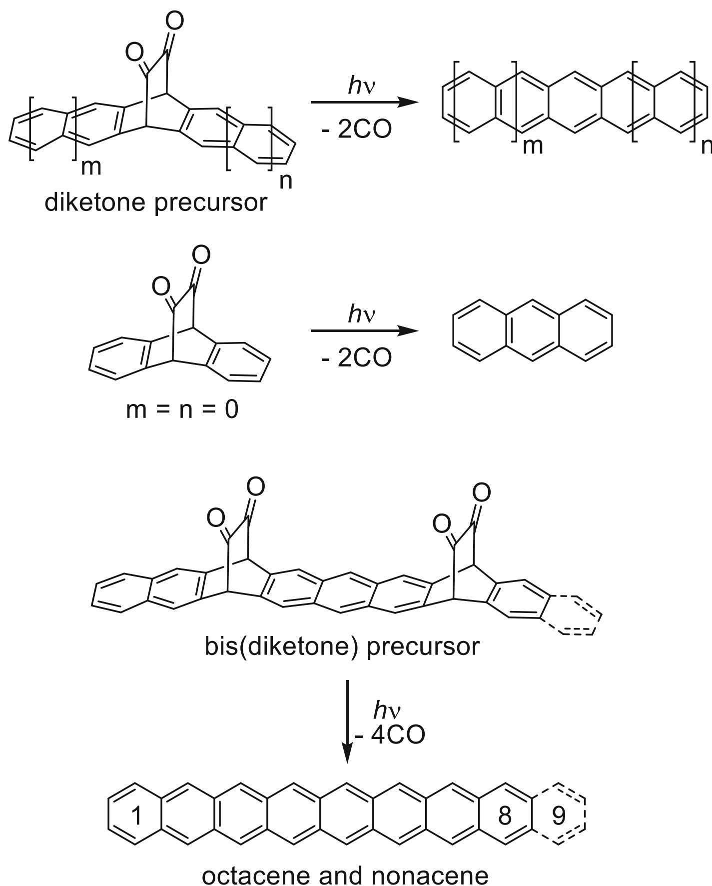

Scheme 7.4 Acene synthesis by the Strating-Zwanenburg reaction

Scheme 7.5 Decacene formation from tetra-epoxide through on-surface chemistry

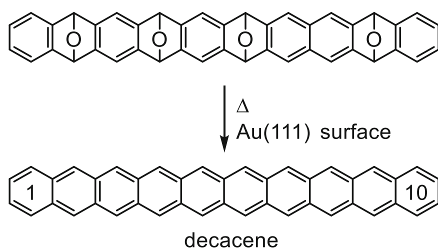

7.3.3 *Attempts to Stabilize Large Acenes*

Large acenes are highly reactive to undergo either oxygenation producing the corresponding endoperoxides or dimerization under light illumination. Many attempts to stabilize large acenes have been proposed from both structural and electronic

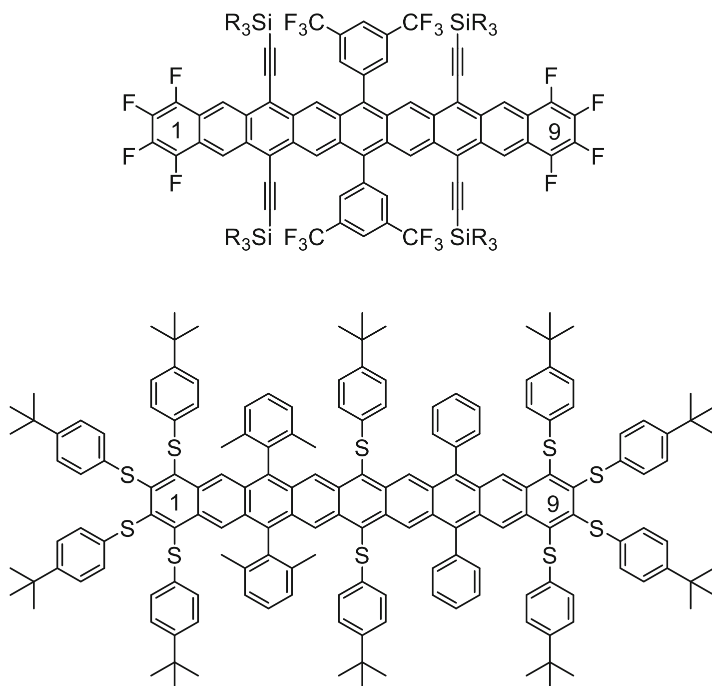

Fig. 7.6 Nonacenes stabilized with fluorine, ethynyl, aryl, and thioaryl substituents

aspects. The introduction of bulky substituents is expected to be useful to kinetically prevent the acene cores from dimerization or reacting with oxygen molecule due to steric repulsion. In this context, large aryl and ethynyl groups were used for kinetic stabilization [35–38]. Sulfur-containing functional groups are considered to stabilize large acenes because they might make the acene electronic system closed structure; however, the exact mechanisms are still under dispute [39]. Partial fluorine substitution is considered to make large acene systems stable during device fabrication [36]. By taking full advantage of these factors, stabilized nonacenes were synthesized, as shown in Fig. 7.6. Nonacene with ethynyl substituents (Fig. 7.6, upper) was isolated and characterized by spectroscopic and X-ray crystallographic techniques [40]. The modified nonacene showed an absorption band at 1033 nm corresponding to a HOMO-LUMO gap of 1.2 eV. The synthesis of arylthio-protected nonacene derivative (Fig. 7.6, lower) was reported, and the HOMO-LUMO gap was estimated to be 1.12 eV [35].

7.3.4 Photochemical Formation of Phenacenes (the Mallory Photoreaction)

Phenacenes are isomers of acenes, i.e., they have a zigzag fusion of benzene rings that exhibits a so-called armchair-edge structure of a graphene sheet (Fig. 7.1).

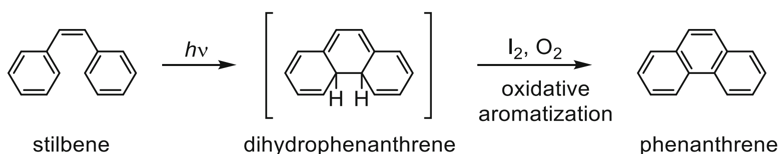

Scheme 7.6 General reaction scheme of Mallory photocyclization

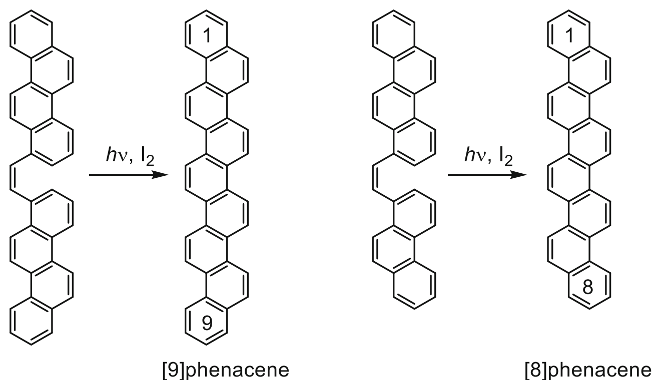

Scheme 7.7 Synthesis of **[8]**phenacene and **[9]**phenacene by Mallory photocyclization

Large phenacenes, such as picene, were extracted from coal tar more than 70 years ago [41]. As they were very rarely used in functional materials, only a few synthetic methods to systematically prepare phenacene frameworks are known. One of the most versatile strategies for constructing the zigzag benzene fusion is the photocylization of *cis*-stilbene to phenanthrene under oxidative conditions (in the presence of I_2 and O_2), which is the so-called Mallory photocylization reaction (Scheme 7.6). The intermediary formed dihydrophenanthrene is generally unstable and reverts to stilbene. However, in the presence of an appropriate oxidant, such as I_2 and O_2, it smoothly produces phenanthrene. Hundreds of examples of the related reactions were already reviewed in the past [42].

The Mallory photocyclization is a powerful method for synthesizing extremely large phenacenes as displayed in Scheme 7.7. Dichrysenylethene, which is a large stilbene homologue with two chrysene moieties instead of phenyl groups, was successfully converted to **[9]**phenacene (Scheme 7.7, left) [43]. Using a similar photoreaction, **[8]**phenacene was conveniently synthesized (Scheme 7.7, right) [44]. Although the prepared **[9]**phenacene was completely insoluble in common organic solvents even at elevated temperatures, its structure was verified by elemental analysis, mass spectrometry, and out-of-plane X-ray diffraction (XRD) analysis [43]. Furthermore, the molecular structure of **[9]**phenacene was definitively and directly observed by STM imaging [45]. Currently, **[9]**phenacene is the largest known phenacene bearing no substituents.

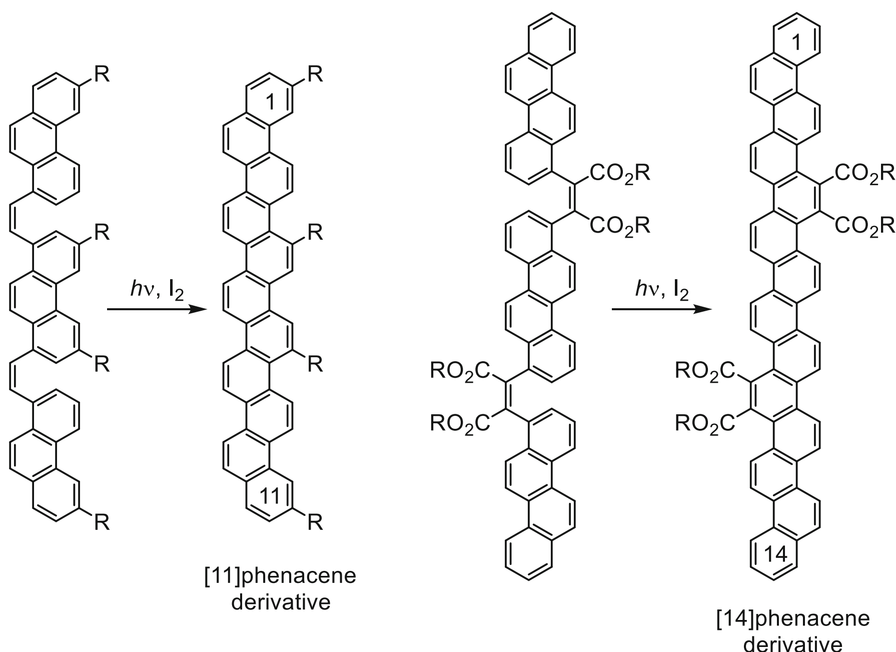

Scheme 7.8 Synthesis of **[11]**phenacene and **[14]**phenacene derivatives by double Mallory photocyclization

Double photocyclization procedures were applied to construct much larger phenacene skeletons up to **[14]**phenacene framework (Scheme 7.8). Mallory synthesized a **[11]**phenacene incorporating alkyl groups by the photocyclization of the precursor possessing three phenanthrene units (Scheme 7.8, left) [27]. The obtained **[11]**phenacene derivative showed an absorption band corresponding to the HOMO-LUMO transition (*p* band) at $\lambda_{max} = 400$ nm (3.1 eV) in solution indicating that the large phenacene maintained a wide HOMO-LUMO band gap. The same double-cyclization protocol was adapted to higher phenacene synthesis (Scheme 7.8, right); a precursor containing three chrysene moieties was converted to a **[14]**phenacene having ester functionalities [46]. The HOMO-LUMO band gap of the **[14]**phenacene estimated from the electronic absorption was reported to be 2.88 eV.

7.3.5 Lewis-Acid Catalyzed Cyclization of Ethynyl-Substituted Biaryl Compounds

A recent trend being followed to prepare phenacene frameworks is the Lewis-acid catalyzed cyclization of biaryl compounds containing ethynyl substituents. The catalysts promote cyclization in an electrophilic manner (Scheme 7.9, upper) [47].

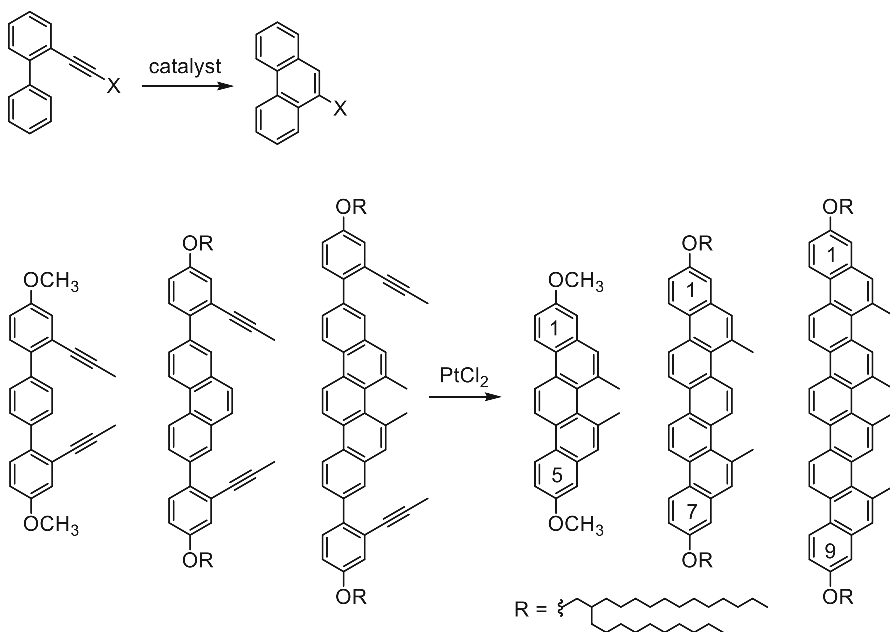

Scheme 7.9 Phenacene synthesis by Lewis-acid catalyzed cyclization of ethynyl-substituted biaryl compounds

It has been documented that $PtCl_2$, AuCl, $AuCl_3$, $GaCl_3$, and $InCl_3$ are effective for synthesizing phenanthrene-type products. The Lewis-acid catalyzed cyclization reaction, as an alternative of Mallory photocyclization, facilitated the construction of phenacene skeletons. For example, **[5]**-, **[7]**-, and **[9]**phenacene skeletons were synthesized by the $PtCl_2$-catalyzed cyclization (Scheme 7.9, lower) [48].

7.4 Reactions of Polycyclic Aromatic Hydrocarbons

7.4.1 Photo-Induced Reactions of Acenes

One of the most widely recognized photodegradation processes of acenes is photodimerization. Photodimerization of acenes is one of the oldest photochemical reactions represented by anthracene dimerization [49]. This photoprocess has been utilized in photochromic systems and photoswitches [50]. However, the photodimerization process faces serious problems in synthesizing, handling, and characterizing large acenes. For example, pentacene is known to undergo dimer formation upon photoirradiation (Scheme 7.10). After illumination with >440-nm light, a symmetric isomer was obtained as the photoproduct. It has also been stated that an isomeric

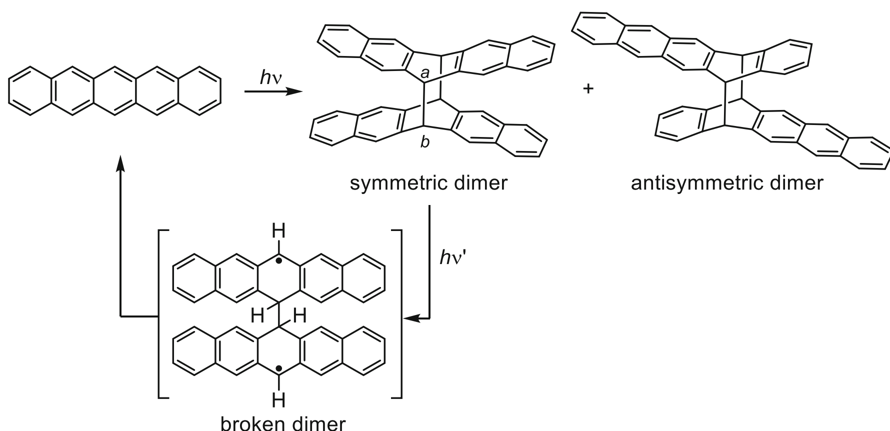

Scheme 7.10 Photodimerization of pentacene and reversion of the dimer

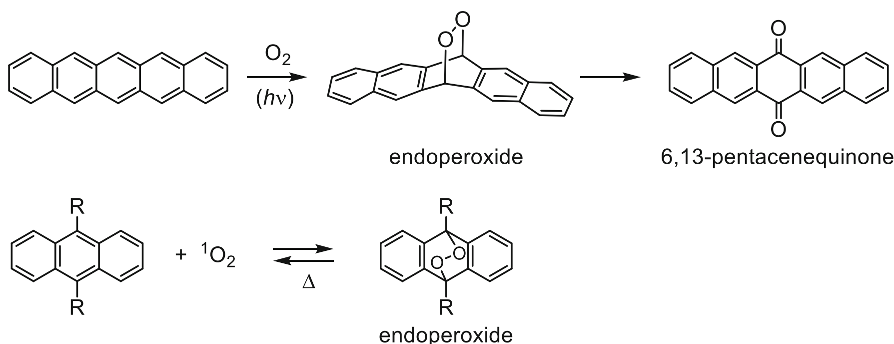

Scheme 7.11 Photochemical oxygenation reactions of acenes and cycloreversion of the endoperoxide to form singlet oxygen

antisymmetric dimer was formed as a minor product [51]. The structure of the symmetric dimer was confirmed by single-crystal X-ray analysis. The length of the bridging C^a-C^b bond was reported to be 1.58 Å, which was slightly greater than that of related anthracene photodimers. The symmetric dimer reverted to the starting form of pentacene upon illumination with UV light in a poly(methyl methacrylate) (PMMA) film. The photodissociation reaction was considered to proceed via a diradicaloid, a broken dimer.

An additional important reaction of acenes is photo-induced oxygenation to form the corresponding endoperoxide which is in turn converted to an acene-quinone product (Scheme 7.11, upper). The oxygenation process is considered to occur either through reactions with a singlet oxygen (concerted reaction) or triplet oxygen (stepwise radical reaction) [52]. This process as well as the photodimerization process prevents large acenes from being used as practical functional materials. Interconversion between acenes and the corresponding endoperoxides is often

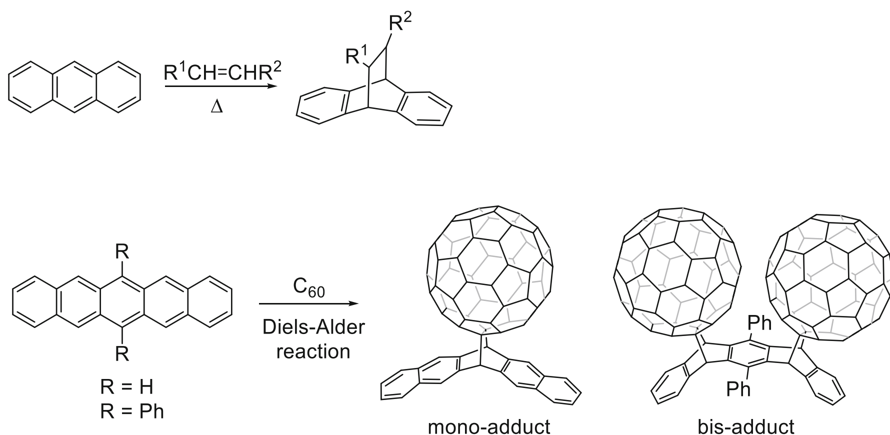

Scheme 7.12 Diels-Alder reactions of acenes

reversible, and thermal reversion of endoperoxides effectively releases singlet oxygen, $^1O_2$ [53]. Thus, acene endoperoxides can be used as a thermal source of $^1O_2$ and have been applied to novel photodynamic therapy systems (Scheme 7.11, lower) [54].

7.4.2 Diels-Alder Reactions of Acenes

Acenes are known to be reactive in their ground state also. A typical reaction pathway in the ground state is Diels-Alder reaction with appropriate dienophiles. The general reaction scheme is illustrated in Scheme 7.12, upper. As described in Sect. 7.3.1, the retro Diels-Alder reaction of the adducts affording original acenes is widely used to prepare large acenes (Scheme 7.2). Interestingly, pentacene derivatives are reported to undergo Diels-Alder reaction with C_{60} fullerene to produce cycloadducts (Scheme 7.12, lower) [55, 56]. In the case of 6,13-disubstituted pentacene, a bis-adduct, in which C_{60} molecules reacted on the same surface of the pentacene plane, was selectively formed. The molecular structure of the latter was established by single crystal X-ray analysis. The two C_{60} moieties were aligned in proximal positions to each other, and the closest carbon-carbon non-bonding distance was reported to be 3.065 Å.

7.4.3 Photochemical Reactions of Phenacenes

As described in Sect. 7.3.4, phenacenes can be effectively prepared by photoirradiation under oxidative conditions. Phenacenes are thus durable under such severe

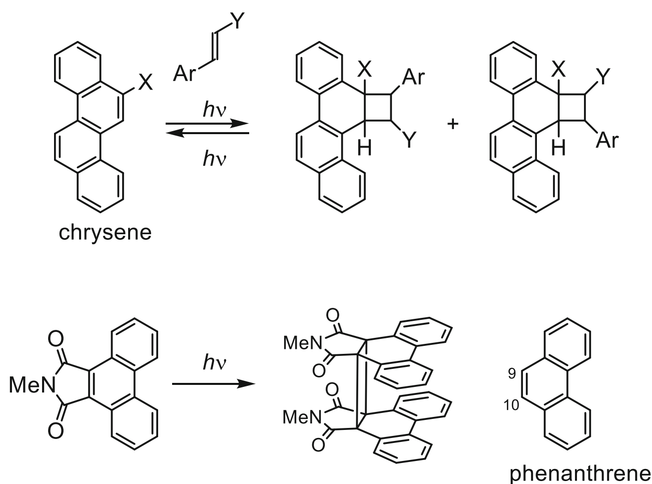

Scheme 7.13 Photochemical reactions of phenacenes

conditions under which acenes usually do not survive. As a result, generally, phenacenes are photochemically inert, and there are a few reactions reported for the same in the literatures (Scheme 7.13). Chrysenes, with four fused benzene rings, reacted with *trans*-cinnamates (Ar = substituted phenyl, Y = CO_2CH_3) to produce cyclobutane photoadducts through [π2s + π2s] cycloaddition (Scheme 7.13, upper) [57]. Phenanthrenes, with three fused benzene rings, undergo the [π2s + π2s] cycloaddition reaction at the $C^9 = C^{10}$ double bond with an olefinic compound to produce a cyclobutane photoproducts as in the case of chrysene. Additionally, intermolecular cycloaddition affording a photodimer has been reported (Scheme 7.13, lower) [58]; thus, upon photolysis with 400-nm light, phenanthrene-9,10-carboximide effectively reacted to afford a photodimer. The $C^9 = C^{10}$ double bond of phenacene is considered to be rather olefinic than aromatic in nature.

7.5 Summary

In this chapter, the representative features of acenes and phenacenes are compared. The two categories of PAHs displayed clear differences in various aspects. Generally, acenes are labile under exposure to oxygen and photoillumination conditions; in contrast, phenacenes are quite stable. Experimentally, acenes with benzene ring numbers up to 7 were prepared in bulk, and larger acenes were characterized only under matrix isolation or STM observation conditions. As for phenacene series, [n]phenacene derivatives with the benzene rings up to n = 14 were obtained as durable molecules. The synthesis and characterization of extremely π-extended PAHs are still intriguing and highly challenging. Furthermore, extremely large

π-conjugated PAHs will open up new materials science and organic electronics research avenues via appropriate molecular design and development of new synthetic protocols. For phenacenes, there are much fewer studies on this series of materials as compared to acenes. By taking advantage of the unique features, robustness, and electronic structures of phenacenes, they can be adapted and developed as novel hydrocarbon-based functional materials [59].

References

1. A. Operamolla, G.M. Farinola, Eur. J. Org. Chem. **3**, 423 (2011)
2. H. Dong, X. Fu, J. Liu, Z. Wang, W. Hu, Adv. Mater. **25**, 6158 (2013)
3. K. Zhou, H. Dong, H. Zhang, W. Hu, Phys. Chem. Chem. Phys. **16**, 22448 (2014)
4. J.E. Anthony, Angew. Chem. Int. Ed. **47**, 452 (2008)
5. S. Günes, H. Neugebauer, N.S. Sariciftci, Chem. Rev. **107**, 1324 (2007)
6. Y. Liang, Z. Xu, J. Xia, S.T. Tsai, Y. Wu, G. Li, C. Ray, L. Yu, Adv. Mater. **22**, E135 (2010)
7. J. Peet, A.J. Heeger, G.C. Bazan, Acc. Chem. Res. **42**, 1700 (2009)
8. J.E. Anthony, Chem. Rev. **106**, 5028 (2006)
9. X. Yang, X. Xu, G.J. Zhou, J. Mater. Chem. C **3**, 913 (2015)
10. D.J. Gundlach, Y.Y. Lin, T.N. Jackson, S.F. Nelson, D.G. Schlom, IEEE Electron Device Lett. **18**, 87 (1997)
11. K. Takimiya, I. Osaka, T. Mori, M. Nakano, Acc. Chem. Res. **47**, 1493 (2014)
12. R. Mitsuhashi, Y. Suzuki, Y. Yamanari, H. Mitamura, T. Kambe, N. Ikeda, H. Okamoto, A. Fujiwara, M. Yamaji, N. Kawasaki, Y. Maniwa, Y. Kubozono, Nature **464**, 76 (2010)
13. Y. Kubozono, H. Mitamura, X. Lee, X. He, Y. Yamanari, Y. Takahashi, Y. Suzuki, Y. Kaji, R. Eguchi, K. Akaike, T. Kambe, H. Okamoto, A. Fujiwara, T. Kato, T. Kosugi, H. Aoki, Phys. Chem. Chem. Phys. **13**, 16476 (2011)
14. Y. Kubozono, R. Eguchi, H. Goto, S. Hamao, T. Kambe, T. Terao, S. Nishiyama, L. Zheng, X. Miao, H. Okamoto, J. Phys. Condens. Matter **28**, 334001 (2016)
15. T. Nakagawa, Z. Yuan, J. Zhang, K.V. Yusenko, C. Drathen, Q. Liu, S. Margadonna, C. Jin, J. Phys. Condens. Matter **28**, 484001 (2016)
16. E. Hückel, Z. Physik **72**, 310 (1931)
17. E. Hückel, Z. Physik **70**, 204 (1931)
18. E. Hückel, Z. Physik **76**, 628 (1931)
19. E. Clar, *The Aromatic Sextet* (Wiley, New York, NY, 1972)
20. M. Solà, Front. Chem. **1**, 22 (2013)
21. M.I. Kay, Y. Okaya, D.E. Cox, Acta Cryst. Sec. B **27**, 26 (1971)
22. M. Bendikov, H.M. Duong, K. Starkey, K.N. Houk, E.A. Carter, F. Wudl, J. Am. Chem. Soc. **126**, 7416 (2004)
23. E. Clar, A. McCallum, Tetrahedron **10**, 171 (1960)
24. A.T. Balaban, D.J. Klein, J. Phys. Chem. C **113**, 19123 (2009)
25. M. Klessinger, J. Michl, *Excited States and Photochemistry of Organic Molecules* (VCH, New York, 1995)
26. C. Tönshoff, H.F. Bettinger, Angew. Chem. Int. Ed. **49**, 4125 (2010)
27. F.B. Mallory, K.E. Butler, A.C. Evans, E.J. Brondyke, C.W. Mallory, C. Yang, A. Ellenstein, J. Am. Chem. Soc. **119**, 2119 (1997)
28. M. Watanabe, K.Y. Chen, Y.J. Chang, T.J. Chow, Acc. Chem. Res. **46**, 1606 (2013)
29. C.T. Chien, C.C. Lin, M. Watanabe, Y.D. Lin, T.H. Chao, T.C. Chiang, X.H. Huang, Y.S. Wen, C.H. Tu, C.H. Sun, T.J. Chow, J. Mater. Chem. **22**, 13070 (2012)
30. M. Watanabe, Y.J. Chang, S.-W. Liu, T.-H. Chao, K. Goto, M.M. Islam, C.H. Yuan, Y.-T. Tao, T. Shinmyozu, T.J. Chow, Nat. Chem. **4**, 574 (2012)

31. C.H. Lai, E.Y. Li, K.Y. Chen, T.J. Chow, P.T. Chou, J. Chem. Theory Comput. **2**, 1078 (2006)
32. J. Strating, B. Zwanenburg, A. Wagenaar, A.C. Udding, Tetrahedron Lett. **10**, 125 (1969)
33. R. Mondal, C. Tönshoff, D. Khon, D.C. Neckers, H.F. Bettinger, J. Am. Chem. Soc. **131**, 14281 (2009)
34. J. Krüger, F. García, F. Eisenhut, D. Skidin, J.M. Alonso, E. Guitián, D. Pérez, G. Cuniberti, F. Moresco, D. Peña, Angew. Chem. Int. Ed. **56**, 11945 (2017)
35. I. Kaur, W. Jia, R.P. Kopreski, S. Selvarasah, M.R. Dokmeci, C. Pramanik, N.E. McGruer, G.P. Miller, J. Am. Chem. Soc. **130**, 16274 (2008)
36. B. Purushothaman, S.R. Parkin, M.J. Kendrick, D. David, J.W. Ward, L. Yu, N. Stingelin, O.D. Jurchescu, O. Ostroverkhova, J.E. Anthony, Chem. Commun. **48**, 8261 (2012)
37. I. Kaur, N.N. Stein, R.P. Kopreski, G.P. Miller, J. Am. Chem. Soc. **131**, 3424 (2009)
38. H. Qu, C. Chi, Org. Lett. **12**, 3360 (2010)
39. K.J. Thorley, J.E. Anthony, Isr. J. Chem. **54**, 642 (2014)
40. B. Purushothaman, M. Bruzek, S.R. Parkin, A.F. Miller, J.E. Anthony, Angew. Chem. Int. Ed. **50**, 7013 (2011)
41. K.F. Lang, Angew. Chem. **63**, 345 (1951)
42. F.B. Mallory, C.W. Mallory, Org. React. **30**, 1 (1984)
43. Y. Shimo, T. Mikami, S. Hamao, H. Goto, H. Okamoto, R. Eguchi, S. Gohda, Y. Hayashi, Y. Kubozono, Sci. Rep. **6**, 21008 (2016)
44. H. Okamoto, R. Eguchi, S. Hamao, H. Goto, K. Gotoh, Y. Sakai, M. Izumi, Y. Takaguchi, S. Gohda, Y. Kubozono, Sci. Rep. **4**, 5330 (2014)
45. S.W. Chen, I.C. Sang, H. Okamoto, G. Hoffmann, J. Phys. Chem. C **121**, 11390 (2017)
46. T.S. Moreira, M. Ferreira, A. Dall'armellina, R. Cristiano, H. Gallardo, E.A. Hillard, H. Bock, F. Durol, Eur. J. Org. Chem. **2017**, 4548 (2017)
47. V. Mamane, P. Hannen, A. Fürstner, Chem. Eur. J. **10**, 4556 (2004)
48. T.-A. Chen, T.-J. Lee, M.-Y. Lin, S.M.A. Sohel, E.W.-G. Diau, S.-F. Lush, R.-S. Liu, Chem. Eur. J. **16**, 1826 (2010)
49. H. Bouas-Laurent, A. Castellan, J.P. Desvergne, R. Lapouyade, Chem. Soc. Rev. **30**, 248 (2001)
50. H. Dürr, H. Bouas-Laurent (eds.), *Photochromism-Molecules and Systems (Revised Version)* (Elsevier, Amsterdam, 2003)
51. O. Berg, E.L. Chronister, T. Yamashita, G.W. Scott, R.M. Sweet, J. Calabrese, J. Phys. Chem. A **103**, 2451 (1999)
52. A.R. Reddy, M. Bendikov, Chem. Commun. **42**, 1179 (2006)
53. J.M. Aubry, C. Pierlot, J. Rigaudy, R. Schmidt, Acc. Chem. Res. **36**, 668 (2003)
54. S. Kolemen, T. Ozdemir, D. Lee, G.M. Kim, T. Karatas, J. Yoon, E.U. Akkaya, Angew. Chem. Int. Ed. **55**, 3606 (2016)
55. G.P. Miller, J. Mack, Org. Lett. **2**, 3979 (2000)
56. G.P. Miller, J. Briggs, J. Mack, P.A. Lord, M.M. Olmstead, A.L. Balch, Org. Lett. **5**, 4199 (2003)
57. H. Maeda, S. Waseda, K. Mizuno, Chem. Lett. **29**, 1238 (2000)
58. Y. Kubo, S. Togawa, K. Yamane, A. Takuwa, T. Araki, J. Org. Chem. **54**, 4929 (1989)
59. Y. Kubozono, X. He, S. Hamao, K. Teranishi, H. Goto, R. Eguchi, T. Kambe, S. Gohda, Y. Nishihara, Eur. J. Inorg. Chem. **24**, 3806 (2014)

Chapter 8
Transistor Application and Intercalation Chemistry of π-Conjugated Hydrocarbon Molecules

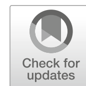

Yoshihiro Kubozono, Shino Hamao, Takahiro Mikami, Yuma Shimo, Yasuhiko Hayashi, and Hideki Okamoto

Abstract In this chapter, field-effect transistors (FETs) are reported using π-conjugated hydrocarbon molecules (polycyclic hydrocarbons). The p-channel FET properties are recorded for the FETs using polycyclic aromatic hydrocarbons. Currently, the highest field-effect mobility (μ) that polycyclic hydrocarbon FETs reach is 21 cm^2 V^{-1} s^{-1} for 3,10-ditetradecylpicene, which is one of phenacene-type molecules. Thus, the recent FETs of polycyclic hydrocarbons show excellent FET characteristics, suggesting that the materials are promising as active layers for future practical organic FET devices. In this chapter, the recent advancement of the FETs using polycyclic hydrocarbons are reported completely, in particular the FETs using extended π-conjugated hydrocarbon molecules, such as phenacene, and the FETs using fullerene molecules are also reported. Furthermore, intercalation chemistry of the π-conjugated hydrocarbon molecules is reported, which facilitates realization of novel physical properties, such as superconductivity and ferromagnetism.

Keywords Field-effect transistor · Fullerene · π-conjugated hydrocarbon · Logic gate circuit · Intercalation chemistry

8.1 Introduction

Over the past two decades, carbon-based field-effect transistors (FETs) have been extensively studied. Many chemists, physicists, and materials scientists have exerted much effort to improve the transistor performance in carbon-based FETs. Carbon is

Y. Kubozono (✉) · S. Hamao
Research Institute for Interdisciplinary Science, Okayama University, Okayama, Japan
e-mail: kubozono@cc.okayama-u.ac.jp

T. Mikami · Y. Shimo · Y. Hayashi
Department of Electric and Electronic Engineering, Okayama University, Okayama, Japan

H. Okamoto
Division of Earth, Life, and Molecular Sciences, Graduate School of Natural Science and Technology, Okayama University, Okayama, Japan

© Springer Nature Singapore Pte Ltd. 2019

Y. Kubozono (ed.), *Physics and Chemistry of Carbon-Based Materials*,
https://doi.org/10.1007/978-981-13-3417-7_8

one of group-14 elements. Carbon (C), silicon (Si), and germanium (Ge) located at the group-14 in the periodic table have been utilized for transistors. In 1947, Bardeen first prepared a bipolar junction transistor using Ge, which is a point-contact transistor [1, 2]. Subsequently, Kahng and Attala succeeded in preparing a new type of transistor using Si crystals, which is presently called "metal-oxide-semiconductor (MOS) field-effect transistor (FET)" [3, 4]. The MOS-FET has many advantages, such as "ease of design for integration and high-reproducibility/low-energy consumption in device-fabrication." Thus, most of the current transistors are categorized as MOS-FET. During the past 50 years, active layers of FET have been formed by Si crystals because of a formation of large conduction path through covalent bonds between Si atoms and an easy fabrication of gate dielectric, SiO_2 (which is easily prepared by thermal oxidation of Si). The filed-effect mobility of Si FET is generally 1000 $cm^2\ V^{-1}\ s^{-1}$ [4].

In 1980s, the FETs were first fabricated using organic molecules and organic polymers [5, 6], instead of Si and other inorganic elements/materials. The most important purpose of using organic molecules and polymers was to make the best use of advantages of organic materials. Namely, it was expected that the new FET devices with the advantages, such as flexibility, light-weight, shock-resistance, and large-area coverage, might be produced using organic materials. Such advantages would emerge because of the weak interaction between molecules, i.e., the van der Waals force. However, the field-effect mobility, μ, was as low as $10^{-5}\ cm^2\ V^{-1}\ s^{-1}$, which means that the weak interaction becomes the demerit for conduction path formation. Throughout the 1990s, the organic FETs exhibiting higher μ value were pursued by searching for the organic molecules suitable for FET device. In 1997, the μ value in the pentacene thin-film FET came to be 1.5 $cm^2\ V^{-1}\ s^{-1}$ [7]. This FET showed the p-channel normally-off characteristics. Since the report, the pentacene molecule that consists of five benzene rings has been recognized as a promising material for the active layer of practical FET. Furthermore, in 1995 a more suitable material, C_{60}, for n-channel FET was discovered, which was composed of 60 C atoms, and it has a soccer ball-shaped structure [8]. The μ value was 0.08 $cm^2\ V^{-1}\ s^{-1}$.

After the year 2000, the μ value has rapidly increased through an application of new organic materials toward FETs, and various materials have attracted much attention owing to the high μ value. The rubrene molecule realized the high-performance single-crystal FET exhibiting the p-channel properties and the μ value as high as 40 $cm^2\ V^{-1}\ s^{-1}$ [9]. The molecule has four phenyl groups and tetracene framework. Furthermore, the thin-film FETs using dioctylbenzothienobenzothiophene (C8-BTBT) showed a very high μ value (9.1 $cm^2\ V^{-1}\ s^{-1}$) [10]. The higher μ value (= 15.6 $cm^2\ V^{-1}\ s^{-1}$) was reported for the FET with thin film of bis (benzothieno) naphthalene (BBTN) [11], which is an analogue of BTBT. The highest μ value among the C8-BTBT thin-film FETs is presently 43 $cm^2\ V^{-1}\ s^{-1}$ [12]. Thus, the high μ value in an organic thin-film FET exceeds 1 $cm^2\ V^{-1}\ s^{-1}$.

In this chapter, the FETs using various π-conjugated hydrocarbon molecules are fully reported. In particular, the characteristics of thin-film and single-crystal

FETs using various fullerenes and phenacene molecules are introduced, which includes the electronic and structural features of their molecules. Furthermore, the applications of FETs with these molecules toward logic gate circuits are reported. Additionally, intercalation chemistry of solids of π-conjugated hydrocarbon molecules is described in this chapter. In particular, the superconductivity observed for metal-doped π-conjugated hydrocarbons is introduced together with the difficulty in the research on their superconductors [13–16]. Finally, a recent progress of intercalation chemistry of phenacene molecules is also introduced.

8.2 Application of Fullerenes Toward FET Devices

8.2.1 FET Devices Using Thin Films of C_{60} and C_{70}

In 1995, the first operation of a fullerene thin-film FET was achieved by Huddon et al. [8]. The C_{60} thin-film FET showed n-channel normally-off characteristics. Subsequently, the thin-film FET using C_{70}, which consists of 70 C atoms (rugby ball-shaped structure), was fabricated by the same group, showing n-channel properties [17]. Figure 8.1 shows the molecular structures of C_{60} and C_{70}. The

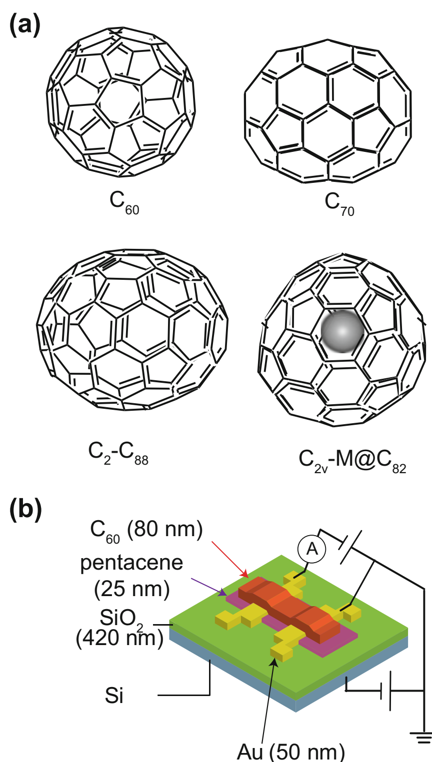

Fig. 8.1 (**a**) Molecular structures of C_{60} and C_{70}, empty higher fullerene and metallofullerene, and (**b**) structure of the middle-contact-type FET device

μ value of C_{60} thin-film FET increased up to 0.56 $cm^2\ V^{-1}\ s^{-1}$, where the FET properties were measured without any exposure to air [18], because the n-channel operation was strongly lowered by O_2 and H_2O. Further, an increase in μ value was achieved by the formation of C_{60} thin film on pentacene layer, in which the thin film has molecular arrangement suitable for FET transport [19]. The μ value was 4.9 $cm^2\ V^{-1}\ s^{-1}$.

Our group succeeded in the fabrication and n-channel operation of C_{60} thin-film FET [20]. Furthermore, the complementary MOS (CMOS) logic gate circuit (inverter) was fabricated using the C_{60} thin-film FET (n-channel) and pentacene thin-film FET (p-channel) [20], which showed a clear inverter property. We observed ambipolar properties in the thin-film FET using heterostructure of C_{60} and pentacene [21]; the middle-contact type structure (Fig. 8.1b) showed the good n-channel/p-channel FET characteristics. The flexible device and the low-voltage operation in the C_{60} thin-film FET was realized using polymer gate dielectric (polyimide) and high-k gate dielectric ($Ba_{0.4}Sr_{0.6}Ti_{0.96}O_3$), respectively, by our group [22]. Subsequently, we fabricated flexible C_{60} thin-film FET with parylene gate dielectric on polyethylene terephthalate (PET), which showed the μ as high as 0.41 $cm^2\ V^{-1}\ s^{-1}$ [23]. We changed metal for source/drain electrodes from Au, and the normally-on FET characteristics were observed when using Eu with a small work function, ϕ (= 2.5 eV) because of no potential barrier between source/drain electrodes and lowest unoccupied molecular orbital (LUMO). The μ value reached 0.50 $cm^2\ V^{-1}\ s^{-1}$ [24]. Although various metal atoms were used for the source/drain electrodes, the p-channel operation could not be observed in the C_{60} thin-film FET. The n-channel operation was realized for the pentacene thin-film FET with Ca source/drain electrodes having a very small ϕ (= 2.9 eV) [25]. The current μ value in the C_{60} thin-film FET reaches 5.3 $cm^2\ V^{-1}\ s^{-1}$ when the C_{60} thin film is formed on self-assembled monolayers of alkylsilanes [26]. Furthermore, the solution-grown aligned C_{60} single-crystal FET showed the μ as high as 2.0(6) $cm^2\ V^{-1}\ s^{-1}$ [27]. Thus, the C_{60} FET is currently one of the most promising n-channel organic FETs from the viewpoint of practical application.

8.2.2 FET Devices Using Thin Films of Other Fullerenes

Fullerene is a general term of diverse molecules consisting of C atoms and taking ball structure. There are many fullerenes other than C_{60} and C_{70}, such as C_{76}, C_{78}, C_{84}, C_{86}, and C_{88}. These are named "empty higher fullerenes" because no elements other than C atoms are included. Moreover, the molecule that metal atoms are encapsulated in the ball-shaped structure consisting of C atoms is termed "metallofullerenes" or "metal endohedral fullerenes." A few typical molecular structures of empty higher fullerene and metallofullerene are shown in Fig. 8.1a. The

Table 8.1 FET parameters of fullerene FETs with SiO_2 gate dielectric

	Polarity	μ [cm^2 V^{-1} s^{-1}]	V_{TH} [V]	References
C_{60}	*n*	5.3	–	[26]
C_{70}	*n*	2×10^{-3}	27	[17]
C_{76}	*n*	3.9×10^{-4}	−5	[28]
C_{78}	*n*	4.6×10^{-4}	35	[28]
C_{82}	*n*	1.9×10^{-3}	–	[29]
C_{84}	*n*	2.1×10^{-3}	–	[30]
C_{88}	*n*	2.5×10^{-3}	–	[31]
$Dy@C_{82}$	*n*	8.9×10^{-5}	–	[20]
$La_2@C_{80}$	*n*	1.1×10^{-4}	−64	[32]
$Ce@C_{82}$	*n*	10^{-4}	–	[33]
$Pr@C_{82}$	*n*	1.5×10^{-4}	37	[34]

Table 8.2 E_{mob} and E_{band} for the fullerenes

	E_{mob} [eV]	E_{band} [eV]	References
C_{60}	–	1.8	[35]
C_{70}	–	2.2	[35]
C_{76}	0.16	1.3	[28]
C_{78}	0.27	0.78	[28]
C_{82}	0.22	1.15	[29]
C_{84}	0.28 or 0.55	1.1	[30, 36]
C_{88}	0.42	–	[31]
$Dy@C_{82}$	0.2	–	[20]
$La_2@C_{80}$	–	0.87 or 1.6	[32, 37]
$Ce@C_{82}$	–	0.4	[33]
$Pr@C_{82}$	0.29	0.7	[34]

FET devices using thin films of empty fullerenes (C_{76}, C_{78}, C_{82}, C_{84}, and C_{88}) were first fabricated by our group [20, 28–31], which show the n-channel FET properties as in the C_{60} and C_{70} FETs. The μ values of these FETs are listed in Table 8.1. The highest μ value was obtained for the C_{88} thin-film FET [31], providing the μ as high as 2.5×10^{-3} cm^2 V^{-1} s^{-1}.

The first metallofullerene FET was prepared using $Dy@C_{82}$, which showed n-channel FET characteristics with the μ as high as 8.9×10^{-5} cm^2 V^{-1} s^{-1} [20]. The n-channel FET characteristics were also recorded in the other metallofullerenes, $La_2@C_{80}$, $Ce@C_{82}$, and $Pr@C_{82}$ [32–34]. As expected from the small mobility gap, E_{mob}, which was determined from the temperature dependence of the resistivity, ρ, most of thin-film FETs using empty fullerenes and metallofullerenes showed normally-on properties [31–34]. Table 8.2 lists the FET properties, E_{mob} and band gap, E_{band}, determined from photoelectron spectroscopy [28–37]. The FET properties of thin film of [6,6]-phenyl-C_{61} butyric acid methyl ester (PCBM) are reported, exhibiting the μ as high as 0.2–0.3 cm^2 V^{-1} s^{-1} [38].

8.3 Application of Phenacene Molecules Toward FET Devices

8.3.1 FET Devices Using Picene Molecule

The phenacene molecule consists of plural benzene rings and takes a W-shaped molecular structure. The first FET of phenacene molecule was fabricated using picene molecule, which consists of five benzene rings (Fig. 8.2a). The FET showed p-channel normally-off FET characteristics with the μ as high as 1.1 cm^2 V^{-1} s^{-1} under O_2 atmosphere [39], which was determined from the reverse transfer curve, while the μ determined from the forward transfer curve was at most 10^{-1} cm^2 V^{-1} s^{-1} in the first picene thin-film FET. The FET showed a clear increase in μ by O_2-exposure for a long time. A subsequent study reported that the μ value of picene thin-film FET determined from the forward and reverse curve came to be 1.4 cm^2 V^{-1} s^{-1} and 3.2 cm^2 V^{-1} s^{-1}, respectively [40]. The quality of thin films of picene was checked using atomic force microscope (AFM), and the FET was fabricated with high-quality thin-film of picene [41], providing μ as high as 1.2 cm^2 V^{-1} s^{-1}. Thus, it was confirmed that picene was a promising material as an active layer for high-performance FET.

The low-voltage operation in picene thin-film FET was successfully achieved using a thin SiO_2 gate dielectric [42], and the absolute threshold voltage, $|V_{TH}|$, of 11 V was realized. Instead of Au electrodes, the conduction polymer poly (3,4-ethylenedioxythiophene)-poly (styrenesulfonate) (PEDOT:TSS) electrodes were used for the source and drain electrodes in the picene thin-film FET [43], which should open to complete metal-less device. The flexible picene thin-film FET was fabricated using parylene gate dielectric on PET substrate, which showed the μ as high as 1.1 cm^2 V^{-1} s^{-1} from the forward/reverse transfer curve [44]. The O_2 sensing properties of picene thin-film FET were fully investigated, and the O_2 sensing ability was quantitatively clarified. The picene thin-film FET was responsive to 10 ppm of O_2, and the drain current, $|I_D|$, quickly increased under 0.01 Torr of O_2 [45]. Further investigation of O_2 sensing properties of picene thin-film FET was performed using high-k gate dielectrics, such as ZrO_2, Ta_2O_5, HfO_2, and $Ba_xSr_{1-x}TiO_3$ (x = 0.4) with/without visible light [46], suggesting that the O_2 sensing properties closely relates to HOMO-LUMO electron excitation. The picene single-crystal FET was first fabricated using various gate dielectrics [47], showing the μ value as high as 1.3 cm^2 V^{-1} s^{-1} in the case of HfO_2 gate dielectric; the μ value was obtained from the forward transfer curve.

Thus, the picene FETs exhibit good FET characteristics in both thin film and single crystal. The typical FET characteristics of picene thin-film FET is shown in Figs. 8.2b, c, which was recently fabricated by our group. The μ was determined to be 8.3×10^{-1} cm^2 V^{-1} s^{-1} from the forward transfer curve, which was measured under Ar atmosphere. Table 8.3 lists the FET parameters of picene thin-film FETs.

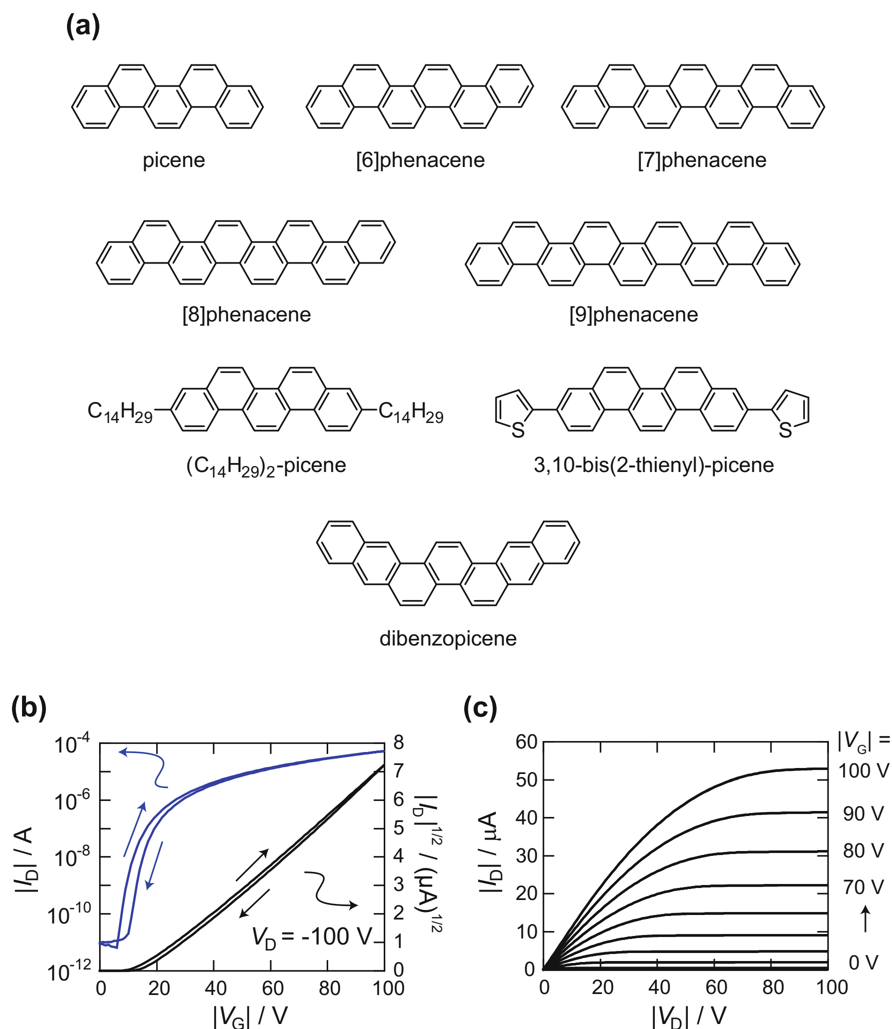

Fig. 8.2 (**a**) Molecular structures of **[n]**phenacenes ($n = 5$–9) and their derivatives. (**b**) Typical transport and (**c**) output characteristics of picene thin-film FET with 400-nm-thick SiO_2 gate dielectric. The SiO_2 surface was treated with hexamethyldisilazane (HMDS)

8.3.2 FET Devices Fabricated Using Phenacene Molecules Other than Picene

The phenacene molecules were synthesized by a repletion of Wittig reaction and Mellory homologation [48–51]; details are shown in Chap. 7. This synthetic route provided the efficient amounts of phenacene samples to proceed to the FET works. The molecules of **[6]**phenacene and **[7]**phenacene (Fig. 8.2a), which

Table 8.3 FET parameters of the picene thin-film and single-crystal FETs

	Active layer	μ [cm^2 V^{-1} s^{-1}]	$\lvert V_{TH} \rvert$ [V]	On/Off	Gate dielectric	Atmosphere	References
Picene	Thin film	1.1	–	1.6×10^5	SiO_2	O_2	[39]
Picene	Thin film	1.4	–	–	SiO_2	O_2	[40]
Picene	Thin film	1.2	–	–	SiO_2	Air	[41]
Picene	Thin film	1.1	93	10^7	Parylene	Vacuum	[44]
Picene	Thin film	0.08	–	–	SiO_2	Vacuum	[45]
Picene	Thin film	0.54	6.2	–	Ta_2O_5	Ar	[46]
Picene	Thin film	0.036	6.7	–	ZrO_2	Ar	[46]
Picene	Thin film	0.015	6.9	–	HfO_2	Ar	[46]
Picene	Thin film	0.0019	4.0	–	BST	Ar	[46]
Picene	SC[a]	0.40	27	–	Ta_2O_5	Ar	[47]
Picene	SC[a]	1.3	30	–	HfO_2	Ar	[47]

[a]SC refers to single crystal

consist of six and seven benzene rings, respectively, were first synthesized using the above synthetic method. The **[6]**phenacene and **[7]**phenacene thin-film FETs showed typical p-channel FET characteristics [52–54], which provided μ as high as 3.7 cm^2 V^{-1} s^{-1} and 0.75 cm^2 V^{-1} s^{-1}, respectively, from the forward transfer curve [52, 53]. The FET characteristics of **[6]**phenacene thin-film FET were fully investigated in a wide temperature range [54]. The μ value of **[6]**phenacene thin-film FET was 7.4 cm^2 V^{-1} s^{-1} in the second report [54], which is one of the best μ values in the organic thin-film FETs. The high-performance flexible FET was also fabricated with the thin film of **[6]**phenacene and the parylene gate dielectric on PET substrate, providing the μ value as high as 2.7 cm^2 V^{-1} s^{-1} [54]. Thus, it was observed that the **[6]**phenacene molecule was an excellent material for the active layer of FET device.

The FET devices were fabricated using single crystals of **[6]**phenacene and **[7]**phenacene [55], which showed p-channel FET characteristics. These single crystals show the plate-type shape, and the *ab*-plane corresponds to the flat surface. Therefore, their crystal shape is suitable for the fabrication of FET device because the channel transport is formed in the *ab*-plane. The μ values of **[6]**phenacene and **[7]**phenacene single-crystal FETs were 5.6×10^{-1} and 6.7–6.9 cm^2 V^{-1} s^{-1} [55, 56], respectively. It is noteworthy that the **[6]**phenacene molecule, which showed the high μ value in the thin-film FET, did not provide the high μ value in the single-crystal FET. The optical microscope image of **[6]**phenacene single crystal showed the aggregation of some crystals and many voids, i.e., a very small flat surface, suggesting that the low FET properties originate from the low quality of **[6]**phenacene single crystals.

Very recently, we retried to make **[6]**phenacene single crystals. Here we reduced the time required for growing the single crystals from several days to 2 h, so as to suppress the aggregation of other crystals except for the target crystal. We could obtain a single crystal without an aggregation of other crystals (Fig. 8.3a). The

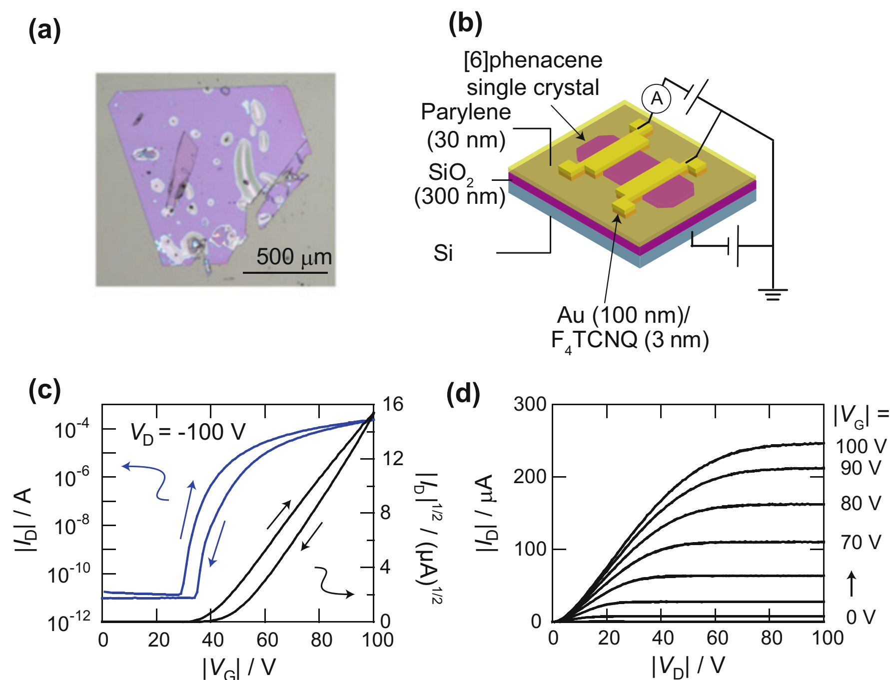

Fig. 8.3 (**a**) Photograph of a single crystal of **[6]**phenacene. (**b**) Device structure of **[6]**phenacene single-crystal FET. (**c**) Transport and (d) output characteristics of the **[6]**phenacene single-crystal FET with 300-nm-thick SiO_2 gate dielectric. The surface of SiO_2 was coated with 30-nm-thick parylene

FET with a single crystal showed the p-channel FET characteristics exhibiting the μ as high as 2.4 $cm^2\ V^{-1}\ s^{-1}$ which is larger by a factor of 4 than that, 5.6×10^{-1} $cm^2\ V^{-1}\ s^{-1}$, of the previous report [55]. The transport and output properties of **[6]**phenacene single-crystal FET are shown in Fig. 8.3b, d together with the device structure.

Furthermore, the molecules of **[8]**phenacene and **[9]**phenacene (Fig. 8.2a) were synthesized by the repletion of Wittig reaction and Mellory homologation [48–51]. The **[9]**phenacene molecule is the most extended phenacene molecule which was utilized for FET device. Both the **[8]**phenacene and **[9]**phenacene thin-film FETs with SiO_2 gate dielectrics showed p-channel normally-off FET characteristics with the average μ, <μ>, values of 1.2(3) $cm^2\ V^{-1}\ s^{-1}$ [57, 58]. Very recently, molecules of [10]phenacene and [11]phenacene were successfully synthesized, but the FET properties are not investigated. The single crystals of these molecules were also applied for the active layer of FET device. Both the **[8]**phenacene and **[9]**phenacene single-crystal FETs with SiO_2 gate dielectric showed p-channel normally-off FET characteristics with the <μ> values of 3(2) and 8(1) $cm^2\ V^{-1}\ s^{-1}$, respectively [58, 59]. The highest μ value in **[9]**phenacene single-crystal FET was

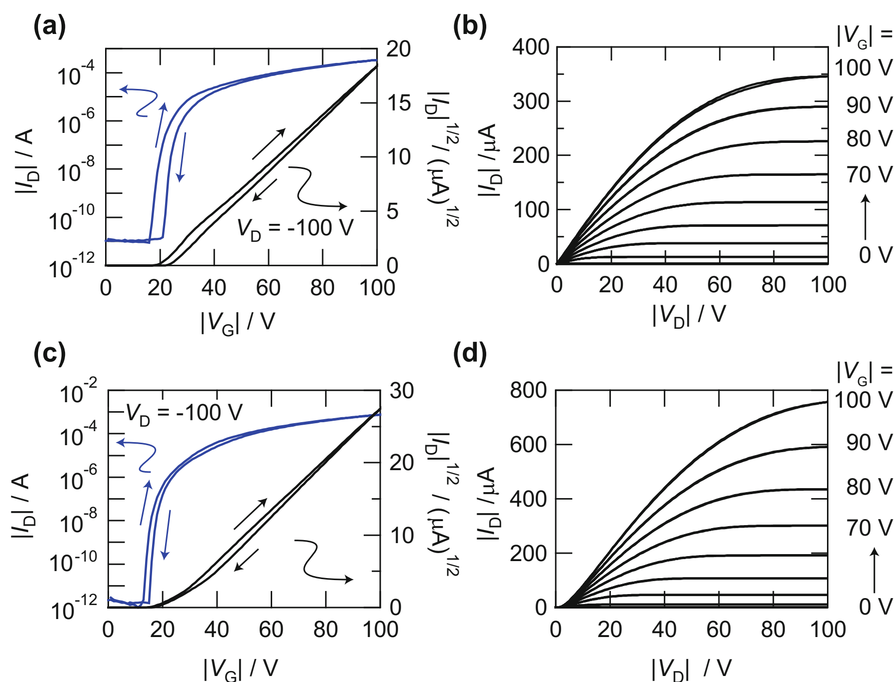

Fig. 8.4 (**a**) Transport and (**b**) output characteristics of **[8]**phenacene single-crystal FET. (**c**) Transport and (**d**) output characteristics of **[9]**phenacene single-crystal FET. 300-nm-thick SiO_2 was used for gate dielectric. The surface of SiO_2 was coated with 30-nm-thick parylene

18 cm^2 V^{-1} s^{-1} in the case of ZrO_2 gate dielectric [58]. This value is comparable to that of rubrene single-crystal FET [9], and it is the highest in the μ values evaluated at two-terminal measurement mode for organic single-crystal FETs. Thus, the extension of π-framework can increase the μ value, probably owing to the increase in π-π interaction between molecules. Typical FET characteristics of **[8]**phenacene and **[9]**phenacene single-crystal FETs are shown in Fig. 8.4a, d; the μ values were 7.5 and 9.1 cm^2 V^{-1} s^{-1}, respectively.

Figure 8.5a shows the plot of μ as a function of number of benzene rings; the maximum μ value is plotted in each **[n]**phenacene single-crystal FET with SiO_2 gate dielectric. The μ value increases straightforwardly with increasing number of benzene rings from five to nine, which indicates the significant correlation between μ and π-π interaction; the $<\mu>$ also increases with increasing number of benzene rings. As shown in Fig. 8.5a, the usage of more extended phenacene molecule is key for the realization of high-performance FET device. This will be further discussed later.

We fabricated the phenacene thin-film FET exhibiting μ as high as 21 cm^2 V^{-1} s^{-1} using the alkyl-substituted picene (3,10-ditetradecylpicene: $(C_{14}H_{29})_2$-picene) [60]; this μ value was estimated at two-terminal measurement

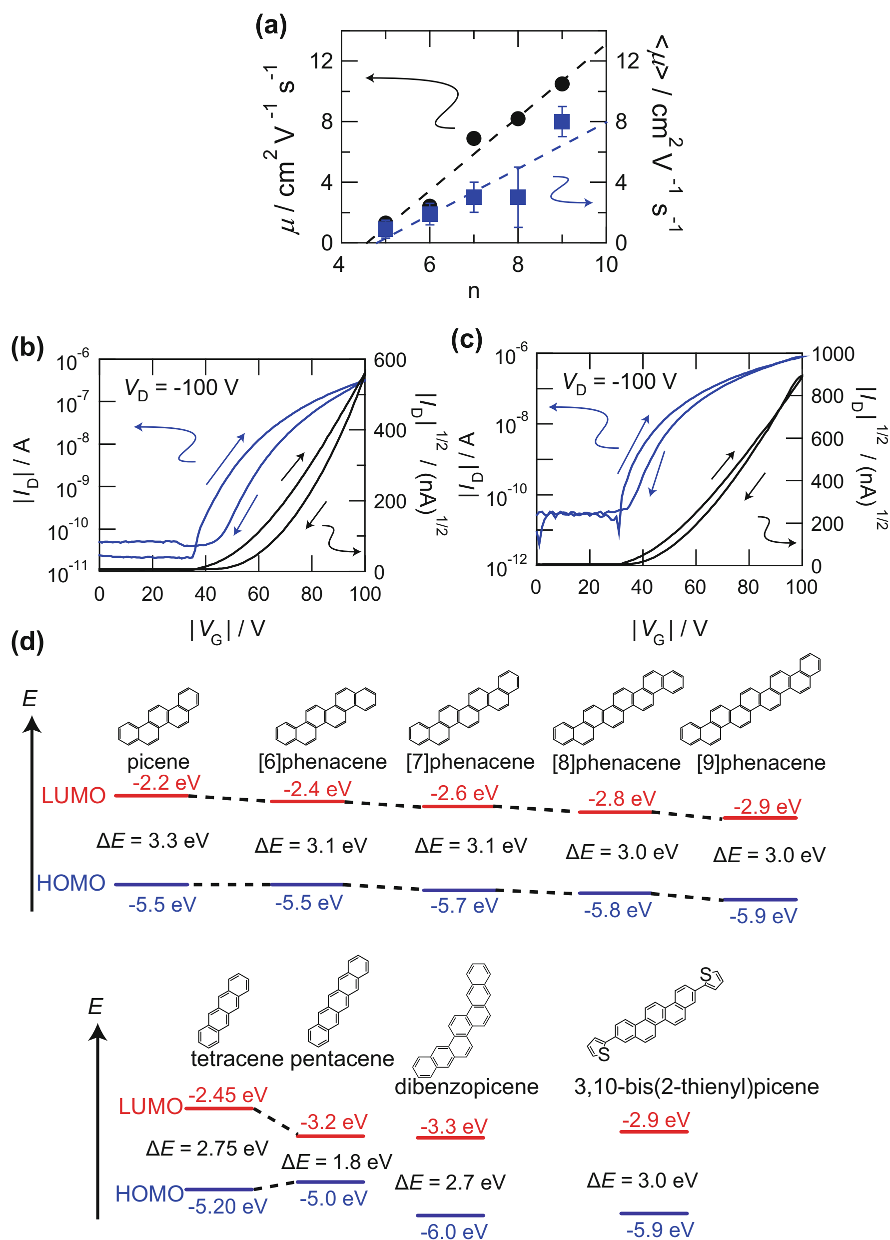

Fig. 8.5 (**a**) Plot of the maximum μ (μ_{max}) versus number of benzene rings in **[n]**phenacene (n = 5–9). The averaged μ (<μ>) values are also plotted. Transfer characteristics of (**b**) dibenzopicene and (**c**) 3,10-bis(2-thienyl)picene thin-film FETs with 400-nm-thick SiO_2 gate dielectrics. The surface of SiO_2 was treated HMDS. (**d**) Energy diagram of phenacenes and acenes

mode. The $(C_{14}H_{29})_2$-picene molecule may produce the strong π-π interaction between molecules because of a fastener effect accompanied by alkyl substituents. Thus, the suitable addition of substituents is also important for recording the high μ value. To investigate the effect of substituents on the FET properties, the FETs using thin films of dibenzopicene and 3,10-bis(2-thienyl)picene molecules (Fig. 8.2a) were fabricated, which showed p-channel FET properties. The transport properties are shown in Fig. 8.5b, c. The μ values of dibenzopicene and 3,10-bis(2-thienyl)picene thin-film FETs were 4.1×10^{-2} and 6.8×10^{-2} cm^2 V^{-1} s^{-1}, respectively; the $<\mu>$ values evaluated from plural FETs are $2.0(9) \times 10^{-2}$ and $5(2) \times 10^{-2}$ cm^2 V^{-1} s^{-1}, respectively. Therefore, the alkyl-substitution to picene provided the high-performance FET device. The energy diagram of dibenzopicene and 3,10-bis(2-thienyl)picene are shown in Fig. 8.5d. The band gaps and HOMO levels are almost the same as those of other phenacenes. Consequently, the low mobility may originate from the stacking between molecules. In other words, the fastener effect due to alkyl substituents may be important for the strong coupling between molecules.

The phenacene molecule is chemically stable even in atmospheric condition, because of their wide band gap and deep HOMO level. The energy diagram of **[n]**phenacene molecules ($n = 5$–9) are shown in Fig. 8.5d**.** The band gap gradually decreases with an increase in number of benzene rings, while the HOMO lowers gradually. This deeper HOMO produces the larger Schottky barrier because of the larger energy difference between the Fermi level of Au (−5.0 eV) and HOMO level, leading to the lowering of p-channel FET characteristics. Therefore, the design for lowering the Schottky barrier height must be required for increasing the μ value in addition to strengthen the π-π interaction through the extension of benzene network. Instead of Au, the metal (ex. Pt: $E_F = -5.65$ eV [61]) with larger work function, ϕ, may be utilized for the source/drain electrodes for the lowered Schottky barrier height. All FET parameters for the FET devices with phenacenes other than picene are listed in Table 8.4.

Table 8.4 FET parameters of **[n]**phenacene thin-film and single-crystal FETs with SiO_2 gate dielectric

	Active layer	μ [cm^2 V^{-1} s^{-1}]	$\|V_{TH}\|$ [V]	On/Off	S [V decade^{-1}]	References
[6]phenacene	Thin film	7.4	69	3.60×10^7	–	[54]
	SC[a]	2.42	31.74	1.12×10^7	1.73	This work
[7]phenacene	Thin film	0.75	–	–	–	[53]
	SC[a]	6.9	50	1.0×10^9	0.93	[56]
[8]phenacene	Thin film	1.74	51.3	5.6×10^6	3.90	[57]
	SC[a]	8.2	28	3.5×10^8	1.6	[59]
[9]phenacene	Thin film	1.7	42	2.6×10^7	3.9	[58]
	SC[a]	17.9	2.12	2.9×10^7	0.212	[58]

[a]SC refers to single crystal

8.3.3 Logic Gate Circuits Fabricated Using Phenacene FET

The CMOS logic gate circuits were fabricated using phenacene FETs which operate as p-channel FET and N,N′-bis(n-octyl)-dicyanoperylene-3,4:9,10-bis(dicarboximide) (PDI8-CN2) FET for n-channel operation; the molecular structure of PDI8-CN2 is shown in Fig. 8.6a. Figure 8.6b, d shows the equivalent circuit, the schematic representation, and the photograph of CMOS inverter. The FET parameters of individual FETs are listed in Table 8.5. The plot of output (V_{out}) against input (V_{in}) is shown in Fig. 8.6e. The voltage of 100 V was applied to the drain-drain voltage (V_{DD}) shown in the equivalent circuit. As shown in Fig. 8.6e, the NOT property (low V_{out} for high V_{in} and high V_{out} for low V_{in}) is clearly observed; the low V_{out} and high V_{out} in $V_{out} - V_{in}$ plot are called V_L and V_H, respectively. The V_{TC}, which corresponds to the V_{in} providing $V_{out} = (V_H + V_L)/2$, was estimated to be 33 V for the forward $V_{out} - V_{in}$ plot, with being lower than the ideal V_{TC} ($= V_{DD}/2 = 50$ V).

The V_{TC} of CMOS inverter circuit is expressed by

$$V_{TC} = \frac{V_{THn} + \sqrt{\frac{k_p}{k_n}}\left(V_{DD} + V_{THp}\right)}{\left(1 + \sqrt{\frac{k_p}{k_n}}\right)}, \tag{8.1}$$

where $k = \frac{\mu WC}{L}$. k_p and k_n correspond to k for p-channel and n-channel FETs, respectively, and the V_{THn} and V_{THp} refer to the V_{TH} values for p-channel and n-channel FETs, respectively [62]. The W, L, and C refer to the channel width, channel length, and capacitance per area for each FET, respectively.

The V_{TC} value can be calculated using the expression (8.1) and the FET properties of **[8]**phenacene and PDI8-CN2 thin-film FETs evaluated individually. The calculated value of V_{TC}, V_{TC}(cal) was estimated to be 31 V for the inverter, which is consistent with that determined from the $V_{out} - V_{in}$ plot, 33 V. The lower V_{TC} than $V_{DD}/2 = 50$ V originates from the unbalance of FET properties of **[8]**phenacene and PDI8-CN2 thin-film FETs, i.e., $V_{TH} = -59$ V for the **[8]**phenacene thin-film FET and $V_{TH} = -2.1$ V for PDI8-CN2 thin-film FET. To come close to the ideal V_{TC} value, the $|V_{TH}|$ of **[8]**phenacene thin-film FET should be decreased by using high-k gate dielectric, while the PDI8-CN2 thin-film FET must be modified to show the normally-off properties. The normally-off properties in the PDI8-CN2 thin-film FET may be achieved by a depletion of electrons from channel region using electron-acceptor. The gain was evaluated to be 56 from the steepest slope of $V_{out} - V_{in}$ plot (Fig. 8.6e) of the **[8]**phenacene/PDI8-CN2 inverter. The numerical derivative of $V_{out} - V_{in}$ plot at 1 V step is shown in Fig. 8.6f, indicating that the maximum derivative value corresponds to "gain."

The $V_{out} - V_{in}$ plots of **[n]**phenacene/PDI8-CN2 inverters consisting of **[n]**phenacene FET (n = 5–9) (p-channel) and PDI8-CN2 FET (n-channel) are shown in Fig. 8.7a; $V_{DD} = 100$ V. The NOT property is found for all inverters.

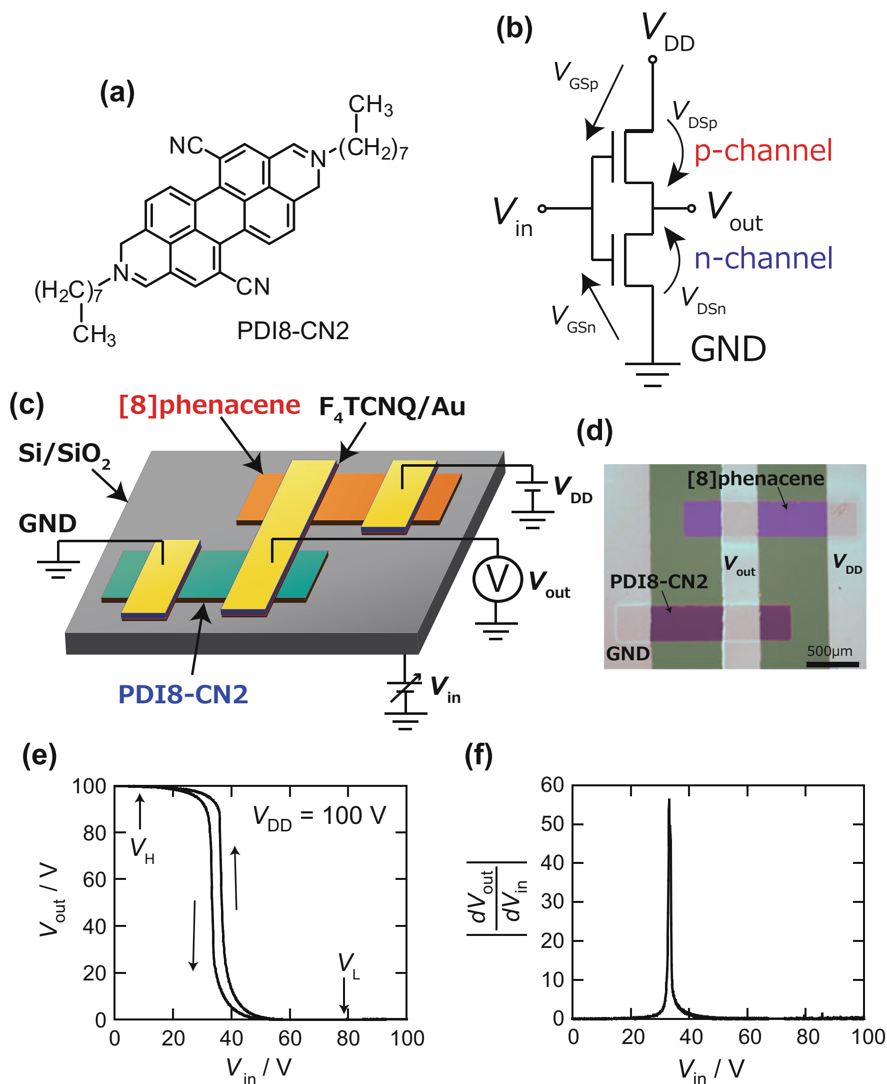

Fig. 8.6 (**a**) Molecular structure of PDI8-CN2. (**b**) Equivalent circuit of CMOS inverter. (**c**) Schematic representation and (**d**) photograph of CMOS inverter using thin films of **[8]**phenacene and PDI8-CN2. (**e**) Plot of $V_{out} - V_{in}$ for the CMOS inverter using thin films of **[8]**phenacene and PDI8-CN2. (**f**) Absolute numerical derivative ($|\frac{dV_{out}}{dV_{in}}|$) of $V_{out} - V_{in}$ for the CMOS inverter; the maximum value corresponds to gain of inverter

Table 8.5 FET parameters of **[n]**phenacene (n = 5–9) and PDI8-CN2 thin-film FETs with SiO_2 gate dielectric and inverter-parameters of CMOS inverter using **[n]**phenacene (n = 5–9) and PDI8-CN2

	μ [$cm^2 V^{-1} s^{-1}$]	V_{TH} [V]	S [V dec.$^{-1}$]	on/off	L [μm]	W [μm]	C [F cm^{-2}]	V_{TC} [V]	V_{TC}(cal) [V]	Gain
Picene	0.82	−17	10	1.1×10^3	772	2443	1.02×10^{-8}	58	73	104
PDI8-CN2	0.018	4.8	9.1	8.7×10^2	610	2047				
[6]phenacene	0.74	−23	1.0	3.8×10^7	933	1575	1.02×10^{-8}	57	64	80
PDI8-CN2	0.0099	−13	71	13	473	1642				
[7]phenacene	0.0041	−62	2.8	3.5×10^4	528	600	1.02×10^{-8}	17	9.6	30
PDI8-CN2	0.013	−7.6	27	58	606	600				
[8]phenacene	0.34	−59	8.7	2.7×10^3	848	600	1.02×10^{-8}	33	31	56
PDI8-CN2	0.02	−2.1	33	1.5×10^2	582	600				
[9]phenacene	0.0098	−53	4.6	1.3×10^4	598	2093	1.02×10^{-8}	22	20	31
PDI8-CN2	0.015	1.6	8.0	1.4×10^3	456	2211				

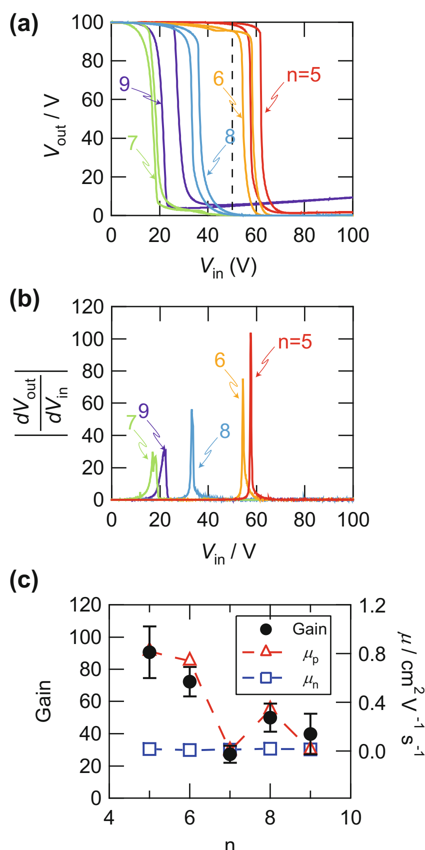

Fig. 8.7 (**a**) Plots of $V_{out} - V_{in}$ for **[n]**phenacene/PDI8-CN2 inverters. (**b**) Absolute numerical derivatives ($|\frac{dV_{out}}{dV_{in}}|$) of $V_{out} - V_{in}$ plots for the **[n]**phenacene/PDI8-CN2 inverters; the maximum value corresponds to the gain of inverter. (**c**) Gain versus *n* in the **[n]**phenacene/PDI8-CN2 inverters, i.e., n means number of benzene rings of phenacene molecule. The μ_p (μ of **[n]**phenacene thin-film FET) is also plotted as a function of n. The μ_n – n plot is made from the μ value of PDI8-CN2 thin-film FET combining with **[n]**phenacene FET in the inverter

As seen from Fig. 8.7a, the V_{TC} values in the inverters using **[7]**phenacene and **[9]**phenacene much deviate from the ideal V_{TC} (= 50 V). The FET parameters are listed in Table 8.5 together with V_{TC}, and gain determined from the $V_{out} - V_{in}$ plots. The highest gain was 104 for the inverter using picene (n = 5) and PDI8-CN2 (Fig. 8.7b). This value is one of the highest gains recorded for the inverter using organic thin films. The highest gain of the inverter fabricated using organic thin films is currently 250 for the inverter consisting of pentacene (p-channel) and N,N′-ditridecylperylene-3,4,9,10-tetracarboxylic diimide (PTCDI-C13) (n-channel) thin-film FETs [63]. Some reports on the inverters showing the high gain (>100) have already been published in refs. [64, 65].

Therefore, it was suggested that the phenacene thin-film FET was suitable for the CMOS inverter. The gain of inverter and the n-channel mobility (μ_n) and p-channel mobility (μ_p) of the PDI8-CN2 and **[n]**phenacene (n = 5–9) FETs are shown in Fig. 8.7c. The clear correlation between μ_p and gain is found in the plots (Fig. 8.7c). Namely, the gain is dominated by the higher μ value between p-channel

and n-channel FETs. Instead of PDI8-CN2, more superior n-channel FET should be pursued to increase the gain of the inverter.

Finally, we tried to fabricate the ring oscillator combining five inverters consisting of **[6]**phenacene and N,N′-dioctylperylene-3,4,9,10- tetracarboxylic diimide (PTCDI-C8) thin-film FETs; the PTCDI-C8 FET (Fig. 8.8a) was used as n-channel FET. The device structure was shown in Fig. 8.8b for the convenience of understanding how to fabricate the ring oscillator. As shown in Fig. 8.8b, the Au electrodes was formed on the SiO_2/Si substrate, and 500-nm-thick parylene was covered on the Au electrodes/SiO_2/Si substrate. The 60-nm-thick thin films of **[6]**phenacene and PTCDI-C8 were thermally deposited on the parylene. Finally, the Au electrodes for the V_{out}, which connects to the V_{in} electrodes of the next inverter adjacent to the first inverter, were formed. Therefore, the gate dielectric is parylene in this ring oscillator. The actual ring oscillator's photograph is also shown in Fig. 8.8b together with the equivalent circuit of ring oscillator.

Figure 8.8c shows the V_{out} as a function of time, t, for the five-stage ring oscillator fabricated using thin films of **[6]**phenacene and PTCDI-C8. The oscillation of V_{out} is observed, but the frequency is still too small. Nevertheless, the successful observation of V_{out} oscillation may be the first step for the practical ring oscillator using phenacene molecule. The frequency, f, of the ring oscillator is expressed by

$$f = \frac{1}{2n < \tau_p >}, \tag{8.2}$$

where n refers to the number of inverters. The $<\tau_p>$ is the averaged τ_p of the ring oscillator. Here, the τ_p is given by

$$\tau_p = \left(\tau_{p\mathrm{LH}} + \tau_{p\mathrm{HL}}\right)/2, \tag{8.3}$$

where the $\tau_{p\mathrm{LH}}$ corresponds to the difference between the time providing $(V_\mathrm{H} + V_\mathrm{L})/2$ in V_{in} in the case of decrease in V_{in} and that providing $(V_\mathrm{H} + V_\mathrm{L})/2$ in V_{out} in the case of the increase in V_{out}, while the $\tau_{p\mathrm{HL}}$ corresponds to the difference between the time providing $(V_\mathrm{H} + V_\mathrm{L})/2$ in V_{in} in the case of increase in V_{in} and that providing $(V_\mathrm{H} + V_\mathrm{L})/2$ in V_{out} in the case of the decrease in V_{out}; for convenience of understanding the $\tau_{p\mathrm{LH}}$ and $\tau_{p\mathrm{HL}}$, the schematic V_{out} and V_{in} in the inverter constituting the ring oscillator is shown as a function of time in Fig. 8.8d. Equations (8.2) and (8.3) suggest that increasing the response speed of all inverters is a key for the realization of high f. To sum up, the ring oscillator should be improved through optimizing the **[6]**phenacene and PTCDI-C8 FETs based on the following equations [62].

$$\tau_{p\mathrm{HL}} = \frac{C_\mathrm{load}}{k_n\left(V_\mathrm{DD} - V_{\mathrm{TH}n}\right)}\left[\frac{2V_{\mathrm{TH}n}}{V_\mathrm{DD} - V_{\mathrm{TH}n}} + \ln\left(\frac{4\left(V_\mathrm{DD} - V_{\mathrm{TH}n}\right)}{V_\mathrm{DD}} - 1\right)\right] \tag{8.4}$$

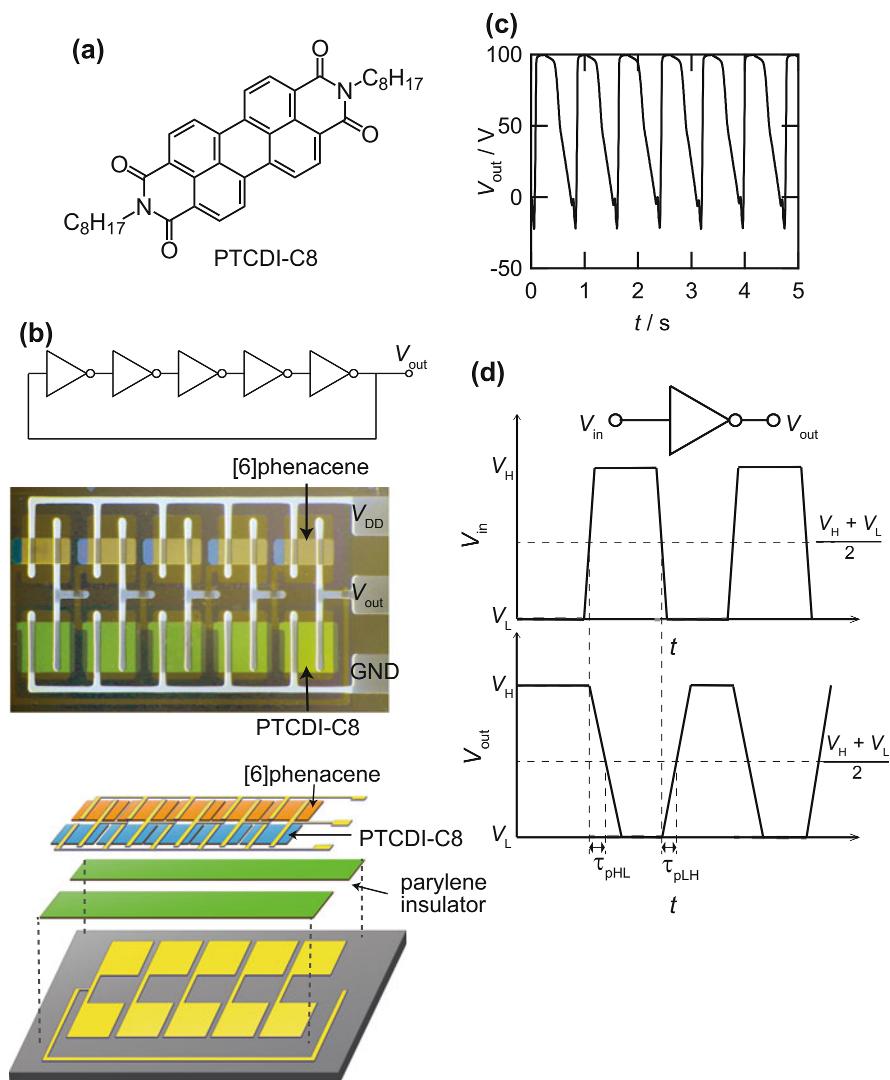

Fig. 8.8 (**a**) Molecular structure of and PTCDI-C8. (**b**) Equivalent circuit of five-step ring oscillator. Device structure of five-step ring oscillator using thin films of **[6]**phenacene and PTCDI-C8. How to fabricate the ring oscillator is also shown. (**c**) Observed V_{out} versus *time* in the ring oscillator. (**d**) Schematic graphs of V_{out} and V_{in} against *time* in the ring oscillator. $\tau_{p\mathrm{HL}}$ and τ_{pLH} are shown in this graph

and

$$\tau_{p\mathrm{LH}} = \frac{C_{\mathrm{load}}}{k_p\left(V_{\mathrm{DD}} - \left|V_{\mathrm{TH}p}\right|\right)}\left[\frac{2\left|V_{\mathrm{TH}p}\right|}{V_{\mathrm{DD}} - \left|V_{\mathrm{TH}p}\right|} + \ln\left(\frac{4\left(V_{\mathrm{DD}} - \left|V_{\mathrm{TH}p}\right|\right)}{V_{\mathrm{DD}}} - 1\right)\right]. \tag{8.5}$$

The C_{load} refers to the total capacitive load of the inverter as seen from Ref. 62. For obtaining the high f in the ring oscillator, the $\tau_{p\mathrm{LH}}$ and $\tau_{p\mathrm{HL}}$ must be reduced based on Eqs. (8.4) and (8.5). Namely, the increase in μ and the decrease in $|V_{\mathrm{TH}}|$ are very important for each FET in the ring oscillator.

8.4 Intercalation Chemistry of Phenacene Solids

Intercalation of metal atoms into phenacene solids, i.e., metal doping of phenacene solids, has been studied by many researchers. The first successful intercalation of metal doping of phenacene was achieved using picene solids by the authors' group [13]; picene has five benzene rings and W-shaped structure (Fig. 8.2), which is called "**[5]**phenacene." Metal doping of picene solids showed the superconductivity. The values of T_c were 7 and 18 K for K-doped picene ($K_x$picene) [13]. The metal doping was carried out by annealing the powder of picene and metal under vacuum, which were introduced into glass tube. The shielding fraction from the magnetic susceptibility (*M*/*H*) at zero field cooling (ZFC) was 15% for 7 K phase and 1.2% for 18 K phase; *M* and *H* refer to magnetization and applied magnetic field, respectively. Subsequently, the superconductivity of $K_x$picene (T_c = 22 K) was confirmed by the US group, but the shielding fraction was too low [66]. Furthermore, the superconductivity in $K_x$picene was confirmed by Chinese group, but the shielding fraction was low [67]. Therefore, the superconductor has not been recognized as "bulk superconductor." In addition, a new superconducting phase was recently discovered in $K_x$picene, with the T_c being as high as 14 K [16, 68]. The shielding fraction was 5.4% at 2.5 K. The shielding fraction increased with applying pressure up to 1 GPa, and it reached 18.5%. The T_c value also increased with increasing the pressure applied for the sample. The 14 K phase was fully characterized using energy-dispersive X-ray spectroscopy (EDX) [68], showing the presence of only K and C in this sample and the chemical stoichiometry of $K_{4(1)}$picene. The time-of-flight (TOF) mass spectrum showed intense peaks of picene and K together with weak peaks due to fragments of picene [68]; the fragments did not show superconductivity. Thus, the superconducting sample prepared by annealing picene and K metal was assigned to "$K_x$picene" [68].

Furthermore, Rb-doped picene showed the superconductivity with the T_c as high as 7 K and the shielding fraction of 10% at 2 K [13, 14]. Recently, Rb doping of picene solid provided the superconductivity with the T_c of 11 K and the shielding fraction of 14% at 3 K [15]. Moreover, Ca doping of picene showed the 7 K

superconductivity with the shielding fraction of 1.25% [14]. Subsequently, Italian group reported the superconductivity of Sm-doped picene with the T_c as high as 4 K [69]. However, the shielding fraction was as low as 1%.

The systematic studies of metal doping of other phenacene molecules have also been performed for phenanthrene, which has three benzene rings in phenacene-type structure [70–72]. The K and Rb doping of phenanthrene solids provided the superconductivity with the T_c values as high as 4.95 and 4.75 K, respectively, the shielding fractions of which were 5.3 and 6.7% at 2.5 K, respectively [70]; the shielding fraction of pellet sample of K_3phenanthrene was 15.5% at 2.5 K. $Sr_{1.5}$phenanthrene and $Ba_{1.5}$phenanthrene showed the T_c values as high as 5.6 and 5.4 K, respectively [71]. The X-ray photoemission spectroscopy (XPS) of $Sr_{1.5}$phenanthrene showed no elements other than Sr and C [15], indicating that the superconducting phase is probably assigned to Sr_xphenanthrene. It was reported that the Sm- and La-doped phenanthrene solids showed the superconductivity with the T_c values as high as 6.1 and 6.0 K, respectively [72], with the high shielding fractions, 46.1 and 49.8%. However, the superconductivity of the sample of La-doped phenanthrene may be ambiguous because La also shows the superconductivity with T_c of 5.0–6.0 K [73]. More careful study of La_xphenanthrene may be indispensable. Moreover, the superconductivity of Ba-doped anthracene (T_c = 35 K) was also reported, but the superconductivity was still filamentary. The new superconductors were prepared by metal doping of dibenzopentacene (DBP) [74]. The T_c of M_xDBP sample was 33.1 K, which showed the shielding fraction of 3.2% at 25 K; the nominal x value was 3.45. Actually, the $K_{3.45}$DBP solids provided multiple T_c values of 33.1, 20 and 5 K. The $K_{3.17}$DBP sample showed the T_c as high as 28.2 K, and its shielding fraction was 5.5% at 5 K. Recently, K-doped pentacene exhibited the superconductivity with the T_c value as high as 4.5 K [75], indicating the presence of ferromagnetic phase near superconducting phase; the shielding fraction was 1% at 2 K. Very recently, it was reported that K-doped p-terphenyl and p-quaterphenyl, which were prepared by high-pressure synthesis, provided the T_c value of 125 K [76], but the shielding fraction was too small. Such a high T_c is quite interesting, but this report must be more carefully examined because of no observation of negative M/H.

Thus, the superconductivity of metal-doped π-conjugated hydrocarbon molecules including phenacenes is a very interesting research subject. However, the shielding fractions observed for metal-doped π-conjugated hydrocarbon molecules are still too low, and some of materials did not show any diamagnetic behavior but only a drop of magnetic susceptibility, although the diamagnetic behavior is observed for most of materials; possible assignment to magnetic transition rather than superconducting transition may also be persuasive for the samples without observation of diamagnetic behavior [77]. The resistance (R) drop (or zero resistance) of metal-doped picene, which is a direct evidence for superconductivity, was confirmed for $K_x$picene [15, 78], but the suppression of R drop by applying magnetic field has not yet been investigated. The investigation is significant for the final confirmation of superconductivity. Additionally, the increase in superconducting volume fraction in metal-doped π-conjugated hydrocarbon

molecules is necessary to study the structure and fundamental physical properties of superconducting phase. To sum up, the study on metal doping of π-conjugated hydrocarbon solids is vigorously advanced by many researchers in all over the world.

8.5 Conclusion

This study describes the recent topics of carbon-based FETs, in particular fullerene and phenacene FETs. The studies performed by our group are mainly introduced. The fullerene FETs showed n-channel FET properties, while the phenacene FETs showed p-channel properties. The highest μ value among the fullerene FETs was obtained for the C_{60} FET; $\mu = 5.3$ cm^2 V^{-1} s^{-1} for C_{60} thin-film FET [26] and $\mu = 2.0$ cm^2 V^{-1} s^{-1} for its single-crystal FET [27]. The μ values of FETs with thin films of fullerenes other than C_{60} were smaller than those of C_{60} FET, because of the decrease in π-π interaction caused by the lowering of molecular symmetry.

The phenacene thin-film and single-crystal FETs exhibited p-channel FET characteristics. The μ value of **[n]**phenacene single-crystal FET increased with the increasing the number of benzene rings from five to nine. The highest μ value was 18 cm^2 V^{-1} s^{-1} for **[9]**phenacene single-crystal FET [58], which is one of the highest μ values measured at two-terminal measurement mode. The $(C_{14}H_{29})_2$-picene thin-film FET provided the μ of 21 cm^2 V^{-1} s^{-1} [60]. The high μ value must originate from the fastener effect produced by the alkyl substituents, which means the tight packing through the interaction between alkyl substituents. This would lead to strengthen the π-π interaction between molecules. The phenacene molecule is stable even in the atmospheric condition; thus, the high mobility observed in their FETs suggests high potentiality for future practical electronics. Moreover, C_{60} is the most important molecule for n-channel FET, although the n-channel transport is not observed in atmospheric condition because of the trap of electron by OH group or H_2O on the gate dielectric. In summary, C_{60} and phenacene must be key materials for the future organic electronics.

Finally, carrier-accumulation by doping of π-conjugated hydrocarbon molecules with metal atoms was discussed based on recent studies [13–16, 66–72, 74–77]. The superconductivity in metal-doped π-conjugated hydrocarbon molecules has been reported by some research groups; however, the superconducting volume fraction is still low. Consequently, the detailed experimental studies on the structure and physical properties of superconducting phases have not been successful yet. Recently, studies using single crystals of metal-doped picene, which was prepared by using a solution method, were reported [79], which suggested that K_2picene provided the behavior of spin liquid. The decisive study to confirm the superconductivity in metal-doped π-conjugated hydrocarbon solids and to determine the structure and fundamental properties of superconducting phase is strongly desirable.

References

1. J. Bardeen, W.H. Brattain, Phys. Rev. **74**, 230 (1948)
2. W. Shockley, Bell Syst. Tech. J. **28**, 435 (1949)
3. D. Kahng, M.M. Attala, *IRE Solid-State Device Research Conference* (Carnegie Institute of Technology, Pittsburg, 1960)
4. J.P. Colinge, C.A. Colinge, *Physics of Semiconductor Devices* (Springer, Boston, 2002)
5. Y. Kudo, M. Yamashita, T. Moriizumi, Jpn. J. Appl. Phys. **23**, 1 (1984)
6. A. Tsumura, H. Koezuka, T. Ando, Appl. Phys. Lett. **49**, 1210 (1986)
7. Y.-Y. Lin, D.J. Gundlach, S.F. Nelson, T.N. Jackson, IEEE Electron. Device Lett. **12**, 606 (1997)
8. R.C. Haddon, A.S. Perel, R.C. Morris, T.T.M. Palstra, A.F. Hebard, R.M. Fleming, Appl. Phys. Lett. **67**, 121 (1995)
9. J. Takeya, M. Yamagishi, Y. Tominari, R. Hirahara, Y. Nakazawa, T. Nishikawa, T. Kawase, T. Shimoda, S. Ogawa, Appl. Phys. Lett. **90**, 102120 (2007)
10. C. Liu, T. Minari, X. Lu, A. Kumatani, K. Takimiya, K. Tsukagoshi, Adv. Mater. **23**, 523 (2011)
11. N. Kurihara, A. Yao, M. Sunagawa, Y. Ikeda, K. Terai, H. Kondo, M. Saito, H. Ikeda, H. Nakamura, Jpn. J. Appl. Phys. **52**, 05DC11 (2013)
12. Y. Yuan, G. Giri, A.L. Ayzner, A.P. Zoombelt, S.C.B. Mannsfeld, J. Chen, D. Nordlund, M.F. Toney, J. Huang, Z. Bao, Nat. Commun. **5**, 3005 (2014)
13. R. Mitsuhashi, Y. Suzuki, Y. Yamanari, H. Mitamura, T. Kambe, N. Ikeda, H. Okamoto, A. Fujiwara, M. Yamaji, N. Kawasaki, Y. Maniwa, Y. Kubozono, Nature **464**, 76 (2010)
14. Y. Kubozono, H. Mitamura, X. Lee, X. He, Y. Yamanari, Y. Takahashi, Y. Suzuki, Y. Kaji, R. Eguchi, K. Akaike, T. Kambe, H. Okamoto, A. Fujiwara, T. Kato, T. Kosugigh, H. Aoki, Phys. Chem. Chem. Phys. **13**, 16476 (2011)
15. Y. Kubozono, H. Goto, T. Jabuchi, T. Yokoya, T. Kambe, Y. Sakai, M. Izumi, L. Zheng, S. Hamao, H.L.T. Nguyen, M. Sakata, T. Kagayama, K. Shimizu, Physica C **514**, 199 (2015)
16. Y. Kubozono, R. Eguchi, H. Goto, S. Hamao, T. Kambe, T. Terao, S. Nishiyama, L. Zheng, X. Miao, H. Okamoto, J. Phys. Condens. Matter **28**, 334001 (2016)
17. R.C. Haddon, J. Am. Chem. Soc. **118**, 3041 (1996)
18. S. Kobayashi, T. Takenobu, S. Mori, A. Fujiwara, Y. Iwasa, Appl. Phys. Lett. **82**, 4581 (2003)
19. K. Itaka, M. Yamashiro, J. Yamaguchi, M. Haemori, S. Yaginuma, Y. Matsumoto, M. Kondo, H. Koinuma, Adv. Mater. **18**, 1713 (2006)
20. T. Kanbara, K. Shibata, S. Fujiki, Y. Kubozono, S. Kashino, T. Urisu, M. Sakai, A. Fujiwara, R. Kumashiro, K. Tanigaki, Chem. Phys. Lett. **379**, 223 (2003)
21. E. Kuwahara, Y. Kubozono, T. Hosokawa, T. Nagano, K. Masunari, A. Fujiwara, Appl. Phys. Lett. **85**, 4765 (2004)
22. Y. Kubozono, T. Nagano, Y. Haruyama, E. Kuwahara, T. Takayanagi, K. Ochi, Appl. Phys. Lett. **87**, 143506 (2005)
23. Y. Kubozono, S. Haas, W. Kalb, P. Joris, F. Meng, A. Fujiwara, B. Batlogg, Appl. Phys. Lett. **93**, 033316 (2008)
24. K. Ochi, T. Nagano, T. Ohta, R. Nouchi, Y. Kubozono, Y. Matsuoka, E. Shikoh, A. Fujiwara, Appl. Phys. Lett. **89**, 083511 (2006)
25. T. Yasuda, T. Goto, K. Fujita, T. Tsutsui, Appl. Phys. Lett. **85**, 2098 (2004)
26. Y. Ito, A.A. Virkar, S. Mannsfeld, J.H. Oh, M. Toney, J. Locklin, Z. Bao, J. Am. Chem. Soc. **131**, 9396 (2009)
27. H. Li, C. Fan, M. Vosgueritchian, B.C.-K. Tee, H. Chen, J. Mater. Chem. C **2**, 3617 (2014)
28. H. Sugiyama, T. Nagano, R. Nouchi, N. Kawasaki, Y. Ohta, K. Imai, M. Tsutsui, Y. Kubozono, A. Fujiwara, Chem. Phys. Lett. **449**, 160 (2007)
29. Y. Kubozono, Y. Rikiishi, K. Shibata, T. Hosokawa, S. Fujiki, H. Kitagawa, Phys. Rev. B **69**, 165412 (2004)

30. K. Shibata, Y. Kubozono, T. Kanbara, T. Hosokawa, A. Fujiwara, Y. Ito, H. Shinohara, Appl. Phys. Lett. **84**, 2572 (2004)
31. T. Nagano, H. Sugiyama, E. Kuwahara, R. Watanabe, H. Kusai, Y. Kashino, Y. Kubozono, Appl. Phys. Lett. **87**, 023501 (2005)
32. S. Kobayashi, S. Mori, S. Iida, H. Ando, T. Takenobu, Y. Taguchi, A. Fujiwara, A. Taninaka, H. Shinohara, Y. Iwasa, J. Am. Chem. Soc. **125**, 8116 (2003)
33. Y. Rikiishi, Y. Kubozono, T. Hosokawa, K. Shibata, Y. Haruyama, Y. Takabayashi, A. Fujiwara, S. Kobayashi, S. Mori, Y. Iwasa, J. Phys. Chem. B **108**, 7850 (2004)
34. T. Nagano, E. Kuwahara, T. Takayanagi, Y. Kubozono, A. Fujiwara, Chem. Phys. Lett. **409**, 187 (2005)
35. T. Rabenau, A. Shimon, R.K. Kremer, E. Sohmen, Z. Phys. B **90**, 69 (1993)
36. Y. Rikiishi, Y. Kashino, H. Kusai, Y. Takabayashi, E. Kuwahara, Y. Kubozono, T. Kambe, T. Takenobu, Y. Iwasa, N. Mizorogi, S. Nagase, S. Okada, Phys. Rev. B **71**, 224118 (2005)
37. T. Miyazaki, S. Okita, T. Ohta, H. Yagi, R. Sumii, H. Okimoto, Y. Ito, H. Shinohara, S. Hino, Chem. Phys. **447**, 71 (2015)
38. K.-J. Baeg, D. Khim, D.-Y. Kim, S.-W. Jung, J.B. Koo, Y.-Y. Noh, Jpn. J. Appl. Phys. **49**, 05EB01 (2010)
39. H. Okamoto, N. Kawasaki, Y. Kaji, Y. Kubozono, A. Fujiwara, M. Yamaji, J. Am. Chem. Soc. **130**, 10470 (2008)
40. N. Kawasaki, Y. Kubozono, H. Okamoto, A. Fujiwara, M. Yamaji, Appl. Phys. Lett. **94**, 043310 (2009)
41. S. Gottardi, T. Toccoli, S. Iannotta, P. Bettotti, A. Cassinese, M. Barra, L. Ricciotti, Y. Kubozono, J. Phys. Chem. C **116**, 24503 (2012)
42. Y. Kaji, N. Kawasaki, X. Lee, H. Okamoto, Y. Sugawara, S. Oikawa, A. Ito, H. Okazaki, T. Yokoya, A. Fujiwara, Y. Kubozono, Appl. Phys. Lett. **95**, 183302 (2009)
43. Y. Kaji, R. Mitsuhashi, X. Lee, H. Okamoto, T. Kambe, N. Ikeda, A. Fujiwara, M. Yamaji, K. Omote, Y. Kubozono, Org. Electron. **10**, 432 (2009)
44. N. Kawasaki, W.L. Kalb, T. Mathis, Y. Kaji, R. Mitsuhashi, H. Okamoto, Y. Sugawara, A. Fujiwara, Y. Kubozono, B. Batlogg, Appl. Phys. Lett. **96**, 113305 (2010)
45. X. Lee, Y. Sugawara, A. Ito, S. Oikawa, N. Kawasaki, Y. Kaji, R. Mitsuhashi, H. Okamoto, A. Fujiwara, K. Omote, T. Kambe, N. Ikeda, Y. Kubozono, Org. Electron. **11**, 1394 (2010)
46. Y. Sugawara, K. Ogawa, H. Goto, S. Oikawa, K. Akaike, N. Komura, R. Eguchi, Y. Kaji, S. Gohda, Y. Kubozono, Sens. Actuators B Chem. **171/172**, 544 (2012)
47. N. Kawai, R. Eguchi, H. Goto, K. Akaike, Y. Kaji, T. Kambe, A. Fujiwara, Y. Kubozono, J. Phys. Chem. C **116**, 7983 (2012)
48. F.B. Mallory, K.E. Butler, A.C. Evans, C.W. Mallory, Tetrahedron Lett. **37**, 7173 (1996)
49. F.B. Mallory, K.E. Butler, A.C. Evans, E.J. Brondyke, C.W. Mallory, C. Yang, A. Ellenstein, J. Am. Chem. Soc. **119**, 2119 (1997)
50. F.B. Mallory, K.E. Butler, A. Bérubé, E.D. Luzik Jr., C.W. Mallory, E.J. Brondyke, R. Hiremath, P. Ngo, P.J. Carroll, Tetrahedron **57**, 3715 (2001)
51. F.B. Mallory, C.W. Mallory, Org. React. **30**, 1 (1984)
52. N. Komura, H. Goto, X. He, H. Mitamura, R. Eguchi, Y. Kaji, H. Okamoto, Y. Sugawara, S. Gohda, K. Sato, Y. Kubozono, Appl. Phys. Lett. **101**, 083301 (2012)
53. Y. Sugawara, Y. Kaji, K. Ogawa, R. Eguchi, S. Oikawa, H. Gohda, A. Fujiwara, Y. Kubozono, Appl. Phys. Lett. **98**, 013303 (2011)
54. R. Eguchi, X. He, S. Hamao, H. Goto, H. Okamoto, S. Gohda, K. Sato, Y. Kubozono, Phys. Chem. Chem. Phys. **15**, 20611 (2013)
55. X. He, R. Eguchi, H. Goto, E. Uesugi, S. Hamao, Y. Takabayashi, Y. Kubozono, Org. Electron. **14**, 1673 (2013)
56. X. He, S. Hamao, R. Eguchi, H. Goto, Y. Yoshida, G. Saito, Y. Kubzoono, J. Phys. Chem. C **118**, 5284 (2014)
57. H. Okamoto, R. Eguchi, S. Hamao, H. Goto, K. Gotoh, Y. Sakai, M. Izumi, Y. Takaguchi, S. Gohda, Y. Kubozono, Sci. Rep. **4**, 5330 (2014)

58. Y. Shimo, T. Mikami, S. Hamao, H. Goto, H. Okamoto, R. Eguchi, S. Gohda, Y. Hayashi, Y. Kubozono, Sci. Rep. **6**, 21008 (2016)
59. Y. Shimo, T. Mikami, H.T. Murakami, S. Hamao, H. Goto, H. Okamoto, S. Gohda, K. Sato, A. Cassinese, Y. Hayashi, Y. Kubozono, J. Mater. Chem. C **3**, 7370 (2015)
60. H. Okamoto, S. Hamao, H. Goto, Y. Sakai, M. Izumi, S. Gohda, Y. Kubzoono, R. Eguchi, Sci. Rep. **4**, 5048 (2014)
61. H.B. Michaelson, J. Appl. Phys. **48**, 4729 (1977)
62. S.-M. Kang, Y. Leblebici, *CMOS Digital Integrate Circuits Analysis and Design* (McGRW-HILL, New York, 2002)
63. M.P. Walser, W.L. Kalb, T. Mathis, T.J. Brenner, B. Batlogg, Appl. Phys. Lett. **94**, 053303 (2009)
64. X.-H. Zhang, W.J. Potscavage Jr., S. Choi, B. Kippelen, Appl. Phys. Lett. **94**, 043312 (2009)
65. H. Klauk, U. Zschieschang, J. Pfaum, M. Halik, Nature **445**, 745 (2007)
66. D. Hillesheim, K. Gofyk, S.A. Sefat, Nov. Supercond. Mater. **1**, 12 (2014)
67. Q.-W. Huang, G.-H. Zhong, J. Zhang, X.-M. Zhao, C. Zhang, H.-Q. Lin, X.-J. Chen, J. Chem. Phys. **140**, 114301 (2014)
68. T. Kambe, S. Nishiyama, H.L.T. Nguyen, T. Terao, M. Izumi, Y. Sakai, L. Zheng, H. Goto, Y. Itoh, T. Onji, T.C. Kobayashi, H. Sugino, S. Gohda, H. Okamoto, Y. Kubozono, J. Phys. Condens. Matter **28**, 444001 (2016)
69. G.A. Artioli, F. Hammerath, C.M. Mozzati, P. Carretta, F. Corana, B. Mannucci, S. Margadonnad, L. Malavasi, Chem. Commun. **51**, 1092 (2015)
70. X.F. Wang, R.H. Liu, Z. Gui, Y.L. Xie, Y.J. Yan, J.J. Ying, X.G. Luo, X.H. Chen, Nat. Commun. **2**, 507 (2011)
71. X.F. Wang, Y.J. Yan, Z. Gui, R.H. Liu, J.J. Ying, X.G. Luo, X.H. Chen, Phys. Rev. B **84**, 214523 (2011)
72. X.F. Wang, X.G. Luo, J.J. Ying, Z.J. Xiang, S.L. Zhang, R.R. Zhang, Y.H. Zhang, Y.J. Yang, A.F. Wang, P. Cheng, G.J. Ye, X.H. Chen, J. Phys. Condens. Matter **24**, 345701 (2012)
73. V.G. Tissen, E.G. Ponyatovskii, M.V. Chernogolovka, F. Porsch, W.B. Holzapfel, Phys. Rev. B **53**, 8238 (1996)
74. M. Xue, T. Cao, D. Wang, Y. Wu, H. Yang, X. Dong, J. He, F. Li, G.F. Chen, Sci. Rep. **2**, 389 (2012)
75. T. Nakagawa, Z. Yuan, J. Zhang, K.V. Yusenko, C. Drathen, Q. Liu, S. Margadonna, C. Jin, J. Phys. Condens. Matter **28**, 484001 (2016)
76. W. Liu, H. Lin, R. Kang, X. Zhu, Y. Zhang, S. Zheng, H.-H. Wen, Phys. Rev. B **96**, 224501 (2017)
77. S. Heguri, M. Kobayashi, K. Tanigaki, Phys. Rev. B **92**, 014502 (2015)
78. K. Teranishi, X. He, Y. Sakai, M. Izumi, H. Goto, R. Eguchi, Y. Takabayashi, T. Kambe, Y. Kubozono, Phys. Rev. B **87**, 060505(R) (2013)
79. Y. Takabayashi, M. Menelaou, H. Tamura, N. Takemori, T. Koretsune, A. Štefančič, G. Klupp, A.J.C. Buurma, Y. Nomura, R. Arita, D. Arčon, M.J. Rosseinsky, K. Prassides, Nat. Chem. **9**, 635 (2017)

Chapter 9
Nanostructure Control of Crystalline Organic Thin Films by Solution Processes

Hiroko Yamada

Abstract Solution-processed organic semiconductor devices are expected to provide flexible, large-area, light-weight, low-cost, and environment-friendly electronic products for next-generation devices. As small molecular crystals have intrinsically high electrical properties, this chapter focuses on the fabrication technique of single crystalline and polycrystalline organic electronic devices using solution processes. It starts with a description of the relationship between the crystal structure and electrical properties of organic semiconductors. Then, several techniques for preparing single-crystalline organic field effect transistors are discussed. Next, a precursor approach to preparing polycrystalline films is addressed. With this approach, well-soluble and stable precursor compounds are deposited on substrates and then quantitatively converted into target materials by applying external stimuli, such as heat or light. The recent progress of organic field effect transistors and organic photovoltaics with this approach is summarized.

Keywords Organic semiconductor · Solution process · Crystalline film · Organic field effect transistor · Organic photovoltaics

9.1 Introduction

Development of high-performance printed organic semiconductor devices, such as organic field-effect transistors (OFETs), organic photovoltaics (OPVs), and organic light emitting diodes (OLEDs), is highly desired for the next-generation technologies of 'printable electronics'. Organic semiconductors are expected to provide flexible, large-area, light-weight, low-cost, and environment-friendly electronic

H. Yamada (✉)
Nara Institute of Science and Technology, Takayama-cho, Ikoma, Nara, Japan
e-mail: hyamada@ms.naist.jp

© Springer Nature Singapore Pte Ltd. 2019

Y. Kubozono (ed.), *Physics and Chemistry of Carbon-Based Materials*,
https://doi.org/10.1007/978-981-13-3417-7_9

products, including wearable and/or transparent sheet-type solar cells, flexible displays, and so on. The performances of organic electronic devices largely depend on the charge transport efficiency in the organic active layers and carrier injection at the interface of organic/metal electrodes.

The organic semiconducting materials can be classified as crystalline small molecules; soluble small molecules, including oligomers and liquid crystalline materials; and π-conjugated conductive polymers. The key structure of these materials is the π-electron conjugation over the molecule frameworks. The π-conjugated polymers have π-electron conjugation through the polymer backbones. Thus, the charge carriers can travel along the main polymer chains. Small molecular semiconducting materials have aromatic frameworks over which the π-electrons spread; however, the electrons are localized in each molecule. For efficient charge carrier transport, charge carriers must efficiently move between the molecules. An immense number of compounds have been developed since the 1990s for small-molecule organic semiconductor materials [1–3].

For efficient intermolecular charge transport between molecules, a π-π interaction with neighbouring molecules is necessary, and a crystalline film with a proper packing structure is desirable. Single-crystal devices are optimal devices with high intrinsic electrical properties; however, the preparation of numerous large single crystals was not practical. Recently several noteworthy solution-processing techniques for single-crystal devices have been reported. It will be surveyed in Sect. 9.4.

Polycrystalline film is the second choice, while vacuum deposition is a well-known technique for the preparation of polycrystalline films. It enables the very pure polycrystalline film to have good electrical properties. Nevertheless, the preparation of large devices on plastic film is difficult with this method, and molecules with a larger molecular weight cannot be deposited on account of the decomposition before sublimation. To apply the polycrystalline organic electronic devices, a preparation technique of polycrystalline films by a solution process is required. Recently, high-performance devices with solution-processed polycrystalline films have been reported. In Sects. 9.5 and 9.6, the preparation and morphology control of crystalline organic semiconductor layers by a solution process are addressed.

9.2 Organic Devices for Evaluating Charge Transport Efficiency

To evaluate the intrinsic charge transport abilities of organic semiconducting materials, the charge carrier mobilities are estimated by various techniques. These techniques include the time-of-flight (TOF), space-charge-limited current (SCLC), time-resolved microwave conductivity (TRMC), OFETs, etc. [4]. In this section, the morphology and charge carrier mobilities of the prepared crystalline films are discussed in terms of OFET and OPV performances. The basic structures and mechanisms of the OFET and OPV devices are first described.

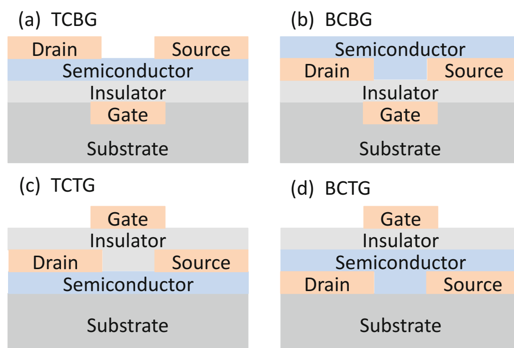

Fig. 9.1 Four OFET architecture types: TCBG, top-contact bottom-gate (**a**); BCBG, bottom-contact bottom-gate (**b**); TCTG, top-contact top-gate (**c**); and BCTG, bottom-contact top-gate (**d**) structures

9.2.1 Organic Field-Effect Transistors

OFETs are crucial components for organic electronic devices using organic semiconductors in the channel. An OFET is a three-electrode system with gate, source, and drain electrodes. There are four OFET device structure types: top-contact bottom-gate (TCBG), bottom-contact bottom-gate (BCBG), top-contact top-gate (TCTG), and bottom-contact top-gate (BCTG) structures, depending on the relative structure of electrodes and organic semiconductors (Fig. 9.1).

The amplitude of the drain–source current (I_{DS}) is controlled by the applied gate voltage (V_G) and drain–source voltage (V_{DS}). The field applied to the gate electrode induces a charge (channel) in the semiconducting layer. The polarity of the gate bias determines the channel polarity. When the hole (electron) is a main charge carrier, it is called a p-type (n-type) OFET. The polarity depends on the electronic properties of the semiconductor materials. The carrier travels horizontally between source and drain electrodes in the channel, and a large π–π interaction between neighbouring semiconductor molecules in a horizontal direction is desirable.

The carrier mobility (μ) indicates the rate of the carrier moving through the channel in the semiconductor layer under an electrical field. The μ value is calculated using Eq. (9.1):

$$I_{SD} = (W/2L)\,\mu C_i(V_G - V_{th})^2 \tag{9.1}$$

where I_{SD} is the drain current, W and L are the channel width and length, respectively, C_i is the capacitance per unit area of the gate dielectric, and V_G and V_{th} are the gate voltage and threshold voltage, respectively. In Fig. 9.2, an example of output curves of I_{SD} at several V_G's (a) and a transfer curve at a certain V_{SD} (b) are shown. The OFET properties are discussed mainly in terms of μ, V_{th}, and the on/off current ratio (I_{ON}/I_{OFF}). V_{th} is the voltage required for driving charges that are mobile; a value close to zero is desirable. I_{ON}/I_{OFF} is the ratio of the drain current at the on and off states. The larger the I_{ON}/I_{OFF} is, the better it is, and at least $I_{ON}/I_{OFF} > 10^3$ is required.

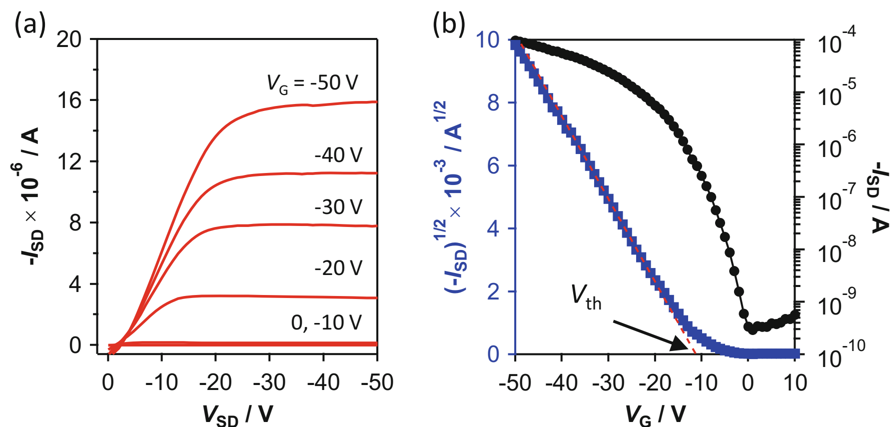

Fig. 9.2 Example of FET data: (**a**) Output curves of I_{SD} at each V_G and (**b**) transfer curve at a certain V_{SD}. The μ value is calculated from the inclination of the tangential line (red dotted line) and V_{th} from the intercept of the tangential line and x-axis

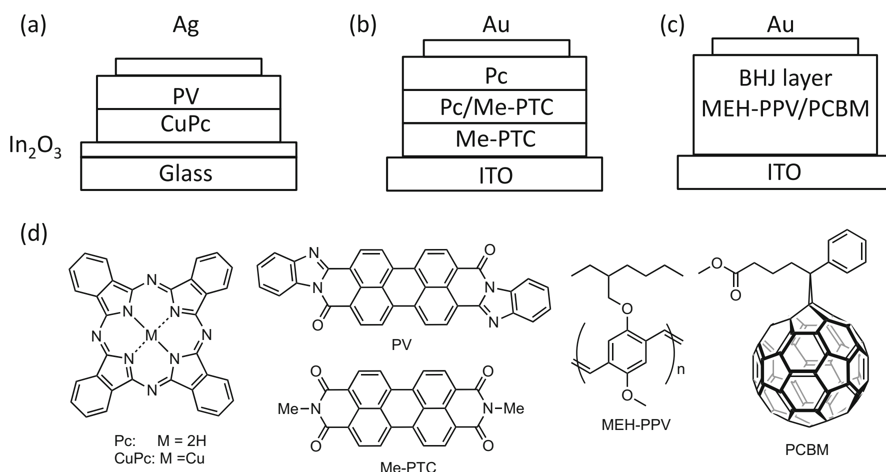

Fig. 9.3 Structures of a (**a**) planar heterojunction OPV, (**b**) p-i-n OPV, (**c**) BHJ OPV, and (**d**) structures of organic semiconductor materials employed in these devices [5–7]

9.2.2 Organic Photovoltaics

A two-layer OPV fabricated by vacuum deposition using copper phthalocyanine for the p-material and a perylene tetracarboxylic derivative (PV) for the n-material (Fig. 9.3a) with a photocurrent conversion efficiency (PCE) of 0.95% was reported by Tang in 1986 [5]. In 1991, Hiramoto et al. reported a three-layered OPV with an interlayer of co-deposited pigments of p-type metal-free phthalocyanine (H_2Pc) and n-type perylene tetracarboxylic derivative (Me-PTC) between respective p- and n-pigment layers (Fig. 9.3b) [6]. The 0.7% PCE performance was two times

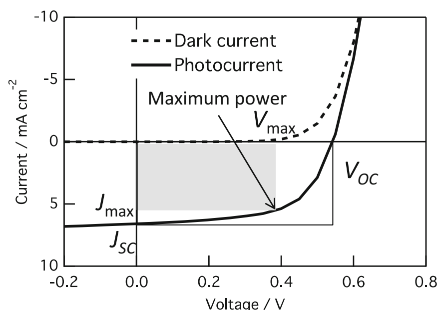

Fig. 9.4 Typical current–voltage curves. Solid line, photocurrent; dashed line, dark current

higher than that of the two-layered device on account of the efficient carrier photo-generation in the interlayer. The single p- and n-type pigment layers, which sandwich the interlayer, effectively provide the built-in potential to the photo-active interlayer. The single p- and n-layers also play an important role as carrier transport layers.

Another key advancement was reported by Heeger et al. in 1995 as a monolayer bulk-heterojunction (BHJ) OPV using a mixture of semiconducting polymer (MEH-PPV) for p-type material and PCBM for n-type material with PCE = 2.9% (Fig. 9.3c) [7]. Efficient charge separation resulted from a bicontinuous network of an internal donor-acceptor heterojunction, and the PCE performance surpassed 11%.

Typical current–voltage (J-V) curves with and without photo-irradiation are shown in Fig. 9.4. The OPV performance is evaluated by power conversion efficiency (PCE), as shown in Eq. 9.2.

$$\mathrm{PCE} = P_{\mathrm{out}}/P_{\mathrm{in}} = J_{\mathrm{SC}} \times V_{\mathrm{OC}} \times \mathrm{FF}/P_{\mathrm{light}} \tag{9.2}$$

where P_{out} is the output power, P_{in} is the input power, J_{SC} is the short-circuit current density, V_{OC} is the open-circuit voltage, FF is the fill factor, and P_{light} is the power of the incident light. In addition, J_{SC} is the maximum current that can be obtained under conditions of a zero-resistance load. The larger absorption coverage of organic molecules and the larger charge transport efficiency of the organic layer increase J_{SC}. Moreover, V_{OC} is the maximum voltage with no load applied. V_{OC} largely depends on the difference of energy level of the highest occupied molecular orbital (HOMO) of the donor material and the lowest unoccupied molecular orbital (LUMO) of the acceptor material. The crystal packing structure of the materials in the active layer also influences V_{OC} by changing the ionization energy of the materials. FF is the ratio between the maximum power and the full square spanned by the J_{SC} and V_{OC} values, as described in Eq. 9.3. FF is influenced by the electrical properties of the active layers and depends on the competition between charge carrier recombination and transport processes.

$$\mathrm{FF} = J_{\mathrm{max}} \times V_{\mathrm{max}}/J_{\mathrm{SC}} \times V_{\mathrm{OC}} \tag{9.3}$$

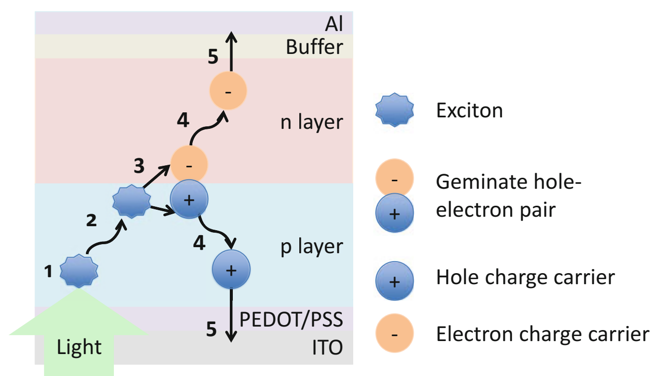

Fig. 9.5 Five-step mechanism to generate photocurrent in a typical planar p-n-type OPV device

The fundamental mechanism to generate photocurrent in OPV is summarized in Fig. 9.5. Conversion of light energy to electric energy can be classified into five steps:

Step 1: Absorption of light by donor and/or acceptor materials generates an exciton (a coulombically bound electron-hole pair).
Step 2: The exciton diffuses into the interface of the donor and acceptor materials.
Step 3: The charge separates from the exciton geminate hole-electron pair.
Step 4: The free charge carrier is transported toward the electrodes.
Step 5: The charge carrier is injected into the electrodes.

To improve the PCE performance, all five steps should efficiently progress. The film morphology plays important roles in each step.

In Step 1, the excited state (exciton) of the donor and/or acceptor molecules is due to incident light absorption. The exciton generation efficiency strongly relates to the molar extinction coefficient of the donor and acceptor materials. By the π–π interaction between molecules in the film, the absorption is broadened and the absorption peaks shift from the peak of the unimolecular spectrum in solution. With H-aggregation (parallel orientation) of the molecules, the absorption shows a hypsochromic (blue) shift; the J-aggregation (head-to-tail orientation) shows a bathochromic (red) shift.

The exciton is deemed an electron and hole pair. The charges are located in the same molecule and strongly bound by a Coulombic interaction. An energetic barrier to transferring the charge from the exciton to the neighbouring molecules exists. In Step 2, the exciton must diffuse to the donor-acceptor interface to encounter the partner for transferring an electron from the donor to acceptor molecule. The exciton diffusion length of organic semiconductors is approximately 10 nm in crystalline films, depending on the packing structure. The packing structure influences the diffusion direction. In p-n-type OPV systems, excitons less than 10 nm from the interface of the two layers can contribute to carrier generation, while excitons far

from the interface cannot reach it. The BHJ structure is superior to the p-n structure owing to the increased interface area. The morphology control of the mixed layer to improve the charge separation probability is important.

For Step 3 charge separation, the ionization potential (IP) and electron affinity (EA) of donor and acceptor materials directly influence the OPV performance. V_{OC} is closely related to the difference between the donor-material IP and acceptor material EA. Donor IP and acceptor EA in crystalline film are different from those for the gas-phase-isolated molecule (the difference is called polarization energy; see Sect. 9.3.3). The difference is greatly influenced by the molecular packing structure.

After charge separation, positive and negative charges travel to anode and cathode electrodes, respectively (Step 4). Charge carrier mobilities in crystalline films are influenced by many factors, including the molecular packing structure, grain size, disorder, presence of impurities, temperature, electric field, charge carrier density, molecule size/molecular weight, and pressure [4]. Molecular packing in single crystals influences the charge transport efficiency and anisotropy, especially by electron coupling (or transfer integral), reorganization energy, and polarization energies [8]. These three key factors are overviewed in Sect. 9.3. Even for the bulk hetero layer from combined polymers and fullerene derivatives, the partial crystallinity of the materials was reported as being crucial for good carrier mobilities and stability [9].

For a good electrical property and effective charge injection at the interface of the active layer and electrodes, the crystalline structure of the p- and n-layers is favourable (Step 5). The crystalline p- and n-layers in the p-i-n structure prevent a current leak and support charge injection to electrodes [6].

9.3 Charge Transport Mechanism of Organic Semiconductors

9.3.1 Organic Versus Inorganic Semiconductors

Compared to inorganic semiconducting materials, the charge transport properties of organic semiconductors are intrinsically low. The exciton nature of organic materials (Frenkel exciton) is very different from those of inorganic semiconductors (Wannier exciton) [10]. In inorganic semiconductors (such as doped silicon, GaAs, ZnS, etc.), atoms are covalently bound, and the exciton electron is only weakly bound to the hole with minimal binding energy. Thus, the average exciton orbital radius ($\sim$16 nm) is larger than the lattice unit. The carrier diffusion length is $\sim$100 μm; the charge carrier mobilities are over the order of 10^0 cm^2 V^{-1} s^{-1}.

For small molecular crystalline organic semiconductors (Fig. 9.6), the lattice unit is based on molecules. The average exciton radius is approximately 1 nm, the carrier diffusion length is approximately several tens of nanometres, and the charge carrier mobilities are less than the order of 10^0 cm^2 V^{-1} s^{-1}. To increase the

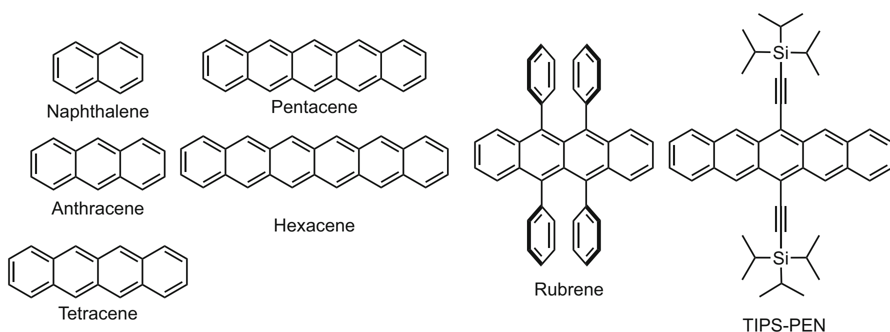

Fig. 9.6 Structures of acene-type semiconductors discussed in this chapter

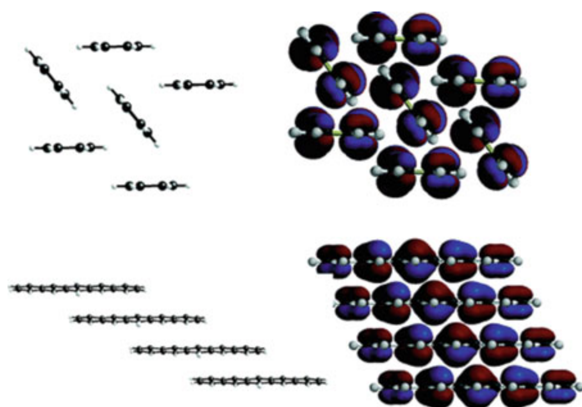

Fig. 9.7 Pentacene herringbone (top) and 1D π-stacking (bottom) structures. (Reproduced with permission from [11]. Copyright 2006 American Chemical Society)

charge carrier mobility of organic semiconductors, the morphologies of the organic molecules are very important. The crystalline molecules are weakly bound by CH–π, π–π, and van der Waals interactions.

Figure 9.7 shows typical packing structures observed for organic semiconducting materials: the herringbone and 1D π-stacking structures of pentacene [11]. In the herringbone arrangement, an aromatic edge-to-face (CH-π) interaction dominates, yielding 2D electronic interactions. In the 1D π-stacking arrangement, a face-to-face (π–π) interaction of electron-rich faces dominates, yielding a coplanar-stacked structure with some degree of displacement along molecule long and short axes. In the 1D π-stacking arrangement, the electron coupling in the stacking direction tends to be large. Substituents on π-frames efficiently influence the packing structure by van der Waals interactions between substituents, steric hindrance, and the π-frame electronic structure.

9.3.2 Transfer Integral and Reorganization Energy

Charge transport efficiency depends on the transfer integral among neighbouring molecules. The transfer integral is a theoretically estimated electronic coupling using the single-crystal structure molecular configuration. It strongly depends on the molecule electronic structure, neighbouring-molecule mutual distances and orientations, and displacement degree along long and short molecule axes.

In 2012, Watanabe et al. were successful in isolating hexacene for the first time [12] (Sect. 9.5.1 for synthesis). They compared its single-crystal structures, transfer integrals, reorganization energies, and hole mobilities with those of naphthalene, anthracene, tetracene, and pentacene. All acenes showed a herringbone motif single-crystal structure [13–15], and Fig. 9.8 shows the hexacene packing structure. A higher electronic coupling (t^+) along both T_1 and T_2 directions is observed by increasing the number of benzene rings (Table 9.1). A significantly higher hole mobility (μ^+) of hexacene than the other acenes was theoretically estimated: hexacene, 1.461 cm^2 V^{-1} s^{-1}; pentacene, 0.832 cm^2 V^{-1} s^{-1}; tetracene, 0.470 cm^2 V^{-1} s^{-1}; anthracene, 0.158 cm^2 V^{-1} s^{-1}; and naphthalene, 0.0511 cm^2 V^{-1} s^{-1}. The hole mobilities are well fitted by an equation relating to the number (x) of aromatic rings, ax^b ($x = 2$–6), where $a = 0.00584$ and $b = 3.09$. The calculation suggests that hexacene μ^+ is most efficient along the *a–b* plane. The best single-crystal (SC)-FET performance of hexacene was 4.28 cm^2 V^{-1} s^{-1} with an on/off ratio of 1×10^5 and threshold of 37 V, while pentacene SC-FET prepared in the same manner showed a hole mobility of 1.2 cm^2 V^{-1} s^{-1} with an on/off ratio of 3×10^6 and a threshold at −7 V.

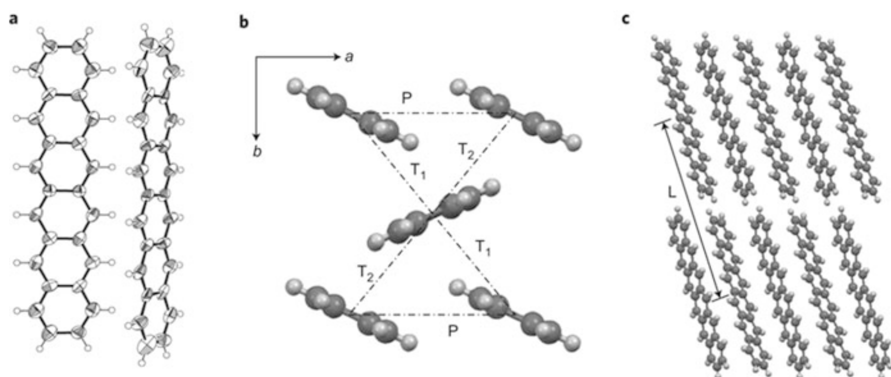

Fig. 9.8 X-ray hexacene crystallographic analysis: (**a**) two adjacent hexacene molecules (the Oak Ridge Thermal Ellipsoid Plot (ORTEP) drawing), (**b**) hexacene molecule layer arrangement on a–b plane, and (**c**) hexacene arrays along a-axis. Transfer-integral computation distances: T_1 and T_2 transverse, P parallel, L longitudinal. (Reproduced with permission from [12]. Copyright 2012 Nature Publishing Group)

Table 9.1 Calculated hole-transporting properties

Compound	HOMO*/eV	λ^{+*}/meV	R/Å, t^{+}/meV†				μ^{+}‡/cm^2 V^{-1} s^{-1}
			T_1	T_2	P	L	
Naphthalene	−5.80	183	5.01, 8	5.01, 8	5.93, 36	8.64, 0	0.0511
Anthracene	−5.24	138	5.22, 19	5.22, 19	6.01, 42	11.12, 0	0.158
Tetracene	−4.87	113	4.77, 70	5.13, 22	6.06, 37	13.44, 1	0.470
Pentacene	−4.61	95	4.76, 79	5.21, 45	6.27, 31	16.11, 1	0.832
Hexacene	−4.42	79	4.72, 88	5.22, 60	6.31, 37	18.61, 1	1.461

Adapted with permission from [12]. Copyright 2012 Nature Publishing Group
B3LYP/6-31G(d,p) level
†PW91/DZ2P level calculated at 300 K (t^{+} is given as the absolute value)
‡Averaged value along the four directions (T1, T2, P, and L) under consideration

Reorganization energy (λ) is an important quantity associated with local electron–phonon coupling [16]. It is described in Marcus theory as energy consumption during molecular-level carrier transfer. High mobility can be attained by small reorganization energy of the hopping model [2]. Reorganized energy is divided into intramolecular (inner) and intermolecular (outer) types. In a solution, the outer contribution from surroundings is greater than the inner one. In molecular crystals, intramolecular reorganization energy ranges from 100 to 200 meV, while the intermolecular type is <10 meV. With π-expanded and delocalized molecules, reorganization energy tends to be small because the generated charge is delocalized in the molecule. Hexacene reorganization energy (λ^{+}) is much smaller than smaller acenes (Table 9.1). Fullerene has a 3D spherical or rugby ball-type shape. The reorganization energy is small owing to the spherical-surface delocalized electronic structure. This is an important reason why fullerene derivatives are commonly used for OPV n-materials.

9.3.3 Polarization Energy

Polarization energy is charge energetic stabilization through interaction with the electrostatic environment surrounding the charged molecule in the crystal. Lichtenberger et al. measured high-resolution gas-phase and solid-phase ultraviolet photoelectron spectroscopy (UPS) of pentacene and TIPS-PEN to obtain intra- and intermolecular electronic effects (Fig. 9.9) [17]. By gas-phase UPS measurement, ionization energy at the pentacene single-molecule level and TIPS-PEN can be obtained. In the solid phase, the cation is stabilized by polarizing the surrounding medium, and ionization energies are lowered from the gas phase to solid phase. Solid-phase pentacene ionization energy is lowered by 1.7 eV from the gas phase; that of TIPS-PEN is lowered by 0.4 eV from the gas phase to the solid phase. The pentacene ionization order and TIPS-PEN are reversed in these phases.

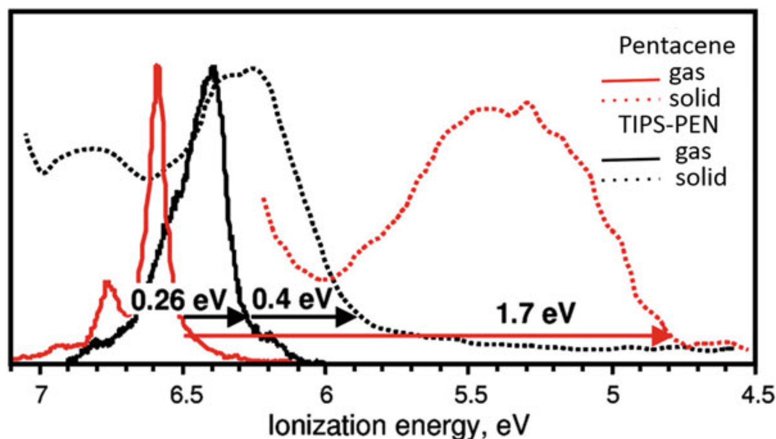

Fig. 9.9 He I UPS: first ionization energy bands of pentacene (red) and TIPS-PEN (black) (solid lines, gas phase; dotted lines, solid phase). (Adapted with permission from [17]. Copyright 2010 American Chemical Society)

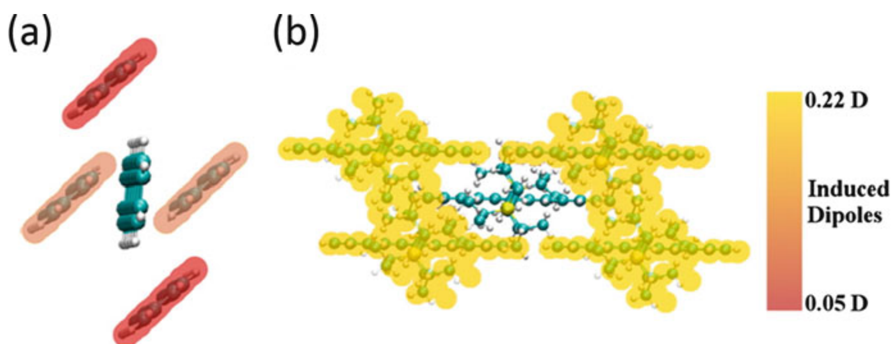

Fig. 9.10 Induced dipoles on the nearest neighbours of a positively charged pentacene (**a**) and TIPS-PEN (**b**), respectively, determined by the parameterised atomic multipole optimized energetics for biological applications (AMOEBA) force field. Dark red molecules in (**a**) have induced dipoles of 0.059 D; those in light red have induced dipoles of 0.063 D. All nearest neighbours in (**b**) have induced dipoles of 0.214 D. (Adapted with permission from [18]. Copyright 2014 American Chemical Society)

A larger polarization of the surrounding medium leads to a larger intermolecular reorganization energy. Ryno et al. described the relationship of polarization energy to crystal structure [18]. Figure 9.10 shows the magnitudes of the dipole moments induced by a positive charge on the central molecule of five-molecule clusters for pentacene (herringbone packing) and TIPS-PEN (brickwork packing). A slight asymmetry in induced dipole moments (0.063 D vs. 0.059 D) is evident in the pentacene herringbone packing configuration, while the TIPS-PEN brickwork configuration shows a larger induced dipole (0.21 D) moment with no asymmetry.

These differences indicate that induced dipole moments are very important to charge carrier stabilization in the brickwork-packed TIPS-pentacene. These results elucidate those of Fig. 9.9, where the TIPS-PEN brickwork configuration shows a fundamental change in the quadrupole and induced dipole interactions, resulting in smaller bulk polarization energy compared to pentacene.

9.4 Deposition of Crystalline Structure by a Solution Process

Charge carrier mobility of organic semiconductors is influenced by the film crystal structure, as described in Sect. 9.3. Fundamental research on the large single-crystal (SC) device is important; development of a preparation method of a flat, regular crystalline film by a solution process is critical. In this section, approaches to preparing SC-FET devices by a solution process are outlined.

9.4.1 Single-Crystal FET by a Solution Process

The FET device size has decreased owing to technological advancements. A smaller FET enables more sophisticated devices. To address this size demand, SC-FET has been studied because the single-crystalline device has good charge transport performance (20–40 $cm^2\ V^{-1}\ s^{-1}$) with few grain boundaries compared to polycrystalline film [19]. To realize solution-processed SC-FETs, Briseno et al. patterned organic SC-FET arrays [20]. Figure 9.11 shows the preparation of patterned SC-FET devices, as well as scanning electron microscope (SEM) images of patterned pentacene, rubrene, and C_{60} arrays. Rubrene- and pentacene-based transistor arrays yielded $\mu = {\sim}0.6 \pm 0.5\ cm^2\ V^{-1}\ s^{-1}$ with $I_{ON}/I_{OFF} > 10^7$ and $\mu = 0.3\ cm^2\ V^{-1}\ s^{-1}$ with $I_{ON}/I_{OFF} > 10^5$, respectively. Devices from patterning n-channel materials, C_{60} and tetracyanoquinodimethane (TCNQ), exhibited mobilities of 0.03 and $10^{-4}\ cm^2\ V^{-1}\ s^{-1}$, respectively.

9.4.2 TIPS-PEN

Another strategy for solution-processed SC-FET is introducing substituents to improve compound solubility in the organic solvents. TIPS-PEN was reported as a soluble pentacene derivative by Anthony in 2001 [21]. The performance of field-effect mobility of TIPS-PEN fabricated by thermal deposition was 0.4 $cm^2\ V^{-1}\ s^{-1}$, [22]. The BGBC FET prepared by blading TIPS-PEN toluene solution and evaporating solvent produced a 0.17 $cm^2\ V^{-1}\ s^{-1}$ hole mobility with I_{ON}/I_{OFF} of 10^5 [23].

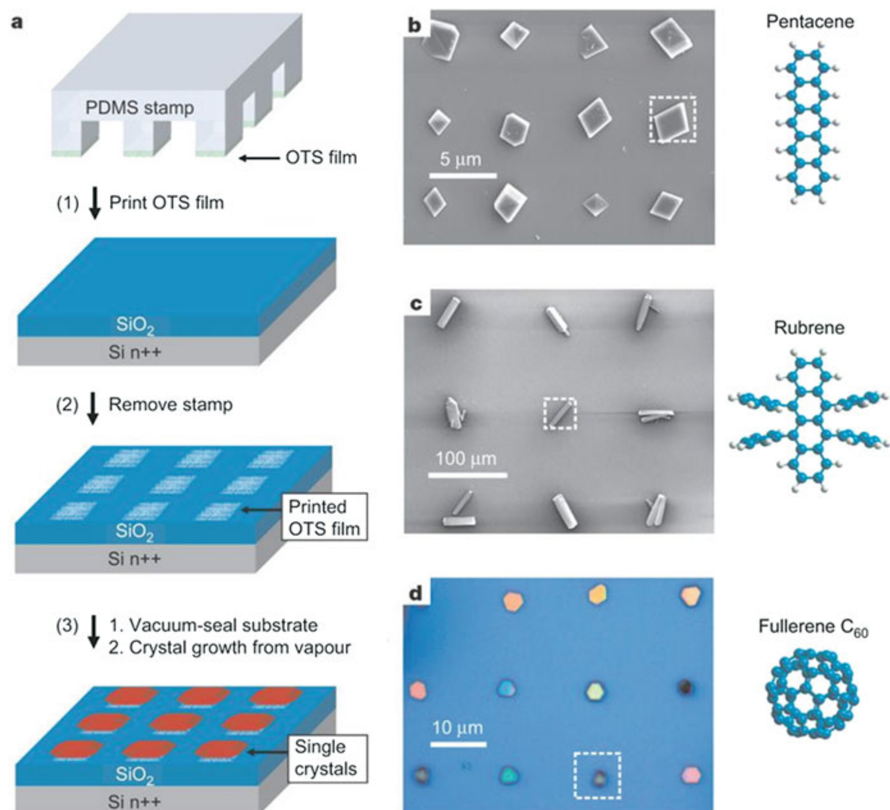

Fig. 9.11 (**a**) Procedure for growing organic single crystals on substrates patterned by micro-contact printing, which uses polydimethylsiloxane (PDMS) stamps with relief features inked with thick octadecyltriethoxysilane (OTS) film and then pressed onto the substrates. To grow the patterned single crystals, the patterned substrate is placed in a glass tube with the organic source material, vacuum-sealed (0.38 mm Hg), and placed in a temperature gradient furnace tube. (**b**–**d**) Patterned single-crystal arrays of different organic semiconductor materials. Dotted squares denote the size and location of the OTS-stamped domain. The organic material molecular structure is shown beside the image of its single-crystal array. (**b**) Pentacene (SEM, 4 × 4-μm stamped domain size), (**c**) rubrene (SEM, 25 × 25 μm), and (**d**) C_{60} (optical micrograph, 8 × 8 μm). (Reproduced with permission from [20]. Copyright 2006 Nature Publishing Group)

Kim et al. produced 1D single-crystalline micro-ribbons through TIPS-PEN self-assembly by injecting a minimum volume of TIPS-PEN concentrated toluene solution in acetonitrile [24]. The typical micro-ribbon dimensions are as follows: 100–600 nm (height), 4–13 μm (width), and 40–800 μm (length). The average field-effect mobility (0.75 $cm^2\ V^{-1}\ s^{-1}$) and I_{ON}/I_{OFF} (ca. 10^5) were obtained for 18 devices from 4 different batches. The highest TIPS-PEN FET mobility was 1.42 $cm^2\ V^{-1}\ s^{-1}$.

In 2007, Park et al. compared carrier mobilities of simple bottom-contact TIPS-PEN FETs by drop casting, dip coating, and spin depositing [25]. X-ray diffraction analysis showed similar peak patterns of a well-organized molecular structure with vertical intermolecular spacing of 16.8 Å. However, the peak intensity suggested the drop-cast films had the best ordering, while the spin-cast film had the worst. The improved molecular ordering and device performance related to the film formation speed. The device with the drop-cast film prepared from 1 wt% toluene solution (b.p. 110.6 °C) had FET mobilities of 0.2–1.8 cm^2 V^{-1} s^{-1} (73 devices, average 0.65 cm^2 V^{-1} s^{-1}) with V_{th} of 0–10 V (3.4 V average). The dip-coated film from 1 wt% chlorobenzene solution was 0.1–0.6 cm^2 V^{-1} s^{-1}, and the spin-cast film from 0.2 wt% film was 0.05–0.2 cm^2 V^{-1} s^{-1}.

Giri et al. reported a solvent shearing method to control the TIPS-PEN π–π stacking distance from 3.33 to 3.08 Å by changing the film-preparation shearing speed [26]. The film lattice strain correlated with the nearest-neighbour charge transfer integral change from 11.7 meV to −36.9 meV. The hole carrier mobility was 0.8 cm^2 V^{-1} s^{-1} for unstrained film and 4.6 cm^2 V^{-1} s^{-1} for strained film.

For solution-process enlargement of TIPS-PEN single crystal, Diao et al. used a fluid-enhanced crystal engineering method (Fig. 9.12) [27]. By controlling film thickness and solvent, nucleation and crystal growth was controlled, resulting in preparation of millimetre-wide, centimetre-long enlargement of TIPS-PEN single-crystalline domains. By excellent domain alignment and omitting grain boundaries, a 11 cm^2 V^{-1} s^{-1} maximum mobility was attained.

9.4.3 Thioacene Derivatives

Takimiya et al. controlled the crystalline structure by adding alkyl groups on the thienoacene derivatives. Alkyl chains influence the crystalline-film packing motif via the van der Waals interaction between alkyl chains. They are soluble in organic solvents; hence, various solution processes were developed. In 2007, Eibata et al. prepared 2,7-dialkyl-substituted [1]benzothieno[3,2-*b*][1]-benzothiophene (C_n-BTBT: n = 5∼14) and compared the solubility, interlayer spacing (d-spacing), and FET performance (Fig. 9.13) [28, 29]. The spin-coated film showed (00 l) reflections in the in-plane XRD pattern, indicating the spun-cast film of C_n-BTBT yielded an end-on orientation on the substrates. The best performance of the spun-cast film was obtained for C_{13}-BTBT film as $\mu = 1.20$–2.75 cm^2 V^{-1} s^{-1}. This C_8-BTBT crystalline film performance was improved by preparing a terrace and step structure in micrometre scale using molecule self-assembly with edge–casting method. The FET mobility improved as high as 5 cm^2 V^{-1} s^{-1}. OFET mass production with an average mobility of 3.5 cm^2 V^{-1} s^{-1} at specified positions on substrates were possible with this method [30, 31].

Minemawari et al. achieved inkjet printing of SC films of C_8-BTBT. The anti-solvent ink (pure anhydrous dimethylformamide (DMF)) was first printed and then overprinted with the solution ink (C_8-BTBT solution in dichlorobenzene (DCB)), yielding TCTG thin-film transistors with average carrier mobility as high

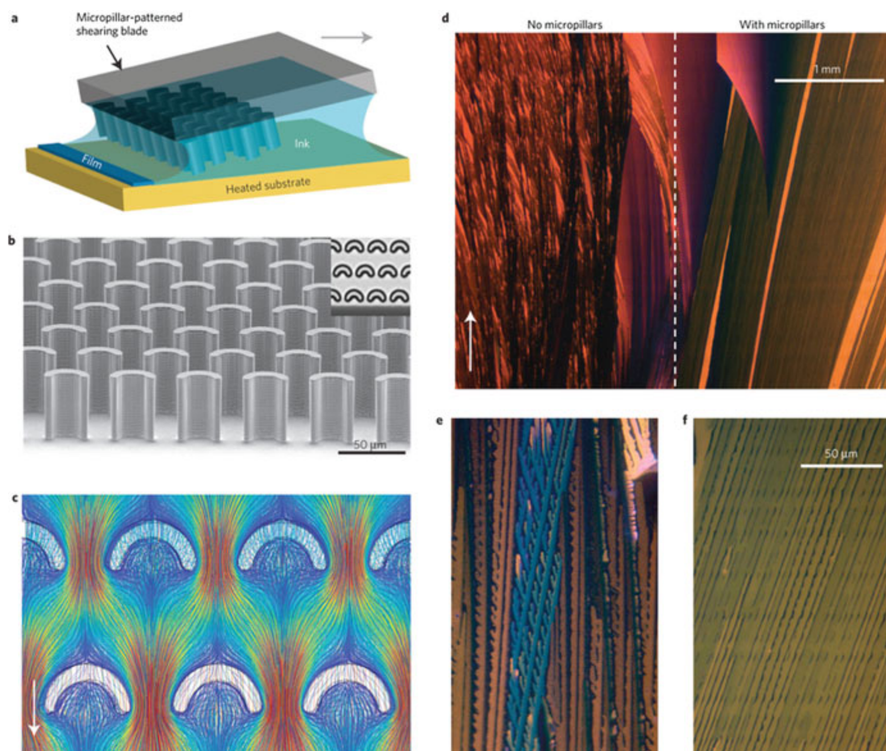

Fig. 9.12 (**a**) Solution shearing using a micropillar-patterned blade (micropillars are not drawn to scale; arrow, shearing direction). (**b**) Micropillar-patterned blade (SEM): top view of micropillars (35 μm wide; 42 μm high) under optical microscope (inset). (**c**) Simulated fluid flow streamlines around micropillars (arrow, flow direction); colour coding indicates velocity scale (mm s^{-1}) from 0 (deep blue) to 1.3 mm s^{-1} (dark red). (**d**–**f**) Cross-polarized optical micrograph of TIPS-PEN film coated from mesitylene solution with (**d**, right; **f**) and without micropillars (**d**, left; **e**) at a 0.6 mm s^{-1} shearing speed. (Reproduced with permission from [27]. Copyright 2013 Nature Publishing Group)

as 16.4 cm^2 V^{-1} s^{-1} (31.3 cm^2 V^{-1} s^{-1} as maximum) (Fig. 9.14) [32]. Phase separation between organic semiconducting molecules and insulating polymers caused by the difference in the surface energies have also been utilized for preparing highly ordered single crystals for SC-FETs. C_8-BTBT single crystals have been prepared from polymer (poly(methyl methacrylate) (PMMA) or polystyrene (PS)) blends by solvent annealing, affording SC-FETs showing high mobility (9.1 cm^2 V^{-1} s^{-1}) and band-like transport behaviours [33].

Dinaphtho[2,3-b:2′,3′-f]thieno[3,2-b]thiophene (DNTT) showed herringbone packing in a single crystal (Fig. 9.13). Non-substituted DNTT top-contact FET was prepared by vacuum deposition on octyltrichlorosilane (OTS)-treated substrate at T_{sub} = 60 °C to give 2.0 cm^2 V^{-1} s^{-1} and I_{ON}/I_{OFF} of 10^7 [34]. Alkyl-substituted C_n-DNTTs were not adequately soluble for the solution process, in contrast to C_n-BTBT. However, vapour-deposited C_{10}-DNTT yielded a high crystalline film with

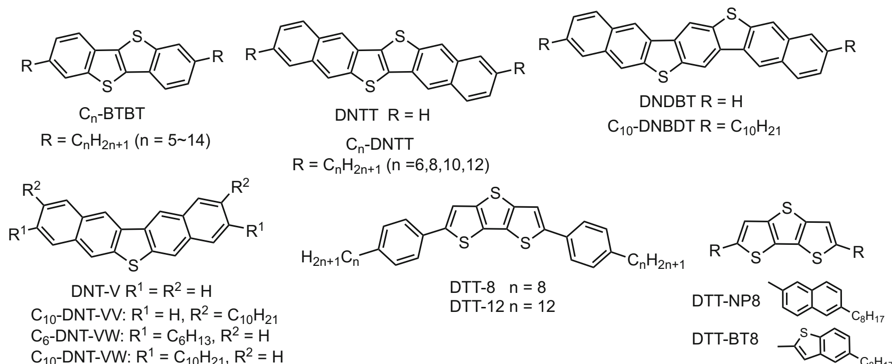

Fig. 9.13 Typical thienoacenes for solution-processed SC-FETs described herein [28–40]

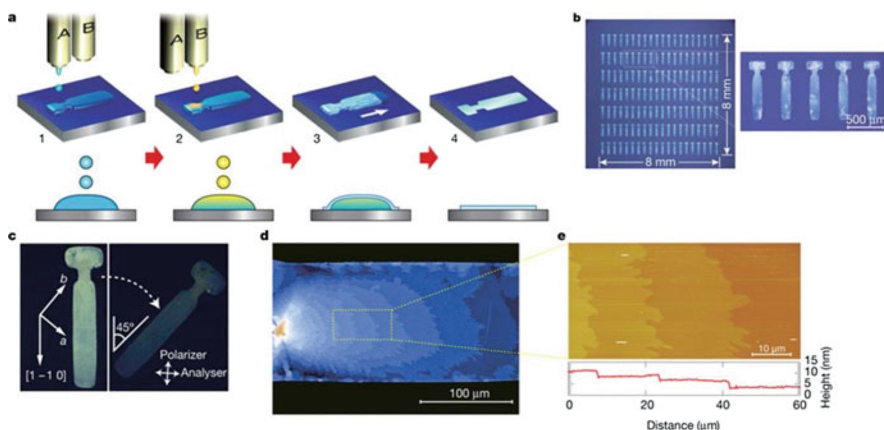

Fig. 9.14 (**a**) Inkjet printing process of SC films of C_8-BTBT. Anti-solvent ink (A) is the first inkjet-printed (Step 1). Solution ink (B) is sequentially overprinted to form intermixed droplets confined to a predefined area (Step 2). Semiconducting thin films grown at droplet liquid–air interfaces (Step 3). Solvent fully evaporates (Step 4). (**b**) Micrographs of a 20 × 7 array of inkjet-printed C_8-BTBT single-crystal thin films. (**c**) Film crossed-Nicol polarized micrographs. (**d**) Expanded micrograph of the film with stripes caused by molecular-layer steps. (**e**) Atomic-force microscopy image and height profile (bottom) showing the step-and-terrace structure on the film surfaces. (Reproduced with permission from [32]. Copyright 2011 Nature Publishing Group)

FET mobility close to 8.0 $cm^2\ V^{-1}\ s^{-1}$ [35]. C_{10}-DNTT was used for patterning solution-crystallized BGTC-OFET. C_{10}-DNTT in hot o-dichlorobenzene (100 °C) was set and gradually dried with crystal growth, and 7 $cm^2\ V^{-1}\ s^{-1}$ average mobility was obtained.

In 2013, V-shaped DNT-V and its alkylated compounds were reported by Okamoto and Takeya et al. (Fig. 9.13) [36]. Depending on the alkylated position and the alkyl chain length, transfer integral changed, and the mobility in vapour-deposited polycrystals and solution-processed single crystals changed. The best performance of C_6-DNT-VW single crystal was 9.5 $cm^2\ V^{-1}\ s^{-1}$ [36].

DNDBT was reported in 2014 with a high carrier mobility of 16 $cm^2\ V^{-1}\ s^{-1}$ by edge–casting method (Fig. 9.13) [37]. All solution-processed DNDBT SC-FET with a mobility of 6.6 $cm^2\ V^{-1}\ s^{-1}$ was reported using POMIRAN™ substrate and EPRIMA™AL insulator [38].

Dithieno[*3,2-b:2′,3′-d*]thiophene derivatives (DTT-8, DTT-12, DTT-NP8, and DTT-BT8) as high-performance p-type organic semiconductors were reported in 2013 by Yasuda and Adachi et al. [39, 40]. The drop-casting deposition of DTT-8 in 1,2-dichlorobenzene solution followed by drying for 12 h gave micro-ribbons, extending uniformly in one dimension up to several hundreds of micrometres or even longer, with widths ranging from 4 to 50 mm and thicknesses of 100–300 nm. The DTT-8 molecules form a nanosegregated lamellar structure consisting of alternately stacked π-conjugated cores and aliphatic chains along the a-axis. In each layer, the molecules are densely packed in a herringbone arrangement, which is cooperatively reinforced by intermolecular S•••S and S•••C(π) interactions. The hole mobility (μ) of the DTT-8 micro-ribbon was found to reach 10.2 $cm^2\ V^{-1}\ s^{-1}$ with a high on/off current ratio on the order of 10^7.

9.5 Precursor Approach for Field-Effect Transistors

Aromatic semiconducting materials without substituents are often low soluble in common organic solvents. Therefore, it is difficult to deposit them on the substrate by a solution process, except for some examples described in Sect. 9.4. In the so-called precursor approach, well-soluble, stable precursor compounds are used as starting materials, and the precursors are quantitatively converted into target materials with released leaving groups in gas phase, solution, film, powders, and crystals by applying external stimuli, such as heat or light. The polyacetylene precursor was first reported in 1980, then tert-butoxycarbonyl (Boc)-DPP, a latent pigment, was reported in 1997 (Fig. 9.15) [41, 42].

In synthetic terms, leaving groups improve precursor solubility; thus, purification and derivatisation of insoluble and/or unstable compounds becomes possible. After precursor purification, the final conversion step yields pure target compounds without further purification. The precursor approach can be applied to insoluble-crystalline-film deposition and morphology control in a solution process. FET and OPV performances via the precursor approach are now addressed [43–45].

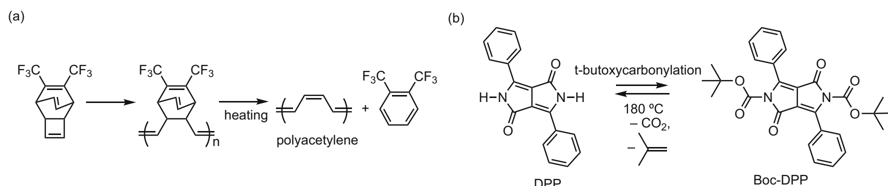

Fig. 9.15 (**a**) Polyacetylene synthesis from the precursor with release of ditrifluoromethylbenzene [41]. (**b**) Synthesis of precursor Boc-DPP and de-protection of Boc groups to yield DPP [42]

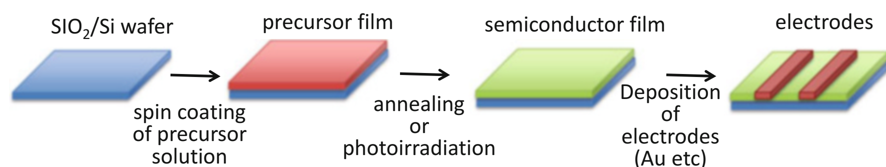

Fig. 9.16 Device fabrication of BGTC-FET by the precursor approach

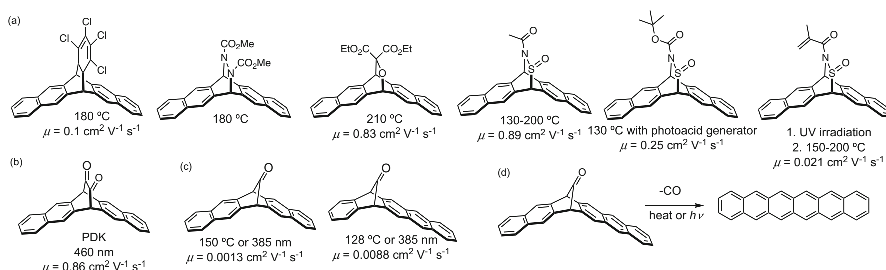

Fig. 9.17 (**a**) Thermal precursors [46–51], (**b**) photo-precursor [52, 53], and (**c**) thermal and photo-precursors [66] of pentacene and FET performance of pentacene prepared by the precursor approach. (**d**) Synthetic scheme of hexacene from precursor [67] for hexacene SC-FET performance

A typical fabrication of the BGTC-OFET device with a precursor approach is shown in Fig. 9.16. After precursor-solution spin-coating, the precursor film is annealed or photo-irradiated to convert the precursor into the target semiconductor materials in situ. The film morphology can be controlled by film-preparation conditions: a selection of solvent to dissolve the precursor, precursor-solution concentration, spin-coating rotation rate and time, substrate temperature during spin-coating and post-annealing, solvent-annealing condition, etc. The polycrystalline film enables preparation of stable devices compared to amorphous film.

9.5.1 Pentacene Precursors

Several thermally convertible pentacene precursors were prepared by adding leaving groups (dienophile) to pentacene (diene) by the Diels–Alder reaction. This reaction is reversible. The precursor can be quantitatively reconverted to pentacene by heating in film. FET performance of pentacene film prepared by the precursor approach is shown in Fig. 9.17a [46–51]. Yamada et al. reported in 2005 6,13–dihydro-6,13-ethanopentacene-15,16-dione (α-diketone precursor: PDK) as a photo-convertible precursor of pentacene (Fig. 9.17b) [52, 53]. PDK is thermally stable over 300 °C but is converted to pentacene by 460 nm irradiation or UV light. This reaction was used for synthesizing substituted pentacene and higher acenes (hexacene, heptacene, octacene, nonacene) by Yamada et al. [54, 55], Neckers et al. [56–59], and Bettinger et al. [60–62].

Acene FET performance using a photo-precursor approach was studied [63–66]. Pentacene using PDK achieved a hole mobility of 0.86 $cm^2\ V^{-1}\ s^{-1}$, $V_{th} = -1.4$ V, and $I_{ON}/I_{OFF} = 4.3 \times 10^6$ [67]. Photo-converted-film high FET mobility was attributed to continuously connected grain boundaries from partial crystallinity obtained by deposition condition optimisation (1% addition of high boiling point solvent to spin-coating solvent, irradiation intensity and duration, and substrate temperature during irradiation).

Watanabe et al. reported a pentacene monoketone precursor (CO-PEN) that extrudes a CO unit upon heating at 150 °C or UV irradiation (Fig. 9.17c) [68]. CO-PEN is unsuitable for FET device fabrication by the precursor approach because it reacts from heating and UV irradiation. Nevertheless, Watanabe et al. prepared pure hexacene single crystal by direct crystal growth on OcTS/SiO_2/silicon substrate by heating the precursor in a nitrogen atmosphere using the physical vapour-transport (PVT) method (Sect. 3.2, Fig. 9.17d) [69]. Table 9.1 outlines the FET performance.

9.5.2 DNTT Precursors

DNTT is a promising material for use in organic semiconductors because DNTT exhibits high carrier mobility and heat resistance as a result of its molecule packing structure and high ionization potential. Since DNTT has a very low solubility in organic solvents, a soluble DNTT precursor was developed [70]. Soeda et al. reported a thermal reaction in ionic liquid to produce DNTT single crystals as large as 200 μm square with a thickness of 50–200 nm hole mobility as high as 2.4 $cm^2\ V^{-1}\ s^{-1}$ in the saturation region, which is comparable to recently reported results for DNTT single-crystal transistors based on vapour-grown crystals (Fig. 9.18) [71]. It was a comparable value with the pentacene OFET prepared with this method: a hole mobility as high as 2.1 $cm^2\ V^{-1}\ s^{-1}$ in the saturation region, and 0.9 $cm^2\ V^{-1}\ s^{-1}$ in the linear region. This method yields a 'single crystal' phase, the most thermodynamically stable structure below 190 °C for pentacene.

High-performance short channel (20 μm) OTFTs with a maximum mobility of 4.7 $cm^2\ V^{-1}\ s^{-1}$ were fabricated by solution process using the DNTT precursor/PS blend, followed by annealing at 200 °C for 10 min [72]. Changing the stereoisomer ratio of the DNTT precursors in the blend, in combination with the surface treatment

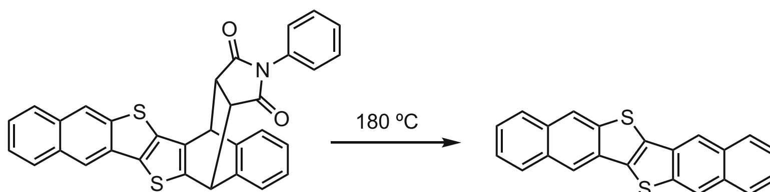

Fig. 9.18 Thermal reaction of DNTT precursor

of substrates, can control the position of the DNTT layer and the crystal size after the thermal conversion of the precursor to DNTT [73]. By using solution phosphorous-doped Si nanoparticle floating gate in combination with DNTT precursor/PS blend, the solution-processed transistor memory was attained [74].

9.5.3 Tetrabenzoporphyrin

Tetrabenzoporphyrin (BP) is a p-type organic semiconductor. Because of BP insolubility in common organic solvents, soluble BP precursors were developed for BP synthesis [43, 75–77]. Bicyclo[2.2.2]octadiene-fused porphyrin (CP) can be quantitatively converted to BP by releasing four ethylene equivalents as a solid and in film by heating over 150 °C (Fig. 9.19). With the quantitative conversion from CP to BP, pure BP can be obtained from purified CP without further purification. The amorphous spun-cast film of CP is changed to polycrystalline BP film during thermal conversion. BP film morphology and grain size can be controlled by the annealing temperature and time [78]. Okujima et al. reported more soluble precursors (MeCP) that release four isoprene equivalents by heating [77].

The BP packing structure of single crystals is the herringbone motif (Fig. 9.20) [80, 81]. Aramaki et al. reported in 2004 a BP FET by the precursor

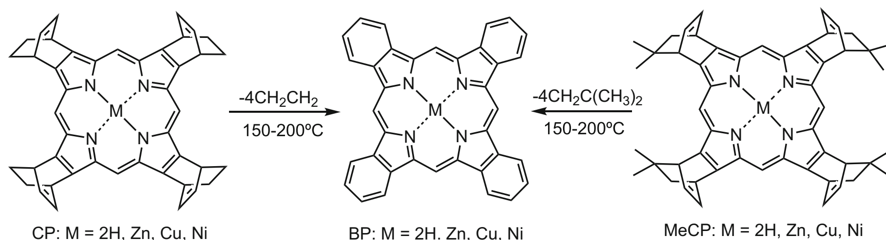

Fig. 9.19 Thermal precursors of BPs (CPs and MeCPs) and the retro-Diels–Alder reaction from precursors to BPs [77, 79]

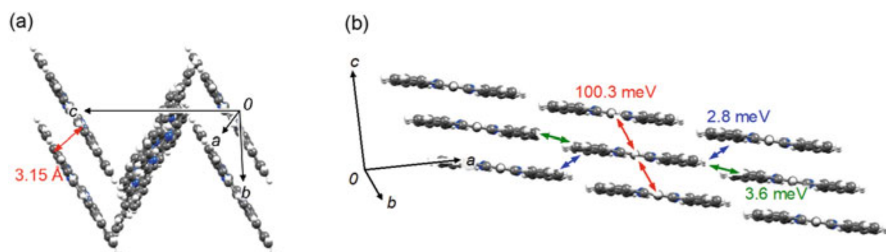

Fig. 9.20 BP herringbone packing structure with (**a**) π–π stacking distance and (**b**) transfer integrals. Rewritten using the crystallographic information file data of [80]

approach with 0.017 cm^2 V^{-1} s^{-1} mobility [78] and Noguchi et al. in 2010 with 0.070 cm^2 V^{-1} s^{-1} [81]. The mobility was better than that prepared by BP direct vacuum deposition (10^{-4} to 10^{-8} cm^2 V^{-1} s^{-1} order). The annealing temperature and presence of an underlying BP layer affected the phase-transition behaviour. Grain size was determined by the balance between nucleation and growth rate. A higher annealing temperature tended to increase them. High growth rates caused rough surfaces. At 150 °C, although the nucleation rate was low, the grains had adequate time to grow up to 5–8 μm with smooth surfaces. At 210 °C, the grains were small and the surface was rough because many nucleates arose [81].

Metalation has a primary influence on the BP electronic structure and film morphologies [82], although the framework of the porphyrin is the same. Kanicki et al. and Aramaki et al. reported FET performances of polycrystalline films of BP and its metal complexes (Ni, Cu, Zn) prepared by the thermal precursor approach [43, 78, 83–86]. The limiting factors in electronic devices fabricated from polycrystalline organic semiconductors are the crystalline grain size and grain boundary density. However, the polycrystalline CuBP thin film has crystalline domains of approximately 20 μm wide (Fig. 9.21) [86]. This was confirmed by the CuBP parallel-aligned nanorods of 55 nm wide, 300 nm long, and 100 nm tall. This parallel nanorod orientation was evident with a higher coverage density. CuBP OFETs demonstrated hole mobilities typically on the order of 0.1 cm^2 V^{-1} s^{-1}, V_{th} around 5 V, I_{ON}/I_{OFF} near 10^4. NiBP showed a similar rod with an average rod height of 110 nm, width of 200 nm, and lengths up to 2 μm [84]. Close to the gate insulator surface, or when there was a low density of molecules, NiBP rods aligned parallel to the interface. These rod piles with random orientations in thicker film produced rough surfaces. The OFETs demonstrated hole mobilities typically on the order of 0.22 cm^2 V^{-1} s^{-1}, V_{th} around −13 V, I_{ON}/I_{OFF} near 10^3.

BP can be deposited on pre-patterned trenches for precise control and placement of long- and short-range ordering of the organic semiconductor [85]. Shea et al.

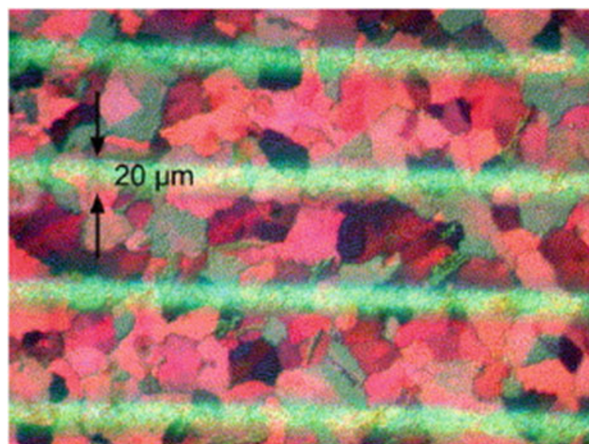

Fig. 9.21 Polarized optical micrograph of a continuous, spun-cast CuBP thin film on thermally oxidized c-Si. The electrodes shown in the figure are 20 μm wide. Colour variations in the film indicate individual nanorod domains. (Reproduced with permission from [86]. Copyright 2007 Elsevier)

prepared BP film from CP on the substrates pre-patterned by photoresisting. The best dimensions observed for the preferred molecular alignment were obtained for substrates with widths of 100 nm, depths of 40 nm, and a nanogroove periodicity of 460 nm. Grooves with smaller periodicity appeared to prevent nucleation within the trenches; crystals instead randomly formed on the top surfaces of the grooves. The height should be adequately large to induce a molecular orientation yet sufficiently small to prevent film roughness. A charge carrier field-effect mobility at $V_{GS} = -40$ V of 2.0×10^{-3} cm^2 V^{-1} s^{-1} was extracted for trenches parallel to L; for trenches aligned perpendicular to L, $\mu = 2.5 \times 10^{-4}$ cm^2 V^{-1} s^{-1}.

9.5.4 TMS-BP and TIPS-BP

As mentioned above, TIPS-PEN is a good semiconducting material with 1D or 2D π-stacking, while pentacene shows a herringbone packing structure. Introducing triisopropylsilylethyny groups to pentacene affects the packing structure in a single-crystal and solution-processed nanocrystalline film. Yamada et al. thus prepared 5,15-bistrimethylsilylethynybenzoporphyrin (TMS-BP) and 5,15-bistriisopropylsilylethynybenzoporphyrin (TIPS-BP) [87–90]. TMS-BP and TIPS-BP X-ray single-crystal structures are shown in Fig. 9.22. TMS-BP shows a herringbone motif. The π–π stacking between BP frameworks is 3.21 Å.

Takahashi et al. found that TIPS-H_2BP has two different packing structures in the single-crystalline state [91]. The first polymorph consists of a 1D extended columnar π-stacking motif (Fig. 9.22b). The second polymorph is arranged in a brickwork motif; π-stacking extends in 2D (Fig. 9.22c). The charge transfer integral based on the TMS-BP and TIPS-BP single-crystal structure is shown in Fig. 9.22. The calculated transfer integral (t) in the TMS-BP crystal is higher than those of TIPS-BP.

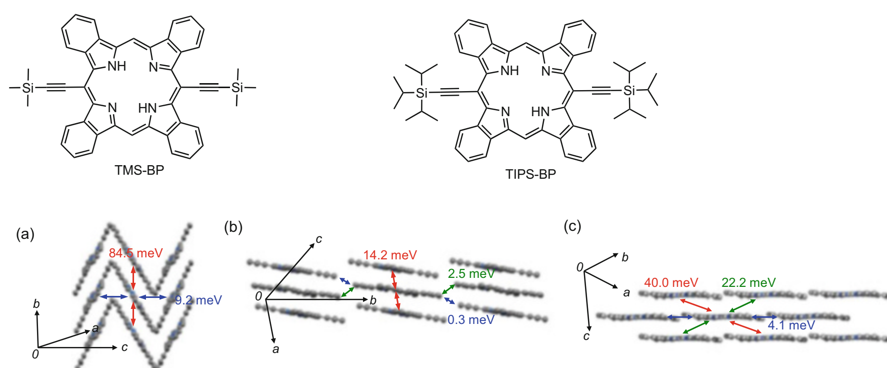

Fig. 9.22 TMS-BP and TIPS-BP molecular and packing structures with transfer integrals of TMS-BP herringbone (**a**), 1D-stacked (**b**), and TISP-BP 2D-stacked (brickwork) structures (**c**). (Adapted with permission from [90] Copyright 2015 World Scientific Publishing Co. and [91] Copyright 2017 American Chemical Society)

Table 9.2 FET performance of TMS-BP and TIPS-BP prepared by the precursor approach [90]

Compounds	μ/cm^2 V^{-1} s^{-1}	V_{th}/V	I_{ON}/I_{OFF}
TMS-BP	0.11	−12.3	2.4×10^6
TIPS-BP	4.36×10^{-5}	−17.8	4.3×10^4

Table 9.3 FET performance of TIPS-BP prepared by drop casting and dip coating

Method	Solvent	SAM[a]	μ^b/cm^2 V^{-1} s^{-1}	$V_{th}{}^c$/V	$I_{on}/I_{off}{}^c$
Drop casting	$C_6H_5CH_3$	MODPA	0.029 (0.018)	0.9	4.9×10^2
Dip coating	CH_2Cl_2	MODPA	0.47 (0.29)	−15.2	1.9×10^5
	CH_2Cl_2 + 10% $CHCl_3$	CDPA	1.1 (0.90)	−0.7	7.0×10^4

[a]MODPA: 12-methoxydodecylphosphonic acid [92]; CDPA: 12-cyclohexyldodecylphosphonic acid [93]
[b]The best values followed by the average of at least six devices in parentheses
[c]Data of champion devices

TMS-BP and TIPS-BP BGTC-FET was fabricated by the precursor approach. The best hole mobility, $\mu = 0.11$ cm^2 V^{-1} s^{-1}, was obtained for TMS-H_2BP, as shown in Table 9.2 [90]. As predicted by the transfer integrals, TMS-BP showed better μ than TIPS-BP.

TIPS-BP is soluble in organic solvents; thus, an intrinsic TIPS-BP solution process is possible. Takahashi et al. compared FET performances of TIPS-BP films prepared by drop casting and dip coating. The performance and packing structure were strongly affected by the use of a suitable deposition method (dip coating), proper solvent (dichloromethane/chloroform, 9:1), and an appropriate self-assembled monolayer (SAM) material as the substrate surfactant [92, 93]. Using CH_2Cl_2 or a mixture of CH_2Cl_2 and $CHCl_3$ as solvents for dip coating, the TIPS-BP films with a 2D π-stack-rich motif were obtained. The maximum field-effect hole mobility of 1.1 cm^2 V^{-1} s^{-1} was achieved with 12-cyclohexyldodecylphosphonic acid (CDPA) as SAM (Table 9.3). This value is higher by orders of magnitude than the record mobility for pristine freebase BP (0.070 cm^2 V^{-1} s^{-1}) [81].

9.5.5 *Other Precursors for OFET*

Murphy et al. reported in 2004 a sexithiophene (T6) solution-processed OFET using thermolysis of diester-functionalized oligothiophene derivative (Fig. 9.23) [94, 95]. Near-edge X-ray absorption fine structure spectroscopy tracked the thermal processing effects on the oligothiophene precursor film chemistry and structure [96]. Thermolysis began at 150 °C for T6. The mobility increased from 150 to 200 °C. During conversion, vertical molecule orientation on substrate occurred.

Hirao et al. prepared thermal precursors (Pc-pre and Nc-pre) of phthalocyanine and naphthalocyanine and deposited BGTC-FET (Fig. 9.24) [97, 98], marking the first examples of solution-processed FETs of phthalocyanines.

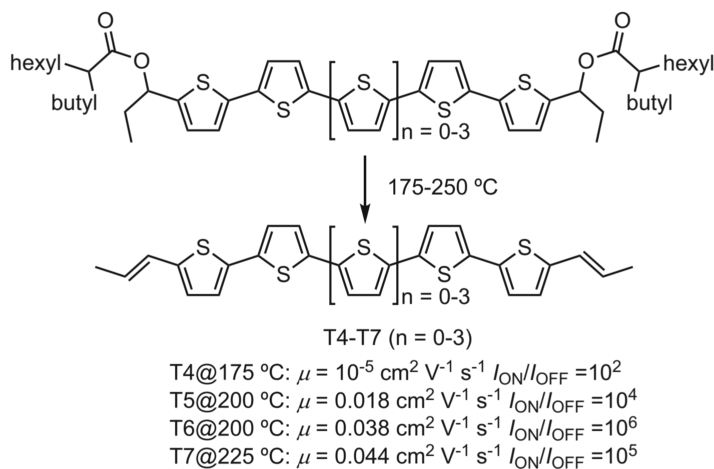

Fig. 9.23 Oligothiophene T4–T7 thermal reaction and FET performance by the precursor approach [96]

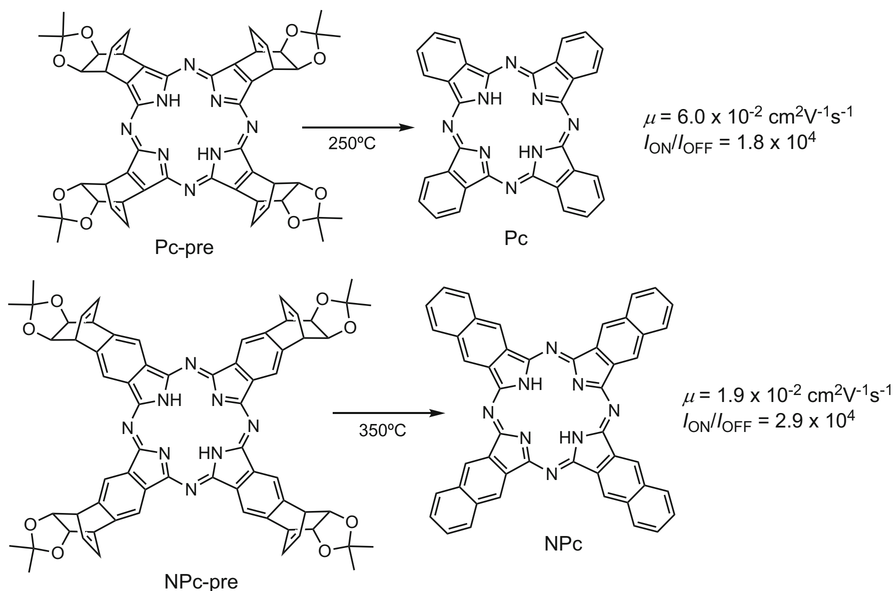

Fig. 9.24 Thermal reaction and FET performance of phthalocyanine and naphthalocyanine by the precursor approach [97, 98]

9.6 Organic Photovoltaics

The precursor approach can be used for OPV devices. In Fig. 9.25, the preparation process of p-n-, BHJ-, and p-i-n-type OPVs by the thermal precursor approach is described. Precursors of p-materials have been mainly developed to date, while few precursors of n-materials have been reported. BHJ layer can be prepared by spin coating a mixed solution of a p-material precursor and a soluble n-material, such as PCBM. It was converted to a p- and n-material mixed film by heating or irradiating. The layered structure was fabricated by repeating spin coating and converting. The film morphology and surface roughness can be controlled by the condition of the conversion from the precursors to the target materials, thermal or solvent annealing, etc.

9.6.1 Solution-Processed p-n Structure Using BP Precursors

BP has been studied as a p-material for solution-processed OPV. As a counterpart of BP, PCBM, a common acceptor, was the first choice. However, the OPV performances of p-n junction solar cells were not satisfactory, as shown in Table 9.4 [99]. With the combination of BP and PCBM (run 1 in Table 9.4), V_{OC} value is small owing to the small energy gap between the highest occupied molecular orbital

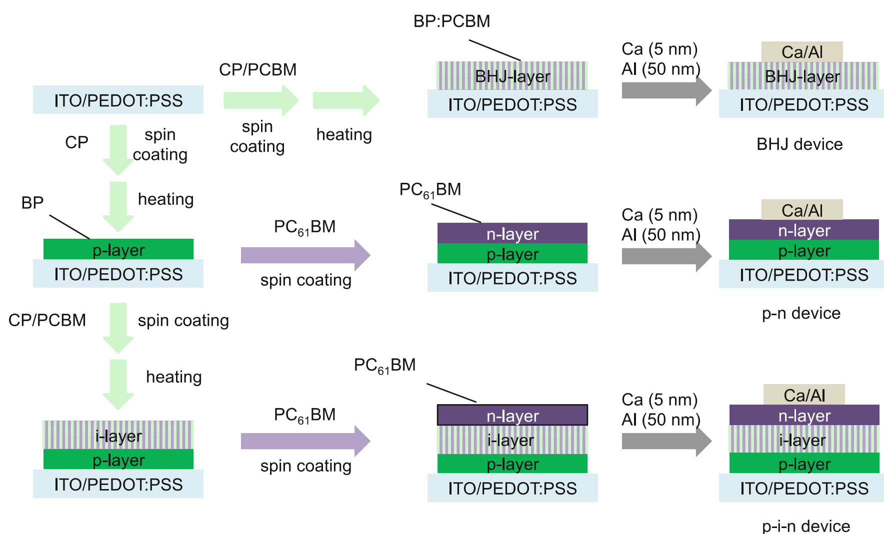

Fig. 9.25 Fabrication of p-n, BHJ, and p-i-n OPV devices by the thermal precursor approach using BP for the p-material and PCBM for the n-material. For the photo-precursors, photo-irradiation instead of heating was applied for the conversion

Table 9.4 OPV performance using BP derivatives for the p-material by the precursor approach

Run	Structure	Donor	Acceptor	J_{SC}/mA cm^{-2}	V_{OC}/V	FF	PCE/%
1	p-n [99]	BP	PCBM	6.3	0.61	0.67	2.6
2		CuBP	PCBM	1.3	0.38	0.61	0.30
3	p-i-n [101]	BP	PCBM	7.0	0.55	0.51	2.0
4		BP	SIMEF	10.5	0.75	0.6	5.2
5	p-i-n [104]	BP	PCBM	5.66	0.44	0.61	1.5
6		BP	PCBNB	7.22	0.60	0.64	2.8
7	p-n [105]	BP	SIMEF2	5.9	0.77	0.68	3.1
8		BP:CABP (75:25)	SIMEF2	8.3	0.81	0.54	3.6
9		CABP	SIMEF2	2.5	0.65	0.65	0.9

(HOMO) energy level of BP and the lowest unoccupied molecular orbital (LUMO) energy level of PCBM. J_{SC} is not adequately large because BP cannot absorb sufficient light at 500–600 nm and over 700 nm. Owing to the high crystallinity of BP, the precursor approach yields polycrystalline BP film with grain sizes of 100 nm, which is larger than the average exciton diffusion length in organic materials (Fig. 9.30a in Sect. 9.6.3) [100–102]. In spite of the drawbacks, various attempts have been tried to use BP derivatives for p-material in OPVs.

Guide et al. reported the effect of copper metalation of BP (CuBP) donor material in a p-n-type OPV combined with PCBM for the acceptor material (run 2 in Table 9.4) [99]. Compared with the BP/PCBM system, the CuBP/PCBM system has a lower J_{SC}, and, in turn, a lower PCE. The authors investigated the cause of the difference between the two materials. The overall average current under the same applied bias of +0.01 V (relative to the substrate) was an order of magnitude higher for CuBP films (260 $\pm$ 100 pA) than for BP films (14 $\pm$ 7 pA) of very similar thicknesses. The charge carrier mobility of CuBP was sufficiently high both in and out of the plane. These data suggest that the charge transport is not a limiting factor in CuBP devices. Despite similar light absorption characteristics, the external quantum efficiency (EQE) showed that the conversion of incident photons to collected electrons was extremely inefficient precisely in the spectral region where CuBP absorption dominated (650–690 nm). Differences in the dependence of EQE and J_{SC} on the donor film thickness for bilayer OPVs with the two different donors suggested a short effective exciton diffusion length (L_D) in CuBP as the factor limiting solar cell performance. That is, an effective L_D of 14.6 $\pm$ 2.2 nm for BP and 5.5 $\pm$ 1.1 nm for PCBM were calculated for BP/PCBM system, while an effective L_D of 2.0 $\pm$ 0.7 nm for BP and 4.3 $\pm$ 1.5 nm for PCBM were calculated for CuBP/PCBM system.

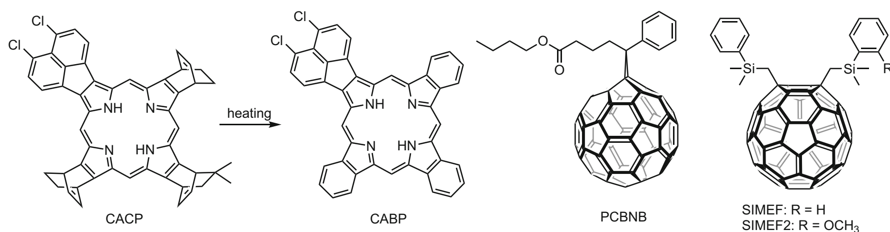

Fig. 9.26 Chemical structures of precursors and compounds discussed in Table 9.4 [101, 104, 105]

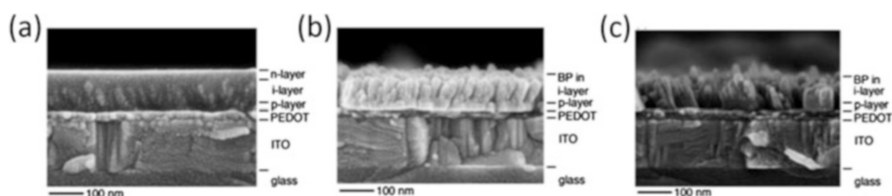

Fig. 9.27 SEM images of the (**a**) side view of p-i-n structure made from BP and SIMEF (glass/ITO/PEDOT-PSS/BP/BP-SIMEF/SIMEF), (**b**) column/canyon region of the p-i structure after toluene washing, and (**c**) side view of the toluene-washed BP/PCBM device, where rectangular BP crystals irregularly grow (Adapted with permission from [101]. Copyright 2009 American Chemical Society)

9.6.2 Solution-Processed p-i-n Structure

The p-i-n device of BP and PCBM showed a comparable performance with the p-n structure as PCE = 2.0% owing to $V_{OC} = 0.55$ V, $J_{SC} = 7.0$ mA/cm, and FF = 0.51 (run 3 in Table 9.4) [100]. With bis(dimethylphenylsilylmethyl)[60]fullerenes (SIMEF) as an acceptor (Fig. 9.26), OPV performance was improved to PCE = 5.2% owing to $V_{OC} = 0.75$ V; $J_{SC} = 10.5$ mA/cm^2; FF = 0.6 (run 4 in Table 9.4) [101]. The important difference between PCBM and SIMEF is the crystallization temperature: SIMEF crystallizes from an amorphous state at 149 °C; for PCBM, it occurs at 195 °C [100]. To deposit the i-layer, a homogeneous mixture (a typical weight ratio of 3:7) of CP and an acceptor SIMEF in chloroform/chlorobenzene is spin coated. CP is converted in situ to BP at 180 °C to form an interdigitated i-layer. The choice of 180 °C is crucial for conversion from CP to BP because SIMEF is crystalline at this temperature. In the i-layer, the desired interdigitated BHJ is achieved with the average size of the columns at 65 nm in height and 26 nm in diameter (Fig. 9.27a, b). This is comparable to the exciton diffusion length of common organic semiconducting separation and carrier transport. When PCBM is used in place of SIMEF, the BP crystal morphology in the i-layer is far less uniform in size than that in the SIMEF device. In addition, the BP crystals are rectangular (a usual bulk morphology of BP crystals) rather than round columnar (Fig. 9.27c). This difference is due to the difference of crystallization

temperatures of SIMEF (149 °C) and PCBM (195 °C). BP crystal formation at 180 °C in the SIMEF device occurs in the matrix of SIMEF crystals, whereas it occurs in amorphous PCBM in the PCBM device.

Tamura and Matsuo theoretically analysed the exciton diffusion length and charge mobility in BP and SIMEF crystals using density functional theory (DFT) and Fermi's golden rule [103]. Because of the herringbone packing structure of the BP crystal, the value of the intermolecular electronic coupling of the hole transfer, V_{hole}, and the exciton coupling, V_{XT}, of the parallel H-aggregate were relatively large compared with other directions. Because the charge transfer coupling of the parallel H-aggregate was large, the electron exchange—i.e. Dexter transfer—significantly contributed to the exciton coupling. For other directions, the electron exchange was small. Thus, the Coulomb coupling, i.e. the Förster transfer, was dominant. Intermolecular electronic coupling for the electron transfers, V_{el}, of SIMEF was also anisotropic because V_{el} was affected by the steric hindrance of the functional groups in SIMEF. As a result, the electron transport was efficient only along a direction that did not cross the functional groups.

Nguyen et al. reported the nanoscale morphology and conductivity/photoconductivity of a recently developed OPV system based on BP and either PCBM or [6,6]-phenyl-C61-butyric acid n-butyl ester (PCBNB) using conducting atomic force microscopy (C-AFM) and photoconductive atomic force microscopy (PC-AFM) (runs 5 and 6 in Table 9.4 and Fig. 9.26) [104]. Although the published values for the (LUMO energies of both PCBM and PCBNB are nearly identical, the p-i-n device fabricated using PCBNB as an acceptor consistently exhibits higher PCEs than the device with PCBM (2.8% versus 1.5%) owing to an increase in V_{OC} from 0.44 to 0.60 V; in J_{SC} from 5.66 to 7.22 mA cm^{-2}; and in FF from 0.61 to 0.64. The BP in the i-layer forms columnar structures with a diameter of approximately 70 nm; however, the slight difference in the alkyl chains of PCBM and PCBNB has a large impact on the film morphology, phase separation, and device performance. For devices with PCBM, unfavourable vertical morphology, large-phase separation, and thus lower PCE are observed. When PCBNB is used, a more homogeneous morphology, finer-phase separation, and higher PCE are observed.

Zhen et al. found a solid solution of 75:25 mixture of BP and CABP produced a higher PCE value than the devices using the single donor BP and CABP, respectively (Fig. 9.26) [105]. CABP has three important features for improving the PCE performance: structural similarity with BP to be intercalated in BP crystals, an acenaphthylene fragment that decreases the band gap, and two chlorine atoms that lower the HOMO energy level, which may otherwise not match well with that of BP. Different ratios of two soluble donor precursors (CP and CACP) were tested in combination with SIMEF2 for the i-layer of p-i structure OPV. Then a very smooth surface reminiscent of a molten solid was achieved by the combination of 75:25 mixture of BP and CABP in a SIMEF2 matrix (porphyrin: SIMEF2 = 3:7), shown by a low-landing-voltage high-resolution SEM (Fig. 9.28). These characteristic nanoscale morphologies occurred only when the CP:CACP mixture was thermolysed in the presence of SIMEF2 and the BP undercoating layer. The 100:0 or 0:100 BP:CABP showed a nano-columnar morphology of considerable

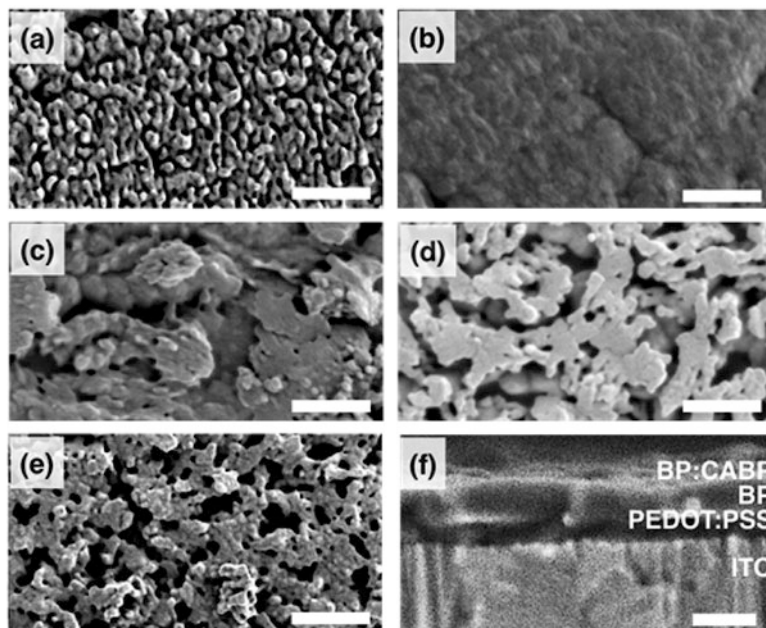

Fig. 9.28 SEM images (**a**–**f**) for blended BP and CABP on the BP layer after removing SIMEF2 by washing with toluene. Top view images at the BP:CABP blend ratios of 100:0 (**a**), 75:25 (**b**), 50:50 (**c**), 25:75 (**d**), and 0:100 (**e**), and a cross-sectional view of the 75:25 blend (**f**). Scale bar, 200 nm (Reproduced with permission from [105]. Copyright 2015 American Chemical Society)

regularity. The 75:25 mixture showed the highest PCE with the increase of J_{SC} (runs 7–9 in Table 9.4). The most noticeable feature in EQE spectrum was the remarkable enhancement at 350–700 nm, where both BP and CABP were strongly absorbed (Soret bands at 440 and 420 nm, respectively). This enhanced EQE was attributed to the improvement of the internal quantum efficiency (IQE) rather than the absorption efficiency. Even though the HOMO (donor)-LUMO (acceptor) energy level differences were the smallest for the solid solution cell among the three cells (BP, BP/CABP, and CABP), the highest V_{OC} was obtained. This is explained by the suppressed recombination current, J_{SO}. CABP molecules intercalated in the BP crystal lattice induced partial disordering of the structure, which decreased J_{SO} and hence increased V_{OC} [106].

9.6.3 BP-C60 for BHJ Layer

Donor–acceptor (D–A) dyads have been widely studied to understand charge separation and recombination processes between donor and acceptor units. Various

Table 9.5 OPV performance using BP derivatives for the p-material by the precursor approach

Run	Structure	p-layer	i(BHJ)-layer	n-layer	J_{SC}/mA cm^{-2}	V_{OC}/V	FF	PCE/%
1	p-n [102]	BP	–	PCBM	5.16	0.57	0.64	1.8
2	BHJ [110]	BP	–	PCBM	0.57	0.14	0.23	0.02
3		–	f-BP-C_{60}	–	1.82	0.48	0.29	0.26
4		–	r-BP-C_{60}	–	2.11	0.62	0.29	0.38
5	p-i-n [110]	BP	–	PCBM	5.9	0.59	0.46	1.6
6		BP	f-BP-C_{60}	PCBM	5.27	0.60	0.63	2.00
7		BP	r-BP-C_{60}	PCBM	3.46	0.60	0.32	0.67

Adapted with permission from [102, 110]. Copyright 2014, 2016 Royal Society of Chemistry

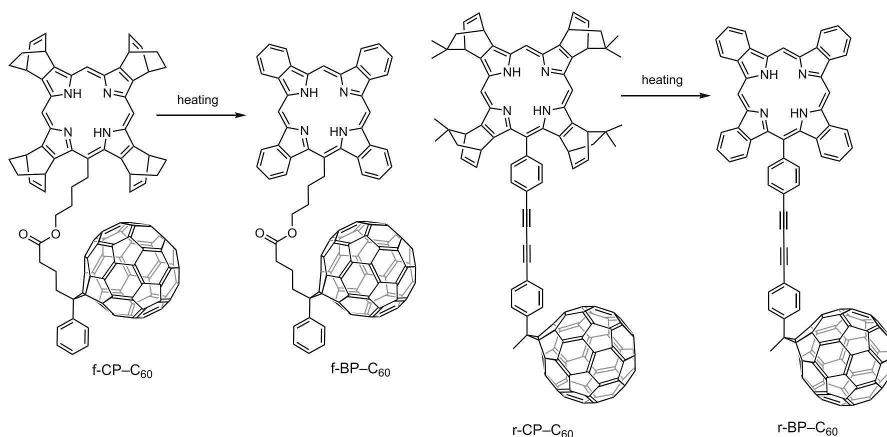

Fig. 9.29 Chemical structures and thermal conversion from precursors to BP–C_{60} compounds described in Table 9.5 [102, 110]

dyad compounds have also been examined for use as active materials in BHJ OPVs. This is because the direct connection of donor and acceptor components can be beneficial for forming a maximal D–A interface within a film, thereby providing high charge separation efficiency [107–109]. Tamura et al. reported a p-i-n-type OPV with a covalently linked BP-fullerene (D–A) compound for the i-layer, while BP was used for the p-layer, and $PC_{61}BM$ was used for the n-layer. It was compared with the p-n-type and BHJ-type solar cell (Table 9.5) [102, 110]. The comparison of flexible versus rigid D–A compounds (f-BP–C_{60} and r-BP–C_{60}, respectively, in Fig. 9.29) as i-layer materials suggest that flexible f-BP–C_{60} is suitable for the i-layer on the highly crystalline BP layer because the BP film roughness is levelled by the f-BP–C_{60} and the device electrical properties are improved by the smooth interface (Fig. 9.30).

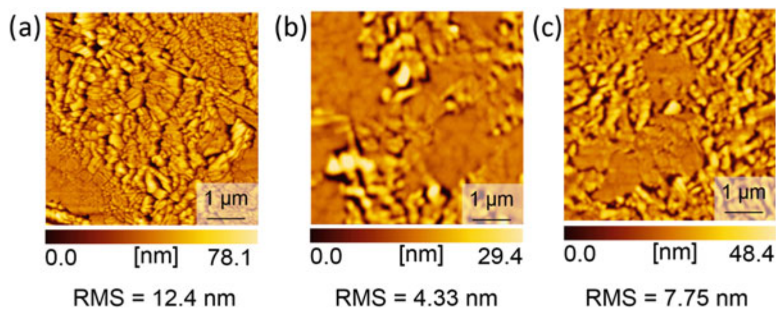

Fig. 9.30 AFM height images of (**a**) BP, (**b**) f-BP-C60 layer on BP layer, and (**c**) r-BP-C60 layer on BP layer (Reproduced by permission of The Royal Society of Chemistry [102, 110])

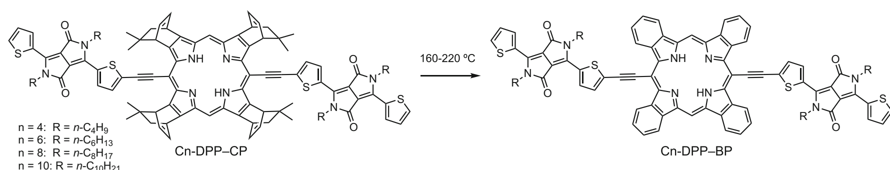

Fig. 9.31 Thermal conversion from Cn-DPP–CP to Cn-DPP–BP [111]

9.6.4 BP-DPP for BHJ

BP has a high photo-absorption coefficient of more than 10^5 M^{-1} cm^{-1} around 450–500 nm, where the solar light intensity is strongest. However, it has rather narrow absorption bands at Soret and Q bands (600–700 nm). It is transparent at 500–600 nm and over 700 nm. To overcome this drawback, DPP-linked BP with different alkyl chains on the DPP unit was synthesized to control the film morphology [111]. They prepared BHJ OPV of Cn-DPP-BP ($n = 4$, 6, 8, or 10, depending on the alkyl chain length) in combination with PCBM by the precursor approach because of the insolubility of Cn-DPP-BP in common organic solvents (Fig. 9.31). The PCE performance drastically changed in accordance with the alkyl chain length because of the drastic change of J_{SC} (Table 9.6). The grazing-incidence wide-angle X-Ray diffraction (GIWAXD) measurements suggested that C4-DPP–BP in blended films tends to have larger amounts of crystallites derived from π–π stacking in the out-of-plane direction. This is more suitable for charge carrier transport of OPV than the C10-DPP–BP oriented to the edge against the substrate. In addition, PCBM tended to produce a more crystalline structure in combination with C4-DPP–BP than C10-DPP–BP.

Table 9.6 OPV performance using BP for the p-material using the precursor approach

Materials	J_{SC}/mA cm^{-2}	V_{OC}/V	FF	PCE/%
C4-DPP–BP	15.19	0.67	0.52	5.24
C6-DPP–BP	13.56	0.69	0.49	4.52
C8-DPP–BP	9.12	0.70	0.48	3.06
C10-DPP–BP	0.88	0.66	0.33	0.19

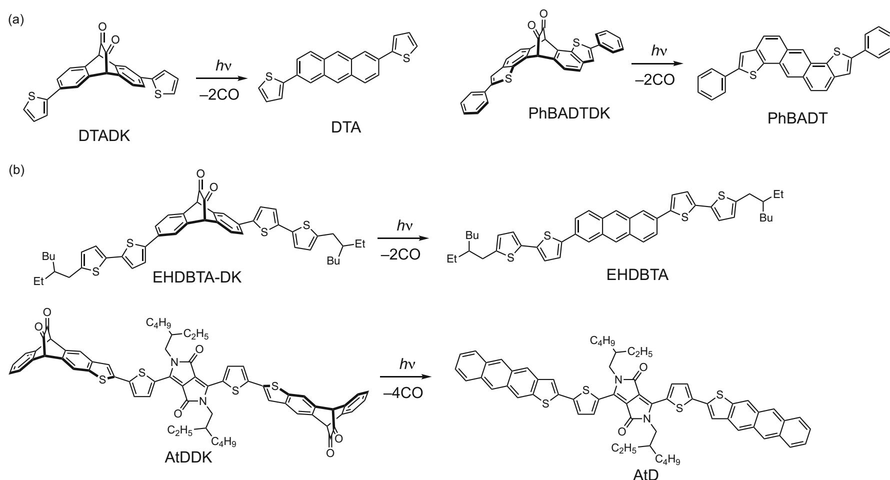

Fig. 9.32 The p-type materials for p-layer (**a**) and BHJ (i)–layer (**b**) with their photo-precursors used in Table 9.7 [114, 115]

9.6.5 *Photo-Precursor Approach*

The photo-precursor approach was applied to OPV fabrication [112–115]. In this approach, in situ photoconversion reaction of precursors to the target materials is performed instead of thermal conversion in the previous sections (Fig. 9.32). When 2,6-dithienylanthracene (DTA) and a fullerene derivative $PC_{71}BM$ were used as the donor and acceptor, respectively, the best p-i-n OPV produced a higher photovoltaic efficiency than the corresponding p-n device by 24% and bulk-heterojunction device by 67% (run 1–3 in Table 9.7). A systematic comparison of different device types indicated that the neat p- and n-layers enhanced charge extraction and carrier injection and the blended i-layer improved charge photo-generation [114].

Furthermore, the prototype hetero p-i-n system was examined with 2,6-bis(5′-(2-ethylhexyl)-(2,2′-bithiophen)-5-yl)anthracene (EH-DBTA) for the i-layer and DTA for the p-layer (run 4). The resulting devices showed significantly enhanced photovoltaic performances compared to the homo p-i-n devices. The PCE enhancement was attributed to the better miscibility with $PC_{71}BM$ and higher photo-absorption capability inherent in EH-DBTA compared to DTA. This three-component system, employing the proper materials for each layer, was enabled by the precursor approach for the solution process.

Table 9.7 OPV performances prepared by the photo-precursor approach in combination with $PC_{71}BM$ as n-material

Run	Device structure	p-Materials		J_{SC}/mA cm^{-2}	V_{OC}/V	FF	PCE/%
		p-Layer	BHJ(i)-layer				
1	p-n [114]	DTA	–	2.81	0.80	0.54	1.2
2	BHJ	–	DTA	2.92	1.05	0.29	0.90
3	p-i-n	DTA	DTA	3.78	0.89	0.45	1.5
4	p-i-n	DTA	EH-DBTA	5.78	0.91	0.55	2.9
5	BHJ [115]	–	AtD	1.6	0.83	0.235	0.30
6	p-i-n	PhBADT	AtD	10.6	0.89	0.498	4.7
7	p-i-n (with SVA)[a]	PhBADT	AtD	12.7	0.88	0.526	5.9

[a] Annealed with THF vapour for 120 s

Suzuki et al. designed the improved materials for the photo-precursor approach [115]. PhBADT is suitable for p-layer because of the transparency in a wide range of the visible region and forming three-dimensionally extended π–π contacts in the solid state, which is favourable in achieving effective hole-transport paths. AtD is suitable for i-layer because of the efficient absorption of the sunlight and good miscibility with $PC_{71}BM$. Compared to BHJ structure (run 5), the p-in structure after solvent annealing afforded the 5.9% PCE (run 7), which was the highest PCE value reported for p-i-n-type OPVs prepared by solution process.

9.6.6 Other p-type Materials for OPV

Benzoporphycene (BPc) is a structural isomer of benzoporphyrin (BP) (Fig. 9.33) [116]. Owing to its lower symmetry compared to BP, the absorption of the Q-band region is stronger than in BP. Saeki et al. investigated BPc as a p-material for BHJ OPV combined with PCBM. The precursor CPc molecules were converted to BPc by annealing above 125 °C in the film. When the CPc/PCBM mixed film was annealed at 200 °C, a phase-separated structure composed of BPc and PCBM crystals was formed. In the presence of CPc/PCBM, PCBM played the role of both a matrix and an aggregation inhibitor of BPc under the thermal conversion process [117]. The process of spin coating of the CPc/PCBM solution and heating at 200 °C for 10 min was repeated five times to produce the multi-stacked film. The BPc homo-epitaxial crystallization was observed with a height of 100 nm, which was approximately five times the height of a single layer of BPc grains [118]. Thus, the precursor approach enabled the preparation of thick film by repeating the deposition process of spin coating and converting.

A dialkoky-substituted copper Pc precursor, $CuPc(OMe)_2$ was reported in 2011 (Fig. 9.34) [119]. The solution-processed OPV with thermal conversion of the precursors showed a solvent-dependent performance, which can be explained by the film morphology. The flat surface morphology obtained using a solvent with a

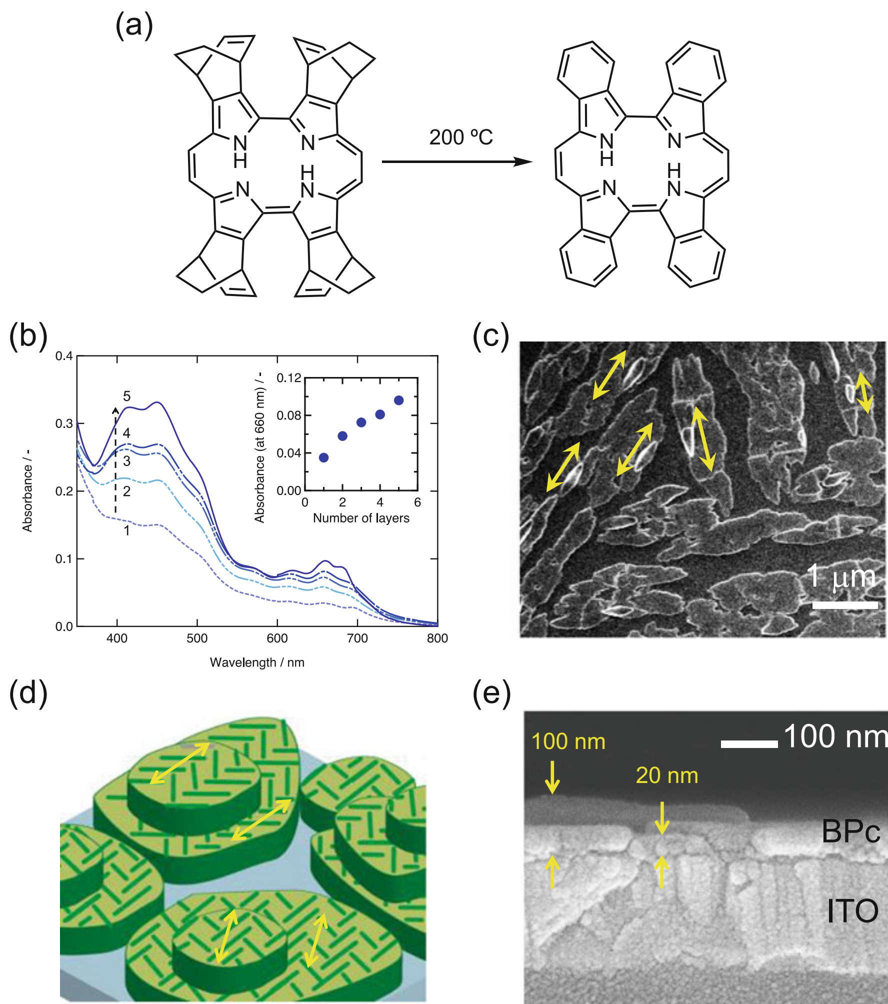

Fig. 9.33 (**a**) Synthetic scheme of BPc from precursor CPc. (**b**) UV-vis absorption spectra of multi-stacked BPc/PCBM films. Inset: dependence of absorbance at 660 nm on the number of alternating spin-coating/annealing cycles. (**c**) Topological SEM image of a BPc/PCBM film containing five layers prepared at 200 °C after rinsing of PCBM. The long axis of the crystal in the upper layer is aligned to be parallel to that of the lower layer, as indicated by arrows. (**d**) Schematic representation of the homo-epitaxial growth of BPc. (**e**) Cross-sectional SEM image of a BPc/PCBM film with five layers after rinsing (Adapted with permission from [118]. Copyright 2013, Japan Society of Applied Physics)

low b.p., such as toluene or chloroform, resulted in a device with better photovoltaic performance because of a lower charge leakage (i.e. a higher FF) [120]. The best PCE performance of the p-n structure with mix-PCBM (a mixture of $PC_{61}BM$ and $PC_{71}BM$) was 1.35%.

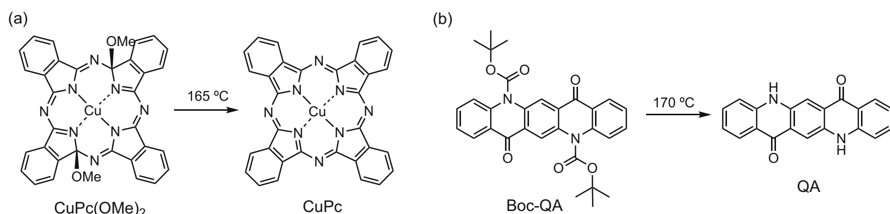

Fig. 9.34 Reaction scheme of (**a**) dialkoky-substituted copper Pc precursor, $CuPc(OMe)_2$, to CuPc and (**b**) Boc–QA to QA [119–121]

Table 9.8 Device parameters for three kinds of OPVs using QA and $PC_{61}BM$ [121]

Devices	Structures	V_{OC}/V	J_{SC}/mA cm^{-2}	FF	PCE/%
Bilayer (p-n)	QA/PCBM	0.53	2.50	0.46	0.61
BHJ (i)	QA:PCBM (1:1.5)	0.70	2.54	0.32	0.57
Trilayer (p-i-n)	QA/QA:PCBM (1:1.5)/PCBM	0.79	2.34	0.44	0.83

Chen et al. reported a solution-processed p-i-n OPV device with quinacridone (QA) and $PC_{61}BM$ using Boc–QA as a soluble precursor of QA [121]. The p-i-n trilayer structure PCE performance was 0.83%; it was 0.61 and 0.57% for the p-n bilayer and BHJ structures, respectively (Table 9.8). V_{OC} of the p-in system was better than that in the BHJ system. It was achieved by reducing the electron leakage current through introduction of carrier blocking layers (QA and $PC_{61}BM$) between the organic layers and electrodes.

9.6.7 Precursors for n-type Materials

A few precursors of n-materials have been reported to date. Lee et al. reported a thermal precursor C_{60}-$CpCO_2R$ (R = hexyl, octyl and ethylhexyl groups), which can be converted to C_{60} by annealing at 120 °C (Fig. 9.35). BHJ OPV performance of P3HT/C_{60} using C_{60}-$CpCO_2R$ as a precursor was improved more than that of direct spin coating of P3HT/C_{60}. The best performance was obtained from P3HT/C_{60}-$CpCO_2$Hex at 120 °C annealing (PCE = 2%), which was twice that of the intrinsic P3HT/C_{60} device. An AFM image showed that as-prepared P3HT/C_{60} had micrometre-order grains, whereas the film from P3HT/C_{60}-$CpCO_2$Hex was smooth [122].

A thermal precursor of C_{60}, $C_{60}(9MA)_2$, was reported in 2016 by Umeyama et al. (Fig. 9.35) [123]. The PCE value of the OPV devices based on PCDTBT:C60–9MA adducts improved from 0.69% to 3.51% by a factor of approximately five, which was associated with a significant enhancement of J_{SC} and FF when the device was annealed at 140 °C. A factor that hampered the achievement of excellent PCE was

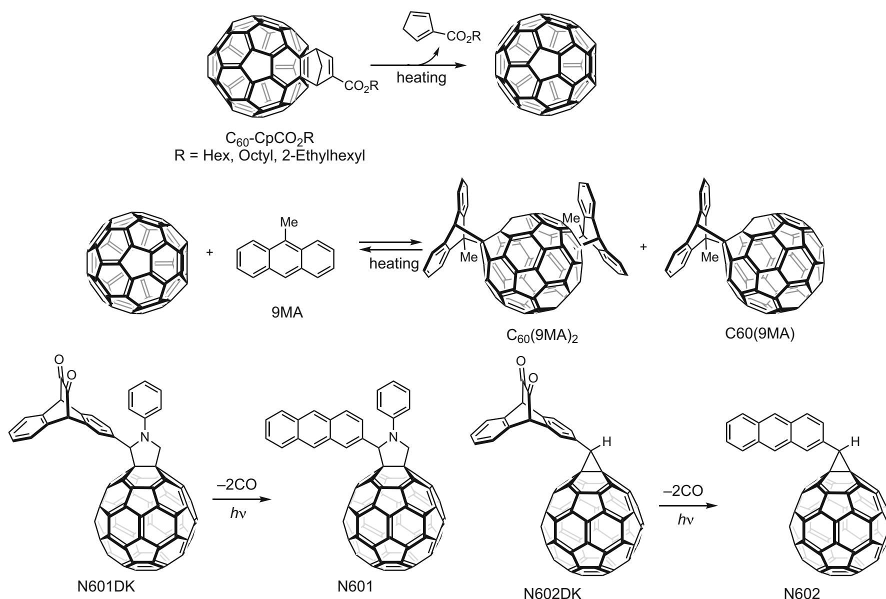

Fig. 9.35 Precursors of n-materials [122–124]

the recovery of the p-conjugation and the consequently lowered LUMO levels of fullerenes by the thermal annealing.

Fullerene derivatives, N601 and N602, were quantitatively converted from diketone precursors, N601DK and N602 DK, by irradiation of 460 nm of light [124]. N601 film prepared by the photo-precursor approach showed comparable electron mobility with PCBM film. The PCE performance of BHJ OPV of P3HT/N601 was 2.43%, which of P3HT/PCBM was 2.16%.

9.7 Summary

In this chapter, solution-process procedures for single crystalline and polycrystalline films for organic semiconductor devices were summarized. The organic crystalline films have intrinsic potential for high-performance devices; however, the solution process was not easy on account of their high crystallinity, namely, the low solubility in common organic solvents. One breakthrough in addressing this problem was the development of soluble materials with high crystallinity. The soluble compounds with alkyl substituents were believed to have low electrical properties on account of the insulating substituents. Nevertheless, some materials were found to have good electrical properties with assistance from the substituents for a good packing motif from the van der Waals interaction. The soluble materials encouraged the progress

of the deposition technique to attain a 10^2 cm^2 V^{-1} s^{-1} order of mobilities. The precursor approach showed potential for improving device performance by controlling the deposition condition, such as the annealing temperature, photo-irradiation condition, solvents, post-annealing, solvent annealing, etc. Further development for new materials can advance organic electronic devices.

Acknowledgment This work was supported by CREST, Japan Science and Technology Agency (JST), Grants-in-Aid for Scientific Research (Nos. 16H02286, 26105004, 26620167), and the Program for Promoting the Enhancement of Research Universities in NAIST sponsored by the Ministry of Education, Culture, Sports, Science and Technology (MEXT), Japan.

References

1. J.E. Anthony, Angew. Chem. Int. Ed. **47**, 452 (2008)
2. K. Takimiya, S. Shinamura, I. Osaka, E. Miyazaki, Adv. Mater. **23**, 4347 (2011)
3. J. Mei, Y. Diao, A.L. Appleton, L. Fang, Z. Bao, J. Am. Chem. Soc. **135**, 6724 (2013)
4. V. Coropceanu, J. Cornil, D.A. da Silva Filho, Y. Olivier, R. Silbey, J.-L. Brédas, Chem. Rev. **107**, 926 (2007)
5. C.W. Tang, Appl. Phys. Lett. **48**, 183 (1986)
6. M. Hiramoto, H. Fujiwara, M. Yokoyama, Appl. Phys. Lett. **58**, 1062 (1991)
7. G. Yu, J. Gao, J.C. Hummelen, F. Wudl, A.J. Heeger, Science **270**, 1789 (1995)
8. J.-L. Brédas, D. Beljonne, V. Coropceanu, J. Cornil, Chem. Rev. **104**, 4971 (2004)
9. V. Vohra, K. Kawashima, T. Kakara, T. Koganezawa, I. Osaka, K. Takimiya, H. Murata, Nat. Photonics **9**, 403 (2015)
10. S. Blumstengel, S. Sadofev, C. Xu, J. Puls, F. Henneberger, Phys. Rev. Lett. **97**, 237401 (2006)
11. J.E. Anthony, Chem. Rev. **106**, 5028 (2006)
12. M. Watanabe, Y.J. Chang, S.-W. Liu, T.-H. Chao, K. Goto, M.M. Islam, C.-H. Yuan, Y.-T. Tao, T. Shinmyozu, T.J. Chow, Nat. Chem. **4**, 574 (2012)
13. S.C. Capelli, A. Albinati, S.A. Mason, B.T.M. Willis, J. Phys. Chem. A **110**, 11695 (2006)
14. C.P. Brock, J.D. Dunitz, Acta Cryst **B46**, 795 (1990)
15. D. Holmes, S. Kumaraswamy, A.J. Matzger, K.P.C. Vollhardt, Chem. Eur. J. **5**, 3999 (1999)
16. V. Coropceanu, O. Kwon, B. Wex, B.R. Kaafarani, N.E. Gruhn, J.C. Durivage, D.C. Neckers, J.-L. Brédas, Chem. Eur. J. **12**, 2073 (2006)
17. O.L. Griffith, J.E. Anthony, A.G. Jones, D.L. Lichtenberger, J. Am. Chem. Soc. **132**, 580 (2010)
18. S.M. Ryno, C. Risko, J.-L. Brédas, J. Am. Chem. Soc. **136**, 6421 (2014)
19. T. Hasegawa, J. Takeya, Sci. Technol. Adv. Mater. **10**, 024314 (2009)
20. A.L. Briseno, S.C.B. Mannsfeld, M.M. Ling, S. Liu, R.J. Tseng, C. Reese, M.E. Roberts, Y. Yang, F. Wudl, Z. Bao, Nature **444**, 913 (2006)
21. J.E. Anthony, J.S. Brooks, D.L. Eaton, S.R. Parkin, J. Am. Chem. Soc. **123**, 9482 (2001)
22. C.D. Sheraw, T.N. Jackson, D.L. Eaton, J.E. Anthony, Adv. Mater. **15**, 2009 (2003)
23. M.M. Payne, S.R. Parkin, J.E. Anthony, C.-C. Kuo, T.N. Jackson, J. Am. Chem. Soc. **127**, 4986 (2005)
24. D.H. Kim, D.Y. Lee, H.S. Lee, W.H. Lee, Y.H. Kim, J.I. Han, K. Cho, Adv. Mater. **19**, 678 (2007)
25. S.K. Park, T.N. Jackson, J.E. Anthony, D.A. Mourey, Appl. Phys. Lett. **91**, 063514 (2007)
26. G. Giri, E. Verploegen, S.C.B. Mannsfeld, S. Atahan-Evrenk, D.H. Kim, S.Y. Lee, H.A. Becerril, A. Aspuru-Guzik, M.F. Toney, Z. Bao, Nature **480**, 504 (2011)

27. Y. Diao, B.C.-K. Tee, G. Giri, J. Xu, D.H. Kim, H.A. Becerril, R.M. Stoltenberg, T.H. Lee, G. Xue, S.C.B. Mannsfeld, Z. Bao, Nat. Mater. **12**, 665 (2013)
28. H. Ebata, T. Izawa, E. Miyazaki, K. Takimiya, M. Ikeda, H. Kuwabara, T. Yui, J. Am. Chem. Soc. **129**, 15732 (2007)
29. T. Izawa, E. Miyazaki, K. Takimiya, Adv. Mater. **20**, 3388 (2008)
30. T. Uemura, Y. Hirose, M. Uno, K. Takimiya, J. Takeya, Appl. Phys. Express **2**, 111501 (2009)
31. J. Soeda, Y. Hirose, M. Yamagishi, A. Nakao, T. Uemura, K. Nakayama, M. Uno, Y. Nakazawa, K. Takimiya, J. Takeya, Adv. Mater. **23**, 3309 (2011)
32. H. Minemawari, T. Yamada, H. Matsui, J. Tsutsumi, S. Haas, R. Chiba, R. Kumai, T. Hasegawa, Nature **475**, 364 (2011)
33. C. Liu, T. Minari, X. Lu, A. Kumatani, K. Takimiya, K. Tsukagoshi, Adv. Mater. **23**, 523 (2010)
34. T. Yamamoto, K. Takimiya, J. Am. Chem. Soc. **129**, 2224 (2007)
35. M.J. Kang, I. Doi, H. Mori, E. Miyazaki, K. Takimiya, M. Ikeda, H. Kuwabara, Adv. Mater. **23**, 1222 (2011)
36. T. Okamoto, C. Mitsui, M. Yamagishi, K. Nakahara, J. Soeda, Y. Hirose, K. Miwa, H. Sato, A. Yamano, T. Matsushita, T. Uemura, J. Takeya, Adv. Mater. **25**, 6392 (2013)
37. C. Mitsui, T. Okamoto, M. Yamagishi, J. Tsurumi, K. Yoshimoto, K. Nakahara, J. Soeda, Y. Hirose, H. Sato, A. Yamano, T. Uemura, J. Takeya, Adv. Mater. **26**, 4546 (2014)
38. S. Sakai, J. Soeda, R. Häusermann, H. Matsui, C. Mitsui, T. Okamoto, M. Ito, K. Hirose, T. Sekiguchi, T. Abe, M. Uno, J. Takeya, Org. Electron. **22**, 1 (2015)
39. Y.S. Yang, T. Yasuda, H. Kakizoe, H. Mieno, H. Kino, Y. Tateyama, C. Adachi, Chem. Commun. **49**, 6483 (2013)
40. H. Mieno, T. Yasuda, Y. Seok, C. Adachi, Chem. Lett. **43**, 294 (2014)
41. J.H. Edwards, W.J. Feast, Polymer **21**, 595 (1980)
42. J.S. Zambounis, Z. Hao, A. Iqbal, Nature **388**, 131 (1997)
43. H. Yamada, T. Okujima, N. Ono, Chem. Commun. **2957** (2008)
44. M. Watanabe, K.-Y. Chen, Y.J. Chang, T.J. Chow, Acc. Chem. Res. **46**, 1606 (2013)
45. M. Suzuki, T. Aotake, Y. Yamaguchi, N. Noguchi, H. Nakano, K.-I. Nakayama, H. Yamada, J. Photochem. Photobiol. C Photochem. Rev. **18**, 50 (2014)
46. A.R. Brown, A. Pomp, D.M. De Leeuw, D.B.M. Klaassen, E.E. Havinga, P. Herwig, K. Müllen, J. Appl. Phys. **79**, 2136 (1996)
47. P.T. Herwig, K. Müllen, Adv. Mater. **11**, 480 (1999)
48. A. Afzali, C.D. Dimitrakopoulos, T.L. Breen, J. Am. Chem. Soc. **124**, 8812 (2002)
49. A. Afzali, C.D. Dimitrakopoulos, T.O. Graham, Adv. Mater. **15**, 2066 (2003)
50. A. Afzali, C.R. Kagan, G.P. Traub, Synth. Met. **155**, 490 (2005)
51. G.S. Tulevski, Q. Miao, A. Afzali, T.O. Graham, C.R. Kagan, C. Nuckolls, J. Am. Chem. Soc. **128**, 1788 (2006)
52. H. Uno, Y. Yamashita, M. Kikuchi, H. Watanabe, H. Yamada, T. Okujima, T. Ogawa, N. Ono, Tetrahedron Lett. **46**, 1981 (2005)
53. H. Yamada, Y. Yamashita, M. Kikuchi, H. Watanabe, T. Okujima, H. Uno, T. Ogawa, K. Ohara, N. Ono, Chem. Eur. J. **11**, 6212 (2005)
54. S. Katsuta, H. Yamada, T. Okujima, H. Uno, Tetrahedron Lett. **51**, 1397 (2010)
55. S. Katsuta, H. Saeki, K. Tanaka, Y. Murai, D. Kuzuhara, M. Misaki, N. Aratani, S. Masuo, Y. Ueda, H. Yamada, J. Mater. Chem. C **2**, 986 (2014)
56. R. Mondal, B.K. Shah, D.C. Neckers, J. Photochem. Photobiol. A Chem. **192**, 36 (2007)
57. R. Mondal, R.M. Adhikari, B.K. Shah, D.C. Neckers, Org. Lett. **9**, 2505 (2007)
58. R. Mondal, A.N. Okhrimenko, B.K. Shah, D.C. Neckers, J. Phys. Chem. B **112**, 11 (2008)
59. R. Mondal, C. Tönshoff, D. Khon, D.C. Neckers, H.F. Bettinger, J. Am. Chem. Soc. **131**, 14281 (2009)
60. C. Tönshoff, H.F. Bettinger, Angew. Chem. Int. Ed. **49**, 4125 (2010)
61. C. Tönshoff, H.F. Bettinger, Chem. Eur. J. **18**, 1789 (2012)
62. H.F. Bettinger, R. Mondal, M. Krasowska, D.C. Neckers, J. Org. Chem. **78**, 1851 (2013)

63. H. Yamada, C. Ohashi, T. Aotake, S. Katsuta, Y. Honsho, H. Kawano, T. Okujima, H. Uno, N. Ono, S. Seki, K.-I. Nakayama, Chem. Commun. **48**, 11136 (2012)
64. C. Ohashi, H. Yamada, K. Nakayama, Mol. Cryst. Liq. Cryst. **580**, 103 (2013)
65. S. Masuo, K. Tanaka, M. Oe, H. Yamada, Phys. Chem. Chem. Phys. **16**, 13483 (2014)
66. C. Quinton, M. Suzuki, Y. Kaneshige, Y. Tatenaka, C. Katagiri, Y. Yamaguchi, D. Kuzuhara, N. Aratani, K.-I. Nakayama, H. Yamada, J. Mater. Chem. C **3**, 5995 (2015)
67. K.-I. Nakayama, C. Ohashi, Y. Oikawa, T. Motoyama, H. Yamada, J. Mater. Chem. C **1**, 6244 (2013)
68. K.-Y. Chen, H.-H. Hsieh, C.-C. Wu, J.-J. Hwang, T.J. Chow, Chem. Commun., 1065 (2007)
69. R.A. Laudise, C. Kloc, P.G. Si, pkins, and T. Siegrist. J. Crysst. Growth **187**, 449 (1998)
70. J. Soeda, T. Okamoto, A. Hamaguchi, Y. Ikeda, H. Sato, A. Yamano, J. Takeya, Org. Electron. **14**, 1211 (2013)
71. M. Uno, Y. Tominari, M. Yamagishi, I. Doi, E. Miyazaki, K. Takimiya, J. Takeya, Appl. Phys. Lett. **94**, 223308 (2009)
72. Y. Kimura, T. Nagase, T. Kobayashi, A. Hamaguchi, Y. Ikeda, T. Shiro, K. Takimiya, H. Naito, Adv. Mater. **27**, 727 (2014)
73. A. Hamaguchi, T. Negishi, Y. Kimura, Y. Ikeda, K. Takimiya, S.Z. Bisri, Y. Iwasa, T. Shiro, Adv. Mater. **27**, 6606 (2015)
74. W. Li, M. Yi, H. Ling, F. Guo, T. Wang, T. Yang, L. Xie, W. Huang, J. Phys. D: Appl. Phys. **49**, 125104 (2016)
75. C.M.B. Carvalho, T.J. Brocksom, K.T. de Oliveira, Chem. Soc. Rev. **42**, 3302 (2013)
76. S.-D. Jeong, B. Min, S.Y. Cho, C. Lee, B.K. Park, K.-S. An, J. Lim, J. Org. Chem. **77**, 8329 (2012)
77. T. Okujima, Y. Hashimoto, G. Jin, H. Yamada, H. Uno, N. Ono, Tetrahedron **64**, 2405 (2008)
78. S. Aramaki, Y. Sakai, N. Ono, Appl. Phys. Lett. **84**, 2085 (2004)
79. S. Ito, T. Murashima, N. Ono, H. Uno, Chem. Commun., 1661 (1998)
80. S. Aramaki, J. Mizuguchi, Acta Cryst **B59**, o1556 (2003)
81. N. Noguchi, S. Junwei, H. Asatani, M. Matsuoka, Cryst. Growth Des. **10**, 1848 (2010)
82. P.B. Shea, J. Kanicki, J. Appl. Phys. **111**, 073709 (2012)
83. P.B. Shea, J. Kanicki, N. Ono, J. Appl. Phys. **98**, 014503 (2005)
84. P.B. Shea, J. Kanicki, L.R. Pattison, P. Petroff, M. Kawano, H. Yamada, N. Ono, J. Appl. Phys. **100**, 034502 (2006)
85. P.B. Shea, C. Chen, J. Kanicki, L.R. Pattison, P. Petroff, H. Yamada, N. Ono, Appl. Phys. Lett. **90**, 233107 (2007)
86. P.B. Shea, L.R. Pattison, M. Kawano, C. Chen, J. Chen, P. Petroff, D.C. Martin, H. Yamada, N. Ono, J. Kanicki, Synth. Met. **157**, 190 (2007)
87. H. Yamada, K. Kushibe, T. Okujima, H. Uno, N. Ono, Chem. Commun., 383 (2006)
88. H. Yamada, K. Kushibe, S. Mitsuogi, T. Okujima, H. Uno, N. Ono, Tetrahedron Lett. **49**, 4731 (2008)
89. K. Takahashi, D. Kuzuhara, N. Aratani, H. Yamada, J. Photopolym. Sci. Tech. **26**, 213 (2013)
90. K. Takahashi, N. Yamada, D. Kumagai, D. Kuzuhara, M. Suzuki, Y. Yamaguchi, N. Aratani, K. Nakayama, H. Yamada, J. Porphyrins Phthalocyanines **19**, 465 (2015)
91. K. Takahashi, B. Shan, X. Xu, S. Yang, T. Koganezawa, D. Kuzuhara, N. Aratani, M. Suzuki, Q. Miao, H. Yamada, ACS Appl. Mater. Interfaces **9**, 8211 (2017)
92. D. Liu, X. Xu, Y. Su, Z. He, J. Xu, Q. Miao, Angew. Chem. Int. Ed. **52**, 6222 (2013)
93. D. Liu, Z. He, Y. Su, Y. Diao, S.C.B. Mannsfeld, Z. Bao, J. Xu, Q. Miao, Adv. Mater. **26**, 7190 (2014)
94. A.R. Murphy, J.M.J. Fréchet, P. Chang, J. Lee, V. Subramanian, J. Am. Chem. Soc. **126**, 1596 (2004)
95. A.R. Murphy, P.C. Chang, P. VanDyke, J. Liu, J.M.J. Fréchet, V. Subramanian, D.M. DeLongchamp, S. Sambasivan, D.A. Fischer, E.K. Lin, Chem. Mater. **17**, 6033 (2005)
96. D.M. DeLongchamp, S. Sambasivan, D.A. Fischer, E.K. Lin, P. Chang, A.R. Murphy, J.M.J. Fréchet, V. Subramanian, Adv. Mater. **17**, 2340 (2005)
97. T. Akiyama, A. Hirao, T. Okujima, H. Yamada, H. Uno, N. Ono, Heterocycles **74**, 835 (2007)

98. A. Hirao, T. Akiyama, T. Okujima, H. Yamada, H. Uno, Y. Sakai, S. Aramaki, N. Ono, Chem. Commun., 4714 (2008)
99. M. Guide, J.D.A. Lin, C.M. Proctor, J. Chen, C. García-Cervera, T.-Q. Nguyen, J. Mater. Chem. A **2**, 7890 (2014)
100. Y. Matsuo, A. Iwashita, Y. Abe, C.-Z. Li, K. Matsuo, M. Hashiguchi, E. Nakamura, J. Am. Chem. Soc. **130**, 15429 (2008)
101. Y. Matsuo, Y. Sato, T. Niinomi, I. Soga, H. Tanaka, E. Nakamura, J. Am. Chem. Soc. **131**, 16048 (2009)
102. Y. Tamura, H. Saeki, J. Hashizume, Y. Okazaki, D. Kuzuhara, M. Suzuki, N. Aratani, H. Yamada, Chem. Commun. **50**, 10379 (2014)
103. H. Tamura, Y. Matsuo, Chem. Phys. Lett. **598**, 81 (2014)
104. M. Guide, X.-D. Dang, T.-Q. Nguyen, Adv. Mater. **23**, 2313 (2011)
105. Y. Zhen, H. Tanaka, K. Harano, S. Okada, Y. Matsuo, E. Nakamura, J. Am. Chem. Soc. **137**, 2247 (2015)
106. M.D. Perez, C. Borek, S.R. Forrest, M.E. Thompson, J. Am. Chem. Soc. **131**, 9281 (2009)
107. J.L. Segura, N. Martín, D.M. Guldi, Chem. Soc. Rev. **34**, 31 (2005)
108. M. Wang, F. Wudl, J. Mater. Chem. **22**, 24297 (2012)
109. H. Imahori, T. Umeyama, K. Kurotobi, Y. Takano, Chem. Commun. **48**, 4032 (2012)
110. Y. Tamura, D. Kuzuhara, M. Suzuki, H. Hayashi, N. Aratani, H. Yamada, J. Mater. Chem. A **4**, 15333 (2016)
111. K. Takahashi, D. Kumagai, N. Yamada, Y. Yamaguchi, T. Koganezawa, D. Kuzuhara, M. Suzuki, N. Aratani, S. Masuo, K.-I. Nakayama, and H. Yamada, Proceeding of International Conference on Hybrid and Organic Photovoltaics (HOPV2016) (2016)
112. T. Motoyama, T. Kiyota, H. Yamada, K.-I. Nakayama, Solar Energy Mater. Sol. Cells **114**, 156 (2013)
113. H. Yamada, Y. Yamaguchi, R. Katoh, T. Motoyama, T. Aotake, D. Kuzuhara, M. Suzuki, T. Okujima, H. Uno, N. Aratani, K. Nakayama, Chem. Commun. **49**, 11638 (2013)
114. Y. Yamaguchi, M. Suzuki, T. Motoyama, S. Sugii, C. Katagiri, K. Takahira, S. Ikeda, H. Yamada, K.-I. Nakayama, Sci. Rep. **4**, 7151 (2014)
115. M. Suzuki, Y. Yamaguchi, K. Uchinaga, K. Takahira, C. Quinton, S. Yamamoto, N. Nagami, M. Furukawa, K. Nakayama, H. Yamada, Chem. Sci. **9**, 6614 (2018).
116. D. Kuzuhara, J. Mack, H. Yamada, T. Okujima, N. Ono, N. Kobayashi, Chem. Eur. J. **15**, 10060 (2009)
117. H. Saeki, O. Kurimoto, M. Misaki, D. Kuzuhara, H. Yamada, Y. Ueda, Appl. Phys. Express **6**, 035601 (2013)
118. H. Saeki, M. Misaki, D. Kuzuhara, H. Yamada, Y. Ueda, Jpn. J. Appl. Phys. **52**, 111601 (2013)
119. Y. Kikukawa, T. Fukuda, A. Fuyuhiro, N. Ishikawa, N. Kobayashi, Chem. Commun. **47**, 8518 (2011)
120. H. Wang, N. Su, L.-C. Wang, X. Wu, S. Bui, A. Nielsen, H.-T. Vo, Y. Luo, X.-J. Ma, Methods Mol. Biol. **1211**, 139 (2014)
121. T.L. Chen, J.J.-A. Chen, L. Catane, B. Ma, Org. Electron. **12**, 1126 (2011)
122. J.K. Lee, Y.-M. Wang, S. Cho, F. Wudl, A.J. Heeger, Org. Electron. **10**, 1223 (2009)
123. T. Umeyama, S. Shibata, H. Imahori, RSC Adv. **6**, 83758 (2016)
124. K. Kawajiri, T. Kawanoue, M. Yamato, K. Terai, M. Yamashita, M. Furukawa, N. Aratani, M. Suzuki, K. Nakayama, H. Yamada, ECS J. Solid State Sci. Technol. **6**, M3068 (2017)

Chapter 10
Solar Cell Applications of π-Conjugated Molecules

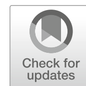

Kouki Akaike and Kaname Kanai

Abstract Because organic molecules possessing extended π-conjugation show strong absorption in the visible region of the solar spectrum, they have been used as dyes in solid-state photovoltaic devices known as organic solar cells (OSCs). The power-conversion efficiency of tandem OSCs already reportedly exceeds 17% by processing state-of-the-art polymer donors and non-fullerene acceptors from their mixed solution, but this efficiency is still far below that of silicon-based solar cells (∼25%). Deep understanding of the fundamental aspects of OSC operation, such as the mechanism for free-charge generation and the interfacial electronic and morphological properties, is now recognized as being vital to establishing well-defined guidelines for designing material interfaces and device structures and for improving the performance of OSCs. In this chapter, we give a brief historical review of solar cells and the operational mechanism of OSCs, as well as recent developments of new donors, acceptors, and interface modifiers. We then give a thorough explanation of the electronic structure of photoactive π-conjugated molecules and their interfaces used in OSCs based on recent studies, with links to OSC performance.

Keywords Organic photovoltaics · Organic semiconductors · Molecular design · Interfaces · Electronic structure

K. Akaike (✉)
Nanomaterials Research Institute, National Institute of Advanced Industrial Science and Technology, Tsukuba, Japan
e-mail: kouki.akaike@aist.go.jp

K. Kanai
Department of Physics, Faculty of Science and Technology, Tokyo University of Science, Tokyo, Japan

© Springer Nature Singapore Pte Ltd. 2019

Y. Kubozono (ed.), *Physics and Chemistry of Carbon-Based Materials*,
https://doi.org/10.1007/978-981-13-3417-7_10

10.1 Introduction

Fossil fuels have been consumed abundantly to produce the energy that has been essential for developing and sustaining human civilization. However, with global economic growth and improved quality of life, electricity demand is increasing steadily, as are concerns about how much fossil fuel remains. This urgent problem regarding the natural environment has prompted researchers to develop devices that can produce energy in ways that are environmentally friendly, renewable, and sustainable. The solar cell is a promising energy device that utilizes the photovoltaic effect to convert the energy of sunlight into electrical energy. As most readers already recognize, silicon-based solar cells are well-established in the market; they can be found to be mounted on buildings and houses or placed on the ground to generate electricity collectively from an abundant natural resource. The discovery of the photovoltaic effect can be traced back to Becquerel's work on liquid electrolytes in 1839 [1]. In 1954, Chapin et al. at Bell Laboratory reported a *p-n* junction silicon solar cell with a power-conversion efficiency of 6% [2]. Since then, many different semiconducting materials have been used as the photoactive layer (or simply the active layer) in solar cells.

Let us describe briefly the solar spectral irradiance distribution collected by the National Renewable Energy Laboratory (NREL) [3] (Fig. 10.1a). Outside the Earth's atmosphere (extraterrestrial), the solar spectrum is approximated as the irradiance emitted from a black body at 5800 K with a peak at ~500 nm. However, we have to consider the influence of the atmosphere when considering the solar irradiance that reaches the Earth. This is because photons with higher energies

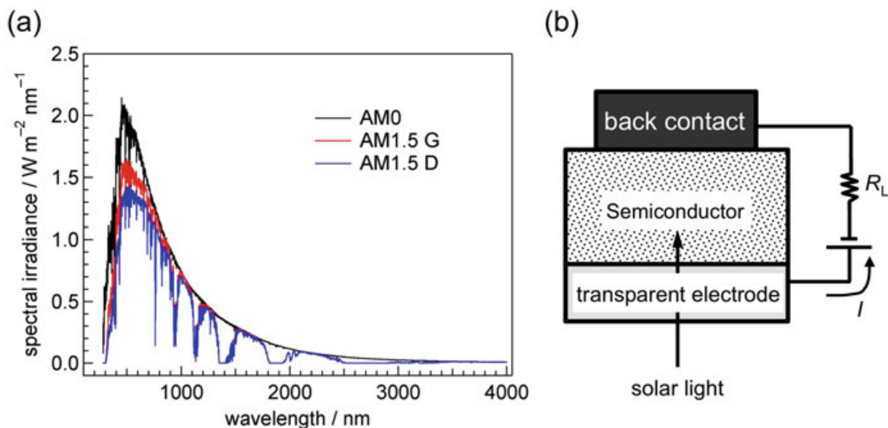

Fig. 10.1 (**a**) Solar spectral irradiance distribution. G and D after AM1.5 denote global total spectral irradiance and direct normal spectral irradiance, respectively. AM1.5 G includes the surrounding ground and the blue sky. AM1.5 D includes the direct beam from the sun plus the circumsolar component in a 2.5° disk around the sun. (**b**) Schematic structure of solar cell with load R_L and photocurrent I

(i.e., ultraviolet and blue light) are scattered (Rayleigh scattering) and absorbed by water vapor in the atmosphere, thereby reducing the spectral irradiance that reaches the Earth.

To express the atmospheric influence on solar spectra, we use the air mass (AM) expressed by $1/\cos\theta$, where θ is the zenith angle. The AM denotes the volume of air that solar light travels through before reaching the Earth's surface. An angle of $\theta = 48.19°$ gives an AM of 1.5, which is often denoted as AM1.5. For the standard characterization of solar cells, a light source with an energy of 100 mW cm^{-2} is used that is filtered to match the AM1.5 spectral irradiance (Fig. 10.1a). The semiconducting material used in the solar cell must absorb photons corresponding to the AM1.5 irradiance, ideally up to the near-infrared range, in order to produce more photocurrent from sunlight. The absorption ability of the material is related to its optical band gap ($E_{g,opt}$), which is defined as the energy difference between the valence band and the conduction band. For organic molecules, $E_{g,opt}$ is determined by the energy difference between the highest occupied molecular orbital (HOMO) and the lowest unoccupied molecular orbital (LUMO) and by the exciton binding energy due to the low dielectric constant of organic molecules. Photons with energies greater than $E_{g,opt}$ can excite electron from occupied states into unoccupied states. The smaller $E_{g,opt}$ is, the more photons are absorbed from sunlight. For example, Si has a (indirect) band gap of 1.1 eV, which enables photoabsorption at wavelengths below 1200 nm.

The basic structure of a solar cell is a semiconductor (e.g., Si, GaAs) sandwiched between a transparent electrode [e.g., indium tin oxide (ITO)] and a back contact such as Al (Fig. 10.1b). Free carriers generated upon photoabsorption within the semiconductor photoactive layer result in a photocurrent I, and electrical energy is extracted from a load R_L.

Among the various types of solar cell, we focus here on organic solar cells (OSCs) that are based on π-conjugated small molecules and polymers. OSCs have attracted tremendous amounts of interest, and the current record for power-conversion efficiency is held by a multi-junction (tandem) OSC at over 17% [4]. Compared to inorganic semiconductors, hydrocarbon solids tend to be "soft"

Fig. 10.2 (**a**) Photograph of the standing meniscus during slot-die coating of the active layer of an OSC comprising many very tightly spaced stripes. (**b**) A total of 48 stripes are coated simultaneously. (**c**) Knife coating with an open ink reservoir and a manual feed hose. (Reprinted with permission from Ref. [5])

because the molecules aggregate in the solid state as a result of van der Waals intermolecular interaction (mainly the London dispersion force). The mechanical softness of organic semiconductors allows us to fabricate flexible solar cells on plastic substrates that could be attached even to curved walls and windows and to fabricate such flexible OSCs by means of the roll-to-roll processes (Fig. 10.2) [5]. In addition, thanks to advanced organic synthesis, it is possible to functionalize organic semiconductors in order to dissolve them into common solvents. Using solution processes such as dip coating and spin coating to fabricate OSCs can therefore reduce the associated production costs, resulting in a shorter payback time (i.e., the time required to recoup the initial investment).

The first reported use of organic molecules for photoelectric conversion was in 1906 [6]. Subsequently, Prof. Inokuchi referred to π-conjugated molecules that show electrical conduction as an *organic semiconductor* after he found photoconduction in thin films of violanthrone [7, 8]. Since then, the potential of organic semiconductors as electronic components in devices such as light-emitting diodes [9, 10] has been explored rigorously. In the early stages of OSC research, porphyrins, phthalocyanines, and merocyanines were used as the active layer in Schottky-barrier OSCs [11]. However, in spite of their high absorption coefficients in the visible range of the solar spectrum and the high crystallinity of their vacuum-deposited films, power-conversion efficiency of OSCs based on these molecules was limited to 0.7% at most in the early 1980s [11]. This was despite efforts to increase carrier concentration and thus conductivity by doping with oxygen and gaseous halogens, for example [11].

However, C. W. Tang of Kodak achieved the efficiency of 1.0% for an OSC with a bilayer structure consisting of copper phthalocyanine (CuPc; molecular structure is shown in Fig. 10.3) and a perylene derivative [12–14]. This prompted worldwide interest in the synthesis of photoactive materials, the optimization of device configurations, and interface engineering to develop more efficient OSCs.

Figure 10.3 shows representative organic semiconductors for the photoactive layer of an OSC. Before use, the semiconducting organic molecules have to be purified sufficiently because material purity severely influences the fill factor and hence the overall device efficiency [15–17]. The abbreviation for each molecule is given in the figure caption. For Schottky-barrier OSCs, one organic semiconductor is used as the sole component for photoelectric conversion and is sandwiched between the anode (hole-collecting electrode) and cathode (electron-collecting electrode) (Fig. 10.4a). By the late 1980s, most OSC devices were based on this simple structure. At that time, the performance based solely on phthalocyanine and merocyanine was poor, as already mentioned. However, fullerenes and SubPc have recently been found to work more efficiently as the photoactive layer in Schottky-barrier OSCs using MoO_3-covered ITO substrates [18, 19]. Because the work function of MoO_3 can be as high as 6.8 eV, it is possible to form a huge electric field at the MoO_3/organic interface as a consequence of the electronic equilibrium there (see Sect. 10.4 for details). The resulting electric field may support carrier extraction and separation within the organic layer. Inserting an exciton blocking layer between the MoO_3 and the active layer can lead to a significantly improved

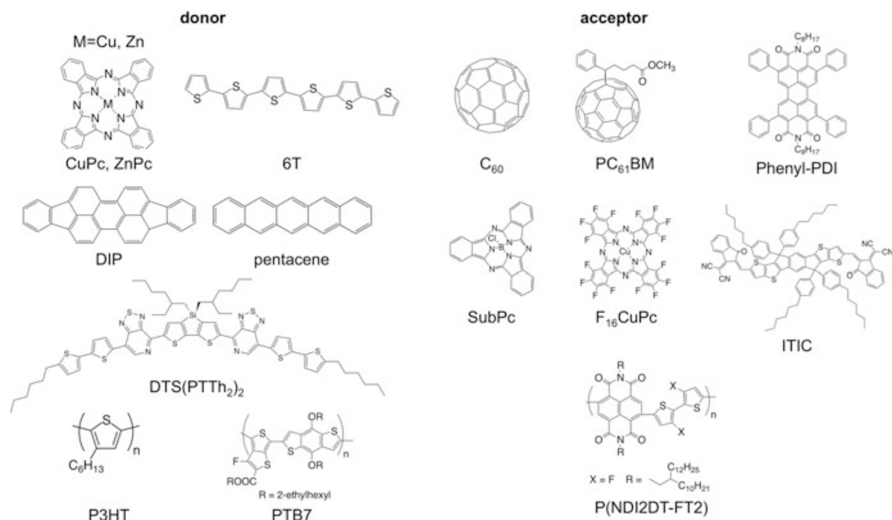

Fig. 10.3 Molecular structures of donors and acceptors used in OSCs. CuPc and ZnPc, copper and zinc phthalocyanine; 6T, sexithiophene; DIP, diindenoperylene; $DTS(PTTh_2)_2$, 5,5′-*bis*{(4-(7-hexylthiophen-2-yl)-[1,2,5]thiadiazolo[3,4-c]pyridine)-3,3′-di-2-ethylhexylsilylene-2,2′-bithiophene; P3HT, poly(3-hexylthiophene); PTB7, thieno[3,4-b]thiophene-*alt*-benzodithiophene copolymer; $PC_{61}BM$, [6,6]-phenyl-C_{61}-butyric acid methyl ester; SubPc, subphthalocyanine; $F_{16}CuPc$, perfluorinated CuPc; phenyl-PDI, *N*,*N*-bis(n-octyl)-2,5,8,11-tetraphenyl-PDI; P(NDI2DT-FT2), polymer composed of a 3,3′-difluoro-2,2′-bithiophene and a NDI with 2-decyltetradecyl side chains; ITIC, 3,9-bis(2-methylene-(3-(1,1-dicyanomethylene)-indanone))-5,5,11,11-tetrakis(4-hexylphenyl)-dithieno[2,3-d:2′,3′-d’]-s-inddaceno[1,2-b,5,6-b’]dithiophene

short-circuit current and fill factor and hence to a power-conversion efficiency of 2% [19]. Single-component OSCs comprising a donor-acceptor copolymer also show relatively high performance because photoelectric conversion occurs between the donor and acceptor components within a single molecule, thereby forming a clear carrier-transport path for charge extraction in the solid state [20, 21].

For more efficient carrier generation, a planar heterojunction (PHJ) of two dissimilar organic semiconductors (Fig. 10.4b) is preferable. This is because strongly bound excitons can split efficiently into free holes and electrons by using the energy offsets of the highest occupied molecular orbitals (HOMOs) or lowest unoccupied molecular orbitals (LUMOs) between the interfacing molecules as driving forces (see Fig. 10.5). Besides, transporting holes and electrons in the different materials supports that they can individually travel toward respective electrodes, which suppresses charge recombination. Molecules that transport holes and electrons are referred to as donors and acceptors, respectively. The molecules shown in Fig. 10.3 are classified roughly into these two categories.

A standard choice as the acceptor is C_{60} because of its high electron affinity, excellent electron-transport ability, and low relaxation energy upon the formation of photo-generated anions. However, C_{60} has relatively poor photoabsorption in the visible range, although that of C_{70} is better because of a breakdown in molecular symmetry. There is also the difficulty of developing a synthesis

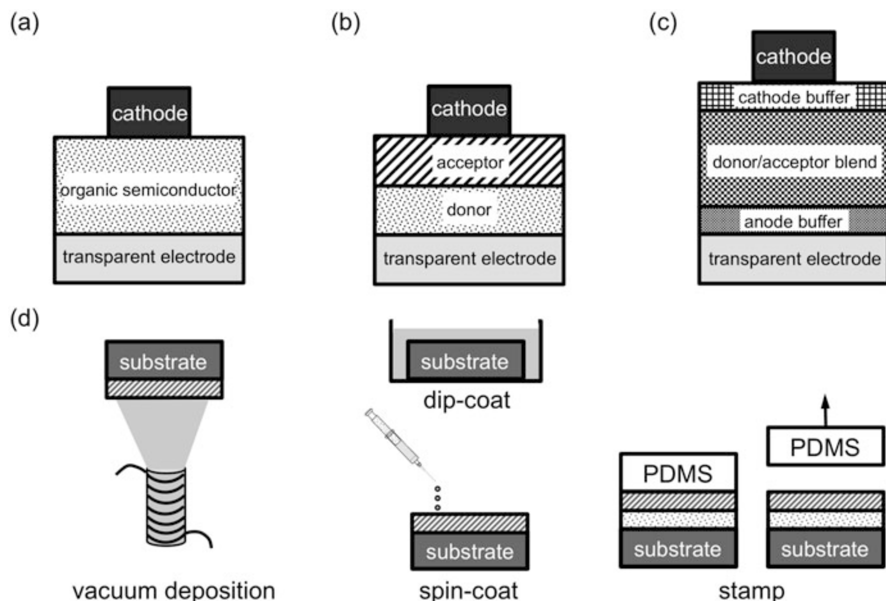

Fig. 10.4 Device structure (top) and corresponding energy diagrams (bottom) of an OSC. (**a**) Schottky-barrier OSC, (**b**) planar heterojunction (PHJ) OSC, (**c**) bulk heterojunction (BHJ) OSC. (**d**) Methods for preparing an OSC

method to modify the molecular structure in order to improve the photophysical and transport properties of such fullerene-based compounds, which escalates the associated costs. Instead, a series of small molecules based on perylene diimide, phthalocyanines, subphthalocyanines, truxenones, quinacridones, fluorenes, and *n*-type polymers with low energy gaps have been reported as promising acceptor molecules [22]. These have the advantages of low LUMO energy (which is achieved by introducing electron-withdrawing groups into its molecular structure), strong absorption in the visible region, adjustable frontier orbital energies by molecular design, morphological stability of the active layer in which they are used in, high thermal stability, and high solubility. For instance, the molecular architecture of the polymers enables them to have high solubility and a broad absorption spectrum. The many superior features of non-fullerene acceptor compounds and rapid developments in their method of synthesis mean that these compounds will play an important role in efficient OPVs in the near future [23, 24].

A disadvantage of a PHJ is that the donor/acceptor interface has a limited area. Hence, some of the formed excitons do not separate into free carriers and thus recombine before reaching the interface. To overcome this drawback, the concept of a bulk heterojunction (BHJ) has been proposed (Fig. 10.4c), wherein donor and acceptor molecules are blended [25, 26]. Because the BHJ interfacial area is much bigger than the PHJ one, tremendous opportunities are provided for exciton dissociation. The most efficient OSCs reported to date are based on this BHJ structure. Some BHJ-based OSCs with non-fullerene acceptors, combined

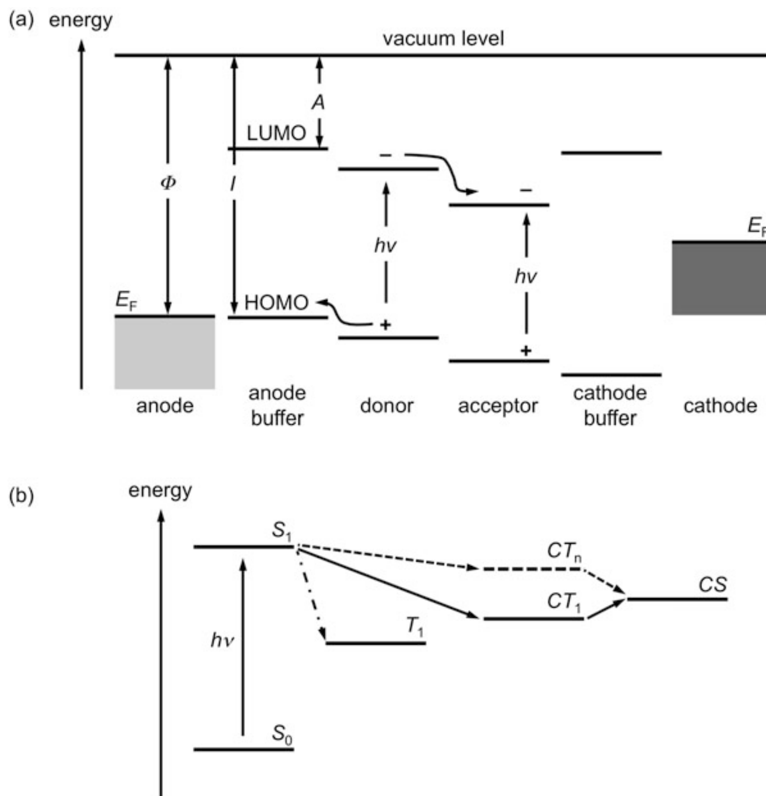

Fig. 10.5 (**a**) Schematic energy diagram of an OSC under the assumption of no built-in potential. Here the case for a planar heterojunction cell is shown. E_F is the Fermi level of the electrodes, hv denotes the photon energy of sunlight, Φ is the work function of the electrode, I is the ionization energy, and A is the electron affinity. (**b**) Corresponding electronic diagram: S_0 is the ground state; S_1 is the excited singlet state; T_1 is the excited triplet state; CT_1 and CT_n are the lowest and higher charge-transfer states, respectively; and CS is the charge-separation state

with state-of-the-art donor polymers, outperform their fullerene-based counterparts. For instance, the use of PTB7-Th as the donor and ITIC as the acceptor leads to efficiencies in excess of 11% [27], which demonstrates again that fullerenes and their derivatives are not the sole choice for OSC acceptors.

In these standard OSCs, holes (electrons) are extracted from the transparent electrode (Al and Ag cathode). However, the inverted geometry is also used (often called an inverted OSC), in which electrons are extracted from the bottom electrode while the top contact collects holes. In a standard OSC, acidic poly(3,4-ethylenedioxythiophene):poly(4-styrenesulfonate) (PEDOT:PSS) and calcium are the prototypical anode and cathode buffer layers, respectively. In spite of their versatility, these materials are sensitive to humidity and oxygen, and as such the long-term stability of OSCs employing these materials is poor. An inverted OSC can avoid the use of these materials because of (i) the commercially available of

relatively inert materials to lower the work function of the ITO bottom substrate (e.g., Cs_2CO_3 [28] and polyethyleneimine ethoxylated (PEIE) [29]) and (ii) the fact that the work function of the top electrode can also be controlled by, for example, evaporation of MoO_3.

The device architectures shown in Fig. 10.4a–c can be prepared using the methods illustrated in Fig. 10.4d. Vacuum deposition is the conventional way to prepare an organic thin film with high purity and crystallinity. The film thickness can be controlled precisely by using a quartz oscillator to monitor the amount and speed of deposition at the angstrom scale; these deposition features are estimated from changes in the intrinsic frequency of the quartz. A crucible containing the organic compound is heated resistively in a vacuum chamber, whereupon the sublimed molecules solidify on a substrate that is placed above the evaporation source. The substrate is ultrasonicated with solvents such as isopropanol, acetone, and pure water prior to the use, followed by UV-ozone treatment. Heating the substrate during the vacuum deposition increases the molecular mobility on the substrate surface, thereby improving the crystallinity of the formed film; this leads in turn to a thermodynamically stable molecular arrangement. However, vacuum deposition is of course applicable only to the sublimation of molecules with relatively low molecular weights.

Spin coating and dip coating offer alternative ways to form a thin film from compound solution on a desired substrate. A number of parameters can affect the morphology and crystallinity and consequently the charge transport and photophysical properties of the solution-processed film (e.g., the boiling point and evaporation rate of the organic solvent that is used, the film thickness, and the ratio of the mixed solvent). As for BHJ active layer, donor and acceptor components should preferably distribute in the normal direction for the selective charge transport (vertical phase separation), while attaining a large donor/acceptor interfacial area for efficient carrier generation. It is well known that P3HT molecules segregate upon being spin-coated on the surface of P3HT:PC_{61}BM-blend film because the P3HT surface energy is lower than the PC_{61}BM one [30, 31]. Thermal annealing after deposition of the top electrode can suppress the surface segregation of P3HT [32].

Stamping is the other method for fabricating a multilayer OSC. A poly(dimethylsilane) (PDMS) stamp is used to transfer the active layer onto the substrate. With this stamping technique, one can fabricate multilayered BHJ and PHJ OSCs [33].

10.2 Operation Mechanism and Characterization of OSC

10.2.1 Photoabsorption

This process is the initial step in the operation of an OSC. If the photons have enough energy to excite electrons in the organic semiconductor from occupied states into unoccupied ones, light passing through a molecule will vibrate electrons bound to its positive nucleus by means of the time-dependent electric field of

the electromagnetic wave. As a result, the molecule gains (excitation) energy. For instance, electrons in the HOMOs of the donors and acceptors are excited into the respective LUMOs (Fig. 10.5a). As a result, an electrostatically bound hole-electron pair (exciton) is generated. To efficiently harvest the photons in the spectral irradiance distribution of sunlight, it is essential to engineer the band gaps of the organic semiconductor by introducing appropriate substituents and incorporating more than two semiconductors into the active layer. The absorption takes place on a femtosecond (10^{-15} s) timescale. The transition probability upon photoabsorption is proportional to the square of the transition moment $m = \int \psi_i \, e\mathbf{r} \, \psi_f \, d\tau$, where Ψ_i is the initial wave function [the ground state S_0 in Fig. 10.5b], Ψ_f is the final wave function [the excited state S_1 for a singlet exciton in Fig. 10.5b], and $e\mathbf{r}$ is the transition dipole operator. According to this relationship, the wave-function overlap between the initial and final states affects the magnitude of photoabsorption. The nature of photoabsorption of π-conjugated molecules is strong absorption in the visible range. Besides, the large geometrical relaxation upon excitation leads to broad absorption [34].

The direction of the transition dipole is determined by how the transition charge is distributed within the molecule. For most planar aromatic molecules, the transition dipole orients itself parallel to the atomic bond. Because the electric field of the incident light should match the direction of the transition dipole moment of the organic semiconductors, especially for elongated π-conjugated molecules, the likes of pentacene and phthalocyanine show the anisotropy of photoabsorption in the solid states. In this sense, it is critical to control the molecular orientation in order to produce a photocurrent. Specifically, for light absorption by π-conjugated molecules, the face-on and edge-on orientations (Fig. 10.6) are preferable to the end-on orientation (Fig. 10.6).

In addition to the absorption ability of each component in an OSC, we must take account of light interference within the OSC to understand the actual absorption within the device. This is because an OSC is made of multi-stacked organic and inorganic layers with different refractive indexes (Fig. 10.5a). The transfer-matrix method is widely used to model the light interference. In this method, the light traveling upstream and traveling downstream through the interfaces is added

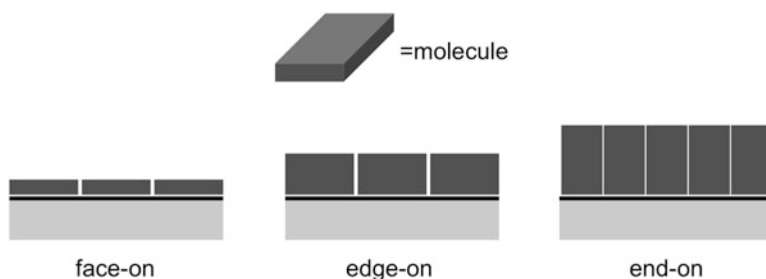

Fig. 10.6 Molecular orientations of a planar π-conjugated molecule

coherently to calculate the electric field strength of the standing waves in the stacks [34]. In this sense, metal reflectivity also plays a decisive role. For instance, calcium and samarium, which are at times used for the cathode electrode, show a relatively low photocurrent because of their weaker reflectance compared to the commonly used Al cathode [16].

10.2.2 Exciton Diffusion

The excitons that are generated upon photoexcitations have to diffuse to the donor/acceptor interface for free-charge separation. The state in which the spins in the occupied and unoccupied states are antiparallel is referred to as a singlet exciton. When the spins are parallel to each other, the state is referred to as a triplet exciton. This is generally spin-forbidden and thus does not form directly upon photoexcitation. However, in the case of strong spin-orbit coupling (e.g., in heavy-atom molecules such as sulfur or metals), transition from the singlet state to the triplet state is allowed. Exciton diffusion takes place through two energy-transfer mechanisms (Fig. 10.7):

(a) *Förster mechanism*

An electron that has been photoexcited into an unoccupied state moves more vigorously than it did when it was in the original occupied state because of the

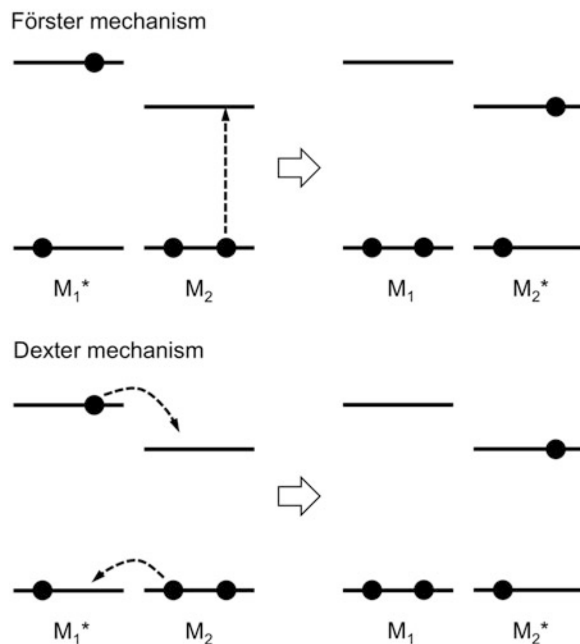

Fig. 10.7 Förster and Dexter mechanisms for exciton transfer. Singlet excitons transfer via both schemes, whereas triplet excitons diffuse via only the Dexter mechanism. M_2 has a smaller band gap than M_1. M_1* and M_2* denote their excited states

increase in the number of state nodes, and this results in the variance of the electric field within a molecule (call it M_1). If a neighboring molecule M_2 near the excited molecule $M_1{}^*$ can resonantly interact with the alternating electric field in M_1, M_2 will obtain excitation energy from M_1 and hence energy transfer occurs. In this mechanism, direct contact between M_1 and M_2 is unnecessary. Therefore, long-range (order of 10 nm) exciton diffusion is possible. As a rule of thumb, if the fluorescence spectrum of M_1 overlaps the absorption spectrum of M_2, an exciton can transfer via the Förster mechanism. Because this involves electronic transition from occupied to unoccupied states, only spin-allowed singlet excitons may diffuse using this mechanism.

(b) *Dexter mechanism*

In contrast to the Förster mechanism, the Dexter mechanism operates through direct molecular contact because it occurs via electron exchange through orbital overlaps. As a result, there is no spectral requirement and thus, in addition to singlet excitons, even triplet excitons can diffuse using this mechanism.

The exciton diffusion length L_D is given by $(D\tau)^{1/2}$, where D is the exciton diffusion constant and τ is the exciton lifetime. As mentioned previously, singlet excitons appear to have larger values of D than those of triplet excitons, but the latter have much longer lifetimes τ (on the order of microseconds) because relaxation of a triplet exciton to the ground state is spin-forbidden. In the solid state, the diffusion length as determined by, for example, photoluminescence quenching is 5–20 nm for both small molecules [35] and polymers [36], although an extremely long exciton diffusion length has been reported for single rubrene crystal (2–8 μm) [37]. In BHJ OSCs, excitons with short diffusion length L_D can reach the donor/acceptor interface efficiently because the domain sizes of donor and acceptor are comparable to L_D.

It is well known that metal can quench excitons at the interface to the photoactive layer. To prevent exciton quenching at the electrode interface, wide-band-gap molecules such as bathocuproine (BCP) and bathophenanthroline (Bphen) are inserted at the cathode interface (Fig. 10.5a).

10.2.3 Free-Carrier Generation

Excitons that reach the donor/acceptor interface may dissociate into free holes and electrons. Because of the relatively low dielectric constant (ε_r) of organic semiconductors ($\varepsilon_r = 3$–5), some driving force is necessary to generate free charges (typically several tenths of an electron volt). At the interface, photo-induced electron (hole) transfer occurs within 100 fs and is driven by the energy difference in the LUMO (HOMO) for excitons generated in donors (acceptors).

An important step on the way to free-charge separation is that, even after the photo-induced charge transfer, a hole in a donor and an electron in an acceptor are still bound to each other by Coulombic attraction before reaching the charge-separation (CS) state in which holes and electrons are completely free. This state

is referred to as the charge-transfer (CT) state. Although "hot" CT states [CT_n in Fig. 10.5b] have generally been regarded as the exclusive pathway to free charges [38, 39], Vandewal et al. showed that the internal quantum efficiency of many OSCs depends neither on whether band gap or CT states are excited nor on how energetic the CT states are [40]. These results suggest that "cold" CT states [the relaxed CT state CT_1 in Fig. 10.5b] could lead to the CS state. Apparently, CT_1 requires an activation energy to generate free charges. One possibility is that the binding energy of the CT states could be much lower than expected when we consider the change in the free energy of the system, namely, the entropy gain from charge dissociation [35, 41].

Some organic semiconductors such as acenes and diphenylisobenzofuran show singlet fission, in which a photoexcited high-energy exciton is converted into a pair of low-energy triplet excitons [T_1 in Fig. 10.5b] [42]. It is generally agreed that photoexcitation generates a triplet-pair state either coherently or incoherently from the singlet exciton and that this state may subsequently separate into two triplet excitons [42]. The underlying mechanism of singlet fission is now the subject of intense study.

10.2.4 Carrier Transport and Extraction

Once the charges are completely free, they drift and diffuse toward their respective electrodes with efficiencies that depend on their carrier mobilities. Because of the large electron-vibration coupling and the disordered nature of organic semiconductor layers, each charge is associated with a local geometrical relaxation and constitutes a polaron [34]. The molecular orientation of π-conjugated molecules is critical to enhancing carrier mobility. For small planar molecules, the face-on orientation is preferable for carrier transport. Recently, Ma et al. demonstrated that the end-on orientation of polythiophene further enhances hole mobility [43], although light absorption becomes weaker because of the orientational mismatch between the transition dipole moment of the polymer and the electric field of the incident light.

Carrier extraction at the electrode/organic interface is the final step in the operation of an OSC. The efficiency regarding this process is not determined simply by the frontier orbitals of the organic semiconductor and the Fermi levels of the electrodes. The electric field near the electrode interfaces, which is caused by the charge transfer in the ground states upon contact formation (see Sect. 10.4), also assists with carrier extraction. In addition, atomic diffusion of the metal electrode and the buffer materials may further complicate the interfacial phenomena. It is well recognized that to obtain long-term stability of an OSC, physical contact between the electrode and the active layer is critical, that is, matching the surface energies of the contacting materials. However, deep and comprehensive understanding of this process still appears to be lacking.

10.2.5 Characterization of OSC

A solar cell is characterized by measurements of its current density (J)-voltage (V) curve under AM1.5 illumination. Its power-conversion efficiency (η) is given by

$$\eta = \frac{J_{max} V_{max}}{P_{in}} = \frac{J_{sc} V_{oc} FF}{P_{in}}, \tag{10.1}$$

where P_{in} is the power of the incident light, J_{max} and V_{max} are the maximum current density and voltage, respectively, J_{sc} is the short-circuit current, V_{oc} is the open-circuit voltage, and FF is the fill factor (Fig. 10.8a). Here, FF can be regarded as the ratio of J_{max} V_{max} to J_{sc} V_{oc}. According to Eq. (10.1), it is necessary to optimize J_{sc}, V_{oc}, and FF to improve the overall power-conversion efficiency. The equivalent circuit for the solar cell is illustrated in Fig. 10.8b. It consists of a diode with a reverse-saturation-current density (J_0) and ideality factor (n), a current source corresponding to the photocurrent (J_{ph}), a series resistance (R_s) resulting from the contact resistance between the semiconducting material and the electrode and from the conductivity of the building components of the OSC, and a shunt resistance (R_p) derived from the loss of carrier recombination centers. The measured J-V curves are often analyzed using the generalized Shockley equation

$$J = \frac{1}{1 + R_s/R_p} \left[J_0 \left\{ \exp\left(\frac{V - JR_sA}{nkT/e} \right) - 1 \right\} - \left(J_{ph} - \frac{V}{R_pA} \right) \right], \tag{10.2}$$

where e denotes the elementary charge, kT is the thermal energy, and A is the area of the cell. From the above equation, J_{sc} can be expressed as

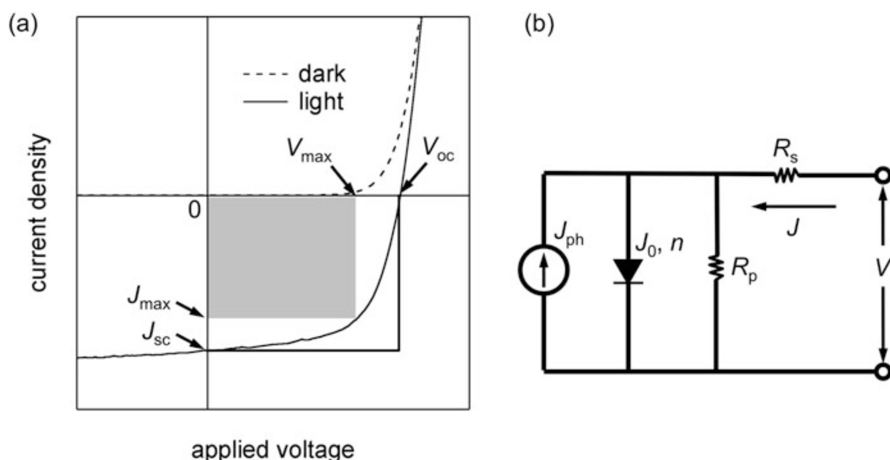

Fig. 10.8 (**a**) Current-density-voltage characteristics of solar cell in dark and illuminated conditions. (**b**) Equivalent circuit for solar cell. The notation is defined in the text

$$J_{sc} = -\frac{1}{1 + R_s/R_p}\left\{J_{\text{ph}} - J_0\left(\exp\left(\frac{|J_{\text{sc}}|\,R_s A}{nkT/e}\right) - 1\right)\right\}. \quad (10.3)$$

By fitting the measured J-V curve with Eq. (10.2), we can obtain values for the parameters R_s, R_p, and n.

10.2.5.1 Short-Circuit Current Density (J_{sc})

The maximum photocurrent J_{sc} is calculated by

$$J_{\text{sc}} = \int_{\text{AM1.5}} e\eta_{\text{EQE}}\,(\lambda)\,N_{\text{ph}}\,(\lambda)\,d\lambda, \quad (10.4)$$

where $N_{\text{ph}}(\lambda)$ is the photon flux density in the incident AM1.5 G spectrum at wavelength λ and $\eta_{\text{EQE}}(\lambda)$ is the external quantum efficiency that indicates the fraction of photons that are converted into current at wavelength λ. The upper limit of J_{sc} is calculated by integrating Eq. (10.4) from the high photon energy side to the wavelength corresponding to the optical band gap of the material. For example, silicon's band gap is 1.1 eV, yielding $J_{\text{sc}} = 43.6$ mA cm^{-2}. To enhance J_{sc}, the optical band gaps of the organic donor and acceptor should be low enough and cover sufficiently different optical ranges of sunlight.

According to Eq. (10.3), large R_s (contact resistance and bulk resistance) is detrimental to obtaining high J_{sc}. Therefore, the more conductive is the semiconducting material, the more current density is available. Charge density and mobility within the organic layer also impact J_{sc}.

10.2.5.2 Open-Circuit Voltage (V_{oc})

The physical origin of V_{oc} for an OSC has been discussed rigorously, and it has been found that its value is influenced by the work function of the electrode material, the donor ionization energy, and the acceptor-electron affinity [44–47]. According to conventional semiconductor physics, the maximum value of V_{oc} is the difference between the quasi-Fermi levels of the semiconductor holes and electrons (E_{Fp} and E_{Fn}): [48]

$$qV_{\text{oc, max}} = \left(E_{\text{Fn}} - E_{\text{Fp}}\right)_{\text{max}}. \quad (10.5)$$

That is, the band gap of the semiconductor determines the maximum value of V_{oc} for an inorganic solar cell. If we simply apply the same principle to an OSC, the maximum V_{oc} can be determined by the energy difference between the donor HOMO and the acceptor LUMO (i.e., the photovoltaic gap). Actually, this relationship was confirmed by comparing the photovoltaic gaps determined by photoelectron spectroscopy and by measured V_{oc} (Fig. 10.9) [49, 50].

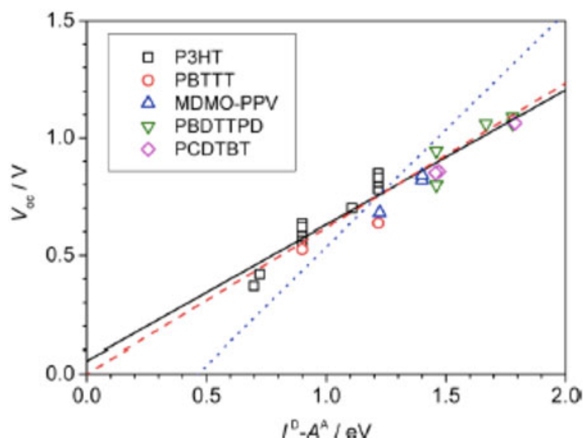

Fig. 10.9 Correlation between measured V_{oc} and ionization energy of donor and electron affinity of acceptor. (Reprinted with permission from Ref. [49]. Copyright 2017 American Chemical Society)

However, there is an empirical relationship that V_{oc} is 0.5–0.7 V smaller than the photovoltaic gap, which is confirmed experimentally by comparing V_{oc} and the gap measured with photoelectron spectroscopy [50]. To understand the origins of V_{oc} and its loss comprehensively, it has been proposed that V_{oc} be determined by the energy of the CT state (E_{ct}) [51]:

$$E_{ct} = E_0 - E_B, \tag{10.6}$$

where E_0 denotes the difference in energy between donor-ionization energy and acceptor-electron affinity (the energy difference between peaks of Gaussian donor-HOMO and acceptor-LUMO) and E_B is the average binding energy of the CT state:

$$E_B = \frac{q^2}{4\pi \varepsilon r_{ct}}, \tag{10.7}$$

where ε denotes the dielectric constant of the material and r_{ct} is the average separation between holes and electrons in the CT state. Burke et al. recently established a model in which CT states and free carriers are in equilibrium [52] and derived the following relationship for V_{oc}:

$$qV_{oc} = E_{ct} - \frac{{\sigma_{ct}}^2}{2kT} - kT\log\left(\frac{qfN_0L}{\tau_{ct}J_{sc}}\right), \tag{10.8}$$

where σ_{ct} denotes the dispersion of the CT state (Gaussian in shape), k is the Boltzmann constant, T is temperature, f is the volume fraction of the mixed region in the active layer, N_0 is the density of states in the organic material, and τ_{ct} is the lifetime of the CT state. From Eq. (10.7), one can easily see that the value of V_{oc} is influenced by not only E_{ct} but also the degree of disorder of the CT state, the interfacial area between donor and acceptor, and how recombination at the

donor/acceptor interface is suppressed. Besides, Eq. (10.7) indicates that increasing the distance between holes and electrons in the CT state weaken the Coulomb interaction between the states, presumably resulting in an improved V_{oc}.

10.2.5.3 Fill Factor (FF)

As mentioned before, *FF* is the ratio of the obtainable maximum power to the product of J_{sc} and V_{oc}. For an OSC with a high *FF*, the photocurrent should remain unchanged when forward bias is applied. In turn, photo-generated carriers drift efficiently through the active layer and electrode interfaces. In other words, series resistance R_s should be low enough for achieving high *FF*. Therefore, the organic and inorganic materials used in an OSC must be "neat" in relation to both purity and molecular order in the film without a carrier-extraction barrier at the electrode interfaces through which free charges pass. In general, relatively high mobility and appropriate control of molecular orientation are required. Impurities in organic semiconductors may act as charge traps [15, 16] and thus must be removed by train sublimation and solvent purification, for instance. Besides, the hole/electron mobility balance affects the fill factor because such an imbalance leads to carrier accumulation near the donor/acceptor interface, which leads to an *S*-shaped *J-V* curve and lowers *FF* [53].

Ohmic contact at the electrode interfaces, where contact resistance is negligible for both carrier injection and extraction, is also required for enhancing *FF*. The ideal contact can be achieved by modifying the electrode surface appropriately to obtain the desired work function, thereby achieving Fermi-level pinning (see Sect. 10.4). For example, the value of R_s of a DIP/C_{60} PHJ OSC prepared on unannealed PEDOT:PSS is 42 kΩ, whereas thermal annealing of PEDOT:PSS increases its work function and concurrently leads to a significantly reduced R_s (down to 55 Ω). Consequently, the *FF* of the OSC increases to 0.74 [54].

10.3 Electronic Properties of π-Conjugated Molecules

The electronic structure of donor and acceptor molecules is known to have a great influence on the device performance of OSCs, particularly the optical absorption, carrier injection, and carrier transport because they have a good deal to do with the operation principle of the devices. As mentioned in Sect. 10.2.5.2, V_{oc} is proportional to the energy difference between the donor's HOMO and the acceptor's LUMO. Therefore, whether intentionally or not, manipulating the molecular structure of donors or acceptors sometimes changes their electronic structure and can affect the device performance. Determining the correlation between the electronic structure of the materials and the function of the OSCs would guide the future material design.

It has been reported that the C_{60} fullerene is a good acceptor for OPVs because of its high electron transfer rate from donor molecules. However, because of the necessity to use soluble compounds when making a device with a BHJ structure, fullerene derivatives such as $PC_{61}BM$ (Fig. 10.3) were developed. The C_{60}- and C_{70}-based PCBMs have been used frequently as acceptor molecules in OPVs, together with π-conjugated polymers such as P3HT as the donor. By using BHJs that combine PCBMs (thereby maintaining a high electron transfer rate) and π-conjugated polymers (thereby ensuring high carrier mobility), we guarantee devices with high power-conversion efficiency. The point of interest here is that by tuning the molecular structure of the fullerenes to achieve soluble derivatives, we end up unintentionally modifying the electronic structure. In some cases, this change in electronic structure can be measured in the device performance.

10.3.1 Fullerene Derivatives

The high symmetry of the molecular structure of fullerenes C_{60} and C_{70} yields a low back electron transfer rate after charge separation occurs. It is also responsible for a highly efficient intersystem crossing from singlet to triplet excited states, giving excited states with long lifetimes. These characteristics make these compounds indispensable as acceptors for OSCs. Fullerenes C_{60} and C_{70} are incompatible with the solution processes such as spin coating because of their low solubility in common organic solvents. Soluble derivatives have been synthesized by adding functional groups to these fullerene backbones [55, 56], thereby allowing OSC devices to be produced using solution processes such as spin coating [57]. Now, C_{60} and C_{70} derivatives bearing various functional groups, which improve solubility and processability, have been used as acceptors in BHJ-OSC with high-efficiency photoelectric conversion [58–62]. PCBMs based on C_{60} and C_{70} are well-known soluble derivatives and have been used frequently as an acceptor in OSCs [55, 58]. It has been reported that the side chains of $PC_{61}BM$ affect the film morphology, which may improve the device performance [63–66].

Akaike et al. [62, 66] reported that adding a side chain to a C_{60} backbone affects not only its solubility but also the electronic structures of $PC_{61}BM$ and [6,6]-diphenyl-C_{62}-bis(butyric acid methyl ester) (bis$PC_{61}BM$). They concluded that a subtle charge transfer from the side chain to the C_{60} backbone destabilizes the frontier orbitals of the molecule. They also suggested that the effects of the side chain on the electronic structures of $PC_{61}BM$ and bis$PC_{61}BM$ may improve the performance of the OSC devices compared with devices containing C_{60} [67, 68]. Their work demonstrates that measures of OSC device performance such as V_{oc} can be discussed in terms of electronic structure.

The results of ultraviolet photoemission spectroscopy (UPS) and inverse photoemission spectroscopy (IPES) for $PC_{61}BM$, bis$PC_{61}BM$, C_{70}, and $PC_{71}BM$ are shown in Fig. 10.10. The simulated spectra based on the molecular orbital calculation are also displayed (filled in gray). The combined UPS and IPES spectra

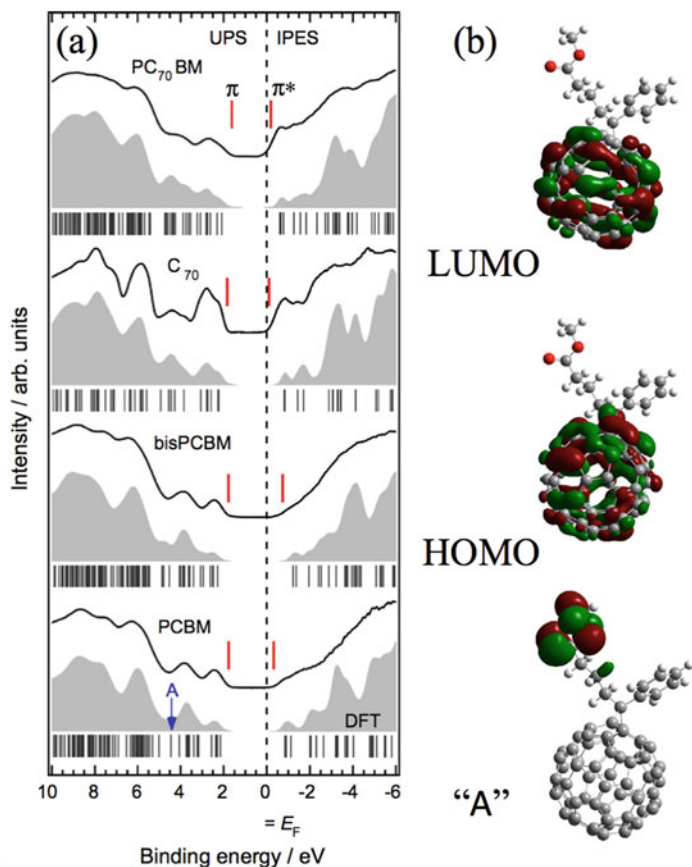

Fig. 10.10 (**a**) Ultraviolet photoemission spectroscopy (UPS) and (**b**) inverse photoemission spectroscopy (IPES) spectra for fullerene derivatives. (Reprinted with permission from Ref. [65])

replicate the molecular orbitals (MOs) of the specimen. Indeed, the simulated spectra reproduce the observed spectra well. The HOMO, LUMO, and highest occupied MOs in the side chain labeled "A" are displayed in Fig. 10.10b. The MOs in the side chain are located at binding energies in excess of 4 eV. Basically, the π-orbitals of the C_{60} backbone contribute greatly to the HOMO and LUMO of the derivatives as seen in the case of $PC_{61}BM$ in Fig. 10.10a, b. The vertical bars in Fig. 10.10a indicate the onsets of the UPS and IPES spectra that correspond to the HOMO (π) and LUMO (π^*) energies. The energy difference of the HOMO measured from E_F is the height of the hole injection barrier ${\phi_h}^{exp}$, and the energy difference between the LUMO and Fermi level (E_F) is the height of the electron injection barrier ${\phi_e}^{exp}$ from the electrode. The adiabatic ionization energy I^{exp}, electron affinity A^{exp}, and energy gap ${E_g}^{exp}$ can be calculated from ${\phi_h}^{exp}$, ${\phi_e}^{exp}$, and E_{vac}. Here, E_{vac} denotes the vacuum-level energy obtained directly by the UPS

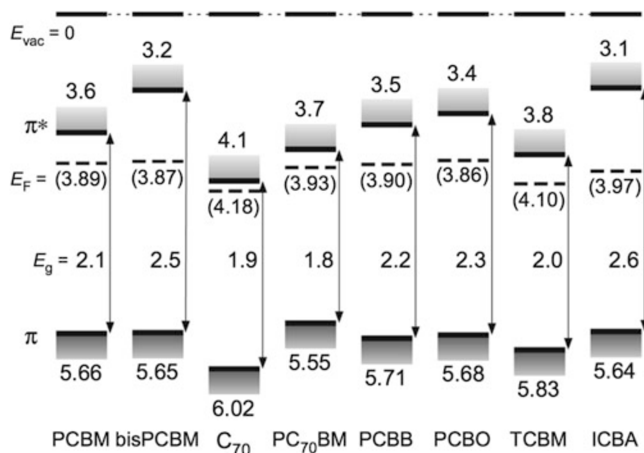

Fig. 10.11 Energy diagrams for various fullerene derivatives determined by UPS and IPES

experiments. The values of ϕ_h^{exp}, ϕ_e^{exp}, and E_g^{exp} calculated from the UPS-IPES spectra for the compounds in Fig. 10.10a are summarized in Fig. 10.11. The LUMOs of all the compounds are very close to E_F, and the low-lying LUMO explains the *n*-type electric characteristics of the devices in which they are used. The LUMOs of C_{70} and $PC_{71}BM$ are right above E_F, indicating very small ϕ_e^{exp}. In contrast, the LUMOs of bisPCBM and ICBA are higher than the LUMOs of the other fullerene derivatives, which probably causes the larger V_{oc} of the OPV devices containing bisPCBM or ICBA.

The values of I_{exp}, A_{exp}, and E_g^{exp} differ among all the fullerene derivatives. There is more variation in the LUMO energies than in the HOMO ones. The I_{exp} and A_{exp} values of C_{70} are larger, and the A_{exp} values of bisPCBM and ICBA are smaller than those of the other compounds. The E_g^{exp} values of C_{70} and $PC_{71}BM$ are smaller, and the E_g^{exp} values of bisPCBM and ICBA are larger than those of the other compounds. The small E_g^{exp} value of $PC_{71}BM$ causes a wide absorption range in the visible region, which leads to the high power-conversion efficiency of the OSC devices in which $PC_{71}BM$ is used as an acceptor [59–61].

Akaike et al. [62, 66] explained the effects of the side chain on the electronic structure of $PC_{61}BM$ and $bisPC_{61}BM$ by slight polarization of the electron density inside the molecules. A subtle electron transfer from the side chain to the C_{60} backbone destabilizes the frontier orbitals spreading over the fullerene backbone. The side chain donates a certain amount of electron density to the C_{60} backbone. The amounts of charge in $PC_{61}BM$ and bis-$PC_{61}BM$ donated to the backbone are estimated at roughly 0.23*e* and 0.46*e*, respectively, from the density functional theory (DFT) calculations, where *e* is the elementary charge. Thus, the partial electrical charge donated from the side chain to the C_{60} backbone of $PC_{61}BM$ and bisPCBM destabilizes the HOMO and LUMO of the molecule and lowers both the I_{exp} and A_{exp} values. This indicates that PCBM and bisPCBM are weaker acceptors than C_{60}.

10.3.2 π-Conjugated Donor Polymers

Semiconducting π-conjugated polymers such as polyphenylenes, polyphenylenes, polyanilines, and polypyrroles have been used frequently in organic electronic devices including OPVs because they possess high solubility in organic solvents and can be formed into smooth films by solution processes. A series of conjugated polymers, poly(3-alkylthiophene)s (P3ATs), is widely used as a hole-transporting material in organic field-effect transistors (OFETs) and OSCs [57, 69–73]. The mobilities of the OFETs with P3HT reach 0.1 $cm^2\ V^{-1}\ s^{-1}$ [69–73], which is comparable to that of amorphous silicon-based FETs. This dramatic improvement in hole mobility has been attributed to the high degree of intra-chain and interchain orders in the P3AT films. The structure of P3HT films as deduced by X-ray diffraction (XRD) analysis is composed of polycrystalline domains embedded in an amorphous matrix [74, 75]. In the polycrystalline domain, P3HT stacks in one-dimensional chains and forms a lamellar structure consisting of two-dimensional conjugated sheets through interchain stacking. The degree of structural order in P3AT films depends strongly on the degree of regioregularity of the polythiophene backbone [76]. It is thought that the conformation and packing of the polymer backbone play a dominant role in determining the transport properties of the material. As mentioned above, OFETs with highly regioregular P3HT have high mobility, whereas OFETs with regiorandom P3HT have mobilities in the range of only 10^{-5}–10^{-4} $cm^2\ V^{-1}\ s^{-1}$ [77]. The high mobility of regioregular P3HT films is partly attributable to the highly ordered structure of the film.

The morphology of the regioregular P3HT polycrystalline film or domains in the active layer in OSCs changes considerably upon annealing, as shown in Fig. 10.12a. Figure 10.12b displays a schematic of the microcrystalline structure

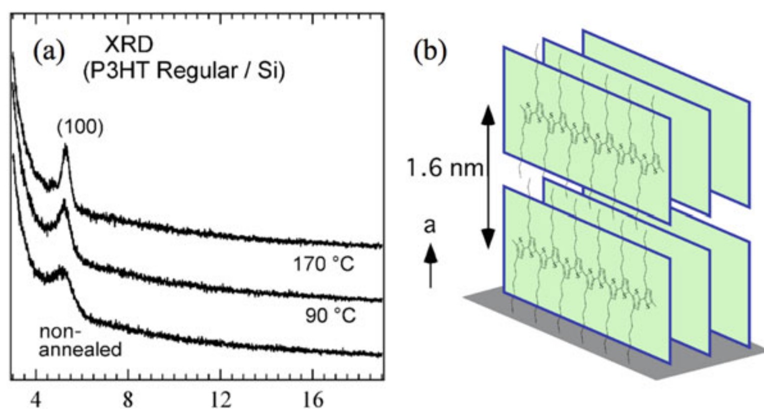

Fig. 10.12 (**a**) XRD of P3HT film prepared under different conditions coated on silicon substrates. (**b**) Schematic illustration of molecular arrangement of P3HT. (Reprinted with permission from Ref. [79])

of P3HT. In the polycrystalline domain, P3HT stacks in one-dimensional chains and forms a lamellar structure consisting of two-dimensional conjugated sheets through interchain stacking. The structural order in P3AT film depends strongly on the degree of regioregularity of the polythiophene backbone [76]. The electrical properties of P3HT films are also affected by annealing: the mobility is dramatically improved [78]. The increased mobility due to annealing is accompanied by increased structural order as observed by atomic force microscopy and X-ray analysis [79]. This result is in contrast to the interpretation that grain boundaries are the major cause of low mobility in low-molecular-weight P3HT films since the annealed films have high crystallinity [79]. Zen et al. have suggested that the main cause of the low mobility of the low-molecular-weight P3HT films is the disordered conformation of the backbones of a majority of the polymer chains, which hinders interchain charge transport as a result of fewer interchain contacts [77]. Alternatively, polymer chains of higher-molecular-weight P3HT possibly have more extensive π-conjugation, which would provide more opportunities for charge carriers passing along the polymer chain to hop to a neighboring polymer through an interchain contact.

Also, we have measurable effects induced by annealing in the electronic structure of the P3HT films. It was found that annealing strongly influences the energy gap, the energy of vacuum level, and the π- and π^*-band energies. Consequently, the carrier injection barriers at the interfaces between the P3HT film and the electrodes are significantly affected. Figure 10.13 shows the combined UPS and IPES spectra of the regioregular P3HT films on ITO substrates. The π-band onset in the non-annealed sample is very close to E_F and shifts to higher binding energies after annealing, whereas the vacuum level and the π*-band onset are less affected. The high-resolution IPES spectra of the annealed films are more structured with the appearance of shoulders, denoted in the figure by arrows. In addition, the UPS spectra at the onset of the π-band become more structured after annealing. Simulated spectra derived from the calculations based on DFT are shown in Fig. 10.13. The simulations were performed using a hexylthiophene oligomer with 10 repeating units of 3-hexylthiophene rings ($n = 10$; 10HT) as a model system. Ten repeating units of HT are enough to reproduce the polymer qualitatively; therefore, 10HT is a good model system for discussing the electronic structure of P3HT. The simulated spectra reproduce the measured spectra well. Based on a comparison of the observed and simulated spectra, the shoulder structures at ~3.5 eV above E_F (indicated by arrows) are assigned to the π*-band. The energy of the band is almost independent of the number of repeating units, and the HOMO and LUMO of 10HT are composed primarily of the π- and π*-orbitals distributed over the conjugated polymer chain. It is clear that the π- and π*-bands grow after annealing as the π-conjugation length increases by a conformation change of the polymer chain. These results are consistent with the change in the UV-visible spectra after annealing [79].

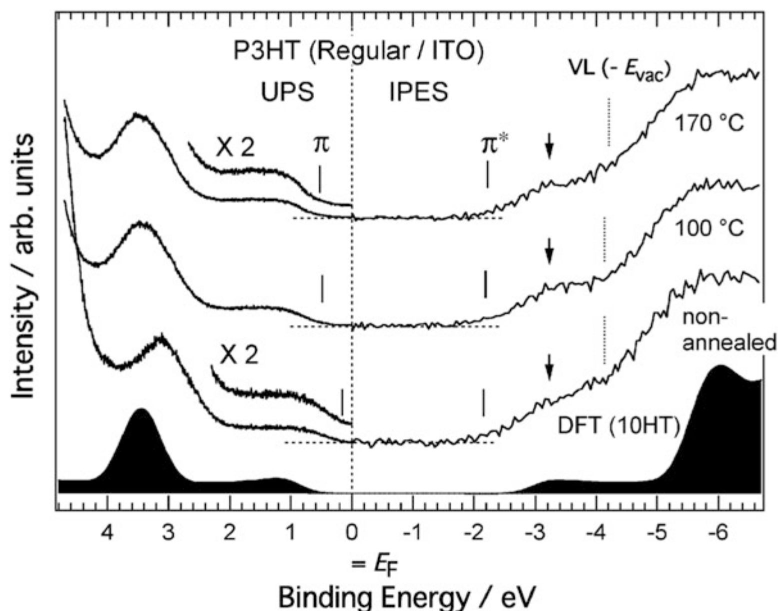

Fig. 10.13 UPS and IPES spectra of rr-P3HT thin films spin-coated on ITO substrate. (Reprinted with permission from Ref. [79])

10.4 Electrode/Organic Interface and Organic Heterointerface

The interface between the electrode and organic semiconductor in an active layer should be free from any energetic barrier to carrier extraction. Thus, we have to realize ohmic contact (i.e., negligible contact resistance with respect to the total resistance) of an OSC. A question arises as to what constitutes ohmic contact for an electrode/organic interface. In the case of an inorganic semiconductor, it is known that high doping concentration and a low energy barrier reduce the contact resistance [48]. Although organic semiconductors are typically *undoped*, the molecules at the interface to the electrode can be *doped* as a result of electron transfer to achieve thermodynamic equilibrium upon contact formation. Such a contact-induced doping has been demonstrated for a high-work function substrate/donor polymer interface and low-work function substrate/C_{60} interfaces [80–83]. Besides, the charge density distribution leads to evolution of an electrostatic potential near the electrode interface, thereby impacting the relative energy of the frontier orbitals with respect to the electrode Fermi level (E_F). Because the energetic landscape near the interface can significantly affect carrier processes and hence OSC performance, knowledge of the mechanism for charge-density and potential distribution is essential for designing the interface.

In this section, we introduce a recently proposed model that simulates energy-level alignment at the interface, which is applicable to electrode/organic interfaces as well as to organic heterointerfaces. Next, we discuss the technique that control electrode work function and wettability to improve energy matching and physical contact between the organic semiconductor and the electrode surface, along with correlating the interface property with the OSC performance.

10.4.1 Theoretical Model for Energy-Level Alignment

Recently, Oehzelt et al. proposed a comprehensive electrostatic model of the energy-level alignment, which is applicable even to organic heterointerfaces [84]. The model assumes that (1) the conductive substrate is an electron-reservoir, (2) the electron occupation obeys Fermi-Dirac statistics under thermodynamic equilibrium and electrons move through the organic layer toward the electrode E_F or vice versa, and (3) organic layers are grown ideally in a layer-by-layer manner on a conductive substrate with experimentally determined HOMO and LUMO onsets, density of states width, and a discrete height z. The charge density at each layer is calculated by

$$\rho(z) = e \cdot n \cdot \left\{ \int_{-\infty}^{+\infty} f_H(E) \cdot D_H\left[E + eV(z)\right]\, dE - \int_{-\infty}^{+\infty} f_L(E) \cdot D_L\left[E + eV(z)\right]\, dE \right\}, \tag{10.9}$$

where e is the elementary charge; n is the molecular number density per area layer; f_H and f_L are Fermi-Dirac functions; D_H and D_L are the peak shapes for the HOMO and LUMO, respectively (typically Gaussian); and $V(z)$ is the potential at distance z from the substrate surface. The charge density so obtained is used to calculate the potential in the respective layer using a generalized one-dimensional Poisson equation:

$$\nabla\left(\varepsilon_r(z)\nabla V(z)\right) = -\frac{\rho(z)}{\varepsilon_0}, \tag{10.10}$$

where $\varepsilon_r(z)$ is the dielectric constant of the layer and ε_0 in the permittivity in a vacuum. The obtained potential is used to calculate charges by solving Eq. (10.9) again, and then a new $V(z)$ is calculated. This self-consistent calculation can simulate depth-resolved charge density and potential distributions. The simulation results can reproduce the trend of thickness-dependent UPS measurements, which are traditionally used to determine the potential distribution along the surface normal. Combining the model simulation and UPS analysis, Wang et al. revealed that the upward band bending at the Ag(111)/NaCl/C_{60} heterostructure, which is attributed to electron transfer from Ag to C_{60} through the NaCl layers, is caused by the evolution of electron density in the C_{60} layers up to 150 nm [80].

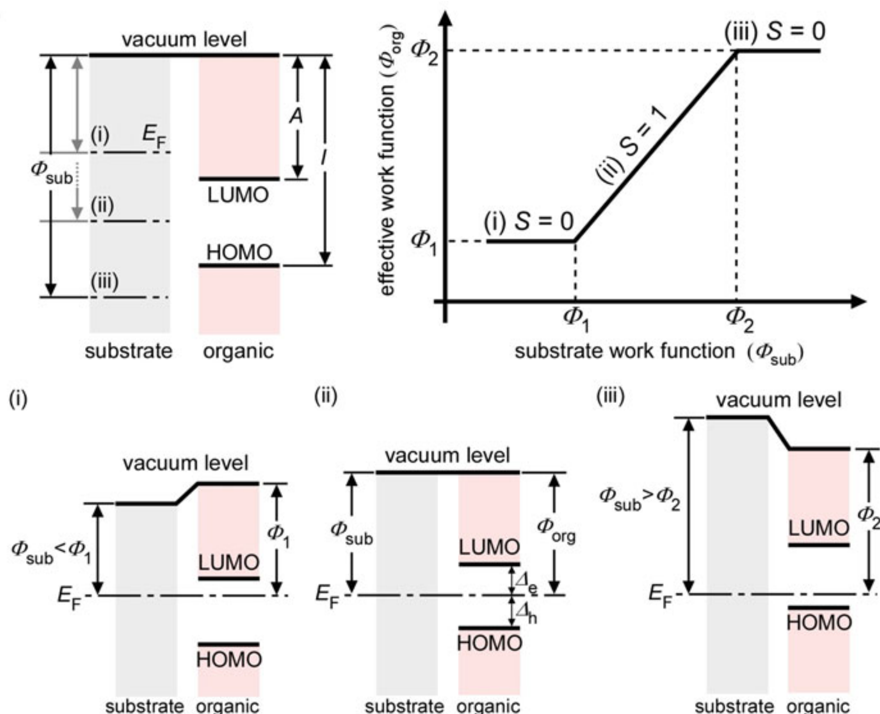

Fig. 10.14 Energy-level alignment at organic interface. Φ_{sub} denotes substrate work function, A is the electron affinity, and I is the ionization of the organic molecules. When Φ_{sub} exceeds I (A), the effective work function of the organic layer (Φ_{org}) is independent of Φ_{sub} [regions (i) and (iii)]; otherwise, Φ_{org} depends on Φ_{sub} [region (ii)]. In the regions (i) and (iii), Fermi-level pinning occurs. S denotes the slope parameter that is defined as $d\Phi_{org}/d\Phi_{sub}$

The model also predicts the dependence of energy-level alignment at the interface on the substrate work function. As already demonstrated by UPS measurements [85, 86], when the substrate work function is higher (lower) than the ionization energy (electron affinity) of the molecule, the vacuum and energy levels are independent of the substrate work function (Fig. 10.14). This phenomenon is known as “Fermi-level pinning,” [85] being reminiscent of the constant charge-injection barrier occurring at a metal/inorganic semiconductor junction because of the dangling bonds.

Typically, the electronic structure at metal/organic interfaces is investigated for organic molecules adsorbed on a metal surface. However, if an interface between the photoactive layer and the top cathode is formed by vacuum deposition, the morphology and electronic structure at the interface can be different from those of the interface with the reversed deposition sequence. For instance, whereas an Au(111)/NPD interface seems to be inert and there is no strong interaction between the two constituents, gold atoms vacuum-deposited on NPD lead to a new chemical species as revealed by XPS [87]. The asymmetry of the electronic structure actually

leads to different charge-injection barriers in diode devices. Usually, injecting from the top contact is more efficient than doing so from the bottom contact [88].

10.4.2 *Modification of Electrode/Organic Interfaces*

As mentioned above, controlling the work function and morphology is critical to achieving ohmic contact for a more efficient device. So far, various materials including transition metal oxides, alkali halides, a polymer electrolyte, an inorganic salt, and a self-assembled monolayer (SAM) have been employed as interface modifiers for an OSC [89, 90]. In addition, here we introduce interface organic materials that are often used for OSCs to control their electronic, morphological, and photophysical properties.

10.4.2.1 Control of Electrode Work Function

To realize an ohmic contact, the Fermi levels of the anode and cathode should be close to the HOMO of the donor and the LUMO of the acceptor, respectively. Actually, Fermi-level pinning is important for reducing the series resistance of an OSC, leading to improved J_{sc} and *FF* [16]. Therefore, appropriate control of the work function of the anode and cathode is required. It was found for ITO substrates that the surface treatments such as UV/ozone, oxygen plasma, and dipping in aqueous alkaline hydroxide solution alter the surface chemical composition and work function because of the formation of surface dipoles and the removal of carbon contamination from the substrate surface. Among anode interface materials, PEDOT:PSS (whose molecular structure is shown in Fig. 10.15) has been used as a polymer-based anode interface layer to improve hole extraction. Its work function ranges from 4.5 to 5.6 eV, depending on its composition and heat treatment [91, 92], which can pin the HOMO levels of most donors to the Fermi level of the substrate. Figure 10.16 shows the importance of the Fermi-level pinning of the donor HOMO in optimizing the OSC behavior. Wagner et al. demonstrated that Fermi-level pinning is necessary to avoid an undesirable S-shaped *I-V* curve due to a high series resistance that can lower the *FF* of the OSC [16, 54].

Despite its wide-ranging applicability, the long-term stability of OSCs prepared on PEDOT:PSS is poor because of traps that form through water diffusion and because of the increased contact resistance due to water damage to the cathode [93]. Instead of the polymer buffer layer, transition metal oxides such as MoO_3 and V_2O_5, and phosphonic SAM, have been employed to control the anode work function. The oxides have very high work functions up to 7 eV, independent of the bottom substrate work function because of its *n*-type character that results from a finite concentration of oxygen defects even in pristine MoO_3 evaporated films [94]. This high work function leads to a downward energy shift in the photoactive layer because of the hole accumulation therein, probably leading to exciton dissociation

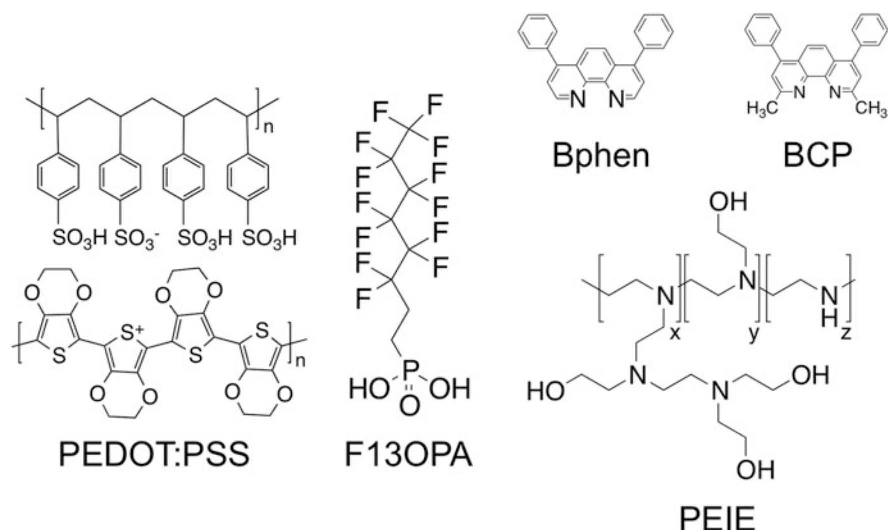

Fig. 10.15 Molecular structure of representative interface modifier

and efficient hole extraction. Actually, the Schottky-barrier OSC based on C_{60} and SubPc shows relatively high performance [18, 19].

The substrate work function actually affects not only the interface energetics but also the photophysical behavior of an OSC. Knesting et al. investigated the correlation between work function modification with V_{oc} and carrier lifetimes [95]. A higher work function leads to a higher electric field at the anode/photoactive-layer interface, suppressing carrier recombination in the bulk. Wang et al. recently reported that the contact-induced doping, which is due to the Fermi-level pinning, may decrease the photocurrent. Thus, there is an optimal work function for the respective polymer to keep its built-in field [96], in contrast to other reports that there is no dependence of OSC performance on substrate work function [97, 98]. A detailed study of carrier distribution (in the ground states) and carrier generation/recombination processes is necessary to obtain a comprehensive understanding of the impact of interface energetics on the device characteristics.

In standard OSCs, lithium fluoride (LiF), bathocuproine (BCP), and bathophenanthroline (Bphen) have often been used as cathode modifiers. By inserting thin films of these materials at the interface between C_{60} and Al, the overall performance of PHJ OSCs improves significantly because of suppression of nonradiative recombination of excitons at the C_{60}/Al interface [99], thereby increasing the interfacial electric field [100]. Toyoshima et al., employing UPS, reported a large work function reduction upon depositing BCP onto metallic substrates [101, 102]. Despite the findings that the large downward energy shift at the C_{60}/BCP interface leads to efficient electron extraction [103, 104] and BCP-thickness-dependent energy-level alignment at the Ag/BCP/C_{60} heterostructure

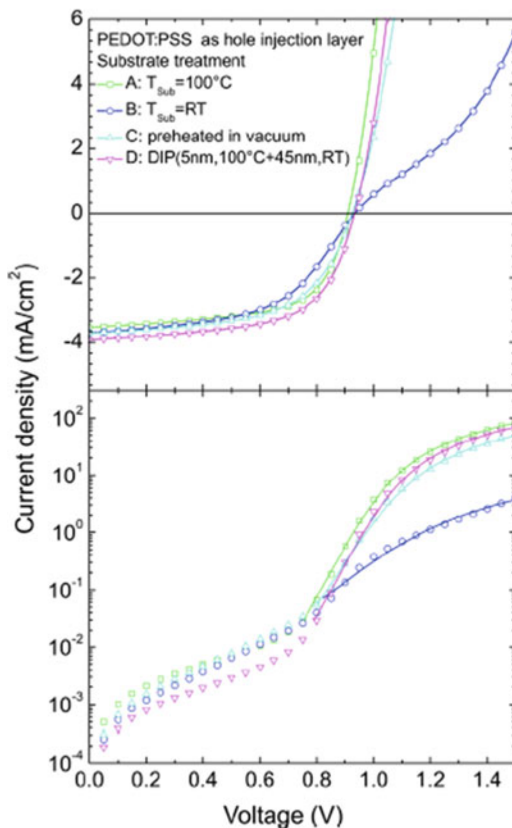

Fig. 10.16 Impact of thermal annealing of PEDOT:PSS layer. Fermi-level pinning reduces series resistance and thus fill factor of DIP/C60 planar heterojunction OSC. (Reprinted with permission from Ref. [16])

[105], direct correlation between the interfacial electronic structure and OSC performance remains elusive.

For an inverted OSC, the work function of the ITO substrate has to be lowered in order to extract electrons. Cs_2CO_3 is one of the candidates for decreasing the work function by either spin coating or vacuum deposition. Upon annealing, the carbonate part desorbs and the metallic Cs produces substrate electrons, forming an interfacial dipole that is responsible for reducing the work function [106]. In 2012, the insulating polymers poly(ethylene imine ethoxylated) (PEIE) and poly(ethylene imine) (PEI) were found to be versatile for producing low-work function electrodes that can be used in OLEDs, OSCs, and OFETs [29]. The origin of the decrease in work function was attributed to the formation of a local dipole on the substrate surface, as suggested by density functional theory calculations. However, the volatile ethyleneimine dimer or trimer impurities contained in the PEI water solution were also found to act as *n*-dopant (electron dopant) for the electrodes, and the resulting interfacial dipole decreased the effective work function [107]. For the hole-extracting electrode in an inverted OSC, one must pay attention to atomic and/or molecular diffusion of buffer materials such as MoO_3 into the

organic layers [108, 109]. This diffusion increases the magnitude of electron transfer from the strong *p*-dopant MoO_3 to the organic molecules. Very recently, doped polymers have been used universally to control the substrate work function in the range of 3.0–5.8 eV [110]. Such a versatile method for producing the desired surface work function would enable the design of well-established interfaces.

Controlling the electrode work function in an OSC is very important for not only making electrode contacts ohmic but also for maximizing V_{oc}. The dependence of V_{oc} on the substrate work function has been measured [96], and it appears to be necessary that the donor HOMO and acceptor LUMO be pinned to the electrode Fermi levels in order to obtain the maximum V_{oc}.

10.4.2.2 Improvement of Physical Contact and Interface Morphology

The physical adhesion of the photoactive layer to the electrode surface is critical to sustaining the lifetime of an OSC and determining the charge-transfer kinetics at the electrode interfaces. So far, surface modification of a representative transparent electrode, ITO, has been examined. An ITO film is often fabricated on a glass substrate by sputter deposition followed by thermal annealing. This fabrication processes results in a highly polar surface with finite roughness and hydroxyl groups. As a result, the ITO surface has a surface energy of 60–70 mJ m^{-2}, which is much higher than that of an organic semiconductor film (10–50 mJ m^{-2}). Such a surface-energy difference leads to delamination of the organic semiconductor and consequently poor sustainability of the charge-transfer kinetics and thus the OSC performance [111]. An example of a surface modifier for ITO is phosphonic acid SAM that is functionalized with a fluorinated alkyl chain (Fig. 10.15) to tune the ITO surface work function, thereby decreasing the ITO surface energy and leading to long-term stability of the work function. An OSC based on this SAM demonstrated a longer lifetime [111]. For ZnO and AZO, alkaline hydroxide solution treatment was found to suppress the light-soaking effect, thereby leading to longer lifetimes of BHJ OSCs [112].

Another technique for changing the interfacial morphology is to use the nanostructure of the interfacial modifier. Nanorods of ZnO are now well established as a way to produce a large interfacial area at the electron-extracting electrode interface. In addition, PDMS stamps can increase the interfacial area. Both techniques contribute to increases in FF and J_{sc}.

10.4.3 *Energetics and Charge Generation at Donor/Acceptor Interface*

10.4.3.1 Energetics

Multilayered organic devices, both OSCs and OLEDs, encompass organic heterointerfaces whose function critically influences their performance. In particular,

evolution of the carrier transport levels (HOMO and LUMO) is essential for understanding the behavior of exciton and free carriers generated at the donor/acceptor interface. For example, any built-in potential near the interface can support the sweeping away of the photo-generated holes and electrons toward the respective electrode.

Together with metal/organic semiconductor interfaces, the energetics at organic heterointerfaces have been investigated by employing surface science techniques [88, 113, 114]. At this early stage of research, vacuum-level alignment appears to hold at most organic heterointerfaces because of van der Waals interaction at the interfaces. However, findings that show that the magnitude of the vacuum-level shift depends on the substrate work function [88, 113] and that electrons are injected through the bottom organic layer to the overlayer [86, 87] confirm the existence of a potential drop even at inert organic heterointerfaces. These studies advance the establishment of a comprehensive model for predicting the energy-level alignment at the interfaces.

Recently, it was found that the electrostatic model [84] (see Sect. 10.4.1) can describe the energy-level alignment at organic heterointerfaces [119] and that the simulation well reproduces the energy-level shift measured by UPS. Strongly motivated by the agreement between the simulations and experimental data, thorough theoretical simulations of energy-level alignment at all types of organic heterointerface have been carried out [115]. Figure 10.17 shows the simulated energy-level alignments for OSC-relevant donor/acceptor interfaces with various substrate work functions. As for the anode/donor/acceptor structure (Fig. 10.17a), when the substrate work function is high enough (cases for $E_F = 6.0$ and 7.0 eV), holes accumulate at the anode/donor interfaces because of the Fermi-level pinning, but no charges accumulate at the donor/acceptor interface; thus the potential drop is negligible. For the cathode/acceptor/donor structure (Fig. 10.17b), when the substrate work function is low enough (cases for $E_F = 3.0$ and 4.0 eV), the Fermi-level pinning again causes electron accumulation at the cathode/acceptor interface. Thus, the energy levels shift upward, whereas no potential change occurs at the donor/acceptor interface.

Poelking et al. demonstrated that the aggregated long-range quadrupole interaction is critical for obtaining the correct energetic landscape at an organic heterointerface [116, 117]. The electrostatic model is capable of including such an influence of the electrostatic potentials of π-conjugated molecules by considering the orientational dependence of the ionization energy and electron affinity.

The electrostatic model assumes the Frank-van der Merwe growth (layer-by-layer) of the respective organic film and therefore ideally sharp interfaces. However, at actual interfaces, intermixing [118] and molecular reorientation [119] may occur, thereby complicating the interfacial electronic structure. Actually, a phthalocyanine/fullerene interface, which is a prototypical donor/acceptor interface used in OSCs, tends to show an unusual potential distribution (Fig. 10.18a). This is independent of the types of substrate, phthalocyanine, and fullerene and of their thicknesses and evaporation speed during formation of the interface [103, 120]. The observed downward-and-then-upward shift has been interpreted as being caused

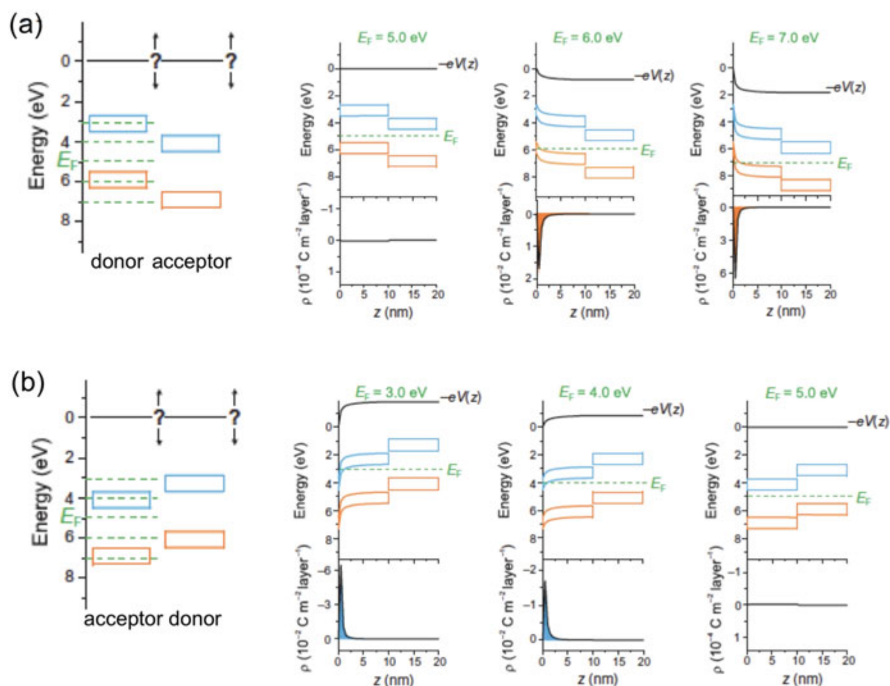

Fig. 10.17 Simulations of the energy-level alignment at donor/acceptor interfaces. (**a**) The very left panel shows the initial energies of the HOMO (orange rectangular) and LUMO (blue rectangular). The green-dashed lines correspond to the work function of the bottom substrates. The dependence of the simulation results on the electrode work function is shown in the second left to right panels. In each panel, the upper and lower plots illustrate the evolutions of the energies of the frontier orbitals and charge density as a function of the distance from a substrate surface (z), respectively. (**b**) Same for the reversed stacking sequence [115]

by an increase in the structural inhomogeneity in the phthalocyanine layers upon interfacial formation [120].

The energetic landscape across the donor/acceptor interface severely impacts the carrier generation and bimolecular recombination. The three-phase model was proposed to explain the widely observed efficient charge generation. The model assumes an amorphous mixed region between the pure donor and acceptor phases. In this amorphous region, the band gaps of the donor and acceptor increase because of shorter conjugation lengths. The existence of such a mixed region has been explored with UPS and cyclic voltammetry in the solid state [124].

An energy cascade designed by any method leads to an increase in free-carrier generation. The model in which the charge-transfer state and free carriers are in equilibrium predicts that more charges are generated in the donor and acceptor phases if an energy offset of 100 meV exists between the mixed and pure phases [52]. Actually, Izawa et al. confirmed that the energy cascade reduces bimolecular

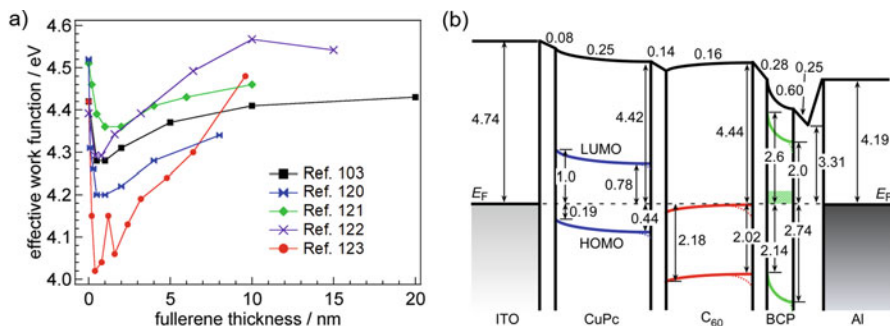

Fig. 10.18 (**a**) Downward-and-then-upward shift at phthalocyanine/fullerene interfaces. A dip in the vacuum level can be seen with increasing fullerene coverage [103, 120–123]. (**b**) Energy diagram of a planar heterojunction OSC determined by Kelvin probe (KP) measurements [103]. (Reprinted with permission from Ref. [103])

recombination at the donor/acceptor interface in the planar heterojunction OSC and increases *FF* and V_{oc} [125].

A more complicated issue is that the molecular orientation may change upon interface formation, which has been reported for a metal-free phthalocyanine/perfluorinated phthalocyanine interface [119]. Besides, chemical interaction in the solid phase can further alter the interfacial properties. The Diels-Alder reaction at a pentacene/C_{60} interface, which shows a PCE of ~4% [47], can produce pentacene-C_{60} adducts [126]. Further investigation is necessary to elucidate the impact of the interface compound on OSC performance.

To reveal the full electronic structure of an OSC, several groups have analyzed the evolution of the vacuum-level and HOMO energies [103, 104, 127–129]. For a small-molecule-based OSC, a huge potential drop was observed at a C_{60}/BCP interface (Fig. 10.18b), which was attributed to the giant surface potential of BCP [103]. The measured shift would support efficient electron extraction toward the cathode. Davis et al. examined the electronic structure under ambient conditions using photoelectron yield spectroscopy and optical absorption spectroscopy [129]. Despite these measurements, a full picture of the energy and charge-density profiles remains elusive because surface science techniques can only probe up to ~2 nm. Therefore, cross-sectional Kelvin probe (KP) measurements and simulation would help to deduce the complete energy diagram within an OSC, which would facilitate our understanding of carrier behavior in the device.

Utilization of the energy transfer across an organic heterostructure is also an important issue for enhancing device performance. As mentioned in Sect. 10.2.2, excitons diffuse to the donor/acceptor interface before recombination. The strategy is to use organic semiconductors that absorb different wavelengths and to transfer excitons to a specific donor/acceptor interface, which would lead to a significant improvement in J_{sc}. Figure 10.19 shows *J*-*V* curves and an energy diagram for 6 T/SubNc/subphthalocyanine (SubPc) OSC [130]. These three materials cover a wide range of the spectral distribution of sunlight. The important point is that

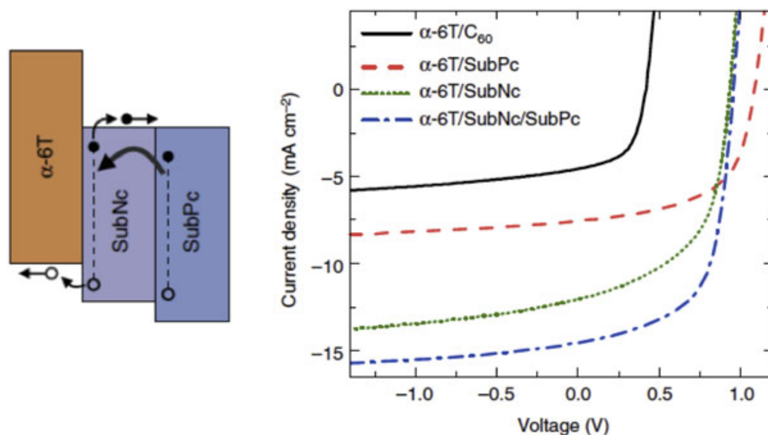

Fig. 10.19 Cascade energy transfer leads to high efficiency for a non-fullerene OSC. (Figures were reproduced with permission of Ref. [130])

because SubNc has a narrower band gap due to an extended π-conjugated ring, excitons generated in SubPc can transfer to SubNc. As a result, excitons generated in both the SubPc and SubNc layers are converted into free holes and electrons at the 6 T/SubNc interface. With this strategy, a PCE of 8.4% was achieved without a sole acceptor, namely, fullerene. This promising result paves a new way to harvest photons in the wide-ranged portion of the solar spectrum by controlling the energy structure.

10.4.3.2 Strategy to Enhance Free-Charge Generation

(a) *Increase of Average Distance of CT State*

As mentioned in Sect. 10.2, electrostatically bound CT states that form at the donor/acceptor interface can be a path to the CS state (free charges). For efficient photocurrent generation, the binding energy of the CT state (E_B) needs to be lowered. One strategy to reduce E_B is to increase the average distance between holes and electrons (r_{ct} in Eq. 10.7) [131–133]. Zhong et al. inserted an insulating wide-band-gap polymer, CYTOP, between P3HT and $PC_{61}BM$ in their planar heterojunction OSC. Insertion of CYTOP increased V_{oc} up to a thickness of 1 nm, while J_{sc} decreased concurrently with increasing thickness because of the reduced electron transfer between P3HT and $PC_{61}BM$ [131]. This decrease in J_{sc} was compensated by adding a dye into the CYTOP layer. This was attributed to more efficient exciton collection by energy transfer and charge separation with the charge cascade.

(b) *Molecular Orientation*

The molecular orientation at the donor/acceptor interface critically impacts the electronic coupling between the two materials and the degree of intermixing and thus the process of photocurrent generation. Rand et al. first suggested for a ZnPc/C_{60} bilayer OSC that the face-on orientation of ZnPc is favorable for photocurrent generation because of a larger electronic coupling between ZnPc and C_{60} [134]. However, it was also found from XPS and X-ray scattering studies that the degree of intermixing between ZnPc and C_{60} increased when ZnPc molecules were in the face-on orientation. This increased intermixing was attributed to higher J_{sc} than for its edge-on-oriented counterpart [135]. However, modifying the molecular orientation should also change the energy levels because the orientation of the molecular quadrupole determines the molecular surface potential [136], as well as the exciton diffusion and carrier mobility. Therefore, the impact of molecular orientation on photovoltaic performance is likely a diverse one.

(c) *Energy Cascade*

The equilibrium model for the CT state proposed by Burke et al. suggests that the energy cascade results in longer free-carrier lifetimes and a drastic increase in charge densities [52]. An energy offset of 100 meV in the HOMO and LUMO leads to tenfold increases in the charge densities in the donor and acceptor phases. Such an energy cascade is believed to exist in the interface between a polymer donor and a fullerene acceptor [124, 137]. The three-phase model assumes the formation of an amorphous mixed region between the aggregated donor and acceptor phases, in which the band gap of the polymer donor is larger than those of the pure phases. Analysis of UPS measurements on a polymer donor/C_{60} interface revealed that the HOMOs of the polymers donor shifted toward higher binding energies upon incremental deposition of C_{60}.

Izawa et al. reported extended carrier lifetimes and a higher charge density [125]. By combining contact film transfer and surface-segregated monolayer techniques, they designed an energy cascade and trap structure across a donor/acceptor interface. A PHJ OSC with an energy cascade could have an increased V_{oc} because of the elongated r_{ct} and a decreased bimolecular recombination because of the energy barrier. However, the lowest LUMO of the SSM layer in the system acts as recombination center for the trap-structured OSC. These results appear to correspond to the prediction made by Burke et al. [52]

(d) *Energy-Level Control of Quadrupole Potential*

Schwarze et al. reported recently that the ionization energy and electron affinity of organic donors such as ZnPc and SubPc can be controlled to 0.5–1.2 eV by mixing them with halogenated counterparts [138]. Concurrently, a ternary OSC with C_{60} as an acceptor shows V_{oc} variation when mixing ratio of the halogenated phthalocyanine varies. Such a new technology will provide optimal guidelines for producing efficient OSCs.

10.5 Summary and Outlook

This chapter has summarized the fundamental aspects of OSCs and given background knowledge on π-conjugated molecules and their interfacial properties. Newly synthesized polymer donors and (non-fullerene) acceptors will further increase the power-conversion efficiency of OSCs. However, economical and environmentally friendly methods of synthesis and device building should be explored simultaneously. Engineering long-ranged quadrupole interactions in organic semiconductors will open new designs for the photoactive layer. Besides, the use of electrostatic-potential models and the simulation of energy diagrams for OSC devices, including the impacts of the top electrode and light illumination, are required if we are to understand the carrier behavior within the device correctly and believably. By merging all these various streams of fundamental knowledge, we hope that optimal device design, based on both know-how and a bottom-up approach, will be possible in the near future.

References

1. E.C.R. Becquerel, Acad. Sci. **9**, 561–567 (1839)
2. D.M. Chapin, C.S. Fuller, G.L. Pearson, A new silicon p-n junction photocell for converting solar radiation into electrical power. J. Appl. Phys. **25**, 676 (2004). https://doi.org/10.1063/1.1721711
3. Solar Spectra: Air Mass Zero. Available at: http://rredc.nrel.gov/solar/spectra/am0/am0_index.html. Accessed 26 Dec 2016
4. L. Meng et al., Organic and solution-processed tandem solar cells with 17.3% efficiency. Science **361**, 1094 (2018). https://doi.org/10.1126/science.aat2612
5. R. Søndergaard, M. Hösel, D. Angmo, T.T. Larsen-Olsen, F.C. Krebs, Roll-to-roll fabrication of polymer solar cells. Mater. Today **15**, 36–49 (2012)
6. A. Pochettino, Acad. Lincei. Rendiconti. **15**, 355 (1906)
7. H. Inokuchi, Photoconductivity of the condensed polynuclear aromatic compounds. Bull. Chem. Soc. Jpn. **27**, 22–27 (1954)
8. H. Inokuchi, The discovery of organic semiconductors. Its light and shadow. Org. Electron. **7**, 62–76 (2006)
9. C.W. Tang, VanSlyke. Appl. Phys. Lett. **51**, 913 (1987)
10. J.H. Burroughes et al., Nature **347**, 539 (1990)
11. G.A. Chamberlain, Organic solar cells: A review. Sol. Cells **8**, 47–83 (1983)
12. Tang, C. W., Marchetti, A. P., Young, R. H. & Company, E. K. Organic photovoltaic elements. US Patent 4125414A. (1978)
13. Tang, C. W. & Company, E. K. Multilayer Organic Photovoltaic Elements. US Patent 4281053A. (1978)
14. C.W. Tang, Two-layer organic photovoltaic cell. Appl. Phys. Lett. **48**, 183–185 (1986)
15. R.F. Salzman et al., The effects of copper phthalocyanine purity on organic solar cell performance. Org. Electron. **6**, 242–246 (2005)
16. J. Wagner et al., Identification of different origins for s-shaped current voltage characteristics in planar heterojunction organic solar cells. J. Appl. Phys. **111**, 054509 (2012)
17. J.H. Bannock et al., The influence of polymer purification on the efficiency of poly(3-hexylthiophene): Fullerene organic solar cells. Sci. Rep. **6**, 23651 (2016)

18. M. Zhang, Irfan, H. Ding, Y. Gao, C.W. Tang, Organic Schottky barrier photovoltaic cells based on MoOx/C60. Appl. Phys. Lett. **96**, 183301 (2010)
19. F. Jin et al., Interface engineering of organic Schottky barrier solar cells and its application in enhancing performances of planar heterojunction solar cells. Sci. Rep. **6**, 26262 (2016)
20. C. Guo et al., Conjugated block copolymer photovoltaics with near 3% efficiency through microphase separation. Nano Lett. **13**, 2957–2963 (2013)
21. C. Grieco et al., Molecular rectification in conjugated block copolymer photovoltaics. J. Phys. Chem. C **120**, 6978–6988 (2016)
22. Y. Lin, X. Zhan, Non-fullerene acceptors for organic photovoltaics: An emerging horizon. Mater. Horiz. **1**, 470 (2014)
23. C.B. Nielsen, S. Holliday, H.-Y. Chen, S.J. Cryer, I. McCulloch, Non-fullerene Electron acceptors for use in organic solar cells. Acc. Chem. Res. **48**, 2803–2812 (2015)
24. C. Zhan, J. Yao, More than conformational "Twisting" or "Coplanarity": Molecular strategies for designing high-efficiency nonfullerene organic solar cells. Chem. Mater. **28**, 1948–1964 (2016)
25. G. Yu, J. Gao, J.C. Hummelen, F. Wudl, A.J. Heeger, Nature **270**, 1789 (1995)
26. J.M. Halls et al., Nature **376**, 498 (1995)
27. W. Zhao et al., Fullerene-free polymer solar cells with over 11% efficiency and excellent thermal stability. Adv. Mater. **28**, 4734–4739 (2016)
28. H.-H. Liao, L.-M. Chen, Z. Xu, G. Li, Y. Yang, Highly efficient inverted polymer solar cell by low temperature annealing of Cs_2CO_3 interlayer. Appl. Phys. Lett. **92**, 173303 (2008)
29. Y. Zhou et al., A universal method to produce low-work function electrodes for organic electronics. Science **336**, 327–332 (2012)
30. A. Orimo et al., Surface segregation at the aluminum interface of poly(3-hexylthiophene)/fullerene solar cells. Appl. Phys. Lett. **96**, 043305 (2010)
31. M.D. Clark, M.L. Jespersen, R.J. Patel, B.J. Leever, Predicting vertical phase segregation in polymer-fullerene bulk heterojunction solar cells by free energy analysis. ACS Appl. Mater. Interfaces **5**, 4799–4807 (2013)
32. J.-H. Huang et al., Fabrication of multilayer organic solar cells through a stamping technique. J. Mater. Chem. **19**, 4077 (2009)
33. B. Kippelen, J.-L. Brédas, Organic photovoltaics. Energy Environ. Sci. **2**, 251 (2009)
34. K. Nakano, K. Tajima, Organic planar heterojunctions: From models for interfaces in bulk heterojunctions to high-performance solar cells. Adv. Mater. **29**, 1603269 (2017)
35. R.R. Lunt, N.C. Giebink, A.A. Belak, J.B. Benziger, S.R. Forrest, Exciton diffusion lengths of organic semiconductor thin films measured by spectrally resolved photoluminescence quenching. J. Appl. Phys. **105**, 053711 (2009)
36. Y. Tamai, H. Ohkita, H. Benten, S. Ito, Exciton diffusion in conjugated polymers: From fundamental understanding to improvement in photovoltaic conversion efficiency. J. Phys. Chem. Lett. **6**, 3417–3428 (2015)
37. H. Najafov, B. Lee, Q. Zhou, L.C. Feldman, V. Podzorov, Observation of long-range exciton diffusion in highly ordered organic semiconductors. Nat. Mater. **9**, 938–943 (2010)
38. G. Grancini et al., Hot exciton dissociation in polymer solar cells. Nat. Mater. **12**, 29–33 (2012)
39. A.E. Jailaubekov et al., Hot charge-transfer excitons set the time limit for charge separation at donor/acceptor interfaces in organic photovoltaics. Nat. Mater. **12**, 66–73 (2012)
40. K. Vandewal et al., Efficient charge generation by relaxed charge-transfer states at organic interfaces. Nat. Mater. **13**, 63–68 (2013)
41. T.M. Clarke, J.R. Durrant, Charge photogeneration in organic solar cells. Chem. Rev. **110**, 6736–6767 (2010)
42. M.B. Smith, J. Michl, Singlet fission. Chem. Rev. **110**, 6891–6936 (2010)
43. J. Ma, K. Hashimoto, T. Koganezawa, K. Tajima, End-on orientation of semiconducting polymers in thin films induced by surface segregation of fluoroalkyl chains. J. Am. Chem. Soc. **135**, 9644–9647 (2013)

44. V.D. Mihailetchi, P.W.M. Blom, J.C. Hummelen, M.T. Rispens, Cathode dependence of the open-circuit voltage of polymer: Fullerene bulk heterojunction solar cells. J. Appl. Phys. **94**, 6849–6854 (2003)
45. B.P. Rand, D.P. Burk, S.R. Forrest, Offset energies at organic semiconductor heterojunctions and their influence on the open-circuit voltage of thin-film solar cells. Phys. Rev. B **75**, 115327 (2007)
46. C. Uhrich et al., Origin of open circuit voltage in planar and bulk heterojunction organic thin-film photovoltaics depending on doped transport layers. J. Appl. Phys. **104**, 043107 (2008)
47. W.J. Potscavage, A. Sharma, B. Kippelen, Critical interfaces in organic solar cells and their influence on the open-circuit voltage. Acc. Chem. Res. **42**, 1758–1767 (2009)
48. Wiley: Physics of Semiconductor Devices, 3rd Edition – Simon M. Sze, Kwok K. Ng. Available at: http://www.wiley.com/WileyCDA/WileyTitle/productCd-0471143235.html. Accessed 24 Jan 2017
49. H. Yoshida, Low-energy inverse photoemission study on the Electron affinities of fullerene derivatives for organic photovoltaic cells. J. Phys. Chem. C **118**, 24377–24382 (2014)
50. A. Wilke et al., Correlation between interface energetics and open circuit voltage in organic photovoltaic cells. Appl. Phys. Lett. **101**, 233301 (2012)
51. K. Vandewal, K. Tvingstedt, A. Gadisa, O. Inganäs, J.V. Manca, Relating the open-circuit voltage to interface molecular properties of donor: Acceptor bulk heterojunction solar cells. Phys. Rev. B **81**, 125204 (2010)
52. T.M. Burke, S. Sweetnam, K. Vandewal, M.D. McGehee, Beyond Langevin recombination: How equilibrium between free carriers and charge transfer states determines the open-circuit voltage of organic solar cells. Adv. Energy Mater. **5**, 1500123 (2015)
53. W. Tress et al., Imbalanced mobilities causing S-shaped IV curves in planar heterojunction organic solar cells. Appl. Phys. Lett. **98**, 063301 (2011)
54. J. Wagner et al., High fill factor and open circuit voltage in organic photovoltaic cells with diindenoperylene as donor material. Adv. Funct. Mater. **20**, 4295–4303 (2010)
55. M.M. Wienk et al., Efficient methano[70]fullerene/MDMO-PPV bulk heterojunction photovoltaic cells. Angew. Chem. Int. Ed. **42**, 3371–3375 (2003)
56. J.Y. Kim et al., Efficient tandem polymer solar cells fabricated by all-solution processing. Science **317**, 222–225 (2007)
57. S.E. Shaheen et al., 2.5% efficient organic plastic solar cells. Appl. Phys. Lett. **78**, 841–843 (2001)
58. S.H. Park et al., Bulk heterojunction solar cells with internal quantum efficiency approaching 100%. Nat. Photonics **3**, 297–302 (2009)
59. Z. He et al., Enhanced power-conversion efficiency in polymer solar cells using an inverted device structure. Nat. Photonics **6**, 593–597 (2012)
60. L. Dou et al., Tandem polymer solar cells featuring a spectrally matched low-bandgap polymer. Nat. Photonics **6**, 180–185 (2012)
61. X. Li et al., Dual plasmonic nanostructures for high performance inverted organic solar cells. Adv. Mater. **24**, 3046–3052 (2012)
62. K. Akaike et al., Ultraviolet photoelectron spectroscopy and inverse photoemission spectroscopy of [6,6]-phenyl-C_{61}-butyric acid methyl ester in gas and solid phases. J. Appl. Phys. **104**, 023710 (2008)
63. E.L. Ratcliff et al., Energy level alignment in PCDTBT:PC70BM solar cells: Solution processed NiOx for improved hole collection and efficiency. Org. Electron. **13**, 744–749 (2012)
64. L. Mattias Andersson, H. Tanaka, Empirical evidence for identical band gaps in substituted C_{60} and C_{70} based fullerenes. Appl. Phys. Lett. **104**, 043304 (2014)
65. R. Nakanishi, A. Nogimura, R. Eguchi, K. Kanai, Electronic structure of fullerene derivatives in organic photovoltaics. Org. Electron. **15**, 2912–2921 (2014)
66. K. Akaike, K. Kanai, Y. Ouchi, K. Seki, Side chain effect on electronic structure of spin-coated films of [6,6]-phenyl-C61-butyric acid methyl ester and its bis-adduct. Chem. Phys. **415**, 31–35 (2013)

67. C.-W. Chu, V. Shrotriya, G. Li, Y. Yang, Tuning acceptor energy level for efficient charge collection in copper-phthalocyanine-based organic solar cells. Appl. Phys. Lett. **88**, 153504 (2006)
68. M. Lenes et al., Fullerene bisadducts for enhanced open-circuit voltages and efficiencies in polymer solar cells. Adv. Mater. **20**, 2116–2119 (2008)
69. H. Sirringhaus, Integrated optoelectronic devices based on conjugated polymers. Science **280**, 1741–1744 (1998)
70. Z. Bao, A. Dodabalapur, A.J. Lovinger, Soluble and processable regioregular poly(3-hexylthiophene) for thin film field-effect transistor applications with high mobility. Appl. Phys. Lett. **69**, 4108–4110 (1996)
71. F.-C. Chen, H.-C. Tseng, C.-J. Ko, Solvent mixtures for improving device efficiency of polymer photovoltaic devices. Appl. Phys. Lett. **92**, 103316 (2008)
72. M.D. Irwin, D.B. Buchholz, A.W. Hains, R.P.H. Chang, T.J. Marks, p-Type semiconducting nickel oxide as an efficiency-enhancing anode interfacial layer in polymer bulk-heterojunction solar cells. Proc. Natl. Acad. Sci. **105**, 2783–2787 (2008)
73. T.-A. Chen, X. Wu, R.D. Rieke, Regiocontrolled synthesis of poly(3-alkylthiophenes) mediated by rieke zinc: Their characterization and solid-state properties. J. Am. Chem. Soc. **117**, 233–244 (1995)
74. T. Thurn-Albrecht, R. Thomann, T. Heinzel, S. Hugger, Semicrystalline morphology in thin films of poly(3-hexylthiophene). Colloid Polym. Sci. **282**, 932–938 (2004)
75. C. Yang, F.P. Orfino, S. Holdcroft, A phenomenological model for predicting thermochromism of regioregular and nonregioregular poly(3-alkylthiophenes). Macromolecules **29**, 6510–6517 (1996)
76. A. Tsumura, H. Fuchigami, H. Koezuka, Field-effect transistor with a conducting polymer film. Synth. Met. **41**, 1181–1184 (1991)
77. A. Zen et al., Effect of molecular weight and annealing of poly(3-hexylthiophene)s on the performance of organic field-effect transistors. Adv. Funct. Mater. **14**, 757–764 (2004)
78. R.J. Kline, M.D. McGehee, E.N. Kadnikova, J. Liu, J.M.J. Fréchet, Controlling the field-effect mobility of regioregular polythiophene by changing the molecular weight. Adv. Mater. **15**, 1519–1522 (2003)
79. K. Kanai et al., Effect of annealing on the electronic structure of poly(3-hexylthiophene) thin film. Phys. Chem. Chem. Phys. **12**, 273–282 (2010)
80. H. Wang et al., Band-bending in organic semiconductors: The role of alkali-halide interlayers. Adv. Mater. **26**, 925–930 (2014)
81. R.C. Shallcross et al., Quantifying the extent of contact doping at the Interface between high work function electrical contacts and poly(3-hexylthiophene) (P3HT). J. Phys. Chem. Lett. **6**, 1303–1309 (2015)
82. J. Niederhausen et al., Doping of C 60 (sub)monolayers by fermi-level pinning induced electron transfer. Phys. Rev. B **86**, 081411 (2012)
83. P. Amsalem et al., Role of charge transfer, dipole-dipole interactions, and electrostatics in fermi-level pinning at a molecular heterojunction on a metal surface. Phys. Rev. B **87**, 035440 (2013)
84. M. Oehzelt, N. Koch, G. Heimel, Organic semiconductor density of states controls the energy level alignment at electrode interfaces. Nat. Commun. **5**, 4174 (2014)
85. C. Tengstedt et al., Fermi-level pinning at conjugated polymer interfaces. Appl. Phys. Lett. **88**, 053502 (2006)
86. M.T. Greiner et al., Universal energy-level alignment of molecules on metal oxides. Nat. Mater. **11**, 76–81 (2011)
87. G. Ligorio, M.V. Nardi, C. Christodoulou, N. Koch, Organic semiconductor/gold interface interactions: From Physisorption on planar surfaces to chemical reactions with metal nanoparticles. ChemPhysChem **16**, 2602–2608 (2015)
88. J. Hwang, A. Wan, A. Kahn, Energetics of metal-organic interfaces: New experiments and assessment of the field. Mater. Sci. Eng. R. Rep. **64**, 1–31 (2009)

89. L.-M. Chen, Z. Xu, Z. Hong, Y. Yang, Interface investigation and engineering – achieving high performance polymer photovoltaic devices. J. Mater. Chem. **20**, 2575 (2010)
90. R. Steim, F.R. Kogler, C.J. Brabec, Interface materials for organic solar cells. J. Mater. Chem. **20**, 2499 (2010)
91. G. Greczynski et al., Photoelectron spectroscopy of thin films of PEDOT-PSS conjugated polymer blend: A mini-review and some new results. J. Electron Spectrosc. Relat. Phenom. **121**, 1–17 (2001)
92. N. Koch, A. Vollmer, A. Elschner, Influence of water on the work function of conducting poly(3,4-ethylenedioxythiophene)/poly(styrenesulfonate). Appl. Phys. Lett. **90**, 043512 (2007)
93. T. Yamanari, T. Taima, J. Sakai, J. Tsukamoto, Y. Yoshida, Effect of buffer layers on stability of polymer-based organic solar cells. Jpn. J. Appl. Phys. **49**, 01AC02 (2010)
94. K. Kanai et al., Electronic structure of anode interface with molybdenum oxide buffer layer. Org. Electron. **11**, 188–194 (2010)
95. K.M. Knesting et al., ITO Interface modifiers can improve V_{OC} in polymer solar cells and suppress surface recombination. J. Phys. Chem. Lett. **4**, 4038–4044 (2013)
96. J. Wang et al., Effects of contact-induced doping on the behaviors of organic photovoltaic devices. Nano Lett. **15**, 7627–7632 (2015)
97. Z.R. Hong, C.J. Liang, X.Y. Sun, X.T. Zeng, Characterization of organic photovoltaic devices with indium-tin-oxide anode treated by plasma in various gases. J. Appl. Phys. **100**, 093711 (2006)
98. R.M. Cook et al., An electrode design rule for organic photovoltaics elucidated using molecular Nanolayers. Adv. Energy Mater. **1**, 440–447 (2011)
99. M. Vogel, S. Doka, C. Breyer, M.C. Lux-Steiner, K. Fostiropoulos, On the function of a bathocuproine buffer layer in organic photovoltaic cells. Appl. Phys. Lett. **89**, 163501 (2006)
100. H. Gommans et al., On the role of bathocuproine in organic photovoltaic cells. Adv. Funct. Mater. **18**, 3686–3691 (2008)
101. S. Toyoshima et al., Electronic structure of bathocuproine on metal studied by ultraviolet photoemission spectroscopy. Jpn. J. Appl. Phys. **46**, 2692 (2007)
102. S. Toyoshima et al., Ultraviolet photoemission study of interaction between bathocuproine and calcium. Jpn. J. Appl. Phys. **47**, 1397 (2008)
103. K. Akaike, Y. Kubozono, Correlation between energy level alignment and device performance in planar heterojunction organic photovoltaics. Org. Electron. **14**, 1–7 (2013)
104. Y. Nakayama et al., Complete demonstration of the valence electronic structure inside a practical organic solar cell probed by low energy photoemission. Adv. Energy Mater. **4**, 1301354 (2014)
105. S. Wang, T. Sakurai, R. Kuroda, K. Akimoto, Energy band bending induced charge accumulation at fullerene/bathocuproine heterojunction interface. Appl. Phys. Lett. **100**, 243301 (2012)
106. J. Huang, Z. Xu, Y. Yang, Low-work-function surface formed by solution-processed and thermally deposited nanoscale layers of cesium carbonate. Adv. Funct. Mater. **17**, 1966–1973 (2007)
107. S. Fabiano et al., Poly(ethylene imine) impurities induce n-doping reaction in organic (semi)conductors. Adv. Mater. **26**, 6000–6006 (2014)
108. Y. Nakayama et al., Origins of improved hole-injection efficiency by the deposition of MoO_3 on the polymeric semiconductor poly(dioctylfluorene- *alt* -benzothiadiazole). Adv. Funct. Mater. **19**, 3746–3752 (2009)
109. R.T. White, E.S. Thibau, Z.-H. Lu, Interface structure of MoO3 on organic semiconductors. Sci. Rep. **6**, 21109 (2016)
110. C.G. Tang et al., Doped polymer semiconductors with ultrahigh and ultralow work functions for ohmic contacts. Nature **539**, 536–540 (2016)
111. P.J. Hotchkiss et al., The modification of indium tin oxide with phosphonic acids: Mechanism of binding, tuning of surface properties, and potential for use in organic electronic applications. Acc. Chem. Res. **45**, 337–346 (2012)

112. H. Zhang et al., Overcoming electrode-induced losses in organic solar cells by tailoring a quasi-Ohmic contact to fullerenes via solution-processed alkali hydroxide layers. Adv. Energy Mater. **6**, 1502195 (2016)
113. S. Braun, W.R. Salaneck, M. Fahlman, Energy-level alignment at organic/metal and organic/organic interfaces. Adv. Mater. **21**, 1450–1472 (2009)
114. N.R. Armstrong et al., Organic/organic′ heterojunctions: Organic light emitting diodes and organic photovoltaic devices. Macromol. Rapid Commun. **30**, 717–731 (2009)
115. M. Oehzelt, K. Akaike, N. Koch, G. Heimel, Energy-level alignment at organic heterointerfaces. Sci. Adv. **1**, e1501127–e1501127 (2015)
116. C. Poelking et al., Impact of mesoscale order on open-circuit voltage in organic solar cells. Nat. Mater. **14**, 434–439 (2014)
117. C. Poelking, D. Andrienko, Design rules for organic donor-acceptor heterojunctions: Pathway for charge splitting and detrapping. J. Am. Chem. Soc. **137**, 6320–6326 (2015)
118. Y. Wakayama, D.G. de Oteyza, J.M. Garcia-Lastra, D.J. Mowbray, Solid-state reactions in binary molecular assemblies of F_{16} CuPc and Pentacene. ACS Nano **5**, 581–589 (2011)
119. A. Opitz et al., Organic heterojunctions: Contact-induced molecular reorientation, interface states, and charge re-distribution. Sci. Rep. **6**, 21291 (2016)
120. K. Akaike, N. Koch, G. Heimel, M. Oehzelt, The impact of disorder on the energy level alignment at molecular donor-acceptor interfaces. Adv. Mater. Interfaces **2**, 1500232 (2015)
121. Y.C. Zhou, Z.T. Liu, J.X. Tang, C.S. Lee, S.T. Lee, Substrate dependence of energy level alignment at the donor-acceptor interface in organic photovoltaic devices. J. Electron Spectrosc. Relat. Phenom. **174**, 35–39 (2009)
122. A. Wilke, T. Mizokuro, R.-P. Blum, J.P. Rabe, N. Koch, Electronic properties of Cu-Phthalocyanine/fullerene planar and bulk heterojunctions on PEDOT:PSS. IEEE J. Sel. Top. Quantum Electron. **16**, 1732–1737 (2010)
123. H.X. Wei et al., Electronic structures of planar and mixed C70/CuPc heterojunctions in organic photovoltaic devices. Org. Electron. **12**, 1422–1428 (2011)
124. S. Sweetnam et al., Characterization of the polymer energy landscape in polymer: Fullerene bulk heterojunctions with pure and mixed phases. J. Am. Chem. Soc. **136**, 14078–14088 (2014)
125. S. Izawa, K. Nakano, K. Suzuki, K. Hashimoto, K. Tajima, Dominant effects of first monolayer energetics at donor/acceptor interfaces on organic photovoltaics. Adv. Mater. **27**, 3025–3031 (2015)
126. T. Breuer, A. Karthäuser, G. Witte, Effects of molecular orientation in acceptor-donor interfaces between pentacene and C_{60} and diels-alder adduct formation at the molecular Interface. Adv. Mater. Interfaces **3**, 1500452 (2016)
127. J. Frisch et al., Full electronic structure across a polymer heterojunction solar cell. J. Mater. Chem. **22**, 4418 (2012)
128. A. Opitz, J. Frisch, R. Schlesinger, A. Wilke, N. Koch, Energy level alignment at interfaces in organic photovoltaic devices. J. Electron Spectrosc. Relat. Phenom. **190**, 12–24 (2013)
129. R.J. Davis et al., Determination of energy level alignment at interfaces of hybrid and organic solar cells under ambient environment. J. Mater. Chem. **21**, 1721–1729 (2011)
130. K. Cnops et al., 8.4% efficient fullerene-free organic solar cells exploiting long-range exciton energy transfer. Nat. Commun. **5**, 3406 (2014)
131. Y. Zhong, A. Tada, S. Izawa, K. Hashimoto, K. Tajima, Enhancement of V_{OC} without loss of J_{SC} in organic solar cells by modification of donor/acceptor interfaces. Adv. Energy Mater. **4**, 1301332 (2014)
132. D.M. Stevens, J.C. Speros, M.A. Hillmyer, C.D. Frisbie, Relationship between diode saturation current and open circuit voltage in poly(3-alkylthiophene) solar cells as a function of device architecture, processing conditions, and alkyl side chain length. J. Phys. Chem. C **115**, 20806–20816 (2011)
133. I.H. Campbell, B.K. Crone, Improving an organic photodiode by incorporating a tunnel barrier between the donor and acceptor layers. Appl. Phys. Lett. **101**, 023301 (2012)

134. B.P. Rand et al., The impact of molecular orientation on the photovoltaic properties of a Phthalocyanine/fullerene heterojunction. Adv. Funct. Mater. **22**, 2987–2995 (2012)
135. G.O. Ngongang Ndjawa et al., Impact of molecular orientation and spontaneous interfacial mixing on the performance of organic solar cells. Chem. Mater. **27**, 5597–5604 (2015)
136. S. Duhm et al., Orientation-dependent ionization energies and interface dipoles in ordered molecular assemblies. Nat. Mater. **7**, 326–332 (2008)
137. F.C. Jamieson et al., Fullerenecrystallisation as a key driver of charge separation in polymer/fullerene bulk heterojunction solar cells. Chem. Sci. **3**, 485–492 (2012)
138. M. Schwarze et al., Band structure engineering in organic semiconductors. Science **352**, 1446–1449 (2016)